CLUSTERING IN THE UNIVERSE

Structuration de l'Univers

Cover illustration :

The image shows an intermediate stage of a gravitational N-body simulation using 16.8 million particles with standard Cold Dark Matter initial conditions. The region shown is 100 Mpc across, and the color of each pixel represents the logarithm of the projected particle density along the line of sight through the periodic computational volume. This treecode N-body simulation performed over 10^{15} floating point operations (1 petaflop), which took about 80 hours on the 512 node Intel Paragon at Caltech.

Credits :
Michael S. Warren, Wojciech H. Zurek, Benjamin Bromley (Los Alamos National Laboratory) John Salmon (Caltech)

XXXth Rencontre de Moriond
Les Arcs, Savoie, France - March 11-18, 1995

CLUSTERING IN THE UNIVERSE
Series : Moriond Astrophysics Meetings

ISBN 2-86332-189-7
© Copyright 1995 by Editions Frontières

All rights reserved.
This book, or parts thereof, may not be reproduced in any form or by any means, electronic or mechanical, including photocopying, recording or any information storage retrivial system now known or to be invented, without written permission from the Publisher.

EDITIONS FRONTIERES
B.P. 33
91192 Gif-sur-Yvette Cedex - France

Printed in Singapore

Proceedings of the XXXth RENCONTRES DE MORIOND
Series : Moriond Astrophysics Meetings
Les Arcs, Savoie, France March 11-18, 1995

CLUSTERING IN THE UNIVERSE

edited by

S. MAUROGORDATO
C. BALKOWSKI
C. TAO
J. TRÂN THANH VÂN

C
CERN BIBLIOTHÈQUE
Les Arcs
1995

EDITIONS
FRONTIERES

The Astrophysics Session of the XXXth Rencontre de Moriond

International Advisory Committee

J. Audouze	*(Paris)*
E. Bertschinger	*(Cambridge, USA)*
C. Cesarsky	*(Saclay)*
G. Chincarini	*(Milan)*
L. da Costa	*(Paris)*
J. Cronin	*(Chicago)*
M. Davier	*(Orsay)*
M. Davis	*(Berkeley)*
A. Dekel	*(Jerusalem)*
R. Ellis	*(Cambridge, UK)*
G. Efstathiou	*(Oxford)*
G. Fontaine	*(Paris)*
M. Geller	*(Cambridge, USA)*
G. Hasinger	*(München)*
J. Huchra	*(Cambridge, USA)*
J. Ostriker	*(Princeton)*
J. Peebles	*(Princeton)*
R. Pellat	*(Paris)*
B. Rocca-Volmerange	*(Paris)*
B. Sadoulet	*(Berkeley)*
R. Schaeffer	*(Saclay)*
S. Shandarin	*(Lawrence)*
J. Silk	*(Berkeley)*
M. Spiro	*(Saclay)*
P. Vettolani	*(Bologne)*
L. Vigroux	*(Saclay)*
A. Yahil	*(New York)*
S. White	*(München)*

Program Committee

C. Balkowski	*(Meudon)*
A. Blanchard	*(Strasbourg)*
S. Maurogordato	*(Meudon)*
M. Moniez	*(Orsay)*
C. Tao	*(Paris)*
J. Trân Thanh Vân	*(Orsay)*

Contents

Avant-Propos ..... **xiii**

Foreword ..... **xv**

Session 1: Large Scale Structure from redshift surveys

Studying Galaxy and Structure Formation with Complete Redshift Surveys.
L. Nicolaci da Costa *3*

The Power Spectrum of galaxy density fluctuations: Current results and improved techniques.
M. S. Vogeley *13*

Biasing in the Southern Sky Redshift Survey.
C. Benoist, S. Maurogordato, L. N. da Costa, A. Cappi, R. Schaeffer *23*

Constraining Ω and bias from Stromlo-APM survey.
J. Loveday *29*

The Power Spectrum of Galaxy Clustering in the Las Campanas Redshift Survey.
H. Lin, R. P. Kirshner, S. A. Shectman, S. D. Landy, A. Oemler, D. L. Tucker, and P. L. Schechter *35*

Large-scale color-segregation of galaxies in the Las Campanas Redshift Survey.
D. Tucker, A. A. Oemler, Jr. , R. P. Kirhner, H. Lin, S. A. Shechtman, S. D. Landy, and P. L. Schechter *39*

First results from the ESO Slice Project (ESP).
E. Zucca, G. Vettolani, A. Cappi, R. Merighi, M. Mignoli, G. Stirpe, G. Zamorani, H. MacGillivray, C. Collins, C. Balkowski, J. M. Alimi, V. Cayatte, P. Felenbok, S. Maurogordato, D. Proust, G. Chincarini, L. Guzzo, D. Maccagni, R. Scaramella, A. Blanchard, M. Ramella *43*

Estimating power spectra from 3D galaxy surveys.
M. Tegmark *49*

Topology of the galaxy distribution.
S. Shandarin *55*

Radio-Sources and Large-Scale Structure.
J.Wall, C. R. Benn *63*

Large-Scale Structures in Three Dimensions
A.P. Fairall and W. R. Paverd *67*

Large-scale structures uncovered behind the Southern Milky Way
R. C. Kraan-Korteweg, P. A. Woudt, A. P. Fairall, V. Cayatte, C. Balkowski, P. A. Henning *71*

Search for emission line galaxies towards nearby voids
C. C. Popescu, U. Hopp, H. Elsasser, H. Hagen *77*

Do dwarf and LSB galaxies trace the same density field as bright galaxies ?
R. Dominguez-Tenreiro, J. M. Alimi, A. Serna, T. X. Thuan *81*

Session 2 : Peculiar motions and the density field

Measuring Ω independent of galaxy biasing.
A. Dekel *89*

Ω and biasing from optical galaxies versus POTENT mass.
M. J. Hudson, A. Dekel, S. Courteau, S. M. Faber and J. A. Willick *105*

Mapping the Peculiar Velocity Field of galaxies.
L. da Costa, W. Freudling, R. Giovanelli, M. Haynes, J. Salzer, G. Wegner *111*

The information content of redshift and velocity surveys.
A. Yahil *117*

Dynamical fields and Ω simultaneously from redshift surveys and peculiar velocity surveys.
A. Nusser and A. Dekel *127*

Wiener Reconstruction, SVD and 'Optimal' Functional Bases: Application for Redshift galaxy catalogs.
S. Zaroubi *135*

Session 3 : Statistics and Dynamics

Redshift distortions and Ω in IRAS Surveys.
A. J. S. Hamilton *143*

What does the galaxy pair-wise velocity probe ?
A. Blanchard, J. G. Bartlett *157*

Aspects of Scaling in gravitational clustering.
B. Jain *161*

Clustering statistics and dynamics.
R. Juszkiewicz and F. Bouchet *167*

Properties of the density PDF-s in the quasi-linear regime.
F. Bernardeau *177*

Session 4: Models of formation and numerical simulations

Improved ways to compare simulations to data.
J. R. Primack *185*

On cluster cores and power spectra.
B. C. Bromley, T. G. Brainerd, M. S. Warren,
W. H. Zurek , P. J. Quinn *195*

Large scale structure in N-body simulations.
A. Doroskhevich *205*

Numerical simulations of galaxy formation: Effect of Supernovae feedbacks.
G. Yepes, R. Kates, A. Khokhlov, A. Klypin *209*

Simulating Large-Scale structure formation for BSI power spectra.
V. Müller *213*

Testing DM models against the cluster distribution.
S. Borgani, M. Plionis, L. Moscardini, P. Coles *217*

Observational constraints on blue primordial spectra.
L. Moscardini, S. Colafrancesco, G de Gasperis, F. Lucchin,
S. Matarrese, S. Mei, S. Mollerach, N. Vittorio *221*

The structure and primordial black holes formation in the inflationary models with peculiarities in inflaton potential.
P. Ivanov *225*

Session 5 : Galaxy clusters

Optical/Near-IR Surveys of distant clusters of galaxies.
M. Postman *231*

Is the density distribution of clusters non-gaussian ?
T. Kolatt *241*

The APM cluster survey: Cluster detection and Large-Scale Structure.
G. B. Dalton *249*

The Power Spectrum of APM clusters
H. Tadros *253*

Large scale peculiar velocities: effects from superclusters.
R. Scaramella *257*

A Redshift Survey of a prominent Southern Supercluster Candidate.
K. Slinglend, D. Batuski, C. Balkowski, P. Felenbok, S. Maurogordato, R. Olowin *261*

A 140 Mpc oscillation of the Abell cluster correlation function.
V. Saar *265*

A comparison between bright galaxy and rich cluster correlations.
A. Cappi, C. Benoist, L. N. da Costa, S. Maurogordato *269*

Estimating $\beta \equiv \Omega_0^{0.6}/b$ from the Local Group and cluster peculiar velocities.
M. Plionis *273*

Reconstructing cluster peculiar velocities within 20000 km/s.
E. Branchini and M. Plionis *277*

The ESO Nearby Abell Clusters Survey (ENACS): velocity dispersion distribution.
A. Mazure, P. Katgert, R. den Hartog, A. Biviano, P. Dubath, E. Escalera, P. Focardi, D. Gerbal, G. Giuricin, B. Jones, O. Le Fevre, M. Moles, J. Perea, G. Rhee *281*

Surveys of galaxy clusters detected by ROSAT.
H. Böhringer *285*

The set of non-monotonous correlation functions for very rich Abell clusters: history, modern results and projects.
T. Fetisova *293*

Cluster evolution and gravitational instability theories.
S. Colafrancesco *297*

Session 6 : Common session with particle physics

A review of gravitational microlensing experiments.
C. Magneville *305*

Cold + hot dark matter cosmology.
J. Primack, J. Holtzmann, and A. Klypin *313*

Solar neutrino problem, 1995.
V. Berezinsky *323*

The Russian-American gallium solar neutrino experiment.
S. Elliott et al. *339*

Recent results from GALLEX
C. Tao *345*

Discovery physics at the large hadron collider.
N. Ellis *351*

Solar neutrinos and lepton mixing.
A. Smirnov *361*

Session 7: The Cosmic Microwave Background

Recent results on the Cosmic Microwave Background.
J. Silk *373*

Anisotropies of the microwave background radiation and the large-scale structure of the Universe
G. Efstathiou *381*

Session 8: The Deep Universe

Evolution of galaxies and clustering from the Canada-France Redshift Survey.
O. Le Fèvre, S. J. Lilly, D. Crampton, F. Hammer, D. Hudon, D. Schade, L. Tresse *399*

The angular correlation function of faint field galaxies.
A. Campos, G. Yepes, M. Carlson, A. A. Klypin, M. Moles, and H. Joergensen *403*

Morphological number-counts from ultradeep HST images.
S. P. Driver, R. A. Windhorst *407*

Evolution of the galaxy pair rate.
L. Infante, R. Carlberg, C. J. Pritchet *417*

Clustering properties of the Lyα clouds.
S. Cristiani, S. d'Odorico, V. d'Odorico, A. Fontana, E. Giallongo, and S. Savaglio *421*

Lyman alpha forest clustering using cell counts statistics.
F. Bouchet and A. Meiksin *425*

Quasars and Large Scale Structure of the Universe.
V. Lukash *429*

The clustering of quasars.
P. Andreani, S. Cristiani, F. La Franca *431*

Gravitational lensing of quasar 0957+561 and the determination of H_0.
G. Rhee, G. Bernstein, T. Tyson, P. Fischer *439*

The environments of $z < 0.3$ QSOs
B. Boyle, R. J. Smith, S. J. Maddox *443*

Large groups of quasars
M. Graham, R. G. Clowes, L. E. Campusano *447*

Session 9 : Dark matter

The Nature of Dark Matter: the case for nonbaryonic dark matter.
B. Sadoulet *453*

Can dark matter be fully baryonic ?
J.M. Alimi and A. Serna *465*

Searches for non baryonic Dark Matter: the case for WIMPs
R. Bernabei *471*

Searching for WIMPS: The CfPA Cryogenic Dark Matter Experiment.
D. S. Akerib for the CDMS Collaboration *483*

Axions: Dark Matter and the Strong CP Problem.
L. J. Rosenberg *487*

The Edelweiss Experiment: a status report.
D. Yvon for the Edelweiss collaboration *503*

Giant Luminous Arcs
F. Hammer, I. Gioia, O Le Fèvre, G. Luppino *507*

Session 10: New windows

Gravitational waves and Cosmology.
T. Damour *515*

Scale Relativity and Structuration of the Universe
L. Nottale *523*

Session 11 : New and Future Projects

Two new radio projects: FORT and SKAI.
W. Van Driel *533*

The COBRAS/SAMBA CMB project.
F. Bouchet, R. Gispert, and J.L. Puget *537*

Survey Spectrographs for Cosmology at the ESO-VLT.
O. Le Fèvre, P. Vettolani *545*

Poster Papers

Structures of galaxy clusters with central dominant galaxies.
F. W. Baier, H. Wipper, H. T. MacGillivray *551*

The significance of orientations of galaxy clusters.
F. W. Baier, H. Wipper *553*

Analysis of the 1.936 Jy IRAS survey through the scaling formalism.
R. Dominguez-Tenreiro, M. A. Gomez-Flechoso, G. Yepes *555*

Tidal evolution of disc galaxies in rich clusters.
M. A. Gomez-Flechoso, R. Dominguez-Tenreiro, J. F. Navarro .. *557*

The structure of compact groups of galaxies.
M. L. Montoya, R. Dominguez-Tenreiro, G. Gonzales-Casado, G. A. Mamon, E. Salvador-Solé *559*

Dark matter in clusters of galaxies and the neutrino rest mass.
A. Kull, R. A. Treumann, H. Bohringer *561*

Résumés des exposés en français **563**

List of Participants **597**

AVANT-PROPOS

Pendant la semaine du 11 au 18 mars 1995, 112 Astrophysiciens et Physiciens des Particules provenant de 15 pays différents se sont rassemblés dans la station des Arcs en Savoie, avec un objectif ambitieux: faire le point sur les connaissances actuelles sur la "Structuration" de l'Univers. "Structuration" ou "Structure"? Le choix du mot était hardi, mais nous avons choisi "Structuration" pour sa portée dynamique, "Structure" conduisant à un aspect plus figé. L'opportunité d'une conférence sur ce thème devenait de plus en plus pressante de part l'avancée rapide du sujet aussi bien au niveau des observations qu'au niveau des modèles théoriques. En effet, de nombreux grands relevés de décalages vers le rouge et de vitesses particulières arrivaient alors à terme, livrant leurs premiers résultats. D'autre part, face aux difficultés du modèle CDM Standard à expliquer à la fois toutes les données observationnelles (aussi bien la structure à grande échelle, les champs de vitesses, et les fluctuations du rayonnement de fond cosmologique), de nouvelles alternatives ont été développées comme les scénarios à base de matière sombre froide + chaude, ou à base de matière sombre froide mais de basse densité avec une constante cosmologique non nulle, ou entièrement baryonique mais avec un indice de spectre tilté... C'était donc le moment de proposer une confrontation entre les différents groupes d'observateurs et de théoriciens afin de passer au crible les contraintes imposées par les données et la capacité des différents modèles à reproduire les observations.

La tradition des Rencontres de Moriond implique une interaction forte entre Astrophysiciens et Physiciens des Particules. Sur le sujet abordé, le trait d'union s'est fait grâce à Charling Tao, Louis Fayard et Marc Moniez qui ont permis d'ouvrir pendant une journée et demi les "boites noires" contenant les différents candidats à la matière sombre si souvent invoqués dans les scénarios de formation des galaxies.

La conférence s'est orientée ensuite vers la nouvelle génération de projets visant à caractériser la structure de l'Univers à grande échelle. Il est frappant de constater que la masse de données typique qui était de l'ordre de 10^3 en 1980, de 10^4 aujourd'hui, va passer à $10^5 - 10^6$ dans les prochaines années avec 2DF et SLOAN. Ceci implique une révolution aussi bien au niveau de la conception des programmes que du traitement des données. Devant ces nouveaux ordres de grandeur, une réflexion sur les méthodes a été conduite avec les physiciens des particules.

Ces grands relevés, combinés aux progrès effectués dans le domaine des statistiques, vont permettre de quantifier l'information sur la distribution des galaxies à la fois à des échelles encore supérieures et avec une grande précision. D'autre part, les programmes impliquant le rayonnement de fond cosmologique évoluent eux aussi très rapidement, permettant d'espérer pouvoir mesurer prochainement le spectre de puissance du rayonnement jusqu'à des multipôles

de l'ordre de 1000, par l'intermédiaire de missions longue durée en ballons, de l'interférométrie ou dans le cas idéal grâce à un projet spatial ad-hoc comme par exemple COBRAS/SAMBA. On espère donc pouvoir faire le pont dans un futur proche entre les échelles de mesure du rayonnement de fond et celles de la distribution des galaxies, et même pouvoir effectuer un recouvrement avec une bonne précision. Tous ces efforts combinés devraient apporter de précieuses clés sur le spectre de puissance et la relation de biais entre distribution de galaxies et distribution de matière.

Nous tenons à remercier tous les membres du comité scientifique qui nous ont permis de rendre ce défi possible, Jean Audouze, Edmund Bertschinger, Catherine Cesarsky, Guido Chincarini, Luiz da Costa, Jim Cronin, Michel Davier, Marc Davis, Avishai Dekel, Richard Ellis, George Efstathiou, Gérard Fontaine, Margaret Geller, Gunther Hasinger, John Huchra, Jeremy Ostriker, Jim Peebles, René Pellat, Brigitte Rocca-Volmerange, Bernard Sadoulet, Richard Schaeffer, Sergei Shandarin, Joe Silk, Michel Spiro, Paolo Vettolani, Laurent Vigroux, Amos Yahil, Simon White.

Nous remercions la Section 14 du Centre National de la Recherche Scientifique, le Service d'Astrophysique du CEA-CEN Saclay, l'Observatoire de Paris, l'Université Paris 7, et le Centre National d'Etudes Spatiales pour le soutien financier qu'ils ont bien voulu accorder à cette conférence. Nous remercions le Ministère des Affaires Étrangères pour l'obtention de bourses ACCESS ainsi que la fondation SOROS qui nous ont permis d'inviter de nombreux participants d'ex URSS et d'Europe de l'Est. Nous remercions la Communauté Européenne qui, dans le cadre du Programme Capital Humain et Mobilité a permis le financement de nombreux jeunes européens.

Nous avons tenu à préserver l'équilibre observation/théorie de cette conférence au niveau de l'iconographie. Ceci a été possible grâce à L. da Costa, M. Geller, J. Huchra et E. Falco qui nous ont permis d'utiliser la vue panoramique du CfA2/SSRS2 pour l'affiche , et grâce à M. Warren, W. Zurek, B. Bromley and J. Salmon qui nous ont gracieusement produit une visualisation de leurs simulations numériques pour la couverture des comptes rendus. Nous leur exprimons toute notre gratitude. Nous tenons à exprimer notre reconnaissance toute particulière à Luiz Nicolaci da Costa et à Avishai Dekel pour leur aide inestimable tout au long de la préparation de cette conférence.

Le succès et l'animation de cette Rencontre de Moriond doivent beaucoup à la perfection de l'organisation sur place, menée par J. Trân Thanh Vân et son équipe. Nous tenons à remercier tout particulièrement Joëlle Raguideau et Nicole Bachala, Jacqueline Plancy et Nicole Romain, pour leur aide aussi bien à l'organisation qu'à la réalisation des comptes-rendus ainsi qu' Aida Cherkaoui pour son efficacité au niveau du graphisme.

Nous remercions enfin tous les conférenciers et participants d'avoir suivi avec une telle assiduité cette conférence aussi dense.

Sophie Maurogordato Chantal Balkowski Charling Tao

FOREWORD

During the week of the 11th to the 18th of March 1995, 112 Astrophysicists and Particle Physicists coming from more than 15 different countries have converged to Les Arcs, in Savoie, with a quite ambitious scope: review our present knowledge of "Clustering in the Universe". The opportunity of such a conference was becoming more and more urgent as both observational and theoretical aspects of the topic had undergone a substantial burst. In fact, at this particular time, various redshift surveys were recently or imminently completed, and their first results were coming out.

On the other side, facing the difficulties encountered by the standard CDM model to explain altogether the whole set of observational data: large-scale structure, velocity fields, CBR fluctuations,... new alternatives as CHDM , ΛCDM, or baryonic tilted models had been proposed. It was therefore the right time to organize a confrontation of the various observational and theoretical groups to screen the various constraints emerging from the data and the capacity of the different models to reproduce observations.

The tradition in the Moriond meeting implies a strong interaction between Astrophysicists and Particle Physicists. The link has been done thanks to Charling Tao, Louis Fayard and Marc Moniez for two specific days during which the "black boxes" containing the various dark matter candidates so often invoked in galaxy formation models have been intensively opened.

The conference has then focused on new projects aiming to characterize the large-scale structure of the Universe. It is striking to note that the typical data in a redshift survey has grown from $\sim 10^3$ in the 80's to $\sim 10^4$ nowadays, and is expected to reach $\sim 10^5 - 10^6$ in the forthcoming years with programs as 2DF or SLOAN digital survey. This implies a complete revolution both on the program conception and on the data reduction. Interaction with particle physicists about the methodology used for manipulating such large flows of data could once more be very fruitful.

These redshift surveys, combined to recent progress in the statistical analysis, will soon allow to quantify the information in the galaxy distribution both at still larger scales and with a greater precision. On another side, CMBR programs are evolving also very rapidly, and will probably be able to measure the power spectrum of radiation up to multipoles of ~ 1000 thanks to balloons, ground-based interferometry or to a dedicated spatial program as for instance the ESA COBRAS/SAMBA project.

One can therefore hope in the next future to bridge the gap between the scales previously covered by COBE for the CMBR and those where the galaxy clustering is measured, and even to get a domain of scales on which both will be measured with a good precision. All these

combined efforts should bring determinant keys towards the power spectrum of fluctuations and of the biasing relation between matter and galaxies.

We would like to thank all the members of the International Scientific Committee, Jean Audouze, Edmund Bertschinger, Catherine Cesarsky, Guido Chincarini, Luiz da Costa, Jim Cronin, Michel Davier, Marc Davis, Avishai Dekel, Richard Ellis, George Efstathiou, Gérard Fontaine, Margaret Geller, Gunther Hasinger, John Huchra, Jeremy Ostriker, Jim Peebles, René Pellat, Brigitte Rocca-Volmerange, Bernard Sadoulet, Richard Schaeffer, Sergei Shandarin, Joe Silk, Michel Spiro, Paolo Vettolani, Laurent Vigroux, Amos Yahil, Simon White, who helped us a lot in organizing this conference.

We thank all the institutions and firms who helped us financially: the Centre National de la Recherche Scientifique, the Service d'Astrophysique of the Commisariat à l'Energie Atomique - CEN Saclay, the Observatoire de Paris, The Université Paris 7, the Centre National d'Etudes Spatiales, the European Economical Community through the Human Capital and Mobility Program, the Ministère des Affaires Etrangères (ACCESS program), and the SOROS foundation

We have wished to reflect the Observational/Theoretical equilibrium of this meeting on the iconography. This has been possible thanks to L. da Costa, M. Geller, J. Huchra and E. Falco who allowed us to use their panoramic view of the CfA2/SSRS2 for the poster, and to M. Warren, W. Zurek, B. Bromley and J. Salmon who have kindly provided a visualisation of one of their numerical simulations for the cover of these proceedings. We thank them for their wonderful pictures. We would like to thank Luiz Nicolaci da Costa and Avishai Dekel for their unvaluable help in preparing this conference.

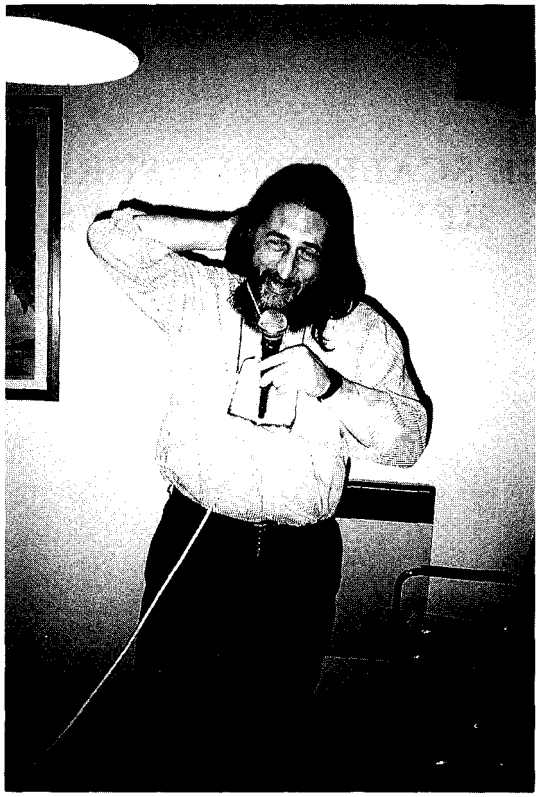
The success and animation of the Moriond Conference is mostly due to the efficiency of the organization provided by Jean Trân Than Vân and all his team. We would like to thank Joëlle Raguideau and Nicole Bachala, Jacqueline Plancy and Nicole Romain, for their help both in the organization and in the typing of the proceedings, as well as Aida Cherkaoui for her efficiency in the graphic realizations.

Last but not least, we would like to thank all speakers and participants for attending with such an assiduity such a dense conference.

Sophie Maurogordato Chantal Balkowski Charling Tao

SESSION I

LARGE SCALE STRUCTURE FROM REDSHIFT SURVEYS



Studying Galaxy and Structure Formation with Complete Redshift Surveys

L. Nicolaci da Costa
Institut d'Astrophysique, CNRS, Paris, France

Abstract

We briefly review the history of "complete" wide-angle redshift surveys of galaxies, highlighting the contribution of each survey to our current understanding of the nature of the galaxy distribution. We also review and discuss the constraints imposed on theories of galaxy and structure formation by the results of analyzes carried out with the CfA2 and SSRS2 surveys, currently the largest samples available for these kinds of studies.

1 Introduction

Among the several tools available to study the large-scale structure of the Universe, redshift surveys have played a pivotal role over the past two decades. If galaxies trace matter redshift surveys are a direct probe of the underlying mass distribution. If not, they contain important information about the way galaxies form. Either way, they represent the benchmark against which the success of any given theory of LSS formation has to be assessed. This has motivated the continuous effort of carrying out complete surveys to greater depths and of refining N-body simulations, most notably by investigating hydrodynamical effects to allow for more realistic galaxy formation.

Beginning in the mid 70s, several surveys covering large areas of the sky have been conducted probing the galaxy distribution to ever increasing depths. Complete optical and radio surveys like the RSA, CfA1, Arecibo, SSRS, CfA2 and SSRS2 have over the years revolutionized our ideas regarding the distribution of luminous matter. The CfA1 survey [18], the first three-dimensional survey to probe distances beyond Virgo, gave us the first hints that the Universe was rather inhomogeneous with the existence of large empty regions, while the Arecibo survey [17] showed the existence of large coherent structures extending over scales $\gtrsim$ 50 Mpc. The existence of voids and large coherent structures were confirmed by the diameter-limited SSRS

[6], with an effective magnitude-limit roughly 0.5 mag fainter than that of CfA1. The fainter magnitude limit produced much sharper maps which allowed the identification of wall-like structures bounding large empty regions. The existence of such structures had already been predicted from the results of the first 6° slice of the CfA2 survey extending the magnitude limit to $m_{B(0)}$= 15.5 [11]. The extension of the CfA2 survey eventually uncovered the remarkable Great Wall [15] within which several clusters are embedded. The SSRS2 [7], with the same magnitude-limit of the CfA2, showed by probing a different region of the sky that wall-like structures and large voids are common features of the galaxy distribution. Their frequency and size may still prove to be important constraints for theoretical models (see section III). Finally, the Las Campanas Survey [23], the first of the new generation of multifiber redshift surveys, has shown that the picture that emerged from the nearby surveys seems to extend to large distances, strongly suggesting that we may have identified the largest scale of inhomogeneities. The activity in the area is still intense with several probe- or slice-like surveys probing greater depths being now near completion [1],[16],[36], [37]. It is important to emphasize that with only sparse or dilute surveys it would have been difficult to uncover the sharp, coherent features observed with dense surveys.

The net result of the effort of the past two decades has been to produce complete surveys of optically and infrared selected galaxies covering large areas of the sky. To a magnitude limit of $m_{B(0)}$= 14.5 the sample consists of about 6000 galaxies covering about 1/2 the sky [31]. A similar sample extending to lower galactic latitudes is also currently available [34]. To $m_{B(0)}$=15.5 the combined CfA2+SSRS2 sample consists of over 15,000 galaxies with a sky coverage approaching 1/3 of the sky. Complementing these dense optical surveys, we also have the more dilute *IRAS* 1.2 Jy survey of $\approx$ 5000 infrared-selected galaxies [14], covering about 95% of the sky to an effective depth comparable to the CfA2+SSRS2 ($\gtrsim 120\ h^{-1}$ Mpc). In addition, there are the sparsely-sampled surveys like the Stromlo-APM survey of optical galaxies [25] and the QDOT survey [33] of infrared selected galaxies probing larger volumes. Although an impressive achievement much remains to be done at large distances and a new generation of wide-angle surveys is about to start with the 2dF and the Sloan Digital Sky Survey.

Below we review some of the results that have been obtained from analyzes of CfA2 and SSRS2 surveys. These analyzes take advantage of the wide-angle coverage and the large number of galaxies in each sample. The wide-angle coverage allows to probe larger pair separations in three-dimensions and to extract information over a wide range of scales. We also use the samples individually and examine the sample-to-sample variations to evaluate the cosmic variance of the results. The large number of galaxies is important because the sample can be sub-divided by different criteria like luminosity, morphological type and colors to investigate the dependence of the the clustering properties on the class of objects considered.

2 Mapping the Galaxy Distribution

The CfA2+SSRS2 sample currently provides the best three-dimensional maps of the present-day galaxy distribution. Confirming growing evidence accumulated over the years there seems to be little doubt that galaxies lie preferentially along thin, coherent wall-like features that define large empty regions devoid of galaxies. While high-density regions can be traced to scales of $\approx 100\ h^{-1}$ Mpc, it is thought that the relevant scale may be the linear extent of voids, typically $\approx 50\ h^{-1}$ Mpc. Inspection of maps like that depicted in the poster of this meeting [7] strongly suggests that the distribution of galaxies consists of a closely-packed, volume-filling network of voids. This picture of the LSS is qualitatively consistent with the redshift maps of

the Las Campanas Survey [23] and the interpretation given to the redshift distribution observed by deep probes [4], while advocating the existence of much larger voids.

Unfortunately, even for the combined sample the surveyed volume is relatively small compared to the scale of voids. Not enough voids are fully contained within the survey volume to adequately test the hypothesis of a void-filled Universe. All we know with some degree of confidence is that a significant fraction of the volume is empty of galaxies and that large walls exist and are common. Whether we chose to think in terms of walls or of voids the relevant point is to determine whether there is a characteristic scale imprinted in the galaxy distribution and if so what it is. These informations are crucial since they may be clues to the process of formation of LSS and they may impose constraints on the amount of power required on large scales to give rise to the observed structures. Equally important is to ask whether small amplitude Gaussian random fluctuations can produce non-linear features with sizes and frequency of the observed walls. Even if galaxies are "painted" and do not delineate real voids in the underlying mass distribution, the existence of a characteristic scale would be important to constrain the biasing mechanism.

We point out that even if the observed distribution is adequately described by a void network, it is not trivial to have a proper definition of what a void should be in a distribution with power on different scales and to define a suitable algorithm to identify voids and to determine their size distribution which will depend on the definition of a void (see [20], [24]). The same difficulties are present in the case of numerical simulations. Claims that current models can produce redshift distributions similar to the observations, having no difficulty producing walls and voids similar to those observed, are as subjective as our claims of a void-filled Universe, leaving open the questions posed above.

It should be pointed out that if one assumes that the distribution is in fact void-filled one can in principle constrain the characteristic scale of the voids. One way of estimating the typical size of voids is by using the zero-crossing of the two-point correlation function, which in the case of a cellular-like distribution should occur at half the size of the cell. Monte-Carlo tests using mock surveys, drawn from a Voronoi tessellation with the same selection and observational mask as real surveys, indicate that current surveys like the combined CfA2+SSRS2 and Stromlo-APM may be large enough to provide a reasonable constraint on the typical size of voids [19] or at least distinguish between the scale seen nearby from that observed with the deep probes.

3 Voids as Constraints to Models

Since the discovery of the Bootes void [21] it has been recognized that the existence of large voids could pose a serious challenge to models of LSS. However, little work has been done in trying to quantify what these constraints would be despite the fact that since this first discovery dense surveys have shown that the voids are not only large but also frequent. They are seen in every direction we have surveyed.

Recently this question has been re-examined under the assumptions that we have a void-filled distribution, that galaxies trace the underlying matter distribution and that structures grow gravitationally [3], [32]. In the scenario advocated by these authors the present-day voids, those surrounded by high-density walls, result from the evolution of small underdense regions reaching shell-crossing today. By analysis of the evolution of inverted top-hat density fluctuations and statistical arguments it can be shown that at any epoch voids reaching shell-crossing are the largest defining a characteristic scale and roughly filling the volume.

From the inverted top-hat model one can also derive the amplitude required at horizon-crossing for the matter fluctuations to form a void of a given size at the present epoch. Equating

this value to the rms density fluctuation on a given scale constrains the amplitude of the linear power-spectrum. Using a generic power-spectrum $P(k) \propto k^n$ we can determine n by requiring the mass power-spectrum to also satisfy the normalization imposed by COBE on large scales, thus relating the value of n to the assumed scale of voids. The main results of this analysis [32] are that the formation of 50 h^{-1} Mpc voids in diameter in an $\Omega = 1$ universe can only be achieved if $n \sim 1.25$, violating the inflationary paradigm. On the other hand smaller voids, 35 h^{-1} Mpc in diameter, would be consistent with $n = 1$. Despite uncertainties in the theoretical calculation the work illustrates how the presence of large voids in the galaxy distribution can provide quantitative constraints to models of structure formation and should stimulate work in methods of extracting information on voids from redshift surveys.

So far calculations have been restricted to generic power-spectra and for a flat Universe with $\Omega = 1$. Extensions of these calculations are currently underway to consider open universes, with or without a cosmological constant, and more realistic power-spectra using the information extracted from redshift surveys as discussed below.

4 Galaxy Power-Spectrum

If galaxies trace matter the galaxy power-spectrum provides important information on the fluctuations of the mass distribution. We have used the CfA2+SSRS2 sample to estimate the redshift space power-spectrum [8]. The main results of this analysis are: 1) that on large scales the PS continues to rise ($n \sim -1.1$) showing only weak signs for a turnover on scales $\gtrsim 200\ h^{-1}$ Mpc; 2) the differences between the PS computed from different samples are consistent with the error estimates based on mock surveys drawn from N-body simulations adopting the same selection criteria as the data; 3) the systematic differences between the PS can be accounted, at least in part, by different amounts of redshift distortions; 4) tests indicate that the results are not sensitive to the magnitude-limit adopted for the CfA2 sample; 5) that the feature on scales 30-50 h^{-1} Mpc [30] are clearly seen in 2 out of 3 samples considered and it is not an artifact of our method since the PS of mock surveys do not show a systematic occurrence of this feature; 6) evidence for the dependence of the amplitude of the PS on the luminosity of the galaxies, suggesting a relative bias between luminous and less-luminous galaxies [35].

A comparison of the PS of galaxies as determined from the combined CfA2+SSRS2 sample and that predicted by CDM models, both in redshift space, is shown in figure 1. The upper solid line represents the PS of a CDM model with $\Omega h = 0.2$ in a flat Universe with cosmological constant. The lower curve is a CDM model with $\Omega h = 0.5$. Both models are unbiased and normalized to $\sigma_8 = 1$. The excess power on scales $\sim 100\ h^{-1}$ Mpc favors a CDM model with minimal bias and $\Omega h = 0.2$. Note that both cases are consistent with the constraints imposed by COBE on large scales. The feature at the $\sim 30\ h^{-1}$ Mpc scale is also clearly seen and it may be a signature of the observed voids. We should point out that our the shape of our PS is consistent with other estimates based on infrared-selected galaxies [12] apart from a shift in the amplitude which reflects the relative bias between the two populations of galaxies.

5 Small Scales Peculiar Velocities

An important constraint on models of structure formation comes from the measurement of peculiar velocities of galaxies on small scales. As it is well known, the prediction of large peculiar velocities on small scale inconsistent with much lower observational estimates [10] is a major drawback of the unbiased $\Omega = 1$ CDM model. Before the COBE era it was possible

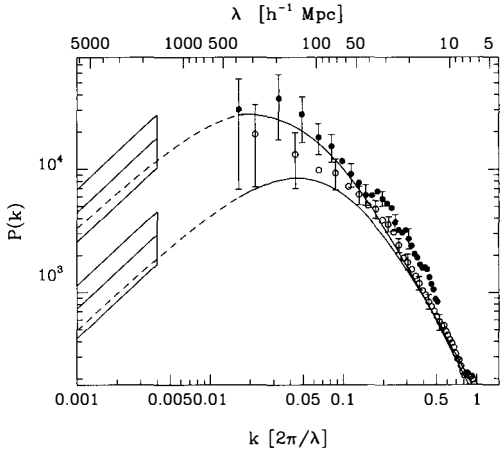


Figure 1: Comparison of the observed power-spectrum of galaxies and that predicted by different CDM models, both represented in redshift space.

to circumvent this problem by arguing that galaxies were biased relative to the mass which allowed some freedom in the normalization of the mass power-spectrum. However, this is no longer possible and demands a new examination of the problem both theoretically and observationally.

On the theoretical side, recent results from high-resolution N-body simulations [38] have shown that simulations with not sufficient mass resolution can significantly overestimate the value of the pairwise radial velocity dispersion used in the comparison to the data. On the observational side, we have used the CfA2+SSRS2 sample to determine the small scale peculiar velocities as measured by the pairwise velocity dispersion σ_{12} [26].

The method used to extract the information of peculiar velocities from redshift surveys is based on the calculation of the two-dimensional correlation function $\xi(r_p, \pi)$ as function of the projected separations perpendicular r_p and along the line-of-sight π. In figure 2 we show a contour plot of $\xi(r_p, \pi)$ calculated for the combined CfA2+SSRS2 sample. Note the significant elongation of the contours along the π axis at small separations, indicative of strong redshift distortions on small scales and the compression along the r_p axis, extending to scales $\gtrsim 15\ h^{-1}$ Mpc, usually attributed to streaming motions.

The correlation function $\xi(r_p, \pi)$ may be expressed as a convolution of the spatial correlation function ξ(r) with the distribution of pairwise peculiar velocities which, under the assumptions of isotropy and slowly varying velocity dispersion, can be expressed in terms of the first two moments, the relative streaming velocity v_{12} and the pairwise velocity dispersion σ_{12} [10]. If one assumes a specific model for the pairwise velocity distribution and for the variation of the streaming motion as a function of the pair separation, fits of $\xi(r_p, \pi)$ at different r_p may be used to derive σ_{12} as a function of r_p.

In the analysis we have assumed that the pairwise velocity distribution is an exponential and that the functional form of v_{12} is given by the self-similar solution of the BBGKY. The derivation of σ_{12} was carried out for different amplitudes of streaming. The main results of the

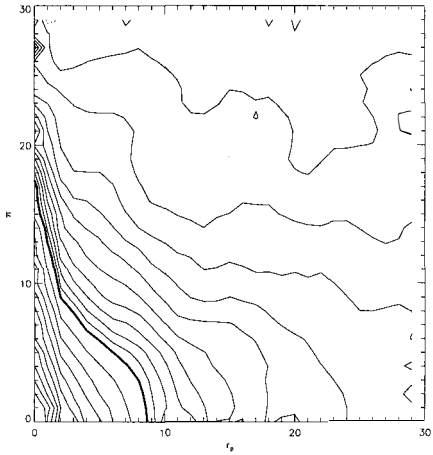


Figure 2: The two-dimensional correlation function $\xi(r_p, \pi)$ of the combined CfA2+ SSRS2 sample from which information on the peculiar velocities of galaxies on small scales is derived.

analysis are the following [26]. We find that our best estimate for the pairwise velocity dispersion is $\sim$ 540 km s^{-1} considerably higher than earlier estimates (340 km s^{-1}). However, this value has a large uncertainty which has been estimated from the variation of σ_{12} as determined from the independent analysis of the SSRS2, CfA2S and CfA2N subsamples. Clusters are the main contributors to σ_{12} . When clusters are removed the value of the dispersion drops to $\sim$ 300 km s^{-1} in agreement with the results for CfA1 and for the IRAS 1.2 Jy [13]. The dominant source of variance in the estimate of σ_{12} is the shot noise of dense virialized systems. An accurate determination of the dispersion would require probing volumes at least 7 times larger than that of the CfA2+SSRS2 sample as estimated from the observed distribution of velocity dispersions in dense systems or the mass distribution of bound systems expected by the Press-Schechter formalism for a COBE normalized CDM model. The main conclusion is that an $\Omega h = 0.2$ CDM model would be consistent with our determination of small scale velocities, consistent with the results obtained with the galaxy power-spectrum.

6 Galaxy Properties

The large number of galaxies and the dense sampling of the galaxy distribution afforded by the CfA2 and SSRS2 surveys make them also suitable to investigate properties of galaxies, their relation with the environment and biasing of different galaxy populations. The use of these surveys for these purposes has so far been limited.

The magnitude limit of the CfA2 and SSRS2 allows the determination of the luminosity function of local galaxies to a relative faint absolute magnitude limit ($M \approx$-14). This function is essential to correct the samples for selection effects and to investigate galaxy evolution. The luminosity function for galaxies of all morphological types has been calculated by for the

CfA2 [27] and the SSRS2[7] samples. The results are somewhat puzzling because there is a significant disagreement between the computed Schechter parameters. While the SSRS2 yields results which are consistent with those computed for the APM survey [25], the value of M_* is considerably fainter as determined from CfA2. Some possible effects that may account for the differences are possible systematic errors in the Zwicky magnitude scale and/or incompleteness of the Zwicky catalog. However, it is important to emphasize that no compelling evidence currently exists to confirm either of these possibilities. Curiously, the peculiar motions in the regions covered by the CfA survey are large, while the volume of space surveyed by the SSRS2 seems to be a particularly quiet region as judged by the small distortions of $\xi(r_p, \pi)$, primarily because of the paucity of rich clusters within the volume. This difference may have a bearing on the discrepancy found between the luminosity functions and should be investigated in more detail.

The large number of galaxies in the samples also allow them to be sub-divided according to different criteria. Taking advantage of this fact, it has been possible to investigate the dependence of the local luminosity function on the morphological types [28]. The results indicate that the LF is similar for all morphological types except for irregular galaxies, which are found to have a much steeper faint-end slope. These results have been confirmed by similar analysis using the SSRS2 [9] which is based in an independent parent catalog and morphological typing. We note that the luminosity functions of early-type galaxies derived from CfA2 and SSRS2 are very similar to those of spirals, in clear disagreement with recent claims that early-type galaxies would have a much flatter faint-end slope.

The overlap which exists between the SSRS2 sample and the ESO-Uppsala Surface Photometry Catalog [22] south of δ = -17.5° allows colors to be assigned for a significant fraction of galaxies in the SSRS2. We are currently using this color information to examine the dependence of the local luminosity function on color. The distinction between color and morphology is important because although correlated the dispersion in the relation is very large to allow a meaningful morphological classification based on color alone. Preliminary results [29] indicate significant differences in the luminosity function of the two populations with blue galaxies having a very steep faint-end slope $\lesssim$ -2, comparable to that obtained for irregular galaxies. This result suggests that a nearby population of blue galaxies may contribute to the faint galaxy counts. Such information is essential to constrain models of galaxy evolution.

Another important application of the large samples available is the study of the relative bias of galaxies of different luminosities and morphological types. This information may be used to place some constraints in the process of galaxy formation. We are currently investigating these effects using the SSRS2. Some preliminary results are reported elsewhere in this volume [2],[5]. For these kind of studies it is critical to be able to examine different classes of objects in the same volume of space in order to distinguish between real clustering differences from effects which may arise when results obtained from different volumes, probing different structures, are compared. This usually requires discarding a significant fraction of the galaxies in the sample. However, with the large samples currently available it is possible to construct suitable volume-limited samples for this kind of analysis. As discussed elsewhere in this volume, preliminary results indicate that galaxies with $L > L_*$ are biased relative to fainter galaxies with the bias depending on the luminosity. Fainter galaxies have clustering properties similar to those of *IRAS* galaxies.

7 Summary

Wide-angle surveys of the nearby Universe have had and will continue to have an enormous impact on studies of LSS providing a wealth of information that one may use to confront and discriminate competing models for the origin of structures.

The CfA2 and SSRS2 surveys have provided dense maps of the distribution of galaxies within a volume 120 h^{-1} Mpc in radius. New instrumentation like the 2dF spectrograph at the AAT and the Sloan Digital Sky Survey (SDSS) will allow large angular coverage to much greater depths which will further contribute to our understanding of the way galaxies are distributed not only locally but at different look-back times. Data from these new generation surveys, new measurements of CMB anisotropies on different angular scales and more detailed maps of the peculiar velocity field of galaxies and clusters will keep theorists busy for a long time.

Acknowledgements. We are grateful to all my collaborators in the SSRS2 survey effort in particular A. Fairall, D. Latham and P. Pellegrini. Special thanks to A. Cappi. C. Benoist, M. Geller, J. Huchra, R. Marzke, S. Maurogordato, M. Vogeley, C. Park, with whom I have conducted the analyzes reported here. I would also like to thank the hospitality of the Hebrew University of Jerusalem where this contribution was written.

References

[1] Bellanger, C., de Lapparent, V., Arnouts,S., Mathez, G., Mazure. A. & Mellier, Y. 1995, *Astr. Astrophys. Suppl. Ser.* **110**, 159

[2] Benoist, C. et. al. 1995, in this volume.

[3] Blumenthal, G.R., da Costa, L. N., Goldwirth, D. S., Lecar, M. & Piran, T. 1992, *Astrophys. J.* **388**, 234

[4] Broadhurst, T. J., Ellis, R. S., Koo, D. C., & Szalay, A. S., 1990, *Nature* **343**, 726

[5] Cappi *et al.* 1995, in this volume

[6] da Costa, L. N., Pellegrini, P. S., Sargent, W.L.W., Tonry, J., Davis, M., Meiksin, A., Latham, D.W., Menzies, J.W. & Coulson, I. 1988, *Astrophys. J.* **327**, 544

[7] da Costa, L. N., Geller, M. J., Pellegrini, P. S., Latham, D. W., Fairall, A. P., Marzke, R. O., Willmer, C. N. A., Huchra, J. P., Calderon, J. H., Ramella, M. & Kurtz, M. J., 1994, *Astrophys. J.* **424**, L1

[8] da Costa, L. N., Vogeley, M., Geller, M. J., Huchra, J. & Park, C., 1994, *Astrophys. J.* **437**, L1

[9] da Costa, L. N., Marzke, R., Pellegrini, P. S. & Santarosa, G. 1995, in preparation.

[10] Davis, M. & Peebles, J., 1983, *Astrophys. J.* **267**, 465

[11] de Lapparent, V., Geller, M.J. & Huchra, J. H., 1986, *Astrophys. J.* **302**, L1

[12] Fisher, K. B., Davis, M., Strauss, M. A., Yahil, A. & Huchra, J. P. 1993, *Astrophys. J.* **402**, 42

[13] Fisher, K. B., Davis, M., Strauss, M. A., Yahil, A. & Huchra, J. P. 1994 , *Mon. Not. R. Astr. Soc.* **267**, 927

[14] Fisher, K., Huchra, J. P., Strauss, M., Davis, M., Yahil, A. & Schlegel, D. 1995, preprint

[15] Geller, M., & Huchra, J. P., 1989, Science, **246**, 897

[16] Geller *et al.* 1995, in preparation

[17] Haynes, M. P. & Giovanelli 1986, *Astrophys. J.* **306**, L55

[18] Huchra, J. P., Davis, M., Latham, D.W. & Tonry, J. 1983, *Astrophys. J. Suppl. Ser.* **72**, 433

[19] Goldwirth, D., da Costa, L. N. & van Weygaert, R. 1995, *Mon. Not. R. astr. Soc.* , in press

[20] Kauffmann, G. & Fairall, A. 1991, *Mon. Not. R. Astr. Soc.* **248**, 313

[21] Kirshner, R. P., Oemler, A., Schecther, P. L. & Schectman, S. A. 1981, *Astrophys. J.* **248**, L52

[22] Lauberts. A. & Valetjin, E. A. 1989, ESO-Uppsala Catalog of Surphace Photometry (Garching:European Southern Observatory)

[23] Lin, H. 1995. in this volume

[24] Lindner, U., Einasto, J., Einasto, M., Freudling, W., Fricke, K. & Tago E. 1995, *Astr. Astrophys.* , in press

[25] Loveday, J., Peterson, B. A., Efstathiou, G., & Maddox, S. J., 1992, *Astrophys. J.* **390**, 338

[26] Marzke, R., & Geller, M. J., da Costa, L. N. & Huchra, J. P. 1995, *Astron. J.*, in press

[27] Marzke, R., Huchra, J. P., & Geller, M. J., 1994, *Astrophys. J.* **428**, 43

[28] Marzke, R., Huchra, J. P., & Geller, M. J., 1994, *Astron. J.* **108**, 437

[29] Marzke, R. & da Costa, L. N. 1995, in preparation

[30] Park, C., Vogeley, M., Geller, M. J. & Huchra, J. P. 1992, *Astrophys. J.* **391**, L51

[31] Pellegrini, P.S, da Costa, L. N., Huchra, J. P., Latham, D. W. & Willmer, C. A. 1990, *Astron. J.* **99**, 751

[32] Piran, T., Lecar, M., Goldwirth, D. S., da Costa, L. N. & Blumenthal, G. R. 1993, *Mon. Not. R. Astr. Soc.* **265**, 681

[33] Rowan-Robinson *et al.* ., 1990, *Mon. Not. R. Astr. Soc.* **247**, 1

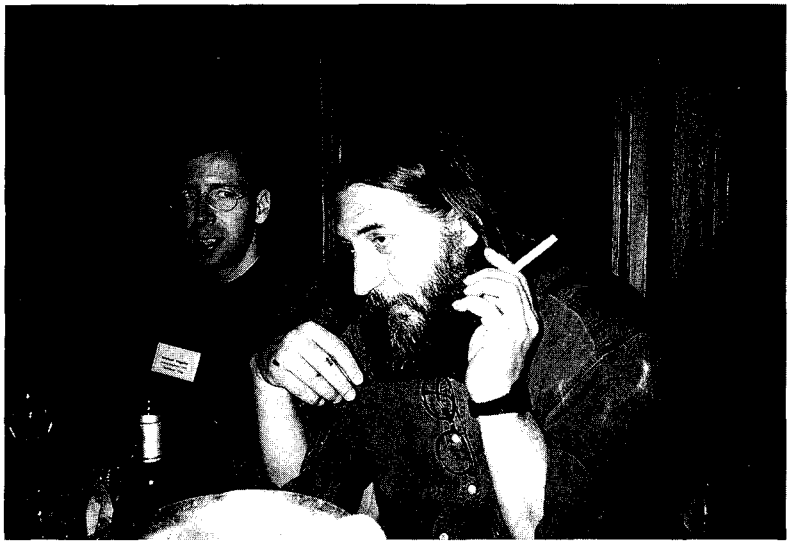
[34] Santiago, B., Strauss,, M.A., Lahav, O., Davis, M., Dressler, A. & Huchra, J. 1994, preprint

[35] Vogeley, M., Park, C., Geller, M. J., Huchra, J.P. & Gott, J.R., 1994 *Astrophys. J.* **420**, 525

[36] Willmer, C.N.A., Koo, D.C., Szalay, A.S. & Kurtz, M.J. 1994, *Astrophys. J.* **437**, 560

[37] Zucca, E, 1995, in this volume

[38] Zureck, W., Quinn, P.J., Salmon. T. K. & Warren, M.S. 1994, *Astrophys. J.* **431**, 559



THE POWER SPECTRUM OF GALAXY DENSITY FLUCTUATIONS: CURRENT RESULTS AND IMPROVED TECHNIQUES

Michael S. Vogeley
Department of Physics and Astronomy, Johns Hopkins University
Baltimore, MD 21218 USA
vogeley@pha.jhu.edu

Abstract

The power spectrum of density fluctuations measured from galaxy redshift surveys provides important constraints on models for the formation of large-scale structure. I review current results for the 3-D power spectrum and examine the limitations of current measurements and estimation techniques. To span the decade of wavelength between the scales probed by galaxy surveys and COBE, measure the detailed shape of the power spectrum, and accurately examine the dependence of clustering on galaxy species, we require deeper samples with carefully controlled selection criteria and improved techniques for power spectrum estimation. I describe a new method for estimating the power spectrum that optimally treats survey data with arbitrary geometry and sampling.

1 Introduction

Recent measurements of galaxy clustering from redshift surveys and angular catalogs, together with limits on the clustering of mass implied by the COBE DMR experiment, yield important constraints on proposed models for the formation of large-scale structure. However, we lack accurate constraints on fluctuations in galaxy density on scales that overlap with those probed by COBE, and the extant measurements have poor resolution on scales where certain theories predict interesting features in the power spectrum. Several surveys, either planned or in progress, promise to yield the desired measurements of the power spectrum of galaxy density fluctuations, but the complex geometry and sampling of these surveys pose a strong challenge to traditional methods of power spectrum analysis. The ultimate measurement of

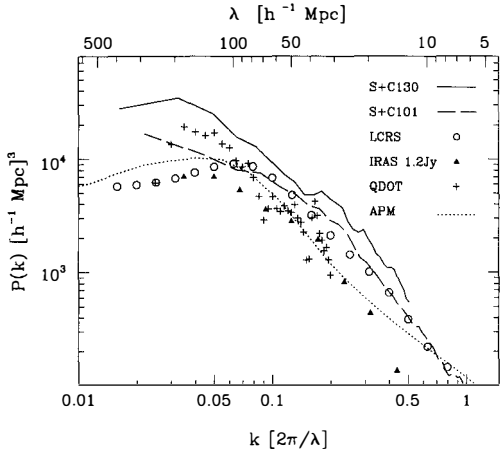


Figure 1. 3-D Power Spectra of Galaxy Surveys. Solid and dashed curves show redshift-space power spectra of volume-limited samples of the optically-selected SSRS2+CfA2 survey. Circles show the power spectrum of the Las Campañas Redshift Survey. Triangles and crosses show the redshift-space power spectra of flux-limited samples of the 1.2Jy and QDOT (1/6 of the 0.6Jy sample) IRAS surveys. The dotted line is the real-space power spectrum inferred from the angular correlations of the APM catalog.

the galaxy fluctuation spectrum will result from combining all of the available data into one sample. This possibility begs the question, how do we obtain the best possible estimate of the power spectrum from a sample with arbitrarily complex geometry and sampling density?

2 Current Estimates of the 3-D Power Spectrum

Using standard estimation techniques (as described in section 3), the 3-D redshift-space power spectrum has been estimated for a variety of galaxy redshift samples. Figure 1 shows power spectra estimated from two volume-limited samples of the combined SSRS2+CfA2 survey [7], the Las Campañas survey [18], the IRAS 1.2Jy survey [10], the QDOT survey of IRAS galaxies [9], as well as the real-space power spectrum inverted from the angular correlation function of the APM catalog [1]. The shapes of the power spectra for the SSRS2+CfA2 samples, the Las Campañas survey, and the IRAS 1.2Jy sample are consistent within the errors. However the amplitudes of the power spectra for optical (SSRS2+CfA2 and Las Campañas) and infrared selected (IRAS 1.2Jy and QDOT) samples spectra differ quite significantly, as do the power spectra for SSRS2+CfA2 sample with different absolute-magnitude limits ($M < -20.3 + 5 \log h$ and $M < -19.7 + 5 \log h$ for the 130 and 101 samples, respectively), suggesting that the bias in clustering amplitude of different species extends over the full range of wavelength scales [20]. The QDOT survey exhibits a large excess in power on scales $\lambda > 75h^{-1}$ Mpc over the shallower but more densely sampled 1.2Jy IRAS sample. This discrepancy may be caused by an extreme overdensity in the Hercules cluster, contained in the QDOT sample [27].

The APM curve in Figure 1 is an estimate of the *real-space* power spectrum, obtained by inverting the angular correlation function. The corresponding redshift-space spectrum would be

steeper than this, and therefore in disagreement with the other optically-selected power spectra plotted here. Luminosity bias might explain this discrepancy: if the clustering amplitude is indeed an increasing function of galaxy luminosity, then the power spectrum inferred from angular correlations (which, by definition, use an apparent-magnitude limited sample) will have too steep a slope because the clustering amplitude increases with depth and therefore with wavelength scale.

These power spectrum measurements yield good constraints on models with CDM-like power spectra, but are insufficient to differentiate among the broad classes of contending models. The data can be well fit by a CDM power spectrum with $\Omega h \approx 0.25$ [17], [21]. The power spectrum of the "standard" $\Omega = 1, H_0 = 50 \mathrm{kms}^{-1}$ model is excluded due to an excess of small vs. large-scale power. Due to the strong influence of peculiar velocities in this model, the shape of the redshift-space power spectrum is roughly correct, but the amplitude is too high (when normalized to COBE, this model requires $\sigma_8 = 1.4$ and, therefore, *anti-biasing* of all but the very brightest galaxies [13]). However, several alternative models predict power spectra with nearly the same shape and the correct normalization, among which the current data do not strongly discriminate. The list of candidates includes (but is not limited to) CDM models with non-zero cosmological constant, open universe CDM, mixed (cold plus hot) dark matter models [24], and warm plus hot dark matter [19].

To further constrain cosmological models, we must (1) close the gap between the scales probed by galaxy surveys and COBE, (2) measure the detailed shape of the galaxy power spectrum, (3) determine the dependence of clustering on galaxy species, and (4) quantify the anisotropy of clustering in redshift space caused by peculiar motions of galaxies. Comparison of power spectra for currently competing models (e.g., Fig. 1 of ref [26]) shows that the shapes of these spectra differ most strongly on scales near and beyond the peak of the spectrum. Unfortunately, the observed spectra plotted in Figure 1 all have resolution of $\delta k \sim 0.02$ or worse. Although there is some evidence of features in the observed power spectrum (e.g., the feature at $\lambda \sim 30h^{-1}$ Mpc in the CfA2 and SSRS2 power spectra [7] and the peaks at $\lambda \sim 30h^{-1}$ and $128h^{-1}$ Mpc seen by [3]), the resolution of the power spectrum near the peak of the galaxy power spectrum is too poor to detect subtle features such as those produced in, e.g., models with a large baryonic mass component [15]. The turnover in the power spectrum seen in Figure 1 at $k \sim 0.03$ is similarly uncertain. More accurate probes of scales $\sim 100h^{-1}$ Mpc and greater are necessary to confidently test for features in the power spectrum on scales where physical processes near the time of matter-radiation equality would leave their imprint and to compare galaxy clustering and the amplitude of mass clustering implied by CMB anisotropy measurements. The latter, along with knowledge of the dependence of clustering on galaxy selection, will elucidate the relationship between clustering of mass and light in the universe. Furthermore, measurement of the anisotropy of clustering in redshift space on the largest (and, therefore, presumably linear-growth) scales can yield a direct measurement of the mean cosmic density [16], [14], [5].

To increase the largest scales that we probe and the resolution of these measurements, we must survey a larger volume of the universe. Several ongoing and planned surveys promise to yield better constraints on the fluctuation spectrum, but the geometries of these samples pose a challenge to standard methods of power spectrum estimation. Deeper surveys of this type that are completed, or are soon to be, include pencil beam surveys [3], [4] and several deep slice surveys: the Las Campañas [25], Century [12], and ESP [29] surveys. Within the next two years we also expect results from the AAT 2df survey and the Sloan Digital Sky Survey (SDSS hereafter). Most of the sensitivity of the AAT survey to large-scale fluctuations will result from an ensemble of 100 randomly spaced pencil beams of 400 galaxies each. Over its five year duration, the SDSS will obtain redshifts for 10^6 galaxies over a contiguous area of π

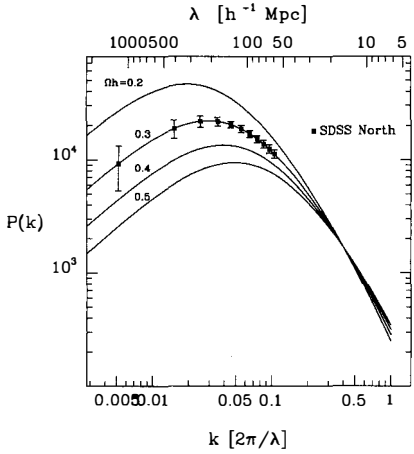


Figure 2. The 1σ uncertainty expected for a volume-limited (to M^*) sample of the SDSS northern redshift survey, assuming Gaussian fluctuations and a $\Omega h = 0.3$ CDM model, compared to power spectra for CDM with different Ωh. Error bars on smaller scales are of similar or smaller size than the symbols.

steradians in the North Galactic Cap, and therefore have a rather simple geometry. Figure 2 shows the uncertainty on the power spectrum that is expected for the full survey. However, the geometry of earlier partial data (e.g., 2×10^5 galaxies over some set of narrow stripes on the sky in the first year), and the survey in the South (three $2.^{\circ}5 \times 100^{\circ}$ stripes), will be more complex. Our goal is to extract the best possible estimate of the power spectrum from such partial data as the survey progresses.

3 Limitations of Standard Estimation Techniques

Standard methods for estimating the power spectrum all follow the same basic scheme. We directly sum the planewave contributions from each galaxy,

$$\tilde{\delta}(\mathbf{k}) = \frac{1}{\sum_j w(\mathbf{x}_j)} \sum_j w(\mathbf{x}_j) e^{i\mathbf{k}\cdot\mathbf{x}_j} - \tilde{W}(\mathbf{k}), \tag{1}$$

where $w(\mathbf{x}_j)$ is the weight given to the j^{th} galaxy and we subtract $\tilde{W}(\mathbf{k})$, which is the contribution to each mode from the finite survey window ($W(\mathbf{x}) = 1$ inside the survey and 0 elsewhere) and the selection function $\bar{n}(\mathbf{x})$. Next we compute the square of the modulus of each Fourier coefficient and subtract the power due to shot noise,

$$\hat{P}(\mathbf{k}) = \frac{|\tilde{\delta}(\mathbf{k})|^2 - \sum_j w^2(\mathbf{x}_j) \,/\, \left[\sum_j w(\mathbf{x}_j)\right]^2}{\frac{1}{(2\pi)^3} \int d^3k' \, |\tilde{W}(\mathbf{k}')|^2}, \tag{2}$$

and average these estimates over a shell in k-space to yield an estimate of $P(k)$. The denominator of equation (2) enforces the convention that $P(k)$ has the units of volume. Methods vary

in the details (compare refs [20], [10], [9]), including the weights applied to each galaxy, how the window function of the survey is computed, corrections (or lack thereof) for the damping of large-scale power (analogous to the integral constraint on the correlation function – see below), and attempts to deconvolve the true power from the window function of the survey.

This method has several weaknesses that become even more serious when applied to surveys with complex geometry and sampling. A critical problem is that the basis functions of the Fourier expansion (plane waves) are not orthonormal over a finite non-periodic volume. Following equations (1) and (2), the power measured at any wavenumber is a convolution of the true power with the window function of the survey,

$$\hat{P}(\mathbf{k}) = \int d^3k' \, P(\mathbf{k}')|W(\mathbf{k}-\mathbf{k}')|^2. \tag{3}$$

The estimates of power at different wavenumber have a covariance that depends on the shape of the survey volume. If the survey is oddly-shaped, then estimates $\hat{P}(\mathbf{k})$ with the same $k = |\mathbf{k}|$ but different direction $\hat{\mathbf{k}}$ sample different ranges of wavenumber because $W(\mathbf{k})$ is anisotropic. Averaging over a shell in k-space combines power estimates with varying bandpass and, therefore, different signal-to-noise ratios.

Further complications arise when we consider how to optimally weight the galaxies (as in eq. [1]) in different regions of a survey. The signal-to-noise for detection of clustering depends on the sampling rate of galaxies in the survey, which may vary due to survey strategy (e.g., the Las Campañas survey, which observes the same number of galaxies in each plug plate field), extinction (for a survey that includes galaxies to a fixed apparent magnitude if uncorrected for extinction), combining different surveys into a single sample, or simply because the selection function varies with distance (in the case where we analyze apparent-magnitude limited samples). In general, the set of weights applied to the galaxies should vary with the wavenumber $\mathbf{k}$ being probed. If the sampling density of galaxies varies with position on the sky, as in the Las Campañas survey, then the variation with wavenumber of the weight per galaxy yields a different pattern on the sky for each mode. Ignorance of this variation with wavenumber of the weighting scheme yields estimates of power with unnecessarily poor signal to noise.

Uncertainty in the mean density limits our ability to detect fluctuations on very large scales. In equation (1), when we subtract the contribution of the window function to each Fourier mode, we attempt to subtract the spike at $k = 0$ in the true power, which is due to the non-vanishing mean density of galaxies. Because this spike is convolved with the window function of the survey and because we typically estimate the mean density from the sample itself (which forces $\langle\delta(\mathbf{x})\rangle = 0$ within the survey), we erroneously subtract the product of the window function with the component of clustering signal on the scale of the survey, $|W(\mathbf{k})|^2\langle|\delta_0|^2\rangle$. A better method would be to simultaneously estimate both the mean density and the power spectrum.

Model testing is made difficult by the non-orthonormality of the Fourier modes, ambiguity about the optimal number of modes to include in the analysis, and necessary assumptions about the probability distribution of the measured power per mode. In principle, we could test models by computing the full covariance matrix of the power spectrum estimates for each model in consideration and compare their likelihoods, as approximated in ref [9]. This procedure requires that we repeatedly invert large, highly nondiagonal matrices. The size of the matrices could be reduced if we choose a limited set of modes, but this method does not specify the optimal set of power estimates; nearby modes have large covariance, but we lose statistical power and resolution if we sample too few. Finally, this method requires that we know the covariance matrix of the *power* per mode (which depends on fourth-order moments of the galaxy density) and the probability distribution of these fourth-order fluctuations for every

model under consideration. To test the likelihood that the observations arise from a model with a particular power spectrum, we only require prediction of the covariance matrix of the expansion coefficients themselves, and knowledge of the probability distribution of second-order fluctuations in the density. A good choice of basis functions eases calculation of this matrix and increases the statistical power of the likelihood function.

4 The Karhunen-Loève Transform

Rather than make small modifications to the standard method for power spectrum estimation, we begin anew and derive the complete set of spatial functions that optimally weight the observed data in order to estimate second-order clustering properties of the galaxy distribution, and describe how this expansion naturally leads to straightforward likelihood analysis of proposed models [31]. The basis functions that we choose are the eigenvectors of the correlation matrix of galaxy density fluctuations. Expansion of the observed density field in this basis is known as the Karhunen-Loève transform (K-L hereafter; see, e.g., refs [28], [23] for discussion of the discrete and continuous forms of this transform, respectively). See ref [2] for a similar analysis of the COBE DMR maps.

Dividing the survey volume into M cells with volume V_i, we observe galaxy counts d_i, which form a vector $\mathbf{D}$. The correlation matrix of the count fluctuations $\mathbf{D} - \langle \mathbf{D} \rangle$ has elements

$$\begin{aligned} R_{ij} &= \langle (d_i - \langle d_i \rangle)(d_j - \langle d_j \rangle) \rangle \\ &= n_i n_j \xi_{ij} + \delta_{ij} n_i + \epsilon_{ij} \end{aligned} \tag{4}$$

where $n_i \equiv \langle d_i \rangle$, $\delta_{ij} = 0$ for $i \neq j$, ϵ_{ij} is the correlation matrix for other sources of noise, and

$$\xi_{ij} \equiv \frac{1}{V_i V_j} \int d^3x_i \int d^3x_j \, \xi(\mathbf{x_i}, \mathbf{x_j}). \tag{5}$$

The three terms in equation (4) are the contributions from clustering of galaxies, shot noise, and extra variance due to, e.g., magnitude errors or uncertainty in the luminosity function. We assume a model for ξ that is consistent with previous observations. The correlation function includes the redshift space distortions, $\xi(\mathbf{x}_i, \mathbf{x}_j) = \xi(r_p, \pi, R)$, where r_p is the projected separation, π the line of sight separation, and R the distance of the pair of cells from the observer.

The division of space into cells is rather arbitrary, therefore we must ensure that our derivation of the eigenmodes does not sensitively depend on the choice of pixellation. To derive the eigenmodes, we first apply a whitening transformation to the binned galaxy counts, $\mathbf{D}' = \mathbf{N}^{-1/2}\mathbf{D}$, where the $N_{ij}^{-1/2}$ are the square roots of the inverse of the noise component of the correlation matrix ($\mathbf{R} = \mathbf{S} + \mathbf{N}$, where $\mathbf{S}$ and $\mathbf{N}$ are the signal and noise correlation matrices, respectively). For the case of shot noise only ($\epsilon_{ij} = 0$ in eq. [4]), this yields a whitened correlation matrix,

$$\mathbf{R}' = \mathbf{N}^{-1/2}\mathbf{R}\mathbf{N}^{-1/2}, \tag{6}$$

with elements

$$\begin{aligned} R'_{ij} &= n_i^{-1/2}[n_i n_j \xi_{ij} + \delta_{ij} n_i] n_j^{-1/2} \\ &= n_i^{1/2} n_j^{1/2} \xi_{ij} + \delta_{ij}. \end{aligned} \tag{7}$$

The K-L transform of the observed galaxy counts has coefficients

$$B_n = \mathbf{\Psi}_n^\dagger \mathbf{N}^{-1/2} \mathbf{D}, \tag{8}$$

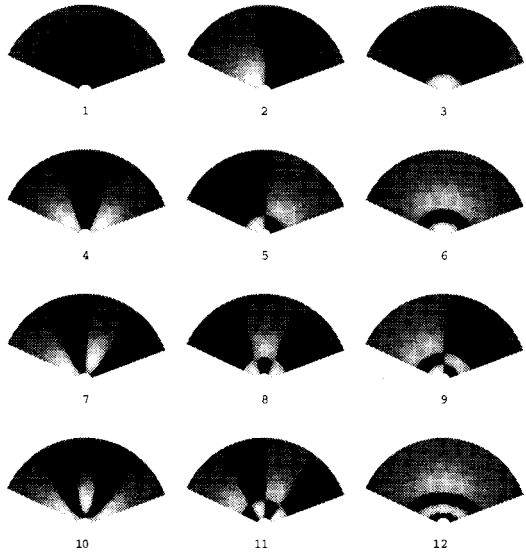


Figure 3. Eigenmodes of the apparent-magnitude limited CfA slice, formed by assuming the selection function and power spectrum measured for the CfA2 survey. This slice covers the region $29\overset{\circ}{.}5 \leq \delta \leq 32\overset{\circ}{.}5$, $8^h \leq \alpha \leq 17^h$, and we restrict the redshift range to $10h^{-1}\mathrm{Mpc} \leq r \leq 120h^{-1}\mathrm{Mpc}$. We plot the twelve modes with largest expected signal-to-noise ratio. These functions closely resemble the multipole moments of the density field, and are most sensitive to structure near the peak of the redshift distribution $r \sim 55h^{-1}\mathrm{Mpc}$.

where the $\mathbf{\Psi}_n$ solve the eigenvalue problem $\mathbf{R}'\mathbf{\Psi}_n = \lambda_n \mathbf{\Psi}_n$. The signal and noise are uncorrelated in this basis and the covariance matrix of these coefficients is diagonal. Figure 3 shows the first 12 eigenmodes for the geometry, selection function, and power spectrum of the first CfA slice [8].

Figure 4 shows the expected power per mode of the K-L transform, analogous to the power spectrum of the Fourier expansion. These modes are sorted by eigenvalue, which (because the expectation value of the noise power is unity for every mode) is equivalent to sorting by signal-to-noise ratio. The total power per mode is

$$\begin{aligned} \langle B_n^2 \rangle &= \langle (\mathbf{\Psi}_n^\dagger \mathbf{N}^{-1/2}\mathbf{D})(\mathbf{\Psi}_n^\dagger \mathbf{N}^{-1/2}\mathbf{D})^\dagger \rangle \\ &= \mathbf{\Psi}_n^\dagger \langle \mathbf{D}'\mathbf{D}'^T \rangle \mathbf{\Psi}_n \end{aligned}$$

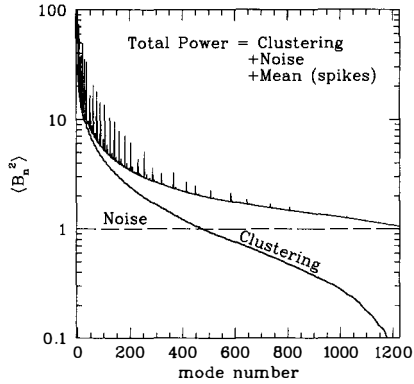


Figure 4. Expectation value of the power per mode for the K-L expansion of the CfA slice, where the modes are ordered by decreasing signal-to-noise ratio. The total power (upper solid line) is the sum of the clustering signal (lower solid line), noise (long-dashed line), and the mean density (spikes in the total power curve).

$$
\begin{aligned}
&= \mathbf{\Psi}_n^\dagger \mathbf{R}' \mathbf{\Psi}_n + \mathbf{\Psi}_n^\dagger \langle \mathbf{D}' \rangle \langle \mathbf{D}' \rangle \mathbf{\Psi}_n \\
&= \mathbf{\Psi}_n^\dagger (\mathbf{S}' + \mathbf{N}' + \mathbf{E}') \mathbf{\Psi}_n. \qquad (9)
\end{aligned}
$$

The contributions from the mean density, noise, and clustering signal are

$$
\begin{aligned}
E_n^2 &= \mathbf{\Psi}_n^\dagger \mathbf{E}' \mathbf{\Psi}_n = \langle B_n \rangle^2 \\
&= \left(\sum_{i=1}^{M} \Psi_n(\mathbf{x}_i) n_i^{1/2} \right)^2 \\
&= \left(\int d^3x \, F_n(\mathbf{x}) \bar{n}^{1/2}(\mathbf{x}) \right)^2, \qquad (10) \\
N_n^2 &= \mathbf{\Psi}_n^\dagger \mathbf{I} \mathbf{\Psi}_n = 1, \qquad (11) \\
S_n^2 &= \mathbf{\Psi}_n^\dagger \mathbf{S}' \mathbf{\Psi}_n \\
&= \sum_{i=1}^{M} \sum_{j=1}^{M} \Psi_n^*(\mathbf{x}_i) \Psi_n(\mathbf{x}_j) n_i^{1/2} n_j^{1/2} \xi_{ij} \\
&= \int \frac{d^3k}{(2\pi)^3} |\tilde{G}_n(\mathbf{k})|^2 P(\mathbf{k}), \qquad (12)
\end{aligned}
$$

where we take the limit $M \to \infty$ and $V_i \to 0$ and define the discrete approximations to the continuous functions of position $F_n(\mathbf{x}) = \Psi_n(\mathbf{x}_i)/V_i^{1/2}$ and $G_n(\mathbf{x}) = \Psi_n(\mathbf{x}_i)\bar{n}^{1/2}(\mathbf{x})/V_i^{1/2}$ for $\mathbf{x} \in V_i$. Each mode samples the power spectrum with the window function $|\tilde{G}_n(\mathbf{k})|^2$. As we increase the volume covered by a survey, the Fourier windows of its eigenmodes narrow and we probe the fluctuations with increasing resolution. In the limit of an infinite volume, these windows approach delta functions, and the K-L eigenmodes become identical to the plane waves of the Fourier expansion, modulated by weighting to account for the variation with distance of the selection function.

We test proposed models for galaxy clustering in a Bayesian fashion, which includes evaluation of the likelihood of the data under a particular hypothesis. Restricting the analysis to large-scale modes, the likelihood is approximately

$$\mathcal{L}(\mathbf{B} \mid \text{model}) = (2\pi)^{-\mathrm{M}/2} |\det \mathbf{C}_{\text{model}}|^{-1/2} \exp\{-(\mathbf{B} - \langle \mathbf{B} \rangle_{\text{model}}) \mathbf{C}_{\text{model}}^{-1} (\mathbf{B} - \langle \mathbf{B} \rangle_{\text{model}})^{\mathrm{T}}/2\}, \quad (13)$$

where M is the number of eigenmodes, and $\langle \mathbf{B} \rangle_{\text{model}}$ and $\mathbf{C}_{\text{model}}$ are predicted by the clustering model. In ref [31], we derive the K-L transform from the requirement that the confidence region of power spectrum parameters be as small as possible, therefore this basis set is *optimal* for testing clustering models. Note that we can explicitly vary the estimated mean density, rather than subtract the mean *a priori*, and thereby avoid the large-scale power damping described above. This method requires an initial guess at the power spectrum (to construct the eigenmodes), but the form of the eigenmodes does not depend sensitively on this assumption, and we can easily iterate the process.

The K-L eigenmodes form a complete basis for representing the observations, with no loss of phase information, and thus may be useful for analyses other than power spectrum estimation. One such application is smoothing of the density field by removal or suppression of modes that sample short wavelength scales. This form of smoothing could be used for studies of the morphology and topology of large-scale structure and for identification of superclusters in sparse data. Another application is optimal reconstruction of the galaxy density field, facilitated by the signal-to-noise properties of the eigenmodes (cf. refs [2] and [11] regarding Wiener filtering for reconstruction of the CMB anisotropy and the galaxy density field, respectively). When applied to spectroscopic observations of galaxies, the K-L transform yields an elegant means of spectral classification [6].

5 Conclusions

Statistical measures of the large-scale structure revealed by redshift surveys of the nearby universe and measurement of the CMB anisotropy successfully narrow the range of acceptable theoretical models, ruling out, for example, the previously 'standard' CDM model, and suggest consideration of several new models. The discriminatory power of galaxy clustering statistics and the increasing predictive power of theoretical models prompt planning for deeper complete redshift surveys such as the SDSS and the AAT 2df survey and the development of more sophisticated methods of analysis, such as the K-L transform.

We plan to apply this method for power spectrum estimation to a variety of data sets, including the pencil beam redshift surveys, early redshift observations from the Sloan Digital Sky Survey, and the spatial distribution of quasar absorption line systems. For future surveys (including planning for the SDSS), we can design the optimal geometry and sampling for the available survey resources, using the K-L transform as a method for estimation of the uncertainty in $P(k)$ for an arbitrary survey. We hope to use this transform method to combine all of the available galaxy redshift data and thereby obtain the best possible measurement of the power spectrum of galaxy density fluctuations.

Acknowledgements. I thank the many individuals who contributed to the work summarized above: Alex Szalay, for development of improved methods for power spectrum estimation; Luiz da Costa, Margaret Geller, John Huchra, and Changbom Park for analyses of the SSRS2 and CfA2 surveys. This research was supported in part by NSF grant AST-9020380 and the Seaver Foundation.

References

[1] Baugh, C. M., & Efstathiou, G. 1993, *M. N. R. A. S.*, **265**, 145.

[2] Bond, J. R. 1994, in *Relativistic Cosmology*, ed. M. Sasaki, (Academic Press), Proc. 8th Nishinomiya-Yukawa Memorial Symposium.

[3] Broadhurst, T. J., Ellis, R. S., Koo, D. C., & Szalay, A. S. 1990, *Nature*, **343**, 726.

[4] Broadhurst, T. J., Szalay, A. S., Ellis, R. S., Ellman, N., & Koo, D. C. 1995 in *Wide-Field Spectroscopy and the Distant Universe, Proc. of 35th Herstmonceux Conference*, eds. S. J. Maddox & A. Aragón-Salamanca, p. 178.

[5] Cole, S., Fisher, K. B., & Weinberg, D. H. 1993, *M. N. R. A. S.*, **267**, 785.

[6] Connolly, A. J., Szalay, A. S., Bershady, M. A., Kinney, A. L., & Calzetti, D. 1995, *A. J.*, in press.

[7] da Costa, L. N., Vogeley, M. S., Geller, M. J., Huchra, J. P., & Park, C. 1994, *Ap. J. Lett.*, **437**, L1.

[8] de Lapparent, V., Geller, M. J., & Huchra, J. P. 1986, *Ap. J. Lett.*, **301**, L1.

[9] Feldman, H. A., Kaiser, N., & Peacock, J. A. 1994, *Ap. J.*, **426**, 23.

[10] Fisher, K. B., Davis, M., Strauss, M. A., Yahil, A., & Huchra, J. P. 1993, *Ap. J.*, **402**, 42.

[11] Fisher, K. B., Lahav, O., Hoffman, Y., Lynden-Bell, D., & Zaroubi, S. 1995, *M. N. R. A. S.*, **272**, 885.

[12] Geller, M. J., Kurtz, M. J., Huchra, J. P., Fabricant, D. G., Thorstensen, J. R., & Wegner, G. 1995, in preparation.

[13] Górski, K. M., Stompor, R. & Banday, A. J. 1995, *Ap. J.*, submitted.

[14] Hamilton, A. J. S. 1992, *Ap. J. Lett.*, **385**, L5.

[15] Holtzman, J. A. 1989, *Ap. J. Suppl.*, **71**, 1.

[16] Kaiser, N. 1987, *M. N. R. A. S.*, **227**, 1.

[17] Kofman, L. A., Gnedin, N., & Bahcall, N. A. 1993, *Ap. J.*, **413**, 1.

[18] Lin, H., Kirshner, R. P., Shectman, S. A., Landy, S. D., Oemler, A., Tucker, D. L., & Schechter, P. L. 1995, in preparation.

[19] Malaney, R. A., Starkman, G. D., & Widrow, L. 1995, preprint astro-ph/9504014.

[20] Park, C., Vogeley, M. S., Geller, M. J., & Huchra, J. P. 1994, *Ap. J.*, **431**, 569.

[21] Peacock, J. A., & Dodds, S. J. 1994, *M. N. R. A. S.*, **267**, 1020.

[22] Peacock, J. A., & Nicholson, D. 1991, *M. N. R. A. S.*, **253**, 307.

[23] Poor, H. V. 1994, *An Introduction to Signal Detection and Estimation* (New York: Springer-Verlag).

[24] Primack, J. R., Holtzman, J., Klypin, A., & Caldwell, D. O. 1995, *Phys. Rev. Lett.*, submitted.

[25] Shectman, S. A., Landy, S. D., Oemler, A., Tucker, D. L., Kirshner, R. P., Lin, H., & Schechter, P. L. 1995, in *Wide-Field Spectroscopy and the Distant Universe, Proc. of 35th Herstmonceux Conference*, eds. S. J. Maddox & A. Aragón-Salamanca, p. 98.

[26] Strauss, M. A., Cen, R., Ostriker, J. P., Lauer, T. R., & Postman, M. 1995, *Ap. J.*, **444**, 507.

[27] Tadros, H., & Efstathiou, G. 1995, preprint astro-ph/9507050.

[28] Therrien, C. W. 1992, *Discrete Random Signals and Statistical Signal Processing*, (Englewood Cliffs: Prentice-Hall).

[29] Vettolani, G, et al. 1995, in *Wide-Field Spectroscopy and the Distant Universe, Proc. of 35th Herstmonceux Conference*, eds. S. J. Maddox & A. Aragón-Salamanca, p. 115.

[30] Vogeley, M. S., Park, C., Geller, M. J., & Huchra, J. P. 1992, *Ap. J. Lett.*, **391**, L5.

[31] Vogeley, M. S., & Szalay, A. S. 1995, *Ap. J.*, submitted.

BIASING IN THE SOUTHERN SKY REDSHIFT SURVEY

C. Benoist [1], S. Maurogordato [1], L.N. da Costa [2], A. Cappi [1,3], R. Schaeffer [4]
[1] *DAEC, CNRS, Observatoire de Paris-Meudon, Meudon, France.*
[2] *Institut d'Astrophysique de Paris, Paris, France.*
[3] *Osservatorio Astronomico di Bologna, Bologna, Italy.*
[4] *Service de Physique Theorique, CEA, CEN-Saclay, France.*

Abstract

We investigate the variation of galaxy clustering with luminosity in the SSRS2 Catalog. Using the two-point correlation function and the variance of counts in cells, we show that a luminosity bias exist in the SSRS2, this latter increasing strongly for galaxies brighter than L^*. This analysis provides a relative bias versus magnitude relation which can be compared to the predictions of models of galaxy formation.

1 Introduction

One of the major difficulties today in relating observational results on galaxy clustering to theoretical models lies in our poor knowledge of the relation between galaxy and mass distribution. In particular, any information on relative biasing between galaxies according to their intrinsic parameters as luminosity, morphological type, or density contrast can bring new constraints on physics of galaxy formation.

We will hereafter analyse how the clustering is affected when selecting galaxies belonging to different luminosity ranges. The existence itself of luminosity biasing has been a controversial topic in the last decades (see for instance [1], [2], [3], [4] and [5]).

On this purpose we will calculate the redshift-space correlation function and of the variance of the counts in cells on various subsamples of the recently completed SSRS2 correponding to different luminosity ranges.

2 Subsamples and indicators

The parent catalog used in this analysis is the SSRS2 [6], consisting of 3592 galaxies within 1.13 str with limiting magnitude $m_B = 15.5$, and angular limits $b_{II} < -40^o$ and $-40^o < \delta < -2.5^o$. In the following analysis we have adopted $H_0 = 100$ and $q_0 = 0.5$. The standard Local Group correction was applied to galaxy radial velocities. The knowledge of an ESO type for each galaxy allowed us to apply an appropriate K-correction $K(z,T)$ [7], to calculate the absolute magnitude. We have selected eight volume and magnitude limited subsamples of the SSRS2 whose main characteristics are defined in Table 1.

Table 1. Subsamples of the SSRS2.

D ($h^{-1}Mpc$)	$M <$	N_g	$\bar{n}$	s_0 ($h^{-1}Mpc$)	γ	σ_8^2
38.35	-17.5	329	1.55×10^{-2}	4.2±1.1	1.7±0.3	
47.83	-18.0	487	1.18×10^{-2}	3.9±0.2	1.9±0.2	0.3
59.52	-18.5	774	9.74×10^{-3}	4.8±0.5	1.3±0.1	0.5
73.86	-19.0	770	5.07×10^{-3}	5.5±0.4	1.4±0.1	0.7
91.37	-19.5	755	2.63×10^{-3}	5.8±0.6	1.7±0.2	0.8
112.6	-20.0	593	1.10×10^{-3}	5.5±0.6	2.0±0.3	0.8
138.12	-20.5	268	2.70×10^{-4}	8.0±0.4	2.0±0.2	1.5
168.52	-21.0	133	7.37×10^{-5}	15.8±2.9	1.5±0.3	2.9

We will present the correlation analysis of data following two different techniques: first calculating the two-point correlation function, counting the number of galaxy pairs in shells of radius s, and secondly computing the variance $\bar{\xi}(s)$ derived from the counts in cells analysis. They are both related in the power law approximation of the correlation function.

We have calculated the two-point correlation function with the algorithm proposed by [8] in order to minimize the uncertainties on $\xi(s)$ due to fluctuations in the mean density:

$$\xi = \frac{N_{gg} N_{rr}}{N_{rg}^2} - 1$$

As working with volume limited samples, we used uniform weighting.

From the pair counts in shells, we have derived by direct summation the J_3 integral, defined as: $J_3(s) = \int_0^s s^2 \xi(s) ds$. It is directly related to the average number of neighbours N_{neigh} of a galaxy within a sphere of radius s: $N_{neigh} = nV + n\int_0^s \xi(s) dV = nV(1 + J_3/V)$, where the second term of this relation represents the excess of mean number of neighbours in a sphere centered on a galaxy relative to the Poisson case. We have used this quantity, smoother than the direct correlation function, for making ratios for different subsamples, in order to determine a relative bias.

Another way of investigating clustering is to compute the variance of the counts in randomly placed spheres which can be expressed as $\Delta^2 = \bar{N}(1+N_c)$, where $N_c = nV\bar{\xi}$ is the mean number of objects in excess of random in a sphere, and $\bar{\xi}(s)$ the volume average of the correlation function.

In the power law approximation for the two-point correlation function $\xi(s) = (s_0/s)^\gamma$, $J_3(s)/V$ and $\bar{\xi}(s)$ are proportional to $\xi(s)$ and the results from the two analysis can be compared alltogether .

three different volumes ($D = 60h^{-1}Mpc$, $D = 74h^{-1}Mpc$, $D = 91h^{-1}Mpc$). For each volume we present two contiguous magnitude bins of 1 magnitude wide. The number of galaxies in each luminosity bin was adequate for the calculation of $\xi(s)$. The depth was chosen to correspond to the maximum distance at which the faintest galaxies considered are visible. Dividing the sample like this allows to test for a luminosity segregation in a way that it is independent of sampling variations.

Our results show that for the first two volumes ($D = 60h^{-1}Mpc$ and $D = 74h^{-1}Mpc$), we cannot detect any significant differences in the amplitude of $\xi(s)$ suggesting that there is little difference in the clustering of galaxies fainter than -20. The behavior changes quite dramatically for galaxies brighter than -20.5 relative to fainter galaxies as can be seen in panel (c) of figure 2.

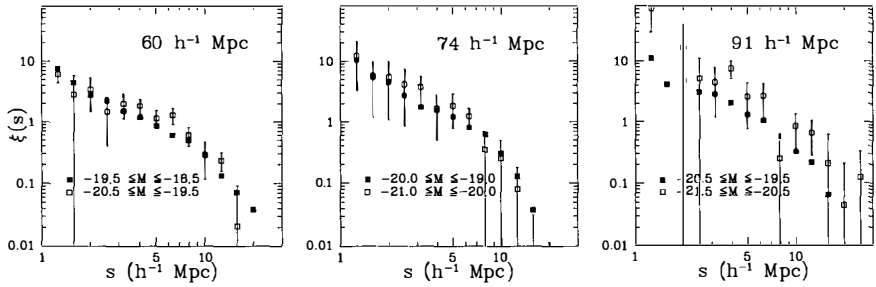


Figure 2: The redshift-space two-point correlation function. Testing the luminosity effect in subsamples of different depths.

The present analysis has been performed in 'redshift space', therefore are expected to be distorted by peculiar velocities. We will analyse in a forthcoming paper [11] how previous effects are affected by redshift space distorsions and remain valid in real space.

4 Luminosity Biasing

The previous tests allows us to interpret the effect of the figure 1 mostly as a dependence of the clustering amplitude of galaxies on luminosity. Here, we would like to determine the relative bias as a function of luminosity. In order to work with relatively smoothed quantities, we have used the J_3 integral (figure 3a).

We define the relative bias

$$\frac{b}{b^*}(s) = \sqrt{\frac{J_3(s)}{J_3^*(s)}}$$

where b is the bias of the galaxies brighter than M, b^* is the bias of the galaxies brighter than M^* (-19.5), J_3^* is the J_3 integral of the galaxies brighter than M^*.

Figure 3b shows that b/b^* is roughly scale independent for all the subsamples between 2 and $13h^{-1}Mpc$. We have thus calculated the mean value of b/b^* over this scale range (figure 3c). This mean relative bias remains quite flat at faint luminosities and increases rapidly for the

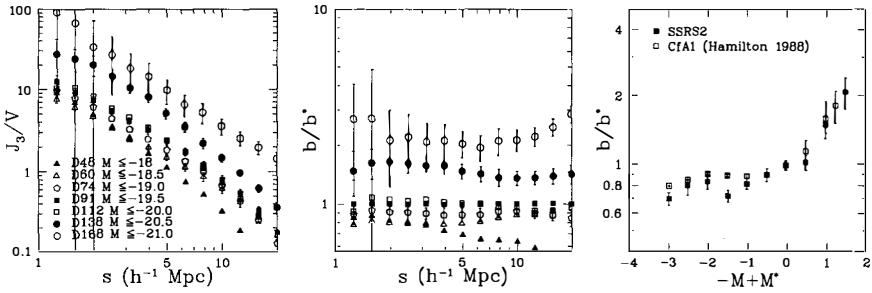


Figure 3: J_3/V (a), the relative bias b/b^* as a function of scale (b), and after averaging over s, the relative bias as a function of the absolute magnitude (c), for the different subsamples as defined in Table 1.

galaxies brighter than M^*, reaching 1.5 for the galaxies brighter than -20.5, and 2 for those brighter than -21.

5 Comparison to previous results and models

Luminosity bias has been evidenced on several wide angle galaxy redshift surveys. The increase of the amplitude of the correlation with the depth and luminosity of the sample has already been shown by [12] on the first diameter-limited SSRS for subsamples ranging from $39h^{-1}Mpc$, $M \leq -18.5$ to $80h^{-1}Mpc$, $M \leq -20.0$. [13] found an amplification factor of about 2 for the J_3 integral from the shallower to the deeper sample, which was shown by [14] to be mostly a luminosity bias. The SSRS2, complete to a fainter magnitude, $m_b = 15.5$, has allowed to confirm this trend for deeper subsamples and with a better accurancy, and to pursue the test up to very bright galaxies, as $M < -20.5$ which reveal a much stronger effect.

Our results are in good agreement with those of [8] on the CfA (figure 3c), who shows a progressive increase of $\xi(s)$ with L for very bright galaxies ($M \leq -20.5$). [2] showed a clear luminosity bias for galaxies brighter than L^* on the power spectrum in volume-limited samples of the CfA2 redshift survey. There are some differences in the singular samples and luminosities at which the effect occurs: but they use a different cut-off in luminosity for selecting 'bright' and 'faint' galaxies, as well as a different way of correcting for k-dimming. So a quantitative comparison is difficult to do. However the same remarkable constancy of bias with scale is evidenced, and the amplification factor of ~ 1.4 between their subsamples at $101h^{-1}Mpc$, $M \leq -19.7$ and $130h^{-1}Mpc$, $M \leq -20.3$ is consistent with our findings.

The recent analysis of the correlation function on the Stromlo-APM redshift survey by Loveday et al (1995) has shown too a luminosity bias in redshift space, but with different characteristics. Galaxies brighter than L^* ($-20 \leq M \leq -19$) are shown to be more clustered than fainter ones ($-19 \leq M \leq -15$), but there is no evidence of increasing the strength of the clustering for $L > L^*$.

6 Conclusion

Independently from the statistical indicator, two-point correlation function $\xi(s)$ or the variance of counts in cells $\bar{\xi}(s)$, we show the existence of a luminosity segregation in the SSRS2, which is particularly strong for the galaxies brighter than M^*. This segregation is characterized by a correlation length, s_0, going from about $5h^{-1}Mpc$, for the faintest galaxies, up to $8h^{-1}Mpc$ for the galaxies brighter than -20.5, and even $15.8h^{-1}Mpc$, for the galaxies brighter than -21. In parallel to this increase of the correlation length, we do not detect any significant tendency for the slope, γ of the correlation function.

References

[1] Hamilton, A.J.S., 1988, *Astrophys. J.* **331**, L59

[2] Park, C., Vogeley, M.S., Geller, M.J., Huchra, J.P., 1994, *Astrophys. J.*, preprint

[3] Maurogordato, S., & Lachièze-Rey, M., 1991, *Astrophys. J.* **369**, 30

[4] Alimi, J.M., Valls-Gabaud, D. & Blanchard, A., 1988, *Astr. Astrophys.* **206**, L11

[5] Loveday, J., Maddox, S.J., Efstathiou, G., Peterson, B.A., 1995, *Astrophys. J.* **442**, 457

[6] da Costa, N.L., Geller, M.J.,Pellegrini, P.S., Latham, D.W., Fairall, A.P., Marzke, R.O., Willmer, C.N.A., Huchra, J.P., Calderon, J.H., Ramella, M. & Kurtz, M.J., 1994, ApJ Letters, 424, L1

[7] Efstathiou, G., Ellis, R.S.& Peterson, B.A., 1988, *Mon. Not. R. astr. Soc.* **232**, 43

[8] Hamilton, A.J.S., 1993, *Astrophys. J.* **417**, 19

[9] Marzke, R.O., Geller, M.J., da Costa, L.N., & Huchra, J.P., 1994, CFA preprint

[10] da Costa, L.N., Vogeley, M., Geller, M.J., Huchra, J., & Park, C., 1995, ApJ

[11] Benoist, C., Maurogordato, S., da Costa, N.L., Cappi, A., & Schaeffer, R. 1995, in preparation

[12] Davis, M., Meiksin, A., Strauss, M.A., da Costa, N.L., & Yahil, A., 1988, *Astrophys. J.* **333**, L9

[13] Maurogordato, S., Schaeffer, R., & da Costa. L.N., 1992, *Astrophys. J.* **390**, 17

[14] Lachièze-Rey, M., da Costa, L.N., & Maurogordato, S., 1992, *Astrophys. J.* **399**, 10



CONSTRAINING OMEGA AND BIAS FROM THE STROMLO-APM SURVEY

J. Loveday
Fermilab, Batavia, USA.



Abstract

Galaxy redshift surveys provide a distorted picture of the universe due to the non-Hubble component of galaxy motions. By measuring such distortions in the linear regime one can constrain the quantity $\beta = \Omega^{0.6}/b$ where Ω is the cosmological density parameter and b is the (linear) bias factor for optically-selected galaxies. In this paper we estimate β from the Stromlo-APM redshift survey by comparing the amplitude of the direction-averaged redshift space correlation function to the real space correlation function. We find a 95% confidence upper limit of $\beta = 0.75$, with a 'best estimate' of $\beta \approx 0.48$. A bias parameter $b \approx 2$ is thus required if $\Omega \equiv 1$. However, higher-order correlations measured from the APM galaxy survey [9] indicate a low value for the bias parameter $b \approx 1$, requiring that $\Omega \lesssim 0.6$.

1 Introduction

Galaxy redshift surveys can provide some of the most important constraints on theories of large-scale structure, but they must be analysed with care. For pure, unperturbed Hubble flow, galaxy clustering measured in both real space and redshift space would be identical and isotropic. However, in practice, peculiar velocities distort the redshift space correlation function. Since the amplitude of peculiar velocities depends on the cosmological density parameter Ω, by measuring this distortion we can hope to constrain the value of Ω. On small scales, the effect of peculiar velocities is to elongate clusters of galaxies along the line of sight in redshift space, leading to the well known 'fingers of God'. However, on large scales, coherent bulk flows dominate the peculiar velocity field resulting in a *compression* in the clustering pattern along the line of sight. This is illustrated for Stromlo-APM Survey galaxies in Figure 1, where we show a contour plot of the full redshift space correlation function $\xi(\sigma, \pi)$ as a function of separation

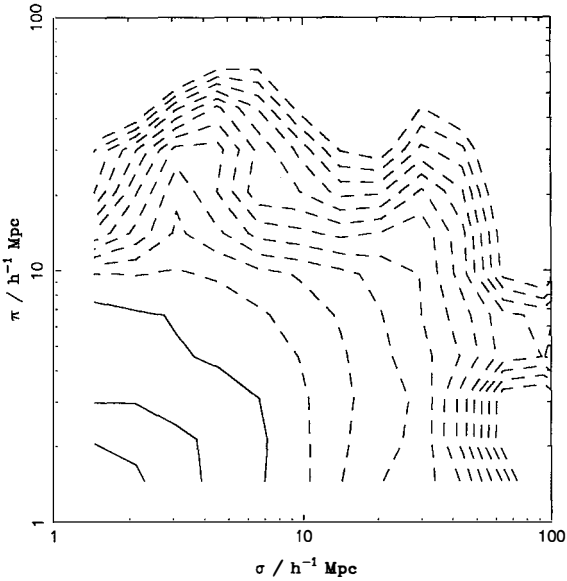


Figure 1: A smoothed contour plot of the full redshift space correlation function $\xi(\sigma,\pi)$ measured from the Stromlo-APM Redshift Survey as a function of separation parallel (π) and perpendicular (σ) to the line of sight. The contours are plotted in fixed steps in $\log\xi$ from -3 to 1. Solid contours show values $\xi \geq 1$, dashed contours show values $\xi < 1$ (*i.e.* in the linear regime).

parallel (π) and perpendicular (σ) to the line of sight. A compression of the low-amplitude ξ contours in the π direction compared with the σ direction is clearly visible for $\pi \gtrsim 10h^{-1}$Mpc.

This large-scale anisotropy in redshift space clustering is most naturally expressed in terms of the power spectrum. Kaiser [14] has shown that in the linear regime of gravitational instability models, the power spectra in redshift space, $P_s(\mathbf{k})$ and real space $P_r(\mathbf{k})$ are simply related by

$$P_s(\mathbf{k}) = (1+\beta\mu_{\mathbf{k}}^2)^2 P_r(\mathbf{k}), \tag{1}$$

where $\mu_{\mathbf{k}}$ is the cosine of the angle between the wavevector $\mathbf{k}$ and the line of sight. The amplitude of the distortion is determined by the parameter $\beta = f(\Omega)/b$, where $f(\Omega) \approx \Omega^{0.6}$

is the dimensionless growth rate of growing modes in linear theory. The bias parameter b relates the fluctuations in galaxy density to the underlying mass density in the linear regime, $\delta_g = b\delta_\rho$ for linear bias. Several practical methods for measuring β have recently been applied: measuring the anisotropy of the correlation function [10, 11, 7, 18], the anisotropy of the power spectrum [2, 3, 22] and spherical harmonics of the density field [8, 12]. Unfortunately, measured anisotropies in redshift space clustering are strongly perturbed by non-linear effects on scales up to $r \sim 30h^{-1}$Mpc [2, 18], and so one needs to be able to measure anisotropies reliably on scales $r \gtrsim 30h^{-1}$Mpc in order for equation (1) to be valid.

As well as causing anisotropy in redshift space, large-scale streaming motions also produce an amplification in the direction-averaged redshift space correlation function. Fortunately, the direction-averaged correlation function is only affected by non-linearities on scales $r \lesssim 5h^{-1}$Mpc [18]. For fluctuations in the linear regime, the direction-averaged redshift space correlation function $\xi(s)$ and the real space correlation function $\xi(r)$ are related by [14],

$$\xi(s) \approx \left(1 + \frac{2}{3}\beta + \frac{1}{5}\beta^2\right)\xi(r). \qquad (2)$$

The large uncertainty in the value of β hinders comparison of $\xi(s)$ with real space predictions of galaxy clustering from various models [15]. In a recent paper [17], we estimated the real-space correlation function of optically-selected galaxies by cross-correlating galaxies in the sparse-sampled Stromlo-APM Redshift Survey with the fully-sampled, parent APM Galaxy Survey. This projected cross-correlation function is unaffected by redshift-space distortions and may be stably inverted to give the real-space correlation function $\xi(r)$. Moreover, the large number of cross-pairs enables clustering to be measured to smaller scales than using the redshift survey data alone. If both $\xi(r)$ and $\xi(s)$ can be reliably measured in the linear regime then the value of β can be constrained using equation (2).

The above formula assumes a plane-parallel approximation for peculiar displacements. In order to approximate this ideal in our analysis, we use only those pairs of galaxies separated by less than 50 degrees on the sky. This rejects about 20% of galaxy pairs, and, as shown in [2], will limit deviations from the plane-parallel approximation to cause no more than a 5% bias in the estimated value of β.

Equation (2) also assumes that linear theory is valid on scales on which ξ can be reliably measured. In order to check the validity of this assumption, we have analyzed an ensemble of CDM-like N-body simulations [4]. See [18] for a description and analysis of the simulations.

2 Stromlo-APM Survey Data

The Stromlo-APM redshift survey consists of 1787 galaxies with $b_J \leq 17.15$ selected randomly at a rate of 1 in 20 from the APM (Automated Plate Measuring) galaxy survey [19, 20]. The survey covers a solid angle of 1.3 sr (4300 square degrees) in the south galactic cap. The APM magnitudes have been calibrated and corrected for photographic saturation using CCD photometry as described in [16]. An approximate morphological type was assigned to each galaxy by visually inspecting the images on the United Kingdom Schmidt Telescope (UKST) survey plates. Redshifts were obtained with the Mount Stromlo-Siding Spring Observatory (MSSSO) 2.3m telescope at Siding Spring. Measured radial velocities were transformed to the local group frame using $v = v + 300\sin(l)\cos(b)$ and we assumed $\Lambda = 0$, $q_0 = 0.5$ and $H_0 = 100$ km s^{-1}Mpc^{-1} with uniform Hubble flow in calculating distances and absolute magnitudes. We adopt k-corrections for different morphological types in the b_J system [6]. More details about the survey are given in ref [16]. Error bars on measurements from survey data are estimated using the bootstrap resampling technique [1] with nine bootstrap resamplings of the survey.

3 Results

3.1 Constraints on β

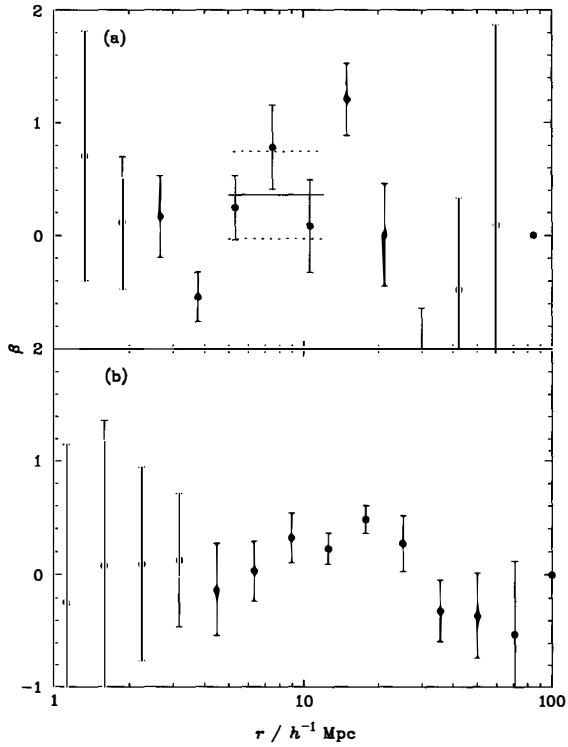


Figure 2: (a) Estimates of β as a function of separation for the Stromlo-APM survey data using $\xi(s)$ and $\xi(r)$ in equation (2). The horizontal line shows the maximum-likelihood fit to β over the range indicated and the dotted lines show 95% confidence limits on β. (b) Same as (a), but using the volume integrals J_3 in place of ξ.

In Figure 2*a*, we plot our estimates of β from the redshift survey, as determined from the ratio $\xi(s)/\xi(r)$. The redshift space correlation function $\xi(s)$ has been calculated in the usual way, directly from the redshift survey data. The real space correlation function $\xi(r)$ has been calculated via inversion of the projected cross-correlation function with the parent APM galaxy catalogue [17]. Although there is quite a wide scatter in the β estimates on different scales, there is no obvious systematic trend with separation, and so we have calculated the maximum-

likelihood value of β using the three data points in the range 5–12 h^{-1}Mpc, since analysis of the N-body simulations [18] shows that $\xi(s)$ and $\xi(r)$ are essentially unaffected by non-linearity on scales $r \gtrsim 5h^{-1}$Mpc. We find $\beta = 0.36$ with 95% confidence limits -0.03–0.75.

One may obtain a less noisy estimate of β by replacing the correlation functions $\xi(s)$ and $\xi(r)$ in equation (2) with the integrated quantities $J_3(s)$ and $J_3(r)$, where $J_3(r) = \int_0^r x^2\xi(x)dx$. Analysis of the N-body simulations [18] shows that the J_3 integrals are unaffected by non-linear effects on scales $r \gtrsim 15h^{-1}$Mpc. Using the $J_3(s)/J_3(r)$ ratio (Fig. 2*b*), we find a value of $\beta = 0.48 \pm 0.12$ at $r = 17.8h^{-1}$Mpc. Our measurements of $\xi(r)$ and hence $J_3(r)$ are not expected to be reliable on scales $r \gtrsim 20h^{-1}$Mpc [17], and hence we do not regard the downturn in β on these scales as being significant.

Both $\xi(s)/\xi(r)$ and $J_3(s)/J_3(r)$ estimates of β give consistent results and exclude the possibility of $\beta \gtrsim 0.75$ at very high confidence.

3.2 Disentangling Ω and b

Ideally, of course, one would like to know the values of the density parameter Ω and the bias parameter b individually. Dekel (these proceedings) describes how peculiar velocity maps can be used to estimate Ω independently of b, and Cole *et al.* [2] have discussed how it may be possible with future redshift surveys to separate the determination of Ω and b by studying the scaling of non-linear effects. An alternative approach is the study of high order correlations to constrain the (possibly non-linear) biasing model using weakly non-linear perturbation theory. Gaztañaga and Frieman [9] have used high order moments of APM galaxies to constrain biasing models. To be consistent with non-linear perturbation theory, one should allow the possibility of *non-linear* bias, in which case second- and third-order non-linear bias coefficients can be chosen which match the observed high order correlations. However, the observations are very well fit by an *unbiased*, low-density CDM model with $b \approx 1$. Applying Occam's razor, this seems the more natural solution.

4 Conclusions

Measuring the projected cross-correlation function of Stromlo-APM galaxies with the parent APM galaxy survey enables a reliable determination of $\xi(r)$ on linear scales $r \gtrsim 5h^{-1}$Mpc. The ratio $\xi(s)/\xi(r)$ on scales 5–12 h^{-1}Mpc yields a value $\beta \approx 0.36$. The integral J_3 is less noisy than $\xi(r)$ and on a scale $r \approx 17.8h^{-1}$Mpc $J_3(s)/J_3(r)$ provides the estimate $\beta = 0.48 \pm 0.12$. Although a little lower than estimates of β from peculiar velocity analyses (eg. Hudson *et al.* [13], who find $\beta = 0.74 \pm 0.13$), the large errors on *all* current estimates of β means they are all consistent. See [5, 21] for reviews of recent measurements of β.

The Stromlo-APM survey is a powerful sample for constraining β since the large volume probed allows us to reliably measure redshift space galaxy clustering in the linear regime, whereas many previous analyses have been limited to measuring $\xi(s)$ in the non-linear regime. Cross-correlation with the fully-sampled APM galaxy survey enables us to measure $\xi(r)$ much more accurately than using the angular correlation function $w(\theta)$, and thus the technique of using the ratio $\xi(s)/\xi(r)$ [or $J_3(s)/J_3(r)$] comes into its own for this survey.

With linear theory and 2-point clustering statistics alone one cannot separate the contributions of Ω and b to β. However, as discussed by Gaztañaga and Frieman [9], higher order correlations may be used to constrain biasing models. Their analysis of APM galaxies favours a linear bias parameter $b \approx 1$, although to be strictly self-consistent, one should allow for a non-linear bias model in non-linear perturbation theory, in which case one can always match the

observed skewness of APM galaxy counts in cells by adjusting the non-linear bias parameters. Further work is clearly required in constraining possible biasing models.

In conclusion, we find that a relatively low value of β is favoured by the Stromlo-APM data; we can certainly exclude an unbiased, $\Omega = 1$ model at more than 95% confidence. If galaxies are indeed unbiased tracers of the mass distribution, then $\Omega \lesssim 0.6$.

Acknowledgments. It is a pleasure to thank my collaborators on the Stromlo-APM survey: George Efstathiou, Steve Maddox and Bruce Peterson. My attendance at this meting was supported by generous grants from the EEC and the NSF.

References

[1] Barrow, J.D., Bhavsar, S.P. and Sonoda, D.M., 1984, MNRAS, 210, 19p

[2] Cole, S., Fisher, K.B. and Weinberg, D.H., 1994, MNRAS, 267, 785

[3] Cole, S., Fisher, K.B. and Weinberg, D.H., 1995, submitted to MNRAS

[4] Croft, R.A.C. and Efstathiou, G., 1994, MNRAS, 267, 390

[5] Dekel, A., 1994, ARA&A, 32, 371

[6] Efstathiou, G., Ellis, R.S. and Peterson, B.A., 1988, MNRAS, 232, 431

[7] Fisher, K.B., Davis, M., Strauss, M.A., Yahil, A. and Huchra, J.P., 1994, MNRAS, 267, 927

[8] Fisher, K.B., Scharf, C.A. and Lahav, O., 1994, MNRAS, 266, 219

[9] Gaztañaga, E. and Frieman, J.A., 1994, ApJ, 437, L13

[10] Hamilton, A.J.S., 1992, ApJ, 385, L5

[11] Hamilton, A.J.S., 1993, ApJ, 406, L47

[12] Heavens, A.F. and Taylor, A.N., 1994, submitted to MNRAS

[13] Hudson, M., Dekel, A., Courteau, S., Faber, S.M. and Willick, J.A., 1995, MNRAS, in press

[14] Kaiser, N., 1987, MNRAS, 227, 1

[15] Loveday, J., Efstathiou, G., Peterson, B.A. and Maddox, S.J., 1992, ApJ, 400, L43

[16] Loveday, J., Peterson, B.A., Efstathiou, G. and Maddox, S.J., 1992, ApJ, 390, 338

[17] Loveday, J., Maddox, S.J., Efstathiou, G. and Peterson, B.A., 1995, ApJ, 442, 457

[18] Loveday, J., Efstathiou, G., Maddox, S.J. and Peterson, B.A., 1995, submitted to ApJ

[19] Maddox, S.J., Sutherland, W.J. Efstathiou, G. and Loveday, J., 1990, MNRAS, 243, 692

[20] Maddox, S.J., Efstathiou, G. and Sutherland, W.J., 1990, MNRAS, 246, 433

[21] Strauss, M.A. and Willick, J.A., 1995, submitted to Phys. Rep.

[22] Tadros, H., Efstathiou, G., Loveday, J. and Peterson, B.A., 1995, in preparation

THE POWER SPECTRUM OF GALAXY CLUSTERING IN THE LAS CAMPANAS REDSHIFT SURVEY

H. Lin [1], R. P. Kirshner [1], S. A. Shectman [2], S. D. Landy [2],
A. Oemler [3], D. L. Tucker [4], and P. L. Schechter [5]
[1] *Harvard-Smithsonian Center for Astrophysics, Cambridge, MA, USA.*
[2] *Carnegie Observatories, Pasadena, CA, USA.*
[3] *Dept. of Astronomy, Yale University, New Haven, CT, USA.*
[4] *Astrophysikalisches Institut Potsdam, Potsdam, Germany.*
[5] *Dept. of Physics, Massachusetts Institute of Technology, Cambridge, MA, USA.*



Abstract

We present the power spectrum $P(k)$, over scales $\lambda = 2\pi/k = 5 - 400\ h^{-1}$ Mpc, for a magnitude-limited sample of 19276 Las Campanas Redshift Survey (LCRS) galaxies, with average redshift $z \approx 0.1$. The LCRS $P(k)$ may be approximated as $\propto k^{-1.8}$ for small scales $\lambda = 5 - 30\ h^{-1}$ Mpc, changing to $\propto k^{1\pm1}$ for large scales $\lambda \approx 200 - 400\ h^{-1}$ Mpc. The overall amplitude corresponds to $\sigma_8 = 1$ in redshift space. We also compare our results to those of several other redshift surveys. For $\lambda \lesssim 100\ h^{-1}$ Mpc, the LCRS $P(k)$ is roughly similar in shape to the $P(k)$ of other surveys, but with an amplitude differing from some of the other samples, possibly because of inherent clustering differences among different types of galaxies. For $\lambda \gtrsim 100\ h^{-1}$ Mpc, the LCRS results are consistent with those of other surveys, given the large errors among all the surveys on these scales.

1 The Las Campanas Redshift Survey Data

The Las Campanas Redshift Survey (LCRS) contains 26400 galaxies, with an average redshift $z \approx 0.1$, distributed over 6 $1.5° \times 80°$ slices, 3 each in the North and South galactic caps. The survey galaxies were selected from an R-band CCD photometric catalog, and were chosen using nominal isophotal magnitude limits $16.0 < R < 17.3$ for the initial 20% of the data and $15.0 < R < 17.7$ for the remainder. Spectroscopy was carried out using the multi-object

fiber-optic spectrograph on the Las Campanas 2.5-m telescope. Additional survey details may be found in [5] and [6]. Figure 1 shows the survey's galaxy distribution, revealing a rich pattern of filaments, clusters, and voids.

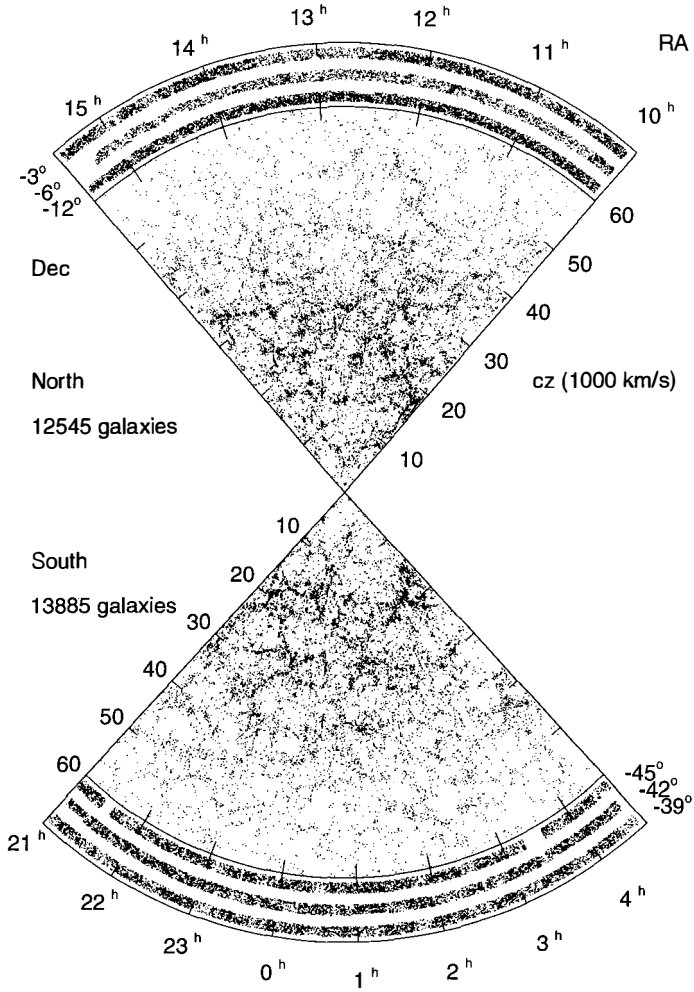


Figure 1. The distribution of galaxies in the LCRS in redshift and right ascension. The distribution of the same galaxies on the sky, in right ascension and declination, is also shown in the outer circular section of the figure.

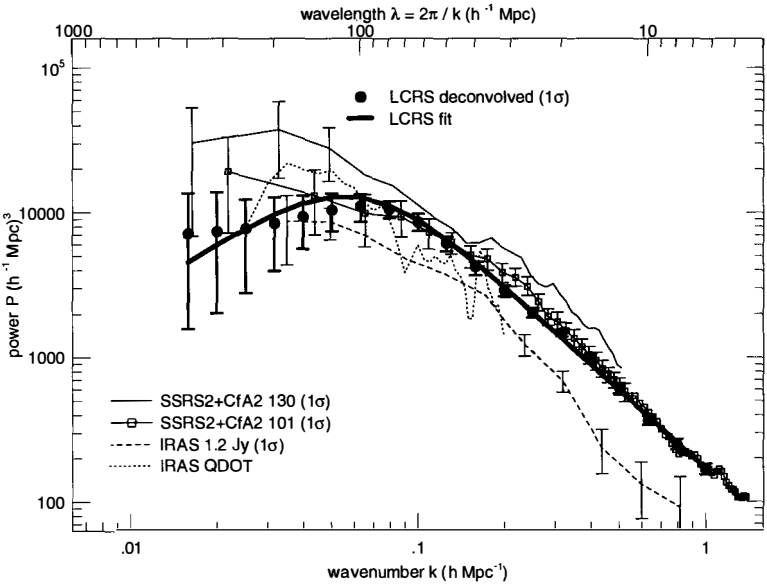


Figure 2. The LCRS power spectrum, obtained from deconvolving or from fitting the directly observed convolved power spectrum, is compared to the power spectra from 4 other redshift survey samples. For clarity some errors bars have been left off the plot.

2 The Power Spectrum of Las Campanas Galaxies

For this analysis we use an apparent-magnitude limited subset of 19276 LCRS galaxies within redshift limits 10000 km/s $< cz <$ 45000 km/s and additional absolute magnitude limits $-22.5 < M_R < -18.5$. We use these limits to keep the survey selection function $\phi \gtrsim 0.05$. To estimate the redshift-space power spectrum we use a method similar to that described in [3]. We have verified our methods and estimated errors using mock redshift surveys drawn from N-body simulations kindly provided by C. Park [4]. Note for an essentially 2D survey geometry like ours, the observed power spectrum differs significantly from the true one because of convolution with the survey window function [3]. We have both deconvolved our observed power spectrum to facilitate comparisons with other surveys, as well as convolved convenient model $P(k)$ to directly fit the observations. The LCRS $P(k)$, shown in Figure 2, may be approximated by $P(k) \propto k^{-1.8\pm0.1}$ for small scales $\lambda = 2\pi/k = 5 - 30\ h^{-1}$ Mpc, and by $P(k) \propto k^{1\pm1}$ for large scales $\lambda \approx 200 - 400\ h^{-1}$ Mpc, with an apparent peak at $\lambda \approx 100\ h^{-1}$ Mpc. However, we want to emphasize that for $\lambda \gtrsim 100\ h^{-1}$ Mpc, the errors are large and we do not claim detection of a turnover, only that our results suggest that $P(k)$ is at least flattening out. The overall amplitude of $P(k)$ may be expressed as $\sigma_8 = 1$ in redshift space. We have also fit our $k \leq 0.1\ h$ Mpc^{-1} data to linear $\Omega + \Lambda = 1$ cold dark matter models, and find $\Omega h = 0.36$.

Figure 2 also shows the power spectra of 2 samples (volume-limited at 130 and 101 h^{-1} Mpc) from the optically-selected Southern Sky (SSRS2) and Center for Astrophysics (CfA2) redshift

surveys [1, 8], and the power spectra of 2 infrared-selected IRAS galaxy surveys, 1.2 Jy [3] and QDOT [2]. On scales $\lambda \lesssim 100\ h^{-1}$ Mpc, the LCRS $P(k)$ is well determined and has an amplitude between that of the SSRS2+CfA2 and IRAS samples. On scales $\lambda \gtrsim 100\ h^{-1}$ Mpc, the LCRS $P(k)$ is consistent with those of the other samples given the large errors common to all the surveys on these scales. The LCRS $P(k)$ agrees best with that of the SSRS2+CfA2 101 sample over most of the range $\lambda = 5 - 150\ h^{-1}$ Mpc. Some of the differences among the surveys have been attributed to inherent differences in clustering amplitude for galaxies of different types. In particular, brighter galaxies may be more strongly clustered than fainter galaxies [4, 1] (*cf.* SSRS2+CfA2 130 and 101) and infrared-selected galaxies seem more weakly clustered than optically-selected galaxies [3] (*cf.* 1.2 Jy and SSRS2+CfA2 or LCRS). In the LCRS there is also evidence for differences in the amplitudes of $P(k)$ among different types of galaxies. Specifically we find roughly a 50% stronger clustering amplitude, relative to our canonical sample, for galaxies brighter than $M_R = -21.5 \approx M_R^* - 1$, as well as an approximately 30% weaker clustering amplitude for emission galaxies with [OII] 3727 equivalent widths > 5 Å. The dependence of clustering on galaxy colors in the LCRS is discussed in [7].

3 Conclusions

We have presented the power spectrum for a sample of 19276 Las Campanas galaxies and compared our results to those of other surveys. For $\lambda \lesssim 100\ h^{-1}$ Mpc, the LCRS $P(k)$ is similar in shape to that of other samples, but with some differences in amplitude that may reflect intrinsic clustering differences for galaxies of different luminosities or types. For $\lambda \gtrsim 100\ h^{-1}$ Mpc, the LCRS results are consistent with those of other surveys given the large errors among all the surveys on these scales. There is a suggestion that the LCRS $P(k)$ is at least flattening out for $\lambda \gtrsim 100\ h^{-1}$ Mpc, but a definitive detection of a turnover will likely require even larger redshift surveys and/or improved power spectrum estimation techniques.

Acknowledgements. The Las Campanas Redshift Survey has been supported by NSF grants AST 87-17207, AST 89-21326, and AST 92-20460. HL also acknowledges support from NASA grant NGT-51093.

References

[1] da Costa, L. N., *et al.*, 1994, *Astrophys. J.* **437**, L1, and this volume

[2] Feldman, H. A., Kaiser, N., and Peacock, J. A., 1994, *Astrophys. J.* **426**, 23

[3] Fisher, K. B., *et al.*, 1993, *Astrophys. J.* **402**, 42

[4] Park, C., Vogeley, M. S., Geller, M. J., and Huchra, J. P., 1994, *Astrophys. J.* **431**, 569

[5] Shectman, S. A., Landy, S. D., Oemler, A., Tucker, D. L., Kirshner, R. P., Lin, H., and Schechter, P. L., 1995, to appear in *Wide-Field Spectroscopy and the Distant Universe*, eds. S. J. Maddox and A. Aragón-Salamanca, World Scientific

[6] Shectman, S. A., Schechter, P. L., Oemler, A., Tucker, D., Kirshner, R. P., and Lin, H., 1992, in *Clusters and Superclusters of Galaxies*, p. 351, ed. A. C. Fabian, Kluwer

[7] Tucker, D. L., *et al.*, this volume

[8] Vogeley, M. S., this volume

LARGE-SCALE COLOR-SEGREGATION IN THE LAS CAMPANAS REDSHIFT SURVEY

D. L. Tucker [1], A. A. Oemler, Jr. [2], R. P. Kirshner [3], H. Lin [3],
S. A. Shectman [4], S. D. Landy [4], and P. L. Schechter [5]
[1] *Astrophysikalisches Institute Potsdam, Potsdam, Germany.*
[2] *Dept. of Astronomy, Yale University, New Haven, CT, USA.*
[3] *Harvard-Smithsonian Center for Astrophysics, Cambridge, MA, USA.*
[4] *Carnegie Observatories, Pasadena, CA, USA.*
[5] *Dept. of Physics, Massachusetts Institute of Technology, Cambridge, MA, USA.*



Abstract

The Las Campanas Redshift Survey (LCRS) is a galaxy survey which extends to a redshift of 0.2 and which is composed of a total of 6 alternating $1.5° \times 80°$ Slices in the North and South Galactic Caps. To date, approximately 26,400 galaxy redshifts have been compiled. Combining b_J–band photometry from the Automated Plate Measuring machine (APM) Galaxy Survey with LCRS R–band photometry has permitted the derivation of $(b_J - R)_o$ rest-frame colors for galaxies in the LCRS $\delta = -39°$ Slice. It is observed that red galaxies [$(b_J - R)_o > 1.25$] cluster more strongly than blue galaxies [$(b_J - R)_o \leq 1.05$] on small scales ($\lesssim 10h^{-1}$ Mpc), but that, on larger scales, there is little evidence for color-segregation.

1 Motivation

Why study color-segregation? First of all, since galaxy color is a rough function of Hubble type — early-type galaxies tend to be red and late-type galaxies tend to be blue — color-segregation should be related to morphological segregation. In analogy to the observed dependence of morphology on environment, one expects that blue galaxies will tend to prefer the field, and red galaxies dense regions like the cores of rich clusters. Therefore, a study of color-segregation may provide clues for the understanding of the much-debated morphology-environment effect. (For a review of the controversy, see [4].)

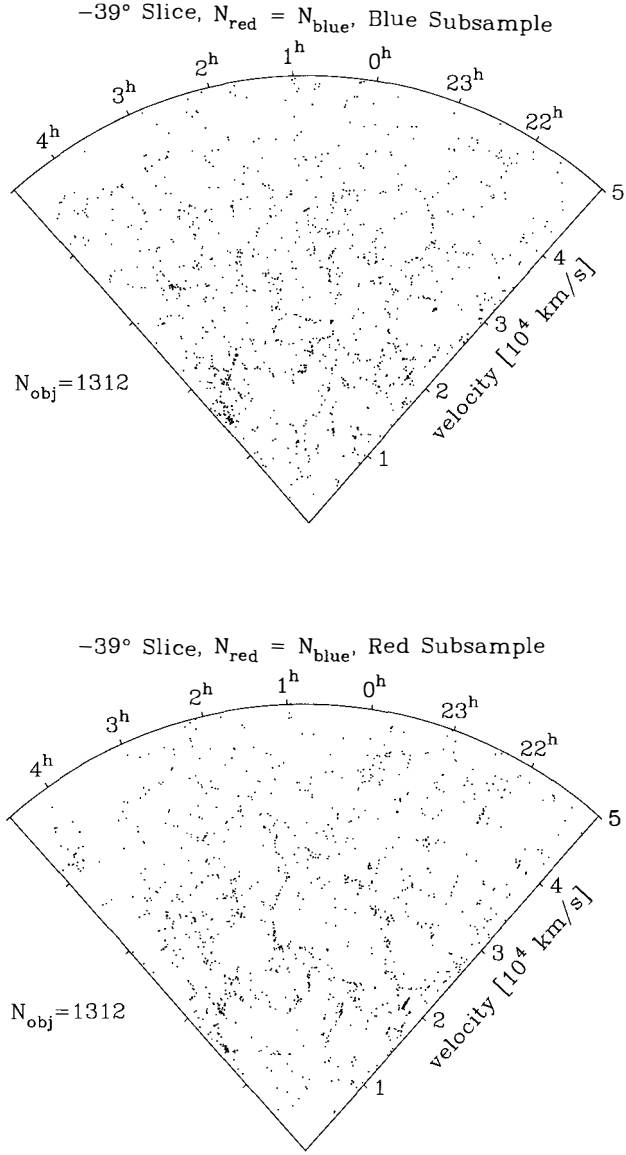


Fig. 1. Velocity/right ascension maps for (a) the Blue Subsample [$(b_J - R)_o \leq 1.05$] and (b) the Red Subsample [$(b_J - R)_o > 1.25$]. A random set of galaxies has been culled from the more numerous Red Subsample so that $N_{red} = N_{blue}$.

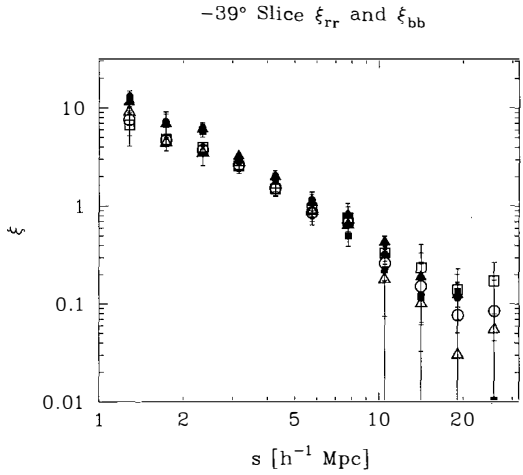


Fig. 2. ξ_{rr} (*filled symbols*) and ξ_{bb} (*unfilled symbols*) for the LCRS −39° Slice. The three different symbol shapes — squares, circles, and triangles — denote the three separate weighting schemes discussed by de Lapparent *et al.* [1]. Squares correspond to de Lapparent *et al.*'s ξ_{11}, circles to their $\xi_{1\phi}$, and triangles to their $\xi_{\phi\phi}$. The general results for the LCRS ξ_{rr} and ξ_{bb} are independent of the weights employed.

Secondly, the study of color-segregation has certain advantages over that of morphological segregation. Galaxy color is a simpler concept than that of galaxy morphology. Whereas Hubble type is a subjective classification which depends upon a variety of parameters (*e.g.*, the presence or lack of a disk, gas and dust content, stellar populations, bulge-to-disk ratio, the weariness of the human classifier, *etc.*), galaxy color is an objective and quantitative measure which depends primarily on a galaxy's recent star formation history. Thus, with fewer parameters to disentangle, color-segregation may be the easier effect to understand.

2 Data, Results, and Conclusions

In this study, we consider the Las Campanas Redshift Survey (LCRS) Slice at $\delta = -39°$. This Slice is 1.5° thick and 80° wide; it contains $\sim$ 3900 galaxies with $cz \leq 50,000$ km/s. (Additional details regarding the LCRS can be found in [2], [5], and [6].)

The Automated Plate Measuring machine (APM) Galaxy Survey is a sky survey which contains $\sim$ 2,000,000 galaxies in the South Galactic Cap [3]. A data trade with the APM Galaxy Survey has permitted, by the combination of APM b_J- and LCRS R-band photometry, the derivation of rest-frame (*i.e.*, k-corrected) colors for $\sim$ 90% of the −39° Slice galaxies. The data have been separated into a "Blue Subsample" [$(b_J - R)_o \leq 1.05$; Figure 1a] and a "Red Subsample" [$(b_J - R)_o > 1.25$; Figure 1b]; the interval $1.05 < (b_J - R)_o \leq 1.25$ was excluded in order to prevent contamination between the two subsamples. In Figure 1b, a random set of red galaxies has been culled, so that $N_{red} = N_{blue}$, in order to eliminate a visual bias which would make a more numerous set of galaxies appear more clustered than a less numerous set.

This simplifies the visual comparison of the two subsamples. Note that, although red and blue galaxies both trace the same large-scale structures, the blue galaxies tend to trace them more diffusely.

The fact that the red galaxies cluster more strongly on small scales ($\lesssim 10h^{-1}$ Mpc) is confirmed by the relative amplitudes of the "red-red" and the "blue-blue" autocorrelation functions (Figure 2). Note, however, that the difference between ξ_{rr} and ξ_{bb} seems to disappear at separations of about $8-10h^{-1}$ Mpc. On larger scales, noise dominates, but the data are not inconsistent with $\xi_{rr} \approx \xi_{bb}$.

To conclude, then, it appears that red galaxies cluster more strongly than do blue galaxies on small scales ($\lesssim 10h^{-1}$ Mpc, or roughly the width of a void wall). On larger scales, however, there is little evidence for color-segregation.

Acknowledgments. The Las Campanas Survey has been supported by NSF grants AST 87-17207, AST 89-21326, and AST 92-20460. One of us (DLT) also wishes to thank the Astrophysikalisches Institut Potsdam for its support, in the form of a post-doctoral research fellowship, of his continued work on the Las Campanas Survey data set. Special thanks are also due to Steve Maddox and Will Sutherland of the APM Galaxy Survey group, without whose help this project would not have been possible.

References

[1] de Lapparent, V., Geller, M. J., and Huchra, J. P., 1988, *Astrophys. J.* **332**, 44

[2] Lin, H., Kirshner, R. P., Shectman, S. A., Landy, S. D., Oemler, A. A., Tucker, D. L., and Schechter, P. L., this volume

[3] Maddox, S. J., Sutherland, W. J., Efstathiou, G., and Loveday, J., 1990, *Mon. Not. R. Astr. Soc.* **243**, 692

[4] Oemler, A. A., Jr. 1992, in *Clusters and Superclusters of Galaxies*, p. 29, ed. A. C. Fabian, Kluwer

[5] Shectman, S. A., Landy, S. D., Oemler, A. A., Tucker, D., Kirshner, R. P., Lin, H., and Schechter, P. L., 1995, to appear in the proceedings of the 35th Herstmonceux Conference, *Wide Field Spectroscopy and the Distant Universe*, in press

[6] Shectman, S. A., Schechter, P. L., Oemler, A. A., Tucker, D., Kirshner, R. P., and Lin, H., 1992, in *Clusters and Superclusters of Galaxies*, p. 351, ed. A. C. Fabian, Kluwer

FIRST RESULTS FROM THE ESO SLICE PROJECT (ESP)

E. Zucca[1], G. Vettolani[1], A. Cappi[2], R. Merighi[2], M. Mignoli[2], G. Stirpe[2], G. Zamorani[2], H. MacGillivray[3], C. Collins[4], C. Balkowski[5], J. Alimi[5], V. Cayatte[5], P. Felenbok[5], S. Maurogordato[5], D. Proust[5], G. Chincarini[6], L. Guzzo[6], D. Maccagni[7], R. Scaramella[8], A. Blanchard[9], M. Ramella[10]

[1] *Istituto di Radioastronomia del CNR, Bologna, Italy*
[2] *Osservatorio Astronomico di Bologna, Bologna, Italy*
[3] *Royal Observatory Edinburgh, Edinburgh, United Kingdom*
[4] *Liverpool John Moores University, Liverpool, United Kingdom*
[5] *DAEC, Observatoire de Paris-Meudon, Meudon, France*
[6] *Osservatorio Astronomico di Brera, Milano, Italy*
[7] *Istituto di Fisica Cosmica e Tecnologie Relative, Milano, Italy*
[8] *Osservatorio Astronomico di Roma, Monteporzio Catone, Italy*
[9] *Universitè Louis Pasteur, Strasbourg, France*
[10] *Osservatorio Astronomico di Trieste, Trieste, Italy*



Abstract

The ESO Slice Project (ESP) is a galaxy redshift survey we are accomplishing as an ESO Key–Project over about 30 square degrees, in a region near the South Galactic Pole. The limiting magnitude is $b_J = 19.4$. Observations were completed in October 1994 and all the obtained data have been just reduced, providing 3348 galaxy redshifts. We present some preliminary results concerning the large scale galaxy distribution and the luminosity function.

1 Introduction

In 1991 we started a galaxy redshift survey over a strip of $22^\circ \times 1^\circ$ (plus a nearby area of $5^\circ \times 1^\circ$, five degrees west of the strip) in the South Galactic Pole region. The right ascension limits are 22^h30^m and 01^h20^m, at a mean declination of -40° (1950). We have filled this area with a regular grid of circular fields with a diameter of 32 *arcmin*, corresponding to the field of view of the multifiber spectrograph OPTOPUS.

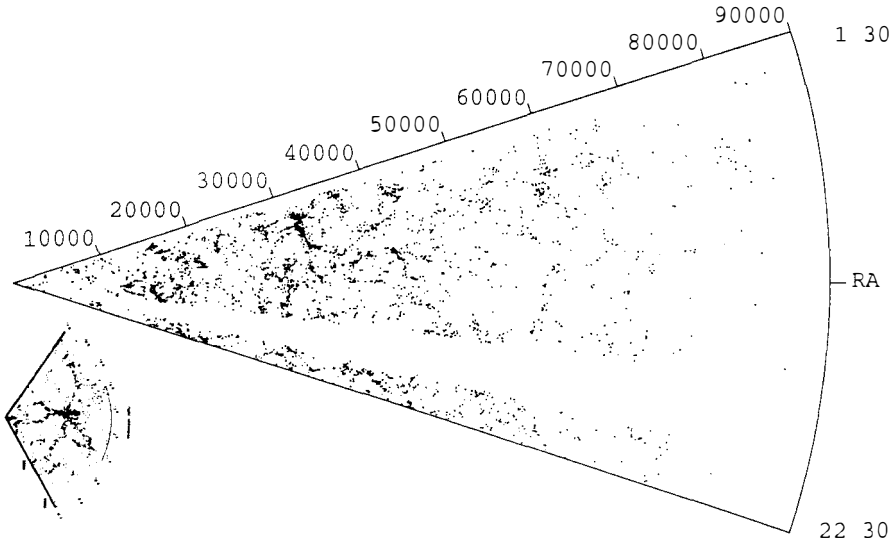


Fig. 1: Wedge diagram in the region $22^h30^m < \alpha < 1^h30^m$ and $-40°45' < \delta < -39°45'$ of the ESP survey.

We have selected the target objects from the Edinburgh–Durham Southern Sky Galaxy Catalogue [4]. The limiting magnitude of the survey is $b_J \leq 19.4$, which optimizes the number of fibers of the spectrograph and corresponds to an effective depth of $\sim 600\ h^{-1}\ Mpc$.
At $z \simeq 0.1$, which corresponds to the peak of the selection function of the survey, the linear dimensions of the main strip are of the order of $110 \times 5\ h^{-1}\ Mpc$, and therefore we sample a volume of $\sim 1.5 \times 10^5\ h^{-3}\ Mpc^3$.

2 Observations and Data Reduction

The observations have been obtained with the multifiber spectrograph OPTOPUS at the Cassegrain focus of the ESO $3.6m$ telescope at La Silla. OPTOPUS has 50 fibers (2.4 *arcsec* diameter) which are manually plugged into holes drilled in aluminum plates. During the last observing run, in order to recover the spectra of missed, sparse objects, we also used MEFOS (at the same telescope), which has 29 fibers moved by mechanical arms over a 1 degree diameter field.
The spectra cover the wavelength range from 3730 Å to 6050 Å, with an effective resolution of about 3.5 Å. Spectra are flat–fielded, extracted and wavelength calibrated. Then the relative transmission of each fiber is computed by normalizing each spectrum through the flux of the OI λ5577 and Na λ5891 sky lines.
After subtraction of the average sky from the galaxy plus sky spectra (the accuracy of the sky subtraction is in the range 2–5%), the redshifts are measured by cross–correlating the spectra with a set of template stars observed by us with the same instrument. The redshifts from emission lines (when present) are also measured, as well as the equivalent width of the most

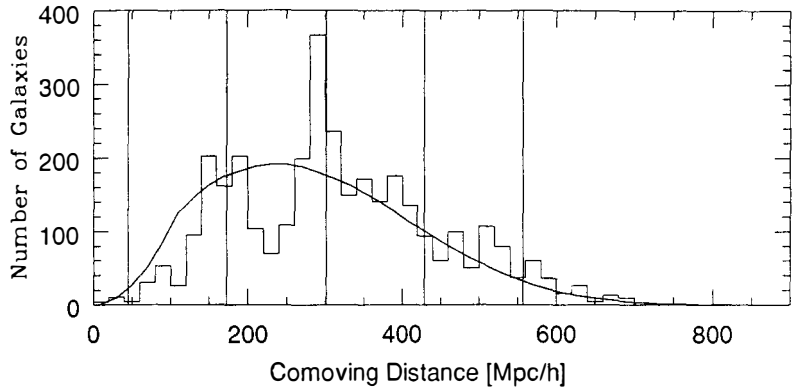


Fig. 2: Galaxy distribution in comoving distance ($q_0 = 0.5$). The solid line shows the expectation resulting from a uniform distribution of the galaxies in the sample. Vertical lines correspond to the position of the BEKS peaks (see text).

common emission lines.
The median error in velocity for the total sample is $\sim$ 50 km/s and more than 80% of the observed fields have a redshift completeness greater than 80%.

3 Large–scale Properties

In Figure 1 it is shown the wedge diagram of the 3348 measured galaxies and on the same scale it is reported, for comparison, the wedge diagram of the CfA2 survey ($m_{lim} = 15.5$). From this figure it is clear that the ESP sample is not contaminated anymore by the local structures, as it happened in almost all previous surveys, and so it will be possible to use these data to obtain information on the large–scale structure unbiased by nearby inhomogeneities.
The histogram in Figure 2 shows the distribution in comoving distance ($q_o = 0.5$) of these galaxies. Note that the outstanding peak at $D \simeq 300\ h^{-1}\ Mpc$ is not due to a single galaxy cluster, but to a structure which extends over almost all the fields. The distance of this peak is almost coincident with the maximum of our selection function. Other peaks seen in Figure 2 at smaller and larger distance are due to less prominent structures, but with a similar contrast with respect to a uniform distribution.
A large fraction of galaxies ($\sim$ 50%) shows the presence of one or more emission lines (OII λ3727, $H\beta$, OIII λ4959 and λ5007). These objects can be either spiral galaxies, where lines originate mostly from HII regions in the disks, or early–type galaxies undergoing a significant burst of star formation.
The large scale distribution of galaxies with emission lines is different from that of galaxies without emission lines: the observed peaks in the galaxy distribution are much less apparent in galaxies with emission lines. This suggests that either spiral galaxies are less frequent in the densest regions, thus confirming a large scale validity of the well known morphology–density relation, or starbursts phenomena occur preferentially in low density environments or both. We

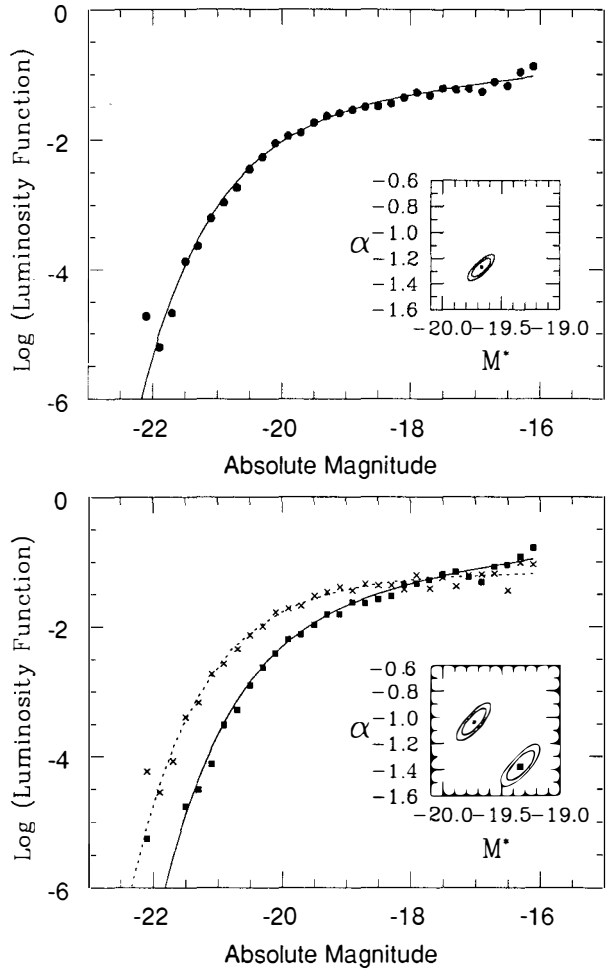


Fig. 3: a) Galaxy luminosity function for the total sample: solid circles have been computed using a modified version of the C-method and the normalization is arbitrary. b) The same as panel a), but for galaxies with emission lines (squares and solid line) and without emission lines (crosses and dotted line).

are going to explore further this point, on the basis of quantitative estimates of densities and of a clearer definition of the structures beyond pure visual impression.
The vertical lines in Figure 2 show the location of the regularly spaced density enhancements found in deep pencil beam survey (BEKS) in the South Galactic Pole region [1], [2]. The two main peaks in our redshift distribution (at comoving distances of ~ 170 and $\sim 300\ h^{-1}\ Mpc$) are in reasonably good agreement with the BEKS peaks and may well be part of the same structures (walls) orthogonal to the line of sight. Under this hypothesis, since the BEKS [2] survey region is located $\sim 10°$ north of the eastern corner of the present survey, the structure at $z \simeq 0.1$ would have minimum linear dimensions of the order of $110 \times 50\ h^{-1}\ Mpc$, comparable with the Great Wall [3].
Although really apparent only in the North Galactic Pole - South Galactic Pole direction, the striking "periodicity" seen in the BEKS deep survey has prompted several speculations and some controversy as well. The latter is mainly based on the criticism on the estimates of levels of statistical significance of the signal found by BEKS to be at $\lambda = 128\ h^{-1}\ Mpc$, due to correlated structures and on the presence of aliasing of power because of the lower dimensionality of the BEKS survey [5]. Even though we cover much less depth than the BEKS survey, it is worthwhile to use the present data to assess the possible presence of peaks in the power spectrum, since in our survey we gain one dimension and this is likely to affect the level of power aliasing. A careful analysis of this point is in progress.

4 The Luminosity Function

The well controlled selection of our sample and the large number of redshifts already obtained allow us to estimate for the first time the shape parameters of the galaxy luminosity function at magnitudes as faint as $b_J = 19.4$.
Since our database was selected in the blue–green, K–corrections are needed to compute the luminosity function even for the moderate redshifts sampled by our galaxies ($z \leq 0.2$). The functional forms of the K–correction as a function of redshift [8] obviously requires the knowledge of the morphological type of each galaxy, which is not available for our fainter galaxies. To overcome this problem, we have adopted the following statistical approach. First, we have assumed that the percentages of late– and early–type galaxies in our sample are approximately the same as those observed in brighter and nearer samples [8], then we have applied the K–correction appropriate for a late–type galaxy to all galaxies showing emission lines. Finally, we have randomly assigned a morphological type to the remaining galaxies in such a way as to obtain the assumed ratio of late and early types in the total sample.
Following the STY method [7], we have then derived the parameters of the Schechter functional form of the luminosity function, through a maximum likelihood technique. The best fit parameters are $\alpha = -1.27$ and $M^*_{b_J} = -19.67$. In order to estimate the maximum amount of uncertainty induced by our "statistical" K–correction scheme, we have also computed the two parameters of the luminosity function with the extreme assumptions that all galaxies are either ellipticals or spirals. The best fit parameters obtained in these way are $\alpha = -1.29$, $M^*_{b_J} = -19.86$ and $\alpha = -1.20$, $M^*_{b_J} = -19.55$, respectively.
Figure 3a shows the luminosity function (with arbitrary normalization) obtained for our sample: the solid line corresponds to the Schechter functional form obtained through the STY method, while the solid circles have been determined through a modified version of the non–parametric C–Method [6]. The fit is based on 3311 galaxies brighter than $M_{b_J} = -16$ and the 68% and 95% confidence ellipses for α and $M^*_{b_J}$ are shown in the inset.
Finally in Figure 3b we show the same function computed for galaxies with and without emis-

sion lines: it is clear that the two functions differ at a very high confidence level, thus suggesting that these two classes of galaxies really represent two different "populations".
Our next steps concern a refinement of the K–correction procedure and the determination of the luminosity function normalization.

Acknowledgements. This work, based on data collected at the European Southern Observatory, has been partially supported through NATO Grant CRG 920150 and EEC Contract ERB–CHRX–CT92–0033.

References

[1] Broadhurst, T.J., Ellis, R.S., Shanks, T., 1988, *Mon. Not. R. astr. Soc.* **235**, 827

[2] Broadhurst, T.J., Ellis, R.S., Koo, D.C., Szalay, A.S., 1990, *Nature* **343**, 726

[3] Geller, M.J., Huchra, J.P., 1989, *Science* **246**, 897

[4] Heydon–Dumbleton, N.H., Collins, C.A., MacGillivray, H.T., 1988, in *Large–Scale Structures in the Universe*, ed. W. Seitter, H.W. Duerbeck and M. Tacke (Springer–Verlag), p. 71.

[5] Kaiser, N, Peacock, J.A., 1991, *Astrophys. J.* **379**, 482

[6] Lynden–Bell, D., 1971, *Mon. Not. R. astr. Soc.* **155**, 95

[7] Sandage, A., Tamman, G., Yahil, A., 1979, *Astrophys. J.* **232**, 252

[8] Shanks, T., Stevenson, P.R.F., Fong, R., MacGillivray, H.T., 1984, *Mon. Not. R. astr. Soc.* **206**, 767

ESTIMATING POWER SPECTRA FROM 3D GALAXY SURVEYS

Max Tegmark[1,2]
[1]*Max-Planck-Institut für Physik, Föhringer Ring 6,D-80805 München.*
[2]*Max-Planck-Inst. für Astrophysik, Karl-Schwarzschild-Str. 1, D-85740 Garching.*
Email: max@mppmu.mpg.de



Abstract

The power spectrum estimated from a galaxy redshift survey is the real spectrum convolved with a window function, so when estimating the power on very large scales (for small k), it is important that this window function be as narrow as possible. A method that achieves this is presented. The optimal estimate of $P(\mathbf{k})$ is found to be the Fourier transform of the number density fluctuations $n/\bar{n} - 1$ weighted by a function ψ_0, and the optimal ψ_0 is found to be the ground-state solution of the Schödinger equation, with the inverse selection function as the potential. This quantum mechanics analogy occurs basically because we want the weight function to be narrow both in Fourier space (to give a narrow window) and in real space (to minimize the variance from shot noise).

1 Introduction

Our observational knowledge of the large-scale structure of the universe is growing at a formidable rate. Fifteen years ago, redshifts had been measured for a few thousand galaxies. Today the figure is around 10^5, and ongoing projects such as the AAT 2dF Survey and the Sloan Digital Sky Survey will raise it to 10^6 within a few years. It is thus very timely to develop analysis techniques that allow us to make the most of this data. One of the most important cosmological quantities that we wish to extract from redshift surveys is the power spectrum $P(k)$. Although this function has been estimated from a wide variety of galaxy samples, *e.g.*, [2, 3, 4, 7, 11], there is still some disagreement about both its overall normalization and its behavior on very large scales. The former problem is related to the issue of biased galaxy formation. Sorting out the behavior on very large scales, however, is more an issue of survey geometry and data analysis. [3] find evidence for $P(k)$ turning over, whereas [7] claim a continued rise up d to $200h^{-1}$Mpc. As pointed out by many authors (*e.g.* [3, 4, 11]), the $P(k)$ we estimate is the true

power spectrum convolved with some window function, and the differences between the window functions of various workers may be part of the explanation for the discrepancies.

The window functions depend on both the survey geometry and the analysis technique employed. Although we may wish we had a method where the window functions were delta functions, it is easy to see that this is impossible given a finite survey volume. Given this constraint, it is natural to ask which analysis technique gives the *narrowest* window functions. The purpose of the present paper is to answer this question.

Before embarking on this program, it is instructive to compare this approach with that of two other recently published methods. Both the method of [3] and the Karhunen-Loève eigenmode method of [11] are optimal in the sense of maximizing the signal-to-noise ratio within a certain class of techniques, without specifically paying attention to the width of the window functions. This corresponds to minimizing the *vertical* error bars that are conventionally placed on power spectrum estimates. To indicate the width of the window functions, *i.e.*, the extent of spectral blurring, one can also place *horizontal* error bars on the estimates. This has recently become fashionable when plotting estimates of the cosmic microwave background power spectrum from various experiments, and would be welcome also in the context of galaxy surveys. The key point to remember is that if we are concerned about both vertical and horizontal error bars, then *there is no one optimal method.* The reason is that there is a trade-off between the two. As pointed out in *e.g.* [4], if one places more weight on the most distant galaxies in a flux-limited survey, then the horizontal error bars get narrower but the vertical ones grow, because of increased shot noise contributions. A method is clearly superior to another if it produces smaller error bars *both* horizontally and vertically. We will find a method that is unbeatable in this sense, with a free parameter β that allows the desired ratio of the two error bars to be specified by the user.

2 The optimal weight function

Just as [3] we model the observed galaxy distribution as a 3D Poisson process $n(\mathbf{r}) = \sum_i \delta(\mathbf{r}-\mathbf{r}_i)$ with intensity $\lambda(\mathbf{r}) = \bar{n}(\mathbf{r})[1+\delta_r(\mathbf{r})]$. The function $\bar{n}$ is the selection function of the galaxy survey under consideration. As is customary, we model the density fluctuations δ_r as a Gaussian random field with power spectrum $P(\mathbf{k}) = P(k)$. We estimate the fluctuation amplitude at wave vector $\mathbf{k}^*$ by[1]

$$\widehat{F}(\mathbf{k}^*) \equiv \int \varphi(\mathbf{r}) n(\mathbf{r}) d^3r \tag{1}$$

and wish to find the optimal choice of the weight function φ. (It is easy to show [10] that this *Ansatz* is essentially unbeatable, since any quadratic power estimator can be written as weighted average of estimates of this form.) A straightforward calculation [10] shows that

$$\langle \widehat{F}(\mathbf{k}^*) \rangle = \widehat{\psi}(0), \tag{2}$$

$$\langle |\widehat{F}(\mathbf{k}^*)|^2 \rangle = |\widehat{\psi}(\mathbf{0})|^2 + \int |\widehat{\psi}(\mathbf{k})|^2 P(\mathbf{k}) d^3\boldsymbol{k} + \int |\psi(\mathbf{r})|^2 \frac{1}{\bar{n}(\mathbf{r})} d^3r. \tag{3}$$

Hats denote Fourier transforms, and we have defined $\psi(\mathbf{r}) \equiv \bar{n}(\mathbf{r})\varphi(\mathbf{r})$. From here on, we will find it convenient to use the standard Dirac quantum mechanics notation with kets and bras, where as usual the wavenumber operator $\widehat{\mathbf{k}} = -i\nabla$. Defining our raw estimate of the power at wave vector $\mathbf{k}$ as

$$Q(\mathbf{k}) \equiv |\widehat{F}(\mathbf{k})|^2 - |\widehat{\psi}(\mathbf{0})|^2, \tag{4}$$

[1]Including a random mock survey as in equation (2.1.3) in [3] can never give minimal error bars, since inclusion of random numbers will always increase the variance of the estimator.

we can write equation (3) simply as $\langle Q(\mathbf{k})\rangle = \langle\psi|P(\widehat{\mathbf{k}}) + V(\widehat{\mathbf{r}})|\psi\rangle$, where we have defined the "potential" function $V(\mathbf{r}) \equiv 1/\bar{n}(\mathbf{r})$. Thus our power estimate is a sum of two terms: a weighted average of the cosmological power $P(\mathbf{k})$, the weights being the window function $|\widehat{\psi}(\mathbf{k})|^2$, and a contribution from shot noise. Since the integral of the window function should be unity, the correct normalization of ψ is evidently $\langle\psi|\psi\rangle = 1$. Subtracting the shot noise contribution, we obtain the unbiased power estimate $Q(\mathbf{k}) - \langle\psi|V(\mathbf{r})|\psi\rangle$. In the approximation of [3] that $\widehat{F}(\mathbf{k})$ is Gaussian, and assuming that the real and imaginary parts have the same variance, the variance of this estimate is simply $\langle|\widehat{F}(\mathbf{k})|^4\rangle - \langle|\widehat{F}(\mathbf{k})|^2\rangle^2 = \langle Q(\mathbf{k})\rangle^2$. (A real-valued $\widehat{F}(\mathbf{k})$ would gives twice this value.) In other words, we minimize the vertical error bars on our power estimate by minimizing $\langle Q(\mathbf{k})\rangle$. Since for any reasonably narrow window function, the cosmic contribution $\langle\psi|P(\widehat{\mathbf{k}})|\psi\rangle \approx P(\mathbf{k}^*)$, independent of ψ, this means that we simply want to minimize the shot noise contribution $\langle\psi|V(\widehat{\mathbf{r}})|\psi\rangle$.

Let us summarize our results so far: a good ψ should be narrow both in Fourier space (to give a narrow window function, *i.e.*, small horizontal error bars) and in real space (to minimize the impact of shot noise and thus give small vertical error bars). In other words, we arrive at the following optimization problem: minimize $\langle\psi|p(\widehat{\mathbf{k}}) + V(\widehat{\mathbf{r}})|\psi\rangle$ subject to the constraint that $\langle\psi|\psi\rangle = 1$. Here p is some *penalty function* that we choose to be small near the $\mathbf{k}^*$ which we wish to estimate and large elsewhere. Introducing a Lagrange multiplier E, this leads to the eigenvalue equation

$$[p(\widehat{\mathbf{k}}) + V(\widehat{\mathbf{r}})]|\psi\rangle = E|\psi\rangle. \tag{5}$$

Throughout this paper, we will estimate the power at wave vector $\mathbf{k}^*$ by chosing the quadratic penalty function $p(\mathbf{k}) = |\mathbf{k} - \mathbf{k}^*|^2/2\beta$, *i.e.*, try to make the window function narrow in the least squares sense. By direct substitution, it is readily seen that equation (5) has the solution

$$\psi(\mathbf{r}) = \psi_0(\mathbf{r})e^{-i\mathbf{k}^*\cdot\mathbf{r}}, \tag{6}$$

where ψ_0 is the solution to the Schödinger equation

$$\left[-\frac{1}{2}\nabla^2 + \beta V(\mathbf{r})\right]\psi_0 = E\psi_0 \tag{7}$$

with the smallest eigenvalue E, the ground state. Continuing our quantum analogy, we see that we arrived at the quantum ground state because we wanted the normalized ψ_0 that minimized the total "energy", where the "kinetic energy" $\langle\psi_0|\widehat{\mathbf{k}}^2|\psi_0\rangle/2$ corresponded to the horizontal error bar and the "potential energy" $\beta\langle\psi_0|V(\widehat{\mathbf{r}})|\psi_0\rangle$ corresponded to the vertical error bar. In conclusion, we see that we can rewrite equation (1) as

$$\widehat{F}(\mathbf{k}^*) \equiv \int e^{-i\mathbf{k}^*\cdot\mathbf{r}}\psi_0(\mathbf{r})\frac{n(\mathbf{r})}{\bar{n}(\mathbf{r})}d^3r. \tag{8}$$

In other words, although there was no mention of Fourier transforms is our *Ansatz* (1), our optimal power estimator $\widehat{F}(\mathbf{k}^*)$ is simply the Fourier transform of the field $F(\mathbf{r}) = \psi_0(\mathbf{r})\frac{n(\mathbf{r})}{\bar{n}(\mathbf{r})}$. Since n is just a sum of delta functions, this reduces to

$$\widehat{F}(\mathbf{k}^*) = \sum e^{-i\mathbf{k}^*\cdot\mathbf{r}_i}\frac{\psi_0(\mathbf{r}_i)}{\bar{n}(\mathbf{r}_i)}, \tag{9}$$

where the sum is to be taken over all galaxies observed in the survey.

3 Examples

In this section, we give the optimal weight function ψ_0 for a few selected survey geometries, and discuss some of their properties. A general feature of all solutions is seen to be that they

fall off smoothly near the survey boundaries, and tend to assign very low weights to points near corners and sharp edges. Basically, this is because it helps a lot in Fourier space without costing much in real space.

3.1 Volume-limited surveys

For a volume-limited survey, $\bar{n}(\mathbf{r})$ equals some constant when r is in the survey volume, and vanishes otherwise. This corresponds to the potential $V(\mathbf{r})$ being infinite outside the survey volume, so we can without loss of generality set $V(\mathbf{r}) = 0$ inside and obtain the quantum-mechanical particle-in-a-box problem: ψ_0 must satisfy the Helmholtz equation $[\nabla^2 + E]\psi = 0$ inside the region and vanish on its boundary. For a volume-limited all sky survey complete out to a radius R, we obtain $\psi_0(\mathbf{r}) \propto j_0(\pi r/R)$, where $j_0(x) = (\sin x)/x$. A more realistic survey contains a *conical* volume of opening angle θ_1, in spherical coordinates defined by $\theta < \theta_1$, $r < R$. Both this case and that of a *slice* $\theta_0 < \theta < \theta_1$, $\varphi_0 < \varphi < \varphi_1$, $r < R$ are treated in [9]. The solutions are a Bessel function of non-integer order in the radial direction, an a non-integer spherical harmonic for the angular part.

3.2 Flux-limited and diameter-limited surveys

For a flux-limited survey, the selection function $\bar{n}(\mathbf{r})$ has the radial dependence (*e.g.* [8], page 214) $\bar{n}(r) \propto \int_{4\pi f r^2}^{\infty} \phi(L) dL$, where ϕ is the galaxy luminosity function and f the flux limit of the survey. The Schechter luminosity function $\phi(L) \propto L^{\alpha} e^{-L/L_*}$, $\alpha = -1.07 \pm 0.05$, gives $\bar{n}(\mathbf{r}) = \Gamma(1 + \alpha, 4\pi f r^2/L_*)$, an incomplete Gamma function. In the crude approximation $\phi(L) \approx L^{-2}$, we obtain $\bar{n}(\mathbf{r}) \propto r^{-2}$. Thus $V(\mathbf{r}) \propto r^2$ and the Schrödinger equation (7) becomes that of the harmonic oscillator, whose familiar ground state is $\psi_0(\mathbf{r}) \propto \exp[-(r/R)^2/2]$, a Gaussian. Here $R \propto \beta^{-1/4}$, where β determined the height of the potential in equation (7). Thus we see that the parameter β, which specifies how concerned we are about shot noise relative to our desire to keep the window function narrow, determines the effective depth of the survey. A greater depth of course narrows the window function, at the price of more shot noise. Notice that in the extreme case of volume-limited surveys discussed above, where the survey depth was completely fixed, the dependence of ψ_0 on β vanished.

3.3 Combinations: realistic pencil beams, slices, etc.

Most realistic surveys are volume-limited in the angular directions (due to incomplete sky coverage) and flux-limited or diameter-limited in the radial direction. They thus result in a Schödinger equation with a radial potential, which is readily attacked by separation of variables. For the case of cones and slices, the angular solution is that mentioned above in the discussion of volume-limited surveys. The ordinary differential equation for the radial part is now straightforward to solve numerically — see *e.g.* [5] for details. If a good approximation is considered satisfactory, the standard variational method (making an *Ansatz* with a few free parameters and minimizing $\langle\psi|H|\psi\rangle/\langle\psi|\psi\rangle$) is recommended, as all one needs is the ground state.

3.4 The **k**-space picture

Figure 1 is an attempt to clarify what is going on in **k**-space. The funnel-shaped surface is the Cold Dark Matter (CDM) power spectrum $P(\mathbf{k}) = P(\sqrt{k_x^2 + k_y^2 + k_z^2})$ of [1], with $h\Omega = 0.5$

and k measured in units of $(h^{-1}\mathrm{Mpc})^{-1}$. If the radial profile looks unfamiliar, it is because the axes are linear rather than logarithmic. For clarity, the third coordinate has been suppressed in the plot ($k_z = 0$). The two surfaces below are examples of window functions. The estimated power is obtained by simply multiplying the window function with the "funnel" and integrating over all $\mathbf{k}$. We have seen that by changing $\mathbf{k}^*$ in equation (8), we can slide our window function around and center it at a point of our choice in $\mathbf{k}$-space, but that its shape will remain unchanged, being simply $|\widehat{\psi}_0|^2$. This simply reflects the well-known fact that the spectral resolution Δk is independent of $\mathbf{k}$. Thus the principal difficulty is to estimate the power at very long wavelengths, near the origin $\mathbf{k} = 0$, where $P(\mathbf{k})$ may change dramatically on the scale of the width of the window function. To accurately probe the largest scales $\lambda = 2\pi/k \gg 30\mathrm{Mpc}$, where $P(k) \propto k$, we thus need a window function that is so narrow that it "fits inside the funnel". Although narrower window functions can always be achieved with deeper surveys (wider ψ_0), the two window functions plotted qualitatively illustrate two subtle problems that can occur even if the survey depth $L \gg 1/k$. The width (standard deviation) of ψ_0 determines the scale on which the central peak of $\widehat{\psi}_0$ falls off. Since the example on the left has a very narrow central peak, we see that it indeed corresponds to a very deep survey. Unfortunately, the "ringing" in Fourier space (often referred to as sidelobes) spoils things, since even if we place the central peak in the middle of the funnel, the dominant contribution will come from the sidelobes picking up power from much larger k. Such sidelobes are caused by sharp edges in ψ_0, caused for instance by incomplete sky coverage, and it is precisely this problem that the method presented in this paper attempts to minimize. The second window function example,

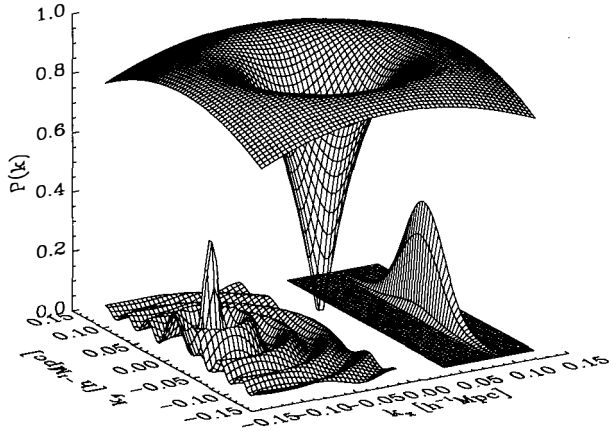


Figure 1. Problems in k-space. The funnel-shaped surface is a standard CDM power spectrum $P(k_x, k_y, k_z)$, with $k_z = 0$. The window-function on the lower left suffers from wide sidelobes due to a sharp edge in the weight function ψ_0. The window function on the lower right suffers from being highly anisotropic, such as is the case for pencil beam and slice surveys.

on the right, has a different problem. Although ψ_0 is evidently smooth (as there are no sidelobes), the geometry is highly isotropic. This is qualitatively what happens for a pencil beam (where $|\widehat{\psi}_0|^2$ will be shaped like a thin disc in $\mathbf{k}$-space) and a thin "slice" (where $|\widehat{\psi}_0|^2$ will be a pencil in $\mathbf{k}$-space). Thus even though the window function $|\widehat{\psi}_0|^2$ is narrow enough in the most favorable direction (because the survey is deep enough in one or two dimensions), it will still not "fit inside the funnel". Rather, the power estimate will be dominated by the ends of the window function protruding out into parts of $\mathbf{k}$-space where k and $P(k)$ are much larger. This well-known phenomenon has been emphasized by *e.g.* [6], who argued that the apparent power excess at $128h^{-1}$ Mpc in a pencil beam survey reported by [2] was probably due to such leakage from shorter wavelengths. In summary, the ability for a survey to probe the longest wavelengths is limited by its weakest link, the dimension in which it is the narrowest.

4 Conclusions

We have presented a method for estimating the 3D power spectrum $P(k)$ that maximizes the spectral resolution, *i.e.*, makes the window functions in k-space as narrow as possible given a level of shot-noise variance. The method decomposes into two separate steps:

1. Estimate $P(\mathbf{k})$ for a 3D grid of $\mathbf{k}$-values with separations of the order of the coherence length.
2. For each k-value of interest, estimate $P(k)$ by taking a weighted average of the estimates of $P(\mathbf{k})$.

We found that Step 1 amounted to the the following:

- Determine the weight function $\psi_0(\mathbf{r})$ from the survey geometry by finding the ground state solution of the Schödinger equation with the inverse selection function as potential.
- Weight the galaxies by the inverse selection function times ψ_0.
- Fourier transform. (This simply involves a sum over all the observed galaxies.)
- As the power estimate, take the square modulus of the Fourier transform minus $|\widehat{\psi}_0(\mathbf{k})|^2$.

Step 2 is described in [10], and generalizes the standard approach of averaging over spherical shells in $\mathbf{k}$-space.
From the discussion at the end of the previous section, we conclude that if a fixed number of square degrees are available for a redshift survey, then

- one should not try to make the area oblong, in a naive attempt to "probe larger scales",
- one should not split the area into several disjoint pieces, and
- the optimal survey shape is a circle, corresponding to a conical 3D geometry.

Acknowledgements. The author wishes to thank George Efstathiou, Karl Fisher, Alan Heavens, John Peacock and Michael Vogeley for useful comments on the manuscript.

References

[1] Bond, J. R. & Efstathiou, G. 1984, *ApJ*, **285**, L45
[2] Broadhurst, T. J., Ellis, R. S., Koo, D. C. & Szalay, A. S. 1990, *Nature*, **343**, 726
[3] Feldman, H. A., Kaiser, N. & Peacock, J. A. 1994, *ApJ*, **426**, 23
[4] Fisher, K. B. *et al.* 1993, *ApJ*, **402**, 42
[5] Hajj, F.Y., Kobeisse, H. & Nassif, N.R. 1974, *J. Comp. Phys.*, **16**, 150
[6] Kaiser, N. & Peacock, J. A. 1991, *ApJ*, **379**, 482
[7] Park, C., Gott, J. R. & da Costa, L. N. 1992, *ApJ*, **392**, L51
[8] Peebles, P. J. E 1993, *Principles of Physical Cosmology*, Princeton University Press
[9] Pockels, F. 1891, *Die Differentialgleichung* $\Delta u + k^2 u = 0$, Teubner Verlag, Leipzig
[10] Tegmark, M. 1995, preprint astro-ph/9502012
[11] Vogeley, M. S. 1994, in *Wide-Field Spectroscopy and the Distant Universe*, eds. Maddox & Aragón-Salamanca, World Scientific

TOPOLOGY OF THE GALAXY DISTRIBUTION

Sergei F. Shandarin
University of Kansas, Lawrence, U.S.A.

Abstract

The history and the major results of the study of the topology of the large-scale structure are briefly reviewed. Two techniques based on percolation theory and the genus curve are discussed. The preliminary results of the percolation analysis of the Wiener reconstruction of the IRAS $1.2Jy$ redshift catalog are reported.

1 Introduction

Looking at the large-scale distributions of galaxies, one may notice that along with clusters and groups of galaxies there are also conspicuously oblong concentrations of galaxies: filaments. One may also get an impression that filaments are connected to each other forming a single network spanning through the entire sample. The two-point correlation function (the most common way of describing the distribution of galaxies) obviously is not sensitive to the geometry and topology of the galaxy distribution. The three- and many- point correlation functions generally speaking are sensitive to the shapes and probably the topology but become cumbersome very quickly. Currently popular averaged moments are easy to interpret, but they loose sensitivity to the geometry after averaging over the volume [1]. There have been suggested various statistics to characterize the geometry and topology of the large-scale structure. In this talk I briefly review the studies of the topology of the large-scale galaxy distribution.

The first mention of topology in the context of the large-scale structure problem (I am familiar with) was in the 1970 paper by Doroshkevich [2]. Studying the formation of the large-scale structure in the pancake scenario Doroshkevich calculated the Euler characteristic of the isodensity surfaces of the initial *Gaussian* density field. Both the Euler characteristic and a common topological measure used in cosmology, genus, are determined by the mean Gaussian curvature of the surface of a constant density.

In 1982 Zel'dovich noticed that the percolation properties of the *nonlinear* density distribution in the HDM (Hot Dark Matter) model are very different from the initial Gaussian field. He also suggested characterizing the topology of the nonlinear density distribution by the percolation thresholds [3]. Percolation theory deals with the number and properties of the "clusters", which are defined as connected regions bounded by the surfaces of a constant density. Following Zel'dovich's idea the author of this talk suggested to use percolation properties of *the galaxy distribution* as an objective quantitative measure of the topology of the large-scale structure and also as a discriminator between cosmological models [4], [5].

The percolation technique was utilized in the study of the CfA I catalog [6]. It was found that the large-scale distribution of galaxies had a network structure. Theoretical studies of the models with the power law initial spectra showed that the $n = -1$ model clearly percolated better than the $n = 0$ model and also in the $\Omega = 1$ universe the $n = -1$ model was in an agreement with the observations [7]. The percolation method showed that the CDM (Cold Dark Matter) model appeared filamentary rather than hierarchical [8], [9]. It was also pointed out that the major disadvantage of percolation technique was the dependence of the percolation thresholds on the mean density of the sample [10] which made it difficult to apply to sparse samples. Similarly, we note that at present some believe that sparse samples can be reliably used for the estimation of the two-point correlation function only [11].

In 1986 Bardeen et al [12] and Gott, Melott and Dickinson rediscovered Doroshkevich's idea of utilizing the Euler characteristic and expanded it to the *nonlinear* distributions as well as *galaxy* catalogs [13]. (Both percolation and genus techniques assumes some kind of smoothing when applied to galaxy distributions.) However, instead of the mean density of the Euler characteristic χ used by Doroshkevich they introduced the mean density of genus, g, which is proportional to the Euler characteristic: $g = -\chi/2$. (For a general review of this method see e.g. [14].) Tomita [15] gave a very elegant analytic expression for the mean Euler characteristic for a D-dimensional Gaussian field which in three-dimensional space yields the familiar equation for the mean genus density

$$g = \frac{1}{4\pi^2}\Big(\frac{< k^2 >}{3}\Big)^{3/2}(1-\nu^2)\exp(-\nu^2/2), \qquad (1)$$

where $\nu = \delta/\sigma_\delta$ is the number of standard deviations by which the threshold density departs from the mean density, $\delta \equiv (\rho - \bar{\rho})/\bar{\rho}$, $< k^2 >= \int k^2 P(k) d^3k / \int P(k) d^3k$, and $P(k)$ is the power spectrum (see e.g. [16]). In a Gaussian field the genus curve has a maximum at $\nu = 0$ with the amplitude determined by the characteristic scale of the density field $< k^2 >$. Since it depends on the slope of the spectrum it is often used as a measure of the "effective" slope of the spectrum (see e.g. [17]); however, it is worth mentioning that $< k^2 >$ has a stronger dependence on the smoothing scale than on the spectral index. Therefore even weak nonlinearity on the smoothing scale may influence the estimate of the spectral index. The genus curve changes sign two times at $\nu = \pm 1$ which signifies the qualitative change of the topology of the surface separating high ($\delta > \delta_c$) and low ($\delta < \delta_c$) density regions where δ_c is a chosen density threshold. As suggested by Eq.1 there are only two types of qualitatively different topologies: 1) one phase percolates and the other does not (negative genus) and 2) both phases percolate (positive genus). In the range $-1 < \nu < 1$ both phases percolate through the whole region and this is often reffered to as sponge topology. At $\nu < 1$ the low density regions do not percolate and at $\nu > 1$ the high density regions do not percolate. The topology of the separating surfaces is obviously the same at $\nu = \pm\nu_c$ as measured by Eq.1. But in cosmological literature it is labeled either as a meatball or bubble topology depending on whether the high or low density phase does not percolate. The network structure obviously has a sponge topology however the term emphasizes a geometrical aspect of a non-Gaussian density field: the high density regions at the percolation threshold

occupy a smaller volume than that of a Gaussian field.

The change of the genus sign is believed to coincide with the percolation thresholds however there is no theorem proving that. Intuitively, it is plausible for distributions resulting from Gaussian fields due to gravitational instability if one believes in a common interpretation of the genus as the mean density of the number of holes minus the number of the isolated regions and that clusters with holes inside do not form. Under these conditions, we assume that percolation thresholds coincide with the changes of the genus sign at least approximately.

One advantage of the genus method is the existence of the analytic expression for Gaussian random fields (Eq.1). Recently there has also been an analytic expression obtained in the weakly nonlinear regime [18]. However, one should not forget that the mean genus is a statistical measure and therefore an estimate of errors is needed before it becomes meaningful. The errors for finite samples having finite resolution can be estimated only from numerical simulations. Percolation parameters are also calculated numerically, but if one can estimate the errors he almost certainly can estimate the mean with similar accuracy.

It has been claimed that the percolation thresholds are the most sensitive discriminators of the models [4]. The recent study of the CfA II catalog using the genus method [16] seems to support that suggestion. The authors reduced the information of the genus curve to three numbers one of which was the genus peak width $W_\nu = \nu_+ - \nu_-$ where ν_+ and ν_- are the levels at which the genus changes the sign. Fig. 12 through 14 in [16] clearly demonstrate that W_ν has the highest discriminating power. However, we still believe that the percolation thresholds, ν_+ and ν_-, should be interpreted separately because they carry independent information about the topology of the structure.

2 Largest "cluster" and largest "void"

Percolation theory deals with the number and properties of the "clusters". In the absence of a better term we label as "clusters" the regions bounded by the surfaces of chosen constant density. In order to avoid confusion with clusters of galaxies, we will use quotation marks when talking about "clusters" with this non-astronomical meaning. The density threshold δ_c separating high ($\delta > \delta_c$) and low ($\delta < \delta_c$) density regions is assumed to be a free parameter $\delta_c > -1$. Analyzing discrete distributions (e.g. galaxy distributions) we assume a smoothing procedure creating a continuous density distribution.

At every density threshold all "clusters" and "voids" are identified and various types of analysis can be performed [20]. However here we present only the results of the study of the largest "cluster" and the largest "void" as functions of a density threshold. (The largest "void" is defined as the largest "cluster" in the low density phase.) The full analysis will be presented elsewhere [21], [22]. The choice of the largest structure is determined by the fact that at the percolation threshold the largest structure become infinite which signifies the change of topology.

The density threshold is not a convenient parameter if linear (Gaussian) and nonlinear density distributions are to be compared. Instead we utilize the filling factor to parameterize the density threshold [19]. The filling factor is the fraction of the volume occupied by the given phase. In this case one can easily compare the properties of "clusters" with that of "voids" and also linear and nonlinear density distributions. It is similar to comparing different patterns provided that the same amount of paint was used to make each pattern. The filling factor as a function of the density threshold is obviously the cumulative distribution function.

The largest "cluster" and "void" are measured as a fraction of the corresponding filling factor. Thus if the largest "cluster" is 0.9 at filling factor of 0.2 it means that the density is

higher than the chosen threshold in 20% of the volume and almost all of that volume (90%) comprised of only one connected region.

The top two panels of Fig.1 show the largest "cluster" and the largest "void" for the density distributions obtained in the N-body simulation of the power law model with $n = -1$ at two stages of evolution: $\lambda_{nl} = 1/8$ and $1/4 L_{box}$. The simulations have been done with 128^3 particles on the equivalent mesh [23] but for this analysis the mesh has been reduced to 64^3. Error bars show 1σ deviations from the mean obtained in four different realizations of the model.

The qualitative behavior of both of the largest structures is universal: at small filling factors the largest structure is negligible then at some filling factor it quickly grows and becomes the only significant structure in the corresponding phase. This is the percolation transition and also the indication of the change of topology. In Gaussian fields there is no statistical difference between "clusters" and "voids" and the transition happens at a filling factor of about 16% corresponding to $\nu = \pm 1$. However, a finite size of the sample as well as finite resolution biases the transition. In order to avoid these effects, we obtain the "Gaussian" distribution by mixing the phases of the Fourier transform of the nonlinear density distributions in question. This automatically includes all finite grid effects in the reference Gaussian field keeping the Fourier amplitudes exactly the same. This allows for the generation of as many Gaussian realizations with identical amplitudes as needed to estimate the dispersion. The Gaussian largest structure is shown as a dotted line in Fig.1 (hidden by the shade of the error bars) lying between the solid and dashed lines.

The major feature of the nonlinear distribution is that the largest "cluster" percolates easier and the largest "void" harder than in the Gaussian case. The significance of this conclusion for the largest cluster is at the many-σ level (see Fig.1). Qualitatively this remains true for all models we have studied ($n = 1, 0, -1, -2, -3$, CDM, and C+HDM [20]), but quantitatively the transitions are different. The high density regions form a connected network spanning through the whole region when the filling factor is relatively small (smaller than in the Gaussian case) and therefore this transition can be labeled as a shift toward the network structure. On the contrary the low density regions do not form a percolating void (remain isolated) even when the filling factor of the low density phase is greater than that in the Gaussian field. This type of transition can be labeled as a shift toward the bubble structure. The range of the sponge topology is typically (but not necessarily) increased compared to the Gaussian case. Thus the above changes also can be labeled as a shift to a sponge topology. However, the major point is not how to label a structure but rather to show that in a general case the two shifts are independent of each other and carry independent information about the structure. Therefore combining them into one parameter (like $W_\nu = \nu_+ - \nu_-$ mentioned above) results in lost information.

At small filling factors the largest structure must be negligible in sufficiently large samples. The actual (finite) sizes of the largest structures can be used as an internal characteristic of the fairness of the sample.

In the past the percolation technique has been successfully applied to volume limited samples [6]. Analyzing the statistically homogeneous distributions is very easy and the largest structures clearly distinguish between the models [21]. However, the analysis is much more difficult if the distribution has a radial gradients, like the IRAS $1.2Jy$ redshift catalog.

3 The IRAS $1.2Jy$ catalog

We analyze the whole-sky galaxy distribution in real space reconstructed from the redshift IRAS $1.2Jy$ catalog using a Wiener filter and an expansion in spherical harmonics [24]. The

Wiener filter effectively uses a variable window size which is about $500km/s$ at $2000km/s$ and increases to $1800km/s$ at $10000km/s$. The resulting smoothed galaxy distribution is not statistically homogeneous. This is the major challenge for applying the percolation technique.

In order to test the effect of the reconstruction we generated two density distributions from the N-body simulation ($n = -1$, $k_{nl} = 8$): one with the Wiener filtering and the other without it. The percolation statistics of these distributions are shown in the middle and bottom panels of Fig.1. The panels on the left hand side show the largest structures in the reconstructed density field without the Wiener filter and on the right hand side with the Wiener filter applied. The panels in the middle row show the results for the sphere with the radius of 30 mesh units and the bottom panels show the results for smaller sphere with the radius of 24 mesh units.

The middle and bottom panels show only one realization which demonstrates a substantial change in the topological properties due to the reconstruction procedure. We plot here only one realization for better visual comparison with the data. Fig.2 shows the largest structures in the filtered galaxy distribution assuming two different $\beta = \Omega^{0.6}/b$. This preliminary result is in a very general agreement with the $n = -1$ model. The models with $\beta = 0.1$ and $\beta = 1$ do not look much different. Unfortunately the method of estimating the dispersion described above does not work in the inhomogeneous case. We are working now on the improved version of estimating the dispersion.

The largest structures in the galaxy distribution are quite large at small filling factors: $30 - 40\%$ of the corresponding filling factor. It may mean that the sample is not large enogh for this kind of analysis.

4 Summary

The quantitative topology proved to be a useful technique for studying the large-scale structure in the universe. There have been suggested two different methods for quantitative characterization of the topology. One widely used method measures the mean density of genus of a constant density surface as a function of the density threshold. It actually measures the mean Gaussian curvature of the surface. The other more geometrical method is based on percolation theory. Here the number and properties of the "clusters" are studied. In particular the volume of the largest "cluster" measured as a function of a density threshold plays an important role.

In general the questions addressed by the two methods are similar but not identical. In the case where the questions coincide the two approaches use different methods of solving them. In particular, they treat the boundaries differently and are probably affected differently by noise.

The genus curve method is more developed and has been applied to many catalogs of galaxies (both two-dimensional and redshift surveys). The major results indicate that. non-Gaussian behavior has been detected in both types of the catalogs (see e.g. [25], [16], [17] and references therein). The characterization of the structure is somewhat conflicting. Almost all possible labels have been assigned to the galaxy distributions: meatball, sponge, network, bubble topology. However, it is likely that the structure seen in different catalogs looks different. The estimate of effective slope is in agreement with $n = -1$ [17].

The percolation method has been tested in various theoretical models and developed to the level when it can be applied to the galaxy catalogs. For the first time we try to apply it to the magnitude limited sample and find the preliminary result encouraging.

Acknowledgements. I am grateful to Capp Yess and Karl Fisher for allowing me to report the preliminary results of a common unfinished work and Francis Bernardeau for useful discus-

sions during the meeting. I acknowledge the AAS travel grant, NSF grant AST-9021414, and University of Kansas GRF-94 grant.

References

[1] Bernardeau, F., 1995, private communication

[2] Doroshkevich A.G., 1970, *Astrophysics* **6**, 320

[3] Zel'dovich Ya. B., 1982, *Sov. Astron. Lett.* **8**, 102

[4] Shandarin S. F., 1983, *Sov. Astron. Lett.* **9**, 104

[5] Shandarin S. F., Zel'dovich Ya. B. 1983, *Comments Astrophys.* **10**, 33

[6] Einasto J., Klypin A.A., Saar E., Shandarin S.F. 1984 *Mon. Not. R. astr. Soc.* **206**, 529

[7] Bhavsar S.P., Barrow J.D. 1983, *Mon. Not. R. astr. Soc.* **205**, 61p

[8] Melott A.L., Einasto J., Saar E., Suisalu I., Klypin A.A., Shandarin S.F., 1983, *Phys. Rev. Lett*, **51**, 935

[9] Davis M., Efstathiou G., Frenk C., White S.D.M. 1985, *Astrophys. J.* **292**, 371

[10] Dekel A., West M.J. 1985, *Astrophys. J.* **288**, 411

[11] Bouchet F. 1995, talk at this meeting

[12] Bardeen J.M., Bond J.R., Kaiser N., Szalay A.S., 1986 *Astrophys. J.* **304**, 15

[13] Gott J.R., Melott A.L., Dickinson M. 1986, *Astrophys. J.* **306**, 341

[14] Melott A.L. 1990, Physics Reports, **193**, 1

[15] Tomita H. 1986, Prog. Theor. Phys. **76**, 952

[16] Vogeley M.S., Park C., Geller M.J., Huchra J.P., Gott J.R. 1994, *Astrophys. J.* **420**, 525

[17] Moore B., et al, 1992, *Mon. Not. R. astr. Soc.* **256**, 477

[18] Matsubara T., 1994, *Astrophys. J.* **434**, L43

[19] de Lapparent V., Geller M., Huchra J.P. 1991, *Astrophys. J.* **369**, 273

[20] Klypin A.A., Shandarin S.F. 1993, *Astrophys. J.* **413**, 48

[21] Yess C., Shandarin S.F. 1995, in preparation

[22] Yess C., Shandarin S.F., Fisher K. 1995, in preparation

[23] Melott A.L., Shandarin S.F. 1993, *Astrophys. J.* **410**, 469

[24] Lahav O., Fisher K., Hoffman Y., Scharf C.A., Zaroubi S. 1994, *Astrophys. J.* **423**, L93

[25] Coles P., Moscardini L., Plionis M., Luchin F., Matarerese S., Messina A. 1993, *Mon. Not. R. astr. Soc.* **260**, 572

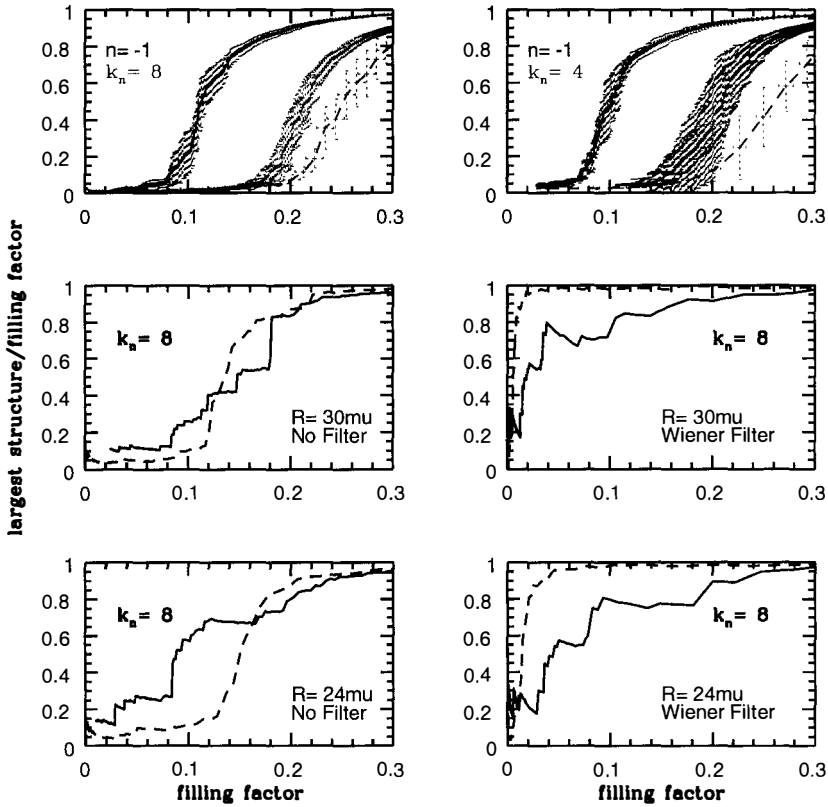


Figure 1: The N-body simulations of the $n = -1$ model. The top row show two stages of evolution $\lambda_{nl} = 1/8$ and $1/4 L_{box}$ before reconstruction. The largest "cluster" (solid line) and largest "void" (dashed line) is shown as a function of filling factor; the Gaussian realization with the identical Fourier amplitudes is shown in between (shaded by the error bars). The middle and bottom panels are the reconstructions without the Wiener filter (on the left hand side) and with the Wiener filter (on the right hand side). Two different radii of the sphere has been used: $R = 30$ and 24 mesh units.

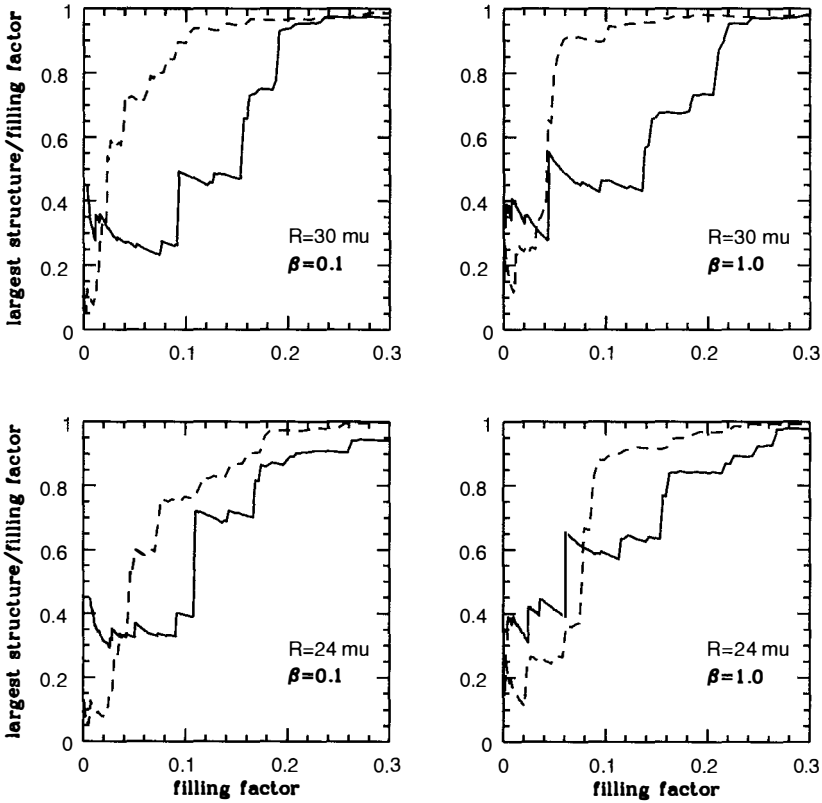


Figure 2: The Wiener reconstruction of the IRAS $1.2Jy$ redshift catalog in spherical harmonics. Solid lines show the largest "cluster" and dashed lines show the largest "void" at two values of $\beta = \Omega^{0.6}/b$ and at two radii of the spherical region.

RADIO SOURCES AND LARGE-SCALE STRUCTURE

J.V. Wall [1], C.R. Benn [2]
[1] *Royal Greenwich Observatory, Cambridge, U.K. CB30EZ.*
[2] *Isaac Newton Group, 38780 Santa Cruz de La Palma, Spain.*

Abstract

Extragalactic radio sources hold the potential to trace large-scale structure throughout the observable universe: serious selection effects present at other wavelengths are overcome through object luminosity, linearity of detectors, large-scale uniformity of surveys and minimal obscuration. Two approaches to extract structural information from radio surveys are described here, (i) the direct tracing of the structure from redshifts in radio surveys, and (ii) the examination of the structure through statistical analyses of the surveys. Both approaches confirm that substantial structural information is present in modern radio surveys, and that the new generation of surveys must be subject to the imprint of the skeleton of the universe.

1 Introduction

The apparently uniform, random and independent distribution of radio sources on the sky (*e.g.* [1]) has led to the view that they have little to contribute to definition of large-scale structure. The very few large-scale anisotropies of low amplitude have now been shown to be due to the presence of the local supercluster[2, 3]. The apparent uniformity of the radio sky arises quite simply: in order to detect anisotropies, surveys must reach a level at which large structures each contribute more than one source to the survey. From the known radio luminosity function, large-area surveys must reach flux-densities of $\lesssim 10$ mJy at a redshift of 1 before this is the case.

However, surveys now exist which cover most of the sky and reach to $(3 - 5) \times 10$ mJy, close to this limit. The VLA has now embarked on surveys of the sky visible to it which will reach levels well below that required to see structure (see *e.g.* [4]). Observational developments now hold out the possibility of direct exploration of structure from the redshifts of identifications in such surveys. In the radio regime the VLA in the north and the Australia Telescope in the south enable accurate positions to be obtained for large samples of sources as a matter of routine. In the optical regime, sky surveys have been digitized facilitating rapid identification of radio sources, while telescopes equipped with fast multi-fibre spectrographs make possible efficient redshift measurements for significant samples of radio sources.

Preliminary explorations for anisotropies in a few small-area radio surveys which reach appropriate levels have provided some indication of clustering[5], while exploration with limited statistics of QSO and radio-galaxy space distribution has likewise provided indication of clustering [6, 7, 8, 9]. Here we describe three investigations, the first involving direct sampling, the second and third statistical in nature, all of which indicate the power of radio surveys to delineate large-scale structure.

2 Tracing structure with redshifts of radio-source samples

It is now straightforward to obtain redshifts of radio galaxies and QSOs out to redshifts of 0.5. But in what sample? To see structure the radio survey must have an opening angle θ large enough to encompass a few clusters or cells at this redshift. (Note 100 comoving h^{-1} Mpc at $z = 0.5$ corresponds to $\theta = 5°$.) The survey must also be deep enough to detect sources at this redshift with $P_{408MHz} << 10^{25.5}$ WHz^{-1}, *i.e.* $S_{408MHz} < 10$ mJy.

The 5C synthesis surveys from the Cambridge One-Mile Telescope, summarized in [10], closely match this requirement[11]. Of these, 5C12 has been the subject of a lengthy series of observations for various cosmological investigations. The survey maps a 4°-diameter region near the NGP and the catalogue contains about 600 sources. Redshifts measured mostly with the WHT faint-object spectrograph are now available for some 60 of the identifications, and Fig. 1 shows the distribution of these on the sky. Several groups and pairs are visible; the *majority* of the redshifts are evidently associated with 1, 2 and even 3 other redshifts in the sample. The group at $z \approx 0.315$ has projected comoving diameter 25 h^{-1} Mpc, and others have projected diameters ranging from 10 to 70 h^{-1} Mpc. These sizes are in accord with the largest structures found in optical/IR surveys; this is the *first direct detection of structure in an unbiassed radio survey.* The extent and nature of the major structure out to $z = 1$ could readily be delineated with multi-feed spectrograph observations of the remainder of the sample.

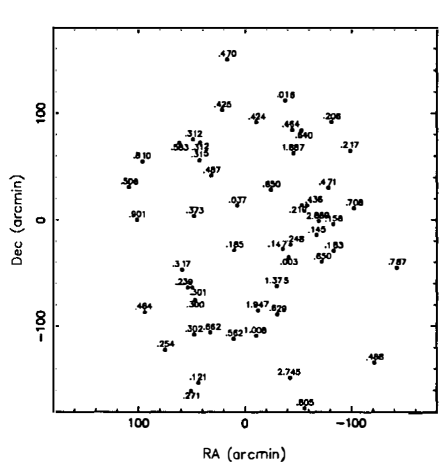


Figure 1: Distribution on the sky of 5C12 sources with measured redshifts.

3 Tracing structure statistically

3.1 Two-point correlation

The two-point correlation function [12] is well suited to surveys of irregular area such as 'all-sky' radio surveys after excision of low Galactic latitudes and confused regions near bright sources. Two surveys at 5 GHz, one covering the northern hemisphere[13] and the other the southern[14], now contain $\approx 10^5$ sources. Early analyses indicated the presence of clustering

signal[15, 16, 17] in different sub-samples. Substantial further analysis is in progress; there are instrumental and observational effects which may affect the strength of such signal. If signal is confirmed then the real power spectrum of the inherent clustering can be determined via a cosmological version of Limber's equation (*e.g.* [18]), because the redshift distribution of the 5-GHz sources is reasonably well established[19].

3.2 A toy cellular universe

In a second form of statistical analysis we considered exactly what kind of radio survey (area, flux-density level) needed to see the imprint of the skeleton of the universe. To do so, we modelled the large-scale structure as a three-dimensional Voronoi tessellation[11]. Poisson Voronoi tessellations are constructed by dividing space into cells around randomly-distributed seeds, such that every point in a given cell is nearer to its seed than to any other seed. The tessellations are thus characterised by one parameter: the mean space density of seeds ρ. We allowed this parameter the range 50 h^{-1} Mpc $< \rho^{-1/3} <$ 800 h^{-1} Mpc. Pencil-beam surveys slicing through typical Voronoi structures are shown in Fig. 2.

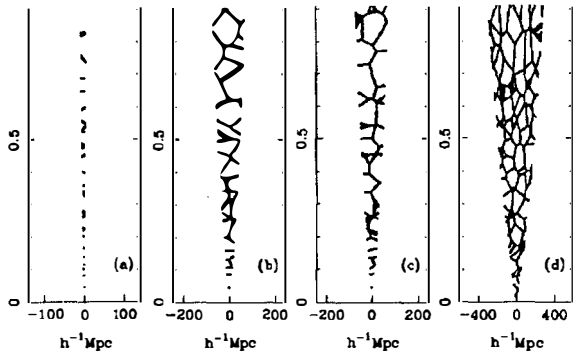


Figure 2: Slices through Voronoi-foam simulations with $\rho^{-1/3}$ =100 h^{-1} Mpc, for pencil-beam surveys of diameter (a) 0.5°, (b) 5°, (c) 5° rotated 90°, and (d) 20°. The horizontal axis is comoving h^{-1} Mpc.

We found the predictions of the model to depend only weakly on the other main parameters: the redshift-dependent luminosity function of the radio sources to be sprinkled on the cell walls; the density parameter Ω; and the distribution of radio sources within the cells.

We tested the isotropy of the sky distribution for each value of $\rho^{-1/3}$ at each of a range of flux densities between 10 μJy and 10 Jy, comparing the area-to-area fluctuations in counts with those expected from statistical noise for a range of survey opening angles. The principal result is that the observed isotropy of the radio-source distribution in surveys currently published at Jy, mJy and μJy levels constrains $\rho^{-1/3} <$150 h^{-1} Mpc. In the context of other constraints on large-scale structure *this limit occupies a critical range between those provided by galaxy surveys and by COBE results.*

The initial region of the FIRST survey[4] now available contains some 27000 sources. Our preliminary analysis[20] (with due allowance for double-structure sources) further refines the

limit to $\rho^{-1/3} \lesssim 50\ h^{-1}$ Mpc. If there are structures up to $\sim 100\ h^{-1}$ Mpc as optical surveys suggest, we must now see the imprint of large-scale structure on this FIRST low-frequency radio sky. 'Cosmologically representative' samples from it and from similar new surveys will have to be chosen with care.

References

[1] Webster, A.S., 1977, in *Radio Astronomy and Cosmology*, Proc. IAU Symp. 74, p. 75, ed. Jauncey, D.L., Reidel

[2] Shaver, P.A., Pierre, M., 1991, *Astr. Astrophys.* **220**, 35

[3] Shaver, P.A., 1991, *Austr. J.Phys.* **44**, 759

[4] Becker, R.H., White, R.L., Helfand, D.J., 1995, *Astrophys. J.* **450**, 559

[5] Windhorst, R.A., Mathis, D., Neuschaefer, L., 1990, in *Evolution of the Universe of Galaxies*, ed. Kron, R.G., *ASP Conf. Ser.* **10**, 389

[6] Rhee, G.R.R.N., Webb, J.K., Katgert, P., 1989, *Astr. Astrophys.* **217**, 1

[7] Crampton, D., Cowley, A.P., Hartwick, F.D.A., 1989, *Astrophys. J.* **345**, 59

[8] Clowes, R.G., Campusano, L.E., 1991, *Mon. Not. R. astr. Soc.* **249**, 218

[9] Peacock, J.A., Nicholson, D, 1991, *Mon. Not. R. astr. Soc.* **253**, 307

[10] Benn, C.R., Grueff, G, Vigotti, M., Wall, J.V., 1982, *Mon. Not. R. astr. Soc.* **200**, 747

[11] Benn, C.R., Wall, J.V., 1995, *Mon. Not. R. astr. Soc.* **272**, 678

[12] Peebles, P.J.E., 1973, *Astrophys. J.* **185**, 413

[13] Gregory, P.C., Condon, J.J., 1991, *Astrophys. J. Suppl. Ser.* **75**, 1011

[14] Griffith, M.R., Wright, A.E., 1993, *Astron. J.* **105**, 1666

[15] Wall, J.V., Rixon, G.T., Benn, C.R., 1993, in *Observational Cosmology*, eds Chincarini, G. *et al.* , *ASP Conf. Ser.* **51**, 576

[16] Wall, J.V., Benn, C.R., Loan, A.J., 1995, in *Examining the Big Bang and Diffuse Background Radiations*, Proc. IAU Symp. 168, eds Kafatos, M. *et al.* , Kluwer, in press

[17] Kooiman, B., Burns, J.O., Klypin, A.A., 1995, *Astrophys. J.* **448**, 500

[18] Fall, S.M., 1979, *Rev. Mod. Phys.* **51**, 21

[19] Dunlop, J.R., Peacock, J.A., 1990, *Mon. Not. R. astr. Soc.* **247**, 19

[20] Benn, C.R., Wall, J.V., 1996, in preparation

LARGE-SCALE STRUCTURES IN THREE DIMENSIONS

A.P. Fairall and W.R. Paverd
Departments of Astronomy and Computer Science, University of Cape Town, Rondebosch, 7700 South Africa.

Abstract

Three-dimensional views are used to explore the character of the large-scale distribution of southern galaxies. They show that within great walls of galaxies, such as the Sculptor great wall, there exists a cellular texture with voids smaller in size than 1000 km s^{-1} (whereas the voids that separate great walls are of order 5000 km s^{-1}) in redshift space. The view from the position of our own galaxy reveals that the concentration of galaxies forming the supergalactic equator is spread in depth from the nearest galaxies out to approximately cz=10000 km s^{-1}, with many small voids embedded. It is therefore suggested that our galaxy is itself within a (Centaurus) great wall structure.

1 Introduction

Our contribution at the Rencontres de Moriond consisted of the presentation of a sequence of images, showing galaxies as colour-coded dots against a black background. The audience was equipped with ChromoDepth(tm) spectacles, that translate colour into stereoscopic depth, thereby enabling the audience to view the structures in three dimensions (3D). A colour-coded video was also shown.

Regrettably, there is no way that the 3D images can be successfully reproduced here with this article. The text and diagrams following give brief descriptions of the images, and convey the verbal information that accompanied the presentation.

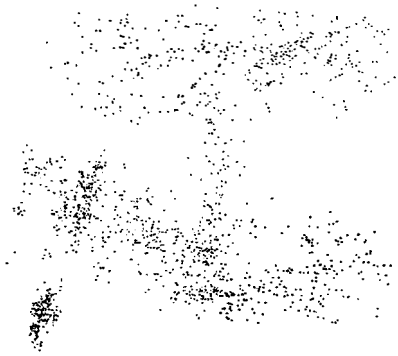


Figure 1: A projection of the distribution of galaxies in the Sculptor (top), Fornax (bottom) and Grus (vertical centre) Walls. The Hydra, Centaurus and Fornax clusters are bottom left, and serve to mark the position of our galaxy. At the conference, this view was presented in 3D.

2 Chromostereoscopic Images

Using ChromoDepth(tm) spectacles, pure red dots may be perceived as being closer than 2 metres, pure blue dots as distant as 40 metres. Only single images need be projected; the spectacles create the stereoscopic pairs. This is a great advantage in the present application, where the eye may otherwise be confused by large numbers of dots.

The colour coded images have been created, using a Silicon Graphics Indigo 2 workstation. The 35mm slides were made by photographing the monitor screen with a pin-registered camera using Fuji Velvia film. Suitable software was developed that converts a selected range of depth into colour. Such colours, when produced on the CRT display, are no longer monochromatic, since the display works by combination of three primary colours; similarly, the photographic emulsion. Nevertheless, the results produced are acceptable and serve for the present purpose.

3 The Database

The database of galaxies used is the first author's Southern Redshift Catalogue (Hereafter SRC [3]), an ongoing compilation of published redshifts that, inter alia, attempts to identify discrepant velocities and exclude them from plots. It is important to realise that the catalogue does not form a statistically-controlled sample, and suitable caution has to be applied. However, the first author [4] has frequently made the point that, nevertheless, such catalogued data can still be successfully used in the mapping and delineating of large-scale structures and voids. Suffice to say that all such features identified in SRC in the early 1980s [9] have all stood the test of time.

Three general views of the database were shown in 3D form. The data are bounded by the equatorial plane, since only southern declinations are covered by SRC. The wedge of obscuration of the Milky Way is also apparent. Wall-like features can be discerned amidst the data, but are better seen in isolated views.

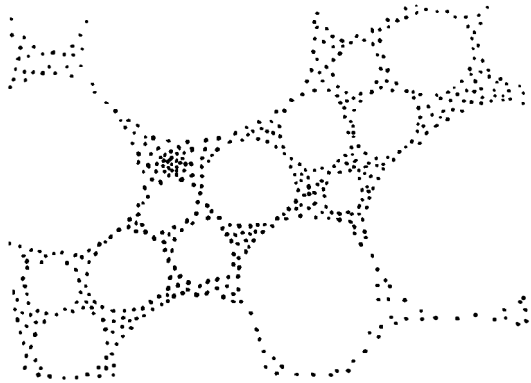


Figure 2: A schematic representation, suggesting that great walls are formed by collective diminution of void size.

4 Great walls

As presented at the conference, the isolated views show only the galaxies in the Sculptor, Fornax and Grus Walls (and the Hydra and Centaurus clusters). An indication is provided in Figure 1. At the workstation, a mouse is used to set the viewpoint.

When displayed in 3D, these views reveal internal structures within the great walls. A great wall, such as the Sculptor Wall (also sometimes referred to as the Great Southern Wall), has a cross section of 5000 X 1000 km s^{-1}. The 3D projections confirm the finding reported previously [5], that there exists a form of cellular structure within the wall. Galaxies in the wall are seen to surround internal voids of diameter <1000 km s^{-1}. These voids are then almost an order of magnitude smaller than the larger voids that separate the great wall structures; for example, the Sculptor Void between the Sculptor and Fornax Walls, has a diameter of approximately 5000 km s^{-1}.

Figure 2 summarizes the finding. It suggests that there is a fabric of small voids within a great wall. Moreover, the wall might delineate a region of retarded void growth - that way the voids would be smaller and the galaxies that surround those voids would be closer.

As yet, this finding is largely qualitative. It remains for a quantitative tool, analogous to the "Voidsearch" algorithm [7] that examined the larger voids, to analyse the distribution within walls.

5 Our View from within a Great Wall

The images also include "all-sky" panels, six of which can cover the hemispherical screen of a planetarium. Three-dimensional views have been created on the dome of the Planetarium of the South African Museum. Like the single-slide images, they serve as a research tool, aside from obvious education potential. The software permits selection of minimum and maximum distances for the range of the colour coding.

At the conference, a sequence of the panel covering RA 10 to 14 hours (and Decl 0 to -90deg) was displayed. The sequence increased in depth: 0 to 1250, 0 to 2500, 0 to 5000, 0 to 10000 and 0 to 20000 km s^{-1}.

This panel includes the nearby galaxies NGC 5128 (Centaurus A) and M83, and the Hydra I and Centaurus clusters. The image confirms a continuous distribution of galaxies between our galaxy and Centaurus, such that what is commonly referred to as the Local (or Virgo) Supercluster is not an independent entity to the Centaurus supercluster.

The panel also shows the most conspicuous segment of the supergalactic equator [2]. The 3D views emphasize that the general concentration of galaxies to the supergalactic plane is continuous in depth, out to approximately cz=10000 km s^{-1}. Furthermore, there are numerous voids intermingled with this concentration. Many of the voids appear large because they are relatively close, but measurements show them to be smaller than 1000 km s^{-1} in diameter - much as those describe above in great wall structures.

It is therefore suggested that the well-known concentration towards the supergalactic equator may represent a great wall structure seen from within [6]. Our galaxy and the Local Supercluster are a part of it.

The Hydra I cluster and associated structures are not a part of this great wall. Although in the past, the existence of a "Hydra-Centaurus" supercluster was often advocated, there are only weak connections [1] between the two, while new structures revealed by Kraan-Korteweg et al [8] suggest that Hydra may form a parallel wall-like structure to our own "Centaurus Great Wall"

References

[1] da Costa, L.N., Nunes, M.A., Pellegrini, P.S., Willmer, C., Chincarini, G. & Cowan, J.J., *Astron. J.* **91,** 6(1986).

[2] de Vaucouleurs, G. & de Vaucouleurs, A., Reference Atlas of Bright Galaxies, Texas, 1964.

[3] Fairall, A.P., Southern Redshift Catalogue, Dept Astronomy, University of Cape Town, (available over Internet from fairall@uctvms.uct.ac.za)

[4] Fairall, A.P., Palumbo, G.C.C., Vettolani, G., Kauffmann, G., Jones, A. & Baiesi-Pillastrini, G., *Mon. Not. R. astr. Soc.* **247,** 21P(1990).

[5] Fairall, A.P., Paverd, W.R., Ashley, R.P., in 4th DAEC Meeting on "Unveiling Large-Scale Structures behind the Milky Way", eds. C. Balkowski and R.C. Kraan-Kortweg, ASP Conf. Ser., 67, 21 (1994).

[6] Fairall, A.P. & Paverd, W.R., in 35th Herstmonceux Conference "Wide-field Spectroscopy and the Distant Universe" (World Scientific), in press.

[7] Kauffmann, G. & Fairall, A.P., 1991, *Mon. Not. R. astr. Soc.* **248,** 313(1991).

[8] Kraan-Korteweg, R.C., Fairall, A.P. & Balkowski, C., 1995, *Astr. Astrophys.* **in** press.

[9] Winkler, H., Mon. N. Astr. Soc. Sthn. Africa, 42, 74 (1983)

LARGE-SCALE STRUCTURES UNCOVERED BEHIND THE SOUTHERN MILKY WAY

R.C. KRAAN-KORTEWEG[1], P.A. WOUDT[2] A.P. FAIRALL[2], V. CAYATTE[1], C. BALKOWSKI[1], P.A. HENNING[3]

[1]*Observatoire de Paris, DAEC, Unité associée au CNRS, D0173, et à l'Université Paris 7, 92195 Meudon Cedex, FRANCE.*

[2]*University of Cape Town, Department of Astronomy, Private Bag, Rondebosch, 7700 South Africa.*

[3]*University of New Mexico, Department of Physics and Astronomy, 800 Yale Blvd., NE, Albuquerque, NM 87131, USA.*

Abstract

In our ongoing deep search for galaxies behind the southern Milky Way by systematic visual inspection of the IIIaJ ESO/SRC-survey to a diameter limit of D$\geq$ 0.'2, we have now charted over 10000 new galaxies within $265° \lesssim \ell \lesssim 340°$, $|b| \lesssim 10°$. Our most recent extension covers a substantial region around the predicted position $(\ell, b, v) = (320°, 0°, 4500$ km/s) of the Great Attractor (GA) [4].

In this report we concentrate on the detection of an extreme overdensity centered on the cluster A3627. This overdensity turns out to be a rich cluster with a large fraction of early type galaxies. Our redshift observations put it close to the GA in velocity-space $(\ell, b, v_{obs}) = (325°, -7°, 4887$ km/s). Moreover, the first mass estimates prove A3627 to be a very massive cluster, $\mathcal{M} \sim 7 \cdot 10^{15} \mathcal{M}_{\odot}$. The mass of the cluster itself cannot fully explain the observed infall motions into the GA ($5 \cdot 10^{16} \mathcal{M}_{\odot}$ [11]), but A3627 seems to be the central peak of a much larger structure/supercluster, which corresponds well with the general predictions of this mass excess.

1 Introduction

The Milky Way obscures about 25% of the optical extragalactic sky. This is a severe restriction in the study of various extragalactic topics:

(a) The connectivity of structures across the Milky Way. Most of the known superclusters disappear in the ZOA. What is their true extent?

(b) The observed infall into the Great Attractor at $(\ell, b, v_{obs}) \sim (320°, 0°, 4500$ km/s) [11, 4]. Is this predicted mass overdensity in the form of galaxies?

(c) The origin of the peculiar motion of the Local Group with respect to Cosmic Microwave Background Radiation (CMB). Can the dipole in the CMB be explained by the gravity of the irregular mass/galaxy distribution in the *whole* sky?

(d) The internal dynamics of the Local Group.

Next to the distribution of clusters, sheets and voids, individual *nearby* galaxies are also relevant as their gravitational perturbation would be significant purely because of their proximity [5].

In order to uncover the galaxy distribution in the 20° wide strip known as the 'Zone of Avoidance', we have embarked on a deep search for partially obscured galaxies down to faint magnitudes and small sizes, i.e. a diameter limit of D= 0.'2. We have started our survey in the southern hemisphere, because of the questions related to the dipole in the CMB and the infall into the GA which both point close to the southern Galactic Plane (marked in Fig. 1).

2 The newly discovered galaxies in the southern ZOA

To date, 50 fields of the ESO/SRC-survey have been visually inspected. The surveyed area lies within $265° \lesssim \ell \lesssim 340°, |b| \lesssim 10°$. Its borders are outlined in Fig. 1. Within the surveyed area of $\sim$ 1200 sq. deg., 10276 new galaxies with D$\geq$ 0.'2 have been identified next to the 269 Lauberts-galaxies [10] with D$\geq$ 1′ in this area. Their distribution is displayed in an Aitoff projection of the southern sky together with all Lauberts galaxies. In the mean, the galaxy

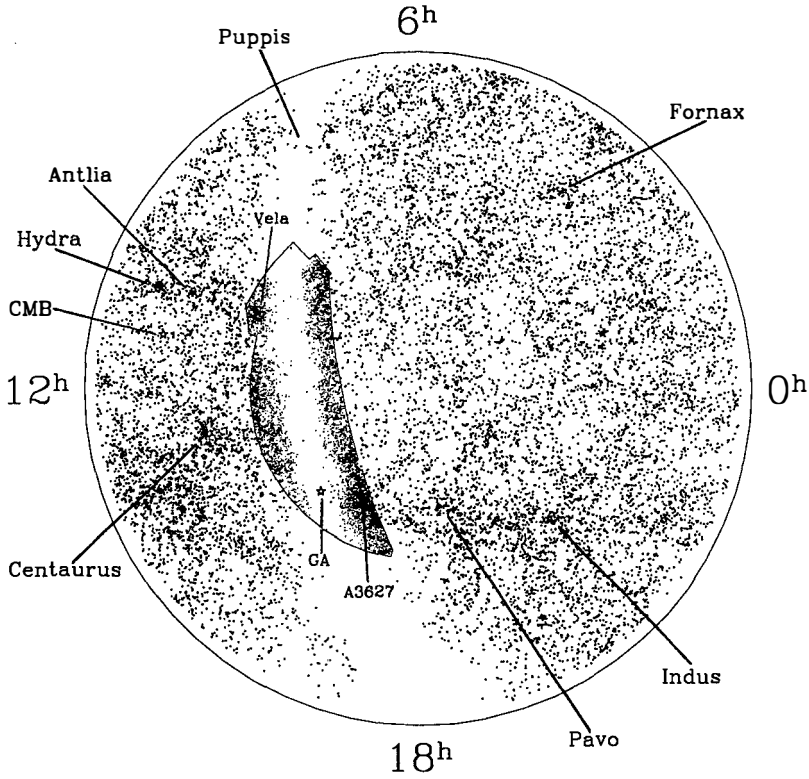


Figure 1: An equal-area projection of the galaxy distribution in the southern hemisphere displaying all Lauberts-galaxies (D$\geq$ 1′), complemented with the 10276 galaxies detected in our deep galaxy search behind the southern Milky Way (D$\geq$ 0.'2). The about 1200 sq. deg. surveyed systematically to date is outlined. The most prominent features are labelled.

density is well correlated with the foreground extinction A_B as traced by the HI-column-density to densities as low as 0.5 gal/sq. deg. For $A_B \gtrsim$5-6mag, respectively $N(HI) \gtrsim 4 - 6 \cdot 10^{21}$ cm^{-2}, the ZOA remains opaque [5, 7].

Above this band, distinct filaments and round concentrations can be recognized. They must have their origin in extragalactic large-scale structures. Some of these features seem to align with the known galaxy distribution, as *e.g.*, a filament above the Galactic Plane (GP) which points toward the Centaurus cluster, and the filament from the Hydra and Antlia clusters across the dipole direction in the CMB towards the prominent overdensity in Vela. However, the 2-dimensional galaxy distribution alone can be misleading. Redshift measurements are required to map the galaxies in 3 dimensions. For instance, our follow-up redshift observations trace a filament/supercluster from Hydra across the ZOA to $b = -10°$ at a mean velocity of 2500-3000 km/s, but the prominent overdensity in Vela is not part of it. The latter is part of a more distant (6000 km/s) shallow overdensity.

Details on the search procedure and earlier results can be found in [6, 7, 8, 9].

The cluster A3627: The most extreme overdensity is found within our recent search extension. It is centered on the cluster A3627 at $(\ell, b) = (325°, -7°)$ and is at least a factor 10 denser compared to regions at similar extinctions and a factor of 3 denser than the Vela-overdensity mentioned above. Although it is (a) the only Abell cluster identified behind the plane of the Milky Way, (b) classified as a rich, nearby cluster by [1], and (c) within a few degrees of the predicted center of the GA [4], this cluster has not received any attention. Part of the reason is the diminishing effects of the foreground obscuration. This cluster is hardly discernable in, for instance, the distribution of Lauberts galaxies (cf. left panel of Fig. 2). However, the diameters

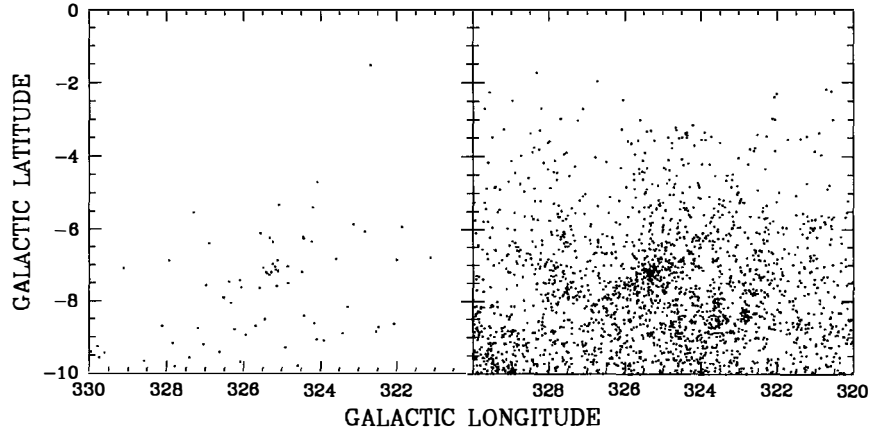


Figure 2: 10° × 10° fields centered on the cluster A3627. The left panel shows the Lauberts galaxies (D≥ 1.′0), the right panel the galaxies identified in our survey (D≥ 0.′2).

of the galaxies in this overdensity peak are just *below* the diameter limit of Lauberts. With slightly lower absorption its presence could have been as prominent as in our survey. This is illustrated in a close-up of the cluster area in Fig. 2. The left panel shows the previously known Lauberts-galaxies and the right panel the galaxies identified by us. In addition, the magnitudes and diameters are significantly brighter and larger than the mean of our survey ($B_J = 16\overset{m}{.}7$, D= 0.′7 compared to $B_J = 18\overset{m}{.}0$, D=0.′4), or the mean at similar latitudes.

The new data support the classification of A3627 as a rich cluster. The core radius of the cluster is $R_c = 10'.4$ with a central density of $N_o = 800$ gal/sq.deg. This translates to $R_c = 0.3$ Mpc for an approximate distance of D= $v_0/H_0 = 93$ Mpc (with $v_0 = 4660$ km/s as determined below and an adopted Hubble constant $H_0 = 50$ km/s/Mpc). Like all rich clusters, A3627 contains a large fraction of early type galaxies (50% in the core of this cluster, 25% within its Abell radius). This probably explains why this cluster is *not evident* at all in the distribution of IRAS-galaxies and IRAS-galaxy candidates which is very smooth in this area.

3 Results based from redshift observations

To assess the implications of the uncovered extragalactic large-scale features for the dynamics of the nearby Universe we are determining their redshifts. This is being pursued with three complementary observational approaches: (a) multifiber spectroscopy with OPTOPUS and MEFOS at the 3.6m telescope of ESO in the densest regions, (b) individual spectroscopy of the brightest galaxies with the 1.9m telescope of the SAAO, and (c) 21cm observations of the extended but low surface-brightness spirals with the 64m Parkes radio telescope (cf. [8, 9]). So far we have obtained 1079 new redshifts in our search area. They allow us to trace large-scale structures out to recession velocities of $v \gtrsim 25000$ km/s.

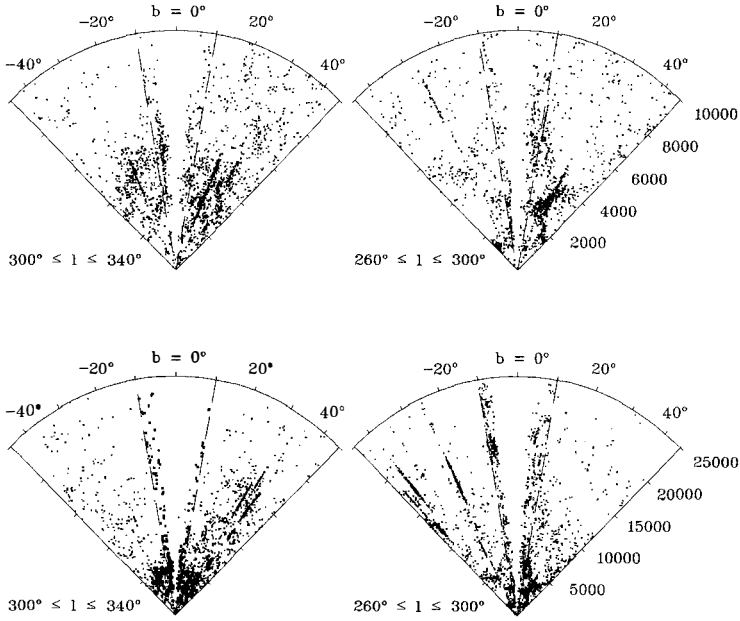


Figure 3: Redshift cones of galaxies in the GA-region ($300° \leq \ell \leq 340°$, left panels) and the Hydra/Antlia region ($260° \leq \ell \leq 300°$, right panels) for velocities $v_0 \leq 10000$ km/s (top) and $v_0 \leq 25000$ km/s (bottom). Within the displayed latitude range ($-45° < b < 45°$), the area investigated here ($|b| \lesssim 10°$) is delineated by dashed lines.

The galaxy distribution in redshift space is shown in Fig. 3 with redshift slices out to 10000 km/s (top) and 25000 km/s (bottom), for the Hydra/Antlia region (right panels) and the GA region (left panels). Our new data ($|b| \lesssim 10°$) is shown together with the data from the *Southern Redshift Catalogue* [3], a compilation of all measured redshifts in the southern hemisphere for the latitude range of $-45° < b < 45°$.

The main earlier results (cf. [6, 8, 9]) are a confirmation of the suspected Hydra/Antlia extension from Hydra $(\ell, b, v) = (270°, 27°, 2800$ km/s) to Antlia (273°, 19°, 2500 km/s) across the GP to about $b = -15°$ where it seems to end at the border of a void (top right panel), and the mapping of a previously unrecognized shallow but significant overdensity in Vela (280°, 6°, 6000 km/s). Note furthermore the seemingly preferred redshift-range of $\sim$ 16-18000 km/s in the lower panels. Is this a chance alignment of clusters, or an indication that the Shapley clusters above the GP are part of a super-structure that crosses the GP and connects to the Horologium clusters 100° further away – hence a coherent structure of about 600 Mpc?

The cluster A3627: Although we have so far covered only part of the cluster A3627 with our redshift measurements, the data already reveal it to be one of the most striking clusters in the nearby slices. The 'finger of God' is quite pronounced (325°, −7°, 4887 km/s) and does not exhibit the bimodal velocity distribution of the Centaurus cluster (302°, 22°, 3000&4500km/s). In fact, the velocity distribution of the 96 galaxies observed by us within the Abell radius of A3627, as displayed in Fig. 4, demonstrates it to be gaussian. The mean velocity and dispersion of the cluster are $< v_{obs} >= 4887$ km/s ($v_0 = 4660$ km/s) and $\sigma = 864$ km/s.

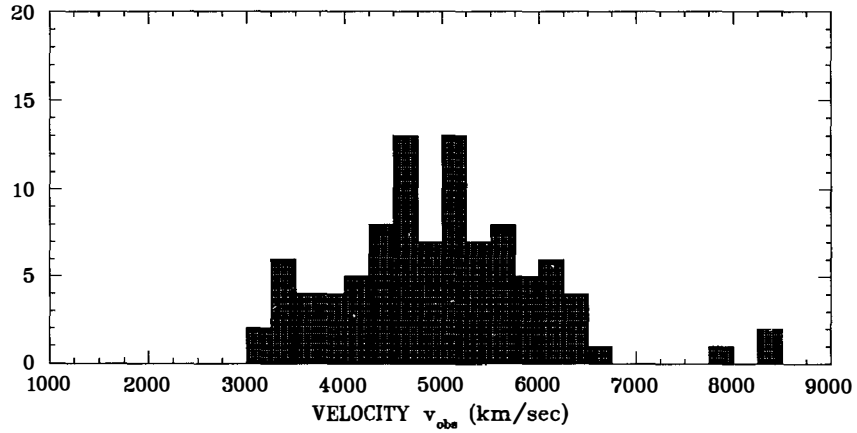


Figure 4: The velocity distribution of the 96 galaxies with measured redshifts within the Abell radius of A3627. The mean velocity and dispersion of the cluster, are $< v_{obs} >= 4887$ km/s, $\sigma = 864$ km/s, not including the 3 galaxies at $\sim$ 8000 km/s.

The large dispersion of A3627 indicates it to be quite massive. Using the formalism given by Rood et al. [12], a preliminary estimate finds (H_0=50 km/s/Mpc)

$$\mathcal{M}_{A3627} = 9 \cdot R_{eff} \cdot \sigma^2/G = 7 \cdot 10^{15} \mathcal{M}_\odot,$$

where the effective radius is $R_{eff} = 155'$. This cluster is hence an order of magnitude more massive than the Centaurus cluster. Its overall properties are similar to the well-studied nearby

rich clusters Perseus and Coma, and although it has not been detected previously in X-ray, ROSAT-observations (0.1-2.4 keV) prove it to be among the brightest 10 galaxy clusters [2].

A3627 versus GA: Is the cluster A3627 responsible for the observed infall into this area?

The predicted mass of the GA is of the order of $5 \cdot 10^{16} \mathcal{M}_{\odot}$ [11]. This is an order higher than the mass derived for A3627. However, the core-radius of the predicted overdensity is large (~20 Mpc). The mass distribution as mapped by POTENT from peculiar velocity fields describes structures only on supercluster scales because of the large smoothing windows (1200 km/s). But these potential wells generally have a rich cluster at their center, which is consistent with our findings. A3627 is embedded in a larger structure. The mean velocity of the cluster does not change within the immediate surroundings of the cluster. Moreover, the nearby slices (Fig. 3, top panels) are suggestive of a very large-scale coherent structure, starting at Pavo ($332°, -24°$) moving towards the density peak of A3627 at slightly larger velocities (left panel). This supercluster then seems to continue to the Vela-overdensity at 6000 km/s. First traces are seen in the left panel above the opaque part of the Milky Way, but it is very apparent in the right panel. A second branch might bend back from A3627 towards the Centaurus and/or Hydra & Antlia clusters (see also Fig. 1).

Although the mass of the here recognized massive cluster A3627 alone does not suffice to fully explain the observed velocity field in this area, the total mass of this supercluster centered on this rich cluster most likely will. A more quantitative analysis will be made with the forthcoming data as soon as we have finished our observations in this region.

References

[1] Abell, G.O., Corwin, H.G. & Olowin, R.P. 1989, ApJSS **70**, 1

[2] Böhringer, H. 1995, priv. commun.

[3] Fairall, A.P. 1994, *Unveiling Large-Scale Structures behind the Milky Way, Proceedings of the 4th DAEC Meeting*, eds. C. Balkowski & R.C. Kraan-Korteweg, A.S.P., p77

[4] Kolatt, T., Dekel, A., & Lahav, O. 1995, MNRAS, in press

[5] Kraan-Korteweg, R.C. 1993, in *2nd DAEC Meeting on The Distribution of Matter in the Universe*, eds. G. Mamon & D. Gerbal, Observatoire de Paris Press: Paris, p202

[6] Kraan-Korteweg, R.C. & Woudt, P.A. 1994, in *9th IAP Astrophysics Meeting and 3rd Meeting of the EARA on Cosmic Velocity Fields*, eds. F. Bouchet & M. Lachièze-Rey, p557

[7] Kraan-Korteweg, R.C. & Woudt, P.A. 1994, in *Unveiling Large-Scale Structures behind the Milky Way, Proceedings of the 4th DAEC Meeting*, eds. C. Balkowski & R.C. Kraan-Korteweg, A.S.P., p89

[8] Kraan-Korteweg, R.C., Cayatte, V., Fairall, A.P., Balkowski, C. & Henning. P.A. 1994, in *Unveiling Large-Scale Structures behind the Milky Way, Proceedings of the 4th DAEC Meeting*, eds. C. Balkowski & R.C. Kraan-Korteweg, A.S.P., p99

[9] Kraan-Korteweg, R.C., Fairall, A.P. & Balkowski, C. 1995, A&A **297**, 617

[10] Lauberts, A. 1982, The ESO/Uppsala Survey of the ESO (B) Atlas, ESO: Garching

[11] Lynden-Bell, D., Faber, S.M., Burstein, D., Davies, R.L., Dressler, A., Terlevich, R.J. & Wegner, G. 1988, ApJ **326**, 19

[12] Rood, H.J., Page, T.L., Kintner, E.C. & King, I.R. 1972: ApJ **175**, 627

SEARCH FOR EMISSION LINE GALAXIES TOWARDS NEARBY VOIDS

C.C. Popescu [1,4] U. Hopp [1,2], H. Elsässer [1], H. Hagen [3]
[1] *Max-Planck Institut für Astronomie, Heidelberg, Germany*
[2] *Universitätssternwarte München, München, Germany*
[3] *Hamburger Sternwarte, Hamburg, Germany*
[4] *The Astronomical Institute of the Romanian Academy, Bucharest, Romania*



Abstract

We present the results of our search for emission line galaxies (ELG) towards nearby voids and the first conclusions concerning their large scale spatial distribution. In order to find emission-line galaxies we started a survey using the IIIa-J objective prism plates from the Hamburg QSO Survey. Follow-up spectroscopy was used to obtain long-slit spectra and thus accurate redshifts of the selected candidates. A sample of 205 objects was finally obtained, of which almost half are newly discovered objects. The first results indicate that there are a few very isolated ELG. Most of these are distributed along the rim of the voids.

1 Introduction

Galaxy redshift surveys carried out over the last decade have revealed a grand picture of the large-scale structure of the Universe with tremendous complexity: coherent structures of galaxies, as well as large empty regions surrounded by filaments and sheets of galaxies and clusters. This view is primarily based on high-luminosity giant galaxies, which are known to constitute the tip of an iceberg of mostly low-luminosity dwarf galaxies. The question therefore arises: are the giant galaxies fair tracers of the large-scale structure? From an observer's point of view, the emptiness of the voids may be a result of observational bias. The above-mentioned galaxy maps may reflect special observational selection effects in surface brightness, integral magnitude or diameter. As we already know from the Local Group of galaxies, dwarf galaxies

can have very small diameters. Many of them also have low or very low surface brightness. These galaxies probably dominate the galaxy number in the Universe, but only very few (a few percent) are contained in the catalogues . They are difficult to detect on Schmidt plates even at the distance of nearby voids because of their small projected diameters. These objects are good candidates to fill up the voids. From the theoretical point of view, there has been the prediction (e.g. [3], [6]) that giants and dwarfs are spatially segregated, based on the concept of "biasing galaxy formation ".

Several studies of the spatial distribution of dwarf galaxies were carried out to test this prediction, though no definitive conclusion was drawn. While the studies concerning low-surface-brightness dwarfs ([2]; [13]; [4]; [11]; [1]; [12]) did not in general favor the models of biasing formation, the results of some objective-prism surveys ([15]; [9]; [17]; [16]; [10]; [18]; [14]) have suggested that star-forming galaxies have been found in voids. Recent work in this field (see [7], [8]) revcled that, while the central part of the voids remains free of galaxies, some of the dwarfs populate the outskirts of the voids, and from these dwarfs, most of them are emission-line galaxies (ELG). As there already have been some hints that such galaxies can provide a positive result to this unresolved question, we have started a project to search for ELG towards nearby voids.

2 Selection of candidates and follow-up observations

We used published cone diagrams to identify nearby ($v_R \leq 7500 km/s$) voids. Four void regions were selected according to the following criteria: diameter larger than 20 Mpc, completely empty of CfA galaxies, galactic latitude $b \geq 30^o$. The candidates were selected on the objective prism IIIa-J plates taken in the frame of the Hamburg Quasar Survey (HQS) ([5]). Automated search software was applied to the low resolution digitized data to select spectra with blue continua. We select candidates only in a certain interval of intensity, missing thus the bright objects, which are not needed for our study, but also some very faint objects, that lie very close to the detection limit of the plate. We estimate that we can miss 2 very faint objects per plate (0.07 objects/deg^2). The selected spectra are rescanned individually with high resolution and the final digitized spectra are visually inspected for emission lines. The objects are mainly selected based on the strong [OIII]λ5007 line, which appears as a distinctive peak near the green head of the objective prism spectra. Often the [OII]λ3727 can be identified too. Though our main selection criteria was the presence of emission features, we have also second priority candidates that were chosen because of their very blue continuum. Digitized direct plates were used to determine coordinates and also overlaps. The total area scanned was 1248 deg^2.

Most of the candidates were observed with the 2.2 m telescope at the German-Spanish Observatory in Calar Alto, Almeria (Spain). We used both the standard Cassegrain Spectrograph and the new focal reducer system. Some observations were made with the focal reducer system at the Calar Alto 3.5 m telescope. The resolution varies between 0.5 and 0.9 nm and covers at least the wavelength region from 420 to 820 nm. Typical exposure times are 10-15 minutes. For 75% of our sample we obtained direct images in R and B, using the focal reducer systems at the 2.2 m and the 3.5 m telescopes.

3 Results of Emission line galaxy search

We obtained a sample of 205 objects, of which 202 are emission-line objects and 3 are galaxies with absorption. From our sample of 205 objects, 96 (47%) are newly discovered objects, 53

(26%) are objects found already in the literature but with no available redshift (sometimes mentioned only as IRAS sources or only as galaxies) and 56 (27%) are objects with redshifts given already in the literature. We have observed all the objects with unknown redshift. From the objects with available redshifts, 6 were reobserved, in order to estimate our redshift errors.

The apparent magnitudes (derived from the Hamburg prism plates) of our sample range between $15.9 \leq B \leq 19.5$. It is customary to give a magnitude for which a survey is complete, but for our sample the incompletness are also described in terms of color, line fluxes and equivalent widths of the emission lines. (A detailed description of the incompletness will be given in a future paper.) Most of our objects seem to be HII galaxies, though some of the direct images indicate the presence of some further morphologies, like HII regions in normal galaxies and irregular dwarfs. There are also some galaxies with disturbed morphologies, that show signs of tidal interactions or mergers. We discovered 3 new QSOs (z=0.785, z=0.954, z=2.996) and 3 Syl galaxies (z=0.0146, z=0.0390, z=0.3447). Some of our spectra suggest

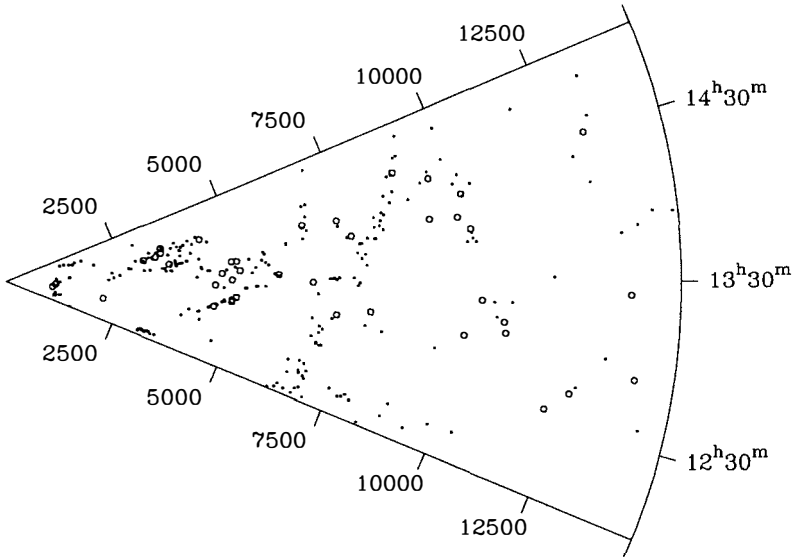


Figure 1: Cone diagram in velocity (km/s) and R.A. of one of our void region. The plot is for a strip of 7° in declination, centred on 36°30′. The small dots are CfA galaxies while the circles are ELG from our sample.

possible candidates for very low metallicity galaxies.

Our results are illustrated in a cone diagram of one of our void regions. We plotted in the same diagram our ELG (open circles), together with the CfA galaxies (small dots), as a comparison sample. There are obviously a few very isolated ELGs in our sample. These galaxies remain isolated also when we plot cone diagrams in declination. Most of the isolated galaxies are distributed along the rims of the voids. A detailed statistical analysis of the spatial distribution of our sample of ELG is in preparation. This analysis will clarify whether we found a more uniformly distributed galaxy population than that of giant galaxies and to which extent our galaxies spread into the voids. We will apply the nearest neighbourhood analysis as well as the two-point correlation function for this purpose.

References

[1] Binggeli B., Tarenghi M., Sandage A., 1990, *Astr. Astrophys.* **228**, 42

[2] Bothun G.D., Beers T., Mould J., Huchra J., 1986, *Astrophys. J.* **308**, 510

[3] Dekel A., Silk J., 1986, *Astrophys. J.* **303**, 39

[4] Eder J.A., Schombert J.M., Dekel A., Oemler A., 1989, *Astrophys. J.* **340**, 29

[5] Hagen H.-J., Groote D., Engels D., Reimers D., 1995, *Astr. Astrophys.* **in press**

[6] Hoffman Y., Silk J., Wyse R.F.G., 1992, *Astrophys. J.* **388**, L13

[7] Hopp U., Kuhn B., 1995, in *Astron. Ges. Review Ser. 8*, p. 277, ed. G. Klare

[8] Hopp U., Kuhn B., Thiele U., Birkle K., Elsässer H., 1995, *Astr. Astrophys. Suppl. Ser.* **109**, 537

[9] Moody J.W., Kirschner R.P., MacAlpine G.M., Gregory S.A., 1987, *Astrophys. J.* **314**, L33

[10] Salzer J.J., 1989, *Astrophys. J.* **347**, 152

[11] Salzer J.J., Hanson, M.M., Gavazzi G., 1990, *Astrophys. J.* **353**, 39

[12] Thuan T.X., Alimi, J.-M., Gott, J.R., Schneider, S.E., 1991, *Astrophys. J.* **370**, 25

[13] Thuan T.X., Gott J.R., Schneider S.E., 1991, *Astrophys. J.* **315**, L93

[14] Thuan T.X., Izotov Y.I., Lipovetsky V.A., Pustilnik, S.A., 1994 in *ESO Conference and Workshop Proceedings No. 49 'Dwarf Galaxies '* p.421, eds. G.Meylan & P. Prugniel

[15] Tifft W.G., Kirschner R.P., Gregory S.A., Moody J.W., 1986, *Astrophys. J.* **310**, 25

[16] Weistrop D., 1989, *Astron. J.* **97**, 357

[17] Weistrop D., Downs R.A., 1988, *Astrophys. J.* **331**, 172

[18] Weistrop D., Hintzen P., Kennicutt R.C., Liu C., Lowenthal J., Cheng K.-P., Oliversen R., Woodgate B., 1992, *Astrophys. J.* **396**, L23

DO DWARF AND LSB GALAXIES TRACE THE SAME DENSITY FIELD AS BRIGHT GALAXIES?

R. Domínguez-Tenreiro [1], J.M. Alimi [2], A. Serna [2], and T.X. Thuan [3]
[1] *Departamento de Física Teórica, C-XI, UAM, 28049 Madrid, Spain*
[2] *Laboratoire d'Astrophysique Extragalactique et de Cosmologie (CNRS, URA173), Observatoire de Paris-Meudon, 92195 Meudon, France*
[3] *University of Virginia, P.O. Box 3818, University Station, Charlottesville, VA 22903, USA*

Abstract

A sample of northern dwarf and low surface brightness (LSB) galaxies selected from the UGC catalog, with complete redshift information, have been analyzed through the scaling formalism. We have constructed volume-limited subsamples which have been compared to bright galaxies from the Center for Astrophysics (CfA) Survey in the same volume-limited samples. The scaling formalism allows for a separate analysis of regions belonging to different density ranges. The null hypothesis that dwarf and LSB galaxies, on one hand, and CfA galaxies, on the other, trace the same density field can be ruled out at a 95% confidence level for areas of high to low density, with CfA galaxies more clustered than dwarf and LSB galaxies. The differences are not statistically significative for the overdense regions of the closer galaxies, presumably due to a higher degree of peculiar velocity contamination in the redshifts of the nearby CfA galaxies. These results are stable against a change in the absolute magnitude interval or the morphological type of the CfA subsamples.

1 Introduction

In most biasing theories, physical processes responsible for biasing are expected to have different effects on protogalaxies of different properties. As a result, dwarfs and bright normal galaxies are expected to have observably different distributions. In a extreme interpretation, some authors [1] have maintained that dwarfs should fill in the voids defined by the distribution of bright normal galaxies.

The first studies of this problem [2] have not led to any clear conclusion. A meaningful comparison between the clustering properties of dwarf and normal galaxies requires a complete dwarf sample, with a sky coverage and depth similar to normal galaxy catalogs. T. X. Thuan and his collaborators have measured the redshifts of all galaxies from the Uppsala General Catalog of Galaxies [3] classified by Nilson as dwarfs, Magellanics or irregulars in the same volume as the CfA catalog [4]. This redshift survey is complete for galaxies with blue apparent diameter larger than $1'$. The data were obtained through the 21 cm line, so that the catalog does not contain H I-deficient objects such as dwarf ellipticals. Objects with a redshift $v \geq 1480$ km s^{-1} are not bonafide dwarfs, but low surface brightness (LSB) objects. This catalog has been analyzed and compared to the CfA1 catalog [5] using the two-point correlation and cross-correlation functions [6]. In agreement with previous studies, it has been found out that dwarfs are slightly less clustered than bright galaxies and they do not fill in voids. However, it is well known that two distributions of points can have comparable two-point correlations and have, nevertheless, very different clustering properties [7, 8], so that it seems desirable to complement previous works with an analysis through another statistical tool.

We present the results of the analysis of the dwarf-LSB catalog and its comparison with the CfA1 catalog by means of the scaling formalism [8, 9, 10]. This formalism gives a deeper insight into the clustering properties of point sets than the two-point correlation function, it provides with a separate description of regions belonging to different density ranges and it is capable to detect contamination by peculiar velocities.

2 The method

Details about the scaling formalism can be found in [8],[10]–[13]. Here we just mention its main points. Let us consider a distribution of N points. We assign to each point, i, in the distribution a) a probability at scale r given by $p_i(r) = n_i(r)/N$, where $n_i(r)$ is the number of points inside a sphere of radius r centered at the i-th point; and b) a radius at probability p, $r_i(p)$, such that the sphere centered at the point i and of radius r contains $n = pN$ points. For every $q \geq 2$ and $\tau \leq -1$ we then form the sums:

$$Z(q,r) \equiv \frac{1}{N} \sum_{i=1}^{N} p_i(r)^{q-1}, \tag{1}$$

$$W(\tau,p) \equiv \frac{1}{N} \sum_{i=1}^{N} r_i(p)^{-\tau} \tag{2}$$

These are the basic ingredients of the so-called correlation sum algorithm and n-nearest neighbor algorithm, respectively [14]. Note that the $Z(q,r)$ moments describe preferentially regions of higher density of the point distribution as q increases, while the $W(\tau,p)$ sums describe preferentially regions of lower density as $\mid \tau \mid$ increases. The slopes of the $Z(q,r), (W(\tau,p))$ moments, when plotted versus r (p) in the log-log plane, provide us with a method for clustering diagnostic: the steeper log $Z(q,r)$ (and log $W(\tau,p)$ for high $\mid \tau \mid$), the less clustered the point set is; for low $\mid \tau \mid$, the steeper log $W(\tau,p)$, the more clustered the point set is.

In order to quantify the statistical significance of the possible clustering differences, we have tested the null hypothesis H_0 that any pair of dwarf-LSB and bright galaxy samples, D and B, have been drawn from a common underlying galaxy population. To this end, for any pair of D and B samples, we have formed the joint BUD sample. We have extracted from BUD M random samples with the same number of galaxies as a) the B sample, and b) the D sample. Then we define:

$$\delta_{lk}(x) \equiv S_l^D(x) - S_k^B(x), \qquad \delta(x) \equiv S^D(x) - S^B(x) \tag{3}$$

for any pair of random realizations of B and D, and for the data, respectively. In these formulae, x is a particular value of the r or p variables and $S(x)$ stands for the $Z(q,x)$ and $W(\tau,x)$ statistics. A measure of the local confidence level at which the null hypothesis, H_0, can be ruled out at point x can be calculated by means of the critical statistics:

$$P_{ij}(x) = \frac{100}{M^2} \sum_{l,k=1}^{M} \log\theta[\delta_{lk}(x) - \delta_{ij}(x)] \tag{4}$$

for the M^2 random realizations and

$$P(x) = \frac{100}{M^2} \sum_{l,k=1}^{M} \log\theta[\delta_{lk}(x) - \delta(x)] \tag{5}$$

for the data. Here θ is the Heaviside step function.

3 The samples

We have compared volume-limited samples of dwarf-LSB and CfA1 galaxies corresponding to the same volumes, defined by the conditions $b \geq 40^0, \delta \geq 0^0, V \leq V_{max}$ (north cap). Dwarf-LSB galaxies are mostly field galaxies. In consequence, we have considered *reference samples* of bright (B) and dwarf-LSB (D) galaxies, where galaxies belonging to rich clusters have been excluded, and with limiting depths of V_{max} =13'75, 2750, 3981 and 5500 km s^{-1} (B13, D13, B27, D27, B39, D39, B55 and D55 samples, respectively). Moreover, to test the stability of the results obtained for the reference samples against changes in the absolute magnitude and intrinsic diameter intervals used to build up them , i) we have also considered samples of bright galaxies whose M_B^{max} corresponds to the limiting value for the following deeper volume-limited reference sample, and ii) we have split dwarf-LSB samples into "big" and "small" galaxies subsamples. To analyze the effects of the presence of galaxies belonging to rich clusters, we have also compared volume-limited samples occupying the same volume as the reference samples but where cluster galaxies have been included. Finally, to test the stability of the results against changes in the morphological type of CfA1 galaxies, we have performed a comparison of the reference dwarf-LSB samples with volume-limited samples where only CfA1 spirals are included.

4 Results

The general result is that CfA1 galaxies are slightly more clustered than dwarf-LSB galaxies.

For the reference samples, the analysis through the $Z(q,r)$ moments reveals that the spatial segregation decreases from areas of moderate density to overdense areas (high q). Only a poor segregation has been detected between the B13 and D13 samples (bonafide dwarfs), presumably due to the high percentage of contamination by peculiar velocities of B galaxies in this volume. The analysis through the $W(\tau,p)$ moments tells us that the clustering differences decrease from areas of moderate density to underdense areas (high $\mid \tau \mid$). We note that, in this case, a positive segregation has been found between the B13 and D13 samples. In Figure 1 we show the regions of the $r-q$ plane where the null hypothesis H_0 can be ruled out at a confidence level $CL \geq 95\%$ (in black) or $95\% > CL \geq 90\%$ (in grey), when the clustering is measured through the $Z(q,r)$ moments. Figure 2 shows the same regions in the $p-\tau$ plane, when the

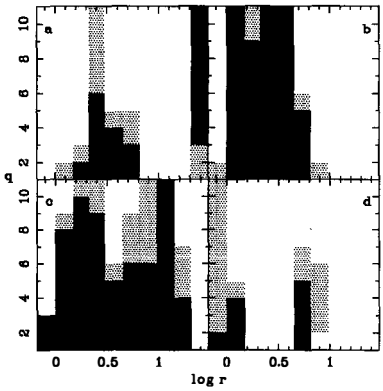


Figure 1

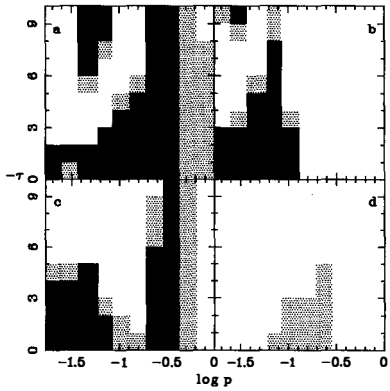


Figure 2

clustering is measured through the $W(\tau, p)$ moments. These results are stable against changes in the intervals of absolute magnitude (for CfA1 galaxies) or intrinsic diameter (for dwarf-LSB galaxies) considered. When cluster galaxies are included, the clustering differences between bright and dwarf-LSB galaxies increase dramatically for the overdense areas of the galaxy distribution (high q), while for the underdense areas the effect is less important. Finally, when only spiral CfA1 galaxies are considered in the bright samples, we get a spatial segregation which is quantitatively intermediate between that detected in the two previous cases.

We conclude that dwarf-LSB galaxies do not seem to trace the same density field as CfA1 galaxies when described by means of the $Z(q, r)$ and $W(\tau, p)$ statistics, at least for some r and q, or p and τ values, respectively. These statistics detect also a morphological segregation between spirals and ellipticals, and also a (slighter) luminosity and size segregation (see [12, 15, 16] and references quoted therein; see also Campos and Benoist, these proceedings, for similar results using other statistical descriptors). All these results put together suggest that the underlying mass density field is not traced exactly in the same way by galaxies of different morphology and/or luminosity and size.

References

[1] Dekel, A., and Silk, J. 1986, ApJ, 303, 39.

[2] Davis, M., and Djorgovski, S. 1985, ApJ, 299, 15; Giovanelli, R., Haynes, M.P., and Chincarini, G.L. 1986, ApJ, 300, 77; Bothun, G.D., Beers, T.C., Mould, J.R., and Huchra, J.P. 1986, ApJ, 308, 510; Thuan, T.X., Gott, J.R., and Schneider, S.E. 1987, ApJ, 315, L93; Eder, J.A., Schombert, J.M., Dekel, A., and Oemler, A. 1989, ApJ, 340, 29; Binggeli, B., Tarenghi, M., and Sandage, A. 1990, A&A, 228, 42. Salcer, J.J., Hanson, M.M. and Gavazzi, G. 1990, ApJ, 353, 39; Santiago, B.X., and da Costa, L.N. 1990., ApJ, 362, 286.

[3] Nilson, P. 1973, Uppsala General Catalog of Galaxies, Uppsala Astr. Obs. Ann., Vol. 6.

[4] Schneider, S.E., Thuan, T.X., Magri, C., and Wadiak, E.J, 1990, ApJS, 72, 245.

[5] Huchra, J., Davis, M., Latham, D., and Tonry, J., 1983, ApJS, 52, 89.

[6] Thuan, T.X., Alimi, J.M., Gott, J.R., and Schneider, S.E. 1991, ApJ, 370, 25.

[7] Peebles, P.J.E. 1980, "The Large Scale Structure of the Universe" (Princeton: Princeton University Press).

[8] Martínez, V.J., Jones, B.J.T., Domínguez-Tenreiro, R. and van de Weygaert, R. 1990, ApJ, 357, 50.

[9] Jones, B.J.T., Martínez, V.J., Saar, E., and Einasto, J., 1988, ApJ Letters, 332, L1.

[10] Borgani, S. 1995, Phys. Rep. in press.

[11] Yepes, G., Domínguez-Tenreiro, R., and Couchman, H.M.P. 1992, ApJ, 401.40.

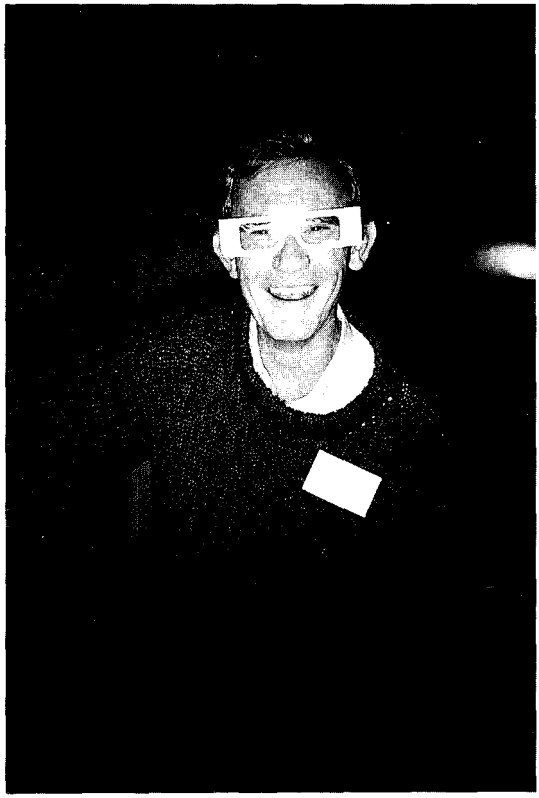
[12] Domínguez-Tenreiro, R., Gómez-Flechoso, M.A. and Martínez, V.J. 1994, ApJ, 424, 42.

[13] Domínguez-Tenreiro, R., Alimi, J.M., Serna, A., and Thuan, T.X. 1995, in preparation.

[14] Grassberger, P., Badii, R., and Politi, A. 1988, J. Stat. Phys. 51, 135.

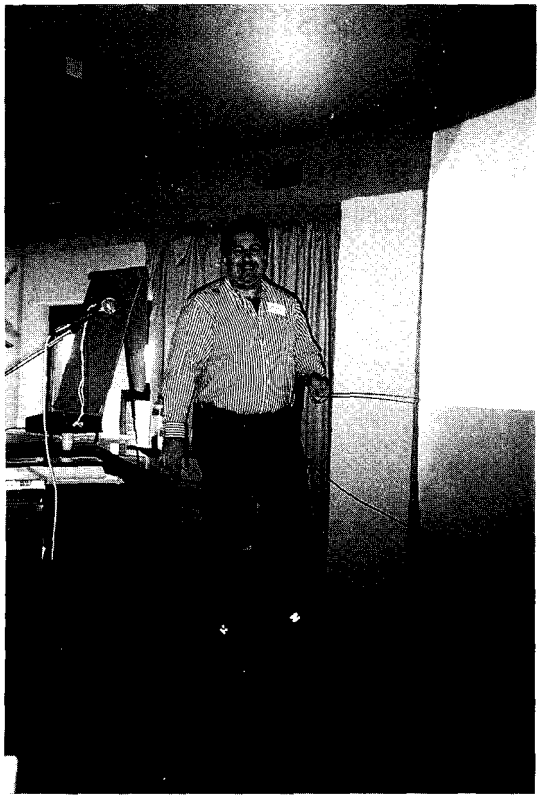
[15] Campos, A., Domínguez-Tenreiro, R., and Yepes, G. 1994, ApJ, 436, 565.

[16] Domínguez-Tenreiro, R., Campos, A., Gómez-Flechoso, M.A., and Yepes, G. 1994, ApJ Letters, 424, L73.



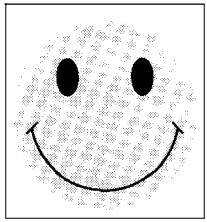
SESSION II

PECULIAR MOTIONS AND THE DENSITY FIELD



MEASURING OMEGA INDEPENDENT OF GALAXY BIASING

Avishai Dekel
Racah Institute of Physics, The Hebrew University, jerusalem 91904, Israel.



Abstract

I describe methods for measuring the cosmological density parameter Ω from the large-scale peculiar velocity field *independent* of galaxy biasing and Λ. Several such methods assume Gaussian initial fluctuations; they use either the velocity field near a void, or the skewness of the probability distribution of $\nabla \cdot \mathbf{v}$, or the initial density fluctuations. All yield $\Omega > 0.3$ with $> 95\%$ confidence.

A new determination is based on comparing the power spectrum of *mass* density fluctuations as derived from the observed velocities with the large-angle fluctuations in the microwave background observed by COBE. For an inflation-motivated flat cosmology with $\Omega + \Lambda = 1$ and cold dark matter, it is found that if the initial fluctuation power index is $n = 1$, maximum likelihood is at $\Omega \simeq (0.7 \pm 0.2)\, h_{50}^{-1.2}$. If $\Omega = 1$, then with no tensor fluctuations $n \simeq (0.8 \pm 0.1) h_{50}^{-0.8}$, and with tensor fluctuations $n \simeq (0.9 \pm 0.1) h_{50}^{-0.8}$.

1 Introduction

Three general kinds of data are used in the effort to determine the cosmological density parameter Ω from large-scale structure: (a) the distribution of galaxies on the sky and in redshift surveys, (b) the large-angle fluctuations in the microwave background (CMB), and (c) the peculiar velocities of galaxies.

As illustrated in Figure 1, these data can be combined to constrain Ω in several different ways. All the methods that use the spatial distribution of galaxies must depend on the unknown relation between the density fluctuations of galaxies and mass, commonly characterized by a linear *biasing* factor b. In the linear approximation to gravitational instability (GI), which is roughly valid for the fields when they are smoothed on large scales, what is actually being measured by these methods is the degenerate parameter $\beta \equiv f(\Omega)/b$ (where $f \approx \Omega^{0.6}$) rather

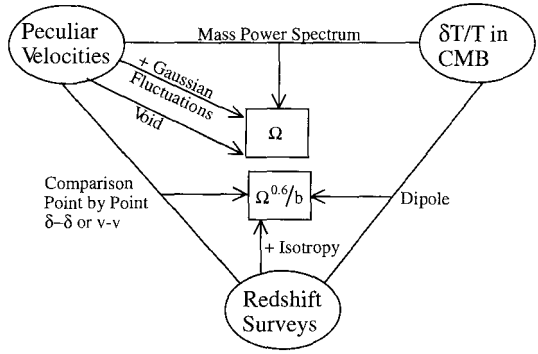


Figure 1: Methods for measuring Ω and β from large-scale observations.

than Ω itself. These methods, reviewed in [18] and [49], include (a) comparisons of the CMB dipole with the acceleration of the Local Group (LG) as predicted via the gravity induced by the galaxy distribution around us, (b) comparisons of the observed peculiar velocities with the galaxy distribution and the predicted velocities deduced from redshift surveys, and (c) measurements of redshift-space distortions under the assumption of global isotropy. The most recent estimates of β for optical and IRAS galaxies lie in the range $0.5 \leq \beta \leq 1$. As argued in §2, the contamination by biasing introduces a significant uncertainty in the translation of the various β measurements to a reliable estimate of Ω.

It is therefore worth considering here alternative methods for determining Ω, which are *independent* of galaxy biasing. These methods are based on the observed peculiar velocities described in §3. One family of such methods uses the velocity data alone, combined with the assumption (supported by observations, e.g. [44]) that the initial fluctuations were drawn from a *Gaussian* random field. Three examples are described in §4: using the velocity field around *voids*, using the *skewness* of $\nabla \cdot \boldsymbol{v}$, and recovering the *initial* probability distribution of density fluctuations.

Another way of determining Ω is based on comparing the observed velocities with the large-angle fluctuations in the *CMB*. Recent comparisons of this sort, via the mass-fluctuation *power spectrum*, are described in §5. These direct estimates of Ω are discussed in §6 in the general context of other cosmological parameters.

2 Uncertainties due to Galaxy Biasing

Galaxy "biasing" clearly exists. The fact that galaxies of different types cluster differently [26] imply that at least some do not trace the underlying mass, and any physical theory would predict non-trivial biasing ([3], [17], [24], [22], [10], [51]). Indeed, simulations of galaxy formation involving gas dynamics ([12], [13]) indicate a biasing relation that is nonlinear in density and is varying with scale. It is therefore not surprising that the various estimates of β show a large scatter. Some of this scatter is due to the different types of galaxies involved, and some may be due to unaccounted for effects of nonlinear gravity or other systematic errors, but a significant fraction of the scatter is likely to reflect non-trivial properties of the biasing scheme. All this means that translating a measured β into Ω is non-trivial; it requires a detailed knowledge of

the relevant biasing scheme.

In order to strengthen this point, I demonstrate here that an obvious source of scatter in β is a straightforward consequence of the inevitable *statistical* scatter in the biasing process. Let $\delta(\boldsymbol{x})$ be the field of mass-density fluctuations smoothed at a given scale, and let $\delta_G(\boldsymbol{x})$ be the corresponding field for galaxies of a given type. Treat them as random fields, both with probability densities of zero mean by definition. Denote $\langle\delta^2\rangle \equiv \sigma^2$ and $\langle\delta^3\rangle \equiv S$. Consider the "biasing" relation between galaxies and mass to be a *random* process, specified by the *conditional probability* function $B(\delta_G|\delta)$ [21]. The common deterministic biasing relation, $\delta_G = b(\delta)\delta$, is replaced by the conditional mean,

$$\langle\delta_G|\delta\rangle \equiv b(\delta)\delta. \tag{1}$$

The statistical character of the relation is expressed by the conditional moments of higher order about the mean, such as

$$\langle(\delta_G - b\delta)^2|\delta\rangle \equiv \sigma_b^2, \quad \text{and} \quad \langle(\delta_G - b\delta)^3|\delta\rangle \equiv S_b. \tag{2}$$

This statistical nature of biasing leads to a different "biasing parameter" for each specific application.

Take for example the ratio of variances, $b_2^2 \equiv \langle\delta_G^2\rangle/\langle\delta^2\rangle$, such as being obtained by a ratio of power spectra or two-point correlation functions, or by comparing the mass function of clusters to the variance of δ_G at $8\,h^{-1}$Mpc [**?**]. One can prove in general that $\langle\delta_G^m\rangle = \langle\,\langle\delta_G^m|\delta\rangle_{\delta_G}\,\rangle_\delta$, and therefore, $\langle\delta_G^2\rangle = \langle b^2(\delta)\,\delta^2\rangle + \langle\sigma_b^2(\delta)\rangle$. Thus, in the simple case where $b(\delta)$ is constant, b_2 is an overestimate of b by

$$b_2 = b\,(1+\Delta_2)^{1/2}, \quad \Delta_2 \equiv \langle\sigma_b^2\rangle/(\sigma^2 b^2). \tag{3}$$

Another common way of estimating β is via linear regression of the noisy field $-\boldsymbol{\nabla}\cdot\boldsymbol{v}(\boldsymbol{x})$ $[\approx f(\Omega)\delta(\boldsymbol{x})]$ on $\delta_G(\boldsymbol{x})$, or via a regression of the corresponding velocities. The slope of the forward regression of δ_G on δ is $b_f = \langle\delta_G\delta\rangle/\langle\delta^2\rangle$, and the slope of the inverse regression of δ on δ_G is $b_i^{-1} = \langle\delta\delta_G\rangle/\langle\delta_G^2\rangle$. In the case where b is constant, $b_f = b$, and b_i is an overestimate,

$$b_i = b\,(1+\Delta_2). \tag{4}$$

Similarly, most methods for determining β lead to an underestimate.

The level of the effect depends on the actual values of Δ_2 and similar parameters. For example, a goodness of fit test of the $12\,h^{-1}$Mpc-smoothed density fields of POTENT mass and optical galaxies [31] yields $\chi^2 \sim 2$ per degree of freedom, instead of ~ 1, unless one adds to the assumed errors a biasing scatter of $\sigma_b \sim 0.15$, corresponding to $\Delta_2 \sim 0.25$ (with $\sigma \sim 0.3$ and $b \sim 1$). Alternatively, hydro simulations [13] yield $\sigma_b = 0.25$ under $10\,h^{-1}$Mpc Gaussian smoothing, i.e. $\Delta_2 \sim 0.4$ (with $\sigma \sim 0.4$). If $b = \Omega = 1$, then the β values derived by the various methods are expected to span the range $0.7 \le \beta \le 1$ just due to the dispersion in the biasing relation. A large skewness in $B(\delta_G|\delta)$ may stretch this range even further.

The moral from the biasing uncertainty is that methods for measuring Ω independent of biasing are desirable.

3 Peculiar Velocity Field

3.1 Data: Mark III

Galaxy distances r_i are estimated by the Tully-Fisher (TF) method for spirals, and by the analogous $D_n - \sigma$ method for ellipticals and SO's. Given a galaxy redshift z_i, the radial

peculiar velocity is $u_i = cz_i - r_i$ (H_0 is set to unity; distances are measured in $\mathrm{km\,s^{-1}}$). Several such samples have accumulated in recent years. Assuming that all galaxies trace the same underlying velocity field, the analysis of large-scale motions greatly benefits from merging the different samples into one self-consistent catalog. The recent Mark III catalog ([53], [54], [55]) combines 544 early type galaxies (mostly [38]) with $\sim$2850 spirals ([1], [29], [40], [30], [52], [15], [39]).

The observers differ in their selection procedures, the quantities they measure, the methods of measurement and the TF calibration techniques, which cause systematic errors and made the merger of Mark III non-trivial, along the following steps. (a) Standardizing the selection criteria, *e.g.* rejecting galaxies of high inclination or low rotation, which are suspect of large errors, and sharpening any z cutoff. (b) Rederiving a provisional TF calibration for each data set using an algorithm that simultaneously groups, fits and corrects for selection bias, and then verifying that inverse-TF distances to clusters are similar to the forward-TF distances. (c) Starting with one data set, adding each new set in succession using the galaxies in common to adjust the TF parameters of the new set if necessary. (d) Using only one measurement per galaxy even if it was observed by more than one observer to ensure well defined errors, and using multiple observations for a "cluster" only if the overlap is small (*e.g.* $<50\%$). (e) Adding the ellipticals from Mark II [11], allowing for a slight zero-point shift. Such a careful calibration and merger procedure is *crucial* for reliable results — in several cases it produced TF distances substantially different from those quoted by the original authors. The Mark III catalog enables a reasonable recovery of the dynamical fields with $\sim 12\,\mathrm{h^{-1}}$ Mpc smoothing in a sphere of radius $\sim 60\,\mathrm{h^{-1}}$Mpc about the LG, extending to $\sim 80\,\mathrm{h^{-1}}$Mpc in certain regions.

3.2 POTENT Analysis

Given the sparsely-sampled radial velocities u_i, POTENT first computes a *smoothed* radial-velocity field in a spherical grid, $u(\boldsymbol{x})$, using a tensor window function corresponding to a Gaussian window of radius $12\,\mathrm{h^{-1}}$Mpc ([19], [6], [18]). Weighting inversely by the local density near each object mimics equal-volume averaging that minimizes the bias due to non-uniform sampling, and weighting inversely by the distance errors, σ_i^2, reduces their random effects.

The 3D velocity field is recovered under the assumption of *potential* flow: $\boldsymbol{v}(\boldsymbol{x}) = -\boldsymbol{\nabla}\Phi(\boldsymbol{x})$ [**?**]. According to linear GI, any vorticity mode decays in time as the universe expands, and based on Kelvin's circulation theorem the flow remains vorticity-free in the mildly-nonlinear regime as long as the flow is laminar. The velocity potential can therefore be calculated by integrating the radial velocity along radial rays, $\Phi(\boldsymbol{x}) = -\int_0^r u(r', \theta, \phi)dr'$. Differentiating Φ in the transverse directions then recovers the two missing velocity components.

The underlying mass-density fluctuation field, $\delta(\boldsymbol{x})$, is computed by the approximation [43]

$$\delta_c(\boldsymbol{x}) = \|I - f(\Omega)^{-1}\partial\boldsymbol{v}/\partial\boldsymbol{x}\| - 1\ , \tag{5}$$

where the bars denote the Jacobian determinant, and I is the unit matrix. This is the solution to the continuity equation under the Zel'dovich assumption that particle displacements evolve in a universal rate, and it reduces to the familiar $\delta = -f^{-1}\boldsymbol{\nabla}\cdot\boldsymbol{v}$ in the linear regime. It approximates the true density in N-body simulations of Gaussian initial conditions, with an *rms* error less than 0.1 over the range $-0.8 \le \delta \le 4.5$.

The results suffer from random and systematic errors due to the distance errors and the non-uniform sampling. The ways to handle these errors are discussed in [19] and [18], where special attention has been paid to correcting for inhomogeneous Malmquist bias. A degree of freedom remains because the inferred distances are only relative. The mean Hubble flow

is tentatively fixed by minimizing velocity residuals within the volume sampled. Therefore, a Hubble-like peculiar velocity error is expeceted, corresponding to a DC offset of order 10% in density fluctuation.

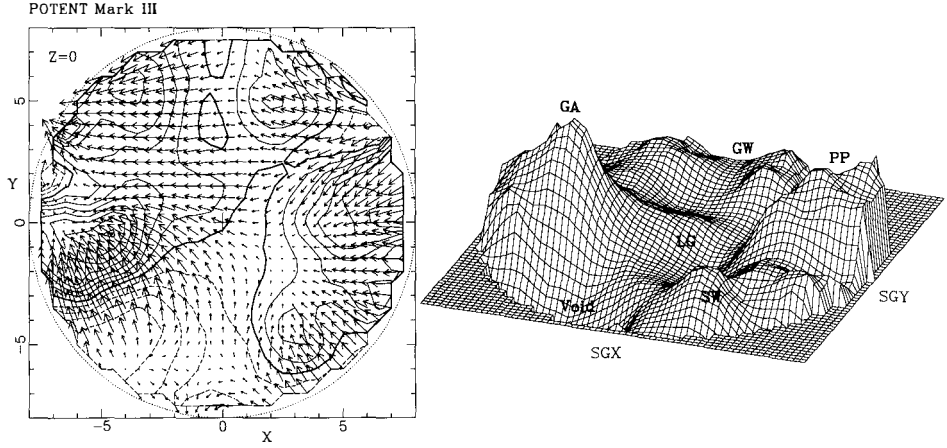


Figure 2: The fluctuation fields of velocity and *mass*-density in the Supergalactic plane as recovered by POTENT from the Mark III velocities of $\sim$ 3000 galaxies with $12\,h^{-1}$Mpc smoothing. The vectors shown are projections of the 3D velocity field in the CMB frame. Distances and velocities are in 1000 $km\,s^{-1}$. Contour spacing is 0.2 in δ, with the heavy contour marking $\delta = 0$ and dashed contours $\delta < 0$. The LG is at the center. The GA is on the left, PP on the right, and Coma is at the top. The grey-scale in the contour map and the height of the surface in the landscape map are proportional to δ (Dekel *et al.* 1994).

Three arguments support our working hypothesis that the peculiar velocities are *real* and that they grew by *GI*: (a) the velocity fields traced separately by spirals and by ellipticals, using different distance indicators, are consistent with each other [34], (b) the COBE detection of $\delta T/T \sim 10^{-5}$, and the local bulk velocity of ~ 350 $km\,s^{-1}$ across $\sim 100\,h^{-1}$Mpc, are consistent with each other (§5.1 and [7]), and (c) the galaxy density from redshift catalogs and the mass density recovered from observed velocities are consistent with each other [20]. We thus adopt the hypothesis that the velocities are real and generated by the gravity induced by the mass-density fluctuations, and we try to determine Ω from them.

4 Omega from Velocities and Gaussian Fluctuations

4.1 Velocities in Voids

A diverging flow in an extended low-density region can provide a robust dynamical lower bound on Ω, based on the fact that large gravitating outflows are *not* expected in a low-Ω universe [23]. In practice, we assume a value for Ω and use the derivatives of the observed velocity field in diverging regions to infer a non-linear approximation to the mass density there, via the approximation δ_c (5). When the true value of Ω is used, this approximation is typically an overestimate, $\delta_c > \delta$. For fluctuations that started Gaussian, the probability that δ_c is an overestimate, in the range $\delta < -0.5$, is well over 99%. Analogously to $\delta_0 \approx -\Omega^{-0.6}\nabla \cdot \boldsymbol{v}$, the

δ_c inferred from a given diverging velocity field is more negative when a smaller Ω is assumed, and for a small enough Ω it may even be smaller than -1. This provides a lower bound on Ω because mass is never negative and therefore $\delta < -1$ is forbidden.

The inferred δ_c field, smoothed at $12\,\mathrm{h}^{-1}$Mpc, and the associated error field σ_δ, were derived by POTENT from the observed radial velocities, and, focusing on the deepest density wells, the assumed Ω was lowered until δ_c became significantly smaller than -1. The most promising "test case" provided by the Mark III data is a broad diverging region centered near the supergalactic plane at the vicinity of $(X, Y) = (-25, -40)$ in h^{-1}Mpc — the "Sculptor void" of galaxies between the GA and the "Southern Wall" extension of PP (Figure 3, compare to figure 2).

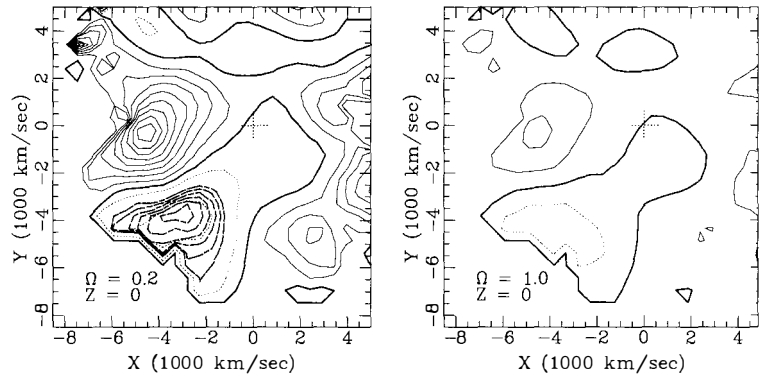


Figure 3: Maps of δ_c inferred from the observed velocities near the Sculptor void in the Supergalactic plane, for two values of Ω. The LG is marked by '+' and the void is confined by the Pavo part of the GA (left) and the Aquarius extension of PP (right). Contour spacing is 0.5, with $\delta_c = 0$ heavy, $\delta_c > 0$ solid, and $\delta_c < 0$ dotted. The heavy-dashed contours mark the illegitimate downward deviation of δ_c below -1 in units of σ_δ, starting from zero (*i.e.* $\delta_c = -1$), and decreasing with spacing -0.5σ. The value $\Omega = 0.2$ is ruled out at the 2.9σ level (Dekel & Rees 1994).

Values of $\Omega \approx 1$ are perfectly consistent with the data, but δ_c becomes smaller than -1 already for $\Omega = 0.6$. The values $\Omega = 0.3$ and 0.2 are ruled out at the 2.4σ and 2.9σ levels in terms of the random error σ_δ.

This result is still to be improved. The systematic errors have been partially corrected in POTENT, but a more specific investigation of the biases affecting the smoothed velocity field in density wells is still in progress. For the method to be effective one needs to find a void that is (a) bigger than the correlation length for its vicinity to represent the universal Ω, (b) deep enough for the lower bound to be tight, (c) nearby enough for the distance errors to be small, and (d) properly sampled to trace the velocity field in its vicinity.

4.2 Skewness of $\boldsymbol{\nabla \cdot v}$

Assuming that the initial fluctuations are a *Gaussian* random field, the one-point probability distribution function (PDF) of smoothed density develops a characteristic skewness due to non-linear effects early in the non-linear regime [33]. The skewness of δ is given according to

second-order perturbation theory by

$$\langle\delta^3\rangle/\langle\delta^2\rangle^2 \approx (34/7 - 3 - n) \ , \tag{6}$$

with n the effective power index of the power spectrum near the (top-hat) smoothing scale [9]. Since this ratio of moments for δ is practically independent of Ω, and since $\boldsymbol{\nabla}\cdot\boldsymbol{v} \sim -f\delta$, the corresponding ratio for $\boldsymbol{\nabla}\cdot\boldsymbol{v}$ must strongly depend on Ω, and indeed in second-order it is [?]

$$T_3 \equiv \langle(\boldsymbol{\nabla}\cdot\boldsymbol{v})^3\rangle/\langle(\boldsymbol{\nabla}\cdot\boldsymbol{v})^2\rangle^2 \approx -f(\Omega)^{-1}(26/7 - 3 - n) \ . \tag{7}$$

Using N-body simulations and $12\,\mathrm{h}^{-1}$Mpc smoothing one indeed finds $T_3 = -1.8 \pm 0.7$ for $\Omega = 1$ and $T_3 = -4.1 \pm 1.3$ for $\Omega = 0.3$, where the error is the cosmic scatter for a sphere of radius $40\,\mathrm{h}^{-1}$Mpc in a CDM universe ($H_0 = 75$, $b = 1$). An estimate of T_3 in the current POTENT velocity field within $40\,\mathrm{h}^{-1}$Mpc is -1.1 ± 0.8, where the errors this time represent distance errors. With the two errors added in quadrature, Ω=0.3 is rejected at the $\sim 2\sigma$ level (somewhat sensitive to the assumed PS).

4.3 Initial PDF

Since the present PDF contains only part of the information stored in the data and is in some cases not that sensitive to the initial PDF (IPDF), a more powerful bound can be obtained by using the detailed present velocity field $\boldsymbol{v}(\boldsymbol{x})$ to recover the IPDF, and using the latter to constrain Ω by measuring it's Ω-dependent deviation from the assumed normal distribution [42]. The necessary "time machine" is provided by an Eulerian interpretation of the Zel'dovich approximation [41].

The velocity out of POTENT Mark II, within a conservatively selected volume, was fed into the IPDF recovery procedure with Ω either 1 or 0.3, and the errors due to distance errors and cosmic scatter were estimated. The IPDF recovered with $\Omega = 1$ is found marginally consistent with Gaussian, while the one recovered with $\Omega = 0.3$ shows significant deviations. The largest deviation, bin by bin in the IPDF, is $\lesssim 2\sigma$ for $\Omega = 1$ and $> 4\sigma$ for $\Omega = 0.3$, and a similar rejection of $\Omega = 0.3$ is obtained with a χ^2-type statistic. The skewness and kurtosis are poorly determined because of noisy tails but the replacements $\langle x|x|\rangle$ and $\langle|x|\rangle$ allow a rejection of $\Omega = 0.3$ at the $(5-6)\sigma$ levels!

5 Omega from Velocities and CMB via Power Spectrum

The observed peculiar velocities constrain the amplitude of dynamical fluctuations on scales $\lesssim 100\,\mathrm{h}^{-1}$Mpc, while The fluctuations observed in the CMB by COBE span an angle range corresponding to $\gtrsim 1000\,\mathrm{h}^{-1}$Mpc, comoving, at $z \sim 10^3$. The relation between the two measurements involves Ω via the fluctuation growth rate and the shape (power index n) of the linear power spectrum (PS) on large scales. I describe the acquisition of two related statistics from the peculiar velocities, the bulk velocity and the mass PS, and the conclusions from comparing them with COBE's measurements. The bulk velocity provides a general confirmation of GI for $n \sim 1$, while the PS is a more sensitive measure of Ω.

5.1 Bulk Velocity

A robust statistic that is relatively straightforward to obtain is the bulk velocity V within a sphere of radius R centered on the LG. It is computed, for example, by volume-weighted

vector averaging of the smoothed peculiar velocities computed by POTENT at grid points [6] . Alternatively, it is obtained by minimizing the residuals of the observed radial peculiar velocities from a bulk velocity across the sphere [14].

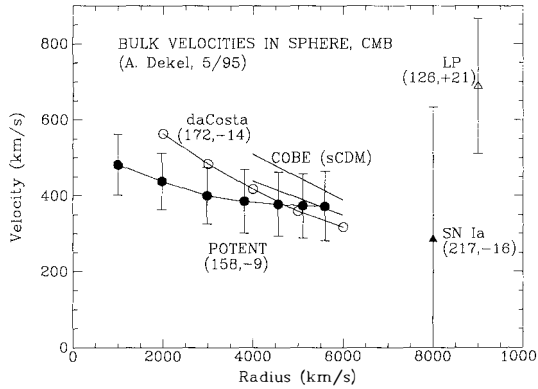


Figure 4: The amplitude of the bulk velocity relative to the CMB frame, in top-hat spheres about the LG. The directions are indicated in supergalactic coordinates (L, B).

The amplitude of the bulk velocity as a function of R, from several recent sources, is shown in Figure 4. The Mark III POTENT result [25] at $R = 50\,\mathrm{h^{-1}Mpc}$ is $V = 374 \pm 85\ \mathrm{km\,s^{-1}}$ towards $(L, B) = (158°, -9°) \pm 10°$. The $\sim 20\%$ error bars are due to distance errors, and one should consider an additional uncertainty of similar magnitude due to non-uniform sampling. Another sample of Sc galaxies by daCosta *et al.* [16] yields at the same R a very similar result (contrary to premature rumors), $V \approx 364\ \mathrm{km\,s^{-1}}$ towards $(172°, -14°)$ [although the slope of the $V(R)$ curve is somewhat steeper in this, still preliminary, analysis]. Within a larger sphere of $R \sim 100\,\mathrm{h^{-1}Mpc}$, the bulk velocity based on Type Ia supernovae [46] is $V = 284 \pm 350\ \mathrm{km\,s^{-1}}$ (consistent with zero!) towards $(217°, -16°) \pm 70°$. This measurement is based on only 13 distances, but the claimed errors of only $\sim 5\%$ enable a meaningful result. This new large-scale result fits nicely any natural extrapolation of the POTENT results from smaller scales, and they all make a bulk of sense within the framework of standard isotropic and homogeneous cosmology.

The only apparently discrepant result comes from the velocities measured on a similar large scale using brightest cluster galaxies (BCG) as distance indicators ([37], LP), which show a large bulk velocity of $V = 689 \pm 178$ towards a very different direction $\sim (126, 21)$. An ongoing effort to measure a larger sample of clusters will soon tell whether this early result is a $\gtrsim 2\sigma$ statistical fluke [27], whether the errors were underestimated, or whether something is systematically different between the BCG distances and the distances measured by other indicators. Until then, it would make sense to put this result on hold.

Shown in comparison are the expected *rms* bulk velocity in a standard CDM model ($\Omega = 1$, $n = 1$) normalized to COBE, for $h = 0.5$ (bottom) and 0.8 (top) [50]. These theoretical curves would not change much if a 20% hot component is mixed with the cold dark matter, or if Ω is lower but still in the range $0.2 - 1.0$, as long as $n \approx 1$. When compared to a theoretical prediction, the error should also include cosmic scatter due to the fact that only one sphere has been sampled from a random field. These errors are typically on the order of the measurement errors.

The CMB fluctuations on scales $\leq 90°$ are of course independent of the local motions, but GI theory predicts an intimate relation between them, which can serve as a basic test for GI. The CMB fluctuations are associated with fluctuations in gravitational potential in the surface of last scattering at $z \sim 10^3$, while their sister fluctuations in our neighborhood have grown by gravity to produce the motions observed. The local surveyed region of $\sim 100\,\mathrm{h}^{-1}$Mpc corresponds to a $\sim 1°$ patch on the last-scattering surface of some hypothetical distant observer. The major effect on scales $> 1°$ is the Sachs-Wolfe effect, where potential fluctuations $\Delta\Phi_g$ induce temperature fluctuations via gravitational redshift, $\delta T/T = \Delta\Phi_g/(3c^2)$. Since the velocity potential is proportional to Φ_g in the linear and quasi-linear regimes, and since linear potential fluctuations do not grow in comoving coordinates, one can write $\Delta\Phi_g \propto Vx$, where x is the scale across which the bulk velocity is V. A typical bulk velocity of ~ 300 km s^{-1} across $\sim 100\,\mathrm{h}^{-1}$Mpc corresponds to $\delta T/T \sim 10^{-5}$ at $\sim 1°$. If the fluctuations are roughly scale-invariant ($n \approx 1$), then $\delta T/T \sim 10^{-5}$ is expected on all scales above $1°$. Several years ago we drew [7] a $\delta T/T$ map of the local GA-PP region as seen by a distant observer, and predicted $\delta T/T \sim 10^{-5}$. Now that such CMB fluctuations have been detected in the range $1° - 90°$ ([48], [47]), they provide an important confirmation of GI, truly addressing the specific *growth rate* of structure as predicted by this theory [2].

The COBE-normalized bulk flow as predicted by theory depends on n but is not that sensitive to Ω or to the nature of the dark matter (DM). The main effect of Ω and H_0 on the PS is via the location of the peak, at $k_{peak} \sim 0.065(\Omega h)^{-1}(\mathrm{h}^{-1}\mathrm{Mpc})^{-1}$, corresponding to the horizon scale at the epoch of equal energy densities in matter and radiation. The DM type mostly affects the shape of the filtered PS at larger k's. The predicted bulk velocity over $\sim 100\,\mathrm{h}^{-1}$Mpc is efectively an integral of the PS over wavenumbers smaller than k_{peak}, and is therefore relatively insensitive to Ω while it is quite sensitive to n. From the bulk velocity by POTENT at $R = 50\,\mathrm{h}^{-1}$Mpc, we obtain for $\Omega = 1$ CDM with no tensor fluctuations that $n \simeq 0.55 h_{50}^{-0.94} \pm 0.3$.

5.2 Mass Power Spectrum from POTENT

The local PS, at $k > k_{peak}$ where the PS is steep, should be more sensitive than the bulk velocity to Ωh (or a similar combination). In a recent work (Kolatt & Dekel [35]), we have derived the PS from the smoothed Mark III POTENT density field, and compared to COBE to yield Ωh and n.

There is a long way between the true fluctuation signal and the observed PS. The data is contaminated by distance errors, and sampled sparsely and non-uniformly. It is then smoothed heavily and is subjected to the POTENT analysis where quasilinear approximations are used to derive the density field and the associated errors on a uniform grid. The density field is taken from within a window of effective radius $\sim 50\,\mathrm{h}^{-1}$Mpc, weighted inverseley by the squares of the local errors, and zero-padded in a larger periodic box before an FFT procedure is applied and the PS is computed by averaging the amplitides of the Fourier transforms in bins of k. Term the product "the observed PS", $O(k)$.

The systematic errors introduced by the above procedure are modeled by

$$O(k) = M(k)[S(k) + N(k)], \tag{8}$$

where $S(k)$ is the true signal PS, $N(k)$ is the noise PS, and $M(k)$ represents the effects of sampling, smoothing, applying a window etc. The correction functions $M(k)$ and $N(k)$ are derived from Monte Carlo mock catalogs based on simulations that mimic in detail the underlying structure of the real universe and the Mark III catalog [36]. The factor $M(k)$ is derived first by $M^{-1} = S/\langle O\rangle_{no-noise}$, where S here is the known signal PS built into the

simulations, and the averaging is over 10 mock catalogs not perturbed by noise. Then $N(k)$ is computed by $N = M^{-1}\langle O\rangle_{noise} - S$, where the averaging this time is over noisy mock catalogs.

Equipped with the correction functions $M(k)$ and $N(k)$, the PS observed from the real universe, $O(k)$, is finally corrected to yield the true PS by

$$S(k) = M(k)^{-1}O(k) - N(k). \tag{9}$$

The recovered mass-density PS is shown in Figure 5 using three thick logarithmic bins covering the range $0.04 \leq k \leq 0.2\,(\mathrm{h^{-1}Mpc})^{-1}$, within which the results are reliable. For example, we find $P(k)f(\Omega)^2 = (4.6 \pm 1.4) \times 10^3(\mathrm{h^{-1}Mpc})^3$ at $k = 0.1(\mathrm{h^{-1}Mpc})^{-1}$ (using the convention where the Fourier transform is defined with no 2π factors in it's coeficient).

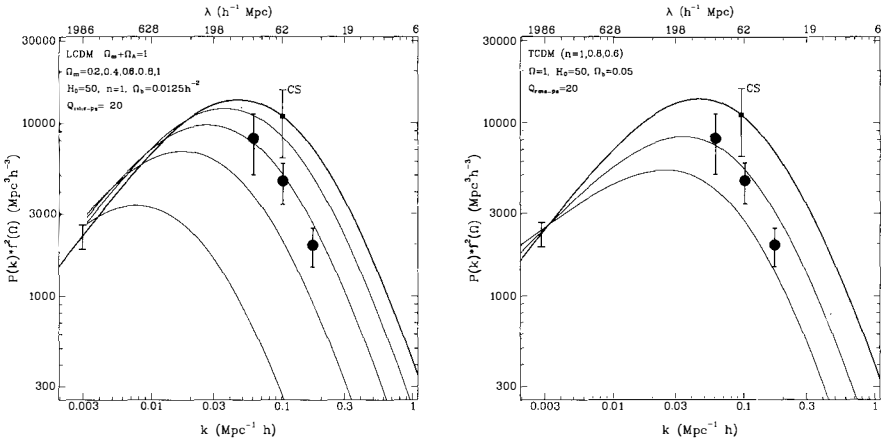


Figure 5: The mass power spectrum $[\times f(\Omega)^2]$ from Mark III POTENT velocities (circles), with 1σ random errors. The curves are COBE-normalized theoretical predictions for flat CDM with $h = 0.5$. Left: $n = 1$ and Ω growing upeards. Right: $\Omega = 1$ and n growing upwards. Cosmic scatter for $\Omega = 1$ and $n = 1$ is indicated (square).

The observed PS is compared in the figure to the linear predictions of a family of Inflation-motivated flat ($\Omega + \Lambda = 1$) CDM models with the Hubble constant arbitrarily fixed at $h = 0.5$. For $n = 1$, maximum likelihood is obtained at $\Omega \simeq 0.55h_{50}^{-1.35} \pm 0.1$. For $\Omega = 1$, assuming that tensor fluctuations do not contaminate the fluctuations observed by COBE, the linear power index is $n \simeq 0.70h_{50}^{-0.8} \pm 0.1$.

5.3 Mass Power Spectrum from Likelihood Analysis

The PS, in a parametric form including Ω, h and n among the parameters, has alternativelly been determined from the velocity data via a Baysian likelihood analysis (Zaroubi, Dekel & Hoffman [56]). According to Bayse, the probability of the model parameters given the data, which is the function one wishes to maximize, can be expresses as

$$P(model|data) = P(data|model)\,P(model)/P(data). \tag{10}$$

$P(data)$ serves here as a normalization constant. Without any external constraints on the model parameters, one assumes that $P(model)$ is a constant in a given range. The remaining

task is to maximize the likelihood as a function of the model parameters, $L = P(data|model)$, which is easier to write down explicitly.

Under the assumption that the velocities and the errors are both Gaussian random fields with no mutual correlations, the likelihood can be written as

$$L = (2\pi|D|)^{-1/2} \exp(-d_i D_{ij}^{-1} d_j/2), \tag{11}$$

where d_i are the data at points $i = 1, ..., N$, and D_{ij} is the covariance matrix, which one can split into covariance of signal (s) and covariance of noise (n),

$$D_{ij} \equiv \langle d_i d_j \rangle = \langle s_i s_j \rangle + \langle n_i n_j \rangle. \tag{12}$$

If the errors are uncorrelated, the noise matrix is diagonal. The signal matrix is computed from the model PS, and is therefore a function of the desired model parameters.

We used a parametric model for the PS of the general form

$$P_k = A\, k^n\, T(\Gamma_i; k), \tag{13}$$

where $T(k)$ is a small-scale filter of an assumed shape characterized by free parameters Γ_i, k^n is the initial PS, which is still valid on large scales today, and A is a normalization factor. The normalization can either be determined by COBE's data (for given Ω, Λ, h, n and tensor/scalar fluctuations), or be left as a free parameter to be fixed by the velocity data alone. The filter $T(k)$ can be taken from a specific physical model (e.g. CDM, where $\Gamma = \Omega h$ [17]), or be an arbitrary function with enough flexibility to fit the data.

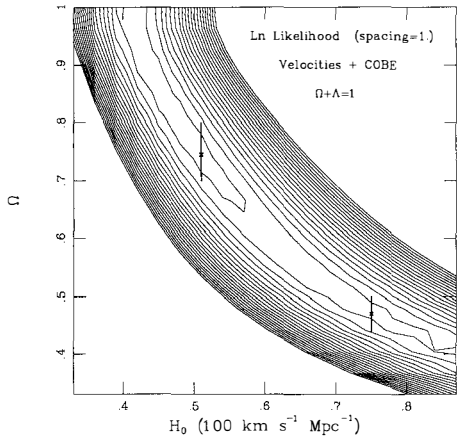


Figure 6: Likelihood contour map in the $\Omega - h$ plane, for flat CDM with $n = 1$. Marked are the most likely values of Ω and the corresponding 1σ error bars for two given values of h.

This likelihood analysis yields for flat CDM with $n = 1$, $\Omega \simeq (0.75 \pm 0.05) h_{50}^{-1.2}$. For $\Omega = 1$ CDM with no tensor fluctuations, $n \simeq (0.90 \pm 0.04) h_{50}^{-0.8}$, and with tensor fluctuations $n \simeq (0.95 \pm 0.02) h_{50}^{-0.8}$.

Focusing on the shape of the PS as constrained by the velocities alone without COBE's normalization, maximum likelihood for a CDM-like filter is obtained with a shape parameter $\Gamma = 0.50 \pm 0.12$, but note that here Γ is not directly related to the cosmological parameters

Ω and h. The normalization as determined for this PS shape can be expressed by $P[k = 0.1(hmpc)^{-1}] = (4.1 \pm 0.6) \times 10^3 (hmpc)^3$, or alternatively by the dispersion in top-hat spheres of radius $8\,h^{-1}$Mpc, $\sigma_8 = 0.8 \pm 0.12$.

Both Ω and n obtained by the likelihood analysis of this section tend to be slightly higher than their estimates based on the PS recovered from the POTENT output in the previous section §5.2. The errors quoted from the likelihood analysis, unlike the errors quoted in the previous section, do not include cosmic scatter. The difference between the results obtained in the two different ways is on the order of the errors in each analysis and the cosmic scatter. Our tentative best guess should probably be a crude average of the two results.

6 Summary

My goal in this paper has been to demonstrate that there are several ways to constrain Ω from dynamical measurements of large-scale structure *independently* of galaxy biasing. The current data enable us to reject values of Ω as low as 0.3 at the 95-99% confidence level in several different ways.

Figure 7 puts our results in perspective, in terms of the ongoing general discussion concerning the cosmological parameters. Shown are various limits derived from observations, on top of theoretical curves relating the age of the universe to the Hubble constant for a given value of Ω, as predicted for the Inflation-motivated family of flat cosmological models.

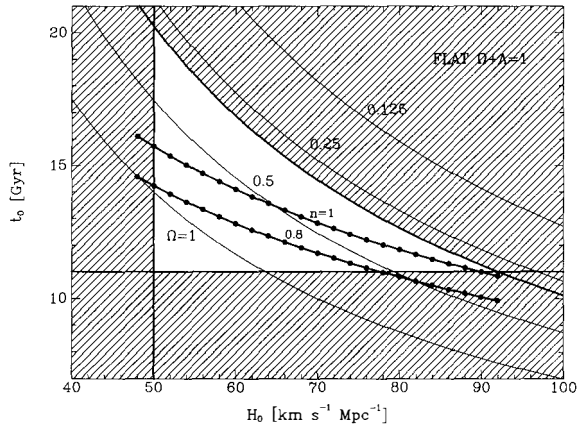


Figure 7: Constraints on the cosmological parameters.

I adopt $\sim 2\sigma$ lower bounds of $h > 0.5$ [45] and $t_0 > 11\,\mathrm{Gyr}$ ([8], [32]). Combined with the limit reported here with similar confidence, of $\Omega > 0.3$, the parameters are confined to a concordence "triangle".

The results of combining the peculiar velocity data with COBE's $\delta T/T$ via the mass-density power spectrum, assuming CDM, are shown as dotted lines for $n = 1$ and for $n = 0.8$ (no tensor fluctuations).

If h is indeed as high as $0.7 - 0.8$, as indicated by recent cepheid measurements [28], then Ω seems to be confined to 0.5 ± 0.2, and then CDM with $n = 1$ could provide an appropriate spectrum. If it turns out that h is only about $0.5 - 0.6$, then an $\Omega = 1$ CDM model becomes

a viable option, provided that n is somewhat smaller than unity, perhaps associated with a nonzero component of tensor fluctuations.

Acknowledgements. Parts of the work described above have been done together with different collaborators, including Bernardeau, Buchet, Burstein, Courteau, Faber, Hoffman, Juszkieicz, Kolatt, Lahav, Nusser, Rees, Willick, and Zaroubi. Parts of this work were supported by the Israel Science Foundation and by the US-Israel Binational Science Foundation.

References

[1] Aaronson, M., Huchra, J., Mould, J.R., Tully, R.B., Fisher, J.R., *et al.* 1982a, *Ap. J. Supp.* **50**, 241.

[2] Babul, A., Weinberg, D., Dekel, A., & Ostriker, J.P. 1994, *Ap. J.* **427**, 1

[3] Bardeen, J., Bond, J.R., Kaiser, N. & Szalay, A. 1986, *Ap. J.* **304**, 15

[4] Bernardeau, F., Juszkiewicz, R., Bouchet, F., & Dekel, A. 1995, *Ap. J.* , *in press*

[5] Bertschinger, E., & Dekel, A. 1989, *Ap. J. Lett.* **336**, L5

[6] Bertschinger, E., Dekel, A., Faber, S.M., Dressler, A., & Burstein, D. 1990, *Ap. J.* **364**, 370

[7] Bertschinger, E., Gorski, K., & Dekel, A. 1990, *Nature* **345**, 507

[8] Bolte, M. & Hogan, C.J. 1995, *Nature* , *submitted*

[9] Bouchet, F., Juszkiewicz, R., Colombi, S., & Pellat, R. 1992, *Ap. J. Lett.* **394**, L5

[10] Braun, E., Dekel, A., & Shapiro, P. 1988, *Ap. J.* **328**, 34

[11] Burstein, D. 1990, *Distributed electronically*

[12] Cen, R., & Ostriker, J.P. 1992, *Ap. J.* **399**, L113

[13] Cen, R., & Ostriker, J.P. 1993, *Ap. J.* **417**, 415

[14] Courteau, S., Faber, S.M., Dressler, A., & Willick, J.A. 1993, *Ap. J. Lett.* **412**, L51

[15] Courteau, S. 1992, *Ph.D. Thesis, UCSC*

[16] daCosta, L. *et al.* , in Cosmic Velocity Fields, eds. F Bouchet & M. Lachieze-Rey (Editions Frontieres)

[17] Davis, M., Efstathieou, G., Frenk, C.S., & White, S.D.M. 1985, *Ap. J.* **292**, 371

[18] Dekel, A. 1994, *Annu. Rev. Astron. Astrophys.* **32**, 371

[19] Dekel, A., Bertschinger, E., & Faber, S.M. 1990, *Ap. J.* **364**, 349

[20] Dekel, A., Bertschinger, E., Yahil, A., Strauss, M., Davis, M., & Huchra, J. 1993, *Ap. J.* **412**, 1

[21] Dekel, A. & Lahav, O. 1996, *in preparation*

[22] Dekel, A. & Rees, M.J. 1987, *Nature* **326**, 455

[23] Dekel, A. & Rees, M.J. 1994, *Ap. J. Lett.* **422**, L1

[24] Dekel, A., & Silk, J. 1986, *Ap. J.* **303**, 39

[25] Dekel *et al.* 1996, *Ap. J.* , *in preparation*

[26] Dressler, A. 1980, *Ap. J.* **236**, 351

[27] Feldman, H.A., & Watkins, R. 1995, *preprint*

[28] Freedman, W. *et al.* 1994, *Nature* **371**, 757

[29] Han, M.S. & Mould, J.R. 1990, *Ap. J.* **360**, 448

[30] Han, M.S. & Mould, J.R. 1992, *Ap. J.* **396**, 453

[31] Hudson, M.J., Dekel, A., Courteau, S., Faber, S.M., & Willick, J.A. 1995, *MNRAS* **274**, 305

[32] Jimenez, R. *et al.* 1995, *submitted*

[33] Kofman, L., Bertschinger, E., Gelb, J., Nusser, A., & Dekel, A. 1994, *Ap. J.* **420**, 44

[34] Kolatt, T. & Dekel, A. 1994a, *Ap. J.* **428**, 35

[35] Kolatt, T. & Dekel, A. 1996, *in preparation*

[36] Kolatt, T., Dekel, A., Ganon, G., & Willick, J. 1996, *Ap. J.* , *submitted*

[37] Lauer, T.R., & Postman, M. 1994, *Ap. J.* **425**, 418

[38] Lynden Bell, D., Faber, S.M., Burstein, D., Davies, R.L., Dressler, A., Terlevich, R. J., & Wegner, G. 1988, *Ap. J.* **326**, 19

[39] Mathewson, D.S., Ford, V.L., & Buchhorn, M. 1992, *Ap. J. Supp.* **81**, 413

[40] Mould, J.R. *et al.* 1991, *Ap. J.* **383**, 467

[41] Nusser, A. & Dekel, A. 1992, *Ap. J.* **391**, 443

[42] Nusser, A. & Dekel, A. 1993, *Ap. J.* **405**, 437

[43] Nusser, A., Dekel, A., Bertschinger, E., & Blumenthal, G.R., 1991, *Ap. J.* **379**, 6

[44] Nusser, A., Dekel, A., & Yahil, A. 1995, *Ap. J.* , *in press*

[45] Press, W. 1995, in *Unsolved Problems in Astrophysics* ed. D. Spergel (Princeton University Press)

[46] Riess, A.G., Press, W.H., & Kirshner, R.P. 1995, *Ap. J. Lett.* **438**, L17

[47] Schuster, J. *et al.* 1993, *Ap. J. Lett.* , in press

[48] Smoot, G.F. *et al.* 1992, *Ap. J. Lett.* **396**, L1

[49] Strauss, M. & Willick, J. 1995, Physics Reports, *in press*

[50] Sugiyama, N. 1995, *Ap. J. in press*

[51] Weinberg, D. 1995, in Wide-Field Spectroscopy and the Distant Universe, eds. S.J. Maddox & A. Aragon-Salamanca (World Scientific: Singapore)

[52] Willick, J. 1991, *Ph.D. Thesis, UC Berkeley*

[53] Willick, J.A., Courteau, S., Faber, S.M., Burstein, D., & Dekel, A. 1995, *Ap. J.* , *in press.*

[54] Willick, J.A., Courteau, S., Faber, S.M., Burstein, D., Dekel, A. & Kolatt, T. 1996a, *Ap. J.* , *submitted.*

[55] Willick, J.A., Courteau, S., Faber, S.M., Burstein, D., & Dekel, A. 1995, *Ap. J. Supp.* , *in preparation*

[56] Zaroubi, S., Dekel, A., & Hoffman, Y. 1996, *in preparation*



Ω and biasing from optical galaxies versus POTENT mass

M.J. Hudson,[1] A. Dekel,[2] S. Courteau,[3] S.M. Faber[4] and J.A. Willick[5]
[1] *Dept. of Physics, Univ. of Durham, South Road, Durham DH1 3LE UK.*
[2] *Racah Institute of Physics, The Hebrew University of Jerusalem, Jerusalem 91904, Israel.*
[3] *Kitt Peak National Observatory, P.O. Box 26732, Tucson, AZ 85726-6732, USA.*
[4] *UCO/Lick Observatory, University of California, Santa Cruz, CA 95064, USA.*
[5] *Carnegie Observatories, 813 Santa Barbara St., Pasadena, CA 91101, USA.*

Abstract

The mass density field in the local universe, recovered by the POTENT method from peculiar velocities of ~3000 galaxies, is compared with the density field of optically selected galaxies. Both density fields are smoothed with a Gaussian filter of radius $12h^{-1}$ Mpc. Under the assumptions of gravitational instability and a linear biasing parameter b_O between optical galaxies and mass, we obtain $\beta_\bullet \equiv \Omega^{0.6}/b_O = 0.74 \pm 0.13$. This result is obtained from a regression of POTENT mass density on optical density after correcting the mass density field for systematic biases in the velocity data and POTENT method. The error quoted is just the 1σ formal error estimated from the observed scatter in the density–density scatterplot; it does not include the uncertainty due to cosmic scatter in the mean density or in the biasing relation. We do not attempt a formal analysis of the goodness of fit, but the scatter about the fit is consistent with our estimates of the uncertainties.

1 Introduction

With the advent of large-scale redshift and peculiar velocity surveys, it has become possible to investigate the relationship between the distribution of mass and galaxies on supercluster scales. Assuming that structures grow through gravitational instability (GI), then, on large scales where linear theory is applicable, the mass density fluctuation, δ, can be determined from the divergence of the peculiar velocity field, $\boldsymbol{v}$,

$$\delta = -f^{-1}\nabla \cdot \boldsymbol{v} \ , \tag{1}$$

where $f(\Omega) \simeq \Omega^{0.6}$ [9], and a generalized approximation is valid in the quasi-linear regime. If we assume that the density fluctuation of optically selected galaxies, δ_O, is related to the density fluctuation of mass by linear biasing $\delta_O = b_O\delta$, then the comparison of densities in the linear regime yields $\beta_O \equiv f(\Omega)/b_O$ (and in the quasi-linear regime it allows a determination of b_O for a given value of Ω). The determination of β_O is the goal of this paper.

In this paper, we summarize our results from the comparison of the mass density field as determined by the POTENT method to that of optically-selected galaxies. Full details of this

work may be found in ref. [7]. The main advantages of the density-density comparison (as opposed to the comparison of predicted and observed peculiar velocities, e.g. [6]) are that (a) the comparison is local (on scales larger than the smoothing scale), and (b) a similar smoothing is applied to *both* fields at a scale on which linear or quasi-linear theory is applicable.

2 Data

The mass density field is determined using an improved version of the POTENT procedure applied to the new Mark III compilation of about 3000 peculiar velocities. The POTENT density field, δ_P, considered in this paper has been reconstructed with Ω set to unity. Details of the Mark III sample, the inhomogeneous Malmquist bias corrections and the new POTENT procedure are summarized in [7] and described in detail in [10] – [12] and [2] – [4]. The errors in the POTENT density field are determined from Monte-Carlo realizations of the raw peculiar velocity data perturbed by their errors. The optical density field is described in [5]. Both density fields are smoothed with a 1200 km s^{-1} Gaussian filter, and are sampled on a cubical grid of 500 km s^{-1} spacing. The optical density field is normalized using the average density within 6000 km s^{-1}, and the POTENT density field is normalized by adjusting the Tully-Fisher and $D_n - \sigma$ zero-points such that $\langle\delta\rangle = 0$ within 6000 km s^{-1}.

3 Determination of β_O

3.1 Method

The density–density comparison is local and the POTENT data are weighted inversely by their local errors. Consequently, we are free to choose the volume considered in the density–density comparison. We therefore limit the comparison volume to regions where the POTENT biases and random errors are smallest and we exclude the Zone of Avoidance and the 'missing equatorial strip' where the optical density field is not well determined. In this paper, the results quoted are for the most conservative choice of selection criteria considered in [7] (the "P1 Small" comparison volume). The comparison volume contains 2197 grid points at 500 km s^{-1} spacing. These grid points oversample by a factor $\simeq 100$ the 1200 km s^{-1} radius Gaussian smoothing. Thus the comparison volume really contains only $N_{\rm eff} \simeq 22$ independent data points.

We cannot perform a direct POTENT – optical comparison because the POTENT density field is known to be biased. This bias is due mainly to the non-uniform sampling of the peculiar velocity tracer galaxies (the so-called "sampling gradient" bias, see [1]). In order to eliminate the effect of this bias on the derived value of $\beta_\bullet$ we subject the optical density field to the same biases as suffered by the POTENT density field. We begin by smoothing the optical density field with a Gaussian filter of 500 km s^{-1} radius. Predicted peculiar velocities are then calculated using the prescription in [8], i.e.

$$\boldsymbol{v}(\boldsymbol{r}) = \frac{f(\Omega)}{4\pi b_O} \int \frac{\delta_O(\boldsymbol{r}')}{1 + 0.18 b_O^{-1} \delta_O(\boldsymbol{r}')} \frac{\boldsymbol{r}' - \boldsymbol{r}}{|\boldsymbol{r}' - \boldsymbol{r}|^3} \mathrm{d}^3\boldsymbol{r}' , \qquad (2)$$

at the observed positions of the galaxies in the Mark III data set. These predicted peculiar velocities are then used as the input to the POTENT procedure with 1090 km s^{-1} Gaussian smoothing which, when added in quadrature with the 500 km s^{-1} smoothing radius of the input field, ensures a total Gaussian smoothing of 1200 km s^{-1}. The result of this procedure, which we label P(O), is a galaxy density field which is affected by biases in the same way as the

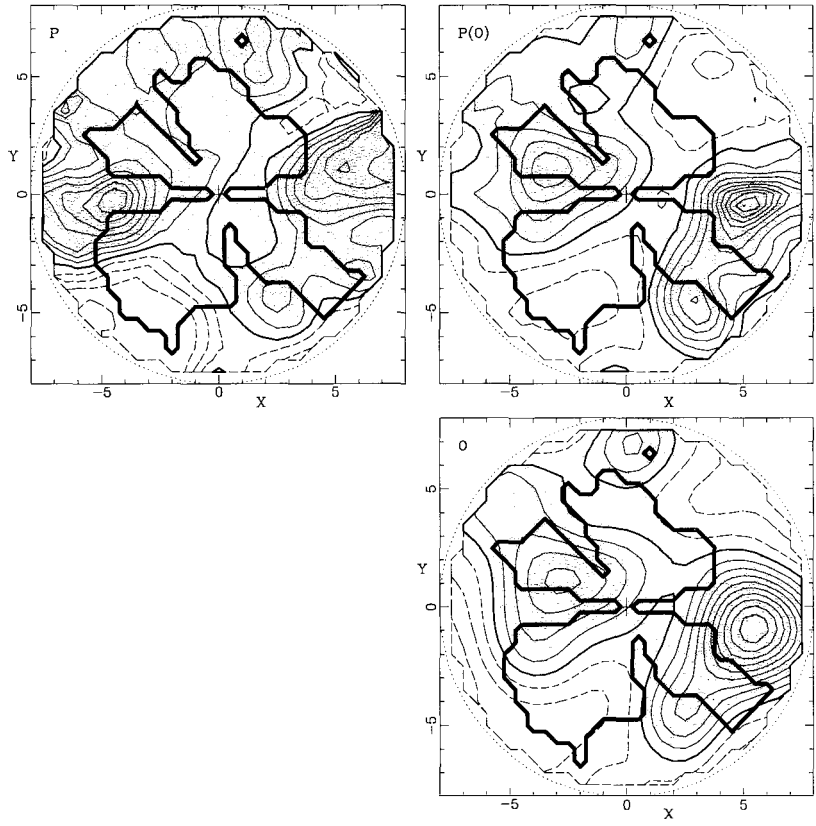


Figure 1: Maps of the density field in the Supergalactic Plane. The contour levels are in steps of $\Delta\delta = 0.2$. The medium-thickness contours indicate the mean density, thin solid contours show overdense regions and dashed contours show underdense regions. The heavy contours indicate the boundary of the "large" comparison volume (see [7] for details). The dotted circle has a radius of 8000 km s^{-1}. The upper left-hand panel shows the POTENT mass density field (P). The upper right-hand panel shows P(O), the POTENT recovery using predicted peculiar velocities from the optical density field at the positions of the Mark III data. The lower right-hand panel shows the optical density field (O). The difference between P(O) and O shows the effect of the biases discussed in the text.

POTENT mass density field recovered from the Mark III data. The comparison of the POTENT density field to P(O) (rather than the raw optical density field) yields an unbiased estimate of β_O. Fig. 1 compares the density fields of POTENT [P], optical through POTENT [P(O)], and raw optical [O].

Assuming a linear biasing relation with no scatter, we expect the densities to be related by

$$\delta_P = \lambda\delta_O + c \tag{3}$$

where the slope, λ, is just equal to b_O^{-1}. The zero-point, c, allows for a relative offset in the

mean density of the two density fields. This parameter is necessary because in practice the volumes within which we have separately normalized the POTENT and optical density fields are slightly different from each other.

The random errors in the inferred peculiar velocities introduce an error in the POTENT density, σ_δ, so of course we expect some scatter in the POTENT – P(O) density scatterplot. We have estimated the random shot-noise errors in the optical density field using the technique of bootstrap resampling. We find these errors to be typically ~ 0.07, and always less than half the random errors of the POTENT density field at a given grid point. In the following analysis we assume that all errors are in the POTENT density field, and thus regress δ_P on δ_O in the determination of λ.

In order to estimate the errors on the slope λ, we use an "effective" χ^2 statistic which corrects for the fact that cubical grid oversamples the smoothed density field. We find that when we set the error in the POTENT density σ_P equal to the error in the Monte Carlo simulations σ_δ, we obtain $\chi^2_{\rm eff} \gtrsim 2N_{\rm eff}$, which is too large for an acceptable fit. It is likely that there are other sources of error, predominantly in the POTENT density field, which are not accounted for by the Monte Carlo perturbations of the distances. We therefore allow for additional errors via an additional parameter, $\sigma_{\rm add}$. The additional errors may or may not be correlated with σ_δ, so we assume a weak correlation by adding *linearly*: $\sigma_P = \sigma_{\rm add} + \sigma_\delta$. We then adjust $\sigma_{\rm add}$ so that $\chi^2_{\rm eff} = N_{\rm eff} - 2$. The required value is $\sigma_{\rm add} = 0.06$. This value of $\sigma_{\rm add}$ is consistent with our estimates of other unmodelled sources of scatter (e.g. imperfect inhomogeneous Malmquist bias corrections, systematic and shot-noise errors in the optical density field or spatial variations in the efficiency of galaxy formation). We therefore conclude that there is no evidence for inconsistency between the data and the assumptions of GI and linear biasing, allowing us to proceed to the parameter fit.

3.2 Results

The comparison between the POTENT density and the POTENT-recovered optical density P(O) removes the biases in the POTENT procedure and thus yields an unbiased estimate of β_O. As discussed above, we assume that the errors in the POTENT density field dominate. We therefore obtain the slope from a regression of δ_P on $\delta_{P(O)}$ with the POTENT error $\sigma_P = \sigma_\delta + \sigma_{\rm add}$. The result of the fit is $\lambda = 0.73 \pm 0.13$ and $c = -0.01 \pm 0.04$. Fig. 2 shows the P – P(O) scatterplot.

We have made a number of tests to check the robustness of the value of λ derived from the regression of δ_P on $\delta_{P(O)}$. We have found that this result is robust to the details of the volume used and to the treatment of Malmquist bias. The sensitivity of β_O to extreme changes in the POTENT weighting scheme is at the 12 per cent level. Its sensitivity to extreme changes in the way in which the optical density field is interpolated across of the Zone of Avoidance is at a similar level (see [7] for details).

We have investigated non-linear effects by setting $\Omega = 0.3$ in the POTENT reconstruction. However, because non-linear effects on this scale are small compared to the scatter in the data, we do not find a significantly different value of β_O nor do we find a significant improvement in $\chi^2_{\rm eff}$. We are thus unable to break the degeneracy between Ω and b_O.

4 Discussion and Summary

Our simple analysis does not allow a formal evaluation of goodness of fit between the data and the assumed model of GI and linear biasing, but we conclude, based on the expected random

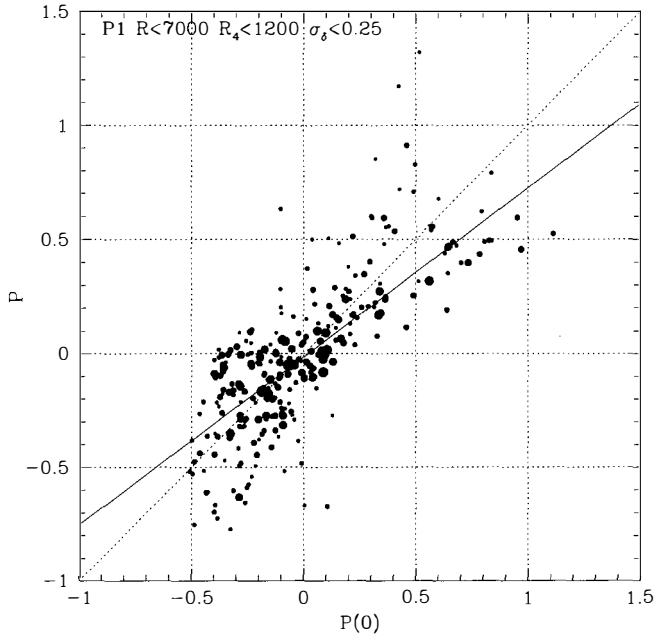


Figure 2: The density–density scatterplot with P(O) plotted on the horizontal axis and the POTENT density (P) plotted on the vertical axis. In this plot, the densities are sampled on a 1000 km s^{-1} grid within the comparison volume, thus the plotted points oversample the number of independent volumes by a factor $\sim$ 12. The areas of the plotted points have been scaled with the inverse squares of their errors. The solid line is the result of the regression of P on P(O); a dotted line of slope unity is also shown for reference. The slope λ is our estimate of $b_{\bullet}^{-1}$ for $\Omega = 1$.

and systematic errors and the possible real scatter in the biasing relation, that the data and model are not in conflict.

Adopting the model of GI and linear biasing, our main goal has been to determine β_O on a scale of 1200 km s^{-1}. We find, from a regression of POTENT density on optical density, the result $\beta_O = 0.74 \pm 0.13$ (formal 1σ error). This result corresponds to $b_O = 1.35 \pm 0.23$ if $\Omega = 1$, and to $\Omega = 0.61 \pm 0.18$ if $b_O = 1$. Although our analysis cannot distinguish between $\Omega = 1$ and $\Omega = 0.3$, we note that low values of the density parameter ($\Omega \lesssim 0.3$) would require optical galaxies to be significantly anti-biased with respect to mass.

One should be cautioned not to interpret the estimated value of β_O too literally. On top of the formal error of 0.13 and the systematic uncertainties of similar order, our estimate of β_O is subject to cosmic scatter in the mean density; the comparison volume of radius $\lesssim$ 6000 km s^{-1} may still be small for a 'fair' sample. This cosmic scatter arises because, in our analysis, both the peculiar velocity data input to POTENT *and* the mean density of optical galaxies are normalized within a volume of radius $\sim$ 6000 km s^{-1}. Note that while the free parameter c

corrects for small differences in the normalizing volumes of the POTENT and optical density fields, and consequent differences in the mean density of these fields with respect to each other, it does not necessarily correct to the universal density. Thus our result is a *local* value of Ω measured within the comparison volume. The rms scatter of the mean density in such a volume is expected to be at the level of $\sim 10 - 15$ per cent according to the fluctuation power spectra in conventional cosmological scenarios. Thus the local value of Ω may differ from the universal value at a similar level.

We have assumed throughout that the additional scatter in the density–density scatterplots (over and above that due to the distance errors which scatter the POTENT densities) is due to other small unquantified errors in the POTENT density fields. As discussed above, the amount of additional scatter is comparable to our estimates of these systematic errors. However, it is also possible that spatial variations in the biasing relation between galaxies and mass may be large on scales of $12h^{-1}$ Mpc. If instead of assigning the additional error $\sigma_{\rm add}$ to the POTENT densities, we assume that there is an astrophysical source of scatter of 0.15 in $\delta_{\rm O}$, then we obtain acceptable values of $\chi^2_{\rm eff}$ and the slope of the regression changes to $\beta_\bullet \sim 1$.

Our results are compatible with the POTENT-IRAS density-density comparison [1], if one allows for the fact that optical galaxies are more clustered than IRAS galaxies by a relative biasing factor of 1.3. Although our results are somewhat higher than the optical velocity-velocity comparison [6], there is no conflict when one allows for the systematic uncertainties in both determinations.

References

[1] Dekel A., Bertschinger E., Yahil A., Strauss M. A., Davis M., Huchra J. P., 1993, *Astrophys. J.* **412**, 1

[2] Dekel A. et al. 1995a, *Astrophys. J.*, in preparation

[3] Dekel A. et al. 1995b, *Astrophys. J.*, in preparation

[4] Dekel A. et al. 1995c, *Astrophys. J.*, in preparation

[5] Hudson M. J., 1993, *Mon. Not. R. astr. Soc.* **265**, 43

[6] Hudson M. J., 1994, *Mon. Not. R. astr. Soc.* **266**, 475

[7] Hudson M.J., Dekel A., Courteau S., Faber S.M., Willick J.A., 1995, *Mon. Not. R. astr. Soc.* **274**, 305

[8] Nusser A., Dekel A., Bertschinger E., Blumenthal G. R., 1991, *Astrophys. J.* **379**, 6

[9] Peebles P. J. E., 1980, The Large Scale Structure of the Universe. Princeton Univ. Press, Princeton

[10] Willick J. A., Courteau S., Faber S. M., Burstein D., Dekel A., 1995a, *Astrophys. J.* **446**, 12.

[11] Willick J. et al. 1995b, *Astrophys. J.*, submitted.

[12] Willick J. et al. 1995c, *Astrophys. J. Supp*, in preparation

Mapping the Peculiar Velocity Field of Galaxies

L. N. da Costa[1,2], W. Freudling[3,4], R. Giovanelli[5], M. Haynes[5], J. Salzer[6], G. Wegner[7]
[1] *Institut d'Astrophysique, CNRS, Paris, France*
[2] *Observatório Nacional, Rio de Janeiro, Brazil*
[3] *Space Telescope–European Coordinating Facility, Garching, Germany,*
[4] *European Southern Observatory, Garching, Germany,*
[5] *Center for Radiophysics and Space Research, Cornell University, Ithaca, U.S.A.*
[6] *Dept. of Astronomy, Wesleyan University, Middletown, U.S.A.*
[7] *Dept. of Physics and Astronomy, Dartmouth College, Hanover, U.S.A*

Abstract

We have recently completed an all-sky redshift-distance survey of spiral galaxies. The sample consists of about 1600 Sbc-Sc galaxies selected according to a redshift-dependent diameter limit. New data were also obtained for galaxies in several clusters which are used to derive an independent I-band Tully-Fisher (TF) relation to estimate distances. These distances are corrected for bias using a Monte-Carlo approach which simultaneously takes into account, homogeneous and inhomogeneous Malmquist bias, selection effects and incompleteness of the sample. We use this new sample to independently reconstruct the fluctuations in the matter density field and the three-dimensional velocity field. Here we present a brief description of the sample and method of analysis. We also discuss some preliminary results.

1 Introduction

In order to understand the origin of large-scale structure we observe today there are several key questions which must be addressed: the nature of fluctuations in the matter density field; the relation between matter and galaxies; the composition of matter; and the value of the cosmological density parameter Ω. Some of these issues may be addressed by studying the peculiar velocity field of galaxies. If large-scale structures grow gravitationally, peculiar velocities of galaxies will be induced by fluctuations in the mass distribution. Mapping of the local cosmic velocity field can thus provide information on the power-spectrum of these fluctuations on intermediate and large scales. Moreover, if galaxies trace matter, comparison of the observed fluctuations in the galaxy distribution with that estimated from peculiar velocity measurements provides an important tool to measure the quantity $\beta = \Omega^{0.6}/b$, where b is the linear biasing factor that relates galaxy and matter fluctuations. Matter fluctuations on intermediate scales can be probed by peculiar velocity measurements, measurements of anisotropies in the CMB radiation at the 1° scale and weak field lensing. Of those, peculiar motion is the most direct, and easy to interpret, way of probing fluctuations of the underlying mass distribution on intermediate scales.

In recent years, a considerable effort has been made to compute matter fluctuations via peculiar velocities [4]. Most of the work has been based on compilations of distance measurements by different authors which are sparse, inhomogeneous and probe a shallow volume in a non-uniform way. Since then new redshift-distance surveys have been carried out but none covers the whole sky in an uniform way. Their use thus requires a great effort to make them consistent as they use different distance relations and corrections. Such an effort is currently being carried out but the final compilation will unavoidably include data of varying quality [11]. Since the bias correction depends crucially on the uncertainty in the individual distance estimate, the use of different samples requires detailed knowledge of the scatter in the distance relation for each sample which is not always well determined.

The importance of the problem and the need for an all-sky homogeneous dataset prompted us to carry out an independent redshift-distance survey of Sbc-Sc galaxies covering essentially the whole sky. The sample has a well-defined selection criteria and new measurements were obtained from observations using modern detectors and reduction techniques.

2 The Sample

Our sample consists of Sbc-Sc galaxies in the region north of δ = -45° and $|b| > 10°$ drawn from the UGC, MCG and ESO catalogs. The redshift-dependent selection criterion adopted was the following: $5' > a > 2.5'$ for $0 < cz < 3000$ km s^{-1}; $5' > a > 1.6'$ for $3000 < cz < 5000$ km s^{-1}; $5' > a > 1.3'$ for $5000 < cz < 7500$ km s^{-1}. Here a is the UGC catalog blue major axis or its equivalent in the ESO-Uppsala catalog converted to the same scale. The sample includes only galaxies with blue axial ratios < 0.7. In addition, similar quality data was obtained for clusters of galaxies out to $cz \sim$ 10,000 km s^{-1}, which are used to determine a suitable I-band Tully-Fisher relation for our sample.

Radio observations were obtained to measure redshifts and high-quality 21 cm line widths. The 21 cm line spectra obtained from different telescopes were all analyzed with the same algorithm to uniformly measure line widths, which were corrected for inclination using ellipticities determined from surface photometry. I-band CCD images were obtained to provide accurate inclinations and total I-band magnitudes. The total magnitudes were corrected for internal extinction as derived from our data itself [7] and differ from those utilized in previous works. Magnitudes were also corrected for extinction within our galaxy adopting the Burstein & Heiles maps of B band extinction converted to I band.

In order to extend our sky coverage southwards of δ = -45° we have used the data of Mathewson *et al.* [10] for galaxies in the same morphological range included in our sample. Using galaxies common to both samples, conversion relations have been derived that allow to correct their line widths and magnitudes to our system. Currently, the combined sample consists of about 1600 galaxies.

The Sc sample is sufficiently dense to delineate the observed structures in the galaxy distribution rather well out to $\sim$ 7000 km s^{-1}. One advantage of our selection criteria is that galaxies are selected roughly in the same range of magnitudes (diameters) as a function of depth, minimizing systematic errors that are introduced as different domains of the Tully-Fisher relation are used for galaxies at different depths.

3 The I-band TF relation

In computing estimated distances, d_{est} and CMB peculiar velocities we have used the direct TF relation obtained from combining data for several clusters. The cluster sample consists of roughly 300 galaxies in 21 clusters. While nearby clusters have a larger dynamical range of absolute magnitudes and widths, they are at the same time more difficult to assign unambiguous membership. Moreover, their depth is comparable to their mean distance and their zero-point more sensitive to peculiar velocities of the clusters. We define an average offset based on clusters in the range 4000 km s^{-1} $< cz <$ 9000 km s^{-1} to define the zero-point of the distance relation. The various biases affecting the TF relation are corrected using an iterative Monte-Carlo approach, taking into account the completeness of the sample. The scatter of the relation has been determined to be ≈ 0.31 mag. A detailed discussion of the construction of our global TF relation is presented elsewhere [8]. We note that in contrast to other works the zero-point of the final TF relation is not defined by a single cluster, but it is instead established by setting the mean peculiar velocity of clusters to zero in the CMB rest-frame [8].

4 Bias Correction

Errors in the distance measurements lead to biased observed peculiar velocities which directly affect the reconstructed density field. For a uniform distribution of galaxies one must correct for the homogeneous Malmquist bias. In addition, one must consider the bias introduced in the distance estimate due to inhomogeneities in the galaxy distribution and due to selection effects. The latter is particularly important for our Sc sample because the adopted redshift-dependent selection criterion implies that near each redshift limit outflowing galaxies are preferentially excluded from the sample. This effect becomes dominant at large distances leading to a systematic infall of galaxies at the outer edge of the surveyed volume.

In order to deal with this problem we have resorted to a Monte-Carlo approach to estimate the bias field at each point in estimated distance space. The method allows the simultaneous correction for the inhomogeneous Malmquist bias, the selection bias and the bias introduced by the incompleteness of the sample. For its implementation it is necessary to know the distribution of optical galaxies in real space. This was obtained using the iterative method of reconstructing a dynamically self-consistent distribution of galaxies from all-sky redshift surveys using linear theory with a non-linear correction applied. The sample used in this reconstruction was the combined CfA1+SSRS and the IRAS 1.9 Jy to fill in the region of low galactic latitudes, which we refer to as the *Optical-IRAS* sample [5].

The basic idea of the method is to assign positions for a large number of particles ($\approx 10^6$) following the same spatial distribution as the density field of galaxies recovered from the *Optical-IRAS* survey. Artificial galaxies are assigned observable properties such as B magnitude, diameters, line widths and I magnitudes, and an UGC-like catalog is generated. Estimated distances for the artificial "galaxies" are computed using the same distance relation, scatter distribution and incompleteness as the data. The difference between the known true distance and the measured distance is the bias. We generate a bias field in estimated distance space and apply this correction on the measured distances for the galaxies and recalculate their peculiar velocities.

The dominant effect to the bias in our Sc sample is the imposed redshift cutoff, especially at large distances. The amplitude of the corrections is relatively small in the central regions but rises steeply beyond 6000 km s^{-1}. A fully corrected model means that distances and peculiar velocities of the galaxies have been corrected by the bias field by interpolating the values defined

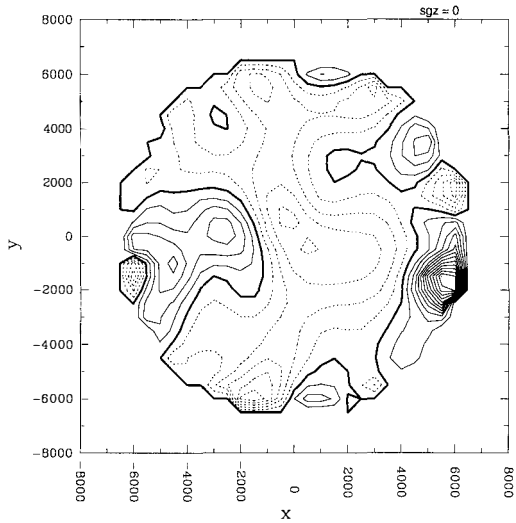


Figure 1: Contours of the reconstructed density field with a smoothing scale of $900 kms^{-1}$s. Solid lines represent overdensities and dashed lines underdense regions. The contours are shown in intervals of 0.2.

on a grid to the position of the galaxies. A detailed discussion of the method can be found elsewhere [6].

5 Preliminary Results

5.1 Density Field

The distances calculated from the TF relation and corrected for the bias, and the radial component of the peculiar velocity $u = cz_{CMB} - d_c$, where d_c is the "fully" corrected distance estimate, are then used as input data to reconstruct the density and the three-dimensional peculiar velocity field. For the reconstruction, we use the POTENT algorithm [3] adopting a grid in spherical coordinates of 20 equal shells out to a maximum radius of 7000 km s^{-1} and 64 latitude and longitude circles. The measured radial peculiar velocities were smoothed using a tensor window with fixed smoothing scale. We have carried out reconstructions with R_w = 900 km s^{-1} or 1200 km s^{-1}.

The reconstructed density field in one of our reconstructions is presented in figure 1. It is defined in a cubic grid of spacing 500 km s^{-1}. We use a Cartesian supergalactic coordinate system with SGX-axis pointing to $L = 0°$ and the SGY-axis pointing nearly to the North Galactic Pole. From this map one can easily recognize some of the major structures in the nearby volume such as the Great Attractor (GA), the Perseus-Pisces (PP) complex and the large void near the origin between the GA and the PP. Comparison of this map with that produced by smoothing the real space *Optical-IRAS* distribution shows the strong correlation between luminous and dark matter. In contrast to earlier reconstructions [1], the PP structure is clearly seen because of the denser sampling of the region.

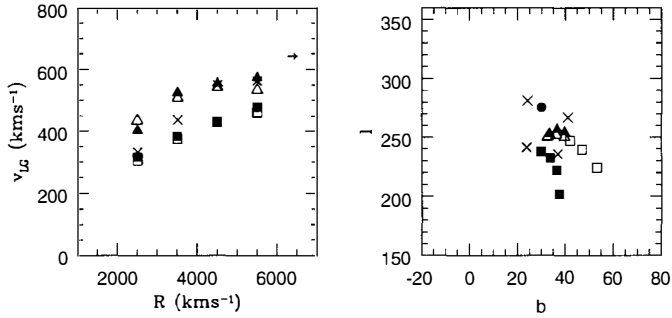


Figure 2: Local Group motion relative to shells 1000 kms^{-1} thick at different distances. In the left panel we show the amplitude as a function of the distance of the shell, with the arrow indicating the amplitude of the LG motion relative to the CMB. In the right panel the direction of the velocity vectors are shown in Galactic coordinates with the lowest point corresponding to the closest shell. The filled circle corresponds to the direction of the LG with respect to the CMB.

Errors in the reconstruction were estimated at each grid point from the variance derived from 100 mock redshift-distance surveys. These mock samples are drawn from the real space distribution of the *Optical-IRAS* model with the same number of galaxies and selection criteria as the data, similar to the procedure described above in connection with the bias correction. The mean fields derived from averaging the reconstruction of these different realizations are also used to evaluate the reliability of the reconstruction.

5.2 Velocity Field

Using the recovered three-dimensional velocity field we can determine the bulk motion in spheres centered at the Local Group. This quantity can, in principle, be used to constrain the power-spectrum of matter density fluctuations since the rms bulk velocity can be directly computed from the mass power-spectrum. Unfortunately, since the available volume is small there are not many independent volumes at any given scale to allow such a determination. Still the measured bulk velocity can be used to evaluate the consistency of a given model with the data.

The bulk velocity was computed using top-hat windows of different sizes by vector averaging the reconstructed three-dimensional velocity field. We find that the amplitude of the bulk motion varies with radius but neither the amplitude nor the direction is very sensitive to the smoothing scale adopted in the reconstruction.

From our preliminary analysis we find that for a top-hat, 6000 km s^{-1} in radius, the amplitude is 312 km s^{-1} in the direction $L = 170°$ and $B = -11°$, in Supergalactic coordinates. These values are in good agreement with those obtained from the analysis of an independent sample which gives an amplitude $\approx$ 300 km s^{-1} in the direction ($L, B = 166°, -20°$) [4]. We note that the direction of the observed bulk motion, as measured within the largest volume available, is very different from that reported from peculiar motions of clusters out to 15000 km s^{-1} [9].

Examination of the velocity field and the variation of the bulk motion with radius already give some indication that the picture of a coherent large-scale bulk flow of the entire region in which all structures partake is not an accurate description of the nearby velocity field [2]. We examine this question further by looking at the motion of the Local Group relative to surrounding shells. This is shown in figure 2 in the LG rest-frame for high (solid squares) and low resolution (open squares) reconstructions. For comparison we also show the points determined directly from the measured radial component of the peculiar velocity (crosses), the mean velocity computed from the mock surveys (open triangles) and that from the *Optical-IRAS* model in real space for $\beta = 1$ (solid triangles). The behavior of the amplitude as a function of distance is similar in all cases and the rise in the amplitude of the velocity suggests that the flow is not coherent within the surveyed volume. It is instead complex with several localized centers of attraction within the volume, the GA and PP systems being the most important. The difference in the predicted direction of the LG motion relative to the outermost shell obtained from the Sc data is about 9° relative to the model and about 22° relative to CMB dipole, suggesting that most of the acceleration imparted to the LG arises from sources within 6000 km s^{-1}.

6 Summary

We have shown some preliminary results from the analysis of the new redshift-distance survey of spiral galaxies. We have outlined the methods used to derive the TF relation appropriate for our data, to correct for bias and to compare the results from the analysis of peculiar velocity measurements with those of the galaxy distribution. Our preliminary results are encouraging and show that this independent sample of peculiar velocity measurements will be an important contribution to the study of the cosmic velocity field and the determination of the parameter β on large scales.

References

[1] Bertschinger, E., Dekel, A., Faber, S. M., Dressler. A. & Burstein, D. 1990, *Astrophys. J.* **364**, 370

[2] Courteau, S., Faber, S.M., Dressler, A. and Willick, J.A. 1993, *Astrophys. J.* **412**, L51

[3] Dekel, A., Bertschinger, E. & Faber, S. M. 1990, *Astrophys. J.* **364**, 349

[4] Dekel, A. 1994, Ann. Rev. Astr. Ap. **32**, 371

[5] Freudling, W., da Costa, L. N. & Pellegrini, P. S. 1994, *Mon. Not. R. Astr. Soc.* **268**, 943

[6] Freudling, W., da Costa, L. N., Wegner, G., Giovanelli, R, Haynes, M. P. & Salzer, J.J. 1995, *Astron. J.*, in press

[7] Giovanelli, R., Haynes, M.P., Salzer, J.J., Wegner, G., da Costa, L.N. and Freudling, W. 1994, *Astron. J.* **107**, 2036

[8] Giovanelli *et al.* 1995, in preparation

[9] Lauer, T.R. and Postman, M. 1994, *Astrophys. J.* **425**, 418

[10] Mathewson, D.S., Ford, V.L. & Buchhorn, M. 1992 *Astrophys. J. Suppl. Ser.* **81,**, 413

[11] Willick, J., Courteau, S., Faber, S. M., Burstein, D. & Dekel, A. 1995, preprint

THE INFORMATION CONTENT OF REDSHIFT AND VELOCITY SURVEYS

A. Yahil
State University of New York, Stony Brook, NY, U.S.A.

Abstract

The pixon-based image reconstruction of Puetter and Piña has achieved significant improvements over other methods in higher spatial resolution, greater sensitivity to faint sources, and immunity to the production of spurious artifacts and signal-correlated residuals. The same technique may be used for those problems of large-scale structure which allow for variable smoothing. The comparison of different datasets is not impaired by the variable smoothing, because a common underlying density/potential field, whatever its smoothing, can be applied to all datasets. By making optimal use of the combined datasets, the pixon method could therefore yield the most sensitive determination of the cosmological density parameter, Ω, from redshift and velocity surveys.

1 Introduction

The mapping of large-scale structures and velocities shares fundamental similarities with image reconstruction/restoration.[1] In both cases, the problem consists of solving an equation which can be written symbolically as

$$D = H \otimes I + N \quad . \tag{1}$$

Here D is the array of data points, I is the underlying field to be determined, image or density/potential, and N is the noise in the data. The operator H transforms the underlying field to data space. For images it is the point-spread function (PSF), typically blurring the image. In the case of large-scale structure it is a dynamical transformation from an underlying density/potential field to the appropriate data space.

[1]The term image restoration is usually reserved for the case in which the image and data spaces are identical, while image reconstruction refers to other cases, for example, the data might be in the form of 1–d scans, while the image is 2–d. For our purposes the distinction is unimportant.

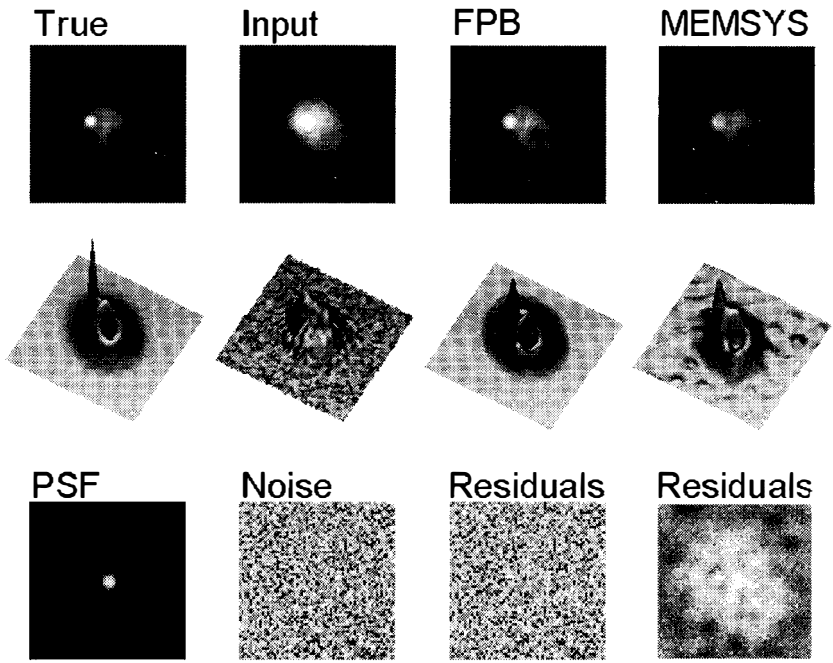


Figure 1: Comparison of pixon (FPB) and maximum entropy (MEMSYS) image restorations of a synthetic dataset, showing the true image, the noisy blurred input image, and the restored images and their residuals.

In solving Eq. (1), the noise is taken to be sufficiently well understood to allow the definition of a goodness-of-fit (GOF) criterion, such as χ^2 or likelihood. It is further assumed that the functional form of the operator H is known, although it may have unknown parameters which are to be determined from the data. In the cosmological case, in fact, the whole point is to determine some of the parameters of H, especially the cosmological density parameter, Ω.

The purpose of this paper is to introduce some recent developments in image processing into the field of large-scale structure. §2 briefly presents some results of the new pixon method of Puetter and Piña [17, 16]. Since this method is based on concepts in information theory which are not generally known in the astronomical community, the paper then veers to a discussion of algorithmic information content, §3, complex adaptive systems, §4, and denoising using localized orthogonal functions such as wavelets and wave packets, §5. (For references see those sections.) A detailed presentation of the pixon method follows in §6, with application to large-scale structure in §7.

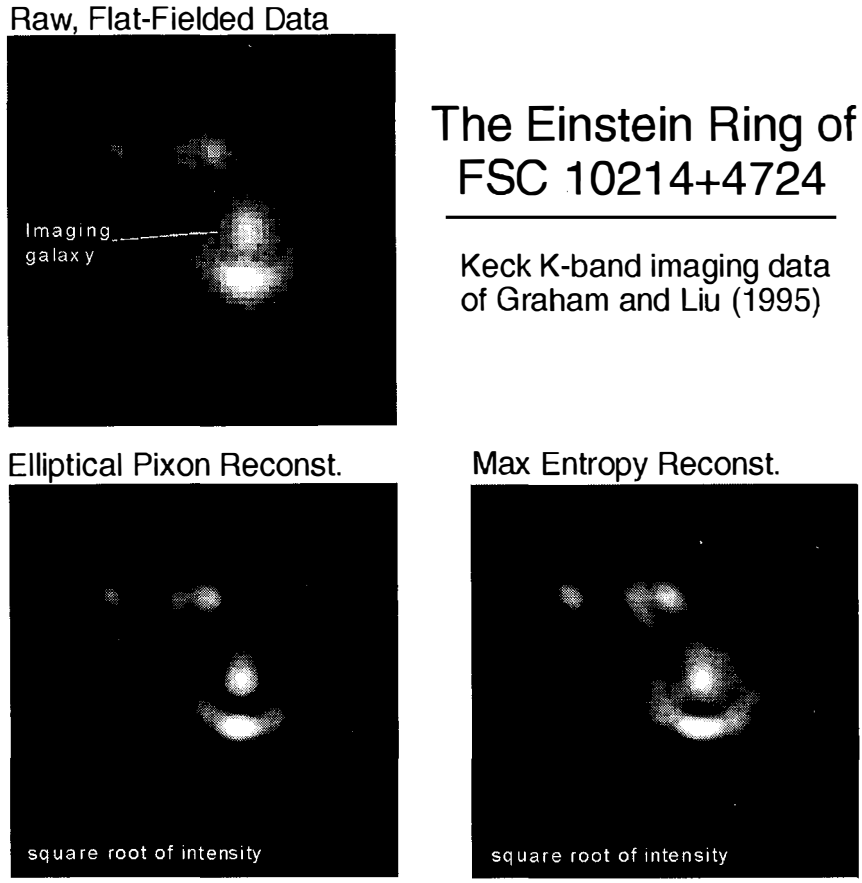


Figure 2: Reconstruction of the entire Einstein ring in FSC10214+4724, showing the raw 2μm data taken at the Keck telescope and the reconstructions using elliptical pixons and maximum entropy. Note that the separation between the peak of the Einstein ring and the lensing galaxy in this ground-based observation is only $1\farcs5$.

2 Image reconstruction/restoration

When the data have high signal-to-noise ratios, Eq. (1) can be solved to obtain information about the image on scales smaller than the width of the PSF, provided that the data are sufficiently finely sampled. This inversion problem is a generalized deconvolution, and suffers from all its problems: (1) There may be less data points than image points, so the inversion is not unique. (2) The PSF is a smoothing operator, but noise introduces a high frequency component to the data. A straight inversion, even if unique, amplifies the noise. (3) A parametric fit of

the image is always possible, but there has to be a model with which to parameterize. (4) If it is not known where to stop a parametric expansion, e.g., the order of a polynomial, a GOF criterion may be used, such as χ^2 or likelihood, but the parameters have to be prioritized.

There is an extensive literature on inversion techniques, the state-of-the-art generally being taken to be the maximum entropy method [1, 15, 21, 13]. Recently Puetter and Piña introduced a new method using a Fractal Pixon Basis [17], to be explained in detail in §6, which is superior at detecting faint sources and resolving extended ones and far more robust against spurious artifacts and signal-correlated residuals. For a recent review with extensive examples see [16]. A synthetic example from that paper is reproduced in Fig. 1, comparing the pixon method with maximum entropy. A second comparison can be seen in the latest pixon restoration [18] of the full Einstein ring in the gravitational lens FSC10214+4724 [12], shown in Fig. 2.

3 Algorithmic information content

The algorithmic information content (AIC) of a dataset is defined as the length of the shortest program that prints the nonrandom content of the data and stops [22, 14, 2]. For example, consider a book whose first ten pages contain only the letter A, the next 10 pages B, and so on, ending with Z on page 260. The rather meager information in this book can be expressed very compactly by a program, making it unnecessary to present the entire data, i.e., the full book. In fact, the second sentence in this paragraph, although written in plain English instead of some computer language, is an accurate instruction for constructing the book.

This definition of information differs significantly from the original entropy introduced by Shannon [20] which uses fixed quanta of information, e.g., letters in the above example, or pixels in an image. Shannon's entropy is invariant under a random scrambling of the units of information and is insensitive to any *correlation* between them. It assigns the same entropy to the above-mentioned book and to one containing a completely random distribution of its letters. The AIC, on the other hand, seeks all possible regularities in order to minimize the description of the information; it recognizes that the book has some information in it beyond the fact that each letter occurs the same number of times. The maximum entropy method uses Shannon's definition of entropy and is therefore invariant under a scrambling of the pixels. As a result, it is not as effective in identifying extended structures.

Unlike the above example, real data always include some unwanted random noise, which is not part of the information content and is due to a physical limit (e.g., photon statistics) or instrumental noise. An artificially high noise level may even be set by the experimenter or analyzer to obscure uninteresting details that could be detected. In any event, the noise is characterized by a lack of correlation with the signal (information), and unpredictability, except in a statistical sense. (Systematic errors are not considered here.)

Clearly, failure to recognize the random component in a dataset leads to an erroneous determination of its information content. Consider, for example, a simple series in an IQ test: 1, 2, 3, 4, 5, 6, 7, 8, ?. The information content in this series can be identified by any child, who recognizes instantly that the next term in the series is 9. Now add noise, for example the following binary series was obtained by flipping a coin: 1, 1, 0, 1, 0, 1, 0, 0, ?. The real data are a sum of the true information and the noise, viz: 2, 3, 3, 5, 5, 7, 7, 8, ?, and the next term in the series is 9 or 10 with equal probability. Most people presented with this series, conditioned as they are on IQ tests, would attempt to find regularity in it assuming it to be noiseless—quite a challenge, actually. On the other hand, if the series were plotted against index, most scientists would recognize the noise component and correctly draw a regression line.

The point is that, even for such a simple series, and certainly for more complicated data, it

is easy to mistake noise for signal and misinterpret the information. Furthermore, the tendency to make this mistake may be a function of how the data are viewed. Any search for information content, especially an automated search, must avoid this pitfall and correctly separate out the noise, so the remaining signal is noise-free. The question is how.

4 Complex adaptive systems

A somewhat surprising result is that, in the presence of noise, the least complex, most economical, description of information, i.e., the AIC, is also the most *faithful*; the data are not overfitted. Intuitive arguments illustrate this manifestation of Occam's razor. (For an example of a rigorous analysis of denoising see [9].) Consider an experiment in which y_i are measured as a function of x_i, and suppose further that the true relation between them is a polynomial

$$y_i = p(x_i) + \epsilon_i \quad , \tag{2}$$

where ϵ_i is an error component. A simple polynomial least-squares fit gives the best coefficients, and a GOF test tells at what order to truncate the polynomial. But suppose that a least-squares fit is made with a sum of exponentials. More terms are typically needed to fit the data with the same χ^2, and the fit is awkward, with correlated residuals. The more economical polynomial fit is also the more faithful one.

But in the absence of a known parameterization, how is one to choose from an infinity of possibilities? Gödel's incompleteness theorem actually guarantees that the entire information content of the data can never be found. The meaning of information content is therefore limited *a priori* by choosing an external language with which to describe it, and this language, in turn, restricts the allowed parameterizations. The choice of language does make a difference. The maximum entropy method makes no allowance for correlations between pixels in an image and assumes that the most probable one is completely gray. The pixon scheme, by contrast, favors images with large correlations.

A language that emphasizes correlations is more complex because of all the possible groupings of pixels. Moreover, these groupings are not known *a priori* and must be learned from the data. This is known as a complex adaptive system. For example, if a photograph of the mountains is taken, with perhaps some friends in the foreground, the information content might be the background mountains and valleys and foreground people. This says that the image is supposed to be made up of these objects, but not where in the image there are mountains and where valleys, and which people are located where in the foreground. The language can impose restrictions on the type of image, but in and of itself it does not specify all the details, which can only be learned from the data.

5 Localized orthogonal basis functions

For data whose expected values are functions of known variables, such as images as functions of position, the language of information has long been spectral. The data are described by means of a sum over spectral functions

$$y_i = \sum_k a_k f_k(x_i) + \epsilon_i \quad , \tag{3}$$

and the information content consists of the length of the series and its coefficients.

Many spectral functions are possible. For pulsed data, the Fourier spectrum might be all that is needed, while if spatial correlation is of no interest, the individual pixel intensities suffice. Images typically consist of extended contiguous structures which are both localized and have spatial correlations. The choice of spectral functions for this intermediate case is constrained by the uncertainty principle which determines the minimum volume of phase-space over which information can be defined. There has to be some give and take between correlation and localization of information.

In the last few years there has been great interest in wavelets [6] and wave packets [4, 5], spectral basis functions that are localized, orthogonal, and translation and dilation invariant. Their advantage is the speed of the transformations between the original and spectral domains, which require only $O(N \log_2 N)$ operations (like a fast Fourier transform). Denoising is achieved by transforming the noisy data into the spectral domain, applying either hard [10] or soft [8] thresholding to the resulting coefficients, thereby suppressing those smaller than a certain amplitude, and then transforming back into the original domain. These methods result additionally in data compression, since fewer spectral coefficients than data points need be kept. They have also been used to identify the important and noisy parts of initial conditions in dynamical problems, e.g., [11].

Despite their strong advantages, however, such denoising techniques have their limitations. First, the speed of the transformations depends on even sampling. More importantly, owing to their orthogonality, they must be both negative and positive. But images and densities are only positive, so a larger number of basis functions is required to "interfere away" the negative holes.[2] The orthogonal functions therefore form a less suitable basis in the AIC sense. This is borne out by the resulting denoised images, which continue to exhibit "visual artifacts" requiring special treatment [3].

6 Pixons

A representation of images which is closer to the AIC, and hence less likely to show residual artifacts, can be obtained by restricting the spectral functions to be positive. This approach, originated by Puetter and Piña [17], indeed leads to significant improvement in image reconstruction and restoration, as evidenced by several examples given in [16] and the image of the gravitational lens FSC10214+4724 [18] shown in Fig. 2. Fainter sources are detected, the angular resolution is better, and spurious features or signal-correlated residuals are largely absent.

The pixon method starts with a finely sampled positive pseudoimage, ϕ, and smoothes it with a positive kernel function, K, to obtain the image.

$$I = K \otimes \phi \quad \Rightarrow \quad D = H \otimes K \otimes \phi + N \quad . \tag{4}$$

In its crudest form, the image model is made up of P contiguous and nonoverlapping cells, called pixons, with constant intensity within each pixon. Unless these pixons have very complex structure, the AIC—the length of the shortest program required to specify the nonrandom part of the data—is likely to depend mainly on the total number of pixons, P, and be a monotonically rising function of it. The goal, then, is to minimize P, but without allowing the residuals to exceed the level expected for random noise. A straightforward way to achieve this is to minimize

$$\mathcal{L} = \mathrm{GOF} + \lambda P \quad , \tag{5}$$

[2] Even for the velocity field, which can have both signs, there are constraints, for example on $\nabla \cdot \mathbf{v}$.

where GOF is a goodness-of-fit criterion, such as χ^2 or likelihood, and λ is a Lagrange multiplier adjusted to give a "reasonable" GOF. (It does not matter if λ is attached to the GOF term or to P.) The procedure is completely analogous to the maximum entropy method; the difference is only in the choice of the entropy term, which in the pixon method seeks images with as much smoothness as possible.

A more refined approach limits the shapes that the kernel function can take, but allows its edges to be fuzzy, overlapping adjacent kernels. For example, the pixons used in the restoration of the gravitational lens FSC10214+4724, Fig. 2, were written as elliptical kernels

$$K(\mathbf{x}|\mathbf{y}) = \det\Big(M(\mathbf{y})\Big)^{1/2} f\Big((\mathbf{x}-\mathbf{y})\cdot M(\mathbf{y})\cdot(\mathbf{x}-\mathbf{y})\Big) \quad , \tag{6}$$

where $\mathbf{y}$ and $\mathbf{x}$ are the positions in pseudoimage and image spaces, respectively, $M(\mathbf{y})$ is a positive-definite, symmetric, matrix which determines the directions and lengths of the axes of the ellipse, and f is the kernel shape function.

The definition of pixons is here a little more subtle, because of their fuzzy edges, but not very difficult. Note first that P need only be specified to within an unknown constant of proportionality, since the latter can always be absorbed by the Lagrange multiplier, λ. A reasonable definition of a pixon density is therefore

$$p(\mathbf{y}) = \det\Big(M(\mathbf{y})\Big)^{1/2} \quad , \tag{7}$$

with the total number of pixons (the entropy term) being the integral

$$P = \int d\mathbf{y}\, p(\mathbf{y}) \quad . \tag{8}$$

The spectacular improvement brought by the pixon method to reconstructed image comes with a price tag of significant complication in numerical computations: (1) There are no simple orthogonal transformations between the original and spectral domains as for wavelets and wave packets. (2) In fact, since the kernel varies over the image, standard techniques for convolution do not apply either. (3) The minimization of $\mathcal{L}$ is nonlinear, with the number of variables proportional to the number of pixels. (4) Unless the signal-to-noise ratio is high, the minimization landscape is very complex, and a program may have to "slalom its way" in complicated terrain toward the minimal value.

When the signal-to-noise ratio (SNR) is not too low, a pixon reconstruction proceeds reasonably well by alternately minimizing the GOF term and P [16]. More elaborate methods are needed for lower SNR. In the case of a γ-ray experiment with lower SNR [7], the derivation of the pixon map required mean field annealing [19], at yet higher computational cost. Effort is now underway by Puetter and the author to develop faster, and more general techniques for minimizing $\mathcal{L}$. Some progress has already been made, but the ultimate goal, a "black box" program which does not require fine adjustments by the user, is not yet at hand.

7 Application to large-scale structure

Galaxies in density and velocity surveys are unevenly sampled in space, both because of real density variations, and for practical reasons, particularly the increase of observational difficulty with distance. Trying to smooth the fields with a fixed window therefore requires compromises, which invariably lead to oversmoothing in some locations and undersmoothing in others.

For some applications, homogeneous smoothing is critical, for example in order to compare with a theoretical probability density function computed for a fixed smoothing window. In

other cases, however, the ideal of homogeneous smoothing may be relaxed in favor of the maximum information contained in the data, introducing at each location the maximum smoothing permitted by the the local data.

Smoothing proceeds in analogy with image reconstruction, except that there is no blurring due to a point-spread-function. Instead, the operator H takes the form of a dynamical transformation from an underlying density/potential field to the appropriate data space. For density determinations, the data are positions in redshift space, while for velocity surveys they are magnitudes and velocity widths. The pseudoimage is the density/potential defined on a fine grid, and the pixon kernel K smoothes it to the maximum degree permitted by a GOF criterion for the data, typically a maximum likelihood estimator for density and a χ^2 for velocity.

The result is a density/potential map with variable smoothing, which can only be interpreted together with its smoothing map. In particular, the comparison of two different density/potential maps is only meaningful when account is taken of differences in their smoothing maps. At first sight, this might seem to limit the usefulness of the method, particularly for the all-important comparison of density and velocity fields, used to determine the cosmological density parameter, Ω. However, in a joint mapping, the same underlying density/potential field can be applied to both datasets. In a region in which the velocity data are more sparse, say, the smoothing scale is determined by the density, and the velocity data are insensitive to the fine structure, and vice versa where velocity data are more abundant. The quality of the fit can then be tested *a posteriori* by verifying that both datasets separately satisfy GOF criteria, and that the residuals are random, showing neither autocorrelation nor correlation with signal.

The success of the pixon method in image reconstruction suggests that, if all goes well, a cosmological pixon fit, which makes optimal use of all the data, could provide the most sensitive determination of Ω from redshift and velocity surveys.

Acknowledgements. I am indebted to R. Puetter for first introducing me to pixons and then for extensive discussions on the subject. This work was supported in part by NASA.

References

[1] Bryan, R. K., Skilling, J. 1980, *Mon. Not. R. Astr. Soc.* **191**, 69

[2] Chaitin, G. J. 1966, *J. Ass. Comput.. Mach.* **13**, 547

[3] Coifman, R. R., Donoho, D. L. 1995, in *Wavelets and Statistics*, A. Antoniadis, ed., (Berlin: Springer-Verlag), in press, http://playfair.Stanford.EDU:80/reports/donoho/

[4] Coifman, R. R., Meyer, Y. 1991, *Comptes Rendus Acad. Sci. Paris* **A312**, 259

[5] Coifman, R. R., Wickerhauser, M. V. 1992, *IEEE Trans. Inform. Theory* **38**, 713

[6] Daubechies, I. 1988, *Comm. Pure Appl. Math.* **41**, 909

[7] Dixon, D. D., Tümer, O. T., Kurfess, J. D., Purcell, W. R., Wheaton, W. A. 1995, in preparation

[8] Donoho, D. L. 1995, *IEEE Trans. Info. Theory.* **41**, 613

[9] Donoho, D. L., Johnstone, I. M. 1994, *Comptes Rendus Acad. Sci. Paris* **A319**, 1317

[10] Donoho, D. L., Johnstone, I. M. 1994, *Biometrika* **81**, 425

[11] Farge, M., Goirand, E., Meyer, Y., Pascal, F., Wickerhauser, M. V. 1992, *Fluid Dyn. Res.* **10**, 229

[12] Graham, J. R., Liu, M. C. 1995, *Astrophys. J.* **449**, L29

[13] Gull, S. F. 1989, in *Maximum Entropy and Bayesian Methods*, J. Skilling, ed., (Dordrecht: Kluwer), p. 53

[14] Kolmogorov, A. N. 1965, *Inf. Transmission* **1**, 3

[15] Narayan, R., Nityananda, R. 1986, *Ann. Rev. Astr. Astrophys.* **24,**, 127

[16] Puetter, R. C. 1995, *Inter. J. Image Sys. Tech.*, in press, ftp://cassir.ucsd.edu/receive/-imrecon/papers/95ijist/

[17] Puetter, R. C., Piña, R. K. 1993, *Proc. S.P.I.E.* **1946**, 405

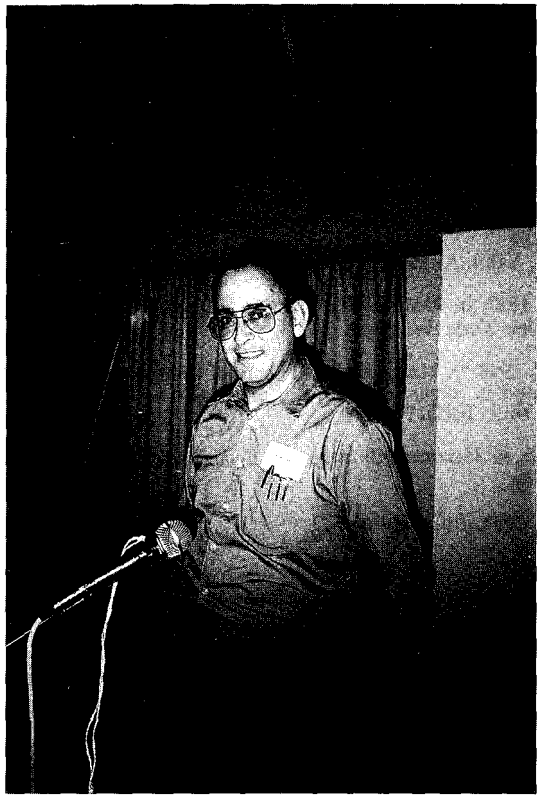
[18] Puetter, R. C., Yahil, A. 1995, in preparation

[19] Reeves, C. R. 1993, in *Modern Heuristic Techniques for Combinatorial Problems*, C. R. Reeves, ed., (New York: Wiley), p. 197

[20] Shannon, C. E. 1948 "A Mathematical Theory of Communication", Bell System Technical Report, reprinted in Slepian, D. 1974, *Key Papers in the Development of Information Theory*, (New York: IEEE Press)

[21] Skilling, J. 1989, in *Maximum Entropy and Bayesian Methods*, J. Skilling, ed., (Dordrecht: Kluwer), p. 45

[22] Solomonoff, R. 1964, *Inf. Control* **7**, 1



DYNAMICAL FIELDS AND Ω SIMULTANEOUSLY FROM REDSHIFT AND PECULIAR VELOCITY SURVEYS

A. Nusser [1] and A. Dekel [2]
[1] *Institute of Astronomy, Madingley Rd, Cambridge, CB3 0HA, England*
[2] *Racah Institute of Physics, The Hebrew University, Jerusalem 91904, Israel*

Abstract

We present a method (termed SIMPOT) for a simultaneous reconstruction of the large-scale density, velocity and potential fields and the parameter $\beta \equiv \Omega^{0.6}/b$ (where Ω is the cosmological density parameter and b is the linear biasing parameter) from the observed radial peculiar velocities and the distribution of galaxies in redshift space. SIMPOT models the velocity potential field by means of an expansion in spherical harmonics and radial Bessel functions, and, assuming a value for β, relates it to the distribution of galaxies in redshift space using linear theory of gravitational instability. The method is tested using realistic mock catalogs of Mark III peculiar velocities and IRAS 1.2Jy redshifts. The mock data are extracted from an $\Omega = 1$ N-body simulation which mimics the nearby universe. If linear biasing prevails in the universe, SIMPOT provides an unbiased estimate for β with an error of ± 0.06. SIMPOT can be applied with different weights to the velocity and redshift data. With high weight assigned to velocities, the recovered fields are mainly determined by the velocities, but properly regulated by the distribution of galaxies in regions of poor velocity data. SIMPOT can be viewed as a general method for recovering large scale dynamical fields from a multitude of heterogenous data.

1 Introduction

Three related objectives of current cosmological research are (a) determination of the universal density parameter Ω, (b) recovery the underlying large scale fields of peculiar velocity and mass density in the local universe, and (c) establishing the relationship between the distribution of galaxies and mass.

Two complementary kinds of data are available: (i) complete redshift surveys of galaxies, which serve as (perhaps biased) tracers of the mass distribution, and (ii) samples of galaxies with redshifts and inferred distances, which serve as tracers of the peculiar velocity field. These data are commonly analyzed separately and compared in retrospect [4]. On one hand, redshift surveys yield the mass distribution and the corresponding velocity field under a given biasing relation and Ω. The apparent anisotropy of clustering in redshift surveys can be used to estimate Ω assuming a biasing relation [10] [8] [2]. Peculiar velocity samples, on the other hand, yield the velocity field based on the potential

nature of gravitating flows, and then the corresponding density field using gravitational instability and an assumed Ω. The recovered velocity field is used to estimate Ω independently of the distribution of galaxies and the biasing relation [17] [7] [1]. At a later stage, the recovered fields from the two inputs are tested for mutual consistency according to gravitational instability and linear biasing, and then compared to yield a value of β [6] [11] [15] [3] [19].

Here we make a first attempt at combining the data from redshift surveys and peculiar velocity samples in recovering the dynamical fields and simultaneously determining β. The simultaneity is advantageous because the data are complementary: the gravitational velocities from the redshift surveys help filling in regions which are poorly sampled by peculiar-velocity data, while the observed velocities help constraining the biasing for the redshift-data analysis, and the bulk velocity which arises from outside the volume covered by the survey. A simultaneous fit is more likely to converge to the true solution than a successive fit. The fact that a simultaneous fit allows applying exactly the same variable effective smoothing to both data sets is important especially because the biasing could be scale dependent.

In §2 we outline the method. In §3 we test the method using mock data. In §4 we discuss the method and its application.

2 The method

The data consist of two independent samples of galaxies: a whole-sky collection of radial peculiar velocities inferred by Tully-Fisher-like distance indicators, and a complete redshift survey with a known selection function. Our goal is to find the velocity potential field $\Phi(\boldsymbol{r})$, and the parameter β, which simultaneously fit the two data sets. We formulate a parametric model $\tilde{\Phi}$ for the velocity potential field by means of a finite expansion in a set of spherical harmonic and radial Bessel functions [18] [9],

$$\tilde{\Phi}(\boldsymbol{r}) = -\frac{1}{2}\mathcal{H}r^2 - \boldsymbol{B}\cdot\boldsymbol{r} + \sum_{l=1}^{l_{max}}\sum_{m=-l}^{l}\sum_{n=1}^{n_{max}} \Phi_{lmn}\, j_l(k_n r)\, Y_{lm}(\hat{r}). \tag{1}$$

We incorporate in the model a monopole term corresponding to a Hubble-like peculiar flow $\mathcal{H}r$ (or a constant offset in density), and a bulk flow term corresponding to a constant velocity $\boldsymbol{B}$. The model free parameters are Φ_{lmn}, B_i, and $\mathcal{H}$. The corresponding model for the radial peculiar velocity field is

$$\tilde{u}(\boldsymbol{r}) = -\frac{\partial\Phi}{\partial r} = \mathcal{H}r + \boldsymbol{B}\cdot\hat{r} + \sum \Phi_{lmn}\, k_n \left(j_{l+1}(k_n r) - l\frac{j_l(k_n r)}{k_n r}\right) Y_{lm}(\hat{r}). \tag{2}$$

Away of triple-value zones in redshift space, the density fluctuation field is related to the velocity potential by linear gravitational instability theory [15],

$$\delta_s(\boldsymbol{s}) = \frac{1}{f(\Omega)}\nabla^2\Phi + \frac{1}{s^2}\frac{\partial}{\partial s}\left(s^2\frac{\partial\Phi}{\partial s}\right), \tag{3}$$

where $f(\Omega) \approx \Omega^{0.6}$. The second term on the r.h.s represents the apparent density enhancement in redshift space as a result of the mapping from distance to redshift. Note that this second term breaks the linear scaling of the potential with f.

The "observed" mass density $\delta_s(\boldsymbol{s})$ has to be inferred from the galaxy redshift survey. The relation between galaxies and mass is modeled by "linear biasing", where the local density fluctuations galaxies and mass are related via a constant biasing factor b. In linear theory, the parameters b and Ω in all the dynamical relations combine into $\beta \equiv f/b$. Since the redshift survey is flux limited, the true number density of galaxies is estimated by weighting the observed number density, $n_0(\boldsymbol{s})$, by the inverse of the selection function of the survey, $\phi(\boldsymbol{r})$. The selection function ϕ must be evaluated at the real space position corresponding to $\boldsymbol{s}$, which is unknown a priori. Approximating $\phi(\boldsymbol{r})$ by the measurable $\phi(\boldsymbol{s})$ leads to systematic biases [12]. Instead, we approximate: $\phi(\boldsymbol{r}) \approx \phi(\boldsymbol{s}) - (\partial\phi/\partial s)u(\boldsymbol{s})$. The field we

choose to express in terms of the model parameters is the fluctuation in $n_0(\boldsymbol{s})/\phi(\boldsymbol{s})$, which can be determined from the observations. We obtain using (1), (3), and (4)

$$\tilde{\delta}_G(\boldsymbol{s}) = -2\frac{\boldsymbol{B}\cdot\hat{s}}{s} + \sum_{lmn}\Phi_{lmn}\left[-\beta^{-1}k_n^2\, j_l(k_n s) + b_{ln}(s)\right]Y_{lm}(\hat{s}), \tag{5}$$

where,

$$b_{ln} = k_n^2 l\left(l+1+\frac{d\ln\phi}{d\ln s}\right)\frac{j_l(k_n s)}{(k_n s)^2} - k_n^2\frac{d\ln\phi}{d\ln s}\frac{j_{l+1}(k_n s)}{k_n s} - k_n^2 j_l(k_n s), \tag{6}$$

and we have omitted the term involving $\mathcal{H}$ so that any uncertainty in the form of a constant offset in the density is absorbed into the Hubble-like flow in the velocity model.

The expansion of an arbitrary radial function into a set of Bessel functions requires a choice of boundary conditions appropriate for the problem in question. These boundary conditions determine the wavenumbers k_n in the expansion. In any realistic application, it is necessary to set a maximum radius, R_{max}, within which the data are sufficiently reliable to constrain the potential field. It is at R_{max} where the outer boundary conditions should be specified. We are guided by the asymptotic behavior of a peculiar velocity field generated by fluctuations in the mass-density distribution. If we assume that the density of matter beyond R_{max} is constant, then potential theory dictates that the radial dependence of the radial velocity u [eq. (2)] at $r > R_{max}$ is $u \propto r^{-(l+2)}$ at $r > R_{max}$ [9]. This leads to the condition $j_{l-1}(k_n R_{max}) = 0$.

2.1 Simultaneous Estimation of β and Φ_{lmn}

In the usual sense of the theory of data modeling, the parameters of the model are found by achieving a maximum in the probability that the model produces the observations within their measurement errors.

There is no ambiguity in formulating the probability for observing the peculiar velocities given the model. If the errors, σ_{ui}, in the measurements of the peculiar velocities, u_{0i}, are uncorrelated and Gaussian, then the probability of the occurrence of the observations given the model $\tilde{\Phi}$ is,

$$\Pr[u_0|\tilde{\Phi}] \propto \exp\left[-\frac{\chi_u^2}{2}\right] \equiv \exp\left\{-\frac{1}{2}\sum_{i=1}^{N_g'}\sigma_{ui}^{-2}\left[u_{0i}-\tilde{u}(\boldsymbol{r}_i)\right]^2\right\}, \tag{8}$$

where the sum is over all galaxies in the sample of peculiar velocities. The errors, σ_{ui}, are mainly a result of the intrinsic scatter of the distance indicator used to derive the peculiar velocities and partly of observational uncertainties, e.g., inclination effects in measuring rotational velocities in the case of the Tully-Fisher distance indicator.

Less obvious is how an "observed" density field. Here we define a density-contrast field in redshift space by [9],

$$\delta_{0s}(\boldsymbol{s}) = \frac{1}{\bar{N}}\sum_{i=1}^{N_g}\frac{1}{\phi(\boldsymbol{s}_i)}\delta_D(\boldsymbol{s}-\boldsymbol{s}_i) - 1, \tag{10}$$

where $\bar{N}$ is the true mean number density of galaxies and the sum is over all galaxies in the survey. Since the contribution of each galaxy is weighted by the selection function at its redshift rather than its distance, the definition (10) is a biased estimate of the true density. However, this bias is properly mitigated by the model (5). In order to estimate the shot-noise errors in (10), we divide space into cubic cells of volume ΔV centered at positions $\boldsymbol{s}_\alpha$ of a uniform grid. We approximate the Dirac delta function by $\delta_D(\boldsymbol{s}-\boldsymbol{s}_i) \approx 1/\Delta V$ if $\boldsymbol{s}$ and $\boldsymbol{s}_i$ fall in the same cell and zero otherwise. Then (10) implies that the number density excess, $\delta(\boldsymbol{s}_\alpha)_{0\Delta V}$, inside a cell α is constant. In this scheme, the variance in the determination of (10) due to shot-noise is the inverse of the number density expected in each cell, i.e., $\sigma_\delta^2(\boldsymbol{s}_\alpha) = \frac{1}{\Delta V\bar{N}\phi(\boldsymbol{s}_\alpha)}$. Clearly the shot-noise errors in different cells do not correlate. Therefore, if

we limit the analysis to modeling the the large scale density field, the probability that $\delta_{0\Delta V}$ is realized in a discrete sampling of $\tilde{\delta}_G$ is Gaussian which, in the limit $\delta V \to 0$, becomes,

$$\Pr[\delta_{0\Delta V}|\tilde{\Phi},\beta] \propto \exp\left[-\frac{\chi_\delta^2}{2}\right] \equiv \exp\left\{-\frac{1}{2}\bar{N}\int d^3s\phi(\boldsymbol{s})\left[\delta_{0s}(\boldsymbol{s})-\tilde{\delta}_G(\boldsymbol{s})\right]^2\right\}. \quad (11)$$

Now we can write the probability for reproducing the observed peculiar velocities and density field as,

$$\Pr[u_0,\delta_0|\tilde{\Phi},\beta] = \Pr[u_0|\tilde{\Phi}]\Pr[\delta_0|\tilde{\Phi},\beta] = A\exp\left[-\frac{1}{2}\left(\chi_u^2+\chi_\delta^2\right)\right], \quad (14)$$

where A is a normalization factor which is independent of β and the model parameters.

The problem of rendering the probability (14) stationary reduces to minimizing the function $\chi^2 = \chi_\delta^2+\chi_u^2$ subject to variations in β and Φ_{lmn}. At the minimum the derivatives $\partial\chi^2/\partial\beta$ and $\partial\chi^2/\partial\Phi_{lmn}$ vanish, yielding a set of equations involving nonlinear coupling between β and Φ_{lmn}. However, for a given β, the equations $\partial\chi^2/\partial\Phi_{lmn}=0$ are linear in Φ_{lmn}. Therefore we choose to determine $\Phi_{lmn}(\beta)$ using standard techniques for solving linear equations. Then we adjust the best estimate for β simply by examining the curve of $\chi^2[\Phi_{lmn}(\beta),\beta]$.

SIMPOT circumvents a major drawback of direct comparisons, say, between the 1.2JyIRAS density and the velocity divergence as derived from POTENT. Were β to be estimated in such comparisons from the regression of the velocity divergence on the density or vice versa, it would be biased due to the presence of errors in the density or the velocity divergence. The reason for the bias in regression lines, is that the dynamical relation between velocity and density is forced to hold between the measured fields which are contaminated by errors. Direct methods usually allude to extensive Monte Carlo simulations in order to take account of the biases in the estimates of β [6]. SIMPOT, however, imposes the dynamical relations in the model. It then seeks best estimates for β and the model parameters by maximizing the probability (14). The dynamical fields which are contrived by SIMPOT are modulated by the observed peculiar velocities and the density field of galaxies. In regions where the velocity data are poor the fields are mainly constructed out of the density field. In regions where the errors in the observed density field are large due to shot-noise while the velocity data are reliable, the fields are affected more by the observed velocities than by the density field.

The constraint on β in SIMPOT is two-faced. On the one hand, the modulation of the potential model by the velocities given β affects the value of χ_δ^2. To see that, consider an unrealistic case of accurate measurements of peculiar velocities and very dilute redshift survey so that the model is solely determined by the velocities independently of β. But then the value of χ_δ^2 strongly depends on β. For β lower the actual value, the density fluctuations as given in terms of potential model by (5) are unrealistically large, causing a large χ_δ^2. For a higher β, larger the actual value, the density fluctuations are underestimated leading to a large χ_δ^2. Note however that according to (5), the density fluctuations do not vanish in the limit $\beta \to \infty$ because the redshift distortion correction terms are independent of β. On the other hand, the value of χ_v^2 is affected by the observed density field in redshift space which introduces an implicit dependence of χ_v^2 on β.

An important question which arises when analyzing two different kinds of data is how well are they consistent given the hypothesis that they describe the same underlying fields? In the rigorous statistical sense, the value of χ^2 per d.o.f is a good indication of a goodness of fit and hence of the agreement between the two kinds of data. However, in the methodology presented here the actual value of the χ^2 is not a good discriminator for the following reasons. First, the χ_δ^2 contains a constant term which is an integration of squares of Dirac delta functions arising from our description of the observed density. This term is infinite but it does not affect the solution for the fit parameters. Clearly, the χ_δ^2 contains a divergent term because the number of d.o.f in the description of the observed density field is infinite. Second, our model does not incorporate small scale velocity scatter present in the peculiar velocities. Third, SIMPOT neglects nonlinear effects in relating the density to the potential model. To some extent these effects might be important in the real universe in some regions such as the Great Attractor.

SIMPOT provides an answer to this question by reconstructing the potential field with different weights assigned to the different data. By inspection of the differences in the reconstructions with different weights one may assess the consistency between the data sets. Thus let us define a function Ξ^2 by,

$$\Xi^2 = \lambda\chi_u^2 + (1-\lambda)\chi_\delta^2, \tag{15}$$

where λ is a free parameter between 0 and 1. A reconstruction of the potential field with $\lambda \dashrightarrow 0$ heavily relies on the observed density field. If $\lambda \dashrightarrow 1$ the reconstruction makes little use of the density field and the recovered potential is dictated by the peculiar velocities. In the reconstruction with $\lambda \neq 0.5$ the value of β derived from minimizing χ^2, i.e, Ξ^2 with $\lambda = 0.5$, must be used. The reason is simply that an estimate β obtained by, $\partial\Xi^2/\partial\beta = 0$ with $\lambda \neq 0.5$, is biased. For instance if $\lambda \dashrightarrow 1$ then the model is determined by the peculiar velocities and χ_u^2 depends very weakly on *beta*. Therefore, the dependence of Ξ^2 on β is due to χ_δ^2 which is mearly a measure of error weighted scatter of the difference between the density as inferred by the velocities given β and the observed density. Therefore estimating β by $\partial\Xi^2/\partial\beta = 0$ is similar, for $\lambda \dashrightarrow 1$, to computing the regression line of the inferred on observed densities. This estimate is clearly biased. Note however that once β is fixed by minimizing χ^2 the potential model is linear in the remaining parameters which can be determined without any bias by minimizing Ξ^2 with $\lambda \neq 0.5$.

3 Testing with with a mock-universe simulation

The systematic biases in the data depend on the morphology of the universe. Therefore it is essential to test the method using a numerical simulation which mimics the large scale structure of the local universe [13]. Such a simulation is generated by integrating forward in time the initial density fluctuations obtained from the 1.2Jy IRAS survey using the Zeldovich-Bernoulli time machine [16]. The simulation was halted at $\sigma_8 = 0.7$. Mock 1.2Jy IRAS and Mark III catalogs were then generated from the simulation. To further improve the realism of the application of SIMPOT and discern the effects of various sources of systematic biases on the estimation of β, 1.2Jy IRAS catalogs with and without attenuation of galaxies in clusters have been generated; the Malmquist bias in the mock Mark III catalog has been corrected for according to the density field from the mock 1.2Jy IRAS using the recipe of Dekel *et al.* (1993). For comparison a mock Mark III free of Malmquist bias has been used as well.

Figure 1 shows maps of the density fluctuations in real space from the mock unbiased 1.2Jy IRAS and Malmquist bias corrected Mark III. The maps are smoothed with a Gaussian window of width 1000km/s. Linear theory was used to derive the density from the potential field. The lower right-hand panel shows a reconstruction which is mainly based on the velocity data. The velocity data, being very noisy and sparse, are not sufficient to constrain the density field in space. Hence SIMPOT was applied with $\lambda = 0.99$, giving some weight to mock IRAS data in order to regularize the minimization procedure. Here the reconstruction overestimates the density fluctuations as expected in linear theory [14]. The lower left panel is a reconstruction from the mock IRAS data with $\lambda = 0$. This is basically a test of the recovery of the density field in real space from the redshift distribution of galaxies. The recovered density field greatly resembles the true field. The reconstruction by SIMPOT with $\lambda = 0.5$ is shown in the upper left panel. The density field in this case correlates very well with the density recovered with $\lambda = 0$ and is consistent, within the errors, with the reconstruction with $\lambda = 0.99$. Given the sparse sampling and the large errors in peculiar velocity surveys the recovery with $\lambda = 0.5$ is in general more sensitive to the density data.

Figure 2 shows curves of $\chi^2(\beta)$ from SIMPOT with $\lambda = 0.5$ for the various variants of the mock Mark III and 1.2Jy IRAS as explained in the figure caption. We see that SIMPOT is successful at recovering the true value of β with random errors of ± 0.06. A key point here is that the systematic uncertainties in the determination of β due to Malmquist bias corrections and the bias of IRAS galaxies around clusters do not amount to a serious discrepancy.

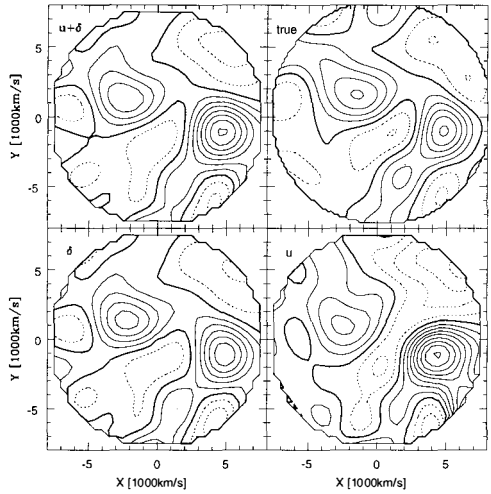


Figure 1: Maps of $-\nabla \cdot \boldsymbol{v}$ in the "supergalactic" plane in the universe simulation. Upper left panel is the true $-\nabla \cdot \boldsymbol{v}$. The three remaining panels are the reconstruction by SIMPOT with $\lambda = 0.5$ (upper right), $\lambda = 0$ (lower left) and $\lambda = 0.99$ (lower right). Contour spacing is 0.2. Heavy, solid and dashed contours denote average, positive and negative fluctuations.

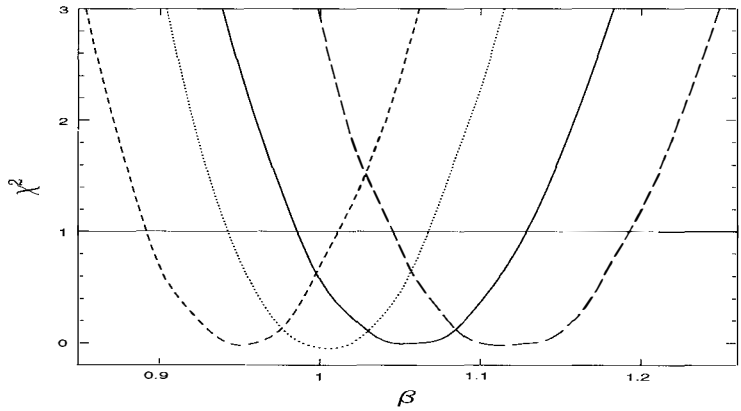


Figure 2: Curves of $\chi^2(\beta) - \chi^2_{min}$ for $\lambda = 0.5$. Short-dashed and dotted lines respectively correspond to unbiased and biased 1.2Jy IRAS mock catalogs with only random errors in the peculiar velocities of mock Mark III . Solid and dotted lines correspond to unbiased and biased mock 1.2Jy IRAS but with random errors and Malmquist bias in Mark III. The Malmquist bias has been corrected for by the density of mock 1.2Jy IRAS.

4 Discussion

In general SIMPOT can be viewed as a method for recovering the underlying large scale fields in the universe given an ensemble of heterogeneous data samples. We have demonstrated that the method, when applied to mock Mark III and 1.2Jy IRAS catalogs, successfully recovers the underlying fields and provides an unbiased estimate for the parameter β. The recovered fields are smoothed independently of the details of individual data sets. This is greatly desirable when assessing the general consistency of different kinds of data on different scales. SIMPOT recovers fields which are locally regulated in space according to the quality of the various data. For example, in the regions where the distribution of galaxies is very dilute but measurements of peculiar velocities are ample, the recovered fields are mainly determined by the velocities. For the purpose of recovering the underlying fields, SIMPOT can in practice be applied with varying weights to the different data. When high weight is given to the velocity data, SIMPOT is essentially a method for recovering the large scale peculiar velocity fields. The interpolation from regions where the velocity data are of good quality to empty regions is modulated self-consistently by the peculiar velocity field as predicted from the distribution of galaxies in redshift space.

Acknowledgements. AN thanks Y.Hoffman for stimulating discussions. AN acknowledges the support of a PPARC postdoctoral fellowship.

References

[1] Bernardeau, F., Juszkiewicz, Dekel, A. and Bouchet, F. 1995, *M.N.R.A.S.* **274** 20

[2] Cole, S., Fisher, K.B., and Weinberg, D. 1994, *M.N.R.A.S.* **267** 785

[3] Davis, M., and Nusser, A. 1995 in *The Maryland Meeting on Dark Matter*

[4] Dekel, A. 1994, Ann. Rev. of A & A

[5] Dekel, A., Bertschinger, E., & Faber, S. M. 1990, *Astrophys. J.* **364** 349

[6] Dekel, A., Bertschinger, E., Yahil, A., Strauss, M., Davis, M., & Huchra, J. 1993, *Astrophys. J.* **412** 1

[7] Dekel, A. and Rees, M. 1993, *Astrophys. J. (Lett.)* **422** L1

[8] Fisher, K.B., Scharf, C.A., and Lahav, O. 1994, *M.N.R.A.S.* **266** 219

[9] Fisher, K.B., Lahav, O., Hoffman, Y., Lynden-Bell, D., and Zaroubi, S. 1995, *M.N.R.A.S.* **272** 885.

[10] Hamilton, A.J.S. 1993, *Astrophys. J. (Lett.)* **406** L47

[11] Hudson, M.J., Dekel, A., Courteau, S., Faber, S.M., and Willick, J. 1995, *M.N.R.A.S.* **274** 305

[12] Kaiser, N. 1987, *M.N.R.A.S.* **227** 1

[13] Kolatt, T., Dekel, A. 1995, to be submitted.

[14] Nusser, A., Dekel, A., Bertschinger, E., & Blumenthal, G. R. 1991,

[15] Nusser, A, & Davis, M. 1994, *Astrophys. J. (Lett.)* **421** L1

[16] Nusser, A, & Dekel, A. 1992, *Astrophys. J.* **391** 443

[17] Nusser, A, & Dekel, A. 1993, *Astrophys. J.* **405** 437

[18] Regös, E., & Szalay, A. 1989, *Astrophys. J.* **345**, 627

[19] Willick, J. *et al.* 1994, in preparation.



Wiener Reconstruction, SVD and 'Optimal' Functional Bases: Application For Redshift Galaxy Catalogs

Saleem Zaroubi
Astronomy Department and Center for Particle Astrophysics
University of California, Berkeley, U.S.A.

Abstract

The formalism of Wiener filtering is applied to reconstruct, in terms of spherical harmonics, the projected 4π galaxy distribution of a mock IRAS 1.2 Jy catalog with a 'Zone of Avoidance' $|b| = 15°$. The Singular Value Decomposition algorithm is utilized as an extra-regularizer in order to stabilize the inversion. This case sheds light on the amount of useful information contained in the data, and also suggests a method for obtaining an 'optimal' functional basis, based on our *prior* knowledge, for the purposes of likelihood analysis and Wiener reconstruction of cosmological data sets. The applicability of such a functional basis for redshift galaxy catalogs is also discussed

1 Introduction

Galaxy catalogs provide the main data base for the purpose of mapping the (continuous) cosmological dynamical fields (density, velocity and gravitational potential), which in turn offer a probe of the early universe and the nature of the primordial perturbation field. However, continuous density maps, constructed from the discrete galaxy distribution, suffer from Poisson 'shot-noise'. This problem become much more severe in the case of magnitude limited samples, where the selection function magnifies the shot-noise contribution as the probability of observing galaxies decreases.

Two other problems appear in analyzing the distribution of galaxies. First, the incomplete sky coverage, due to the obscuration by gas and dust in our local galaxy, the so-called 'Zone of Avoidance' (ZOA), poses an obstacle in mapping the whole-sky distribution. Second, the peculiar velocities in redshift surveys give a distorted picture of the galaxy distribution, even in the linear regime of gravitational instability.

Recovering the underlying field from the measured field can be viewed as an inversion problem

in the following sense. Consider the case in which the observed data points, $\mathbf{d} = \{d_i\}(i = 1, \ldots, M)$ are given by a linear convolution or mapping of the underlying field, $\mathbf{s} = \{s_\alpha\}(\alpha = 1, \ldots, N)$, namely,

$$\mathbf{d} = \mathbf{R}\,\mathbf{s} + \boldsymbol{\epsilon}, \tag{1}$$

where $\mathbf{R}$ is an $M \times N$ matrix which represents a response function and $\boldsymbol{\epsilon} = \{\epsilon_i\}$ $(i = 1, \ldots, M)$, is the statistical uncertainty vector associated with the data. Here the standard notion of the response function is extended to include any theoretical relationship between two fields (*e.g.*, the matrix which relates the redshift space density to the real space density [4] and [19]).
Mathematically, the act of reconstruction amounts to solving equation 1 for $\mathbf{s}$ given $\mathbf{d}$ where $\mathbf{R}$ is assumed to be known. However, direct inversion of equation 1, *i.e.*, $\mathbf{s} = \mathbf{R}^{-1}\mathbf{d}$, suffers from several problems, the most important of which are: First, the number of independent data points is often smaller than the number of degrees of freedom (*d.o.f.*) of the underlying field, and therefore the data do not contain enough information to constrain all of the *d.o.f.*. Second, the inversion might be unstable due to the existence of statistical noise.
As a result of these potential pitfalls of direct inversion, the technique of Wiener filtering (*c.f.*, [14], [20]) as a regularization method is presented and applied for the case of the projected mock IRAS 1.2 Jy catalog with $|b| = 15°$ ZOA.
The Singular Value Decomposition algorithm (SVD) [13] as an extra-regularizer is also applied. An extension of the SVD algorithm is presented and discussed in the context of Wiener reconstruction and maximum likelihood analysis of 3-D redshift catalogs ([20]).

2 Wiener Filter

The derivation of the Wiener filter (WF) requires *prior* knowledge of the the first two moments of the underlying field, namely, $\langle \mathbf{s} \rangle$ (taken in what follows to be 0 for simplicity), and its covariance matrix, $\mathbf{S} = \langle \mathbf{s}\,\mathbf{s}^\dagger \rangle \equiv \{\langle s_i\, s_j^* \rangle\}$. (see [9] [4] and [3] for various applications of WF).
Define an estimator of the underlying field, $\mathbf{s}^{\mathrm{MV}}$(MV stands for minimal variance), as the linear combination of the data, $\mathbf{s}^{\mathrm{MV}} = \mathbf{F}\,\mathbf{d}$, where $\mathbf{F}$ is an $N \times M$ matrix,, chosen to minimize the variance of the residual $\mathbf{r}$ defined by

$$\langle \mathbf{r}\,\mathbf{r}^\dagger \rangle = \langle (\mathbf{s} - \mathbf{s}^{\mathrm{MV}})(\mathbf{s}^\dagger - \mathbf{s}^{\mathrm{MV}\dagger}) \rangle. \tag{2}$$

Carrying out the minimization of equation 2 with respect to $\mathbf{F}$ one finds the so-called WF,

$$\mathbf{F} = \langle \mathbf{s}\,\mathbf{d}^\dagger \rangle \langle \mathbf{d}\,\mathbf{d}^\dagger \rangle^{-1} = \mathbf{S}\mathbf{R}^\dagger(\mathbf{R}\,\mathbf{S}\,\mathbf{R}^\dagger + \mathbf{N})^{-1}, \tag{3}$$

where $\mathbf{N} \equiv \langle \boldsymbol{\epsilon}\,\boldsymbol{\epsilon}^\dagger \rangle$ is the noise correlation matrix, which is assumed to be uncorrelated with the underlying field. WF includes two operations: *inversion* of the response function and *suppression* of the shot noise roughly by the ratio of $\frac{prior}{prior + noise}$. Note that this ratio is less than unity, and therefore the method can not be used iteratively as successive applications of the WF would drive the recovered field to zero (see [20] for more details).
While earlier applications of the WF have focused on estimation, namely suppressing the noise in the measured quantities, one can extend the application of the WF to predict the values of unmeasured quantities, such as the density field in un-sampled regions of space, or to deconvolve blurred data. Within the context of linear gravitational instability theory, the WF can also be used to perform dynamical reconstruction of one field which is dynamically related to some other observed field. This is the case, for example, of the reconstruction of the real space galaxy distribution from its redshift distribution.

2.1 Conditional Probability

The standard model of cosmology assumes that the primordial perturbation field is Gaussian, and therefore on large scales where the fluctuations are still small the perturbations field will be very close to Gaussian, even in the present epoch. The statistical properties of any Gaussian random field depend only on its two-point covariance matrix $\mathbf{S}$ [1]. If the noise is also a Gaussian field, then, since it is independent, one can construct simple estimates of the underlying field $\mathbf{s}$, based on the knowledge of the full probability distribution function.
In our case, if both the signal and the noise are Gaussian, the conditional mean value of the field given the data can also serve as an estimator of $\mathbf{s}$, $\int \mathbf{s} P(\mathbf{s}|\mathbf{d})\, \mathrm{d}\mathbf{s}$, which yields $\mathbf{s}^{mean} = \mathbf{s}^{MV}$. $\mathbf{s}^{MV}$ coincides also with the maximum *a posteriori* estimate (MAP) of the field; namely the one that maximizes the conditional probability $P(\mathbf{s}|\mathbf{d})$. Therefore for Gaussian fields WF coincides with the mean and the MAP estimators, *i.e.*, $\mathbf{s}^{MV} = \mathbf{s}^{mean} = \mathbf{s}^{MAP}$. The residual from the mean coincides with $\mathbf{r}$, and it has Gaussian distribution with zero mean and covariance matrix $(\mathbf{S}^{-1} + \mathbf{R}^{\dagger}\mathbf{N}^{-1}\mathbf{R})^{-1}$. This property is the basis of the constrained realization method [6].
Another estimator can be formulated from the point of view of Bayesian statistics. The main objective of this approach is to calculate the *posterior* probability of the model given the data, which is written according to Bayes' theorem as $P(\mathrm{model}|\mathrm{data}) \propto P(\mathrm{data}|\mathrm{model})P(\mathrm{model})$. The estimator of the underlying field (*i.e.*, model, in Bayes' language) is taken to be the one that maximizes $P(\mathrm{model}|\mathrm{data})$, which is the most probable field. One can show that in the case in which the *prior* assumed to be a Gaussian, the Bayesian estimator coincides with the $\mathbf{s}^{\mathrm{MV}}$ ([20], [8], [17]).

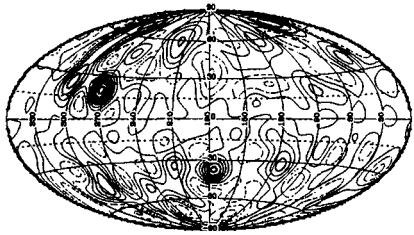
3 Spherical Harmonics Expansion and SVD

Spherical harmonics (SH) have been used to probe the large scale structure from wide angle galaxy surveys ([11],[12],[15],[16]). These analyses consist of expanding the angular galaxy distribution in a set of spherical harmonics which form an orthonormal functional basis when the expansion is carried out over the full, 4π, sky. The expansion coefficients in SH basis constitute a statistically orthogonal set (like the case of k-space), which makes it more comfortable to deal with the data in the case of full sky coverage.
Consider an underlying angular density field, given in terms of its spherical harmonic expansion, $a_{lm} = \int \mathrm{d}\hat{\mathbf{r}}\, \mathcal{S}(\hat{\mathbf{r}})\, Y^{*}_{lm}(\hat{\mathbf{r}})$, where the projected surface density is given by $\mathcal{S}(\hat{\mathbf{r}}) = \sum_{lm} a_{lm} Y_{lm}(\hat{\mathbf{r}})$. This field is sampled by a finite discrete distribution of galaxies, which suffers basically from incomplete sky coverage and shot-noise. The observed harmonics c_{lm} are related to the underlying whole sky harmonics a_{lm} by: $c_{lm} = \sum_{l'm'} W^{mm'}_{ll'} \{a_{l'm'} + \sigma_{l'm'}\}$ where the monopole term ($l' = 0$) is excluded [15]. σ_{lm} is the shot-noise in the 'true' number-weighted harmonics a_{lm}'s. The noise variance is estimated as $\left\langle \sigma^2 \right\rangle = \mathcal{N}$ (the mean number of galaxies per steradian, independent of $\hat{\mathbf{n}}$ in this case). Notice that $W^{mm'}_{ll'}$, the harmonic transform of the mask, introduce 'cross-talk' between different harmonics.
Applying equation 3 to this case, it can be shown that the solution for this inversion is ([9], [20])

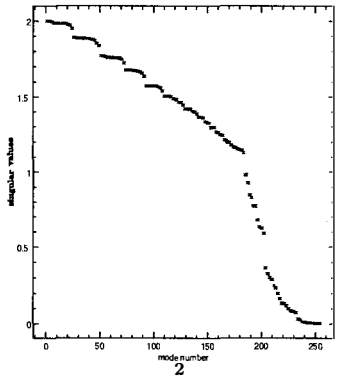
$$\mathbf{a}^{\mathrm{MV}} = diag\Big\{\frac{A_l}{A_l + \mathcal{N}}\Big\}\mathbf{W}^{-1}\mathbf{c} \equiv \mathbf{B}^{-1}\mathbf{c}, \tag{4}$$

where the vectors $\mathbf{a}$ and $\mathbf{c}$ represent the sets $\{a_{lm}\}$ and $\{c_{lm}\}$. Here A_l is the cosmic variance in the harmonics, which is determined by the assumed power spectrum (*i.e.*, the *prior*).
Here, this method is applied to a standard CDM simulation characterized by $\Omega_0 h = 0.5$ with particles selected to mimic the IRAS 1.2 Jy galaxy catalog with ZOA $|b| = 15°$ (see [9] for the case of the true IRAS 1.2 Jy data with ZOA $|b| = 5°$). The simulation evolves the particles until the rms variance of the density field in a sphere of $8Mpc/h$ reache $\sigma_8 = 0.62$ (see [5] for more details). Figure 1 shows the harmonic reconstruction of the projected counts of the simulation

using the raw harmonic coefficients, c_{lm}, up to $l_{max} = 15$. In this case the direct inversion of the matrix **B** is unstable and yields excessive power on small scales. However using the SVD algorithm to invert the matrix **B** sheds a new light on the question of the amount of useful information contained in the data.



1



2

Figure 1: Harmonics reconstruction of the projected counts of the mock IRAS 1.2 Jy catalog with a 'Zone of Avoidance' $|b| = 15°$, in Galactic Aitoff projection, using the observed coefficients c_{lm}, up to $l_{max} = 15$. The contour levels of the projected surface number density are in steps of 100 galaxies per steradian (the mean projected density is $\mathcal{N} \sim 400$ galaxies per steradian).

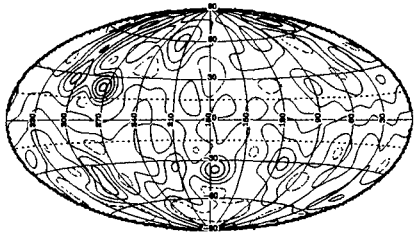
Figure 2: The sorted spectrum of the singular values of the matrix **B**, for the $|b| = 15°$ case. The 'knee' suggests how to choose the cutoff for the SVD, $\lambda_{min}/\lambda_{max} = 0.565$, at the mode 184 ($l_{max} \approx 13$).

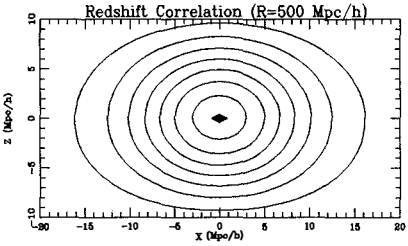
Essentially, the SVD algorithm decompose the square matrix **B** into the product of three matrices $\mathbf{B} = \mathbf{U}\, diag\{\lambda_i\}\, \mathbf{U^T}$ (SVD can also be applied to non-square matrices [13]). The λ_i's and the rows of the matrix **U**, are the eigen-values and eigen-vectors of the matrix **B**. After performing the decomposition, the inversion of **B** is trivial,

$$\mathbf{B}^{-1} = \mathbf{U}^T\, diag\{1/\lambda_i\}\, \mathbf{U}. \tag{5}$$

Formally speaking, equation 4 has a unique solution if and only if **B** is a non-singular matrix, namely if $\lambda_i \neq 0$ for all i. However a meaningful solution to equation 4 can be obtained even in the case where **B** is singular, by requiring the solution to minimize the norm of the residuals, $|\mathbf{Ba} - \mathbf{c}|$. Such a solution is obtained by substituting $1/\lambda_i = 0$ in the expression for the inverse (equation 4) for any $\lambda_i = 0$ ([13]). Realistically, $1/\lambda_i$ is set to zero for any λ_i less than some lower limit, determined by the physical and geometrical properties of the system. The question of how, in general, one should set the lower limit is discussed in §4 . In general, the eigenvalues measure the amount of 'information' carried by each mode in the problem; the small eigenvalues are those that might destabilize the inversion, so they do notcontribute significantly to the reconstruction.

Figure 2 shows the sorted spectrum of the eigenvalues (λ_i) of **B**, versus the harmonic number, l. The 'knee' in this figure suggests that the cutoff for the SVD, should be at $\lambda_{min} = 0.565\lambda_{max}$. Note that this cutoff suggest that only the largest 184 modes are significant ($l \approx 13$). Figure 3 shows the reconstructed a_{lm}'s map using WF and the above cutoff for SVD. Note that here, contrary to the $|b| = 5°$ case discussed by Lahav *et al.* [9] where the structure was recovered in the ZOA, the reconstructed ZOA remains empty. This illustrates that WF, even with the use of SVD extra-regularization, can not create structures out of nothing, unless the structures are dictated by the correlations ([9]).





3 4

Figure 3: The reconstructed a_{lm}'s using Wiener filter and the cutoff shown in figure 2

Figure 4: The correlation function for SCDM model with $8Mpc/h$ smoothing, as measured in the redshift space according to the exact linear calculation around point at $500Mpc/h$ distance. Z is the *l.o.s.* direction.

4 'Optimal' Functional Basis

Frequently, it is useful to expand the cosmological perturbation field as a linear combination of a complete orthogonal functional basis. Such a basis defines a space in which all of the physical, statistical and geometrical properties of the field are retained. In the framework of linear gravitational instability, spaces of a special interest are Fourier space ([12]) and the space defined by SH and spherical Bessel functions ([4],[20]). These spaces are commonly used for the following reasons: a) Their expansion coefficients are statistically orthogonal (*e.g.*, $\langle \delta_{\mathbf{k}} \delta_{\mathbf{k}'} \rangle = P(k)\delta_D(\mathbf{k}-\mathbf{k}')$). b) They are eigen-functions of the Laplacian operator (and the ∇ operator, in case of Fourier space).

However, the problems from which galaxy catalogs suffer complicate the picture since they introduce cross-talk between different modes, both in the signal covariance matrix itself and in the noise correlation matrix, as shown in §3 just above equation 4. For instance, in the linear regime, the redshift distortion, due to its anisotropy 'squeezes' the configuration space correlation function along the line of sight. Figure 4 shows the correlation matrix in redshift configuration space, around $R = 500Mpc/h$, for SCDM model in the framework of linear theory ([7],[19]). In k-space this is reflected in a cross-talk between different Fourier modes [19].

A different approach to the question of the functional basis, is to construct a statistically orthogonal functional basis according to our *prior* knowledge of the survey geometry, clustering properties and weighting scheme.

One possibility, which is useful for Wiener reconstruction, is to find the eigen-functions and eigen-values of the matrix $\mathbf{F}$ defined by equation 3. Indeed this is the case presented in §3, where the expansion was used to stabilize the inversion by means of data compression (*i.e.*, excluding small eigen-values). However, that was is a special case, in the sense that it had a characteristic scale (defined by the mask width) that corresponds to the position of the 'knee' in figure 2. Generally speaking, diagonalizing $\mathbf{F}$ does not guarantee such a 'natural' choice for the cutoff. Moreover, this expansion is not, necessarily, useful for other cases, especially for likelihood analysis.

Another possibility, is to find the eigen-functions of the matrix $\left\langle \mathbf{d}\,\mathbf{d}^{\dagger} \right\rangle$ (signal + noise)[10], which appears both in WF and in the Gaussian likelihood probability. However, the main problem of this approach, is that one can't distinguish between the contribution of the signal and the contribution of the noise to the eigen-values. Therefore it can not be used for data compression, nor for stabilizing the inversion, without throwing away useful information.

Here we suggest an 'improved SVD' approach, which basically solves the following generalized eigen-value problem,

$$\mathbf{R}\mathbf{S}\mathbf{R}^{\dagger}\mathbf{a}_i = \lambda_i \mathbf{N}\mathbf{a}_i \qquad (6)$$

where $\mathbf{a}_i$ and λ_i are the eigen-vector and its eigen-value respectively. This equation diagonalizes $\mathbf{N}$ and $\mathbf{RSR}^\dagger$ simultaneously[1]. Note that the orthogonality condition of the vectors $\mathbf{a}$ is $\mathbf{N}$ weighted [18] (see also [2]).
This approach provides a natural way to compress the data, since here the eigen-values represent the relative contribution of the signal with respect to the noise in each mode. Hence, if $\lambda_i \geq 1$, the mode is dominated by the signal, and it is dominated by the noise otherwise. Note also that the eigen-vectors constitute a functional basis, although not complete, which includes all the *prior* knowledge about the data.
To summarize, this 'optimal' functional basis together with the WF formalism, the constrained realization method, and the Bayesian likelihood analysis (parameter estimation) provide a comprehensive and self contained prescription for analyzing the (linear) LSS of the Universe.

Acknowledgements. I am grateful to K. Fisher, Y. Hoffman, O. Lahav for their contribution to the work presented here and for many stimulating discussions

References

[1] Bardeen, J.M., Bond, J.R., Kaiser, N., & Szalay, A.S. 1986, *Astrophys. J.* **304**, 28

[2] Bunn, E., 1995, *PhD Thesis*, University of California, Berkeley

[3] Bunn, E., *et al.* , 1994, *Astrophys. J.* **432**, L75

[4] Fisher, K.B., *et al.* , 1995, *Mon. Not. R. astr. Soc.* **272**, 885

[5] Fisher, K.B., Scharf, C.A., & Lahav, O. 1994, *Mon. Not. R. astr. Soc.* **266**, 219

[6] Hoffman, Y., & Ribak, E., 1991, *Astrophys. J.* **380**, L5

[7] Kaiser, N., 1987, *Mon. Not. R. astr. Soc.* **227**, 1

[8] Kaiser, N. & Stebbins, A. 1991, in *Large Scale Structure and Peculiar Motions in the Universe*, eds. D.W. Latham & L.N. DaCosta (ASP Conference Series), p. 111

[9] Lahav, O., Fisher, K.B., Hoffman, Y., Scharf, C.A., & Zaroubi, S. 1994, *Astrophys. J.* **423**, L93

[10] Vogeley, M., *this proceedings*

[11] Peebles, P.J.E., 1973 *Astrophys. J.* **185**, 413

[12] Peebles, P.J.E. 1980, *The Large-Scale Structure of the Universe*, Princeton University Press

[13] Press, W.H., *et al.* , 1992, *Numerical Recipes* (2nd Edition), Cambridge University Press

[14] Rybicki, G.B., & Press, W.H. 1992, *Astrophys. J.* **398**, 169

[15] Scharf, C., Hoffman, Y., Lahav, O., & Lynden-Bell, D. 1992, *Mon. Not. R. astr. Soc.* **256**, 229

[16] Scharf, C.A. & Lahav, O. 1993, *Mon. Not. R. astr. Soc.* **264**, 439

[17] Stebbins, A. 1994, Proc. of the 9$^{\text{th}}$ IAP Conference on *Cosmic Velocity Fields*, eds. F. Bouchet and M. Lachiéze-Rey,(Gif-sur-Yvette Cedex: Editions Frontiéres) p. 253

[18] Zaroubi, S., 1995, *in preparation*

[19] Zaroubi, S., & Hoffman, Y., 1995, *Astrophys. J.* , submitted.

[20] Zaroubi, S., & Hoffman, Y., Fisher, K.B., & Lahav, O., 1995, *Astrophys. J.* , in press

[1] This is similar to the problem of small oscillations in classical mechanics, where the noise and the signal matrices are analogous to the kinetic energy and potential energy matrices.

SESSION III

STATISTICS AND DYNAMICS



REDSHIFT DISTORTIONS AND OMEGA IN IRAS SURVEYS

A. J. S. Hamilton
JILA, U. Colorado, Boulder, CO 80309, USA.



Abstract

Redshift space distortions on large scales can be used to measure the linear growth rate parameter $f \approx \Omega^{0.6}/b$. I report here measurements of such distortions in the *IRAS* 2 Jy, 1.2 Jy, and QDOT redshift surveys, finding $f = 0.69^{+.21}_{-.19}$ from a merged QDOT plus 1.2 Jy catalogue. Unfortunately, confidence in this result is undermined by a marked (4σ) change in the pattern of clustering in QDOT beyond about $80h^{-1}$Mpc. A similar effect may be present at a mild level in the 1.2 Jy survey. The effect may be caused by systematic variation in the effective flux limit of the *IRAS* PSC over the sky, with a dispersion of ~ 0.1 Jy on scales $\sim 7°$. If so, then the value of f inferred from redshift distortions in *IRAS* surveys may be systematically underestimated.

1 Redshift Correlation Function

Peculiar velocities cause line of sight distortions in the pattern of clustering of galaxies observed in redshift space. The most familiar distortion is the finger-of-god effect, caused by large velocities of galaxies in collapsed clusters. A more subtle effect is the squashing effect on large scales induced by peculiar infall towards overdense regions. Both kinds of distortion can be used to estimate the cosmological density Ω, from the virial theorem on small scales, and from linear theory on large scales.

The recent growing interest in the large scale squashing effect has been encouraged by the availability of the *IRAS* redshift surveys, which seem for the first time to probe a sufficiently large volume of the Universe to allow a statistically significant measurement of Ω from the effect. Figure 1 illustrates the distortion of the redshift space correlation function $\boldsymbol{\xi}$ in the *IRAS* 2 Jy [14], [15], [16], 1.2 Jy [6], and revised QDOT [13] redshift surveys. In each case, the full survey (left panels) shows plainly the expected large scale squashing effect, while fingers-of-god show up as the $\sim 4h^{-1}$Mpc wide by $15h^{-1}$Mpc long enhancements along the line of sight axis.

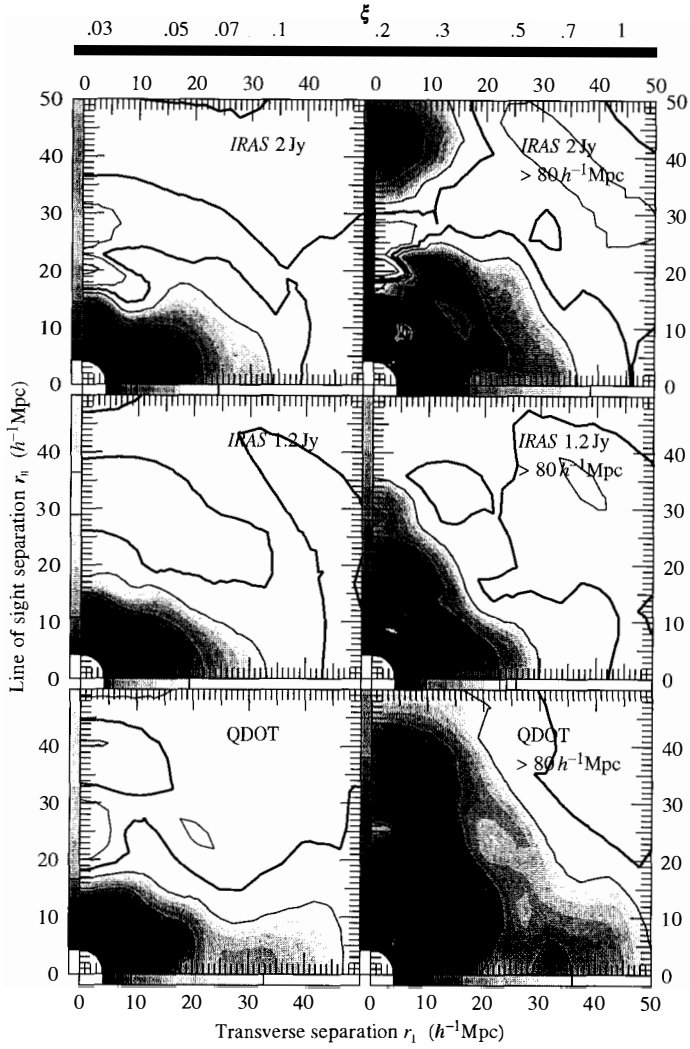


Figure 1: Contour plots of the redshift space two-point correlation function ξ in the *IRAS* 2 Jy (top), 1.2 Jy (middle), and QDOT (bottom) surveys. Left panels show the full survey in each case (excluding the region within $25h^{-1}$ Mpc so as to eliminate local bias), while right panels show the region beyond $80h^{-1}$ Mpc. The thick contour signifies $\xi = 0$, and other contours are logarithmically spaced at intervals of 0.5 dex above $10^{-1.5}$, or below $-10^{-1.5}$ for negative contours. Shading is graduated at intervals of 0.1 dex above $10^{-1.5}$. The correlation function here has been smoothed over pair separation $r = (r_\perp^2 + r_\parallel^2)^{1/2}$ with a tophat window of width 0.2 dex, and over angles $\theta = \tan^{-1}(r_\perp / r_\parallel)$ to the line of sight with a gaussian window with a 1σ width of 10°. Bars along the two axes of each frame are contour plots of the 1σ uncertainties in the plotted correlation function in the two particular directions parallel ($\theta = 0°$) and perpendicular ($\theta = 90°$) to the line of sight. The uncertainties are greater along the line of sight axis because the volume element $\sin\theta d\theta$ is smaller.

2 Theory

The mathematical relation between Ω and the squashing effect was clarified by Kaiser [8] whose approach demonstrated, amongst other things, the power of working in Fourier space when in the linear regime. Kaiser showed that in the linear regime a wave of amplitude $\delta(\boldsymbol{k})$ appears amplified in redshift space by a factor $1 + f\mu^2$, where μ is the cosine of the angle between the wavevector $\boldsymbol{k}$ and the line of sight, and f is the growth rate of growing modes in linear theory, which is related to Ω by

$$f \approx \frac{\Omega^{0.6}}{b} \tag{1}$$

in standard pressureless Friedmann cosmology with mass-to-light bias b. Kaiser concluded that the redshift space power spectrum $\boldsymbol{P}(\boldsymbol{k})$, the Fourier transform of the correlation function $\boldsymbol{\xi}$, appears amplified by a factor $(1 + f\mu^2)^2$ over the true power spectrum $P(k)$ (boldface distinguishes redshift space power spectra and correlation functions from their unredshifted counterparts)

$$\boldsymbol{P}(\boldsymbol{k}) = (1 + f\mu^2)^2 P(k) \; . \tag{2}$$

Equation (2) predicts that the redshift space power spectrum in the linear regime is a sum of monopole, quadrupole, and hexadecapole harmonics [9], [2]

$$\boldsymbol{P}(\boldsymbol{k}) = \boldsymbol{P}_0(k)\mathrm{P}_0(\mu) + \boldsymbol{P}_2(k)\mathrm{P}_2(\mu) + \boldsymbol{P}_4(k)\mathrm{P}_4(\mu) \tag{3}$$

($\mathrm{P}_l(\mu)$ here are Legendre polynomials) with

$$\boldsymbol{P}_0(k) = (1 + \frac{2}{3}f + \frac{1}{5}f^2)P(k) \; , \quad \boldsymbol{P}_2(k) = (\frac{4}{3}f + \frac{4}{7}f^2)P(k) \; , \quad \boldsymbol{P}_4(k) = \frac{8}{35}f^2 P(k) \; . \tag{4}$$

All the higher order harmonics are predicted to be zero in the linear regime (odd harmonics vanish in any case by pair exchange symmetry, while $m \neq 0$ azimuthal harmonics vanish by symmetry about the line of sight). The hexadecapole harmonic $\boldsymbol{P}_4(k)$ is predicted by equation (4) also to be quite small, only 1/10th of the amplitude of the monopole and quadrupole harmonics even for $f = 1$, so in practice almost all the information about redshift distortions in the linear regime is contained in the monopole and quadrupole harmonics $\boldsymbol{P}_0(k)$ and $\boldsymbol{P}_2(k)$. The ratio $\boldsymbol{P}_2(k)/\boldsymbol{P}_0(k)$ of these harmonics of the redshift power spectrum then provides a way to measure f, hence Ω, independently of the shape of the power spectrum

$$\frac{\boldsymbol{P}_2(k)}{\boldsymbol{P}_0(k)} = \frac{\frac{4}{3}f + \frac{4}{7}f^2}{1 + \frac{2}{3}f + \frac{1}{5}f^2} \; . \tag{5}$$

3 Measuring the Power Spectrum

In measuring the distortion of the power spectrum in a real redshift survey, it is essential to disentangle the true distortion from the artificial distortion introduced by a non-uniform mask and selection function. Now in real space the observed galaxy density is the product of the true density with the catalogue window, whereas in Fourier space this becomes a convolution. Thus the natural place to 'deconvolve' the observations from the catalogue window is real space, where deconvolution reduces to division, and where the observations exist in the first place. The procedure is described in some detail in [11]. In brief, in computing the contribution to the power spectrum from a pair of galaxies at separation r and angle θ to the line of sight, one divides by the probability of finding a pair anywhere in the catalogue with that separation r

and angle θ. The deconvolution procedure is 'exact', stable in practice, and admits minimum variance pair weighting.

The harmonics $\boldsymbol{P}_l$ of the redshift power spectrum are related to those $\boldsymbol{\xi}_l$ of the redshift correlation function by

$$\boldsymbol{P}_l(k) = i^l \int_0^\infty \boldsymbol{\xi}_l(r) j_l(kr) 4\pi r^2 dr \tag{6}$$

where j_l are spherical Bessel functions. Just as it is necessary in a real catalogue to measure the correlation function with finite bins of separation, so also the power spectrum must be measured with finite resolution in k-space. The harmonics of the power spectrum, smoothed over some window $W(k)$, are related to the harmonics of the correlation function by

$$\boldsymbol{P}_l^{\rm smoothed}(k) = \int_0^\infty \boldsymbol{P}_l(k') W(k'/k) 4\pi (k'/k)^2 d(k'/k) = \int_0^\infty \boldsymbol{\xi}_l(r) W_l(kr) 4\pi r^2 dr \tag{7}$$

where the real space window $W_l(r)$ for the l'th harmonic is, from equation (6), the smoothed spherical Bessel function

$$W_l(r) = i^l \int_0^\infty W(k) j_l(kr) 4\pi k^2 dk \ . \tag{8}$$

I choose to use a smoothing window of the form

$$W(k) \propto k^n e^{-k^2/4} \tag{9}$$

which has the desirable properties of being positive definite in k-space, and yielding gaussian convergence in real space for harmonics $l \leq n$ provided n is an even integer. The real space windows corresponding to the window (9) are (if $W(k)$ is normalised so $\int W(k) 4\pi k^2 dk = 1$)

$$W_l(r) = \frac{i^l [(n-l)/2]!}{(3/2)_{(n/2)}} r^l e^{-r^2} L^{l+1/2}_{(n-l)/2}(r^2) \tag{10}$$

where L^λ_ν are Laguerre polynomials, and $(3/2)_{(n/2)} = \Gamma[(n+3)/2]/\Gamma(3/2)$ is a Pochhammer symbol. These real space windows (10) bear an amusing resemblance to hydrogenic wave functions. The resemblance extends to the quantisation condition that the index $(n-l)/2$ must be a nonnegative integer, to ensure gaussian convergence at large separations.

Computation of the smoothed harmonics $\boldsymbol{P}_l(k)$ of the redshift power spectrum thus reduces to taking a suitably weighted sum over galaxy pairs of $W_l(kr)$ times $\mathrm{P}_l(\cos\theta)$, the l'th Legendre polynomial. No correction factors for the shape of the power spectrum are necessary in measuring f from the ratio (5) of the smoothed quadrupole and monopole harmonics of the power spectrum.

The power spectra shown in this paper are smoothed with the window (9) with $n = 2$, the smallest n which allows the quadrupole power to be measured. This smallest n yields the broadest smoothing window of the form (9), so the errors in the ratio $\boldsymbol{P}_2(k)/\boldsymbol{P}_0(k)$ of smoothed power spectrum harmonics are smallest for this n, though the results at different k are also then most correlated.

4 Result for f

Figure 2 shows the ratio $\boldsymbol{P}_2/\boldsymbol{P}_0$ of the quadrupole to monopole power spectra in the *IRAS* 2 Jy, 1.2 Jy, and QDOT surveys, and also in QDOT plus 1.2 Jy merged over the angular region of the sky common to both surveys. At small scales, $\pi/k < 5h^{-1}$Mpc, the quadrupole power

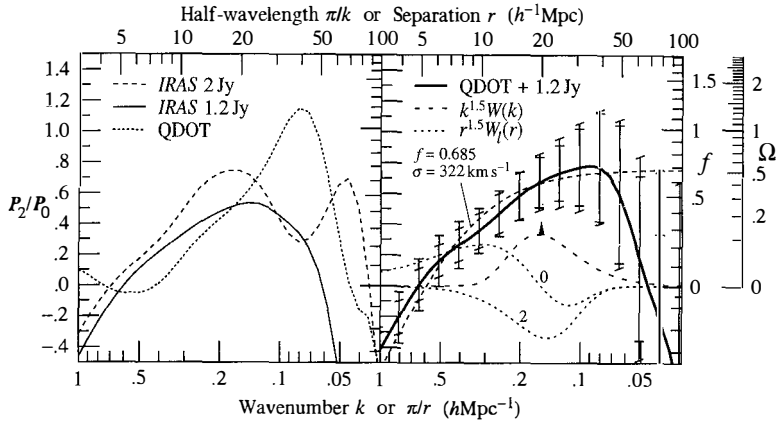


Figure 2: Ratio of the quadrupole to monopole redshift power spectrum in the *IRAS* surveys. The left panel shows separately the 2 Jy, 1.2 Jy, and QDOT surveys, while the right panel shows QDOT plus 1.2 Jy merged over the angular region of the sky common to both surveys. Horizontal and tilted bars on the 1σ errors on the QDOT + 1.2 Jy data distinguish two methods for estimating the uncertainties, described in §5. The dashed curve is a fit with $f = 0.685$ and a 1-dimensional pairwise exponential velocity dispersion of $322\,\mathrm{km\,s^{-1}}$. The smoothing window $W(k)$, equation (9) with $n = 2$, of constant width in $\log k$, gives an impression of the covariance between plotted points. Notice that the smoothing window is broad, so the points are correlated. Also shown are the equivalent real space smoothing windows $W_l(r)$, equation (10), for the monopole and quadrupole harmonics of the correlation function.

is negative, which is the nonlinear finger-of-god effect, while at larger scales the quadrupole power is positive, which is the squashing effect.

Figure 2 shows a best fit to the merged QDOT plus 1.2 Jy survey of a model in which the linear distortion is modulated by a random exponentially distributed pairwise velocity dispersion, which seems to offer a simple but adequate description of nonlinearity [5]. The best fitting value of the linear growth parameter f, equation (1), is $f = 0.69^{+.21}_{-.19}$ (1σ).

The reader should beware that the measured value of f is somewhat sensitive to the relative weight assigned to the near versus far regions of the survey (this reflects the problem discussed in §6; the above-quoted statistical error on f excludes this systematic uncertainty). Differences between values of f obtained by different authors, [3], [5], [7], [10], [12], may be attributable at least in part to differences in pair weighting schemes. The turnover in $\boldsymbol{P}_2/\boldsymbol{P}_0$ evident in Figure 2 at the largest scales, $\pi/k \gtrsim 50h^{-1}\mathrm{Mpc}$, may be caused in part by the same problem, although here the uncertainties become large.

5 Error Estimation

Uncertainties are estimated by two distinct methods, distinguished in Figure 2 (& 4) by horizontal and tilted bars on the errors. Both methods take proper account of the correlated character of the galaxy distribution.

The first method (horizontal bars) is described and justified in detail in [11]. The procedure is to subdivide the survey into a few hundred volume elements, measure the fluctuation in the

power attributable to each volume element, and form a variance by adding up the covariances of the fluctuations between the volume elements. However, there is an integral constraint which implies that the sum of all covariances between all volume elements is exactly zero, so it is necessary to truncate the sum at some point. The procedure adopted is to order the covariances in order of increasing distance between each pair of volume elements, and take the variance to be the maximum value of the cumulative covariance.

The advantage of this method is that it makes minimal assumptions about the origin and nature of the errors. Moreover, systematic errors may be discernible as systematic patterns in the distribution of fluctuations. The main defect of the method is that it necessarily underestimates the variance on scales approaching the scale of the catalogue.

The second method (tilted bars), inspired by [4], is to take the Poisson (i.e. self-pair) variance weighted by $[1 + \Phi_i P(k)][1 + \Phi_j P(k)]$ where Φ_i, Φ_j are the selection functions at the positions of a pair ij. The method has the defect that it is properly valid only for gaussian fluctuations, but it should be correct to a factor of order unity also for nongaussian fluctuations.

6 Systematics

Ideally one would like to 'map out' the redshift distortions, to check that the signal is generally consistent through the survey, and is not dominated by just a few structures.

Figure 3 is an attempt to present such a detailed breakdown of the distortion signal, in what can be thought of as 'Kolmogorov-Smirnov' type plots. The error analysis (method one) described in §5 provides a list of fluctuations of the power in many volume elements in the catalogue. Figure 3 plots these fluctuations cumulatively as a function of depth, and within each shell of depth as a function of 22 angular regions on the sky (Figure 6, inset). In interpreting the plots in Figure 3 one should bear in mind that the fluctuations are correlated.

The cumulative distribution of power in the 2 Jy survey (Figure 3, top) looks encouraging. The most prominent features in the survey are the Great Attractor (GA), and Perseus-Pisces (PP) complexes [15]. The GA, which is elongated along the line of sight, produces the negative steps in quadrupole power in angular region 19 in the two radial shells at depths $25-40h^{-1}$Mpc, while PP, which is flattened, causes the positive step in quadrupole power in angular region 2 at depth $40-50h^{-1}$Mpc. The overall impression, however, is that the cumulative quadrupole power rises consistently, indicating that the squashing effect is pervasive throughout the survey.

By contrast, the cumulative distribution of power in the QDOT survey (Figure 3, bottom) looks quite peculiar. While the quadrupole power increases consistently to a depth of about $80h^{-1}$Mpc, beyond this point it turns over and declines, again consistently, at all measured wavelengths. Thus while the near region shows the expected squashing effect, the far region is 'finger-of-goddy'. Associated with the turnover in quadrupole power is an enhancement, albeit less marked, in monopole power. Figure 3 indicates that at larger wavelengths, $\pi/k \gtrsim 40h^{-1}$Mpc, there is a dominant feature in Hercules, angular region 5 at $80-100h^{-1}$Mpc. However, it will be seen below that Hercules is not the only problem area.

The 1.2 Jy survey (Figure 3, middle) appears intermediate between the 2 Jy and QDOT surveys.

The right panels of Figure 1, which show contour plots of the redshift correlation function in the region beyond $80h^{-1}$Mpc depth, confirm visually the indications from Figure 3. For QDOT, the correlation function of the far region (Figure 1, bottom right) shows a broad extension along the line of sight, to separations of $50h^{-1}$Mpc and more, in contrast to the squashing effect observed in the full survey (Figure 1, bottom left). There is a sign of a similar, albeit milder, extension in the far region of the 1.2 Jy survey (Figure 1, middle right). There

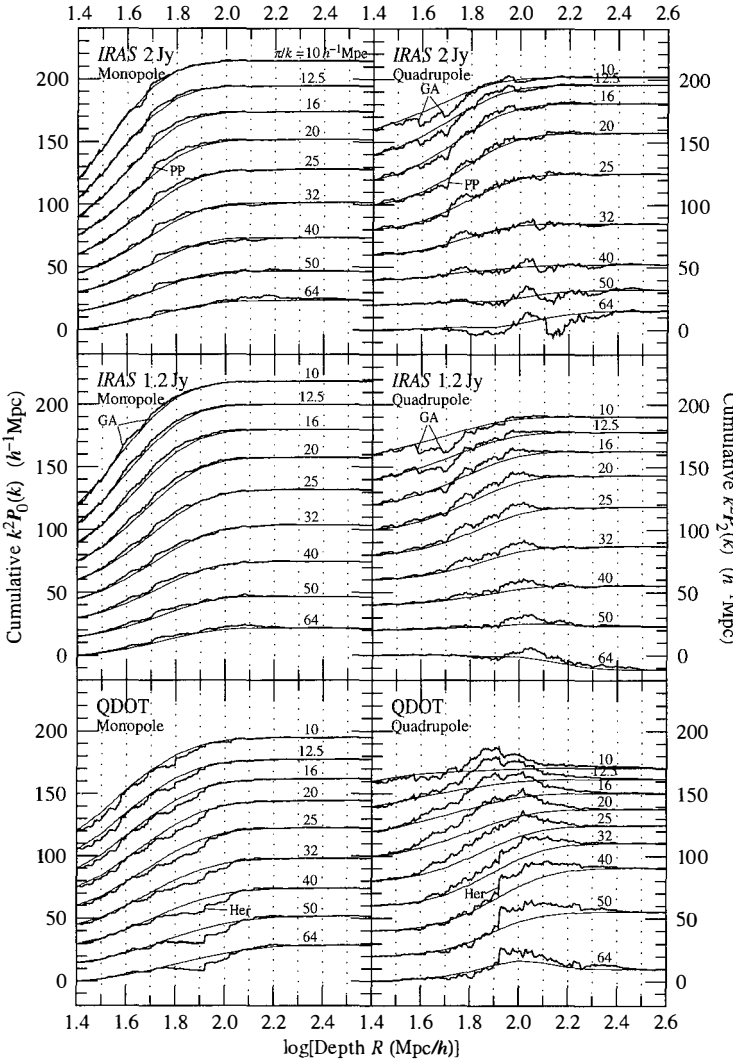


Figure 3: Cumulative monopole (left) and quadrupole (right) power contributed by many volume elements in the *IRAS* 2 Jy (top), 1.2 Jy (middle), and QDOT (bottom) surveys. There are nine curves in each case, each corresponding to a different fixed k, with half-wavelength π/k as labelled. The horizontal axis cycles through 22 angular regions, keyed in Figure 6, within each of 12 radial shells of width 0.1 dex, from $10^{1.4}h^{-1}$Mpc $\approx 25h^{-1}$Mpc to $10^{2.6}h^{-1}$Mpc $\approx 400h^{-1}$Mpc, although in practice there is little contribution to power from the outermost shells (thanks to the minimum variance pair weighting). Along with each observed 'bumpy' curve is a smooth curve which shows how the cumulative power would increase if the clustering around each volume element were the same as for the full survey. The curves are offset to separate them on the graph, and scaled by k^2 so that the curves at different k vary with similar amplitude.

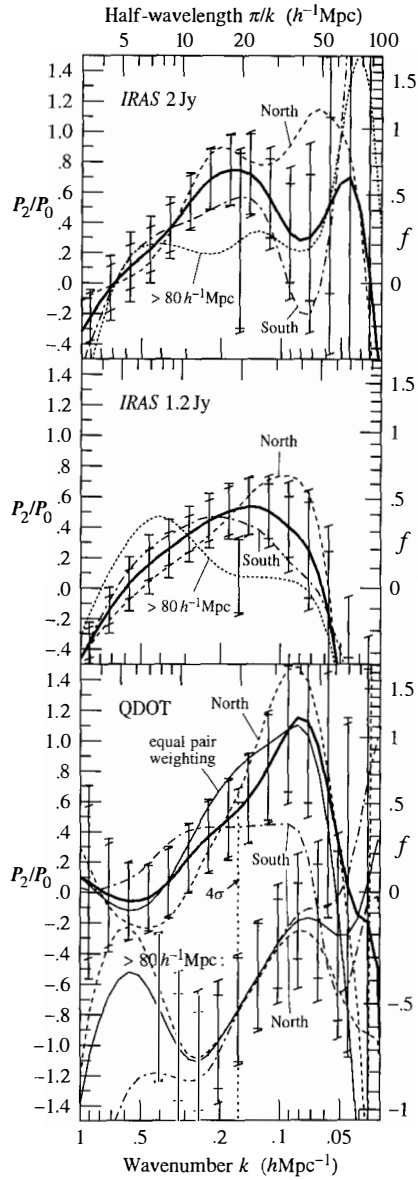


Figure 4: Ratio of the quadrupole to monopole power spectrum in the *IRAS* 2 Jy, 1.2 Jy, and QDOT surveys, showing separately the North and South galactic hemispheres, and the region beyond $80h^{-1}$Mpc. Also shown in QDOT is the result of applying equal pair weighting (which gives relatively more weight to the nearer region than minimum variance pair weighting). The smoothing window is the same as plotted in Figure 2. Estimation of 1σ errors is described in §5.

may even be some hint of the effect in 2 Jy (Figure 1, top right), although the noise here is too great to draw any conclusion.

Figure 4 provides a quantitative assessment of the statistical significance of the discrepancy between the near and far regions. It shows the ratio $\boldsymbol{P_2/P_0}$ of the quadrupole to monopole power in each of the 2 Jy, 1.2 Jy and QDOT surveys, showing separately the region beyond $80h^{-1}$Mpc, and also the North and South galactic hemispheres. The first point to notice is that the North and the South are consistent with each other in all cases, fluctuating from the total at around the 1σ level, as expected for two almost independent halves of a sample.

In the 2 Jy (Figure 4, top) and 1.2 Jy (Figure 4, middle) surveys the $\boldsymbol{P_2/P_0}$ ratio in the region beyond $80h^{-1}$Mpc is again consistent with the full survey, though there is some hint of a downward fluctuation. In QDOT however (Figure 4, bottom) the ratio in the region beyond $80h^{-1}$Mpc is decidedly low compared to the full survey, by about 4σ at the most accurately measured scale, $\pi/k \sim 20h^{-1}$Mpc. The discrepancy in QDOT appears about equally in both North and South, demonstrating that the problem is not confined to Hercules. The region beyond $80h^{-1}$Mpc in QDOT contains 1071 galaxies, about half the galaxies in the survey.

7 Variable Depth of PSC Fluxes over the Sky?

While the discrepancy between the near and far regions of QDOT is not so large as to be conclusive, it is large enough to be worrying. Certainly it is large enough to influence the measurement of cosmological quantities. If the discrepancy is real, what could be causing it?

Several evidences argue against the problem being errors in redshifts. In the first place, if the 'finger-of-goddiness' in the far region of QDOT were caused by redshift errors, then it would tend to reduce the monopole power in the far region, whereas the opposite, an enhancement of power, is observed. Secondly, the 'finger-of-god' in the far region extends to 5,000 $\mathrm{km\,s^{-1}}$ and more, which seems implausibly large for redshift errors. Thirdly, tests of QDOT redshifts against others show no large systematic differences.

The effect appears about equally in intrinsically faint and luminous galaxies. This argues against the hypothesis that the 'finger-of-goddiness' of the far region results from the tendency of infrared-luminous galaxies to occur in interacting systems.

Other tests show the effect to be insensitive to details of the analysis. For example, even gross changes in the selection function have surprisingly little effect. The effect is not caused by cosmological evolution, whether in the volume element, in fluxes, or in the correlation function.

A possible explanation of the problem is that there is some systematic variation in the effective depth of the *IRAS* Point Source Catalog (PSC) across the sky. Such an explanation would be consistent with several facts: (1) Systematic variations in flux limit over the sky would both increase the overall (monopole) power, and at the same time cause more deeply sampled regions to appear elongated along the line of sight. This agrees with what is observed. (2) The change in the pattern of clustering appears at a depth of about $80h^{-1}$Mpc, which is where the selection function in QDOT starts to steepen. Flux variations will cause larger variations in density where the selection function is steeper. (3) The effect is most marked in QDOT, whose flux limit of 0.6 Jy is close to the 0.5 Jy limit of the PSC.

The effect is probably *not* caused by real intrinsic variations in the luminosity function of different regions, because in that case the 2 Jy and 1.2 Jy surveys would be as affected as QDOT.

Figure 5 offers a quantitative assessment of the hypothesis of variations in the flux limit of the PSC across the sky. The plot is motivated by the following rough mathematical argument. Suppose flux variations cause a variable selection function ϕ across the sky. The observed galaxy

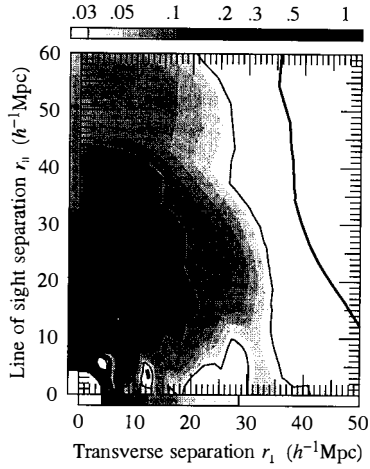


Figure 5: Contour plot of $(\xi_{>80}-\xi)/(1+\xi)$ in QDOT, where ξ and $\xi_{>80}$ denote the redshift correlation functions respectively of the full survey and of the region beyond $80h^{-1}$Mpc, as plotted in Figure 1, bottom. The plotted quantity represents the correlation function ξ_ϕ of a variable angular selection function ϕ, equation (13), which hypothetically modulates the density in the far region of QDOT. Contour levels are the same as in Figure 1. Bars along the two axes are contour plots of the 1σ uncertainties in the parallel and perpendicular directions, as in Figure 1.

density $\rho_{\rm obs}$ is the product of the true galaxy density ρ times the variable selection function ϕ

$$\rho_{\rm obs} = \rho\phi \ . \tag{11}$$

The observed correlation function $\xi_{\rm obs}$ is then related to the true correlation function ξ and the correlation function ξ_ϕ of the variable angular selection function by

$$1 + \xi_{\rm obs} = \langle \rho_{{\rm obs},1}\rho_{{\rm obs},2}\rangle = \langle \rho_1\phi_1\rho_2\phi_2\rangle = \langle \rho_1\rho_2\rangle\langle\phi_1\phi_2\rangle = (1+\xi)(1+\xi_\phi) \ . \tag{12}$$

The third equality of equation (12) assumes that the true density ρ and the selection function ϕ are uncorrelated, which may be false. Equation (12) rearranges into an expression for the correlation function ξ_ϕ of the variable angular selection function,

$$\xi_\phi = \frac{\xi_{\rm obs} - \xi}{1+\xi} \ . \tag{13}$$

Now take the 'observed' correlation function $\xi_{\rm obs}$ in equation (13) to be the correlation function $\xi_{>80}$ of QDOT beyond $80h^{-1}$Mpc (which is more affected by flux variations), and take the 'true' correlation function ξ to be the correlation function of the full QDOT sample (which is less affected). If the hypothesis of a variable flux limit across the sky is true, then Figure 5 represents the correlation function ξ_ϕ of the resulting variable angular selection function (more precisely, the difference in the angular selection functions in the $> 80h^{-1}$Mpc versus full samples).

The prediction then is that the contours in Figure 5, which by hypothesis represents the correlation function ξ_ϕ of an angular selection function, should be more or less vertical (not

quite vertical because the horizontal axis is a physical rather than an angular separation, but this should not make too much difference at a depth of $80h^{-1}$Mpc). Now certainly there are structures in the contours of Figure 5 (for example, the blob on the line of sight axis at $r_\parallel \approx 10h^{-1}$Mpc *is* produced by an excess of luminous interacting pairs), but the general impression is that the contours are consistent with being more or less vertical.

Suppose that the $\xi_\phi = 0.1$ contour level in Figure 5 is believable. The implied rms variation in the density is $\xi_\phi^{1/2} = 0.1^{1/2} \approx 0.3$. The density variation can be converted into a flux variation by dividing by the rms value of the logarithmic slope $d\ln\Phi/d\ln R^2$ of the radial selection function Φ with respect to depth R. This rms slope is $\langle(d\ln\Phi/d\ln R^2)^2\rangle^{1/2} \approx 1.7$ (the Euclidean value would be 3/2) for QDOT beyond $80h^{-1}$Mpc, implying an rms flux variation of $0.3/1.7 \approx 0.18$. At the 0.6 Jy limit of the QDOT, this translates into a flux variation of 0.18×0.6 Jy ≈ 0.10 Jy. Figure 5 suggests that the variation increases somewhat to smaller scales; the scale at which the variation is 0.10 Jy appears to be $r_\perp \sim 15h^{-1}$Mpc, corresponding to an angular scale of $\sim 7°$.

A failing of the above argument is that flux variations should cause at least some line-of-sight elongation of the correlation function also in the near region of QDOT, whereas no obvious elongation is observed. The amplitude of the effect in the near region is reduced by two effects, the shallower slope of the selection function, and the fact that a given transverse separation $r_\perp$ corresponds to a larger angular separation, where the flux variations are (apparently) smaller. All the same, the absence of the effect in the near region is surprising.

8 Map

If there are systematic flux variations in the PSC which affect QDOT more than 1.2 Jy, then one way to try and map out the hypothesised flux variations on the sky is to take the ratio of the QDOT and 1.2 Jy densities on the sky. Figure 6 (bottom) shows the result. The most prominent overdensities in QDOT relative to 1.2 Jy are Hercules ($l = 40°$, $b = 40°$; the peak at $l = 10°$, $b = 50°$ is actually in Serpens) and Leo ($l = 230°$, $b = 50°$) in the North, and Pisces ($l = 130°$, $b = -40°$) and Reticulum ($l = 280°$, $b = -40°$) to Phoenix ($l = 290°$, $b = -70°$) in the South. There is some indication that regions close to the Galactic plane are underdense in QDOT relative to 1.2 Jy, though bear in mind that these and other heavily masked regions are noiser: the Great Attractor region ($l = 310°$), Cygnus ($l = 80°$), Cassiopeia ($l = 130°$), and Taurus ($l = 170°$, $b = -30°$). Other underdense regions include Draco ($l = 110°$, $b = 50°$) and Eridanus ($l = 230°$, $b = -50°$). There is some indication that the 2HCON regions are underdense in QDOT relative to 1.2 Jy (these are two D-shaped regions to the ecliptic east (left and down) of the two masked strips in the top map of Figure 6; see [1] Figure III.D.3).

While Figure 6 may contain some clues as to the distribution of hypothetical flux variations, such inferences should be viewed skeptically, for the level of fluctuations in the map is in fact entirely consistent with Poisson noise fluctuations between QDOT and 1.2 Jy.

9 Conclusion

The large scale squashing effect predicted by linear theory is clearly observed in the *IRAS* 2 Jy, 1.2 Jy, and QDOT surveys. However, the pattern of redshift distortions changes markedly in QDOT beyond its median depth of $80h^{-1}$Mpc, becoming extended along the line of sight rather than squashed. There is some sign of a similar effect at a mild level in the 1.2 Jy survey. I have

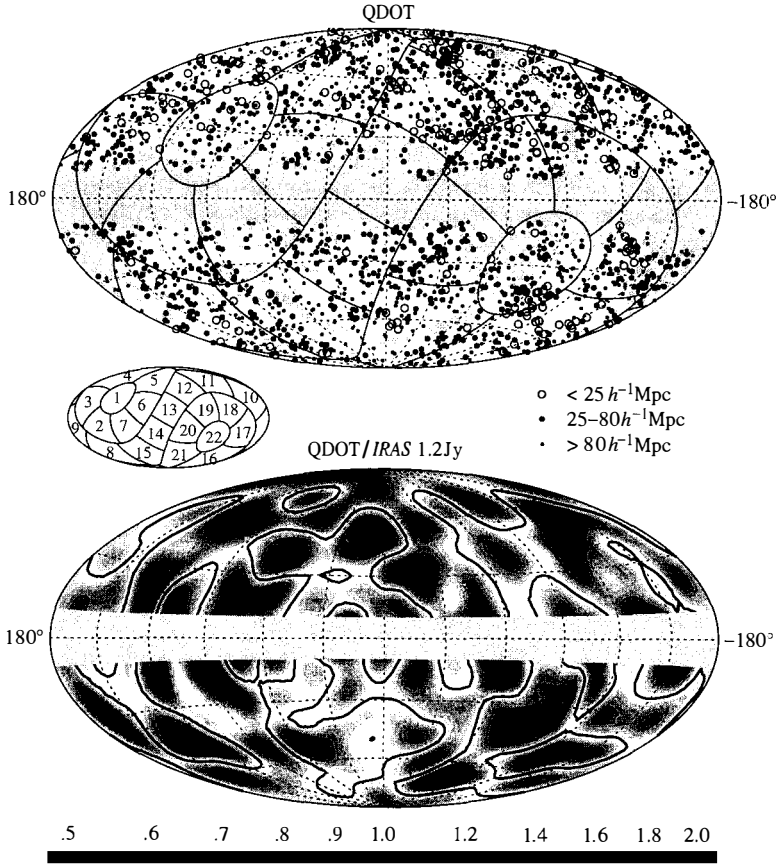


Figure 6: Top: Map of the QDOT galaxy distribution in galactic coordinates. Inset: The 22 angular regions used in the error analysis and in the 'Kolmogorov-Smirnov' plots in Figure 3. The boundaries of the angular regions are lines of constant ecliptic latitude and longitude; angular region 1 is the North ecliptic cap. Bottom: Ratio of QDOT to 1.2 Jy density on the sky. The 1.2 Jy density was radially weighted by the ratio of radial selection functions to give the same density run with depth as QDOT. Only galaxies in the area common to both surveys were used, and the local region within $25h^{-1}$Mpc was excluded. The galaxy densities were smoothed with a gaussian with a 1σ width of 7° before taking their ratio. The thick contour signifies a ratio of unity; other contours are at intervals of 0.1 dex, solid for positive fluctuations, broken for negative fluctuations. Shading is graduated at intervals of 0.02 dex.

argued that systematic variations in the depth of the *IRAS* PSC fluxes of ~ 0.1 Jy on scales $\sim 7°$ could account for several aspects of this discrepancy.

Acknowledgements. I thank George Efstathiou for the hospitality of the Nuclear & Astrophysics Laboratory, Oxford University, where this paper was written. This work was supported by a PPARC Visiting Fellowship, NSF grant AST93-19977, and NASA grant NAG 5-2797.

References

[1] Beichman C. A., Neugebauer G., Habing H. J., Clegg P. E., Chester T. J., 1988, *IRAS Catalogs Volume 1 Explanatory Supplement*, NASA

[2] Cole S., Fisher K. B., Weinberg D. H., 1994, *Mon. Not. R. Astr. Soc.* **267**, 785

[3] Cole S., Fisher K. B., Weinberg D. H., 1995, *Mon. Not. R. Astr. Soc.* submitted

[4] Feldman H. A., Kaiser N., Peacock J. A., 1994, *Astrophys. J.* **426**, 23

[5] Fisher K. B., Davis M., Strauss M. A., Yahil A., Huchra J. P., 1994, *Mon. Not. R. Astr. Soc.* **267**, 927

[6] Fisher K., Huchra J., Strauss M., Davis M., Schlegel D., 1995, *Astrophys. J. Suppl. Ser.* in press

[7] Fisher K. B., Scharf C. A., Lahav O., 1994, *Mon. Not. R. Astr. Soc.* **266**, 219

[8] Kaiser N., 1987, *Mon. Not. R. Astr. Soc.* **227**, 1

[9] Hamilton A. J. S., 1992, *Astrophys. J.* **385**, L5

[10] Hamilton A. J. S., 1993, *Astrophys. J.* **406**, L47

[11] Hamilton A. J. S., 1993, *Astrophys. J.* **417**, 19

[12] Heavens A. F., Taylor A. N., 1995, *Mon. Not. R. Astr. Soc.* in press

[13] Lawrence A., Rowan-Robinson M., Crawford J., Parry I., Xia X.-Y., Ellis R. S., Frenk C. S., Saunders W., Efstathiou G., Kaiser N., 1995 in preparation (QDOT)

[14] Strauss M. A., Davis M., Yahil A., Huchra J. P., 1990, *Astrophys. J.* **361**, 49

[15] Strauss M. A., Davis M., Yahil A., Huchra J. P., 1992, *Astrophys. J.* **385**, 421

[16] Strauss M. A., Huchra J. P., Davis M., Yahil A., Fisher K. B., Tonry J., 1992, *Astrophys. J. Suppl. Ser.* **83**, 29



WHAT DOES THE GALAXY PAIR-WISE VELOCITY PROBE?

A.Blanchard [1,2], J.G.Bartlett [1]
[1] *Observatoire astronomique de Strasbourg, Strasbourg, France.*
[2] *Université Louis Pasteur, Strasbourg, France.*

Abstract

The pair-wise velocity of galaxies, i.e., the mean relative velocity of two galaxies separated by some distance, can be estimated from redshift surveys of galaxies. Peebles has emphasized that this is one of the few ways to directly estimate the mean density associated with galaxies without using an individual system. Provided that galaxies trace the mass (i.e., the unbiased picture), this is generally considered a useful measure of the mean density of the universe. However, this picture has to be modified if galaxies have an extended halo: actually, we show that in this case the pair-wise velocity on small scales remains constant almost independently of the cosmic mean density. We therefore argue that the pair-wise velocity is probing the spatial extension of galaxies and that, taking into account present day observations, galaxies possess halos extending beyond 300 kpc.

1 Introduction

Estimation of the mean cosmic density of the universe is certainly one of the most exiting topics in modern cosmology. Most of the standard procedures rely on the measurement of the mass of a particular system (such as a cluster), through knowledge of its dynamical properties, which is then converted into a measure of the cosmic mean density (or Ω_0) via the M/L ratio. This is not entirely satisfying, because a single object, or a class of objects, is supposed to be representative of the whole universe. In this context, Peebles (1980) has proposed a different way to measure Ω_0: Under the hypothesis of stable clustering, he established a relation between the pair-wise velocity and Ω_0; this relation involves the two- and three-point correlation functions and is known as the *Cosmic Virial Theorem*, hereafter CVT. The great advantage of this method is that it can be considered as a statistical estimate of Ω_0, as the information comes

from the whole ensemble of galaxies. The validity of the CVT has been checked at some level by means of numerical simulations (Davis et al., 1985). More recently, numerical simulations with greater resolution have been performed in which the formation of individual objects on galactic scales can be followed. Perhaps one of the most important advances resulting from these numerical simulations is the fact that the pair-wise velocity could be, at least in some cases, smaller than in the standard scenario, such an effect being called the velocity bias. The theoretical explanation for this velocity bias is largely unknown.

2 The Standard Cosmic Virial Theorem and Beyond

2.1 The Orthodoxy

The CVT relates the pair-wise velocity of galaxies to the mean cosmic density:

$$\frac{d[\xi(r)\sigma^2(r)]}{dr} = -\frac{2G\bar{\rho}}{r}\int d^3z\zeta(r,z,|\vec{r}-\vec{z}|)\frac{\vec{r}\cdot\vec{z}}{z^3}. \qquad (1)$$

The derivation of this relation can be found in Peebles (1980). The actual pair-wise velocity has been estimated from various samples. There is a general agreement that the observed pair-wise velocity is slightly increasing with distance, from $10h^{-1}kpc$ to $1h^{-1}Mpc$, with a typical value of $350km/s$ at $r = 1h^{-1}Mpc$ (for a more pessimistic look at the data, see Mo et al., 1993). The shape of the observed pair-wise velocity is in impressive agreement with the predicted shape, and the fact that the observed pair-wise velocity is in such good agreement with the data provides one of the most convincing arguments for a low density universe (Davis & Peebles, 1983).

2.2 The CVT Revisited

One of the major assumptions in the standard derivation of the CVT is that the galaxies are considered point-like. From observations we know that galaxies do possess and halo presenting a flat rotation curve, and for which the spatial extension is not known. Typically, if galaxies are extended up to the scale r_c, the contribution of galaxies to the mean cosmic density is

$$r_c h = (2.98\,\mathrm{Mpc})\Omega\left(\frac{0.01h^3\,\mathrm{Mpc}^{-3}}{n_g}\right)\left(\frac{200\,\mathrm{km/s}}{v_g}\right)^2. \qquad (2)$$

HI rotation curves probe galaxy halos up to a few tens of kpc, at best up to 100 kpc. There is, however, some evidence that halos extended beyond that. There is therefore clearly a need to account properly for this observational property of galaxies in the derivation of the CVT. This point has been addressed by Bartlett & Blanchard (1995), BB95 hereafter. The main result they obtained was that the pair-wise velocity could fit the data for Ω as large as 1, despite the fact that galaxies trace the mass distribution. Their results are presented in the figure.

They essentially assume that galaxies possess an extended halo which provides the mean density of the universe, i.e., the mean cosmic density can be accounted for by galaxies and the matter directly associated with them. This point is important and its meaning has to be clarified. Essentially, one can have two pictures of the link between galaxies and the mass distribution. The first one is to assume that mass is distributed with 2- and 3- point correlation

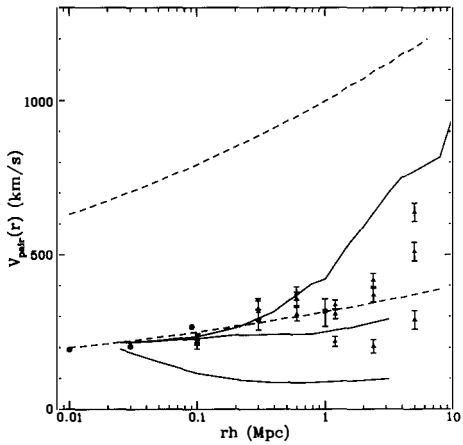


Figure 1: The pair-wise velocity dispersion as a function of physical separation compared to observations. Equation 1 produces the upper dashed curve for a flat universe and the lower dashed curve for $\Omega = 0.1$. Adopting the model discussed in the text, a flat universe will produce the uppermost solid curve. The remaining two curves show the results of this same model for $\Omega = 0.1$ (middle solid curve) and $\Omega = 0.01$ (lowest solid curve).

functions exactly identical those measured for galaxies. In this case, bright galaxies must be regarded as a finite random sub-sample of the distribution of dark matter particles which are themselves in nearly infinite number. For instance, one can think that this distribution is asymptotically reached when one considers fainter and fainter galaxies. An alternative is to consider that the bulk of the mass is associated with bright galaxies, say L_* galaxies, as part of their environment and according to the density profile of the halo ($\propto 1/r^2$). Physically, that is to say that there is not a specific scale at which the galaxy-mass correlation function should stop, but that it instead extends as a power-law up to large scales. This is not to say that the dark matter material necessarily lies in a dynamical halo, but rather that it lies in the vicinity of galaxies and is statistically associated to them, although not necessary to one specific galaxy. These two pictures are rather different: while the galaxy-mass correlation function is nearly identical in both cases (see figure 3 in BB95), the 3-point correlation functions differ (see figure 2 in BB95) - in the second picture, the 3-point correlation function galaxy-galaxy-mass is significantly smaller. This is the critical point for understanding the lower velocity one sees in this picture: In the expression for the CVT, the numerical coefficient involves an integral of the three-point correlation function (Eq. 75.14 in Peebles, 1980) which is almost divergent in the first picture. On the contrary, in the second picture this numerical coefficient is reasonable.

2.3 Interpretation

The result which has been obtained by BB95 is rather surprising at first glance. However, it could be understood intuitively: if galaxies are considered as extended objects, when one is considering the dynamics driving the relative velocity of two galaxies separated by some distance r, the dominant contribution comes from the mass between them. Therefore, the

outer part will not contribute and the pair-wise velocity dispersion will be independent of the actual size of the halo. In this case it is rather intuitive that the pair-wise velocity on small scales will essentially reflect the halo profile and therefore should be of the order of 200/km/s. On larger scales one of two things can happen. Two scales have to be considered - the mean distance to the nearest neighbor and the halo size. If the halo size is smaller than the distance to the nearest neighbor, the dynamics of the two galaxies is essentially a two-body problem and the relative velocity will decrease accordingly. Therefore, *we would expect the relative velocity to exhibit a feature at the distance at which the halo ends.* In the alternative case, when one is looking at two galaxies separated by a distance greater than the distance to the nearest neighbor, then other galaxies exist between them which contribute to the dynamics, and their effect will raise the pair-wise velocity. From the observational point of view, the pair-wise velocity is constant from 10 kpc to several Mpc. However, on scales larger than 1 Mpc the assumption of stable clustering is not expected to hold. Moreover, the data are uncertain on these scales. So probably only scales between 10 kpc and 1 Mpc are to be considered. The fact that the pair-wise velocity is constant primarily indicates that the halo does not end in this range; otherwise, as we already pointed out, the scale associated with it would be visible in the shape of the pair-wise velocity. From BB95, it seems that it is likely that the measured pair-wise velocity shows that galaxy halos extend to at least 300 kpc, although larger halos are perfectly acceptable.

References

[1] Bartlett J.G. & Blanchard A., 1995, preprint astro-ph/9506100, in press

[2] Peebles P.J.E., 1980, The Large-Scale Structure of the Universe, Princeton University Press, Princeton

[3] Peebles P.J.E., 1990, in *Proceedings of the 2nd Blois Conference: Physical Cosmology*, p. 17, eds Blanchard et al., Editions Frontières

[4] Davis M. & Peebles P.J.E., 1983, *Astrophys. J.* **267**, 465

[5] Davis M., Efstathiou G., Frenk C.S., White S.D.M., 1985, *Astrophys. J.* **292**, 371

[6] Mo H.J., Jing Y.P., Borner G., 1993, *Mon. Not. R. astr. Soc.* **264**, 825

ASPECTS OF SCALING IN GRAVITATIONAL CLUSTERING

Bhuvnesh Jain
Max-Planck-Institut für Astrophysik, 85740 Garching, Germany.

Abstract

The scaling ansatz of Hamilton et al. effectively extends the idea of self-similar scaling to initial power spectra of any generic shape. Applications of this ansatz have provided a semi-empirical analytical description of gravitational clustering which is extremely useful. This contribution examines the two theoretical ingredients that form the basis of these applications: self-similar evolution and the stable clustering hypothesis. A brief summary of work verifying self-similar scaling for scale free spectra $P(k) \propto k^n$, with $n < -1$ is given. The main results presented here examine the hypothesis that clustering is statistically stable in time on small scales, or equivalently that the mean pair velocity in physical coordinates is zero. The mean pair velocity of particles can be computed accurately from N-body simulations via the pair conservation equation, by using the evolution of the autocorrelation function $\xi(x,t)$. The results thus obtained for scale free spectra with $n = 0, -1, -2$ and for the CDM spectrum are consistent with the stable clustering prediction on the smallest resolved scales, on which the amplitude of $\xi \gtrsim 200 - 1000$ for $n = -2$ and $n = 0$, respectively.

1 The Universal Scaling Ansatz

The evolution of gravitational clustering in an expanding universe has resisted rigorous analytical attempts at describing the nonlinear regime. A scaling ansatz proposed by Hamilton et al. (1991) (HKLM, reference [3]) has however provided a useful analytical prescription for computing the nonlinear autocorrelation function $\xi(x,t)$, or the power spectrum $P(k,t)$ in Fourier space. This ansatz relates the linear and nonlinear average two-point correlation functions $\bar{\xi}_{\rm L}$ and $\bar{\xi}_{\rm E}$:

$$\bar{\xi}_{\rm E}(x) = F[\bar{\xi}_{\rm L}(x_0)] \ , \ x_0 = [1 + \bar{\xi}_{\rm E}(x)]^{1/3} x. \qquad (1)$$

Here $\bar{\xi}(x) = (3/x^3)\int_0^x y^2\xi(y)\mathrm{d}y$, and F is a universal function assumed to be independent of the initial spectrum. The mapping of scales from x_0 to x takes into account the fact that nonlinear density fluctuations shrink in comoving coordinates as evolution proceeds.

A remarkable aspect of this ansatz was that the same function F appeared to work for all epochs and initial spectra. HKLM found that their ansatz was in good agreement with the N-body simulations of Efstathiou et al. (1988) (EFWD, ref [2]), and used these data to determine the functional form of F. Motivated by this work applications and extensions of the scaling ansatz have been developed by refs [8], [10], [6] and [9]. It has been found that there is in fact a dependence on the initial spectrum in equation (1), and modified formulae that take this into account are given in ref [6].

While the functional form of F in equation (1) is fitted from N-body simulations, it is important to check that the dynamical basis of the scaling ansatz is valid. The primary ingredient is self-similar scaling for scale free spectra $P(k) \propto k^n$ in an Einstein-de Sitter universe. Section 2 contains a brief discussion of the self-similar scaling of spectra with $n < -1$, based on refs [4] and [5]. In Section 3 we examine the validity of the stable clustering hypothesis which describes the deeply nonlinear regime and thus fixes the asymptotic functional form of F. Testing for self-similarity and stable clustering is of course important in understanding gravitational dynamics, quite independent of their applications in implementing the scaling ansatz. These issues have recently been addressed by refs [1] and [9] as well.

2 Self-Similar Evolution

The results of EFWD established self-similar scaling for spectra with $n \geq -1$, but they lacked the resolution to probe the $n = -2$ spectrum. Here we present a direct test of the scaling of the Fourier amplitude $\Delta(\vec{k},t)$ of the density, defined by $\hat{\delta}(\vec{k},t) = \Delta e^{i\phi}$ where $\hat{\delta}(\vec{k},t)$ is the Fourier transform of the overdensity in real space, $\delta(x,t)$. This is based on work done with E. Bertschinger – a detailed analysis of the scaling of the $n = -2$ spectrum, and comparison with other recent results will be presented elsewhere. We use a p^3m simulation of 128^3 particles with the Plummer force softening parameter $\epsilon = 1/2560$ of the box size. For each mode of the Fourier density we compute the deviation of $\Delta(\vec{k},t)$ from the linear evolution $\Delta_1 \propto a(t)$, where $a(t)$ is the expansion scale factor. By averaging the absolute values of the deviations of modes with wavenumber k in the range $k_c - 0.5 < k < k_c + 0.5$, we define characteristic nonlinear scales k_c as follows:

$$\left\langle \frac{|\Delta(\vec{k}_c,a) - \Delta_1(\vec{k}_c,a)|}{\Delta_1(\vec{k}_c,a)} \right\rangle = \Delta_c\,, \tag{2}$$

where Δ_c is a dimensionless constant of order unity. Since the magnitude of the fractional departures from linear growth for each mode within a given k–shell is summed, this statistic probes the scaling properties more directly than comparing a statistic like the power spectrum at different times would [4].

Figure 1 shows the results for four different values of Δ_c. The self-similar scaling, $k_c \propto a(t)^{-2/(3+n)} \propto a^{-2}$ is indicated by a dotted line. Also shown is the scaling $k_c \propto a^{-1}$ which would result if the dynamics were driven by the large scale bulk velocity, a formally divergent quantity for $n < -1$. Some analytical as well as numerical evidence points to the significance of this scaling. However, the results shown in Figure 1 demonstrate that for modes with wavelength less than 1/10 the box size, $k > 10$, the standard self-similar scaling is valid. It also provides an estimate of the effect of large-scale power for the $n = -2$ spectrum, since the growth of the amplitude of modes with wavelengths $< 1/10$ the box-size is slowed down by the

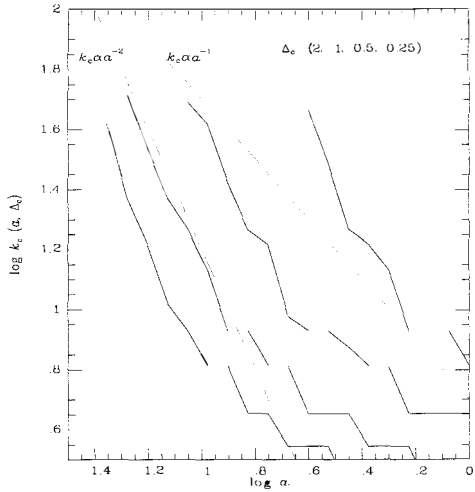


Figure 1: Scaling of the amplitude $\Delta(\vec{k},t)$ for $n=-2$. The scaling in time of characteristic wavenumber scales, derived from the departure of the amplitude from linear growth, $k_c(a,\Delta_c)$ vs. a is shown for 4 different values of Δ_c (see equation (2) for the definition of $k_c(a,\Delta_c)$). The values of a are in arbitrary units, while those of k are in units of the box-size such that $k=1$ is the fundamental mode. All the curves have a slope close to the standard self-similar scaling, $k_c \propto a^{-2}$, shown as the dotted line on the left. For k below about 10 the slope becomes shallower, due to the limitation of a finite box.

absence of power on scales larger than the box.

A detailed analytical analysis also reveals that while a class of statistical measures related to the phase ϕ would show the bulk velocity scaling, the density amplitude should scale self-similarly. Thus the conclusion of our analytical analysis in ref [5], and of a numerical study in preparation, is that self-similar scaling holds for scale free spectra with $-3 < n < 1$ (see also refs [1] and [9]).

3 Stable Clustering

The stable clustering hypothesis fixes the growth of the autocorrelation function $\xi(x,t)$ in the deeply nonlinear regime. This hypothesis states that on sufficiently small scales the mean relative velocity of particle pairs is zero or, equivalently, that the mean number of neighbors remains constant in time at a given physical separation. It relies on the physical picture of a virialized cluster which is no longer expanding or contracting in physical coordinates. The discussion below follows Peebles (1980) [11].

In comoving coordinates the mean pair velocity $v(x,t) = a\dot{x}$. By symmetry this velocity is directed along the line joining the pair of particles. If stable clustering is valid then the peculiar velocity must cancel the Hubble velocity on that scale, so that the net velocity in

physical coordinates is zero:

$$v(x,t) = a\dot{x} = -\dot{a}x\,. \tag{3}$$

To establish the connection of the above statement of the stable clustering ansatz to the growth of the correlation function, consider the equation of pair conservation, obtained by integrating the 2nd BBGKY equation over momenta (Section 71 of [11]):

$$\frac{\partial \xi}{\partial t} + \frac{1}{x^2 a}\frac{\partial}{\partial x}\left[x^2(1+\xi)v\right] = 0. \tag{4}$$

We can re-write equation (4) by integrating over the volume of a sphere, and re-arranging terms to obtain

$$\frac{a}{3(1+\bar{\xi})}\frac{\partial \bar{\xi}}{\partial a} = \frac{-v}{\dot{a}x} = \frac{-v}{Hr}\,, \tag{5}$$

where Hr is the Hubble velocity on the physical scale $r = ax$, and $\bar{\xi}(x,t)$ is the mean interior correlation function. We shall use this form of the pair conservation equation to measure v from the N-body simulations.

On substituting the assumption of equation (3) in (4), the functional form of $\xi(x,t)$ which satisfies (4) becomes restricted to

$$\xi(x,t) = a^3 f\,[ax]\,, \tag{6}$$

where we have approximated $1+\xi \simeq \xi$, as the stable clustering hypothesis is applied on very small scales were ξ is at least of order 100. Equation (6) fixes the growth of ξ in physical coordinates. If the initial spectrum is scale free and the universe is Einstein-de Sitter, then the functional form of equation (6) can be combined with the requirement of self-similarity to obtain the shape of the correlation function as well. The result is

$$\xi(x,t) \propto (x/a^\alpha)^{-\gamma}\;;\; \gamma = (9+3n)/(5+n)\,,\; \alpha = 2/(3+n)\,. \tag{7}$$

3.1 Testing Stable Clustering

N-body simulations provide a useful means of testing the stable clustering ansatz. The results of EFWD suggested that stable clustering might hold for $\xi \gtrsim 100$, but their simulations lacked the small scale resolution required to see evidence of it. Two simple tests of stable clustering are provided by equations (3) and (6) (and for scale free spectra, the more detailed form of equation (7)). Theoretically the two tests are equivalent, but in practice it is far easier to measure the growth and shape of $\xi(x,t)$ than it is to directly measure $v(x,t)$ as $x \to 0$. This is because of the large fluctuations in the mean pair velocity that arise due to the high velocity dispersion of a finite number of particles sampled at a given x.

Therefore we "measure" the mean pair velocity by solving the pair conservation equation in the form given by equation (5). Figure 2 shows $-v/Hr$ plotted as a function of $\bar{\xi}$ for four different spectra. The results are from p^3m simulations with 100^3 particles and a Plummer force softening $\epsilon = 1/2500L$, where L is the box-size, for $n = 0, -1$; 128^3 particles with $\epsilon = L/2560$ for $n = -2$; and 144^3 particles with $L = 100$ Mpc, $h = 0.5$, and $\epsilon = 65$ kpc for the CDM spectrum. Three different output times, chosen to probe the full range of $\bar{\xi}$ accessible in the simulations, are shown for each spectrum. For CDM these are $a = 0.3, 0.5, 0.8$ with a $\sigma_8 = 1$ normalization. The results at the high-$\bar{\xi}$ end are plotted up to $x = 2\epsilon$. The near coincidence of the results for the three different times in each of the scale free spectra establishes consistency with self-similarity. It also shows how small the scatter in the results is, in contrast to a direct measurement of v which would have a scatter about 5 times larger in the nonlinear regime.

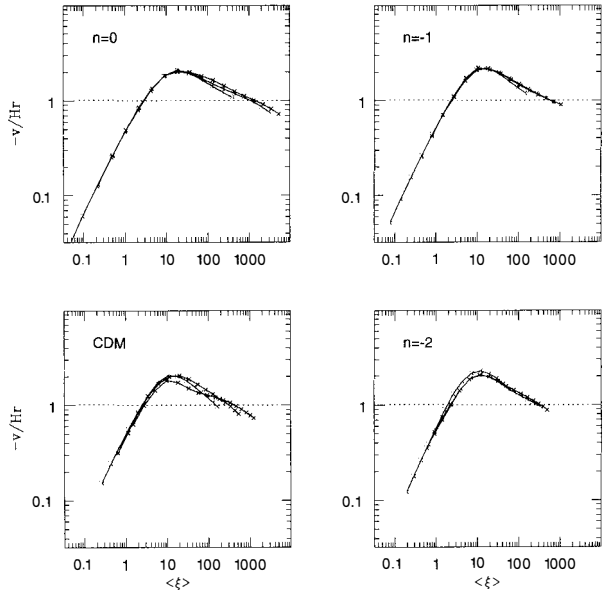


Figure 2: The ratio of the mean pair velocity to the Hubble velocity on the same scale $-v(x,t)/Hr$ vs. mean interior correlation function $\bar{\xi}(x,t)$, denoted here by $< \xi >$, at three different output times for each of the four spectra indicated in the panels. v is computed by using the time evolution of $\bar{\xi}$ to solve the pair conservation equation as described in Section 3. Note that self-similarity requires that the three curves for each of the scale free spectra coincide, stable clustering that they asymptote to the value 1 at the high-$\bar{\xi}$ end, and the scaling ansatz predicts that their functional form is almost independent of the spectrum.

It is evident that at the small scale, highly nonlinear end $-v/Hr \simeq 1$. However there is no evidence for the onset of an asymptotic regime, in which $-v/Hr = 1$ for a wide enough range of scales. Larger simulations which measure small scale nonlinearity well beyond $\xi \sim 1000$ are therefore required to test whether the ratio $-v/Hr$ remains constant as $x \to 0$. Figure 2 hints that this ratio continues to decrease below the value unity, but since the last two points plotted could underestimate $-v/Hr$ due to limited numerical resolution this issue must be addressed with care, as discussed in Section 4.

4 Discussion

Measuring the asymptotic value of $\xi(x,t)$ or $v(x,t)$ as $x \to 0$ requires a careful analysis of the finite numerical resolution of the simulations (see ref [1] for a detailed discussion). We have computed $v(x,t)$ by using the evolution of ξ rather than by measuring it directly, as the high velocity dispersion causes a direct measurement to have much larger scatter. The dominant

source of error in ξ at small scales is force softening which suppress its growth, and can therefore cause the inferred value of $-v/Hr$ to be artificially low. Hence the decreasing trend of $-v/Hr$ with increasing $\bar{\xi}$ at the smallest scales probed (between $2-4\epsilon$) should be viewed with caution. On these scales it is barely above the maximum error expected from the limited numerical resolution over the range of ~ 4 in $\bar{\xi}$ on the high-$\bar{\xi}$ end. Figure 2 also shows that the conclusion $-v/Hr \simeq 1$ is accurate to within $20-30\%$ for this range of scales. These results are supported by a detailed analysis of numerical resolution effects, by checking them with an ensemble of simulations for the $n=-1$ spectrum, and by other tests of stable clustering [7]; a comparison with the results of refs [1] and [9] will also made.

If one adopts the pragmatic point of view that the verification of stable clustering is useful only to the extent that it fixes the nonlinear growth of ξ on a certain range of scales, then Figure 2 indicates that for $\xi \gtrsim 1000$ for $n \simeq 0$, and for $\xi \gtrsim 200$ for $n \simeq -2$ and CDM, the results of the simulations analyzed here are consistent with the stable clustering prediction. This is adequate for most applications such as fixing the strongly nonlinear form of ξ in the formulae obtained from the scaling ansatz. However some interesting dynamical questions need to be addressed. Why is the slope of ξ steeper than the stable clustering prediction, or equivalently, why is there a net infall, $-v/Hr > 1$, for $\xi \lesssim 200-1000$ (for $n=-2$ and $n=0$ respectively)? Can the spectral dependence of the results be physically explained? Does the consistency with stable clustering claimed here hold as $x \to 0$, i.e. is it indeed the asymptotic regime? While analytical models can provide an understanding of the first two questions, the existence of an asymptotic regime can only be verified by higher resolution simulations that probe the nonlinear regime well beyond $\xi \sim 1000$.

Acknowledgements. The work presented here on self-similar scaling was done in collaboration with Ed Bertschinger. I am grateful to him and to Simon White for the use of their simulations and for useful discussions.

References

[1] Colombi S., Bouchet F., Hernquist L. 1995, preprint

[2] Efstathiou G., Frenk C.S., White S.D.M., Davis M. 1988, *Mon. Not. R. astr. Soc.* **235**, 715 (EFWD)

[3] Hamilton A.J.S., Kumar P., Lu E., Matthews A. 1991, *Astrophys. J.* **374**, L1 (HKLM)

[4] Jain B. 1994, PhD. Thesis, MIT

[5] Jain B., Bertschinger E. 1995, *Astrophys. J.* , submitted

[6] Jain B., Mo H., White S.D.M. 1995, *Mon. Not. R. astr. Soc.* **276**, L25

[7] Jain B. 1995, in preparation

[8] Nityananda R., Padmanabhan T. 1994, *Mon. Not. R. astr. Soc.* **271**, 976

[9] Padmanabhan T., Cen R., Ostriker J.P., Summers F.J. 1995, preprint

[10] Peacock J.A., Dodds S.J. 1994, *Mon. Not. R. astr. Soc.* **267**, 1020 (PD)

[11] Peebles P.J.E. 1980, The Large-Scale Structure of the Universe, Princeton, Princeton Univ. Press

CLUSTERING STATISTICS & DYNAMICS

R. Juszkiewicz[1], F. R. Bouchet[2]
[1] *Copernicus Center, Warsaw, Poland.*
[2] *Institut d'Astrophysique de Paris, France.*

Abstract

Since the appearance of the classical paper of Lifshitz almost half a century ago, linear stability analysis of cosmological models is textbook knowledge. Until recently, however, little was known about the behavior of higher than linear order terms in the perturbative expansion. These terms become important in the weakly nonlinear regime of gravitational clustering, when the rms mass density contrast is only slightly smaller than unity. In the past, theorists showed little interest in studying this regime, and for a good reason: only a decade ago, it would have been an academic excercise – at scales large enough to probe the weakly nonlinear regime, all measures of clustering were dominated by noise. This is no longer the case with present data. The purpose of this talk is to provide a brief summary of recent advances in weakly nonlinear perturbation theory. We present analytical perturbative results together with results of N-body experiments, conducted to test their accuracy. We compare perturbative predictions with measurements from galaxy surveys. Such comparisons can be used to test the gravitational instability theory and to constrain possible deviations from Gaussian statistics in the initial mass distribution; they can be also used to study the nature of physical processes that govern galaxy formation ("biasing"). We also show how future studies of velocity field statistics can provide a new way to determine the density parameter, Ω.

1 Perturbation theory

Tests of theories for the origin of the large scale structure of the universe ultimately depend on a comparison of model predictions with measurable quantities, derived from observations. The statistical measures we will discuss here are the low order N-point correlation functions. They have two clear advantages. First, they can be estimated from galaxy surveys with a reasonable degree of precision and reproducibility (see, e.g. [45, 46, 20, 51], and references therein). Second, correlation functions can be relatively easily related to dynamics (e.g. [45]). Their evolution can be studied by taking moments of the hydrodynamical equations of motion of an expanding self-gravitating pressureless fluid with zero vorticity, which is a good approximation of the real universe after the hydrogen recombination. Low order correlation functions can also be measured from N-body experiments.

1.1 Gravitational instability

The full description of gravitational instability is nonlinear. The density contrast

$$\delta(x,t) \;=\; \frac{\rho(x,t)}{\langle\rho\rangle} - 1 \;, \tag{1}$$

the peculiar velocity v and the gravitational potential ϕ are related by the Euler, Poisson and continuity equations. They can be combined into one expression for the density contrast,

$$\ddot{\delta} + 2H\dot{\delta} - \tfrac{3}{2}\Omega H^2\delta \;=\; \tfrac{3}{2}\Omega H^2\delta^2 + a^{-2}\nabla\delta\cdot\nabla\phi + a^{-2}\nabla_\alpha\nabla_\beta[(1+\delta)v_\alpha v_\beta] \;. \tag{2}$$

Here $x = \{x_\alpha\}$ and t are, respectively, the comoving spatial coordinates and the cosmological time, the dots represent time derivatives, $\nabla_\alpha = \partial/\partial x_\alpha$, $a(t)$ is the scale factor, $H = \dot{a}/a$ is the Hubble parameter, and $\Omega = 8\pi G\langle\rho\rangle/3H^2$ is the density parameter. The brackets $\langle \ldots \rangle$ denote ensemble averaging and ρ is the mass density. Perturbation theory rests on a conjecture that when the deviations from homogeneity are small, the first few terms of the expansion

$$\delta \;=\; \delta_1 + \delta_2 + \delta_3 + \ldots \tag{3}$$

provide a reasonable approximation of the exact solution of eq. (2). The first, linear term is the well known Lifshitz [39] solution of eq. (2) with the right-hand side set to zero,

$$\delta_1 \;=\; D(t)\varepsilon(x) \;+\; \textit{decaying mode}\,, \tag{4}$$

where $D(t)$ is the standard growing mode (see, e.g., §11 in [45]) and ε is a random field with statistical properties defined by initial conditions. The term $\delta_2 = \mathcal{O}(\varepsilon^2)$ is the solution of the same equation with quadratic nonlinearities included iteratively by using δ_1 as source terms (as in [45], §18). For a vanishing cosmological constant ($\Lambda = 0$) and arbitrary Ω, the fastest growing mode in this solution is [35]

$$\delta_2 \;=\; D^2(t)\,\left[\tfrac{2}{3}(1+\kappa)\varepsilon^2 + \nabla\varepsilon\cdot\nabla\Phi + (\tfrac{1}{2}-\kappa)\tau_{\alpha\beta}\tau_{\alpha\beta}\right]\,, \tag{5}$$

$$\tau_{\alpha\beta} \;=\; (\tfrac{1}{3}\delta_{\alpha\beta}\nabla^2 - \nabla_\alpha\nabla_\beta)\Phi\,; \quad \Phi(x) \;=\; -\int d^3x'\,\varepsilon(x')/4\pi|x-x'|\,. \tag{6}$$

The parameter κ is a slowly varying function of time; its dependence on Ω is extremely weak, too. In the range $0.05 \le \Omega \le 3$, the Ω-dependence is well approximated by [8]

$$\kappa\,[\Omega(t)] \;\approx\; \tfrac{3}{14}\,\Omega^{-2/63}\,. \tag{7}$$

The higher order terms can be constructed out of the linear solution in a similar way.

1.2 Dynamical evolution of correlations

The main source of difficulties in studies of the dynamics of gravitational instability is the nonlinearity of the equations of motion. Indeed, let us write eq. (2) for $\delta(x,t)$ and $\delta' = \delta(x',t)$, then multiply the first equation by δ', and the second by δ. The result of adding these two equations and averaging is

$$\ddot{\xi} + 2H\dot{\xi} - 3\Omega H^2\xi + 2a^{-2}\nabla^2\xi_v \;=\; 3\Omega H^2\langle\delta^2\delta'\rangle \;+\; \ldots\,, \tag{8}$$

where $\xi = \langle\delta\delta'\rangle$ and $\xi_v = \langle v\cdot v'\rangle$ are the two-point density and velocity correlation functions, while the right-hand side of the equation involves 3- and 4-point correlations, which we left out except for one term given as an example. The full expression is not the point here; the important message is that we have an infinite hierarchy of equations. Mathematically, this is similar to the BBGKY hierarchy: in order to solve for an N-point function, we need to know $(N+1)$- and $(N+2)$-point correlations. Perturbation theory may help, but not without further assumptions, necessary to close the infinite hierarchy of correlation functions. Here we will assume that $\varepsilon(x)$ is a random Gaussian field. This approach, also known as the *random phase approximation*, can be justified theoretically for a wide class of models of the early universe [46]. Independently of whether we take "inflationary" arguments seriously or not, the random phase assumption is observationally testable. As we will show below, comparing model predictions with observations can help us decide whether the early universe was Gaussian or not. The greatest advantage of our assumption is simplicity. Indeed: all odd-order correlation functions of ε vanish, and all even-order moments can be reduced to the two-point function. For example, for the first four moments we have $\langle 1\rangle = \langle 123\rangle = 0$, $\langle 12\rangle = \xi_L\,(|x_1-x_2|,t)\,D^{-2}$, and

$$\langle 1234\rangle = D^{-4}\,\xi_L\,(|x_1-x_2|,t)\,\xi_L\,(|x_3-x_4|,t) \;+\; \textit{cycl.(two terms)}\,, \tag{9}$$

where $\langle 12\ldots N\rangle \equiv \langle\varepsilon(x_1)\varepsilon(x_2)\ldots\varepsilon(x_N)\rangle$, while ξ_L in eq. (9) is $\langle\,\delta_1\,(x_1,t)\,\delta_1\,(x_2,t)\,\rangle$, the linear 2-point correlation function. Using these relations and the perturbative expansion, we can express the

3- and 4-point functions on the right-hand side of eq. (8) in terms of ξ_L. This will close the hierarchy, allowing us to calculate weakly nonlinear corrections for the 2-point function ξ. The same procedure can be applied for higher order correlation functions. This simple idea is at the root of all perturbative results, discussed below.

Perturbative calculations are usually easier after applying the Fourier transform. The Fourier transform of ξ is the power spectrum, $P(k,t)$, where k is the comoving wavenumber. The linear term in the perturbative expansion for $P(k,t)$ is

$$P_L(k,t) = \int \xi_L(r,t) \exp(ik\cdot r)\, d^3k \,. \tag{10}$$

The basic properties of linear evolution, as well as the effect of nonlinear interactions can be deduced from the functional form of δ_1 and δ_2. Indeed, according to eq. (4), all fluctuations evolve without changing the shape of their density profiles, so that we can expect that the linear power spectrum evolves without changing its slope (the growth rate is the same for all scales). This is indeed the case. If $P_L(k,t) \propto k^n$ at some initial time t_0, than at later times $P_L(k,t) = P_L(k,t_0)\, D^2(t)/D^2(t_0) \propto k^n$. A second characteristic property of a linear field is that its distribution function remains Gaussian; only its width, $\langle\delta_1^2\rangle$ grows in time as $D^2(t)$. Neither of these properties remain valid when nonlinear interactions become important. The nonlinear terms, describing tidal interactions in eq. (5) redistribute power across the spectrum, and growth rates may be enhanced at some wavenumbers and suppressed at others: the logarithmic slope $n(k,t) = d(\log P)/d(\log k)$ is no longer constant, it can now change with time. Moreover, the nonlinear evolution introduces deviations from Gaussian statistics. The lowest-order moment which can detect such deviations is the skewness, $\langle\delta^3\rangle$. The Gaussian distribution is symmetric about $\delta = 0$, and its skewness is zero. According to eq. (5), however, the fluctuations with positive initial density contrast δ_1 grow more rapidly than those with $\delta_1 < 0$. Hence, nonlinear interactions introduce asymmetry in the distribution, and we can expect that with time, gravity will induce a non-zero skewness in the distribution.

The earliest (to our knowledge) analytic results of weakly nonlinear calculations were obtained by Zeldovich et al. and Peebles [56, 19, 45]. They considered power-law initial conditions, $P_L \propto k^n$, and showed that unless $n < 4$, the nonlinear terms become larger than linear at large scales, and the perturbation theory breaks down. A somewhat more systematic approach, going beyond scaling relations was introduced in the eighties by Juszkiewicz et al. [33, 34] and Vishniac [53], who used Eulerian perturbation theory and the random phase approximation to study the first non-trivial, weakly-nonlinear corrections for second moments – $P(k,t)$ and $\xi(r,t)$. Peebles [45] used the same approach to calculate the gravitationally induced skewness, while Fry, in a truly seminal paper, showed how to calculate a reduced correlation function of arbitrary order N, using the perturbative expansion, truncated at the $(N-1)$ -st order [23].

Unfortunately, N-body simulations, available in the early eighties were too crude to study the range of validity of perturbative methods. Moreover, the galaxy surveys at scales, large enough to probe the weakly nonlinear regime of clustering, were dominated by noise. This made further progress in analytic calculations difficult and the field became dormant for several years. With time, the dynamical range of the simulations improved by more than an order of magnitude [55]. Simultaneously, the length scales in galaxy surveys, at which correlations can be accurately measured, increased by an order of magnitude [20], making weakly nonlinear theory useful in their analysis. As a result of these developments, the study of the evolution of the mass distribution in the expanding universe has become a rich topic for analytic perturbative methods. The revival of enthusiasm for analytic calculations produced many new results. It is our purpose to briefly summarize some of these new results here. For a more detailed approach, see e.g. the recent lecture notes of Bouchet [?] and the review by Sahni & Coles [48].

1.3 Spatial smoothing

The last issue we need to discuss before moving on to the next section is spatial smoothing. It is useful to employ a field $\bar{\delta}$, such that $\delta(x,t)$ is replaced by $\bar{\delta}_1 + \bar{\delta}_2 + \ldots$, with

$$\bar{\delta}_N(x,t) = \int \delta_N(x',t)\, w(|x-x'|/R)\, d^3x' \,, \tag{11}$$

where $w(x/R)$ is a spherically symmetric window function. R is the characteristic comoving smoothing length: w decreases rapidly for $x/R \gg 1$. Its Fourier representation acts as a low pass filter, suppressing the fuctuations with wavenumbers $k \gg 1/R$. The usual normalization condition requires $\int d^3r\, w(r) = 1$. Smoothing over a ball of radius R is also called "top hat" smoothing; another popular filter is a fuzzy ball with a Gaussian profile of width R. Note that the effects of smoothing and gravitational evolution are interchangeable only for δ_1; for terms of second or higher order, these two effects *do not* commute (this is evident from eq. (5); see also [30]). For a power-law initial spectrum, the smoothed linear variance is

$$\langle \bar{\delta}_1^2 \rangle = \sigma_L^2(R,t) = \int w(x_1/R) w(x_2/R) \xi_L(|x_1 - x_2|)\, d^3x_1 d^3x_2 \propto R^{-(n+3)}\,, \tag{12}$$

so the condition $n > -3$ ensures that the clustering process is hierarchical, and proceeds from small to large scales. (this constraint, together with the Zeldovich-Peebles condition $n < 4$, broadly determines the range of "reasonable" values of n; a mix of observational arguments and theoretical prejudce shrinks this range to $-2 \lesssim n \lesssim 1$, see e.g. [46]). The smoothing procedure is needed for at least two reasons. First, at any stage of the evolution, in order to be able to use the perturbation theory, we need to smooth-out the strong nonlinearities. In all hierarchical models, this can be done by any a low pass filter of width $R > R_{nl}$, where $R_{nl}(t)$ is the current nonlinear scale, defined by the condition $\sigma_L^2(R_{nl}, t) = 1$. The second reason for introducing the smoothing is practical: all observable quantities, derived from galaxy surveys or numerical experiments, involve spatial smoothing. Hereafter, we will deal with smoothed fields almost without exceptions (which will be explicitly stated), so to simplify notation, we will omit the bars over δ and δ_N. Generally, we will also assume Gaussian initial conditions (again, all exceptions will be properly described).

2 New results for the second moment; the previrialization conjecture

The perturbative series (3) can be used to expand the second moment of the density field in powers of the linear variance, σ_L^2. Squaring δ and averaging, we get

$$\sigma^2 \equiv \langle \delta^2 \rangle = \langle \delta_1^2 \rangle + \langle \delta_2^2 \rangle + 2\langle \delta_1 \delta_3 \rangle + \ldots = \sigma_L^2 + (I_{22} + I_{13})\, \sigma_L^4 + \mathcal{O}(\sigma_L^6). \tag{13}$$

The second and third term in this expansion are the lowest order nonlinear corrections to linear theory. These terms are of order σ_L^4 because $\mathcal{O}(\sigma_L^3)$ terms vanish under the random phase assumption. The quantities I_{22} and I_{13} can be determined from perturbation theory. They were recently calculated for power-law initial conditions by Scoccimarro & Frieman [50] and by Lokas et al. [41]. Scoccimarro & Frieman explored the evolution of an unsmoothed density field. Lokas et al. studied spatially smoothed fields, and found that nonlinear tidal interactions redistribute the power in the spectrum in such a way, that for $n > -1$, the correction $I_{22}+I_{13}$ is negative. The growth rate of density fluctuations is inhibited: σ is smaller than the linear prediction σ_L. The magnitude of this suppression increases with n, or with the relative amount of small scale power in the initial spectrum. For $n < -1$, there is an opposite effect – the fluctuation growth rate is enhanced ($\sigma > \sigma_L$). The transition occurs at $n = -1$, when the correction is close to zero and $\sigma \approx \sigma_L$. Lokas et al. compared these perturbative results with a series of N-body simulations and found a good agreement in a wide dynamical range, up to $\sigma \approx 1$. These results are in qualitative agreement with the so-called *previrialization conjecture* of Davis & Peebles [18]. According to Davis & Peebles, tidally induced nonradial motions of small scale inhomogeneities within collapsing mass concentrations should resist gravity and slow down the collapse. Until recently the size of the previrialization effect was still under discussion, with some N-body studies reproducing the effect and others claiming its absence. For example, Peebles [47] found strong support for the previrialization effect, while Evrard & Crone [21] reached opposite conclusions. This apparent controversy can be resolved, using the perturbative results we just discussed. Indeed, Peebles in his simulations assumed $n = 0$, while Evrard & Crone assumed $n = -1$: a spectral index, for which nonlinear effects are minimal.

Jain & Bertschinger [32] used perturbation theory and N-body experiments to investigate the nonlinear transfer of power in a CDM spectrum. Their results are consistent with Lokas et al. and Scoccimarro & Frieman. Finally, we must mention the important work of Makino et al. [42], who succeeded in reducing the dimensionality of the mode coupling integrals of Vishniac and Juszkiewicz et al. [53, 34]. This significantly simplified the derivation of all of the new results described in this section.

3 The third moment and deviations from Gaussian behavior

As we saw in Section 1, nonlinear gravitational evolution drives the field δ away from the initial Gaussian distribution. Deviations from Gaussianity can be measured by *cumulants*, also called "reduced" or "connected" moments. A cumulant of order N is

$$M_N \equiv \partial^N \ln \langle e^{x\delta} \rangle / \partial x^N , \qquad evaluated\ at\ x = 0 . \tag{14}$$

For the first four cumulants, this expression generates the mean, $M_1 = \langle \delta \rangle = 0$, the variance, $M_2 = \langle \delta^2 \rangle = \sigma^2$, the skewness, $M_3 = \langle \delta^3 \rangle$, and the kurtosis, $M_4 = \langle \delta^4 \rangle - 3\sigma^4$. For a zero-mean Gaussian distribution, all cumulants vanish except M_2. The skewness measures the asymmetry of the distribution, while the kurtosis measures the flattening of the tails relative to a Gaussian. Using perturbation theory, Fry [23] showed that in an Einstein-de Sitter universe, M_N scale like σ^{2N-2}. Hence, to lowest non-vanishing order in perturbation theory, the ratio

$$S_N \equiv M_N / \sigma^{2N-2} \tag{15}$$

is time-independent. Juszkiewicz et al. [36] have recently used this property and the Edgeworth series to describe the weakly nonlinear evolution of the probability distribution function (PDF) of the density field. The Edgeworth expansion is a standard statistical tool, used to represent quasi-gaussian probability distribution functions (PDFs). Juszkiewicz et al. obtained an expansion in powers σ, with the first few terms, given by

$$p(\nu) = \left[1 + \tfrac{1}{3!} S_3 H_3(\nu)\sigma + \left\{ \tfrac{1}{4!} S_4 H_4(\nu) + \tfrac{10}{6!} S_3^2 H_6(\nu) \right\} \sigma^2 \right] g(\nu) + \mathcal{O}\left(g(\nu)\sigma^4\right) , \tag{16}$$

where $\nu = \delta/\sigma$, $g = (2\pi)^{-1/2} \exp(-\nu^2/2)$, and H_J is a Hermite polynomial of degree J. A similar expansion was obtained independently by Bernardeau & Kofman [4]. The Edgeworth expansion is particuraly useful when only a few low-order reduced moments are known; it can be also used to estimate low-order S_N -s from the shape of empirically measured PDF near the peak (in realistic situations, the tails, and/or high-N moments are poorly known anyway). An alternative, Laplace-transform representation for the PDF, which does require the knowledge of all S_N -s to $N = \infty$, was proposed by Bernardeau [5].

3.1 Skewness induced by gravity

The acual values of the parameters S_N can be also calculated perturbatively. The results generally depend on the shape of the initial power spectrum and the shape of the window function. Let us begin with the skewness, responsible for the lowest order nonlinear correction to the Gaussian PDF in eq. (16). Upon raising both sides of equation (3) to the third power and averaging, we get

$$\langle \delta^3 \rangle = S_3 \sigma^4 = \langle \delta_1^3 \rangle + \langle 3\delta_1^2 \delta_2 \rangle + \ldots \tag{17}$$

In models, which satisfy the random phase assumption, the lowest order non-vanishing term in this expansion is $\mathcal{O}(\sigma)^4$. The scaling with σ is completely different in models with non-gaussian initial conditions and an intrinsic skewness $\langle \delta_1^3 \rangle \neq 0$: the lowest order term is $\propto \sigma^3$. The skewness parameter, S_3 in eq. (17) was first calculated by Peebles [45], assuming $\Omega = 1$ and no smoothing. The latter

constraint prevents any comparison of this result with observations or N-body simulations. To deal with this problem, we calculated S_3 for a smoothed density field with a power-law initial spectrum and for two different kinds of spatial filters: a gaussian and a top hat [35]. The result is particularly simple in the latter case,

$$S_3 = \tfrac{34}{7} - (n+3) + \mathcal{O}(\sigma^2) , \tag{18}$$

where the allowed range of power indexes is $-3 \leq n < 1$ (outside of this range S_3 diverges). Note that here, as well as in Section 2, we quote only results for the Einstein-de Sitter case. All these results, however, are also true for a much wider class of models with arbitrary Ω and Λ (this is an approximate statement, but the approximation is good enough for all practical purposes). For example, for $0 \leq \Lambda/3H^2 \leq 1 - \Omega$ and $0.05 \leq \Omega \leq 3$, the term '34/7' in eq. (18) should be replaced by

$$4 + 4\kappa(\Omega) = \tfrac{34}{7} + \tfrac{6}{7}(\Omega^{-0.03} - 1) . \tag{19}$$

The corrections, introduced by deviations from the Einstein-de Sitter model were first derived by Bouchet et al. [8] for arbitrary Ω, and by Bernardeau [2] and Bouchet et al. for arbitrary Λ [10]. These results were recently confirmed by Catelan et al. [14], who used a significantly different method of derivation. For our purposes here, the most important implication of all this is that Gaussian initial conditions and weakly nonlinear gravitational instability generate the scaling relation

$$M_N \propto \sigma^{2N-2} \qquad (\sigma < 1) , \tag{20}$$

and S_N, the ratio of the above moments, up to terms of order σ^2 in perturbation theory is time-, Ω- and Λ-independent; it is determined only by the shape of the initial power spectrum. Bernardeau [2] generalized eq. (18) for a smoothing scale-dependent slope, $n = n(R)$. He showed, that this expression for $S_3(R)$ remains valid when n is replaced by the effective local slope,

$$n(R) = -d(\log \sigma_L^2(R))/d(\log R) - 3 . \tag{21}$$

As we have seen, to lowest non-vanishing order in perturbation theory, S_3 is time independent. We can expect that $S_3(R)$ will be scale-independent as well in the range of smoothing scales, for which $n(R)$ is constant. A completely different picture arises when the primeval PDF is significantly skew. The lowest order non-vanishing contribution to skewness gives

$$S_3(R) \propto 1/\sigma_L \propto R^{-(n+3)/2} D(t)^{-1} , \tag{22}$$

so in all hierarchical ($n > -3$) models we can expect a strong scale- and time-dependence, with S_3 "blowing up" at large scales and at high redshift. As pointed out by several authors, this property can be used to distinguish observationally Gaussian initial conditions from their non-gaussian alternatives [17, 35, 49]. Chodorowski & Bouchet [16] find that the distinction can be made even sharper by studying the scaling properties of S_4 (see also Fry & Scherrer [25]).

Using methods similar to those discussed above, Catelan & Moscardini [15], Lokas et al. [40], and Bernardeau [2] calculated the parameter S_4 for power-law spectra and top hat as well as Gaussian windows. The last two papers also provide closed-form expressions for $S_4 = S_4(n)$. Bernardeau [5] solved the problem of calculating S_N -s of arbitrarily high order for top hat smoothing.

Most of the above perturbative results for S_3 and S_4 were tested against N-body simulations [1, 7, 35, 36, 38, 40, 54], showing remarkable agreement up to $\sigma \approx 1$. On a comoving scale R, the Edgeworth expansion agrees with the N-body simulations within $\sim 1/\sigma(R)$ standard deviations from zero [36]. The Laplace transform perturbative PDF agrees with the N-body PDF even when σ is slightly greater than unity [5].

3.2 Velocity statistics

Unlike the reduced moments of the density field, the cumulants of the *expansion scalar*, $\theta = \nabla \cdot v/H$ are very sensitive to the value of Ω. For example, the skewness parameter is given by [3]

$$\langle \theta^3 \rangle / \langle \theta^2 \rangle^2 = -\Omega^{-0.6} \left[\tfrac{26}{7} - (n+3) \right] . \tag{23}$$

In principle, this can provide a new method of determining Ω from the velocity data alone (rather than from the comparison with the density field, as in more conventional methods). The existing velocity surveys, however, are by far too shallow to allow accurate measurements of the variance and skewness of θ. We have to wait for better data. Weakly nonlinear theory can also be used to study the dynamics of relative motions in pairs of galaxies, which induce the anisotropy of the redshift space galaxy correlations [37]. This can improve the accuracy of Ω determinations from presently available redshift surveys.

3.3 Lagrangian methods

So far, we have focused on Eulerian perturbation theory. An interesting alternative is the Lagrangian approach. It follows particle trajectories rather than the evolution of $\delta(x,t)$. The local density is $\delta = 1/J - 1$, where J is the Jacobian of the transformation from initial particle positions to positions at time t. The famous Zeldovich approximation [57] is a linear order Lagrange solution. In its original form, it can not be used for statistical studies because it predicts infinite cumulants for δ. As pointed out by Grinstein & Wise [29], the problem can be at least partially fixed by expanding $1/J - 1$ in powers of spatial derivatives of the linear order Eulerian velocity field. The cumulants, generated by such an expansion are finite. Unfortunately, however, they disagree with the proper Eulerian perturbation theory and with all N-body experiments [15, 35, 36]. The Zeldovich approximation fails particularly badly when applied to the velocity divergence, θ [3, 36]. Two lessons follow from this example. The first is that dynamical estimates of Ω, derived from reconstruction schemes for the initial PDF of δ or θ, which rely entirely on the Zeldovich approximation (see e.g. [44]), should be treated with caution. The second lesson is positive: the Zeldovich approach is more powerful than it seems. For example, under this approximation, $\kappa = 0$ in eq. (19) and therefore for a top hat $S_3 = 4 - (n + 3)$. Depending on n, this causes about 20% to 50% underestimate of the true S_3, derived from second order Eulerian theory. Note however, that we used *first order* Lagrangian theory to derive the Zeldovich prediction for S_3. To make a fair comparison, we should confront this result with its first order Eulerian counterpart: the linear prediction $S_3 = 0$, which is much further away from the true value! What we have just seen, is an illustration of a more general phenomenon: at any fixed order in perturbation theory, the Lagrangian approach is likely to remain valid for stronger density contrasts than the Eulerian approach. This happens because the requirement of the smallness of the (Lagrangian) particle displacements is less restrictive than the requirement of the smallness of $|\delta|$. This idea, which must have motivated Zeldovich, remains valid at higher orders in perturbation theory. The idea to extend the Lagrangian perturbation theory beyond the linear order was introduced by Moutarde et al. [43] and generalized by Bouchet et al. [8] and Buchert & Ehlers [13]. Lagrangian coordinates have been used to derive second- and third-order perturbative solutions in the Einstein-de Sitter case [12, 13], as well as in more general cosmological models [8, 10], and to study distortions of correlations in redshift space [10, 31]. We are convinced that the full potential of this approach to perturbation theory is far from being exhausted.

3.4 Convergence studies

As we have seen, perturbative expansions for $\langle\delta^2\rangle$ and $\langle\delta^3\rangle$, truncated at the lowest-order or next to the lowest-order non-vanishing contribution, are in remarkable agreement with N-body simulations in a wide dynamical range, up to $\sigma \approx 1$. The precise range of validity of perturbation theory is still under investigation. Apart from comparisons with N-body experiments, the convergence can be also studied within the perturbation theory itself, by comparing contributions coming from terms of increasing order. Such studies may answer the question: why does perturbation theory work so well?

Scoccimarro & Frieman [50] obtained closed-form expressions for $I_2 = I_{22} + I_{13}$ in the case of no smoothing ($R = 0$). Although individually, I_{22} and I_{13} suffer from "infrared" ($k \to 0$) divergencies, their sum is finite and approximately n-independent; for $-2 \leq n \leq 2$, $I_2 \approx 1.82$ [41, 50]. The divergent terms cancel each other; the probable source of this phenomenon is the Galilean invariance

of the equations of motion [50]. Łokas et al. studied "ultraviolet" ($k \to \infty$) divergences which occur for $n > -1$, when the smoothing length is finite ($R \neq 0$). They found that I_2 diverges unless $P_L(k)$ has a shortwave cutoff at $k = k_c$. For $k_c R \gg 1$, the correction term is [41] $I_2 \approx -(0.6 k_c R)^{n+1}$ (a shortwave cutoff appears in all N-body experiments, where k_c^{-1} corresponds to the mean interparticle separation, or the Nyquist scale). Scoccimarro & Frieman have also calculated the $\mathcal{O}(\sigma^2)$ term in the expansion for S_3 (eq. (18)). They found that $\mathcal{O}(\sigma_L^2)$ terms in the expansions for S_3 and σ^2/σ_L^2 do not "overtake" the lowest-order non-vanishing terms until $\sigma \approx 0.5$, in agreement with the results of direct N-body tests of perturbation theory, which we already discussed.

4 Observations

Before comparing theoretical predictions to observations, let us discuss two possible sources of confusion.

1. Biasing. If galaxies form with different efficiency in different environments, then the galaxy distribution may paint a biased picture of the underlying mass distribution. Let us suppose that the smoothed galaxy field δ_g is a local, but not necessarily linear function of the smoothed mass density field: $\delta_g(x) = f[\delta(x)]$, where f is an arbitrary function. Then, using a Taylor expansion for $|\delta| \ll 1$, it is possible to prove, as Fry & Gaztañaga [24] did, that local bias preserves the form of the scaling relations (20), while changing the constants S_N. For example, S_3 changes to [24, 36]

$$S_{3g} \equiv \langle \delta_g^3 \rangle / \langle \delta_2^2 \rangle = S_3/b_1 + 3b_2/b_1^2 , \tag{24}$$

where $b_J \equiv d^J f / d\delta^J$, evaluated at $\delta = 0$ (note that the linear bias model with all $b_J = 0$ for $J > 1$ must break down when $b > 1$ and $\delta < -1/b$, since it predicts negative δ_g).

2. Redshift distortions. Redshift surveys use radial velocities of galaxies instead of their true radial coordinates. As a result, galaxy peculiar motions distort the true spatial distribution and the two-point correlation function, ξ (cf. §20 in [46] and references therein). Bouchet et al. [10] and Hivon et al. [31] have used weakly nonlinear perturbation theory and N-body simulations to study the effects of redshift space distortions on the three-point correlation function, ζ, and on S_3. They showed that although ζ, like ξ, is affected by the redshift space distortion, all appreciable, Ω-dependent effects cancel out for the moment ratio S_3. In the weakly-nonlinear domain, when $\sigma < 1$, and for spectral slopes $-3 \leq n \leq -1$, the differences between redshift-space S_3 and its true value are smaller than 10%, whatever the value of Ω. Hence, the comparison between theoretical predictions and observations is not obscured by redshift space distortions provided we use the moment ratio S_3 rather than reduced moments themselves.

The parameters S_3 and S_4 have been estimated from the CfA and SSRS surveys [26], the *IRAS* 1.2 Jy sample [9], as well as for vaious angular catalogues [27, 52]. All these measurements show beautiful agreement with the predicted scaling relation (20). The dependence (24) of S_{3g} on the shape of the bias function may explain why the value measured by Bouchet et al. [9] from the top-hat smoothed, *IRAS* redshift survey is rather low, $S_{3g}^{IRAS} \sim 1.5$. The galaxies observable in the infrared are underrepresented in rich clusters relative to optical galaxies, so the "bias function" that applies to *IRAS* galaxies may have negative curvature ($b_2 < 0$), pushing S_{3g} below the value of S_3 for the mass. If cluster avoidance is indeed the cause of the low value of S_{3g}^{IRAS}, then one would expect that optically selected surveys would yield higher values. The values of S_{3g}, obtained recently by Gaztañaga [27] from the APM survey suggest that this is exactly the case. The value of S_{3g}, deprojected from the two-dimensional APM data onto three-dimensional space is 3.16 ± 0.14, assuming a top-hat filter with a radius $R > 7\, h^{-1}$ Mpc (here h is the Hubble constant in units $100\, km\, s^{-1} Mpc^{-1}$; the latter condition ensures $\sigma_g < 1$). Substituting $n = -1$, appropriate for the slope, seen in the APM survey on these scales, into equation (18) yields $S_3 = 2.9$. Hence, for sufficiently large scales, the APM results are

in perfect agreement with second order perturbation theory: $S_{3g}^{APM} = S_3$. This agreement provides support for three theoretical assumptions: first, that gravitational instability is responsible for the growth of clustering; second, that the initial conditions were Gausssian; and third, that the APM galaxies trace the mass, i.e., in eq. (24) $b_1^{APM} \approx 1$ and $b_2^{APM} \approx 0$ (of course, other combinations of b_1 and b_2 also fit the APM data, but they require a coincidental compensation of the linear, $1/b_1$ factor by the b_2 term arising from nonlinear bias). This is bad news non-local biasing models like the model of Bower et al. [11], invoked in a desperate attempt to explain the mismatch of the observed power spectrum with standard CDM. Indeed, as demonstrated by Frieman & Gaztañaga [22], such models break the scaling relation (20) and are incompatible with observations. Most recently, Gaztañaga & Mähönen [28] have used the APM data to severely constrain the so-called global texture model. The source of problems for this model is its prediction that S_J parameters must 'blow up' at large scales, like S_3 in our example in eq. (22). There is no trace of such behaviour in the APM galaxy distribution. Since the already available data can be used to constrain non-local biasing schemes and deviations from Gaussian distribution, we can expect that in the new generations of catalogues (like the SDSS and the 2dF, described in these proceedings) will finally tell us whether all we are looking at is just a Gaussian random process modified by plain gravity.

Acknowledgements. We are grateful to the Organizers, Chantal Balkowski, Sophie Maurogordato, and J. Trân Thanh Vân, for making this scientifically useful meeting happen; to Mother Nature for providing good skiing conditions, and last but not least, to Chantal and Sophie as Editors, for their incredible patience with the authors, who broke several submission deadlines for this manuscript. This research was supported by the Polish Government KBN grants No. 2-P304-01607, 2-P304-01707, and by an NSF grant No. PHY94-07194. RJ thanks Alain Omont for his hospitality at Institut d'Astrophysique de Paris, CNRS, where part of the work reviewed here was done.

References

[1] Baugh, C.M., Gaztañaga, E., Efstathiou, G., 1994, *Mon. Not. R. astr. Soc.* **274**, 1049.

[2] Bernardeau, F., 1994, *Ap. J.* **433**, 1.

[3] Bernardeau, F., Juszkiewicz, R., Dekel, A., Bouchet, F.R., 1995, *Mon. Not. R. astr. Soc.* **274**, 20.

[4] Bernardeau, F., & Kofman, L., 1995, *Ap. J.* **443**, 479.

[5] Bernardeau, F., 1994, *Astr. Astrophys.* **291**, 697.

[6] Bouchet, F. R. 1995, Proceedings of the "Enrico Fermi" School "Dark Matter in the Universe" held in Varenna (Societa Italiana di Fisica).

[7] Bouchet, F.R., Hernquist, L., 1992, *Ap. J.* **400**, 25.

[8] Bouchet, F.R., Juszkiewicz, R., Colombi, S., Pellat, R., 1992, *Ap. J. (Letters)* **394**, L5.

[9] Bouchet, F.R., Strauss, M., Davis, M., Fisher, K.B., Yahil, A., & Huchra, J.P., 1993, *Ap. J.* **417**, 36.

[10] Bouchet, F.R., Colombi, S., Hivon, E., & Juszkiewicz, R., 1995, *Astr. Astrophys.* **296**, 575.

[11] Bower, R.G., Coles, P., Frenk, C.S., & White, S.D.M., 1993, *Ap. J.* **405**, 403.

[12] Buchert, T., 1994, *Mon. Not. R. astr. Soc.* **267**, 811.

[13] Buchert, T., & Ehlers, J., 1993, *Mon. Not. R. astr. Soc.* **264**, 375.

[14] Catelan, P., Lucchin, F., Mattarrese, S., Moscardini, L., 1995, *Mon. Not. R. astr. Soc.* **276**, 39.

[15] Catelan, P., & Moscardini, L., 1994, *Ap. J.* **426**, 14.

[16] Chodorowski, M., & Bouchet, F.R., 1996, *Mon. Not. R. astr. Soc.*, in press.

[17] Coles, P., Frenk, C.S., 1991, *Mon. Not. R. astr. Soc.* **253**, 727.

[18] Davis, M., & Peebles, P.J.E., 1977, *Astrophys. J. Suppl. Ser.* **34**, 425.

[19] Doroshkevich, A.G., Zeldovich, Ya. B., 1975 *Astrophys. Space. Sci.* **35**, 55.

[20] Efstathiou, G., 1996, *in: Les Houches Lectures, Session LX*, ed. R. Schaeffer, Elsevier Science Publishers (Netherlands).

[21] Evrard, A.E., & Crone, M.M., 1992, *Ap. J. (Letters)* **394**, L1.

[22] Frieman, J., & Gaztañaga, E., *Ap. J.* **425**, 392.

[23] Fry, J.N., 1984, *Ap. J.* **279**, 499.

[24] Fry, J.N., & Gaztañaga, E., 1993, *Ap. J.* **413**, 447.

[25] Fry, J.N., & Scherrer, R.J. 1994, *Ap. J.* **279**, 36.

[26] Gaztañaga, E., 1992, *Ap. J. (Letters)* **398**, L17.

[27] Gaztañaga, E., 1994, *Mon. Not. R. astr. Soc.* **268**, 913.

[28] Gaztañaga, E., & Mähönen, P., 1996, *Ap. J. (Letters)*, in press

[29] Grinstein, B., & Wise, M.B., 1987, *Ap. J.* **314**, 448.

[30] Goroff, M.H., Grinstein, B., Rey, S.-J., & Wise, M.B., 1986, *Ap. J.* **311**, 6.

[31] Hivon, E., Bouchet, F.R., Colombi, S., & Juszkiewicz, R., 1995, *Astr. Astrophys.* **298**, 643.

[32] Jain, B., Bertschinger, E., 1994, *Ap. J.* **431**, 495.

[33] Juszkiewicz, R., 1981, *Mon. Not. R. astr. Soc.* **197**, 931.

[34] Juszkiewicz, R., Sonoda, D.H., & Barrow, J.D., 1984, *Mon. Not. R. astr. Soc.* **209**, 139.

[35] Juszkiewicz, R., Bouchet, F.R., & Colombi, S., 1993, *Ap. J. (Letters)* **412**, L9.

[36] Juszkiewicz, R., Weinberg, D.H., Amsterdamski, P., Chodorowski, M., & Bouchet, F., 1995, *Ap. J.* **442**, 39.

[37] Juszkiewicz, R., Fisher, K.B., & Szapudi, I., 1996, *Ap. J.*, in press.

[38] Lahav, O., Itoh, M., Inagaki, S., & Suto, Y., 1993, *Ap. J.* **402**, 387.

[39] Lifshitz, E.M., 1946, *J. Phys. U.S.S.R.* **10**, 116, (*Zh.E.T.F.* **16**, 587).

[40] Lokas, E.-L., Juszkiewicz, R., Weinberg, D.H., & Bouchet, F.R., 1995, *Mon. Not. R. astr. Soc.* **274**, 730.

[41] Lokas, E.-L., Juszkiewicz, R., Bouchet, F.R., & Hivon, E., 1996, *Ap. J.*, in press.

[42] Makino N., Sasaki M., Suto, Y., 1992, *Phys. Rev.* **D46**, 585.

[43] Moutarde, F., Alimi, J.-M., Bouchet, F.R., & Pellat, R., 1991, *Ap. J.* **382**, 377.

[44] Nusser, A., & Dekel, A., 1993, *Ap. J.* **405**, 437.

[45] Peebles, P.J.E., 1980, *The Large-Scale Structure of the Universe* (Princeton University Press: Princeton).

[46] Peebles, P.J.E., 1993, *Principles of Physical Cosmology* (Princeton University Press: Princeton).

[47] Peebles, P.J.E., 1990, *Ap. J.* **365**, 27.

[48] Sahni, V., & Coles, P., 1995, *Physics Reports*, in press (preprint SISSA astro-ph/9505005).

[49] Silk, J., & Juszkiewicz, R., 1991, *Nature* **353**, 386.

[50] Scoccimarro, R., & Frieman, J., 1995, Fermilab preprint.

[51] Strauss, M.A., & Willick, J.A., 1995, *Physics reports*, 261, 271, inpress (preprint SISSA astro-ph/9502079).

[52] Szapudi, I., Dalton, G., Efstathiou, G., & Szalay, A.S., 1995, preprint.

[53] Vishniac, E., 1983, *Mon. Not. R. astr. Soc.* **203**, 345.

[54] Weinberg, D.H., & Cole, S., 1992, *Mon. Not. R. astr. Soc.* **259**, 652.

[55] White, S.D.M., 1996, *in: Les Houches Lectures, Session LX*, ed. R. Schaeffer (Elsevier Science Publishers: Netherlands).

[56] Zeldovich, Ya.B., 1965, *Adv. Asron. Astrophys.* **3**, 241.

[57] Zeldovich, Ya.B., 1970, *Astr. Astrophys.* **5**, 84.

PROPERTIES OF THE DENSITY PDF-s IN THE QUASI-LINEAR REGIME

F. Bernardeau
Service de Physique Théorique, C.E. de Saclay,
F-91191 Gif-sur-Yvette, France

Abstract

Perturbation Theory applied to large-scale cosmological fields for Gaussian initial condition provides us with a large variety of statistical properties of the cosmological density field, such as the expected behaviour of the high order moments of the counts in cells probability distribution functions. In this contribution I present the general framework of these calculations, and their domain of validity. In particular I apply these statistical indicators to galaxy angular surveys and stress that the observations in the APM angular survey points towards a slightly biased galaxy distribution

1 The Perturbation Theory

In this presentation the perturbation theory (PT) is not used to improve upon the results obtained from the linear theories (like the growing rate of the fluctuation, the density velocity relationship), but to broaden our knowledge of the statistical properties of the large-scale cosmological fields. Indeed, even if the linear theory has been proved to give accurate predictions for the width of the local smoothed density probability distribution function (PDF) when the r.m.s. of the density fluctuation approaches unity, it is unable to predict the actual shape of the density PDF, especially the shape of the rare event tails. These non-Gaussian features are indeed sensitive to nonlinear effects in the dynamical evolution of the fields, that can only be investigated with higher order PT calculations.

1.1 Principles of PT calculations

The principles of these calculations have been initially presented by Peebles [18], then explored in more details in a series of more recent papers [9, 12, 6, 2, 13, 14, 3]. The starting point of all these calculations is the system of field equations, Continuity, Euler and Poisson equations, describing a single stream pressure-less fluid. The density field which satisfies those equations is then expanded with respect to the initial fluctuation field, $\delta(\mathbf{x}) = \sum_i \delta^{(i)}(\mathbf{x})$. As the shape of the density PDF is directly related to the cumulants, $\langle\delta^p\rangle_c$, the latter have to be evaluated in the regime we are interested in. In the quasi-linear regime, when the r.m.s. of the density fluctuations, σ, is small, these cumulants are given by their lowest order in σ which can be calculated by PT techniques. Assuming that the initial field is Gaussian, one can show [9, 12, 2] that the cumulants follow the hierarchy,

$$\langle\delta^p\rangle_c = S_p\langle\delta^2\rangle^{p-1}, \tag{1}$$

and the coefficients S_p can be calculated for $\sigma \to 0$. Their values depend on the shape of the power spectrum and on the *window function*. For the case where the whole series of these coefficients can be calculated the shape of the density PDF is given by the integral,

$$P(\varrho)\mathrm{d}\varrho = \frac{\mathrm{d}\varrho}{2\pi\mathrm{i}\sigma^2}\int_{-\mathrm{i}\infty}^{+\mathrm{i}\infty}\mathrm{d}y\exp\left[\sum_{p=2}^{\infty}\frac{S_p}{p!}\frac{(-y)^p}{\sigma^2}+\frac{\varrho y}{\sigma^2}\right]. \tag{2}$$

Note that in case that only a limited number of S_p coefficients are known this integral can be estimated by expanding it with respect to σ. We are then led to an approximate expression of the density PDF [5, 14], the Edgeworth expansion, which describes accurately the shape of the density PDF around its maximum.

2 The density PDF in 3D catalogues

As a consequence of the remarks of the previous section the whole problem of the determination of the shape of the density PDF, relies on the calculation of the S_p coefficients. They have proved to be difficult to obtain when the shape of the window function is properly taken into account. Results have been obtained, laboriously, for Gaussian window functions [14, 17], but the most complete set of results have been obtained for top-hat window functions [3].

2.1 The theoretical results

I give here the expression of the first two coefficient S_3 and S_4, valid for any power spectrum,

$$S_3 = \frac{34}{7} + \gamma(R_0); \tag{3}$$

$$S_4 = \frac{60712}{1323} + \frac{62\gamma(R_0)}{3} + \frac{7\gamma(R_0)^2}{3} + \frac{2}{3}\frac{\mathrm{d}\gamma(R_0)}{\mathrm{d}\log R_0}; \tag{4}$$

with

$$\gamma = \frac{\mathrm{d}\log\sigma^2(R_0)}{\mathrm{d}\log R_0}. \tag{5}$$

One can notice that S_3 depends only on the local slope, and that S_4 also depends (but weakly) on the variations of that slope. These results are valid for an Einstein-de Sitter Universe but are found to be weakly Ω and Λ dependent [6].

2.2 Comparison with numerical simulation

The comparisons with numerical simulations have been done with a remarkable success for the S_p parameters up to $p = 11$ [1], and also, using equation 2, for the shape of the density PDF [3]. In figure 1 I give the comparison of the predicted density PDF-s (solid lines) compared to their actual measurements in a numerical simulation.

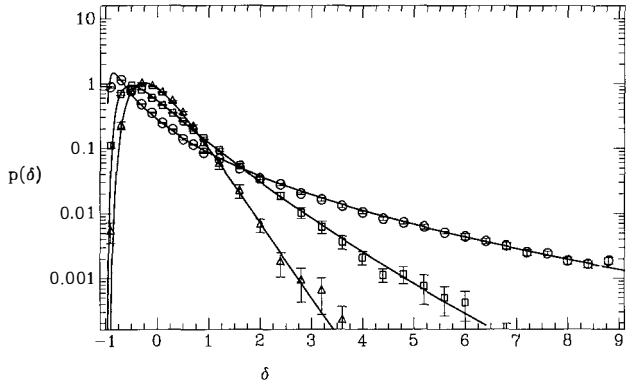


Figure 1. Comparison of the PT predictions with results of a numerical simulation with CDM initial conditions for the one–point probability distribution function of the density contrast. The density PDF has been measured at three different radius, $R = 5$ h^{-1}Mpc (circles), $R = 10$ h^{-1}Mpc (squares), $R = 15$ h^{-1}Mpc (triangles). The values of σ are respectively, $\sigma = 1.52, 0.74, 0.47$.

These results, showing perfect agreement between the theoretical predictions and the numerical results, gave us confidence in the accuracy of the PT predictions.

Direct measurement of such a PDF in the galaxy catalogues is however difficult to obtained. Several difficulties have to be overcome:

- poor statistics with quite sparse samples which induces large errors on the moments [8];
- redshift effects affecting the redshift space-real space transformation, that is however expected to be small in the quasi-linear regime [16];
- possible biases associated with galaxies.

An estimation of S_3 and S_4 in the IRAS catalogue [7] was anyway quite encouraging. The hierarchy given in equation 1 was indeed observed. The value of S_3 was however smaller than the one expected from the theoretical calculations. This is thought to be due to biases affected the IRAS galaxies, known to be relatively rare in clusters.

3 Correlation properties in angular surveys

One way to overcome some of the problems associated with statistics in redshift surveys is to use the angular surveys. The main advantages are that the statistics is far more important (with more than 10^6 objects in the APM angular survey), that the redshift effects are naturally absent.

The results, however, cannot be directly compared to the coefficients S_p obtained for a 3D top-hat filtering as those given in Equations 3 and 4. A new proper calculations of these

coefficients has to be done, taking into account the superposition of scale, in a similar way as in the Limber equations [15].

3.1 The small angle approximation

When one assumes that the filtering angle, θ_0, is small it is possible to simplify dramatically the calculations of the coefficient S_p (denoted s_p for angular surveys in the following) [10, 4]. The coefficients s_p are then expected to take the form

$$s_p = R_p \; \Sigma_p(n) \tag{6}$$

where Σ_p is a function of the power-law index n only and R_p a rather simple function of the index n and the selection function $F(r)$,

$$R_p = \frac{M_1^{p-2}(3) \; M_p[3p - (p-1)(n+3)]}{M_2^{p-1}(3-n)} \tag{7}$$

with

$$M_p(a) = \int_0^\infty \mathrm{d}r \; r^{a-1} \; F^p(r). \tag{8}$$

This is a key property which implies that, in the limit of small angles, the dependence with the shape of the selection function is factorized and very simple. Note that the parameters R_p are generally greater but close to unity.

The actual values of the coefficients Σ_p depend on the angular window function. They can be calculated exactly in case of a top-hat angular window function [4].

3.2 The theoretical results

I give here the first two coefficients Σ_p as a function n,

$$\Sigma_3 = \frac{36}{7} - \frac{3\,(n+2)}{2}, \qquad \Sigma_4 = \frac{2540}{49} - 33\,(n+2) + \frac{21\;(n+2)^2}{4}. \tag{9}$$

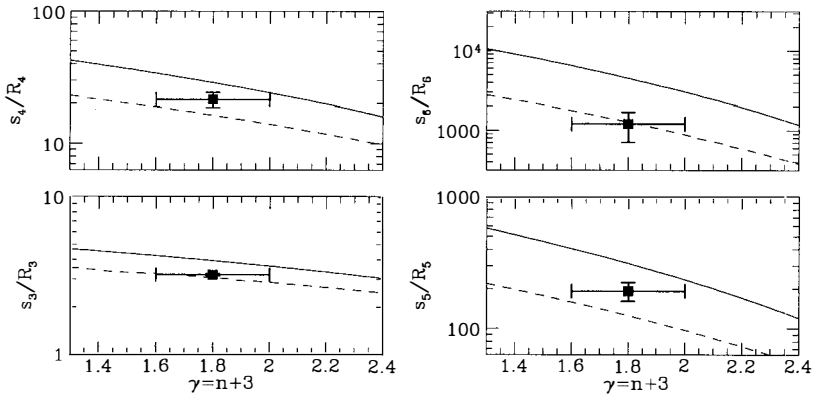


Figure 2. The ratios Σ_p as a function of the power law index, γ (solid lines) for $p = 3, \ldots, 6$ and for an Einstein-de Sitter Universe. The ratios S_p (Eq. [1]) for 3D statistics are represented by dashed lines, and the points are the observed values in the APM angular survey [10]

In Figure 2 I plot these coefficients up to $p = 6$ as a function of $\gamma = n + 3$ and compare them with the S_p coefficients obtained in case of 3D top-hat filtering. The latter are shown to be significantly smaller.

3.3 Comparison with observation and validity of the small angle approximation

For comparison with the observation I use the results obtained by Gaztañaga [10] in the angular APM survey. The observed values are seen to be systematically lower than the theoretical predictions.

One should have in mind however that the theoretical predictions have been obtained with the small angle approximation. This is somehow in conflict with the assumption that we want to test the quasi-linear regime. For the depth of the APM survey the angular scale we are interested in is for $\theta_0 \gtrsim 1^o$. It is not clear, however, that the small angle approximation is valid for such filtering angles. In order to test this approximation I computed the exact (with PT) dependence of s_3 with the filtering angle. The result depends obviously on the selection function $F(r)$. I adopted the following form,

$$F(r) \propto r^{-0.5} \exp\left[-\left(\frac{r}{D}\right)^2\right]. \tag{10}$$

I also assume that the 2-point correlation function is well described by a power-law behavior with $\gamma = 1.7$ and $r_0 = 5h^{-1}$Mpc. It reproduces reasonably well the observed angular mean two-point correlation function in the APM galaxy survey for $\theta_0 \lesssim 2^o$. The resulting s_3 parameters are given in Fig. 3 for two cosmological models, $\Omega = 1$ and $\Omega \ll 1$.

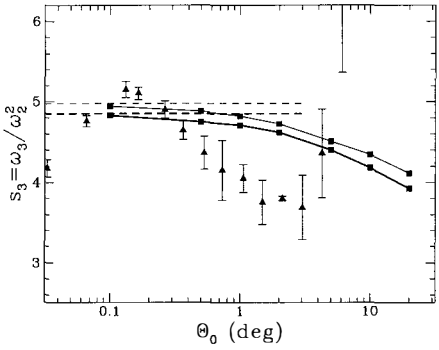


Figure 3. The value of s_3 as a function of the smoothing angle for the model given by equation 10. The dashed lines correspond to the small angle limits; the thin lines to the $\Omega \ll 1$ case; the thick lines to the $\Omega = 1$ case. The triangles correspond to the observations in the APM galaxy survey [10]

The small angle approximation is found to be reasonably good at the angular scale of interest. The two-point correlation function was on the other hand quite crudely parameterized. The power-law behavior is known to break down at angular scale $\theta_0 \gtrsim 2^o$ which may significantly affect the result, and decrease the value of s_3. On the other hand, at angular scales of about $0.2,\ 0.3^o$ nonlinear correction are expected to increase the value of s_3 (see for instance the paper

[1]). The angular scale dependence of the observed value of s_3 is thus roughly in agreement with what is expected but the normalization is not in very good agreement (contrary to conclusions of a previous analysis [11]). Note, however, that the redshift evolution of the number density of galaxies or their correlation properties has also not been taken into account.

If anyway, more precise numerical calculations of $s_3(\theta_0)$ taking into account those effects confirm the results obtained here it would imply that there is a slight discrepancy between the observations and the theoretical predictions. It gives support to the gravitational instability scenario but implies the existence of biases between the galaxy distribution and the matter distribution. The estimated amount of bias would be of the order of 20%. This number, however, should by no means be considered as a measure of the usual bias parameter b.

References

[1] Baugh, C.M., Gaztañaga, E. & Efstathiou, G., 1994, *Mon. Not. R. astr. Soc.* in press

[2] Bernardeau, F. 1992, *Astrophys. J.* **292**, 1

[3] Bernardeau, F. 1994, *Astr. Astrophys.* **291**, 697

[4] Bernardeau, F. 1995, *Astr. Astrophys.* in press

[5] Bernardeau, F. & Kofman, L., 1995, *Astrophys. J.* **443**, 479

[6] Bouchet, F., Juszkiewicz, R., Colombi, S. & Pellat, R., 1992, *Astrophys. J.* **394**, L5

[7] Bouchet, F., Strauss, M.A., Davis, M., Fisher, K.B., Yahil, A. & Huchra, J.P. 1993, *Astrophys. J.* **417**, 36

[8] Colombi, S., Bouchet, F.R. & Schaeffer, R. 1995, *Astrophys. J. Suppl. Ser.* **96**, 401

[9] Fry, J., 1984, *Astrophys. J.* **279**, 499

[10] Gaztañaga, E., 1994, *Mon. Not. R. astr. Soc.* **268**, 913

[11] Gaztañaga, E. & Frieman J. 1994, *Astrophys. J.* **437**, L13

[12] Goroff, M.H., Grinstein, B., Rey, S.-J. & Wise, M.B. 1986, *Astrophys. J.* **311**, 6

[13] Juszkiewicz, R., Bouchet, F.R. & Colombi, S. 1993, *Astrophys. J.* **412**, L9

[14] Juszkiewicz, R., Weinberg, D. H., Amsterdamski, P., Chodorowski, M. & Bouchet, F., 1995, *Astrophys. J.* **442**, 39

[15] Limber, D.N., 1954, *Astrophys. J.* **119**, 655

[16] Lahav, O. Itoh, M. Inagaki, S. & Suto, Y. 1994 *Astrophys. J.* **402**, 387

[17] Łokas, E., Juszkiewicz, R., Weinberg, D.H., Bouchet, F.R., 1995, preprint

[18] Peebles, P.J.E. 1980; The Large-Scale Structure of the Universe; Princeton University Press, Princeton, N.J., USA;

SESSION IV

MODELS OF FORMATION AND NUMERICAL SIMULATIONS



IMPROVED WAYS TO COMPARE SIMULATIONS TO DATA

Joel R. Primack [1]
[1] *Santa Cruz Institute for Particle Physics, University of California, Santa Cruz, CA 95064*

Abstract

Theoretical models for structure formation with Gaussian initial fluctuations have been worked out in considerable detail and compared with observations on various scales. It is on nonlinear scales $\lesssim 10\ h^{-1}$ Mpc that the greatest differences exist between $\Omega = 1$ models that have been normalized to agree on the largest scales with the COBE data; here especially there is a need for better statistical tests which are simultaneously *robust*, *discriminatory*, and *interpretable*. The era at which galaxy and cluster formation occurs is also a critical test of some models. Needs for the future include faster and cleverer codes, better control of cosmic variance in simulations, better understanding of processes leading to galaxy formation, better ways of comparing observational data with models, and better access to observational and simulation data.

1 Introduction

Although many cosmological models have been considered by various authors, I propose to concentrate here on a particular class of such models, namely those inspired by the hypotheses of inflation (hence with $\Omega = 1$, or at least curvature $k = 0$, and a near-Zel'dovich primordial spectrum of adiabatic fluctuations) and (all or mostly) cold dark matter. I do this not only because I believe that such models still have the best prospects of ultimately being found to be consistent with the data. My main motivation for concentrating on these models is that they are *well specified*, in the sense that they are described by a small number of adjustable parameters (unlike general non-Gaussian models, for example), and very *predictive*, in the sense that many of their consequences can be worked out fairly easily with relatively few uncontrolled approximations. Thus they can be confronted rather directly with the observational data, and

eventually most (or all) such theories can actually be ruled out — as standard CDM already has been (or is close to being) ruled out. If a small class of such models survive, they may actually have something to do with the real universe. Even if not, this research should help to develop better statistical methods for comparison of cosmological theories with observational data.

The great advantage of keeping a tentative theory in mind as one thinks about data is that it helps in organizing the facts. If it is a good theory, it will also call attention to particularly important facts — especially those that may contradict it! CDM stimulated the creation of better models of the origin and evolution of galaxies and large scale structure, it helped motivate the acquisition and analysis of crucial data, and it has been a valuable test bed for data analysis tools — allowing, for example, development and testing of the POTENT algorithm [1] for reconstructing the total density field from measured peculiar velocities. Comparison of the original standard $\Omega = 1$ CDM model and its variants (cf. e.g. [2]) with the observational data has certainly been useful during the past decade.

2 Testing Models

It is useful to divide the discussion of how to confront models with the observational data according to the scale of the observations: (a) greater than 100 Mpc, (b) 10-100 Mpc, (c) less than 10 Mpc, and (d) early structure formation. If we restrict attention to CDM-like $\Omega = 1$ models, the data on the largest scales (a) is probably useful mainly for establishing the normalization of the fluctuations, measuring the contribution of gravity waves, and testing inflation. For low-Ω CDM models with a cosmological constant Λ such that the curvature vanishes (i.e. with $\Omega_\Lambda \equiv \Lambda/(3H_0^2) = 1 - \Omega_0$), data on the power spectrum $P(k)$ of galaxies and especially of the mass will be a crucial test, since if normalized to COBE [3] these models predict much higher $P(k)$ than $\Omega = 1$ CDM; however, the available data on the largest scales (mainly from the APM angular correlations and from the CfA2 + SSRS2 data [4]) is not yet a powerful constraint on theories. Comparing with the data on smaller scales tests the gravitational clustering hypothesis, and (assuming gravitational clustering is valid) the spectral shape and other features of the cosmological model, including the cosmological parameters H_0, Λ, and Ω, and the nature of the dark matter — e.g., whether it is a mixture of cold and hot dark matter. With a given normalization of the spectrum, the smaller scale data also tests the shape of the primordial spectrum (e.g., whether there is "tilt"). But there are many problems with actually carrying out this program even when large-scale redshift surveys become available, perhaps the worst of which is the uncertainties about galaxy formation which make identification of "galaxies" in the simulations uncertain. Fortunately, there are several ingenious new techniques that promise to improve this situation. For example, weak gravitational lensing [5] or extension of peculiar velocity surveys to larger scales (which requires new ways of measuring distance independent of redshift, or of measuring the peculiar velocity directly e.g. by the Sunyaev-Zel'dovich velocity term) may allow direct determination of the distribution of mass on large or even very large scales.

2.1 Very large scales

The shape of the power spectrum deduced from the two-year COBE data and other large-angle CBR measurements is consistent with a power-law primordial power spectrum $P(k) = Ak^{n_p}$ with $n_p \approx 1.1 \pm 0.3$, and with the rms amplitude quoted as the quadrupole for an $n_p = 1$ spectrum given by $Q_{\rm rms-ps} \approx 20\,\mu$K [3]. If a CDM spectrum is normalized to this amplitude for

$h = 0.5$, it appears to be consistent with all the available data on large scale structure (LSS) down to scales of approximately 100 h^{-1} Mpc (e.g., [6, 1, 7]). But the amplitude of the LSS is presently known at best to about $\pm 25\%$ — that is roughly the uncertainty on the large-scale bulk velocity, for example (e.g., [1]), which at least measures the mass power spectrum. The amplitude of the galaxy or cluster power spectrum has the further uncertainty that the ratio of the rms fluctuation amplitudes of these objects to that of the mass, i.e. the "bias" $b_{\rm gal} = (\frac{\delta\rho}{\rho})_{\rm gal}/(\frac{\delta\rho}{\rho})_{\rm mass}$, is known rather poorly. Indeed, the extent to which the bias of a given category of astronomical objects can be regarded as a constant even on a given scale is not very well tested.

Within these fairly large uncertainties, the consistency between the CMB data and the LSS data supports the validity of the gravitational clustering hypothesis. In order to really test this both this and the hypothesis of cosmic inflation, it will be necessary to do better. Perhaps the most important issue is the contribution of gravity waves. These tensor modes can contribute to the low spherical harmonics $\ell \lesssim 20$ of the CMB temperature fluctuations, but hardly at all to the higher ℓ ones; and they are of course irrelevant to the formation of structure, to which only the scalar mode density fluctuations contribute. In principle, the tensor contribution can be determined by comparing the large and small angle CMB anisotropies, but in practice this will require more accurate CMB measurements on small scales than are presently available, and also knowledge of Ω_b and the extent of ionization of the universe after the recombination era, both of which have a strong influence on the amplitude of the CMB fluctuations near the first Doppler peak, $\ell \sim 200$. For the time being, it is perhaps best to regard the COBE normalization $Q_{\rm rms-ps} \approx 20$ as an *upper* limit to the density fluctuation amplitude, since the tensor and scalar modes add in quadruature. One of the most urgent issues for CMB studies is to determine a *lower* limit on the density fluctuation amplitude by constraining the tensor mode amplitude. This will allow improved tests of the gravitational clustering hypothesis, and measurement of the "tilt" of the primordial fluctuation amplitude.

All the nearby surveys, such as the CfA2 survey with an effective depth of about 15,000 km/s, have found structures as large as the surveys themselves. This left open the possibility that still larger structures would be found by even larger surveys, which would contradict the gravitational clustering hypothesis (e.g. [8]). Although the very large scale periodicity of peaks in the galaxy distribution with a length scale of $\sim 135\,h^{-1}$ Mpc seen in the BEKS [9] pencil beam redshift survey was unexpected in any cosmological model [10], it is significant that no indications of still larger scales were seen in this data (preliminary reports indicate that pencil beams in different directions also have peaks with such separations but not such strong periodicity). Large scale redshift surveys are now in progress, notably the KOSS southern sky redshift survey and the ESO Key Project. Preliminary reports suggest that no larger structures have in fact been found (Kirshner characterizes this as "the end of greatness"), again supporting the gravitational clustering hypothesis. The much larger scale surveys just beginning — the Two Degree Survey at the AAT, and the Sloan Digital Sky Survey at the Apache Point Observatory — will be able to measure the sizes of these large structures and characterize their correlations, shapes, and other statistical properties. These will provide essential constraints on models of cosmic structure formation. These statistical properties appear on the basis of the data available at present to be consistent with the expectations from CDM-type models, but it remains to be seen whether this is true for topological defect models.

2.2 Large scale structure ($\sim 10 - 100$ Mpc)

On these scales a great deal of galaxy redshift data [11] and peculiar velocity data [1] is already available, although much of it remains unpublished. There are also several redshift surveys for

optically selected clusters, and large-scale redshift surveys for X-ray selected clusters (which are likely to be less affected by projection effects and galactic obscuration) are now in progress. Comparison of the spectrum of fluctuations measured with this data and with the small-angle CMB data when it is available will eventually provide a test of the gravitational clustering hypothesis.

Comparison with specific theories must be done on the basis of nonlinear simulations since on these scales linear theory is no longer reliable. All the available tests — power spectra of galaxies and mass (a preliminary POTENT result), galaxy and cluster correlations, skewness and higher moments of the pdf — suggest that CDM, normalized to fit on scales of 100 Mpc and above, fits increasingly poorly on smaller scales: it has too much power. For example, CDM predicts far too many clusters [12], and it predicts that mass autocorrelations become negative for separations beyond about 30 h^{-1} Mpc, while all measurements of cluster correlations show that they remain significantly positive for separations out to $\sim 50\ h^{-1}$ Mpc. These correlations are sensitive to the slope of the power spectrum, and indicate a steeper decline with increasing k than CDM.

2.3 Intermediate scales (less than 10 Mpc)

It is on scales less than about 10 Mpc that the greatest differences exist between $\Omega = 1$ CDM variants that have all been normalized to agree on the largest scales with the COBE data. It is these scales on which galaxy locations and velocities, as revealed by relatively dense redshift surveys (i.e., with fainter galaxies included), have the greatest potential to help discriminate between cosmological models, for example those containing more or less of various mixtures of cold and hot dark matter, with or without a cosmological constant. (Someday there may be enough galaxy peculiar velocities based on accurate distance measurements independent of redshift to allow these to be used to discriminate between theories on small scales, but for the time being it remains necessary to smooth peculiar velocity data over scales of at least 5 Mpc to overcome the large uncertainty in each such measurement.) The statistics that have been used for this purpose include N-point functions, the void probability function VPF and related functions, skewness and kurtosis coefficients S_3 and S_4, multifractal analyses, the genus density, etc. These statistics indicate that galaxies exhibit hierarchical scaling as expected in gravitational clustering models, but most of these statistics (with the possible exception of the VPF, see e.g. [13]) do not appear to be able to discriminate very efficiently in redshift space between alternative Gaussian models – although they may discriminate between these and non-Gaussian (e.g., [14]) al. 1993) or scale-dependent-bias models (e.g., [15]).

Simulations are of random patches of the universe, so comparisons with observational data must be statistical. There are broadly two different approaches to making such comparisons; one can work either in the "theoretical plane"– i.e., attempt to "correct" the data for selection effects, redshift space effects, etc. – or in the "observational plane" – i.e., "observe" the simulations. As computational power has grown, it has become increasingly advisable to observe the simulations rather than attempt to correct the data, since simulations have much more information – for example, the velocity as well as location of each object identified as a galaxy. Thus it is possible to construct magnitude-limited redshift surveys from simulations with no ambiguity in the conversion to redshift space, but it is more difficult to recover real space information from only redshift space data.

On the other hand, one should not underestimate the difficulties of simulating observational data. Perhaps the greatest problem is determining which objects in the simulations are to be identified with observed galaxies. In dissipationless simulations, with only dark matter included, perhaps the worst problem is overmerging. Nearby dark matter halos merge into

large blobs, even though in the real universe the individual galaxies within a group or cluster can retain their separate identities since the gas can condense a great deal within the larger dark matter halos. Even in hydrodynamical simulations (e.g. [16]) there are serious limitations; only limited spatial resolution is available with even the largest supercomputers, and many relevant physical processes such as energy input from stars and supernovae are neglected or treated superficially. Although the main strengths and limitations of the several different approaches to hydrodynamical simulations seem to be reasonably well understood (see e.g. [17]), the accuracy and resolution currently available is limited.

The necessary art, at the present stage of cosmology, is to invent statistical tests that are both *robust* and *discriminatory*. Robust, in the sense that the difficulties of the sort mentioned above – e.g. in galaxy identification or "illumination" (assignment of luminosity to objects identified as galaxies) – do not significantly affect the statistical results. And discriminatory, in the sense that the statistical tests give significantly different results for the various cosmological models that are of interest. That a given statistical test is actually robust and discriminatory can be checked by trying a wide variety of different approaches to galaxy identification and illumination of simulations of a number of different cosmological models. A further desirable feature of cosmological statistics is *interpretability* in terms of the physical assumptions or observational consequences of the cosmological model in question. For example, the matter two-point correlation function is just the Fourier transform of the (nonlinear, i.e. evolved) power spectrum $P(k)$, which is of fundamental theoretical importance.

For examples of such statistics and tests by my collaborators and students, see e.g. [18, 19] (galaxy group statistics), [13] (void probability function), [20, 21] (shape statistics). To avoid the problem of cosmic variance, discussed in more detail in the next section, we should ideally have compared many cosmological models by running simulations of them with the same random numbers (producing for example the same random phases). In the test-bed of simulations that we had available this was only possible to a limited extent, but we are improving on this.

3 Large-Scale Constrained Realizations

A great deal of effort is being devoted to creating improved methods of doing dissipationless and hydrodynamical cosmological simulations. In a new research project with Avishai Dekel and our students and other collaborators, we propose to complement this by developing more efficient methods for setting up such similations, for comparing the results to observational data.

The distribution and velocities of galaxies on scales of $\sim 1 - 10\ h^{-1}$ Mpc as revealed by redshift surveys are particularly sensitive to the nature of the dark matter, but discriminatory statistics such as relative galaxy velocities are also sensitive to the largest waves in the simulation volume. Because there are only a few such waves, they cannot fairly represent the Gaussian distribution assumed in models. Moreover, the dominant structures — rich clusters, "great walls" — in the largest dense redshift surveys such as PPS, CfA2, and SSRS2 also strongly affect statistics such as velocities. The solution we propose is to do simulations to be compared to **specific** redshift surveys, using the technique of constrained Gaussian realizations to set up initial conditions that will produce these dominant structures, with smaller waves put in and the simulation evolved to the present using the mixture of cosmological parameters (H_0, Ω, Λ) and dark matter types according to each model to be tested. This "Large Scale Constrained Realizations" (LSCR) approach certainly needs much development and testing; but assuming that it works as well as we hope, we anticipate that it could grow into a major addition to the

technology of observational cosmology.

Cosmic variance is perhaps the most serious problem in comparing simulations such as ours to redshift data. The cosmic scatter between random realizations is artificially large because the perturbations of the largest scales are represented by only a few waves and they therefore do not represent properly a Gaussian field. Each such realization is therefore typically dominated by one or a few large-scale waves, with strong systematic effects on the small-scale structure of interest, and especially on the velocities. A brute force way to beat this cosmic scatter is by averaging over many random realizations, but this can be quite expensive and impractical with full N-body simulations, although it is quite practical with the truncated Zel'dovich approximation (e.g. [22]).

A much more economical way would be to fix the large-scale structure in the initial conditions at its true pattern, and generate random realizations of the relevant small-scale structure only. The large waves on scales $> 20\ h^{-1}$ Mpc in regions of our cosmological neighborhood covered by dense redshift surveys can be extracted from the IRAS redshift surveys or from peculiar velocity data (e.g. using the POTENT reconstruction [1]. These large-scale constraints will be imposed on a random Gaussian realization of smaller waves representing each of the models of interest using the technique of Hoffman [23].

We also need to test the effectiveness of the overall LSCR procedure. For example, we plan to impose LS constraints from both CHDM and ΛCDM simulations, use the LSCR procedure to set up initial conditions for each model with the same parameters, and then evolve all four models — CHDM-CHDM, ΛCDM-ΛCDM, and the two crossed models — to the present. We can then see how well we can recover the same statistical results on various tests as in the original CHDM and ΛCDM models, and understand the nature of the biases if any in the crossed models.

4 Early structure formation

A major difference between cosmological models is in their predictions for the origins of galaxies, clusters, and large scale structure, and the evolution of these with redshift. Detection of large-mass collapsed objects at high redshift would certainly be contrary to the predictions of models with $\Omega = 1$, especially models such as CHDM in which small-scale fluctuation power is significantly suppressed compared to standard CDM. For example. a possible detection of a large HI cloud was reported but not confirmed; the upgraded Arecibo telescope and the Giant Meter-wave Radio Telescope will soon provide sensitive tools for searching for such clouds at high redshift. Detections of galaxy clusters and quasar superclusters at redshifts $z \sim 2$ have also been reported, and there are some remarkable HST WFPC2 pictures of clusters at redshifts $z \sim 1$. Although the striking differences between the galaxies in such clusters and those at lower redshift support earlier indications that cluster galaxies have evolved significantly since redshift 1, galaxies in the field appear to have evolved less dramatically since the universe was half its present age (e.g., [24]). The most useful data would provide indications of the number densities of the objects (e.g. galaxies or clusters) considered at various redshifts as a function of their mass (indicated for example by internal velocity dispersion or gas temperature), since that is what simulations predict most directly.

One of the most useful data sets for comparison with theories of structure formation is provided by absorption lines in the spectra of high-redshift quasars. The absorption systems with the highest density of neutral gas – known as damped Lyman α absorption systems – are presumably protogalaxies, and the quantity of gas in such systems at redshift $z \sim 3$ is roughly the same as the amount of ordinary matter in all the stars and gas that we can see in the

universe at the present epoch (see e.g. [25]). An important question that will discriminate strongly between various cosmological models is whether the quantity of gas in such systems peaks at redshifts about 3-4, as expected in models where structure forms relatively late such as CHDM (see e.g. [26]), or increases to still higher redshift, as expected in models such as ΛCDM where structure forms significantly earlier.

5 Needs for the Future

Perhaps the most important information needed as a basis for constructing the first fundamental theory of cosmology is the values of the fundamental cosmological parameters, especially H_0, Ω, and Λ. Below we summarize a number of other areas in which progress is needed.

Bigger computers, faster and cleverer codes, shared software. The greatest dynamical range in force resolution currently available is only a little better than three orders of magnitude in dissipationless simulations, worse in hydrodynamical simulations. This means that in a simulation with a 100 Mpc box, not large enough to simulate large surveys and large structures such as the Great Wall, the resolution is not much better than 100 kpc, an order of magnitude larger than the visible parts of galaxies. Moreover, there is a tradeoff between mass and force resolution: codes that permit better force resolution use fewer particles and thus have poorer mass resolution. A few groups such as the Grand Challenge Cosmology Consortium (GC^3) have recently devoted a great deal of effort to developing new and improved codes that exploit the new generation of massively parallel supercomputers that is now becoming available. It is very desirable that these codes become widely available so that the entire cosmology community can benefit. New technologies for visualization of the results of supercomputer calculations also hold considerable promise.

Cosmic variance. One of the worst problems with all simulations is cosmic variance; since only a random patch of universe is simulated, a number of such simulations must be compared to a number of regions for which galaxy survey data is available, and it is not clear that even the largest redshift surveys yet completed provide fair samples. This problem is exacerbated by the fact that, as many calculations have shown, there is a feed-down of effects from large structures to small; for example, rms pairwise velocities are strongly influenced by the presence of relatively rare rich clusters of galaxies (see e.g. [4]). Controlling cosmic variance is one of the most important challenges for current theory, until really large simulations can be compared to really large data sets such as the SDSS.

Better understanding of processes leading to galaxy formation. Since galaxy formation includes a number of generations of stars, including supernovae and the resulting chemical evolution, and perhaps often also involves more exotic objects such as the massive black holes thought to power active galactic nuclei, developing a secure understanding of these formation processes is likely to take a long time. It is even possible that a general theory of cosmology, including at least a general outline of the initial conditions and the nature of the dark matter, will precede rather than follow a detailed understanding of galaxy formation. No doubt a great deal of data on galaxies in both early and intermediate stages of formation will be necessary. Fortunately, such data is now coming from the new generation of great telescopes in space and on the ground. But present-epoch galaxies are brightest in the near infrared, and higher-redshift galaxies are expected to be brightest in the several micron band which can only be accessed from space. A large space infrared telescope such as SIRTF has long been seen as a high priority for astronomy, and the need

for it was reiterated several times during the Snowmass workshop. Meanwhile, we will need to make use of even indirect data such as the amount of extragalactic background infrared light from early galaxies, which can perhaps be probed by its absorption of TeV photons from AGNs via pair production [27].

Better ways of comparing observational data with models. We need new and better statistical tests, which are both *robust* against the difficulties of galaxy identification in simulations and the biases and selection effects always present in survey data, and *discriminatory* between the classes of cosmological models of interest. On the whole, it is probably better to compare theory with data by "observing" simulations rather than "correcting" data. It is very desirable that standard software become available to theorists and observers, so that standard versions of various statistics can be tried on many datasets from simulations and observations.

Better access to observational and simulation data. It is unfortunate that the only dense redshift survey covering a reasonably large volume which is publicly available is the 1982 CfA1 survey. Many papers have been published analyzing data from newer and larger redshift surveys in the years since then, but the redshift data remains largely unavailable. It is also desirable that simulation data (e.g. catalogs of objects identified as galaxies) be made available. The journals and funding agencies should ask a committee of observers and theorists to establish reasonable rules regarding access to such data – for example, all data used for a given paper must be made publicly accessible within one year of the publication of the paper – and ask referees to help enforce these rules. The POTENT group has set a good example of the sort of public access advocated here, by making their peculiar velocity dataset available in a timely way and in convenient form.

References

[1] A. Dekel, Ann. Rev. Astron. Astroph. 32, 371 (1994).

[2] J. Holtzman and J. R. Primack, *Astroph. J.* **405**, 428 (1993). Cf. also R. K. Shaefer and Q. Shafi, *Phys. Rev. D* **47**, 1333 (1993); **49**, 4009 (1994); A. R. Liddle and D. Lyth, *Phys. Rep.* **231**, 1 (1993).

[3] K.M. Gorski et al., *Astrophys. J. Lett.* **430**, L89 (1994); C.L. Bennett et al., *Astrophys. J.* (in press, 1994); E.F. Bunn, D. Scott, and M. White, *Astrophys. J.* **441**, L9 (1995); R. Stompor et al., *Mon. Not. Roy. Astr. Soc.* (in press, 1995).

[4] L.N. da Costa, M.S. Vogeley, and M.J. Geller, em Astroph. J. **437**, L1 (1994); L.N. da Costa at Moriond XXX, in *Clustering in the Universe*, ed. S. Maurogordato, et al. (Editions Frontieres), in press.

[5] T.J. Broadhurst, at Moriond XXX, ibid., and refs. therein.

[6] J.A. Peacock and S.J. Dodds, *MNRAS* **267**, 1020 (1994).

[7] A. Dekel, at Moriond XXX, ibid.

[8] T. Piran, et al., *MNRAS* **265**, 681 (1993).

[9] T.J. Broadhurst, et al., Nature 343, 726 (1990); A.S. Szalay, *Proc. NAS* **90**, 4853 (1993).

[10] A. Dekel, G.R. Blumenthal, J.R. Primack, and D. Stanhill, *MNRAS* **257**, 715 (1992).

[11] R. Giovanelli and M.P. Haynes, *Ann. Rev. Astron. Astroph.* **29**, 499 (1991).

[12] S.D.M. White, G. Efstathiou, and C.S. Frenk, *MNRAS* **262**, 1023 (1993).

[13] S. Ghigna, *Astrpoph J.* **437**, L71 (1994).

[14] P. Coles, et al., *MNRAS*, **264**, 749 (1993).

[15] J.A. Frieman and E. Gaztanaga, *Astroph. J.* **425**, 392 (1994). J.N. Fry and E. Gaztanaga, *Astroph. J.* **425**, 1 (1994).

[16] A.E. Evrard, F.J. Summers and M. Davis, *Astroph. J.* **422**, 11 (1994).

[17] H. Kang et al., *Astroph. J.* **430**, 83 (1994).

[18] R. Nolthenius, A. Klypin, and J.R. Primack, *Astroph. J.* **422**, L45 (1994).

[19] R. Nolthenius, A. Klypin, and J.R. Primack, *Astroph. J.* in press (1995).

[20] R. Davé, D. Hellinger, A. Klypin, and J.R. Primack, *MNRAS* submitted (1995).

[21] D. Hellinger, A. Klypin, and J.R. Primack, *MNRAS* in prep. (1995).

[22] S. Borgani, et al., *MNRAS* in press (1995). T. Kolatt, Moriond XXX, ibid.

[23] Y. Hoffman and E. Ribak, *Astroph. J.* **380**, L5 (1991); **384**, 448 (1992); G. Ganon and Y. Hoffman, *Astroph. J.* **415**, L5 (1993).

[24] C.C. Steidel, M. Dickinson, and S.E. Persson, *Astroph. J.* **437**, L75 (1994).

[25] A.M. Wolfe, *Texas/PASCOS Proceedings*, *Ann NY Acad. Sci.* 688, 281 (1993).

[26] A. Klypin, S. Borgani, J. Holtzman, and J.R. Primack, *Astroph. J.* **444**, 1 (1995).

[27] D. MacMinn and J.R. Primack, *Space Sci. Rev.* (1995) in press.



ON CLUSTER CORES AND POWER SPECTRA

B. C. Bromley[1], T. G. Brainerd[1], M. S. Warren[1], W. H. Zurek[1] & P. J. Quinn[2]
[1] *Los Alamos National Laboratory, Los Alamos, NM, USA*
[2] *Mt. Stromlo Oservatory, Canberra, Australia*

Abstract

We discuss high-resolution numerical simulations of structure formation with focus on (1) the distribution of dark matter in the cores of Abell clusters and (2) the effects of nonlinear galaxy dynamics on measures of the power spectrum. Scaling arguments suggest that massive clusters have extended soft cores; however, recent observations of gravitational lensing imply that soft cores are bounded by a few tens of kiloparsecs. Working with a 1.1 million particle cold dark matter (CDM) simulation of an isolated cluster we find no extended soft core, in agreement with observations. We examine nonlinear galaxy clustering in the Universe at large using a 17 million particle CDM simulation in a 250 Mpc periodic cube. We focus on the effects of pairwise velocities on the power spectrum measured in redshift space, $P_S(k)$. The simulated data show that peculiar velocities and spatial clustering conspire to make $P_S(k)$ very insensitive to the normalization of the primordial power spectrum on scales as large as 50 Mpc; this effect is modeled with a filter $F(k)$, valid from linear to strongly nonlinear scales, which connects the redshift-space power spectrum to its real-space counterpart by $P_R(k) = F(k)P_S(k)$. We find redshift-space power in the CDM models to be in excellent agreement with observations, however we conclude that this statistic does not strongly constrain cosmological models on the broad range of scales that can be affected by nonlinear peculiar motion.

1 Experimental Cosmology

With the recent advances in both hardware and software, primarily in the area of parallel supercomputing, numerical cosmology is evolving into "experimental cosmology." That is, we are now capable of creating fragments of model universes which are large enough to be Fair Samples while maintaining resolution in force and mass sufficient to reliably identify collapsed halos associated with galaxies. This capability has led to several recent results which challenge both cosmological models and previous conclusions about these models made on the basis of numerical experiments with less dynamical integrity.

The aim of this paper is to focus on two such surprises. The first concerns high-density regions in massive clusters and is sometimes referred to as the "soft core problem," especially in the context of galaxies whose halos have density profiles consistent with formation from

secondary infall ([1], [2], [3], and [4]). On the basis of early simulations with low resolution ([5], [6]) it was concluded that cold dark matter halos form with substantial soft cores of radii $r_c \geq 20$ kpc. In the case of spiral galaxies, a soft core enables the rotation curve to pass from the inner star-dominated regime to the outer dark-matter halo in a "seamless" fashion ([6], [7]), so that the profile shows no sign of a transition from one regime to the other. In such models the core radius is expected to scale with the size of the halo, an effect that was inferred ([6], [7]) from some numerical experiments ([4], [5]). This scaling implies that a very substantial soft core should exist in massive Abell clusters.

The obvious worry was that the soft cores found in simulated halos may be a by-product of the force-softening in the N-body code (see discussion by Quinn, Salmon & Zurek [3]). This concern has been strengthened and justified by recent high-resolution simulations which, for galactic halos, yield core radii of less than 10 kpc, comparable to the force-smoothing scale [8]. To investigate this problem in a somewhat different setting, we have carried out a high-resolution simulation of an Abell cluster collapse in a CDM cosmology. We show that Abell clusters have cores considerably smaller than expected from simply scaling up the galactic halo density profiles to cluster dimensions. This result is consistent with gravitational lensing observations in quite a few objects, which reveal core radii of less than 50 kpc (see the contributions by Broadhurst, by Ellis, and by Hammer in this volume).

As a corollary to our discussion on clusters we shall see that the dark matter halos forming in the vicinity of the cluster can remain essentially intact over time intervals of the order of the lifetime of the cluster, even if they do not become more bound as a result of the formation of a central baryonic "clump". This is intriguing and somewhat unexpected as it was initially anticipated that only dissipative baryonic halos could survive the strong tidal forces near the cluster center.

The other surprise from the high-resolution simulations is the unreliability of redshift power spectra as cosmological constraints. This result comes in the wake of the realization ([9],[10], and [11]) that the galaxy-galaxy velocity dispersion, which for over a decade was thought to provide a solid cosmological constraint in the range of 300–400 km/s, is not a robust statistic when estimated in surveys similar in geometry to the First Center for Astrophysics redshift catalog (CfA I). The standard measure of pairwise velocity dispersion is

$$\sigma_v^2(r) = \frac{1}{\mathcal{N}} \sum_{i,j} \left[v_{ij}(r) - v_{INFALL}(r) \right]^2 \ , \tag{1}$$

where $v_{ij}(r)$ and $v_{INFALL}(r)$ are the relative radial pairwise velocity and mean infall velocity, respectively, between galaxies i and j at separation r, and $\mathcal{N}$ is the number of such pairs. The velocity dispersion is probably twice as big on megaparsec scales ([9], [10], [11], [12], and [13]) as the original value of $\sigma_v \approx 340 \pm 40$ km/s reported by Davis and Peebles [14].

The revised σ_v estimates call for reëvaluations [15] of those models which were condemned on the basis of small-scale velocity statistics. The high value of the recent measurements, with $\sigma_v \sim 700$ km/s, also demands renewed consideration for the effects of small-scale peculiar velocities on clustering statistics. For power measured in redshift space (defined by angular sky positions and redshifts which include both Hubble flow and line-of-sight peculiar motion) pairwise peculiar velocities dominate the signal on scales of several times the velocity dispersion, expressed in distance units as

$$l_v \approx \sigma_v / H \ , \tag{2}$$

where $H \equiv h100$ km/s/Mpc is the Hubble parameter. From the recent estimates of σ_v fluctuation modes on scales as large as tens of megaparsecs can be affected by velocity dispersion. We demonstrate this effect by obtaining power spectra from both real-space coordinates and

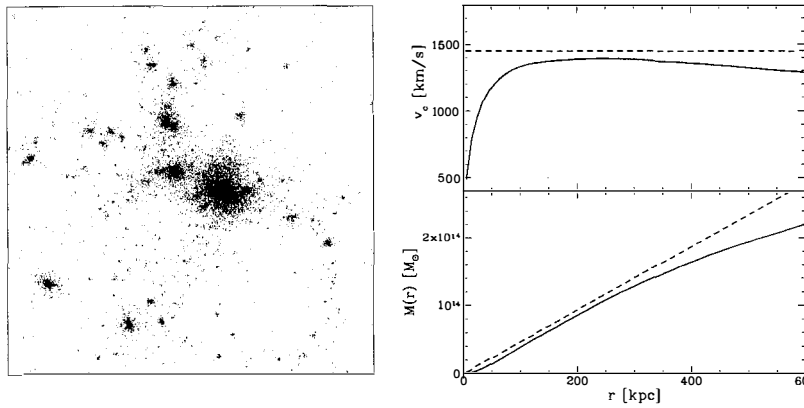


Figure 1: A particle plot (left) of 5×10^{14} $M_\odot$ simulated CDM cluster. A random subset (3%) of the particles is shown in projection within a box of 24 Mpc to a side. The cumulative mass function (top right) and the rotation curve (bottom right) illustrate the presence of a soft core within $\lesssim 50$ kpc. The dashed lines correspond to a singular isothermal sphere.

from the redshift distributions of N-body particles and of collapsed halos. We discuss the implications for the general usefulness of redshift-space power as a model discriminator.

2 Cluster Cores

We have simulated a cluster in an isolated 30 Mpc radius sphere with 1.1 million CDM particles as outlined in reference [16]. Figure 1 shows a particle plot of our cluster. Out to radii of $\sim$ 500 kpc the cluster is dominated by a single central halo, with a mass $M \approx 10^{14}$ $M_\odot$, although smaller halos ($M \approx 10^{12}$ $M_\odot$ each) are also visible. The cumulative mass function and the rotation curve for the central region are shown on the right in Figure 1; for comparison, curves corresponding to the a singular isothermal sphere ($\rho \sim r^{-2}$) are also shown. We believe that with the force softening length of $\epsilon = 5$ kpc the density profile should be reliable down to a few tens of kiloparsec. Evidently, a soft core emerges only below 50 kpc, while above this value the density profile roughly follows the isothermal prediction out to 200 kpc and well beyond.

In addition to the small radius of the softened core, the high resolution of the simulation reveals another phenomenon: the surprising stability of collapsed galaxy halos whose orbits pass very near to the cluster center. As mentioned earlier, it was anticipated that such structures would be destroyed by tidal disruption. While baryons — which are not included in this simulation — can stabilize halos by increasing the gravitational binding via dissipative gas dynamics [17], we find that this mechanism is not required to prevent disruption, as can be seen in the sample trajectories shown in Figure 2.

Perhaps the most immediate source of the intimate information about the cluster mass distribution comes from gravitational lensing. We have looked at the background field shown in Figure 3a through the simulated cluster in the foreground (Fig. 3b). For comparison, lensing through a singular isothermal sphere (Fig, 3c) and a core-softened isothermal sphere (Fig. 3d)

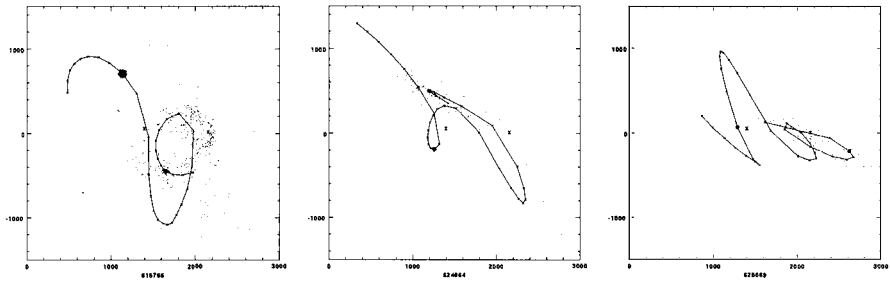


Figure 2: Sample trajectories of halo center-of-mass and constituent particles about the center of the cluster. The orbits run from a redshift of $z = 0.85$ to the present epoch; particle plots correspond to times near the trajectory endpoints. The present-epoch positions show clouds of evaporated particles and reduced but nonetheless intact halos.

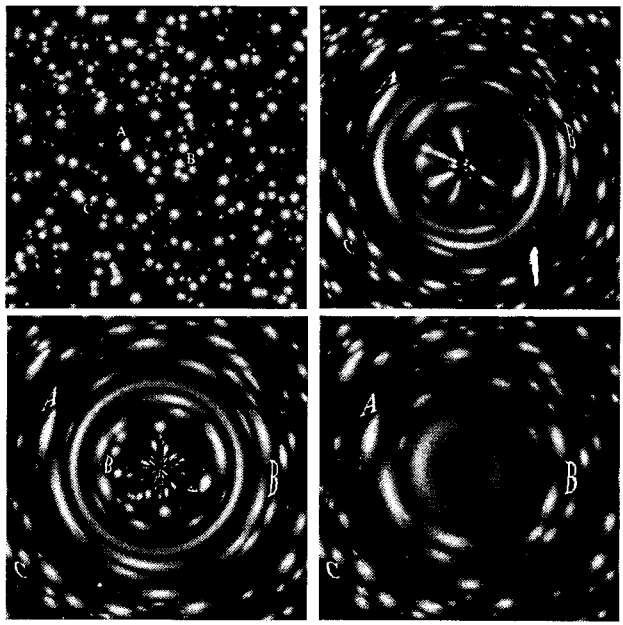


Figure 3: Lensing of a background image (upper left) by the simulated cluster (upper right), a singular isothermal sphere (lower left), and an isothermal sphere with a quadratically softened 40 kpc core (lower right). The size of the frame is 250 kpc at the distance of the lens.

are also shown. In all cases the amplification from lensing is suppressed to highlight the photon deflections. Amplification would strongly brighten the circular arclets (which fall near the Einstein radius).

In the face of evidence for small or nonexistent soft cores in clusters, the presence of soft galactic cores inferred for the dark matter distribution from the rotation curves (e.g., [18]) seems paradoxical. This apparent conflict — the breakdown of a soft-core scaling law — may be resolved through the natural extension of the segregated merging scenario we have advanced to explain morphology-environment correlation [19]).

3 Velocity Dispersions

We begin this section with a brief recapitulation of a recent ([9], [10], and [11]) and now independently confirmed ([12], [13]) revision of a "standard lore." The radial pairwise velocity dispersion (eq. [1]) is a measure of a "temperature" of the Universe, and may be interpreted as a bulk property of a gravitationally interacting system. For instance, σ_v was used to infer the mean mass density parameter Ω on the basis of a Cosmic Virial Theorem (CVT) which draws on a standard statistical mechanics as well as on a few bold assumptions (e.g., galaxies are point particles which represent the entire mass of the Universe; see ref. [20]). Once such assumptions are made,

$$\Omega \approx 2.3 \times 10^{-5} \xi^{-1}(r) \sigma_v^2(r) \qquad \left[r = 1 h^{-1} \mathrm{Mpc} \right] , \tag{3}$$

using spatial clustering statistics derived from CfA I survey, e.g., the two-point correlation function $\xi(r) \sim r^{-1.8}$.

The Davis and Peebles [14] result, $\sigma_v = 340 \pm 40$ km/s, and the CVT imply that $\Omega \approx 0.15$. Even though the CVT in the form of equation 3 is an approximation, it does provide an explanation for why early simulations failed to reproduce such a small σ_v given constraints from observed clustering and the widely held assumption that $\Omega = 1$. Indeed, given the Davis and Peebles value for the velocity dispersion and the observed level of clustering Einstein-de Sitter models seemed doomed. An attempt to salvage the situation for $\Omega = 1$ scenarios called upon a bias mechanism, whereby luminous galaxies and mass have distinct spatial distributions, thus mitigating the constraints from spatial clustering. In a linear bias model with CDM [21], the fluctuations in light exceed those in dark matter by a multiplicative factor of $b \sim 2.5$, hence drastically reducing the predicted power in total mass fluctuations and, consequently, lowering σ_v.

However, initial measurements from the Cosmic Background Explorer (COBE) revealed that CDM fluctuation amplitude should be roughly the same as that for luminous galaxies, that is $b \approx 1$. For example, σ_8, the r.m.s. density fluctuations relative to the mean in a spherical tophat of radius $8\ h^{-1}$ Mpc, is about unity for both dark matter and galaxies. Consequently, it was anticipated that CDM is ruled out because σ_v obtained with this density fluctuation amplitude exceeds 700 km/s, twice as large as the Davis & Peebles observational estimate.

Our reanalysis of the observational estimate of σ_v from the CfA survey, along with numerical experiments that indicate σ_v varies widely between different CfA-sized surveys cut out of fragments of a model CDM universe ([9], [11]), has changed the situation by (i) raising the best observational estimates by nearly a factor of two and (ii) indicating very large samples of the Universe are required to obtain a reliable estimate of σ_v. Both of these points were arrived at independently by Mo et al. [10] and are now confirmed in larger observational datasets ([12], [13]).

An illustration of the velocity dispersions for halos in a CDM scenario is found in Figure 4. We emphasize that the story which seems simple at small scales where the radial pairwise velocities are well-fit by an exponential distribution

$$f(v) \sim \exp(-\sqrt{2}|v - v_{INFALL}|/\sigma_v) \ , \tag{4}$$

becomes more complicated at larger pair separation because of coherent infall. For example, the skewness of the curve at 10 Mpc separation in Figure 4 clearly indicates that equation (4) does not apply.

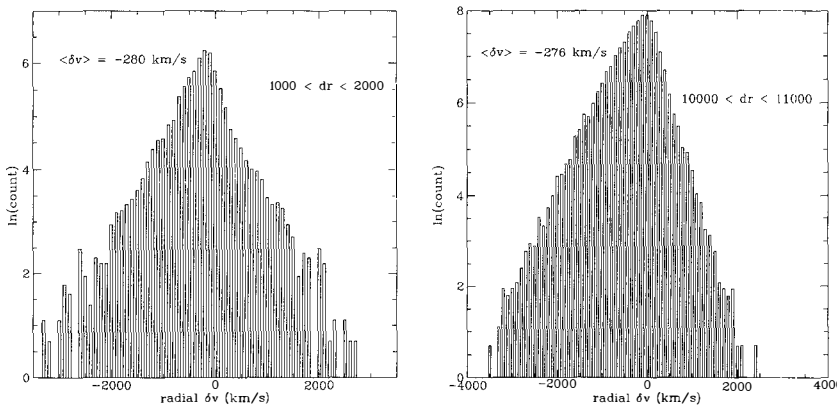


Figure 4: Histograms showing the distribution function of radial pairwise velocity for CDM halos. The figures show δv, the velocity averaged for galaxies whose separation lies in the radial bins dr. The average $< \delta v >$ is approximately v_{INFALL}.

As we shall discuss in the next section, σ_v and the form of $f(v)$ will act as a filter, modulating power inferred from the redshift survey on scales up to tens of megaparsecs (cf. eq. [2]).

4 Effects of Velocities on Redshift-Space Power

In this section we consider the relationship between the real-space power, $P_R(k)$, and the power in redshift space, $P_S(k)$, based on a large N-body simulation ($N \simeq 17 \times 10^6$) of a standard CDM universe. The simulation volume is a periodic cube of length 250 Mpc. We focus on two specific CDM models with fluctuation amplitudes of σ_8 of 0.74 and 1.1, and hence very different small-scale velocity dispersions. At issue here is the effect of peculiar velocities on the direct measurement of power in redshift space. We demonstrate that $P_S(k)$ is a poor cosmological constraint on scales below 100 Mpc because of the erasure of power by peculiar velocities.

Fisher et al. [22] report that the clustering of galaxies in the IRAS 1.2 Jy survey is inconsistent with the predictions of CDM on the basis of the redshift-space power on scales less than several tens of megaparsecs. Their work incorporated an alternative measure of power, which is similar to the conventional definition (e.g., ref. [20]), except that each wavemode is convolved with a cylindrical window in order to handle the finite survey volume. We have determined $P_R(k)$ and $P_S(k)$ for our high-resolution numerical data using the same cylindrical window

function as Fisher et al. (1993) and present results for CDM halos in Figure 5. Evidently, the CDM scenario is quite consistent with the IRAS data at small scales, in agreement with the findings of Brainerd and Villumsen [23] and Gramann, Cen and Bahcall [24]. The discrepancy between these results and those of Fisher et al. [22] are discussed below.

The difference in normalization of primordial power in the two CDM models clearly affects both spatial clustering and peculiar velocities. For example, σ_v in these two models for galaxy halos is roughly 700 km/s and 1,200 km/s, respectively. Evidently all differences between the models at small scales are obscured in the redshift-space power spectrum, hence $P_S(k)$ on small scales is not a robust model discriminant. It is only on very linear scales ($\sim$ 60 Mpc or greater) that $P_S(k)$ is significantly different for the two normalizations.

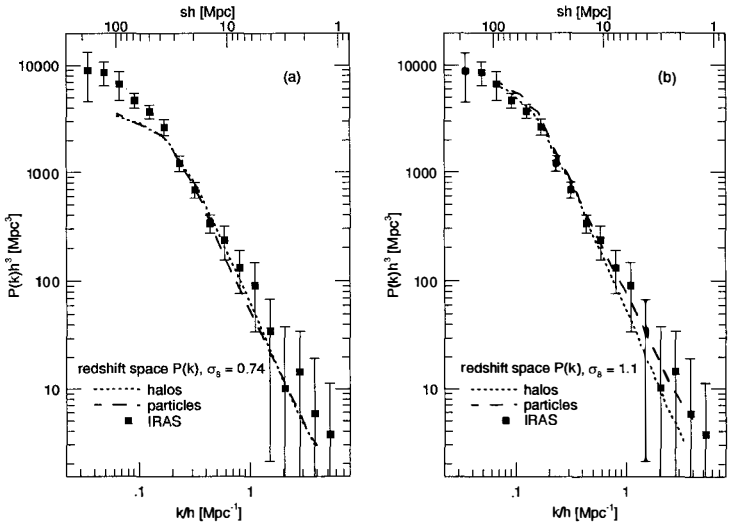


Figure 5: The power spectra of CDM halos and the IRAS 1.2 Jy galaxies. The method of windowing described by Fisher et al. [22] was used to generate these curves; the effects of the window convolution have not been removed.

The effect which is responsible for the observed amplitude of $P_S(k)$ is a simple conspiracy between small-scale peculiar velocities and density such that an increase in real-space power is largely negated by the smearing effects of peculiar motions in redshift space. Formally, the redshift-space correlations are simply given by the real-space correlation function convolved with the pairwise velocity distribution function f (e.g., eq. [4]). In the Fourier domain, $P_S(k)$ is related to its real-space counterpart $P_R(k)$ by a multiplicative filter function, $F(k)$, which is the Fourier transform of f, averaged over possible mode orientations relative to an observer. We model this filter by assuming that equation (4) holds at all scales. If we ignore infall we find that

$$F_{DISP}(k) \approx \frac{k_{DISP}}{k} \tan^{-1}(k/k_{DISP}) \ , \quad k_{DISP} \equiv \frac{\sqrt{2}}{l_v} \ , \tag{5}$$

where $l_v \equiv \sigma_v/H$ (eq. [2]). Hence the filter goes to unity at large scales and falls off as $1/k$ at small scales. We parameterize effects of correlated infall from linear and weakly nonlinear

flows in a similar manner as Fisher et al. [22],

$$F_{INFALL}(k) \approx \frac{k^2 + (28/15)k_{INFALL}^2}{k^2 + k_{INFALL}^2} , \tag{6}$$

where the factor of 28/15 is Kaiser's [25] redshift-space power enhancement for $\Omega = 1$, averaged over all angles relative to an observer's line-of-sight; the mode

$$k_{INFALL} \approx \frac{2\pi}{20\sigma_8^2 h^{-1}\ \mathrm{Mpc}} , \tag{7}$$

corresponds to an effective transition scale between the linear and nonlinear regimes. We introduce a dependence on σ_8 to model the change of this scale with normalization of the primordial power spectrum.

Combining the effects given by equations (5) and (6), we propose a new filter,

$$F(k) = F_{DISP}(k)F_{INFALL}(k) , \tag{8}$$

such that

$$P_S(k) = F(k)P_R(k) . \tag{9}$$

Figure 6 illustrates the effectiveness of this parameterization.

From equation (5) the small-scale insensitivity of $P_S(k)$ to normalization becomes clear. The shape of the spectrum is strongly influenced by the factor of k^{-1}, independent of the real-space power. The amplitude of $P_S(k)$ in this regime is determined by $1/\sigma_v$, which varies roughly as $1/\sigma_8$. However, in the case of halos the amplitude of $P_R(k)$ goes as σ_8^a where a is 2 at linear scales and falls toward unity at small scales. The net result is that the dependence of $P_S(k)$ on σ_8 is weak in the nonlinear regime.

Our results appear to be in direct conflict with those of Fisher et al. [22]. However, their conclusions regarding $P_S(k)$ for CDM were made after they altered the velocities of CDM particles to match $\sigma_v \approx 320$ km/s as measured in the IRAS survey. The effect of reducing σ_v but not σ_8 is evident in equation (5); for a COBE-normalized CDM universe one would predict a redshift-space power spectrum on small scales that is far in excess of the IRAS result (i.e. the conclusion of Fisher et al.). We propose that a more realistic way to identify a halo population in the simulation that is comparable to the late-type galaxies of the IRAS survey is to cut out the fast-moving objects in clusters. With this in mind, we select a subsample of halos, approximately 70% of the original data, which yields a σ_v value around 400 km/s. Even after this radical treatment, our data yield a redshift-space power spectrum that is consistent with the IRAS result.

5 Conclusion

A cosmological model must be judged on the basis of its physical predictions. Our principal goal here is to show the extreme importance of assessing those predictions accurately. In the case of the CDM, simulations in which insufficient resolution influenced the physics on galactic scales were used to condemn the model. Here, we have reexamined the standard CDM scenario with high-resolution simulations and found that the model is in agreement with several key observations which have been used previously to eliminated it. With the caveats that neither σ_v nor redshift-space power are ideal measures of structure in finite surveys, we note that CDM models with small-scale normalizations of $\sigma_8 \approx 0.7$–0.8 yield a surprisingly good fit to the observational data – again a result which contradicts much of the presently prevailing prejudice.

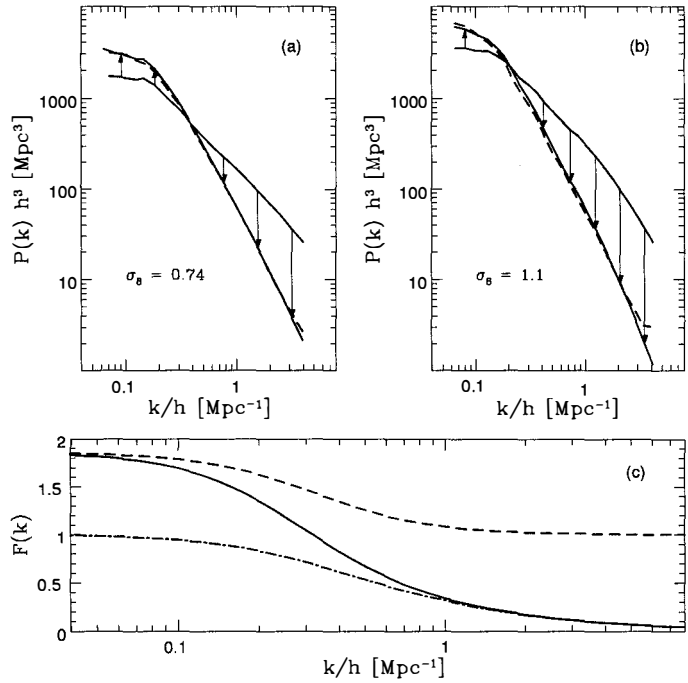


Figure 6: The effect of filtering real-space power spectra. The arrows in (a) and (b) show the transformation from the measured real-space power spectrum of CDM halos to redshift space using the filter $F(k)$ given in equation (8); The dashed lines are the measured redshift-space power spectrum. The filter is shown explicitly in (c) as the solid line; the upper curve is the contribution from infall, and the lower curve, with $1/k$ falloff at large k, is the factor from velocity dispersion.

Indeed, while COBE provides *prima facie* evidence for $\sigma_8 \sim 1.3$, somewhat "undernormalized" CDM models are predicted when the finite duration of a standard inflationary epoch is explicitly considered [26], [11]. The transition from a de Sitter-type inflationary expansion to an Einstein-de Sitter Universe prevents the primordial power spectrum from reaching its conventional $P(k) \sim k$ form; instead the power-law index is slightly less than unity. In addition, the transition generates gravitational tensor modes that can contribute to the COBE signal. Both phenomena lower the predicted σ_8 for CDM from the value that was naively extracted from the COBE data [11]. Whether they suffice to reconcile CDM with observations is not certain at present. However, it is clear that some of the most compelling pieces of evidence that have been mounted against the CDM scenario (as reviewed in ref. [27], for example) now carry much less weight.

Acknowledgements. We extend thanks to Karl Fisher for providing the IRAS power spectrum data. We gratefully acknowledge support from the NASA HPCC program.

References

[1] Gunn, J. E., & Gott, J. R., III, 1987, *Astrophys. J.* **176**, 1

[2] Hoffman, Y., & Shaham, J., 1985, *Astrophys. J.* **297**, 16

[3] Quinn, P. J., Salmon, J. K., & Zurek, W. H., 1986, *Nature* **322**, 329

[4] Efstathiou, G., Frenk, C. S., White, S. D. M., & Davis, M., 1988, *Mon. Not. R. astr. Soc.* **235**, 715

[5] Frenk, C. S., White, S. D. M., Efstathiou, G., & Davis, M., 1985, *Nature* **317**, 595

[6] Blumenthal, G. R., Faber, S. M., Flores, R., & Primack, J. R., 1986, *Astrophys. J.* **301**, 27

[7] Flores, R., Primack, J. R., & Blumenthal, G. R., 1993, *Astrophys. J.* **412**, 443

[8] Warren, M. S., Quinn, P. J., Salmon, J. K., & Zurek, W. H., 1992, *Astrophys. J.* **399**, 405

[9] Zurek, W. H., Warren, M. S., Quinn, P. J., & Salmon, J. K., 1993, in *Proceedings of the 9th IAP Meeting*, ed. Bouchet, F. R., IAP

[10] Mo, H. J., Jing, Y. P., & Börner, G., 1993, *Mon. Not. R. astr. Soc.* **264**, 825

[11] Zurek, W. H., Quinn, P. J., Salmon, J. K., & Warren, M. S. 1994, *Astrophys. J.* **431**, 559

[12] Guzzo, L., Fisher, K. B., Strauss, M. S., Giovanelli, R., & Haynes, M. P., 1995, *preprint*, astro-ph/9504070

[13] Marzke, R. O., Geller, M. J,. da Costa, L. N., & Huchra, J. P. 1995, *preprint*, astro-ph/9503114

[14] Davis, M., & Peebles, P. J. E., 1983, *Astrophys. J.* **267**, 465

[15] Zurek, W. H., Bromley, B. C., & Warren, M. S., 1995, in *Proceedings of the 5th Annual October Astrophysics Conference in Maryland*, eds. Holt, S. S., & Bennett, C. L., AIP

[16] Bromley, B. C., Warren, M. S., Zurek, W. H., & Quinn, P. J., 1995, in *Proceedings of the 5th Annual October Astrophysics Conference in Maryland*, eds. Holt, S. S., & Bennett, C. L., AIP

[17] Ryden, B. S., & Gunn, J. E., 1987, *Astrophys. J.* **318**, 15

[18] Moore, B., 1994, *Nature* **370**, 629

[19] Zurek, W. H., Quinn, P. J., & Salmon, J. K., 1988, *Astrophys. J.* **330**, 519

[20] Peebles, P. J. E., 1980, *Large-Scale Structure of the Universe*, Princeton University Press

[21] Davis, M., Efstathiou, G., Frenk, C. S., & White, S. D. M., 1985, *Nature* **292**, 371

[22] Fisher, K. B., Davis, M., Strauss, M. A., Yahil, A., & Huchra, J. P., 1993, *Astrophys. J.* **402**, 42

[23] Brainerd, T. G. & Villumsen, J. V., 1994, *Astrophys. J.* **425**, 403

[24] Gramann, M., Cen, R., & Bahcall, N. A., 1993, *Astrophys. J.* **419**, 440

[25] Kaiser, N., 1987, *Mon. Not. R. astr. Soc.* **227**, 1

[26] Davis, R. L., Hodges, H. M., Smoot, G. F., Steinhart, P. J., & Turner, M. S., 1992, *Phys. Rev. Let.* 69 1856

[27] Ostriker, J. P., 1993, *Ann. Rev. Astron. Astrophys.*, 31 689

LARGE SCALE STRUCTURE IN N-BODY SIMULATIONS

A.Doroshkevich[12]
[1] *Keldysh Institute of Applied Mathematics, Moscow, Russia.*
[2] *Theoretical Astrophysics Center, Copenhagen, Danmark.*



Abstract

The approximate quantitative theory of the formation and evolution of Large Scale Structure of the universe (LSS) is compared with six N-body simulations with the standard CDM power spectrum and power spectra with broken scale invariance (BSI). The proper dependence of the structure parameters and their evolutionary history on the amplitude and shape of the spectra and on the size of the computational box are found.

1 Introduction

The growth of perturbations in the Universe leads to the appearance of Large and Superlarge Scale Structure (LSS and SLSS). In observational catalogues the LSS is seen as the system of galaxy filaments (or chains of galaxies). The SLSS is formed by the galaxy superclusters and it contains also such elements as the Great Wall and the Great Attractor. This effect was predicted by Zeldovich' nonlinear theory of gravitational instability and has been tested in many numerical simulations. Filaments and sheet like structures were also observed in different large redshift surveys of the galaxy distribution, e.g. in the wedge diagrams of the CfA and the LCDRS. Some quantitative characteristics of LSS and SLSS have been found in [1] using data of deep pencil beam galaxy surveys.

In this paper some *quantitative* results of study of the LSS evolution in numerical simulations are presented. These results will be detailed in [2].

The 'core-sampling' method proposed in [1] allows to discriminate the random and deterministic elements in the spatial structure distribution and to obtain the statistical characteristics of the structure elements. This analysis allows to extract a substantial amount of information from N-body simulations. Eventually, it gives several structure parameters as functions of

redshift and their relation to the considered power spectrum. In this way we can characterize each simulation by a small number of parameters and we are able to distinguish between the influence of the computational box and the characteristics of the power spectra.

2 The theoretical description of structure formation and evolution

A first version of a general theory of structure evolution was developed in [3] on the basis of Zeldovich' nonlinear theory of gravitational instability. According to [3] we can obtain the approximate time dependence of the typical scale of structure, l_{LSS}, for different power spectra. This value corresponds rather to the mean separation of structure elements along a random straight line. This size is determined mainly by two physical processes, the formation of new structure elements and the later merging of these elements. According to Zeldovich' theory the creation of pancakes is described by the eq.

$$l_{LSS}^{-1} \simeq r_c^{-1} \frac{8}{3\pi^2}\sqrt{\frac{15}{7}}\,(\tau^2/2+1)\,\exp(-\tau^2/2) \leq 0.4\; r_c^{-1}, \qquad (1)$$

where z is the redshift and $\tau = (1+z)/(1+z_{cr}) = (1+z)\sqrt{5}/\sigma_\rho$. The variance of the perturbations, σ_ρ, and the typical scale r_c are defined as

$$\sigma_\rho^2 = (2\pi)^{-3}\int p(k)d^3k, \quad r_c^2 = 3\int p(k)d^3k/\int k^2 p(k)d^3k,. \qquad (2)$$

where k is the comoving wave number and $p(k)$ is the power spectrum of perturbations.

Later, during the second period of the structure evolution, the typical separation of structure elements is defined by the merging of elements what leads to the effective growth of the comoving structure scale, l_{LSS}. At this period the evolution of l_{LSS} is characterized by the dissipation scale which depends on the mean comoving displacement of structure elements due to the bulk motion:

$$l_{LSS}^2 \approx \frac{2}{(1+z)^2}\,\frac{1}{2\pi^2}\int_0^\infty p(k)G(kl_{LSS})dk,. \qquad (3)$$

$$G(x) = x^{-3}\int_0^x u^2\exp(-u^2)du$$

For broadband spectra with Harrison-Zeldovich longwave asymptotic $p(k) \propto k$ the equation 3 can be solved approximately by the simple expression [3]:

$$l_{LSS}^2 \approx \frac{3}{4}\frac{l_{max}^4(1+z)^{-2}}{\sqrt{l_0^4 + l_{max}^4(1+z)^{-2} + l_0^2}}, \quad l_0^{-2} = \int_0^\infty kT^2(k)dk, \quad l_{max}^2 = \sqrt{\frac{16}{15}}Q_2R_h^2,. \qquad (4)$$

where $T(k)$ is the transfer function, $R_h = 6\times10^3h^{-1}$ Mpc is the size of the horizon today and $Q_2 = (17/2.73)\times10^{-6}$ is the amplitude of the quadrupole fluctuations of the microwave background radiation.

3 Large Scale Structure in N-body simulations

The spatial distribution of DM structure elements was studied for six numerical simulations with CDM and broken scale invariant (BSI) power spectra for three computationl boxes: $25h^{-1}$ Mpc, $75h^{-1}$ Mpc and $200h^{-1}$ Mpc. It has been found that the spatial distribution of DM is

characterized by a hierarchy of sheet like elements, and only a small fraction of the DM particles forms filaments.

For this sample the period of structure formation varies over a wide range and the same redshifts correspond, in fact, to different evolutionary periods of structure formation. For BSI-200 simulation the end of the period of structure creation is seen at the redshifts $z = 2$ & 2.5. On the contrary, in the CDM-25 simulation the period of the structure disruption is typical for lower redshifts. For the six investigated models our analysis results in a set of structure parameters: the mean separation of sheets, D_s and the mean separation of sheets and filaments, $< l_{LSS} >$, for different redshifts.

3.1 The evolution of DM structure

In all simulations the filamentary structure appears at the smallest scales and incorporates a comparatively small mass fraction. We can estimate roughly the life time of filamentary structure in DM component as following

$$0.25 \leq (1+z)/(1+z_{cr}) \leq 2.5. \tag{5}$$

where the right limit gives approximately the beginning of the merging period of the structure evolution. For the smaller redshifts the influence of DM filaments becomes negligible. DM filaments occupy presumably the underdense regions and, therefore, correspond to the late population of structure elements.

Our analysis confirms that the sheet like DM structure elements dominate at all investigated time steps and that it contains about (60 - 70)% of matter. This fact is in a good agreement with expectations of Zeldovich' theory. During an earlier period of merging a larger and larger portion of the matter is collected in a decreasing number of structure elements, and the separation between structures gradually increases. Later the sheet like structure is disrupted and it becomes more and more important that the matter will be concentrated in a small number of supermassiv elements.

For BSI-200 and BSI-75 simulations the matter concentrated in supermassive elements is negligible. However, for further developed simulations such concentrations play an increasing role. For the CDM-25 simulation a significant fraction of particles is concentrated in supermassive elements. Our analysis restricts the period of the regular evolution of the structure to the interval

$$0.25 \leq (1+z)/(1+z_{cr}) \leq 2.5.. \tag{6}$$

It is approximately the same one as for the filamentary structure 5.

3.2 Time dependence of the typical scale of LSS

The typical scale l_{LSS} is the most important parameter of the LSS and its time dependence characterizes the essence of the structure evolution. The theory presented in eqs. 1 and 3,4 allows us to predict this time dependence for a wide class of the power spectra.

The main results of our analysis are presented in Fig. 1 where two estimates of the mean separation of the structure elements are shown together with the theoretical curves for the analyzed simulations (dases lines) and for the 'reference' volume $L_{box} = 6000h^{-1}Mpc$ with $N_{cell} = 60000$ (full lines).

The upside down triangles present the values D_s. The values take into account only the separation between the sheet like population of the structure elements and, so, they give actually an upper limit of the mean separation. The triangles denote the value $< l_{LSS} >$. This value

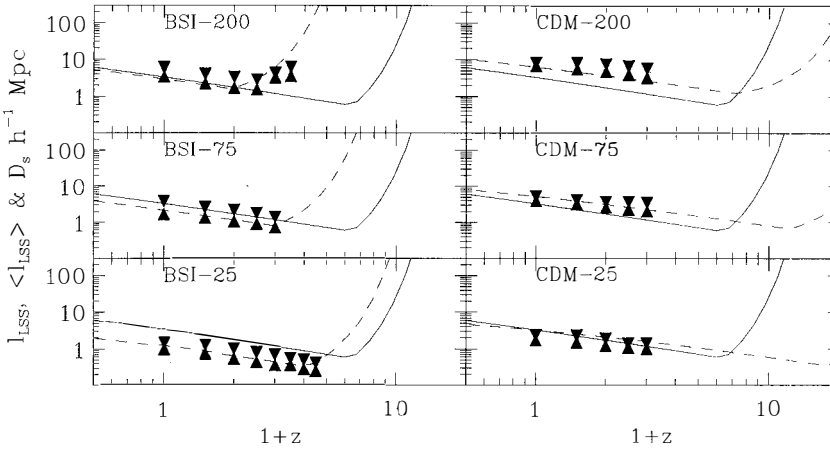


Figure 1: l_{LSS} vs. redshift z for six N-body simulations

takes into account also the filamentary population of the structure elements. Therefore, it can be probably considered as a more reasonable estimate of this separation. However, the obtained $< l_{LSS} >$ must be considered rather as a lower limit of the real separation because all these estimates of the $< l_{LSS} >$ are noisy. This noise is generated mainly by the background of individual particles.

The results, presented in Fig. 1, show that:

1. For all simulations the theoretical curves are located between two set of simulated separations and $< l_{LSS} > \leq l_{LSS} \leq D_0$. Therefore, we conclude that the relationship 1, 3 gives a reasonable description of the time dependence of the typical scale of the LSS over all investigated period of evolution.

2. The difference between the two estimates of the mean structure separation, D_s and $< l_{LSS} >$ may reach a factor of two, what characterizes the precision for our method of structure description.

4 Acknowledgments

This paper was supported by Danmarks Grundforskningsfond through its support for an establishment of Theoretical Astrophysics Center.

References

[1] Buryak, O.E., Doroshkevich, A.G., Fong, R. 1994, *Astrophys. J.* **434**, 24

[2] Doroshkevich, A.G., Fong, R., Gottlöber, S., Mücket, J.P. & Müller, V., 1995, *in preparation.*

[3] Doroshkevich, A.G., Fong, R., Gottlöber, S., Mücket, J.P. & Müller, V., 1995, *Mon. Not. R. astr. Soc.* **0000**, 0000.

NUMERICAL SIMULATIONS OF GALAXY FORMATION: EFFECTS OF SUPERNOVA FEEDBACKS

G. Yepes [1], R. Kates [2], A. Khokhlov [3] and A. Klypin [4]
[1] *Departamento de Física Teórica C-XI, Universidad Autónoma de Madrid, Spain*
[2] *Astrophysikalisches Institut, Potsdam, Germany*
[3] *Department of Physics and Astronomy, University of Texas at Austin, USA*
[4] *Department of Astronomy, New Mexico State University, Las Cruces, USA*



Abstract

We present results of cosmological simulations of galaxy formation in which the effects of radiative and Compton cooling and feedback from supernovae explosions have been taken into account. In our 3D Hydro+N-body numerical simulations, the matter is treated as a multi phase medium having four components: dark matter, hot baryonic gas and cold gas clouds (an analog of molecular clouds) embedded in the hot gas, and stars produced from cold gas clouds. Stars with mass $> 10M_{\bullet}$ explode as supernova, evaporating cold clouds around and heating the hot gas. These combined effects will regulate star formation within the dark matter halos. Stellar Population Synthesis models have been used to compute luminosities and colors of the "numerical galaxies". Supernova feedbacks play an important role on the evolution of dwarf galaxies. Most of the small objects have extremely low luminosities and very red colors. However, dwarf galaxies located near bright ones tend to be significantly brighter than those in low density areas. The amount of luminous matter that is formed within the dark halos depends strongly on the modelization of the supernova feedbacks. Star formation is inhibited when a large fraction of the energy released by supernovae goes into reheating the gas rather than evaporating cold clouds. The total fraction of gas converted into stars in the whole simulation varies from 50%, when half of the supernovae energy is kinetic, to 8% when most of the energy is thermal. The distribution of gas broadly follows the dark matter distribution, except for condensations that are much less diffuse than the local dark matter. In the case of both large and small "galaxies", the distribution of luminous matter is strongly biased with respect to the dark halos. However, the biasing is not a simple function of local density but depends strongly on environment.

1 Description of the model

We have studied the formation and evolution of galaxies in the context of large-scale structure. We focus our attention on the role of supernova feedback and hydrodynamics together with gravitational and radiative processes in determining the observational properties of galaxies, including luminosities and colors, and the extent of their dependence with the environment.

In our model, matter is treated as a multi-phase fluid with different physical processes acting between them: **Collisionless Matter** (Dark + Stars) and **Collisional Matter** (baryonic gas). The gas is treated as two separate phases, depending on its temperature: *Hot Gas* ($T_h > 10^4$K) and *Cold Gas Clouds* ($T_h < 10^4$K)

There are two mechanism for gas to leave the hot phase and enter the cold phase: **Radiative and Compton cooling** and **Thermal Instability** [3]. Star formation is assumed to occur only inside cold gas clouds and leads to a decrease in the average density of the cold component. We take a constant star-formation timescale $t_* \sim 10^8$ yr. Thus most of stars with M_* larger than $(10-20)M_\odot$ will explode as supernovae (SN) during one time-step. The fraction of mass that explode as SN, β, depends on the particular form of the Initial Mass Function (IMF). For a Salpeter IMF with lower mass limit $0.1M_\odot$, $\beta = 12\%$. This value of β has been taken to be valid at all epochs.

We consider two main effects of SN explosions in the surrounding gas: **Evaporation of cold clouds** and **Reheating of hot gas**. Evaporation of cold clouds due to kinetic energy from SN explosions is an important phenomenon in the interstellar medium [5]. We incorporate this effect by supposing that the total mass of cold gas "evaporated" and transferred back to the hot gas phase is a factor A higher than that of the supernova itself. We will refer to A as the *Supernova Feedback Parameter*. Admissible values of the supernova feedback parameter A are constrained by the condition that the energy of a supernova explosion be larger than the energy required for the evaporation of cold clouds. For typical values of SN energy and hot gas temperature this condition implies the restriction $A << 250$. We take values of A ranging from 100 to 20. For $A = 100$, almost half of the SN energy goes into kinetic energy that is able to evaporate clouds.

In order to estimate observational properties of the "numerical galaxies" we have used Stellar Polulation synthesis models [2] to compute luminosities and colors from the stars created in the simulation.

1.1 Numerical Techniques

The gravitational Poisson equation is solved by means of a standard Particle-Mesh code [4]. Hydrodynamical equations are solved by applying an Eulerian code based on the Flux-Corrected-Transport technique [1]. In our code the timestep for advection of gas and motion of dark matter is the same for all cells, but cooling and star-formation processes were integrated with variable timestep for each zone. A detailed description of the code and the tests carried out can be found in ref [6].

2 Results

A number of different simulations have been carried out to study the effects of supernova feedbacks on galaxy formation. We present results for 4 different simulations of an unbiased Cold Dark Matter Model in a comoving box of size 5Mpc ($h_0 = 0.5$). The number of dark matter particles and grid points was 2097152. This gives a minimum resolution of 38kpc . In

two of the simulations we took the same value $A = 100$ and two different realizations of the CDM spectrum.

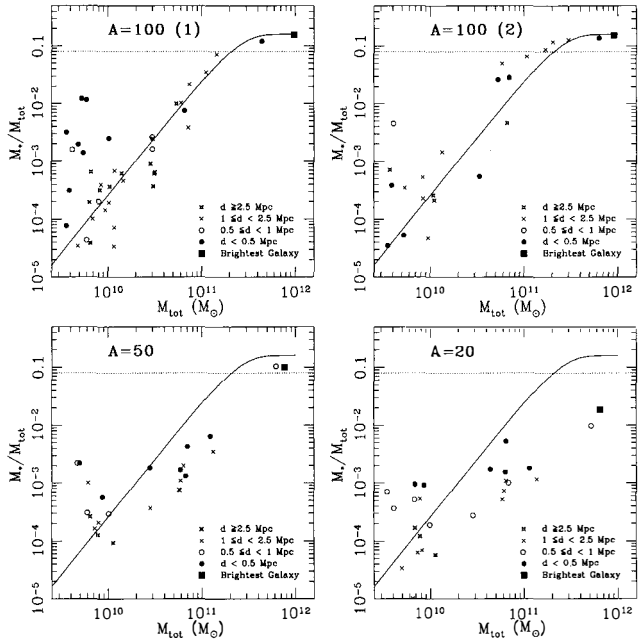


Figure 1 Fraction of Luminous to total mass as a function of total mass for the galaxies in the 4 simulations described in the text. The solid line represents a fit to the large objects in the first simulation.

In the other two, we started with the same initial conditions for dark matter, but varied the value of A. We took $A = 50$ and $A = 20$. In this sense we can check both the effects of the supernovae and environment at the same time. Initial conditions were generated at $z \sim 65$ and evolved until $z = 0$. Numerical "galaxies" are found in the simulation by identifying the Center-of-Mass of dark halos within spheres of 2 cell radius (80 kpc) and 1 cell radius (40 kpc). See ref [6] for further details of this method.

In Figure 1 we show the fraction of luminous mass to total mass in the galaxies identified in the 4 simulations as a function of the total mass of the halos and in terms of their distance to the brightest galaxy in each simulation. The amount of luminous (star) matter depends very strongly on the value of A. For low values of A the energy from supernovae mostly goes to reheat the gas and not to evaporate the cold clouds around. Then, the gas needs more time to cool down to produce cold gas cloud from which stars can be formed. As a result of this, a smaller fraction of gas is converted into stars. For $A = 20$, only 8% of the total gas in the simulation was transformed into stars, while for $A = 100$ almost 50% was converted. Another important feature is that the large mass objects are not very affected by environment. Looking at the two top panels of Figure 1 we see that the amount of stars in the more massive galaxies is almost the same, as well as their colors (Figure 2) and luminosities, although they correspond to 2 different realizations of the spectrum. On the contrary, the low mass objects are very much affected, not only by the environment (dwarfs located near bright galaxies tend to be brighter) but also by the modelization of the supernova feedbacks (value of A).

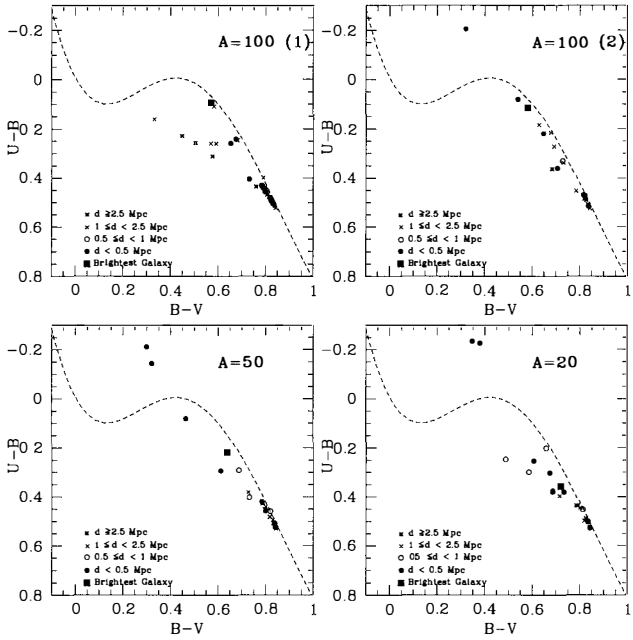


Figure 2 UBV Color indices for the galaxies in the simulations. The dotted line represents the position in the diagram of the main sequence stars of luminosity class V

In Figure 2 we show the color indices of the objects in the UBV diagram. As we can see, most of the dwarf galaxies found in the simulations have very red colors corresponding to old K stars. As A decreases the colors of all objects tend to be redder. In CDM the small objects form first. Star formation begins very early ($z \sim 4 - 9$) for most of the objects. When the first stars form, the supernovae associated with them are able to blow the gas away from the shallow potential wells of dark matter, stopping subsequent star formation. As a result, the colors of the objects are dominated by the older stars. This effect is enhanced for low values of A, when most of the SN energy is assumed to be thermal.

The above results underline the rather complicated interaction of gas dynamics, SN feedback and gravitation in the formation and evolution of observable properties of galaxies in cosmological scenarios.

References

[1] Boris, J.P., Book, D.L., 1973 *J Comp. Phys.*, **11,** 38.

[2] Bruzual, G & Charlot, S. 1993, *Astrophys. J.* **405**, 538

[3] Fall, S.M., Rees, M.J., 1985 *Astrophys. J.* **298**, 18

[4] Kates, R.E., Kotok, N., and Klypin, A.A., 1990 *Astr. Astrophys.* **243**, 295

[5] McKee, C.F. and Ostriker, J.P., 1977 *Astrophys. J.* **218**, 148

[6] Yepes, G., Kates, R., Khokhlov, A. & Klypin A., 1995, *preprint*

SIMULATING LARGE-SCALE STRUCTURE FORMATION FOR BSI POWER SPECTRA

Volker Müller
Astrophysical Institute Potsdam, Germany.



Abstract

A double inflationary model provides perturbation spectra with enhanced power at large scales (Broken Scale Invariant perturbations – BSI), leading to a promising scenario for the formation of cosmic structures. We describe a series of high-resolution PM simulations with a model for the thermodynamic evolution of baryons in which we are capable of identifying 'galaxy' halos with a reasonable mass spectrum and following the genesis of large and super-large scale structures. The power spectra and correlation functions of 'galaxies' are compared with reconstructed power spectra of the CfA catalogue and the correlation functions of the Las Campanas Deep Redshift Survey.

1 Double inflation scenario

We have discussed structure formation in a cosmological model with the dimensionless density parameter $\Omega = 1$, dominated by cold dark matter (CDM). However, alternatively to the standard CDM scenario, we used a primordial perturbation spectrum with a break at a characteristic scale. It is produced by the dominance of two scalar fields in the early cosmological evolution leading to a double inflation scenario. Original the idea goes back to Starobinsky [1], who considered n inflaton fields producing an equivalent n-fold inflation. The logarithmic increase of the scale factor during such a scenario is given by the sum of the initial values of the different scalar field potentials. For a model with two fields we get a break in the primordial perturbation spectrum. We select parameters so that it lies at the comoving scale corresponding approximately to the initial radius of forming galaxy clusters. Then we get a typical scale which separates 'large' and 'small' cosmic structures.

The model used in our simulations was derived by Gottlöber, Müller, & Starobinsky [2]. A description of the power spectrum of primordial potential perturbations $P_\Phi(k)$ is given by

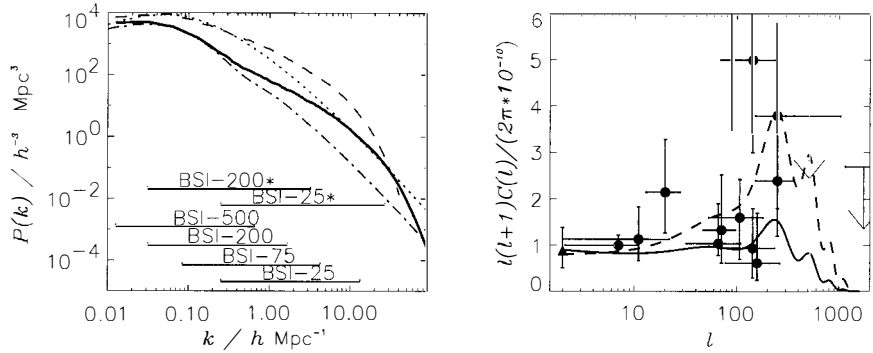


Figure 1: BSI and CDM power spectra (left) and inhomogeneities in the background radiation (right).

the approximate formula (it does not describe the typical oscillations generated during the intermediate power law stage):

$$k^3 P_\Phi(k) = \begin{cases} 4.2 \times 10^{-6} [\log(k_s/k)]^{0.6} + 4.7 \times 10^{-6} & \text{for} \quad k < k_s \\ 9.4 \times 10^{-8} \log(k_f/k) & \text{for} \quad k > k_s \end{cases} \tag{1}$$

with $k_s = (2\pi/24) h^{-1}$Mpc , $k_f = e^{56} h^{-1}$Mpc . After folding this spectrum with the standard CDM transfer functions (using a dimensionless Hubble constant $h = 0.5$ besides $\Omega = 1$) we get the power spectrum shown by the dash-dotted line in Fig. 1 (left). For comparison we show the CDM curve as dotted line, it has more small scale power.

At decoupling the primordial potential perturbations impose imprints in the temperature fluctuations whose angular spectrum differs from the standard CDM prediction. Fig. 1 (right) shows the comparision of the BSI spectrum (solid line) and the CDM spectrum (dashed line) with a set of observations. As indicated the power spectra are normalised by the most reliable measurements at small multipoles (COBE-normalisation), but they differ in the amplitude of the Doppler peak at about $l \approx 200$.

2 N-body simulation and galaxy identification

At presence no theoretical description or simulation scheme exhaust all the various effects of structure formation in the universe. For testing our envisaged model we have to study both the large scale structure formation, i.e. the formation of cluster and superclusters of galaxies, and the formation of the different types of galaxies as the basic building blocks of all large cosmic structures.

Therefore we studied a collection of simulation boxes which range from 25 h^{-1}Mpc for having enough resolution at galactic scales, to 75 h^{-1}Mpc and 200 h^{-1}Mpc for study galaxy clustering, and to 500 h^{-1}Mpc for the super-large scale structure as studied in [3]. We used the PM code of Kates, Kotok, & Klypin [4], taking for BSI in the highest resolution 512^3 cells and 256^3 particles (simulation names with asterisk in Fig. 1) and a set of simulations with half the resolution for comparing BSI and CDM [5]. The range realised by the different simulations is indicated in Fig. 1. The solid line shows the combined non-linear spectrum of the dark

matter after evolving from redshift $z = 25$ to the presence. The higher non-linear power of the corresponding CDM-simulations over a wide range of scales is shown by the dashed line.

During the simulation the code looks for shocks between triplets of originally neighboring particles, i.e. it looks for changes of the sign of the volume spanned by these particles. At shocks we attribute to the particles a 'temperature', which characterises the mean baryonic matter comoving with the dark matter (we suppose a cosmic abundance of 10 percent baryons). Subsequently we solve the cooling (and adiabatic heating) equations for these particles. This recipe leads to a reasonable account of the condensation of baryonic matter in galaxy halos and its clustering [5]. Since we do not alter the dynamics during and after shocks, dark and baryonic matter remains in the same pattern. Further we do not account of secondary shocks and of the heating by the intergalactic UV background. But we allow a certain fraction (85%) of reheating of the baryonic matter which became cold. This is believed to describe a phenomenological feedback mechanism provided by supernovae explosion in the forming galaxies. Finally it is essential that particles can get heated by neighboring high temperature particles.

Due to the nonlinear gravitational instability a large part of 'baryons' (up to 88%) gets 'cold' and transforms to star and star systems. Galaxies are identified with density maxima in the distribution of cold particles, which lie over a certain threshold (2 to 3 times the grid variance), but 'galaxy halos' are assembled by all particles within a search radius of 0.5 times the mean interparticle separation. The resulting mass distribution can be fitted by a Schechter function

$$\mathrm{d}n/\mathrm{d}\log M = n_*(M/M_*)^{-p}\exp(-M/M_*), \tag{2}$$

For BSI-25* we get $M_* = 10^{12}M_\bullet$, $n_* = 2.6 \times 10^{-2}h^3\mathrm{Mpc}^{-3}$ and $p = 0.8$. This is a quite reasonable density of M_* galaxies (corresponding to the characteristic L_* galaxies). Their spatial distribution can be used to evaluate the astrophysical effects of the BSI spectrum.

3 Power spectra and correlation function

Here we describe first the comparison of simulated power spectra with the power spectrum reconstructed from the CfA galaxy catalogue [6]. We impose redshift corrections by placing an arbitrary observer far outside the simulation box. The resulting power spectrum of BSI and CDM galaxies, identified in simulations with a box length of 200 h^{-1}Mpc is shown in Fig. 2 (left), where we select 'galaxies' with more than 10 particles for BSI and over 30 particles for CDM (the higher threshold is due to the more advanced clustering in the CDM model). The CDM model is strongly influenced by the redshift corrections which enhance the power near the maximum and suppress it at higher k values (another cause for suppression of the power at high wave numbers is the subtraction of shot noise). Both spectra can fit the CfA power spectrum, in particular the BSI model leads to a very good fit of the data. The galaxies used in this simulation are biased with respect to the sea of all dark matter particles by an (approximately linear) bias factor of about 2, contrary to the CDM model which has $b \approx 1$.

The galaxy correlation function shown in Fig. 2 (right) supplements the study of the power spectrum. While in principle it has the same information content, the accuracy of its estimation is much higher in the region of nonlinear clustering. Here we compare 'galaxies' composed of a minimum number of 5 and 10 particles in the BSI and CDM simulations, respectively. The data from the Las Campanas Deep Redshift Survey are taken from [7]. Again, due to redshift corrections both curves are able to reproduce the observed galaxy clustering over a wide range of scales (in the contrary, the real space correlation function of CDM galaxies is much steeper than that of BSI galaxies). The lower clustering level of the data at lengths below 2 h^{-1}Mpc

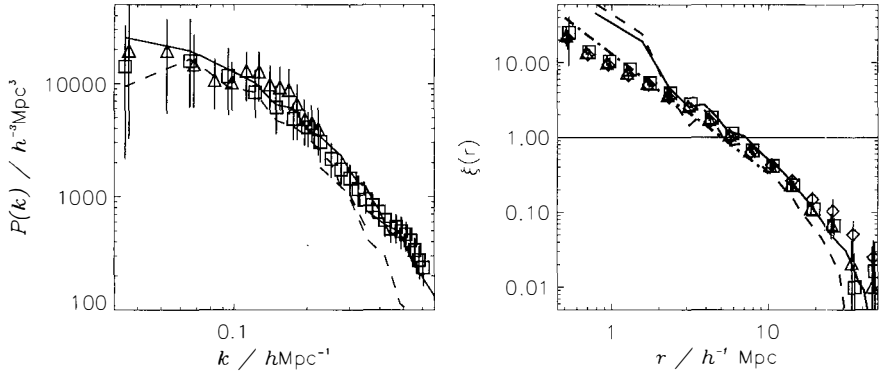


Figure 2: Galaxy power spectra and two-point correlation function.

is probably due to the selection effects. A small difference becomes visible in the length range $(20-30)\ h^{-1}$Mpc , where the higher clustering of the LCDRS galaxies may indicate an enhanced power, it is slightly better reproduced by the BSI model. The dash-dotted line in Fig. 2 (right) shows the best fit power law $\xi = (r/r_0)^{-1.6}$ with a correlation length of $r_0 = 5\ h^{-1}$Mpc .

Strong differences between the properties of galaxies in the two models become visible in the small scale velocity dispersion. Its one dimensional (line of sight) projection value lies at about 250 km/s in the BSI model and at about 600 km/s in the CDM model. This velocity dispersion can be estimated from the anisotropy of the two-point correlation function of redshift catalogues with respect to the line of sight and orthogonal to it. Further strong differences come from the observed mass distribution of galaxy clusters and the cluster-cluster correlation function ([8]). In the BSI model, the latter remains positive on scales up to at least $60\ h^{-1}$Mpc .

Acknowledgements. I am grateful to S. Gottlöber, R. Kates, J. Mücket, J. Retzlaff, and D. Tucker for a stimulating cooperation.

References

[1] Starobinsky, A.A., 1985, *Sov.Astron.Lett.* **9**, 302.

[2] Gottlöber, S., Müller, V., Starobinsky, A.A., 1991, *Phys.Rev.* **D43**, 2510.

[3] Doroshkevich, A.G., Fong, R., Gottlöber, S., Mücket, J.P., Müller, V., 1995, *MNRAS* subm.

[4] Kates, R., Kotok, E., Klypin, A., 1991, *Astron. Astrophys.* **243**, 295.

[5] Kates, R., Müller, V., Gottlöber, S., Mücket, J.P., Retzlaff, J., 1995, *MNRAS* subm.

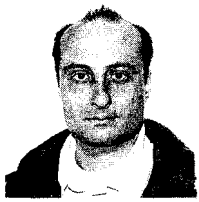
[6] Vogeley, M., Park, C., Geller, M., Huchra, J.P., 1992, *Astroph. J.* **391**, L5.

[7] Tucker, D.L., Oemler, A.A., Kirshner, R.P., Lin, H., Shectman, S.A., Landy, S.D., Schechter, P.L., 1995, this volume.

[8] Müller, V., 1994, in: 'Cosmological Aspects of X-Ray Clusters of Galaxies', ed. W.C. Seitter, Kluver, NATO ASI Series, 441.

TESTING DM MODELS AGAINST THE CLUSTER DISTRIBUTION

S. Borgani[1,2], M. Plionis[2], L. Moscardini[3], P. Coles[4]
[1] *INFN, Sez. di Perugia, Perugia, Italy.* [2] *SISSA – International School for Advanced Studies, Trieste, Italy.* [3] *Dipartimento di Astronomia, Università di Padova, Padova, Italy.* [4] *Astronomy Unit, School of Mathematical Sciences, Queen Mary & Westfield College, London, UK.*



Abstract

We study the clustering properties of numerical simulations of the cluster distribution, which are based on the Zel'dovich approximation, and compare them with an extended redshift sample of Abell/ACO clusters. A detailed comparison of such simulations with "exact" N–body simulations is also discussed. Within the list of the simulated dark matter (DM) models, we find that only that based on a mixture of Cold+Hot DM (with $\Omega_{hot} = 0.3$) and a low–density ($\Omega_o = 0.2$) CDM model with a cosmological constant term ($\Omega_\Lambda = 0.8$) provide a good fit to the data. The standard CDM, the tilted CDM ($n = 0.7$) and a low Hubble constant ($h = 0.3$) CDM models are ruled out.

1 Introduction

The observed strong clustering of clusters makes them potentially powerful probes of the large–scale structure of the Universe, because their clustering can be detected with high statistical significance on scales where density fluctuations are still in the linear (or quasi–linear) regime. For this reason, the cluster distribution is expected to give hints about the nature of primordial fluctuations. The usual technique to investigate the cosmological consequences of the cluster clustering involves N–body numerical simulations, which are however computationally expensive. On the other hand, the wide variety of proposed dark matter (DM) models calls for a flexible analysis technique, which would allow to easily go through the DM parameter space. Moreover, in order to assess correctly the statistical significance of the results obtained, one should ideally perform a large ensemble of simulations and look at the variation of statistical

measures across the ensemble. We present results based on an alternative method for simulating cluster samples in cosmological scenarios which is based on the Zel'dovich approximation [1] (hereafter ZA). The ZA, if used appropriately, reproduces the spatial distribution of matter found in fully dynamical N–body simulations at a fraction of the computational cost. We are therefore able to present a study of a large ensemble of realizations of cluster distributions from various cosmological scenarios with realistic estimation of the cosmic variance[2, 3].

2 The simulations

Let $x(t)$ be the comoving position of a particle. In the ZA, the solution to the equations of motion for the fluid particles can be written as the mapping of Eulerian–to–Lagrangian coordinates

$$x(q,t) = q + b(t)\,\nabla\psi(q)\,, \qquad (1)$$

where q and x are the initial (Lagrangian) and the final (Eulerian) particle positions respectively, $b(t)$ is the growing mode for the linear evolution of density fluctuations and $\psi(q)$ describes the gravitational potential, which is related to the density fluctuation field by Poisson's equation. According to eq.(1), particles do not feel any gravitational field and, although they are correctly moved by gravity at the beginning, they are not held within the minima of the potential field at later times. A detailed study of how to optimize best the ZA [4] suggests that one should filter the initial power–spectrum with a Gaussian k–space filter with a cut-off of the form $W(k) = e^{-k^2/2k_G^2}$. The optimal value for k_G depends upon the form of $P(k)$. We have chosen k_G so as to fix the average number of streams at each Eulerian point [5] at the value $N_s = 1.1$. We generate a random–phase realization of the smoothed fluctuation spectrum and the corresponding potential $\psi(q)$, appropriate to the model in question, on a 128^3 grid within a box of size $L = 320\,h^{-1}$ Mpc. A particle is putted on each grid point and is shifted according to Eq.(1). Then, we reconstruct the density field on the grid and identify all the local density maxima as cluster candidates. If d_{cl} is the mean cluster separation, the expected number of clusters is $N_{cl} = (L/d_{cl})^3$. Clusters are identified as the N_{cl} highest grid peaks.

We present ZA simulations for six different dark matter models: (1) Standard CDM model (SCDM) with $\sigma_8 = 1$; (2) Tilted CDM (TCDM), with primordial spectral index $n = 0.7$ and $\sigma_8 = 0.5$; (4) A cold–plus–hot DM model (CHDM), with 30% HDM and $\sigma_8 = 0.67$; (5–6) Two low–density, flat CDM models with $\Omega_o = 0.2$, $\Omega_\Lambda = 0.8$, one with a low normalization, $\sigma_8 = 0.8$ (ΛCDM$_1$), and one with $\sigma_8 = 1.3$ (COBE–consistent, ΛCDM$_2$). For each model we generated an ensemble of 50 different random realizations.

In order to test the reliability of the ZA cluster simulations, we run a CHDM PM N–body simulation and compared it with the output of a ZA simulation, having the same initial phases. In Figure 1 we compare the cluster positions in the two simulations at two different epoques, $\sigma_8 = 0.67$ and $\sigma_8 = 1$. It turns out that, while the ZA approach accurately reproduces the "true" cluster positions at the less evolved stage, it is less reliable at the more evolved configuration. This is due to the fact that, as fluctuations depart from linear evolution on the cluster mass scale (i.e., $\sigma_8 \gtrsim 1$), the ZA is not longer efficient at determining the individual cluster positions. Therefore, we expect that our simulation approach will be less reliable for the ΛCDM$_2$ model, while it is adequate for the other models. In any case, these results disprove recent claims for a general inadequacy of the ZA for cluster simulations [6].

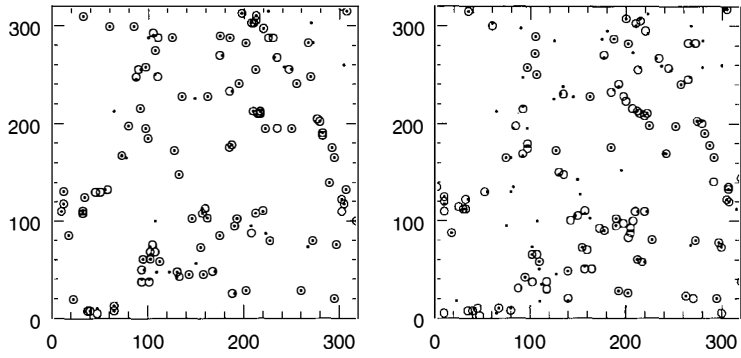


Figure 1: Comparison between ZA and PM cluster simulations, at $\sigma_8 = 0.67$ (left panel) and $\sigma_8 = 1$ (right panel). Open circles are the ZA cluster positions and filled dots give the PM cluster positions.

3 Results

As a test of the clustering developed by the simulated cluster distribution, we analyzed the statistics of the density field traced by clusters. A continuous cluster density field is obtained by smoothing the cluster distribution on a grid with grid-cell width of 20 h^{-1} Mpc with a Gaussian kernel of radius R_g. If $\delta(x_g, R_{sm})$ is the smoothed cluster density fluctuation at the grid-cell position x_g, then its second- and third-order moments,

$$\sigma^2(R_g) = N_{gr}^{-1} \sum_{g=1}^{N_{gr}} [\delta(x_g, R_{sm})]^2 \quad ; \quad \gamma(R_g) = N_{gr}^{-1} \sum_{g=1}^{N_{gr}} [\delta(x_g, R_{sm})]^3 , \qquad (2)$$

($N_{gr} = (16)^3$ is the total number of grid points) are the variance and the skewness, respectively. In Figure 2 we plot the relation between σ^2 and γ for each realization of the six considered models, at two different smoothing scales, $R_g = 20\,h^{-1}$ Mpc and $R_g = 30\,h^{-1}$ Mpc. The crosses are the results of the same analysis on a sample of Abell and ACO clusters [7]. At $R_g = 20\,h^{-1}$ Mpc the models which perform better are CHDM and ΛCDM_1, while almost no realizations of the other four models are consistent with the observational result. At $R_g = 30\,h^{-1}$ Mpc the increase of the cosmic variance makes SCDM, LOWH and TCDM marginally consistent, while the excess clustering of ΛCDM_2 generates too large σ^2 and γ values. Note, however, that for this model we expect the ZA to be in trouble in describing the cluster distribution. Following indication from N-body simulations that cluster correlations are almost independent of σ_8 [3, 6], one would instead conclude that the ΛCDM model substantially agrees with the observed cluster correlation.

As a general conclusion, the ZA approximation is shown to give an excellent representation of the cluster clustering at a very low computational cost. Therefore, it represents a very useful instrument to investigate in detail the parameter space of DM models.

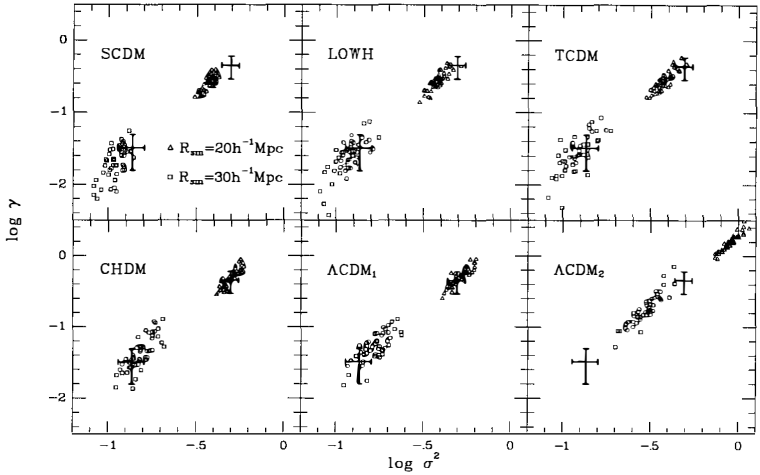


Figure 2: Variance–skewness relation for the six models at two smoothing scales, R_{sm}, as compared to observational results based on the Abell–ACO cluster sample [7].

References

[1] S.F. Shandarin and Ya.B. Zel'dovich, *Rev. Mod. Phys.* (1989), **61**, 185.

[2] M. Plionis, S. Borgani, L. Moscardini and P. Coles, *Astrphys J.* (1995), **441**, L57.

[3] S. Borgani, M. Plionis, P. Coles and L. Moscardini, *Mon. Not. R. Astron. Soc.* (1995), accepted.

[4] A.L. Melott, T.F. Pellman and S.F. Shandarin, *Mon. Not. R. Astron. Soc.* (1994), **269**, 626.

[5] L. Kofman, D. Pogosyan , S.F. Shandarin and A.L. Melott, *Astrophys. J.* (1992), **393**, 437.

[6] E. Gaztañaga, R.A.C. Croft, G.B. Dalton, 1995, MNRAS, submitted, preprint ASTRO-PH/9501115

[7] M. Plionis and R. Valdarnini, *Mon. Not. R. Astron. Soc.* (1995), **272**, 869.

OBSERVATIONAL CONSTRAINTS ON BLUE PRIMORDIAL SPECTRA

L. Moscardini [1], S. Colafrancesco [2], G. de Gasperis [3], F. Lucchin [1],
S. Matarrese [4], S. Mei [3], S. Mollerach [5], N. Vittorio [3]
[1] *Dipartimento di Astronomia, Università di Padova, Italy.*
[2] *Osservatorio Astronomico di Roma, Italy.*
[3] *Dipartimento di Fisica, Università di Roma, Italy.*
[4] *Dipartimento di Fisica "Galilei", Università di Padova, Italy.*
[5] *SISSA – International School for Advanced Studies, Trieste, Italy.*



Abstract

Recently, there has been growing interest on primordial 'blue' ($n > 1$) perturbation spectra, motivated both by a composite set of observational data on large scales (CMB anisotropies, bulk flows, etc.), and from the point of view of theoretical model building (e.g. hybrid inflation). In order to put some observational constraints on this type of spectra, both in the frame of purely Cold Dark Matter (CDM) and in Mixed Dark Matter (MDM) scenarios, we run N–body simulations and we perform a statistical analysis of the matter distribution, velocity field and cluster distribution. The main results show that a pure CDM model with blue primordial spectrum produces too small–scale power; on the contrary, a blue MDM model can reproduce the APM–Stromlo variance of counts–in-cells and the results of other tests, but it tends to produce too many massive clusters.

1 Introduction

The detection by *COBE* of anisotropies in the CMB at large angular scales has provided an insight on the primordial density perturbations. This measurement gives us the amplitude of density perturbations at the largest observable scales. Furthermore, it also constrains the spectral index n that is necessary to fully determine the primordial power spectrum. These constraints, promptly taken into account in the main current cosmological models, allowed to strongly discriminate among possible scenarios. In particular, the standard (i.e. $n = 1$)

Cold Dark Matter model with the *COBE* normalization (hereafter SCDM) produces too much structure on scales of order of 10 h^{-1} Mpc (h is the Hubble constant in units of 100 km sec^{-1} Mpc^{-1}), e.g. in terms of the cluster number and excessive rms pairwise galaxy velocity on Mpc scales. Tilted (i.e. $n < 1$) CDM models are in better agreement with observations on small scales, but the amount of tilt is strongly constrained from data on large scales [1].

The most fashionable alternative to SCDM emerged during recent years to overcome these problems is the Mixed (i.e. cold + hot) Dark Matter (MDM) model: the addition to cold dark matter of a small contribution ($\sim 10 - 30\%$ of the critical density) by massive neutrinos erases, via free–streaming, part of the power on the scale of galaxies and clusters. This scenario, on the other hand, will be reinforced also from the particle physics side, if recent claims for a mass of order 2 eV for the μ and τ neutrinos are confirmed. The standard MDM model is based on the same assumptions as SCDM, in particular, the usual Harrison–Zel'dovich $n = 1$ spectral index is taken. The results of linear analyses and numerical simulations [2] are certainly promising, but some problems are present: an excessive delay of the epoch of galaxy formation, in contrast with observations of quasars and damped Lyα system at redshifts $z \geq 3$.

In this paper we investigate a possible variant of MDM models, by assuming a "blue", i.e. $n > 1$, primordial density perturbation spectrum; such a 'BMDM model' (where 'B' now stands for 'blue'), with the usual *COBE* normalization, may clearly alleviate the small–scale problem of the standard (i.e. $n = 1$) MDM model. Such a choice seems suggested also by a variety of observations. The announced analysis of the first two years of the *COBE* DMR data indicates a most likely value for the spectral index in the range $n = 0.9 - 1.9$. Blue primordial spectra are also suggested by other CMB anisotropy experiments: the Tenerife experiment at the 5° angular scale and measurements at angular scales smaller than 1°, MAX and PYTHON experiments. An $n > 1$ perturbation spectrum can also be at the origin of the claimed bulk flow on scales of 150 h^{-1} Mpc [3] and of the large voids in the galaxy distribution in the CfA survey, at scales of order 50 h^{-1} Mpc, as recently pointed out [4]. On the other hand, it is also possible to put upper bounds on n. The primordial black hole overproduction constraints on nucleosynthesis and the *COBE* data put a limit on the spectral index, $n < 1.5$ [5]. An independent constraint, $n < 1.54$, comes from using recent experimental limits on the CMB spectral distortions found by the *COBE* FIRAS experiment [6]. Most theories for the origin of the primordial fluctuations predict a spectral index $n \leq 1$. In particular, inflationary models based on simple inflaton potentials originate this type of spectra. Nevertheless, in recent years some works have pointed out that suitable inflationary dynamics can easily account for blue spectra [7], in particular, in the frame of hybrid models.

2 N-body simulations

To study the large–scale structure of the Universe in models with blue primordial perturbation spectra we ran N–body simulations of the matter distribution. We used a particle–mesh code with a box of side 260 h^{-1} Mpc (we adopt here $h = 0.5$). We considered three different models: Standard CDM (SCDM), a Blue CDM model (BCDM) with primordial spectral index $n = 1.2$ and a Blue Mixed Dark Matter model (BMDM), still with primordial spectral index $n = 1.2$, but with $\Omega_{cold} = 0.65$, $\Omega_{baryons} = 0.05$ and $\Omega_{hot} = 0.3$. The COBE data imply (in the absence of any relevant gravitational wave contribution) approximately $b = 1$, $b = 0.5$ and $b = 0.9$, for SCDM, BCDM and BMDM respectively. In the case of pure CDM models (SCDM and BCDM), we used 128^3 grid–points and 128^3 particles. Initial conditions have been set using the standard approach based on the Zel'dovich approximation. Our N–body simulation of BMDM includes three sets each having 128^3 particles, one for the cold particles and two for the hot

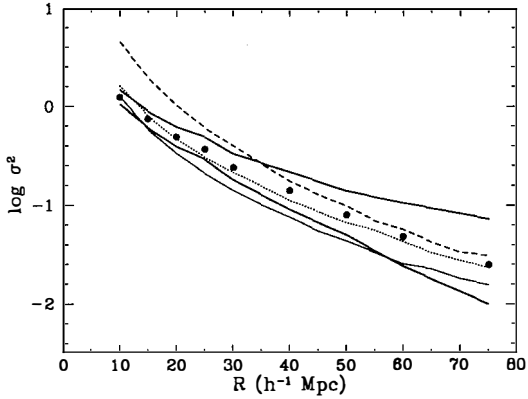


Figure 1: The variance σ^2 as a function of the side R of cubic cells for the three models: SCDM (solid line), BMDM (dotted line), BCDM (dashed line). The results from APM–Stromlo data are also shown: filled circles are the central values and thick solid lines represent the 95% range.

ones; the relative masses are 0.7 and 0.15 respectively. In generating the initial conditions in this case we followed the same method used by [2] (more details can be found in [8]).

3 Results

We present here some results obtained in the statistical analysis of N–body simulations. More tests have been applied in [8], where we also present an analysis, performed in the framework of the linear theory, of the X–ray cluster abundances and bulk flows at various scales.

An interesting insight on the clustering of the mass can be obtained from the counts–in–cells analysis. In particular, we calculate the variance $\sigma^2 \equiv \langle \delta^2 \rangle$. Figure 1 shows σ^2 as a function of the side R of cubic cells for the three models at the present time; shot–noise corrections were applied. For comparison, we also show the results (with 95% error bars) obtained by [9] in the analysis of the Stromlo–APM galaxy redshift survey. According to [9], galaxies in this catalog are nearly unbiased with respect to the mass; this implies that their counts can be directly related to the matter distribution. The SCDM model, as already known [9], has too small a variance on scales ranging from 20 to 60 h^{-1} Mpc. The clustering for BCDM is too strong on small scales: σ^2 is outside the 95% observational range for $R \lesssim 35$ h^{-1} Mpc. On the contrary, the results for BMDM are very close to the observational ones.

The analysis of the cluster distribution represents a potentially powerful tool in discriminating between dark matter models because they sample the universe on scales still in (quasi–)linear regime. In order to identify clusters in our simulations we adopted a standard method [10]. The cumulative mass function $n(> M)$, i.e. the number of clusters per unit volume with a mass larger than M, is presented for the three models in Figure 2. The BCDM model has a larger number of rich clusters compared with SCDM and BMDM, which behave in a similar way. A comparison with the observational estimates can be done using the mass function derived by [11] using both optical (richness, velocities and the luminosity function of galaxies in clusters) and X–ray data (temperature distribution of clusters). All models present too a high mass function for larger masses. The disagreement, already known in the case of SCDM, is

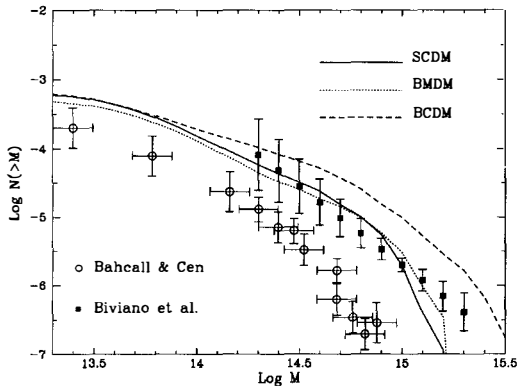


Figure 2: The cluster mass function $N(> M)$ (M in units of the solar mass) for the three different models. For comparison the observational estimates are shown.

significant. However, the estimates of [11] should be reconsidered, because of some underlying assumptions, such as the density profile or sphericity. Independent estimates of the cluster mass function, using masses derived directly from the dynamics (i.e. virial evaluations), give lower values for the mass function [12]. Observational data from [11, 12] are also shown in Figure 2. Considering the [12] data, the agreement with BMDM and SCDM is definitely better, while the number of very rich cluster is still a problem for BCDM model.

References

[1] Moscardini L., Tormen G., Matarrese S., Lucchin F., 1995, *Astrophys. J.* **442**, 469

[2] Klypin A., Holtzman J., Primack J., Regös E., 1993, *Astrophys. J.* **416**, 1

[3] Lauer T., Postman M., 1994, *Astrophys. J.* **425**, 418

[4] Piran T., Lecar M., Goldwirth D.S., da Costa L.N., Blumenthal G.R., 1993, *Mon. Not. R. astr. Soc.* **265**, 681

[5] Carr B.J., Lidsey J., 1993, *Phys. Rev. D.* **48**, 543

[6] Hu W., Scott D., Silk J., 1994, *Astrophys. J.* **430**, L5

[7] Mollerach S., Matarrese S., Lucchin F., 1994, *Phys. Rev. D.* **50**, 4835

[8] Lucchin F., Colafrancesco S., de Gasperis G., Matarrese S., Mei S., Mollerach S., Moscardini L., Vittorio N., 1995, *preprint*

[9] Loveday J., Efstathiou G., Peterson B.A., Maddox S.J., 1992, *Astrophys. J.* **400**, L43

[10] White S.D.M., Efstathiou G., Frenk C.S., 1993, *Mon. Not. R. astr. Soc.* **262**, 1023

[11] Bahcall N.A., Cen R., 1992, *Astrophys. J.* **398**, L81

[12] Biviano A., Girardi M., Giuricin G., Mardirossian F., Mezzetti M., 1993, *Astrophys. J.* **411**, L11

THE STRUCTURE AND PRIMORDIAL BLACK HOLES FORMATION IN THE INFLATIONARY MODELS WITH PECULIARITIES IN INFLATON POTENTIAL

P. Ivanov

Astro Space Centre of Lebedev Physical Institute,
Profsoyuznaya 84/32 , 117810 Moscow, Russia

We discuss the unusual properties of spectrum of primordial adiabatic perturbations produced in the inflationary cosmological models with breaks (the slope changes) in the inflaton potential. We show that such spectrum should be highly unflat contrary to the standard Harrison-Zeldovich case. n breaks in the potential lead to n peculiar features in the form of bumps or depressions in the two point correlation function of matter distribution. The potential with two breaks and nearly flat region in between (plateau-like feature), results in the increase in the spectrum power at relevant scale. This spectrum bump may produce the primordial black holes in the amount sufficient to close the Universe ($\Omega_{PBH} \approx 1$).

1 Introduction

In inflationary cosmology the primordial perturbations arising from quantum fluctuations of matter, may form the seeds of the structure formation in the observable part of the Universe. For the adiabatic perturbations in the "standard" inflationary theory with single scalar field ϕ (inflaton) driving inflation, and with smooth featureless potential $V(\phi)$ the spectrum is determined by well known formula (see, for example[1])

$$\delta_{rms} \propto (\frac{V^{3/2}}{\partial V/\partial \phi})_{k=a(\phi)H(\phi)}, \tag{1}$$

where k is the comoving wave number, a is the scale factor and H is Hubble parameter. The *rms* value of density contrast δ_{rms} is taken at the moment of second horizon crossing and the quantities on right hand side are taken at the moment of first horizon crossing. For the derivation of (1) two standard assumptions are used
1) slow-roll condition (which is neccesary for exponential inflation)

$$\dot{\phi}^2 \ll V(\phi), \tag{2}$$

2) friction-dominated condition

$$\mid \ddot{\phi} \mid \ll 3H \mid \dot{\phi} \mid . \tag{3}$$

According to the conditions (2, 3) field ϕ (and also H) changes very slowly in comparison with a, therefore all scales of astrophysical interest correspond to the small range of values of ϕ in (1) and $\delta_{rms} \approx const.$ Thus the standard inflation predicts nearly flat (Harrison-Zeldovich) spectrum of primordial pertubations. This prediction is to be checked by observations. For example, if one can find the local characteristic features in two point correlation function of matter distribution (CF) or some evidence for the large bump in the spectrum (one of such evidence might be the fraction of dark matter consisting of primordial black holes ($PBH's$)), the standard inflationary models should be ruled out.
Therefore one can consider non-standard inflationary models and find to which extent the highly unflat spectrum is compatible with inflation. In this contribution we consider the non-standard inflation with arbitrary numbers of breaks in the inflaton potential (the case of one break was considered by Starobinsky[2]). The condition (3) is violated each time when ϕ passes the break point ϕ_j and this leads to the strong deviation of spectrum from the flat one. n breaks produce n oscillating modulations of spectrum with frequency $\approx 2/k_j$ where $k_j = a(\phi_j)H(\phi_j)$, $j = 1, ..n$. This gives n features in CF in the form of bump (when potential sharply decreases before the break) or

depression (in the opposite case) at the corresponding scale. When the slope of potential is small between the breaks, the large bump in the spectrum appears. This bump may result in the intense $PBH^{'}s$ production.
This contribution is based on papers[3,4].

2 The modulation function

In our model the spectrum can be expressed as $\delta^2_{rms} = AD(k)$, where normalization $A \approx const$ and modulation function $D(k)$ characterizes the "non-flatness" of the spectrum ($D(k \to \infty) \to 1$). In general $D(k)$ has rather complicated form[3], therefore we consider two limit cases only. For the breaks occuring far from each other $k_{j+1}/k_j \ll 1$ $D(k)$ is the product of modulation functions $D_j(k)$ of one break theory ($D_j(k)$ were calculated by Starobinsky[2]). For $k \propto k_l$, using high frequency approximation for $j > l$, we have

$$D(k) = \prod_{j<l}(\frac{A_j^-}{A_j^+})^2\{1 + 3\sum_{j>l}(1 - \frac{A_j^-}{A_j^+}\frac{k_j}{k}\sin(2k/k_j)\}D_l(k/k_l), \qquad (4)$$

where A_j^-, A_j^+ are the slopes of potential after and before $j-th$ break. In the case of two breaks theory with plateau between the breaks we have

$$D(k) \approx \{1 + \gamma^3\}^2\{1 + 3\frac{\sin(2k/k_2)}{(k/k_2)}\}, \qquad (5)$$

when $k_2 < k < k_1$ and $D(k) \approx 1$ when $k > k_1$ and $k < k_2$. In (5) we assume $\gamma = k_1/k_2 \gg 1$ and $A_1^- \approx A_2^+$. From (5) it follows that the value of δ_{rms} is increased on the factor γ^3 at the scales $k_2 < k < k_1$.

3 The correlation function

In general CF has the form

$$\xi(r) = \frac{b^2}{2\pi^2 r}\int k^2 dk \delta^2_{rms} T(k)\exp(-k^2R_*^2)\sin(kr), \qquad (6)$$

where b is the bias parameter, $T(k)$ is the transfer function (we used approximate expression for CDM $T(k)$ obtained by Holtzmann[5]), R_* is the Gaussian filter scale. It can be shown with help of (4, 6) that at scale $r \approx R_j = 2/k_j$

$$\xi(r) \approx 3(1 - \frac{A_j^-}{A_j^+})\xi(0)\frac{r_0^2}{R_j^2}(1 - \frac{(r - R_j)^2}{2r_0^2}), \qquad (7)$$

where $r_0 \approx 2.5Mpc$ is determined by CF of theory without breaks[3]. From (7) it follows that $\xi(r)$ has a maximum for $\frac{A_j^-}{A_j^+} < 1$ and a minimum for $\frac{A_j^-}{A_j^+} > 1$. Therefore the peculiar features in CF may probably correspond to the breaks in inflaton potential.

4 The formation of primordial black holes

To get $PBH's$ in the amount sufficient to close the Universe we should have $\delta_{rms}^{crit} = 0.06$ for $PBH's$ with masses $M_{PBH} \approx 0.1 M_\odot$. This estimate depends on mass by logariphmical way only, for example $\delta_{rms}^{crit} = 0.04$ for $M_{PBH} \approx 10^{15} g$ and $\delta_{rms}^{crit} = 0.08$ for $M_{PBH} \approx 10^6 M_\odot$. However the $COBE$ and large scale structure data typically give very small $\delta_{rms} \approx 5 \cdot 10^{-6} \div 10^{-5} \approx 10^{-4} \delta_{rms}^{crit}$ [1]. Thus to obtain δ_{rms}^{crit} at some scale one should have a bump in the spectrum of primordial perturbations. It can be obtained by choosing the amplitude A to fit the $COBE$ data and introducing the plateau at $PBH's$ masses scale with $\gamma \approx 20$ (see (5)). Note that the condition $\Omega_{PBH} \approx 1$ can be achieved by the very delicate adjustment of the theory parameters. On the other hand, one can constraint the parameters of plateau-like features in the potential in wide range of scales, implying constraints on $PBH's$ abundance.

Acknowledgements

I am grateful M. Demianski, P. D. Naselsky, D. I. Novikov and I. D. Novikov for many fruitful and stimulating discussions. This work has been supported in part by Russian Foundation for Fundamental Research (code 93-02-2929) and International Science Foundation (code MEZ300).

References

[1] J. M. Bardeen, P. J. Steinhardt, M. S. Turner, *Phys. Rev. D* 1983 **28**, 679
S. W. Hawking, 1982 *Phys. Lett.* **115B**, 295
A. A. Starobinsky, *Phys. Lett.* 1982 **115B**, 175

[2] A. A. Starobinsky, *JETP Lett.* 1992 **55**, 489

[3] M. Demianski, P. Ivanov, D. I. Novikov, *Phys. Rev. D* 1994 **50**, 2488

[4] P. Ivanov, P. Naselsky, I. Novikov, *Phys. Rev. D* 1994 **50** 7173

[5] J. A. Holtzmann, *Astrophys. J. Suppl.* 1989 **71** 1

[6] B. J. Carr, J. E. Lidsey, *Phys. Rev. D* 1993 **48**, 543

[1] Note that the blue type spectra with power law dependance on scale which are compatible with large scale structure data give δ_{rms}^{crit} only for $PBH's$ masses less than $10^{15} g$ [6]. Such $PBH's$ would have evaporated long time ago and cannot contribute to the dark matter.

SESSION V

GALAXY CLUSTERS



OPTICAL/NEAR-IR SURVEYS OF DISTANT CLUSTERS OF GALAXIES

Marc Postman
Space Telescope Science Institute, Baltimore, MD U.S.A.

Abstract

The results from an analysis of an optical/near IR selected catalog of 79 clusters distributed over an area of 5.1 square degrees are presented. The catalog was constructed from images obtained with the 4-Shooter CCD mosaic camera on the Hale 5m telescope operating in "scan" mode. The survey, hereafter known as the Palomar Distant Cluster Survey (PDCS), was conducted in two broad band filters that closely resemble V and I. The 4σ limiting magnitudes for our 300 s exposures are $\sim$ 23.8 (V) and 22.5 (I). A matched filter algorithm was developed and employed to identify the cluster candidates by using positional and photometric data simultaneously. The clusters cover the range $0.2 \lesssim z \lesssim 1.2$, based on the redshift estimates derived in the cluster detection procedure. An accurate selection function is generated from extensive simulations. We find that the cumulative surface density of clusters with richness class R $\geq$ 1 is about a factor of 5 higher than the extrapolated density of R $\geq$ 1 Abell clusters. The PDCS results are consistent with a constant comoving density of clusters to $z \lesssim 0.6$, albeit at the above high density level. Constraints on cluster abundances at $z > 0.6$ will be possible with the acquisition of spectroscopic redshifts for a large subset of these cluster candidates. We have analyzed the richest clusters in this sample and find that the typical Palomar cluster has a surface density profile of $r^{-1.4}$ ($r \geq 0.15\ h^{-1}$ Mpc) and a core radius of $0.1\ h^{-1}$ Mpc. We see some evidence that the slope of the surface density profile steepens with increasing redshift. Our cluster population is inconsistent at a 99.2% confidence level with a population of azimuthally symmetric clusters.

1 Introduction

The evolution of the space density of clusters, of their internal kinematics and spatial structure, of their large scale clustering properties, and of their host galaxy populations are fundamental

predictions of all viable galaxy and cluster formation theories. The accuracy of the observational constraints on these parameters depends on the availability of statistically complete cluster catalogs over a large redshift range ($0 < z \lesssim 1$ and beyond). At redshifts less than 0.2, the available catalogs ([1]; [37]; [33]; [2] (ACO); [24] (Edinburgh-Durham); [12] (APM)) have all been based on the large photographic sky surveys done with the 1.2m Schmidt at Palomar Mountain and at the UK Schmidt at Siding Spring. These surveys have only recently become available in digital format and, consequently, only the Shectman, APM, and Edinburgh-Durham catalogs have been generated using automated and objective cluster detection algorithms. At higher redshifts, the catalogs are based on deep prime focus optical/near IR photographic plates taken on 4-5m class telescopes ([18], hereafter GHO; [9]). The low quantum efficiency of photographic material limits the completeness of these surveys beyond $z \sim 0.5$. These catalogs have yielded important information on galaxy evolution (*e.g.*, [8]; [17]; [32]) and on the clustering properties and space densities of low redshift clusters as a function of richness (*e.g.*, [5]; [11]; [20]; [29]). The Abell/ACO and Zwicky *et al.* cluster catalogs and the previously published optically selected cluster catalogs at higher ($z \gtrsim 0.3$) redshifts were constructed via visual inspection, limiting their utility. For a cluster catalog to be statistically useful, it must be homogeneous and its selection biases must be accurately quantified. Furthermore, in order to compare the predictions of models to the observations reliably, the same cluster selection process that is used on the observations should be applicable to large scale simulations.

The 4-Shooter CCD mosaic camera on the Hale 5m was designed, in part, to conduct digital, two color surveys for distant ($z \lesssim 1$) clusters over a moderate area of sky. We summarize here the properties of the cluster catalog resulting from the first such survey, hereafter referred to as the Palomar distant cluster survey (PDCS). A detailed description of the survey and the corresponding distant cluster catalog are provided in [30].

2 Survey Design

The PDCS consists of five separate fields. The shape of each field is roughly a square that is 1 degree on a side. The fields are all located within or near the original high-latitude [19] survey areas. In addition, field centers were chosen to minimize the number of bright stars in the survey regions and to avoid very low-redshift ($z < 0.1$) clusters and regions with high reddening. The J2000 coordinates of the field centers are given in [30].

The PDCS was performed with the 4-Shooter CCD camera mounted at the cassegrain focus of the Hale telescope. The data are acquired in Time-Delay-and-Integrate, or TDI, mode. (This is frequently called "scan" mode in the literature.) The effective size of the field for this project is $\approx 2 \times 780$ pixels, or a width of $520''$. Images of each field are obtained in two filters, the F555W and F785LP of HST's Wide Field/Planetary Camera [16]. To minimize confusion with the HST photometric systems, we will denote the 4-Shooter passbands as V_4 (F555W) and I_4 (F785LP); see [30] for a complete description of the PDCS photometric system. The 4σ limiting magnitude of the V_4 data (23.8) is fainter than that of the I_4 observations (22.5) due to the fainter sky and higher detector sensitivity at 5500 Å, but the I_4 images are in some respects just as important; at $z \gtrsim 0.6$ the 4000 Å "break" lies redward of the V_4 band, so the I_4 data provides the wavelength coverage needed to detect clusters out to $z \sim 1$.

3 The Cluster Detection Algorithm

We have developed a matched filter cluster selection algorithm which uses both positional and photometric data simultaneously to search for overdensities in the galaxy distribution [30]. We have applied this algorithm to the uniform galaxy catalogs derived from our CCD data. The matched filter method has many attractive features — 1) it is optimal for identifying weak signals in a noise dominated background (exactly the case for distant clusters), 2) photometric information is incorporated in an optimal way, 3) the contrast of overdensities which approximate the filter shape is greatly enhanced, 4) improved suppression of false detections, 5) redshift estimates are produced as a byproduct, and 6) good performance is seen over a large dynamic range in redshift. There are some disadvantages, in particular, one must assume a form for the cluster luminosity function and radial profile. We find that with sensible choices, however, the filters are broad enough to allow detection of systems with a range of properties.

The derivation of the matched filter functions used in our algorithm along with details of the cluster detection parameters are given in [30]. We have used extensive simulations to quantify the selection biases due to the functional form of the matched filter. In addition to providing a redshift estimate, the amplitude of the matched filter signal provides an estimate of the cluster richness. This filter richness, Λ_{cl}, is a measure of the effective number of L^* galaxies in the cluster. We can statistically determine the relation between Λ_{cl} and the actual cluster richness as determined by the specification of [1]. This relation is dependent on profile shape; as the cluster profile slope steepens, a given Λ_{cl} value corresponds to a *lower* richness class. For a cluster which has a surface density profile of r^{-1} (the assumed profile of the radial filter), $\Lambda_{cl} \gtrsim 40$ corresponds to Abell R ≥ 1.

4 The Profiles of Distant Clusters

We have examined the galaxy distributions of the richest clusters of galaxies from the PDCS. Through an analysis of individual cluster profiles and composite profiles as a function of redshift, we find that the typical Palomar cluster has a profile of $r^{-1.4}$ at radii greater than 0.15 h^{-1} Mpc and a core radius of 0.1 h^{-1} Mpc. In at least 20% of the clusters, our fitted core radius is only an upper limit. The average profile parameters of the PDCS clusters are consistent with measures of nearby clusters, as well as other intermediate redshift clusters ([25]; [36]; [35]; [34]). Though the observational uncertainty is large, there is an indication that the mean cluster profile steepens with increasing redshift. In addition, we find that a large fraction of the PDCS clusters have significant degree of asymmetry. The PDCS cluster population is inconsistent with a population of circularly symmetric clusters of galaxies at a greater than 99.2% confidence level. Table 1 summarizes some of the results. A complete analysis of the cluster profiles is presented in [22].

Table 1 : Power-Law Slopes of Composite Surface Density Profiles of the PDCS Clusters

	V_4		I_4	
	#	α	#	α
$0.2 \leq z_{est} \leq 0.4$	26	$1.21^{+0.16}_{-0.23}$	21	$1.23^{+0.15}_{-0.22}$
$0.5 \leq z_{est} \leq 0.7$	22	$1.44^{+0.11}_{-0.14}$	24	$1.43^{+0.14}_{-0.19}$
$0.8 \leq z_{est} \leq 1.2$	9	$1.82^{+0.18}_{-0.27}$	5	$2.06^{+0.19}_{-0.28}$

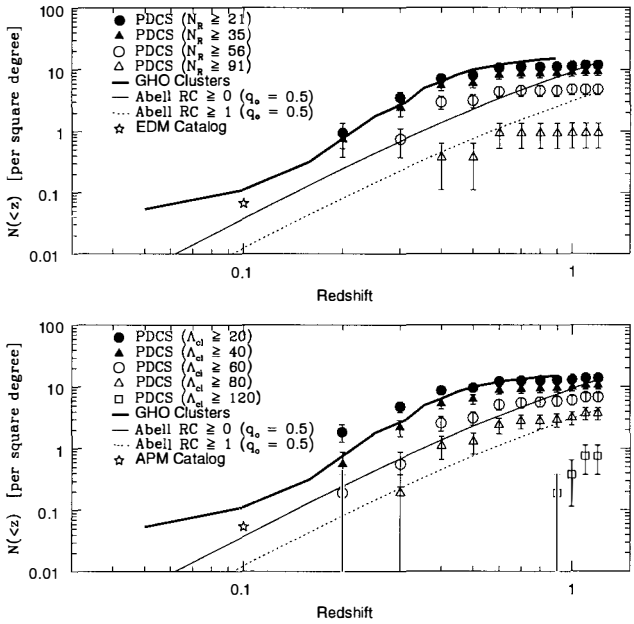


Figure 1: The cumulative number of clusters per square degree as a function of redshift and richness for the PDCS, the GHO catalog, the Abell/ACO catalog, the APM cluster catalog, and the Edinburgh-Durham-Milano (EDM) cluster redshift catalog. The upper plot shows PDCS cluster counts as a function of the Abell richness estimator, N_R. The lower plot shows PDCS cluster counts as a function of the Λ_{cl} richness estimator. For clarity, the APM and EDM values are shown on separate plots.

5 The Abundances of Distant Clusters

One of the prime motivations for conducting this survey is to constrain the comoving density of clusters as a function of redshift. This will be accurately accomplished only when redshifts exist for a substantial number of these distant clusters. At the present time we have spectroscopic redshifts for only a handful and, thus, we present preliminary constraints based upon our estimated redshift data for the 79 clusters in our catalog.

In Figure 1 we plot the cumulative number of clusters per square degree as a function of redshift and richness (Λ_{cl} and $N_R(1.0h^{-1}$ Mpc)) for the PDCS. The $N(< z)$ for the GHO catalog, the Abell/ACO catalog, the APM cluster catalog (Dalton *et al.* 1992), and the Edinburgh-Durham-Milano (EDM) cluster redshift catalog (Guzzo *et al.* 1992) are also shown. The Abell cluster curves are extrapolations normalized to the $z \leq 0.07$, R ≥ 0 Abell cluster space density and assume this density remains constant in comoving coordinates. For reference, a richness class 1 cluster should have $35 \leq N_R < 56$. If the same cluster has $z \lesssim 0.7$ and a $r^{-1.4}$ profile, then it would have $25 \lesssim \Lambda_{cl} \lesssim 60$ in the V_4 band and $30 \lesssim \Lambda_{cl} \lesssim 65$ in the I_4 band. No corrections have been made for false positive detections in Figure 1.

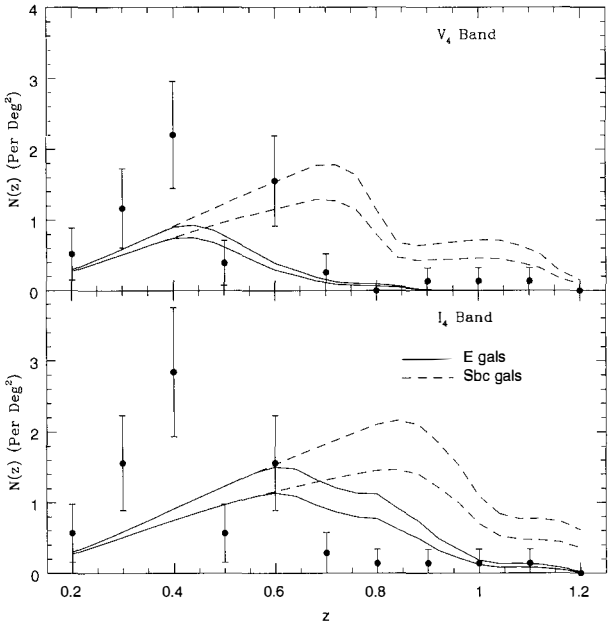


Figure 2: The differential redshift distributions for clusters detected in the V_4 and I_4 bands. The curves show the expected distributions for clusters consisting of non-evolving elliptical (solid line) and Sbc (dashed line) galaxies for $\Omega_o = 0.2$ and $\Omega_o = 1$. The $\Omega_o = 1$ curves always predict fewer clusters at a given redshift.

Figure 2 shows the observed and expected differential redshift histograms for the clusters in our main catalog with richness class ≥ 1. The observed histograms are based solely on our estimated redshifts and we have corrected the counts for false positive detections using the rates estimated from simulations. The expected distributions, for a given passband, are computed from the expression

$$N_{exp}(z, k(z)) = V(z) \sum_{i=0}^{4} (\rho_i P_i(z, k(z))) \tag{1}$$

where $N_{exp}(z, k(z))$ is the expected number of clusters per square degree per unit redshift for an assumed k-correction model specified by $k(z)$, $V(z)$ is the volume of a comoving element from z to $z + \delta z$ subtending a 1 square degree solid angle, ρ_i is the space density of clusters in this volume with richness class i, and $P_i(z, k(z))$ is the probability that a cluster of richness class i at redshift z would be detected by our cluster selection procedure for a given passband. Since the selection probability is a function of projected cluster profile, we need to assume something about the profiles of clusters in order to make our prediction. The projected profile of a typical $z \leq 0.2$ cluster is at least as steep as r^{-1} but flatter than r^{-2} over the range $100 \lesssim \mathrm{r} \lesssim 1000h^{-1}$ kpc ([6]; [26]; [28]; [7]; [22]; [34]; [35]; [36]). For this computation, we adopt the selection function for a $r^{-1.4}$ profile — the mean profile shape for the clusters in

this catalog. Lastly, we assume a constant comoving density of clusters and a constant cluster mass function (*i.e.*, the relative abundances of clusters of different richness classes remains independent of redshift). The actual density of the various richness classes is derived from the cluster luminosity function given by [4], normalized to match the observed space density of low redshift clusters. We compute the predicted cluster counts for two different galaxy population scenarios – one where clusters are made up of nonevolving elliptical galaxies and one where clusters are made up of nonevolving Sbc galaxies. The different scenarios account for the two substantially different expectations as a function of redshift and passband seen the Figure 2, although in the I_4 band cosmological effects are comparable with the effect of varying the k-correction. The estimated redshift distribution of the Palomar survey clusters is consistent with the hypothesis that the typical distant cluster galaxy is bluer than a nonevolving elliptical galaxy at the cluster redshift.

The predicted cluster counts depend critically on which data are used to determine the low redshift normalization. If we normalize to the observed space density of R $\geq$ 1 Abell clusters, we find that the expected number of such clusters with $z \leq 0.3$ per square degree is about a factor of 5 (± 2) smaller than the number in our Palomar catalog even after applying a statistical correction for spurious detections. This "discrepancy" is clearly demonstrated in Figure 1 — PDCS clusters with $N_R \geq 35$ or with $\Lambda_{cl} \gtrsim 40$ should correspond to Abell richness class 1 systems. The PDCS certainly has better completeness for poor clusters than either the Abell or GHO catalogs although assessing the exact incompleteness of these catalog is difficult given the visual selection procedures used in their construction. The space density of clusters in the PDCS is consistent with that previously found by GHO; however, a direct comparison is not very meaningful since there is no richness information for the GHO clusters and the GHO cluster selection function cannot be easily quantified. Extrapolating the density of $z \lesssim 0.1$, R $\geq$ 1 Abell clusters to $z \geq 0.3$ results in a substantial underestimate of the cluster space density inferred from the present survey. The uncertainty in the density of $z \leq 0.3$ clusters from the PDCS is large but improves significantly by $z = 0.6$ where R $\geq$ 1 PDCS clusters still outnumber the predicted R $\geq$ 1 Abell/ACO cluster density by a factor of 5 (after false positive correction). Hence, the expected counts shown in Figure 2 are based on a comoving density of R $\geq$ 1 clusters that is 5 times larger than that derived from the Abell and ACO catalogs.

At $z \leq 0.6$, the slope of the PDCS $N(< z)$ vs z relation is consistent with a constant comoving density, albeit a density 5 times higher than the R $\geq$ 1 Abell cluster density. The flattening of the slope of the $N(< z)$ vs z relation at $z \gtrsim 0.6$ is primarily due to the PDCS selection function. Figure 2 shows that a significant constraint on the spectral evolution of cluster galaxies is the modal redshift of the cluster sample — for clusters dominated by non-evolving elliptical galaxies, the predicted mode of the PDCS cluster redshift distribution is between $0.3 - 0.45$ whereas for clusters dominated by evolving elliptical galaxies (or non-evolving Sbc galaxies), the predicted mode may be as high as 0.75. The uncertainties in the redshift estimates, however, prevent us from constraining the cluster space density at $z \sim 1$. Follow-up spectroscopic surveys should allow a reasonable determination of the behavior of the space density of clusters at $z > 0.6$. A contiguous 13 square degree I band survey which is approximately 1.5 mag deeper than the PDCS has been completed by [31] in an additional effort to address this issue and to study the evolution of large scale structure.

There are several possible explanations for the difference between the abundances of Abell and PDCS clusters. The Abell catalog could easily be missing half the clusters (presumably all R $\leq$ 1). The APM and EDM cluster catalogs, which are objectively derived, yield a somewhat higher space density of clusters than that derived from the R $\geq$ 0 Abell clusters although they are not inconsistent with the Abell value. [21] produced an x-ray selected cluster sample to study cluster evolution. At $z \leq 0.08$, they detect 7 clusters but only 3 of these are in the Abell

catalog. The 4 x-ray selected clusters not in the Abell catalog have x-ray luminosities that are comparable with the ones that are. X-ray luminosity is highly correlated with richness and central density [14].

Previous observations have shown that clusters at $z \sim 0.4$ have galaxy populations which are significantly bluer than their low redshift counterparts ([8]; [27]). At higher redshifts, [3] report that "...by $z \sim 0.9$ there are no cluster galaxies as red as present day ellipticals." Such evolution would enhance the detection rate of high redshift clusters at a given threshold (particularly in the V_4 band). Recent HST image data ([13]; [10]; [15]) reveal that many of the blue ($g-r < 1.2$) galaxies in $z \lesssim 0.5$ clusters are either "normal" spirals or have peculiar morphologies, producing non-elliptical fractions which are 3 to 5 times higher than the average current epoch cluster. A number of physical mechanisms have clearly reprocessed the morphological mix between epochs. It is likely that in the cluster environment a combination of starbursts, tidal destruction, fading, and stripping conspire to produce the observed time variation of photometric and spectroscopic properties.

Our estimated spurious detection rate due to alignments of field galaxies is $\lesssim 30\%$ and we are confident that field galaxy superposition is not the primary source of the factor of 5 discrepancy in cluster counts. [9] claim that the higher cluster density in their J band survey could, in part, be explained by foreground contamination from spiral rich groups. However, 88% of our clusters are detected in both the V_4 and I_4 passbands which argues against severe contamination from such groups. A related effect, which is probably important for our survey, is an enhanced detection rate due to the superposition of poor groups and/or clusters. Systems with redshifts that differ by $\Delta z \lesssim 0.2$ and with projected separations of $\lesssim 1h^{-1}$ Mpc would be detected as a single cluster with richness significantly higher than any of the individual superposed components. The Abell catalog contains a number of such cases (*e.g.*, A419, A1318, A1631). Spectroscopic follow-up is the only unambiguous way to measure the magnitude of this problem. We note, however, that the matched filter algorithm is able to resolve overlapping systems if the projected separation is $\gtrsim 1.25h^{-1}$ Mpc.

Finally, we address the question of how our measuring errors might contribute to this discrepancy. The space density of clusters in the Abell catalog is roughly exponential with Abell's richness parameter. If f is the fraction of clusters at (or above) some richness R, $d\ln f/dR \approx -1.1$; that is, the space density of clusters falls by a factor of ~ 3 for each successive richness class. The richness class is roughly logarithmic with total galaxy population (which is proportional to Λ_{cl}), i.e. $d\ln\Lambda_{cl}/dR \approx 0.45$. Therefore, the fraction of clusters above a given value of Λ_{cl} goes as a power law function of Λ_{cl}.

$$f \propto \Lambda_{cl}^{-2.4} \tag{2}$$

Thus, if we have overestimated the richnesses of all our clusters by a factor of ~ 2, the discrepancy can be explained. We have examined this possibility through extensive simulations of clusters with a broad range of profile shapes and color evolution [23]. Firstly, we examine the relation between the *actual* richness and N_R. For most of the very distant clusters, we severely underestimate their richness; however, for some of the nearby clusters ($z_{est} \leq 0.4$), we can misclassify R = 0 clusters as R = 1 clusters and vice versa due to uncertainties in background subtraction and redshift errors. In the worse case, these misclassifications could cause a factor of ~ 2 overestimate in the space density of clusters at $z \leq 0.4$. Secondly, we have examined the effect of the profile shape on the filter richness parameter Λ_{cl}. The magnitude of Λ_{cl} is proportional to the steepness of the cluster profile. Complete resolution of the discrepancy would require Abell R ≥ 1 clusters to have $\Lambda_{cl} \geq 85$ and $\Lambda_{cl} \geq 70$ in the V_4 and I_4 bands, respectively. These values would correspond to an average cluster surface density profile of r^{-2} or steeper. This profile is not consistent with the PDCS clusters. The average profile shape is $r^{-1.4}$ (see

Table 1). Lastly, we have examined the effect of the shape of the cluster luminosity function on the relation between Λ_{cl} and the Abell richness estimator. The relationship depends on the faint end slope, α, but not on the k-correction. For values in the range $(-0.6 \geq \alpha \geq -1.3)$, the relationship varies by only $\pm 30\%$. The trend is such that if the cluster LF slope is greater (less) than the nominal flux filter value, a R = 1 cluster would yield a lower (higher) Λ_{cl} value.

A more subtle question is the effect of systematic or random redshift errors. One might naively think that the error could be explained by a *relatively* small systematic underestimate of redshift as the volume, and hence the number, increases dramatically with distance. In the Euclidean case, $d\ln V/d\ln z = 3.0$ (where V is the comoving volume), so a factor of five in space density would require a systematic underestimate of the distance by a factor of 0.6. At a redshift of 0.5 in an $\Omega = 1$ Einstein-deSitter universe, the value of $d\ln V/d\ln z$ is smaller, about 2.2; to explain the discrepancy, we would have to underestimate the distances by slightly more than a factor of 2. This seems hardly possible; however, the situation may be more complex as our estimate of richness is also distance-dependent. If we underestimate the distance, we may underestimate the richness as we have assumed a brighter characteristic m^*. The richness measured relative to this m^* would be smaller than that measured relative to the actual, fainter m^*. The result is that we would confuse very rich clusters at great distance, of which there are few, with poorer ones nearby. We can estimate the magnitude of the effect as follows. From the simulations, we find that in the vicinity of the correct redshift, the inferred richness changes with the assumed redshift like $d\ln \Lambda_{cl}/d\ln z_a \approx 2.1$. Now let us focus on some assumed redshift z_a and richness Λ^a_{cl} and suppose that the clusters that we think are at that redshift are really at some other (say larger) redshift z. Let us then ask how the total measured number of clusters at $z < z_a$ and $\Lambda_{cl} > \Lambda^a_{cl}$ changes as the real redshift z changes. The number of clusters that we infer to be in our sample as we change z is the product of the total number of clusters, which we assume is proportional to the comoving volume, and the fraction of clusters at z which are sufficiently rich to have measured richness Λ^a_{cl} at the inferred redshift z_a. Thus

$$\begin{aligned} \frac{d\ln N}{d\ln z} &\propto \frac{d\ln V}{d\ln z} + \frac{d\ln f}{d\ln z} \\ &\propto \frac{d\ln V}{d\ln z} + \frac{d\ln f}{d\ln \Lambda_{cl}} \frac{d\ln \Lambda_{cl}}{d\ln z} \\ &\approx 2.2 - (2.4)(2.1) \\ &\approx -2.8 \end{aligned} \tag{3}$$

This richness effect is opposite in sign to the volume effect and more than cancels the former; the numbers change with almost the inverse third power of the redshift. We need to have *overestimated* the redshift by a factor of about 1.8 to explain the discrepancy. This is extremely unlikely. The validity of this richness correction calculation depends on the origin of the redshift errors. Any systematic redshift error is most likely due to our assumption of no evolution, rather than the choice of an inappropriate luminosity function. First, there is no evidence of gross variation of luminosity function among clusters; second, our simulations, which are all based on a single Schechter luminosity function, display errors similar to the real sample and no substantial redshift biases. Therefore, we see no evidence to suggest that there are large luminosity function variations which would invalidate the notion of "richness" as measured by either the matched filter (Λ_{cl}) or the Abell technique (N_R) and the calculation for the richness correction (Eq. 3).

Let us now consider the ("Malmquist") bias due to *random* errors. As long as the number-distance relation is concave up (which is the case for both the richness-uncorrected and the richness-corrected relation in Eq. 3), the effect of random errors in the distances is to cause one to overestimate the galaxy density in a cluster. If the distribution of errors in $\ln z$ is assumed

to be Gaussian with standard deviation σ, the density overestimate is the factor

$$F = \frac{\Lambda_{cl}^{inferred}}{\Lambda_{cl}^{true}} = \exp(\frac{\gamma^2\sigma^2}{2}) \quad (4)$$

Here $\gamma = d\ln N/d\ln z \approx -2.8$, so the factor is approximately $F = \exp(3.9\sigma^2)$, which is 5 for $\sigma \approx 0.64$ and 2 for $\sigma \approx 0.42$. At our mean cluster redshift of ~ 0.6, the former corresponds to a mean redshift error of ~ 0.4, the latter to an error of ~ 0.25. We believe the errors in our estimated redshifts to be ~ 0.2. Therefore, perhaps one-half of the discrepancy can be accounted for by the Malmquist effect, and it seems likely that evolution and incompleteness in the Abell sample can account for the rest. However, we must wait for a substantial number of real redshifts for this sample before it is possible to clarify this issue satisfactorily. We have already begun a number of related spectroscopic surveys. Over the next five years, results from these and other ground-based spectroscopic surveys plus imaging with HST and x-ray satellites should yield a substantial improvement in our understanding of the formation and evolution of galaxy clusters.

References

[1] Abell, G. O. 1958, *Astrophys. J. Suppl. Ser.* **3**, 211

[2] Abell, G. O., Corwin, H. G., & Olowin, R. P. 1989, *Astrophys. J. Suppl. Ser.* **70**, 1

[3] Aragón-Salamanca, A., Ellis, R. S., Couch, W. J., & Carter, D. 1993, *Mon. Not. R. astr. Soc.* **262**, 764

[4] Bahcall, N. 1979, *Astrophys. J.* **232**, 689

[5] Bahcall, N., & Soneira, R. M. 1983, *Astrophys. J.* **270**, 20

[6] Beers, T. C., & Tonry, J. L. 1988, *Astrophys. J.* **300**, 557

[7] Broadhurst, T. 1995, private communication.

[8] Butcher, H., & Oemler, A. 1984, *Astrophys. J.* **285**, 426

[9] Couch, W.J., Ellis, R.S., Malin, D.F., & MacLaren, I. 1991, *Mon. Not. R. astr. Soc.* **249**, 606

[10] Couch, W.J., Ellis, R.S., Sharples, R.M., Smail, I. 1994, *Astrophys. J.* **430**, 121

[11] Dalton, G. B., Efstathiou, G., Maddox, S. J., & Sutherland, W. J. 1992, *Astrophys. J.* **390**, L1

[12] Dalton, G. B., Efstathiou, G., Maddox, S. J., & Sutherland, W. J. 1994, *Mon. Not. R. astr. Soc.* **269**, 151

[13] Dressler, A., Oemler, A., Butcher, H., & Gunn, J. E. 1994, *Astrophys. J.* **430**, 107

[14] Edge, A. C. & Stewart, G. C. 1991, *Mon. Not. R. astr. Soc.* **252**, 428

[15] Ellis, R.S. 1994, STScI Workshop on *Quantifying Galaxy Morphology at High Redshifts.*

[16] Griffiths, R. 1990, *Hubble Space Telescope Wide Field & Planetary Camera Instrument Handbook Version 2.1* (Baltimore, Space Telescope Science Institute).

[17] Gunn, J. E., & Dressler, A. 1988, in *Towards Understanding Galaxies at Large Redshift*, R. Kron and A. Renzini, eds., Dordrecht, p. 29.

[18] Gunn, J. E., Hoessel, J. G., & Oke, J. B. 1986, *Astrophys. J.* **306**, 30

[19] Gunn, J. E., & Oke, J. B. 1975, *Astrophys. J.* **195**, 255

[20] Guzzo, L., Collins, C. A., Nichol, R. C., & Lumsden, S. L. 1992, *Astrophys. J.* **393**, L5

[21] Henry, J. P., Gioia, I. M., Maccacaro, T., Morris, S. L., Stocke, J. T., & Wolter, A. 1992, *Astrophys. J.* **386**, 408

[22] Lubin, L. M., & Postman, M. 1995, *Astron. J.*, submitted

[23] Lubin, L. M., 1995, *Ph.D.* Thesis, Princeton University.

[24] Lumsden, S. L., Nichol, R. C., Collins, C. A., & Guzzo, L. 1992, *Mon. Not. R. astr. Soc.* **258**, 1

[25] Molinari, E., Banzi, M., Buzzoni, G., Chincarini, G. & Pedrana, M.D. 1994, *Astron. & Astrophys. Suppl.*, **103**, 245

[26] Oegerle, W. R., Hoessel, J. G., & Jewison, M. S. 1987, *Astron. J.* **93**, 519

[27] Oemler, A. 1992, in *Clusters and Superclusters of Galaxies*, A.C. Fabian, ed., Kluwer Academic Publishers, London.

[28] Postman, M., Geller, M. J., & Huchra, J. P. 1988, *Astron. J.* **95**, 267

[29] Postman, M., Huchra, J. P., & Geller, M. J. 1992, *Astrophys. J.* **384**, 404

[30] Postman, M., Lubin, L.M., Gunn, J.E., Oke, J.B., Schneider, D.P., Hoessel, J.G. & Christensen, J.A. 1995, *Astron. J.*, submitted

[31] Postman, M., Oegerle, W. R., Hoessel, J. G., & Lauer, T. R. 1995, in progress.

[32] Schombert, R., & Rakos, K. 1994, *Astrophys. J.*, in press.

[33] Shectman, S. 1985, *Astrophys. J. Suppl. Ser.* **57**, 77

[34] Smail, I., Ellis, R., Fitchett, M. & Edge, A.C. 1995, *Mon. Not. R. astr. Soc.* **273**, 277

[35] Squires, G., Kaiser, N., Babul, A., Fahlman, G., Woods, D., Neumann, D.M. & Böhringer, H. 1995, *Astrophys. J.*., submitted

[36] Tyson, J.A. & Fischer, P. 1995, *Astrophys. J.* **446**, L55

[37] Zwicky, F., Herzog, E., Wild, P., Karpowicz, M., & Kowal, C. T. 1968, *Catalogue of Galaxies and Clusters of Galaxies*, California Institute of Technology, Pasadena.

IS THE DENSITY DISTRIBUTION OF CLUSTERS NON-GAUSSIAN ?

Ts. Kolatt [1]
[1]*Harvard-Smithsonian Center for Astrophysics, Cambridge, Massachusetts, 02138 USA.*

Abstract

The one-point probability distribution function (*PDF*) is computed for the 25 h^{-1}Mpc-smoothed density field of rich clusters of galaxies in the Abell/*ACO* catalogs. The observed *PDF* is compared to the *PDF*s drawn similarly from mock catalogs of clusters in cosmological simulations of Gaussian and several non-Gaussian initial conditions. Several statistics allow significant rejection of the non-Gaussian models tested here, and fail to reject the Gaussian model. A comparison with the predictions of second-order perturbation theory and a log-normal model for *CDM* Gaussian initial conditions yield a linear biasing factor $b_c/b_o \simeq 4$ and $b_c/b_o \simeq 3.7$ for $R \geq 0$ clusters.

1 Introduction

There exist various cosmological scenarios that consider different physical processes that led to the initial mass-density fluctuations. All scenarios agree in that starting at a certain time gravitational instability took over and became the dominant process for the growth of density fluctuations. As for the initial conditions in different models, these can be categorized according to the Gaussian nature of their *PDF*. In most models that arise from the inflating universe paradigm [9] Gaussian density fluctuation fields originate naturally. Within the same framework of inflation some scenarios do lead to non-Gaussian density fields [15, 11]. In other models cosmic strings, monopoles and textures (see [5] for a review) all serve as high-density seeds for gravitational instability to start with, thus forming non-Gaussian fields. Some of these non-Gaussian models are motivated by observations [6, 16].

Assuming the initial fluctuations form a Gaussian random field, one may use either the gravitational potential field, the velocity field or the density field in order to reveal the Gaussian nature of them. The former two, however, are not yet well determined within a large enough volume to allow for conclusive results about their distribution function. The analysis

of the spatial distribution of the density fluctuations is somewhat easier. By employing a biasing scheme we may use the object field as a probe for the distribution function. Since the density field may appear highly non-linear on small scales while we are looking for the (semi) linear phase of the distribution function, heavy smoothing is compulsory. This requirement, in conjunction with the requirement of having as many independent volumes as possible for the assessment of the *PDF*, lead to the natural choice of a big volume-limited sample of objects. The best candidates for this are the rich-cluster catalogs.

The direct calculation of a smoothed field *PDF* is preferential over the evaluation of n-order correlations (very noisy) or moments of distribution for discrete objects (subject to selection effects).

In the following we derive the *PDF* of the smoothed field of the rich-cluster catalogs (§2), compare with mock catalogs drawn from simulations with well known *PDF*s (§3), and demonstrate the rejection power of this test for some non-Gaussian *PDF*s (§4). We finally use the comparison between the first few moments as observed and as predicted-by-theory in order to obtain the linear biasing factor for the rich clusters.

2 Data and measuring method

Three combinations of two data sets were used in order to estimate the *PDF* of the rich clusters; The north Abell (*NORTH*) catalog [1] with richness class $R > 0$, the *ACO* [2] catalog, and the unification of the two sets including many more measured redshifts ($R > 0$ and $R \geq 0$).

Distances to the clusters, D_c, included in the *NORTH* and *ACO* sets are inferred by the procedure described in Scaramella *et al.* [21]. For the unified set of the above two (*ALL*), we use the compilation done by Peacock & West [18] and follow their procedure of distance estimation. In the present analysis we confine ourselves to include clusters within $D_c < 450$ h^{-1}Mpc . For the angular selection, $\phi(\boldsymbol{r})$, we use the formula of Bahcall & Soneira [3] for the *NORTH* sample, and Scaramella *et al.* [21] for atmospheric obscuration. The robustness of the results as a function of the different D_c and $\phi(\boldsymbol{r})$ is discussed in detail elsewhere [13, 14]. The similar results for the *PDF* for each data set when analyzed separately (fig. 1) is due to this robustness. For the sake of the statistical noise reduction, we prefer to use the *ALL* data set.

We evaluate the 25 h^{-1}Mpc Gaussian smoothed *PDF* on grid points of 30 h^{-1}Mpc linear dimension. A key point is that the correction for selection is done for a smoothed field, any other choice doesn't allow appropriate weighting of low density cites. We weigh by setting $N_g = 50$ as the mass-unit measure of the clusters, where N_g is the number count of galaxies within the Abell radius. Alternative weighting is discussed in [13]. In order to account for missing volume near the survey boundaries, the effective smoothing volume about each grid point, V_{eff}, is computed. The density assigned to a grid point is the weighted count of clusters times V_{eff}^{-1}. The *PDF* and its first moments are obtained from the distribution of smoothed density values at the grid points. In order to overcome the systematic errors and to reduce the random ones, we consider only regions in space where the selection function is not too low ($\phi \geq 0.4$) and points for which the effective window volume within the catalog boundaries is relatively large ($V_{eff} \geq 0.8V$).

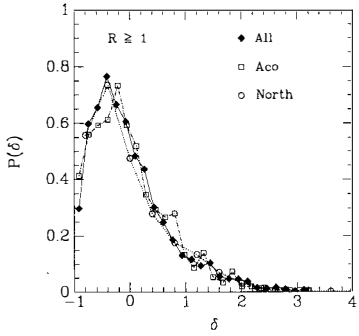


Figure 1: *PDF*s of the 25 h^{-1}Mpc smoothed three data sets ($D_c \leq 450$ h^{-1}Mpc , $R \geq 1$)

3 Comparison with simulations

3.1 Gaussian simulations

In order to quantify the rejection level of the hypothesis that the smoothed density distribution of the rich clusters of galaxies reconciles with Gaussian initial fluctuations, we create artificial catalogs out of N-body simulations. We use Zel'dovich mapping [25] for the simulations as an approximation for the mildly non-linear regime (for the quality of this *cf.* [12]). We take the power spectrum to be the 3 h^{-1}Mpc Gaussian smoothed *CDM* ($\Omega = 1, h_0 = 0.5, n = 1$) model [8] within a box of 900 h^{-1}Mpc side and 128^3 particles and grid points. The identification of the considered cell as a cluster or a center for a super cluster, is done by applying the joint condition of both exceeding a threshold density and being a local peak of the density field.

We weigh each peak for which $\delta \geq \delta_{th}$ by $\delta - \delta_{th} + 1$. This allows to take the richness degree of freedom into account or alternatively to account for dense regions with more than one cluster. The specific locations of the clusters are then determined randomly within the boundaries of the considered cell. The observed number density is obtained by adjusting δ_{th}.

In the upper left panel of figure 2 we notice the similarity between the *PDF* of the *ALL* clusters and the *PDF* from the simulation of the Gaussian field. Both *PDF*s are not Gaussian and several reasons account for that: **1.** Small non-linearities tend to change the original Gaussian density field. **2.** The biases due to the analysis contribute to mildly non-Gaussian effects. **3.** The identification of clusters is a process that may take us away from the original Gaussian nature of the density field [4].

The consistency of the *ALL* catalog distribution with the simulation's catalog, should, however, convince us that there is no contradiction between the two fields after they experience the measurement machinery. In order to make sure that such an agreement is not achieved by the combination of a high degree of statistical noise and heavy smoothing we should find at least one density field for which its derived distribution function differs considerably from the processed Gaussian field.

3.2 Non-Gaussian simulations

We divide the non-Gaussian fields into two categories: Local non-Gaussian where a local, continuous, non-linear transformation (mapping) is applied to a Gaussian field, and Global non-Gaussian where the construction of the field is by a process that induces strong correlations between the *phases* in the k-space distribution.

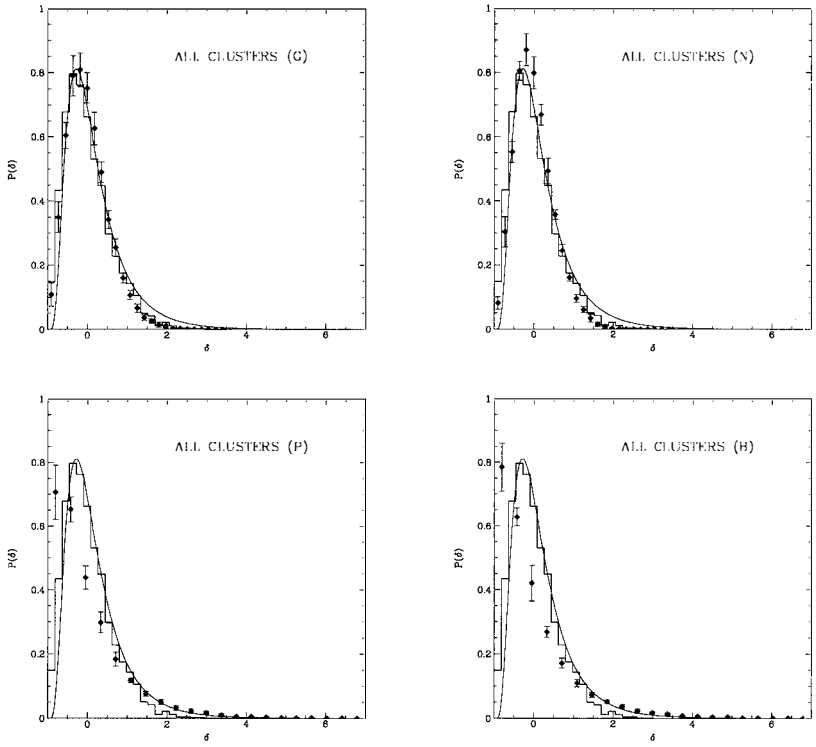


Figure 2: *PDF* drawn from 10, 25 h^{-1}Mpc smoothed artificial catalogs (diamonds, 1σ errors) Vs. real data (*ALL*, solid histogram) and log-normal model (solid line). all for $R \geq 0$. **a.** Non-distorted Gaussian (G) **b.** Negatively skewed (N) **c.** Positively skewed (P) **d.** Broaden (B) (distortion parameter for (b-d), $a = 0.8$).

3.2.1 Local non-Gaussian fields. We follow Weinberg & Cole [24] and parameterize the local distortion from Gaussianity by one parameter, a. The transformations are applied to the field $\delta(\vec{r})$ with a Gaussian *PDF* of σ^2 variance. We force the distorted distribution to preserve the first and second moments of the Gaussian distribution. Three distortion schemes are given by considering the following transformations: positive, negative and broad.

$$Dis(\delta) = \begin{cases} \delta(\vec{r}) & (G) \\ (\exp(a\delta/\sigma) - \exp(a^2/2)) \times \sigma \left(\exp(2a^2) - \exp(a^2)\right)^{-1/2} & (P) \\ -(\exp(-a\delta/\sigma) - \exp(a^2/2)) \times \sigma \left(\exp(2a^2) - \exp(a^2)\right)^{-1/2} & (N) \\ \delta \left(\exp(a\delta/\sigma) + \exp(-a\delta/\sigma)\right) \times \sigma \left(2[1 + (1+4a^2)\exp(2a^2)]\right)^{-1/2} & (B) \end{cases} \quad (1)$$

A value of $a = 0.8$ is adopted since it yields similar distribution to that of the global texture model [17] in the (P) case.

In figure 2 the *PDF*s of the Gaussian and distorted fields are shown against the *PDF* of the (*ALL*) rich clusters ($R \geq 0$). In each plot the continuous line is the one parameter log-normal fit.

3.2.2 Global non-Gaussian fields. In the global non-Gaussian density field we use a "toy" explosion model [23]. Spheres of equal radius are embedded at random. Clusters are

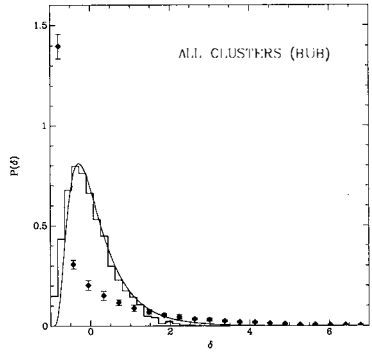


Figure 3: *PDF* from 30, 25 h^{-1}Mpc smoothed artificial bubbles catalogs (diamonds) Vs. *ALL* ($R \geq 0$) *PDF*. Marks as in figure 2.

positioned at each of the two intersection points of every three spherical shells. The radius of the spheres and their filling factor are adjusted to obtain the desired number density of clusters, and several of their other observed statistical properties such as the auto-correlation function. Figure 3 shows the *PDF* obtained for the bubbles simulations (BUB) with bubbles of 50 h^{-1}Mpc radius and a filling factor of 1.5 .

4 Comparison with theoretical approximations

In this attempt, the 25 h^{-1}Mpc smoothing brings us to the slightly non-linear regime for which the second order perturbation theory is designed ([20] §18). In this framework the expression for the skewness, S, is obtained given a power spectrum, $P(k)$, and an arbitrary filter, W_k, [10]. For the standard *CDM* and the relevant current filter, numerical integration of the expression yields $S \approx 3.07\sigma$ (here $\sigma^2 \equiv \mu_2$).

A log-normal distribution may serve as an alternative approximation to the mildly non-linear evolution of the primary Gaussian distribution [7]. In this approximation we use the first (average, μ) moment and the second (variance, σ^2) moment of the *Gaussian* distribution to express the entire moments of the *log-normal* distribution. In the current case where the first two moments should be preserved, the log-normal distribution becomes the mapping: $Dis(\delta) = \exp(\delta) - \exp(\sigma/2)$. Predictions for the skewness, by the two theoretical models, can be compared to the skewness as measured for the smoothed cluster density field. However the comparison may suffer from the following drawbacks: **1.** The approximations were made for the continuous field, while the data calculation is for a smoothed discrete field. **2.** The second order perturbation calculation underestimates the skewness. **3.** A time dependence may be required for the log-normal approximation [7].

Comparing an S value as predicted by a model with the observed value according to $S^{model}(b_c\sigma) = S^{data}$ can then give a solution for b_c. In table 1 we quote the values of b_c for standard *CDM* ($\sigma_8 = 1$, *i.e.* $b_o = 1$). From the second order perturbation theory we get 4.0 ± 0.6, and from the log-normal model 3.7 ± 0.5. The 1σ errors are estimated from the simulations. These biasing factors are consistent with each other, and more important consistent with other calculations for rich cluster biasing factor ([19], $b_c/b_o = 4.5 \pm 0.6$).

STATISTICS OF PDF OF DISTORTED FIELDS AND RICH CLUSTERS

	$\sqrt{\mu_2}$	S_r	K_r	S	K
ALL CLUSTERS ($R \geq 0$)	0.58	1.47	4.34	1.00	1.14
(G)	0.52 ± 0.02	1.25 ± 0.17	4.36 ± 0.04	0.86 ± 0.12	1.07 ± 0.45
DISTORTED					
(P)	0.95 ± 0.09	1.28 ± 0.11	1.85 ± 0.09	2.43 ± 0.70	11.0 ± 7.8
(N)	0.48 ± 0.02	1.09 ± 0.13	4.40 ± 0.03	0.71 ± 0.09	0.50 ± 0.21
(B)	1.05 ± 0.09	1.39 ± 0.07	1.78 ± 0.10	2.78 ± 0.67	13.2 ± 7.1
(BUB)	1.61 ± 0.12	1.59 ± 0.08	1.67 ± 0.11	2.83 ± 0.52	10.96 ± 4.75
CDM (2^{nd} ORDER)				0.25 ($b_c = 4.0 \pm 0.6$)	
LOG-NORMAL				0.27 ($b_c = 3.7 \pm 0.5$)	

Table 1: Statistics (see text) of the *PDF* for the real ($R \geq 0$) *ALL* data and artificial catalogs (1σ errors).

KOLMOGOROV - SMIRNOV REJECTION LEVEL (D)

	ALL	ACO
(G)	NR(0.07 ± 0.04)	NR(0.07 ± 0.04)
(P)	$0.992(0.54 \pm 0.06)$	$0.979(0.47 \pm 0.08)$
(N)	NR(0.18 ± 0.08)	$0.956(0.34 \pm 0.06)$
(B)	$0.999(0.58 \pm 0.03)$	$0.997(0.51 \pm 0.02)$
(BUB)	$0.999(0.56 \pm 0.00)$	$0.999(0.63 \pm 0.01)$

Table 2: KS test rejection level (D) for *ALL* sample versus artificial catalogs ($R \geq 0$). NR=Not-Rejected.

5 Statistical tests

One way of rejecting the hypothesis that two *PDF*s are consistent with each other is by comparing moments of the two distributions, rational functions of moments, or other statistics such as the "reduced skewness" $< \delta|\delta| >$. In Table 1 we show five statistics as applied to the $R \geq 0$ clusters. The statistics are: **(a)** standard deviation: $\sqrt{< \delta^2 >} = \sqrt{\mu_2}$, **(b)** reduced skewness, defined as $S_r \equiv < \delta|\delta| > / \sqrt{\mu_2}$, **(c)** reduced kurtosis: $K_r \equiv (< |\delta| > - \frac{2}{\pi}) / \sqrt{\mu_2}$, (d) skewness: $S \equiv \left[(\mu_3)^2/(\mu_2)^3\right]^{1/2}$, and **(e)** kurtosis: $K \equiv \mu_4/\mu_2^2$. The (P) model is formally ruled out by the K_r statistic at the $\sim 27\sigma$ level. Similar results hold for the (B) model ($\sim 25\sigma$) and the (BUB) model ($\sim 24\sigma$). The (N) model can be rejected only at the $\sim 3\sigma$ level by S_r and S statistics. As for the (G) model, leaving aside the issue of $\sqrt{\mu_2}$, all the statistics yield a $\sim 1.5\sigma$ agreement between the data and the model. The 3σ deviation of $\sqrt{\mu_2}$ may be interpreted as the inadequacy of standard *CDM* power spectrum, or a biasing scheme somewhat different from the chosen one. The quoted numbers for the observational data can now serve as references for any theoretical model which predicts a certain pattern of a density field.

In order to allow consideration of the entire *PDF* in the comparison, we use the Kolmogorov-Smirnov (KS) test [22]. Table 2 sets the rejection levels drawn from the KS tests for the *PDF* of the rich clusters ($R \geq 0$), and those for the ensembles of artificial catalogs. Both *PDF*s are treated as experimental data. According to this test one can rule out consistency between the data and all the models but the (G) and the (N). In the case of the *ACO* catalog even the (N) model fails and the (G) model stays alone (NR = Not Rejected) to be consistent with the rich clusters distribution.

6 Conclusions

The smoothed density field of the Abell, ACO cluster catalogs provide a suitable probe for the mildly non-linear range of the evolution of density fluctuations, and may serve as a discriminatory tool for various initial distributions of matter fluctuations. In this contribution we confronted the smoothed PDF of the rich clusters with several non-Gaussian model PDFs and demonstrated its rejection power. No non-Gaussian model among those tested here (3 local non-Gaussian and 1 global) passed the test of being consistent with the data. We were unable to reject the Gaussian PDF model by any of the statistics we used here.

Our test is not a good discriminatory tool between different power spectra. In a biasing scheme it is subject to changes via multiplication by b_c. The power spectrum can however, be uniquely related to the other moments in the Gaussian case. Under the assumption of Gaussian field, the biasing factor can be found almost independently of the value of Ω, by using second order perturbation theory ($b_c = 4.0 \pm 0.6$) or a log normal approximation (3.7 ± 0.5).

This work was supported in part by the US National Science Foundation (PHY 91-06678).

References

[1] Abell, G.O. 1958, ApJ. Supp., **3**, 211

[2] Abell, G.O., Corwin, H.G., Olwin, R.P. 1989, ApJ. Supp., **70**, 1

[3] Bahcall, N.A. and Soneira, R.M. 1983, ApJ, **270**, 20

[4] Bardeen J.M.,Bond, J.R.,Kaizer,N.,Szalay,A.S. 1987, ApJ, **304**, 15

[5] Bertschinger, E. 1989, *Ann. Ny. Acad. Sci.* **57**, 151

[6] Broadhurst, T.J., Ellis, R.S., Koo, D.C. & Szalay, A.S. 1990, Nature, **343**, 726

[7] Coles, P. & Jones, B.J.T. 1991, MNRAS, **248**, 1

[8] Davis, M., Efstathiou, G., Frenk, C. and White, S.D.M. 1985, ApJ, **292**, 371

[9] Guth, A.H. & Pi, S.-Y. Phys. Rev. Lett., **49**, 1110

[10] Juszkiewicz, R. & Bouchet, F.R., 1991, in *"the distribution of Matter in the Universe" 2nd DAEC Meeting*, ed. G.A. Mamon & D. Gerbal (Meudon: Observatoire de Paris), p. 301

[11] Kofman, L. 1991, in Primordial Nucleosynthesis and Evolution of Early Universe, Eds. Sato, K. and Audouze, J. (Dordrecht: Kluwer)

[12] Kofman, L., Bertschinger, E., Gelb, J. M., Nusser A. & Dekel, A. 1994, ApJ, **420**, 44

[13] Kolatt, Ts.S., 1994, Ph.D. Thesis, The Hebrew University, Jerusalem, Israel

[14] Kolatt, Ts.S., Dekel, A. & Primack, J.R., 1995, in preparation

[15] Linde, A. 1990, Particle Physics and Inflationary Cosmology (Harwood, Chur, Switzerland)

[16] Ostriker, J. P. 1988, in *IAU Symp. No. 130*, ed. J. Audouze and A. Szalay (Dordrecht: Reidel)

[17] Park, C., Spergel, D.N. & Turok, N. 1991, ApJ, **372**, L53

[18] Peacock, J.A. & West, M.J. 1992, MNRAS, **259**, 494

[19] Peacock, J.A., & Dodds, S.J. 1994, preprint

[20] Peebles, P.J.E. 1980, *The Large Scale Structure of the Universe*, Princeton University Press

[21] Scaramella, R., Zamorani,G., Vettolani, G., Chincarini, G. 1991, Ast. J, **101**, 342

[22] Smirnov, N.V. 1938, Byull. Moskov. Gos. Univ., Ser A.; 2 no. 2; 3

[23] Weinberg, D.H., Ostriker, J.P. , Dekel, A. 1989, ApJ, **336**, 9

[24] Weinberg, D.H., Cole, S. 1992, MNRAS, **259**, 652

[25] Zel'dovich, Ya.B. 1970. A&A, **5**, 20

[26] Zel'dovich, Ya. B., 1980, MNRAS, **192**, 663

THE APM CLUSTER SURVEY: CLUSTER DETECTION AND LARGE-SCALE STRUCTURE

G. B. Dalton
Department of Physics, Oxford, UK.



Abstract

The APM Cluster Survey was based on a modification of Abell's original classification scheme for galaxy clusters. Here we discuss the results of an investigation of the stability of the statistical properties of the cluster catalogue to changes in the selection parameters. For a poor choice of selection parameters we find clear indications of line-of-sight clusters, but there is a wide range of input parameters for which the statistical properties of the catalogue are stable. We conclude that clusters selected in this way are indeed useful as tracers of large-scale structure.

1 Introduction

For many years, all statistical analyses of the distribution of clusters of galaxies has relied on the work of [1] and [2]. In recent years, however, the uniformity of these catalogues, and hence their usefulness as tools for studying the large-scale structure, have come into question ([7], [10] and [6]). With the aim of resolving these questions and producing a uniform cluster catalogue we have applied a modified version of Abell's algorithm to the APM Galaxy Survey ([8] and [9]). Here we describe an investigation of the properties of a wide range of possible catalogues based on different parameter choices. We find the statistical properties of the catalogue to be fairly stable to changes of the input parameters, but we will also describe some potential pitfalls. A full account of this work will be published in [5].

2 The Cluster Selection Algorithm

Abell's algorithm defined clusters in terms of the number of galaxies seen on the photographic plate above the estimated background, within two magnitudes of $m_3{}^\star$, and within a projected

*We use the notation m_i to denoth the ith ranked galaxy in the cluster field after subtraction of the background.

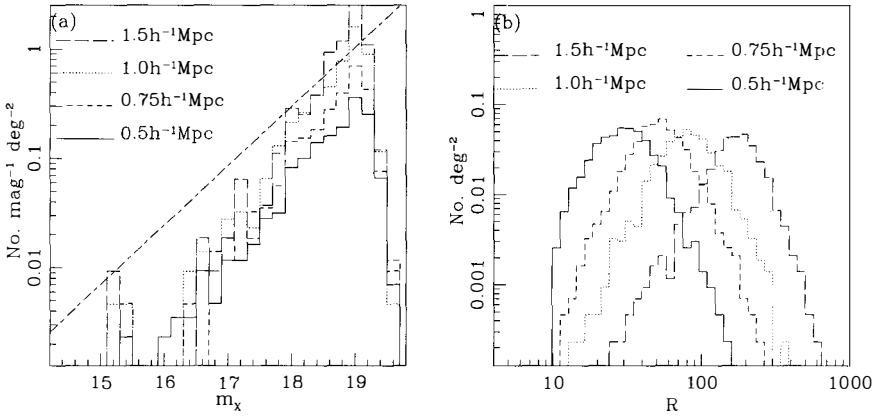


Figure 1: **(a)** The number-magnitude histograms for catalogues with different search radii (see legend), $X = \mathcal{R}/4$. and richnesses determined from the range $[m_X - 0.5, m_X + 1.5]$. The magnitude limits adopted for comparison samples are 19.0, 18.9, 18.8, and 18.7, respectively. The diagonal shows the Euclidean slope of 0.6 for comparison, and successive histograms have been offset by 0.3 in log$N$ for clarity. For each catlogue we only show data for clusters above the richness limit adopted for the comparison. **(b)** The number-richness histograms for these catalogues, with magnitude limits as above. The richness limits for 500 clusters to these magnitude limits are 190, 99, 67, and 39, respectively.

radius of $1.5\mathrm{h}^{-1}$Mpc at the distance estimated from the magnitude of $m_{1\bullet}$. For a range of projected radii, r_C, we estimate the cluster distance from m_X, where X is a function of the cluster richness ($X = \mathcal{R}/\kappa$), which is in turn determined from a magnitude range about m_X. This definintion is recursive, and so we apply the convergence criteria that $\delta m_X < 0.025$ mag and that the centroid of the galaxies within the projected radius changes by $< 40''$.

3 Comparison Samples and Completeness

For each catalogue we calibrate the distance estimator as described by [4]. We expect a catalogue to be useable out to the point at which the faint limit of the richness determination is equal to the magnitude limit of the APM Galaxy Survey ($b_J = 20.5$). We compare the properties of groups of catalogues by selecting equal numbers of clusters from each catalogue to a common estimated distance. Figure 1 shows the number-magnitude and number-richness relations for four catalogues with different selection radii (see figure caption). For each catalogue the $N(m_X)$ relation rises smoothly to $m_X = 19.0$ where the catalogue definition becomes invalid. The $N(\mathcal{R})$ relations show that each catalogue is still complete in terms of richness at the comparison limit.

The limiting feature of the catalogues shown in Figure 1 is that the richness is defined by a broad magnitude range about m_X which hits the survey magnitude limit by a redshift of $z \sim 0.1$. We attempted to improve on this limit by reducing the magnitude range by 0.5mag at the faint end to give a limiting m_X of 19.5. However, since the definition of m_X is tied to the richness count, it then becomes necessary to adopt a different value for X to prevent m_X from

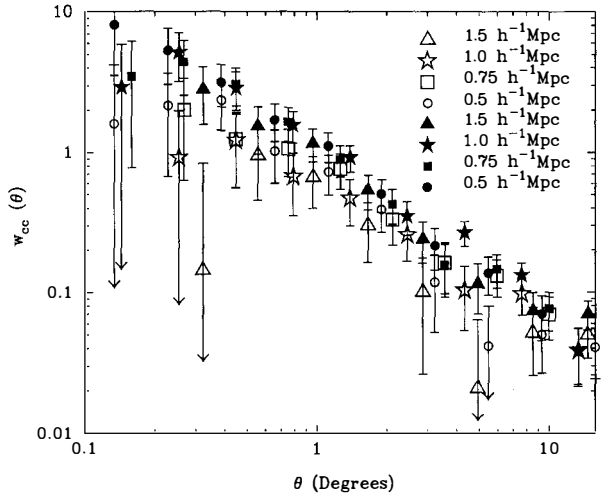


Figure 2: The angular correlation functions for the comparison samples shown in Figure 1 (solid symbols). Also shown are the data for similar catalogues generated with richnesses estimated from the range $[m_X - 0.5, m_X + 1.0]$ (open symbols). Note the depression of clustering due to spurious line-of-sight associations.

sampling the luminosity function at an absolute magnitude brighter than $M_\star$. If this is not corrected, the cluster selection algorithm becomes extremely sensitive to spurious, line-of-sight associations of galaxies in preference to real clusters [3]. This effect is most noticeable for a large selection radius. Reducing X to a value closer to $X = 2$ compensates adequately for the change in the richness definition, but careful tuning is required to optimise the desired gain in the catalogue depth. One should also be aware that the depth of the catalogue is increased at the expense of increased noise in the richness estimates for nearby clusters, as the background count in a small magnitude range becomes uncertain at brighter magnitudes.

4 Angular Clustering Measures

For each comparison set of catalogues we calculated the two-point angular correlation functions, $w(\theta)$, using the standard, $F(DD/DR) - 1$, estimator. Figure 2 shows the results for the catalogues shown in Figure 1, together with results for similar catlogues generated using the smaller magnitude range for the richness estimator as discussed above. It can be seen that the original catalogues (filled symbols) are in good agreement with one another over the whole range of scales for which estimation is possible, and we may conclude that there is no intrinsic variation in the clustering properties introduced by changing the selction radius. For the second set of catalogues (open symbols) there a systematically lower amplitude for $w(\theta)$ and a much greater variation between the catalogues. As noted above, the largest excursions from the solid symbols occur for those catalogues with large selection radii.

At smaller selection radius, $r_C = 0.75\mathrm{h}^{-1}\mathrm{Mpc}$, we also investigated the effect of varying κ.

At the depth of the comparison samples considered for $2 \leq \kappa \leq 4$ we find no variation within the amplitude of $w(\theta)$ within the errors, and conclude that the catalogues are stable to such variation at this selection radius. This implies that the reduced amplitude seen in Figure 2 for small radii catalogues (open circles and squares relative to filled circles and squares) must be generated by incompleteness at the low richness end in these catalogues. This is not surprising, given that in Figure 2 we have matched to the lowest effective depth estimate from Figure 1 and hence we are sampling only those clusters in the deeper catalogue with the noisiest richness estimates.

We conducted similar tests on the angular cluster–galaxy correlation functions. These provide a much clearer signal of the line-of-sight effects discussed above. For the original set of catalogues we see evidence for a shoulder in $w_{cg}(\theta)$ which corresponds to the projected cluster selection radius at the mean depth of the sample considered. This effect is significantly more pronounced for catalogues with large r_C, and is almost undetectable by $0.75h^{-1}$Mpc. For the narrower richness definition we see a similar trend as we increase r_C until we reach $r_C = 1.5h^{-1}$Mpc. For this catalogue the line-of-sight effects are so pronounced that there is *no signal* in the cross-correlation function beyond this radius.

5 Conclusions

We have shown that it is possible to select clusters of galaxies in a way that does not affect the large-scale statistical properties of the distribution. There is some gain to be made by a careful choice of distance estimator, but one must be wary of the potential problems associated with a distance estimator which samples the luminosity function at very bright magnitudes. We conclude that clusters of galaxies selected from a high quality galaxy catalogue may be usefully used as a tracer of the matter distribution on large scales.

References

[1] Abell G. O., 1958. ApJS, 3, 211.

[2] Abell G. O., Corwin H. C., Olowin R. P., 1989. ApJS, 70, 1.

[3] Dalton G. B., 1992. *D.Phil. thesis*, Oxford University.

[4] Dalton G. B., Efstathiou G., Maddox S. J., Sutherland W. J., 1994. MNRAS, 269, 151.

[5] Dalton G. B., Maddox S. J., Sutherland W. J., Efstathiou G., 1995, in preparation.

[6] Dekel A., Blumenthal G. R., Primack J. R., Olivier S., 1989. ApJ, 338, L5.

[7] Lucey J. R., 1983. MNRAS, 204, 33.

[8] Maddox S. J., Sutherland W. J., Efstathiou G., Loveday J., 1990a. MNRAS, 243, 692.

[9] Maddox S. J., Efstathiou G., Sutherland W. J., 1990. MNRAS, 246, 433.

[10] Sutherland W. J., 1988. MNRAS, 234, 159.

THE POWER SPECTRUM OF APM CLUSTERS

H.Tadros
Oxford University, Oxford, England.



Abstract

We present the power spectrum analysis of the APM cluster redshift survey and compare it with the predictions from various Cold Dark Matter (CDM) models. We find that standard CDM (SCDM) fails to match the observations. Mixed dark matter (MDM) and CDM with a cosmological constant (ΛCDM) are a better fit to the data. We also examine the question of the biasing of the cluster distribution with respect to that of galaxies and attempt to estimate the bias parameter between galaxies and mass within the context of specific cosmological models.

1 Survey Data and Cosmological Models.

The APM cluster redshift survey (described in detail in ref.[3]) consists of 364 clusters selected from the APM galaxy survey. The sample of clusters has a mean depth of 450 h^{-1}Mpc and a mean space density of 3.4×10^{-5} h^3Mpc^{-3}. Previous results from the correlation function analysis, measured on scales $2 \lesssim s \lesssim 50$ h^{-1}Mpc ([3]), give a correlation length $r_0 = 14.3 \pm 1.75$ h^{-1}Mpc (2 σ errors). The correlation function is inconsistent with SCDM, but consistent with ΛCDM (with $\Gamma = \Omega h = 0.2$) and MDM. With the power spectrum analysis we can extend this comparison to larger scales.

We also use simulated APM cluster surveys taken from three cosmological models. The details of these simulations and the method for creating mock APM cluster surveys is described in detail in refs. [1] and [2]. We use three cosmological models:

1. Standard CDM with a normalization such that the amplitude of mass fluctuations in spheres of radius 8 h^{-1}Mpc, $\sigma_8 = 1$.

2. ΛCDM with $\Omega_\Lambda = 0.8$, and $\Omega_{tot} = 1$, and a normalization of $\sigma_8 = 1$.

3. A model where the Mixed Dark Matter transfer function is used, with $\Omega_{tot} = 1$ and $\Omega_\nu = 0.3$, and $\sigma_8 = 0.83$

These normalizations were chosen to match as closely as possible the COBE normalization (refs. [5] and [7]). The simulations are run with a P^3M code and have 10^6 particles in a box of side 300 h^{-1}Mpc. The spatial resolution is $\sim 80h^{-1}$kpc (see refs. [1] and [2]).

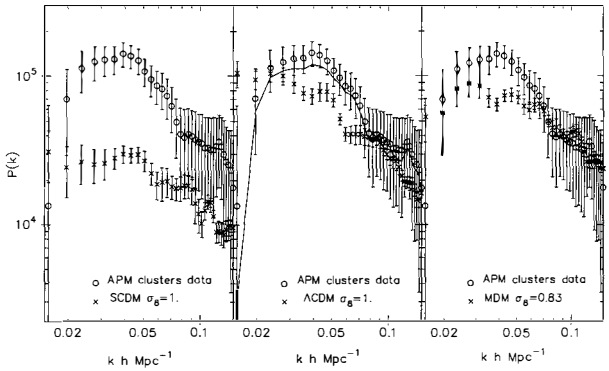


Figure 1: The power spectrum of the APM cluster survey (circles) compared with predictions from cosmological models (crosses). The model power spectra are obtained from the average over ten realizations of mock APM cluster surveys taken from N-body simulations and the error is the error on the mean. The error bars on the APM cluster power spectrum are calculated as in FKP. All power spectra are in redshift space.

2 Power Spectrum Analysis.

Since the cluster redshift survey has a radially varying selection function (i.e. it is not accurately volume limited), we treat it as we would a flux limited survey. We apply the formalism of Feldman *et al.* ([4], hereafter FKP) to find the power spectrum and the errors on each point. The radial selection function is obtained by smoothing the velocity histogram of the data with a Gaussian of width 4000 km s^{-1}. Further details such as the exact weighting schemes used may be found in Tadros *et al.* ([8]).

In Figure 1 we compare the power spectrum obtained from the real APM clusters with that obtained from mock APM cluster catalogues with the same mean space density as the data. It can be seen that the results from the SCDM model lie 3 - 4σ below the data. The MDM and ΛCDM match the data more closely, but there is still an indication of more power in the data than in the models on large scales. However it must be kept in mind that at these large scales the power spectrum results are sensitive to the selection function. (For example a smaller smoothing width results in less power. For reference the solid line in the central panel shows the result for a Gaussian smoothing width of 1000 km s^{-1}).

3 Biasing of Clusters and Galaxies with respect to Mass.

We define the following linear bias parameters:

$$P_g(k) = (b_m^g)^2 P_m(k), \quad P_{cl}(k) = \left(b_m^{cl}\right)^2 P_m(k), \quad P_{cl}(k) = \left(b_g^{cl}\right)^2 P_g(k) \tag{1}$$

where the subscript m refers to mass, g to galaxies and cl to clusters. We can therefore write the linear bias parameter of galaxies with respect to the underlying mass as:

$$(b_m^g)^2 = P_g(k)/P_m(k) = \left(1/\left(b_g^{cl}\right)^2\right) \times \left(b_m^{cl}\right)^2 \tag{2}$$

We are going to utilize these identities to get a handle on the value of the linear bias parameter b_m^g via the observations presented here, measurements from the APM/Stromlo galaxy redshift survey ([6]), and results from N-body simulations. The above equations allow us

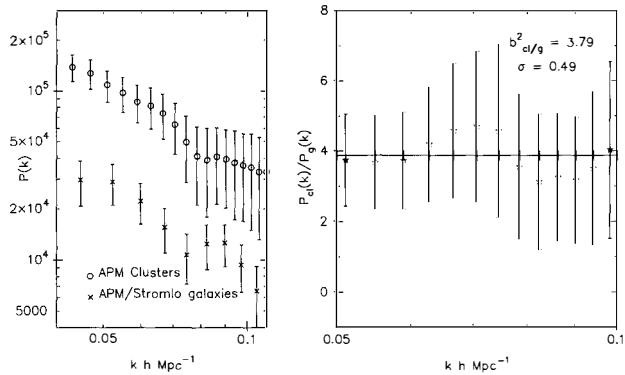


Figure 2: Left hand panel shows the power spectrum of APM clusters (circles) and the power spectrum of galaxies in the APM/Stromlo survey (crosses) while the right hand panel shows the ratio between the two.

to estimate b_m^g from the data in two ways, while never having to identify galaxies from the simulations. We would like to see whether we can get consistent results for b_m^g, and to estimate its value. We compare the ratio of the power spectrum of galaxies to that of clusters in the real universe using the cluster power spectrum of Figure 1 and the galaxy power spectrum as found from the APM/Stromlo survey([9]). This gives us the first ratio on the RHS of equation 2. Then assuming a cosmological model, we can use the N-body simulations described in Section 2 to find the power spectrum of the underlying mass and compare this with the power spectrum of the clusters drawn from these simulations, to give us the second ratio on the RHS of equation 2. (Note: in these comparisons we have used all the clusters in a simulation box, without applying the APM cluster catalogue mask or selection function). In this way we can indirectly estimate the linear bias parameter between galaxies and mass, within the context of a given cosmological model. This parameter can also be measured directly by comparing the APM/Stromlo galaxy power spectrum with the power spectrum of mass points from the cosmological simulations (again, the whole box is used).

In the left hand panel of Figure 2 we show the power spectrum of the APM clusters as presented here together with the power spectrum of the APM/Stromlo galaxies ([9]). Plotted in the right hand panel is the ratio of these two power spectra. It can be seen to be accurately constant over the range of scales being considered, its value being ~ 3.8. (This range in wavenumber is chosen because at wavenumbers less than $\sim 0.04\ h\ \mathrm{Mpc}^{-1}$ the power spectrum of APM/Stromlo galaxies is poorly determined. We have an upper limit on wavenumber of $0.1\ h\ \mathrm{Mpc}^{-1}$ to ensure that we are in the linear regime.) In Figure 3 the circles show the ratio of the power spectrum of the clusters in an N-body simulation to the power spectrum of the mass points. This is generally constant as a function of scale, except possibly in the MDM model. The crosses are the ratio of the power spectrum of the APM/Stromlo galaxies to the power spectrum of mass points.

4 Results.

From the data in Figure 2, we have $1/(b_g^{cl})^2 = 0.26 \pm 0.03$ and using the values of $\left(b_m^{cl}\right)^2$ in Figure 3, we can estimate b_m^g. These values can now be compared with the direct measurement of b_m^g, also given in Figure 3. The results are summarized in Table 1.

These results support the claim that SCDM is not a consistent model. The indirect and

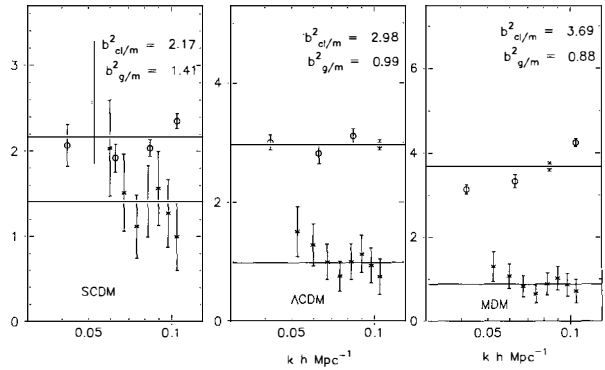


Figure 3: Circles show the ratio of the power spectrum of clusters to that of mass points for the three cosmological models, while crosses show the ratio of the power spectrum of galaxies in the APM/Stromlo galaxy survey to the power spectrum of mass points for the three cosmological models.

	Indirect	Direct
SCDM	0.75 ± 0.05	1.19 ± 0.07
MDM	0.98 ± 0.06	0.93 ± 0.05
ΛCDM	0.88 ± 0.06	0.99 ± 0.06

Table 1: Values for the linear bias parameter b^g_m from the direct and indirect measurement.

direct measures of the bias parameter give significantly different results. This is to be expected, since the SCDM model is generally in poor agreement with measured large scale structure statistics. The MDM and ΛCDM models provide a consistent picture. The indirect and direct measures of the bias parameter agree and indicate that its value is of order unity.

Acknowledgements. I acknowledges the receipt of a PPARC research studentship.

References

[1] Croft R. A. C., Efstathiou G., 1994, *Mon. Not. R. astr. Soc.* **267**, 390

[2] Croft R. A. C., Efstathiou G., 1994, *Mon. Not. R. astr. Soc.* **268**, L23

[3] Dalton G. B., Croft R. A. C., Efstathiou G., Sutherland W. J., Maddox S. J. 1995, *Mon. Not. R. astr. Soc.* **271**, L47

[4] Feldman H. A., Kaiser N., Peacock J. A., 1994 *Astrophys. J.* **426**, 23

[5] Górski K. M., Stompor R., Banday A. J. *preprint*

[6] Loveday J., Peterson B. A., Efstathiou G., Maddox S. J., 1992 *Astrophys. J.* **390**, 338

[7] Stompor R., Górski K. M., Banday A. J. *preprint*

[8] Tadros H., Efstathiou G., Croft R. A. C., Dalton G. *in preparation*

[9] Tadros H., Efstathiou G., Loveday J., Peterson B. A. *in preparation*

LARGE SCALE PECULIAR VELOCITIES: EFFECTS FROM SUPERCLUSTERS

Roberto Scaramella[1]
[1]*Osservatorio Astronomico di Roma, 00040 Monteporzio Catone, Italy.*



Abstract

We study the gravitational influence of very large scale structures, as traced by clusters of galaxies, on the Local Group [LG] motion and the large scale flows.

We derive from the distribution of Abell clusters within 300 Mpc/h the overdensity field on a 3-D grid of spacing 5 Mpc/h, then we solve the Poisson equation for the peculiar potential and finally obtain the peculiar velocity field.

Quite interestingly, from *this global solution* we:

i) recover within $\sim 10^o$ the direction of the LG motion in the Cosmic Microwave Background [CMB] frame,

ii) find that the Great Attractor itself moves wrt to the CMB frame,

iii) derive $\beta_c^{-1} \equiv b_c \Omega_0^{-0.6} = 5.3 \pm 0.20$ from a preliminary comparison with the Mark II catalog of peculiar velocities,

iv) derive estimates for the bulk flow in spheres which fairly agree with the level derived from POTENT and the Spiral samples,

v) find that the Lauer & Postman [L&P] bulk flow has too a large amplitude to be in agreement with our results.

1 Sample and method

A fuller discussion can be found in [5]. Our starting point are the Abell and ACO catalogs of clusters. Here we use data from an all-sky sample of $\simeq$ 860 clusters of galaxies, obtained by joining the Abell and ACO catalogs, considering a region complete in volume with limiting depth of 300 Mpc/h and with $|b| > 20^o$. We place the clusters on a 128^3 grid, of side 640 Mpc/h. The clusters are allocated to the nearest grid point two different weights (number and mass, see [5]) which give an estimate of the intrinsic uncertainty of the results. We divide this field (Gaussianly smoothed with $\sigma = 15$ Mpc/h) by the average of 200 pseudo-random samples [6] and solve the Poisson equation for the peculiar potential of this field with periodic b.c. Finally we derive the linear velocity field by differencing the potential.

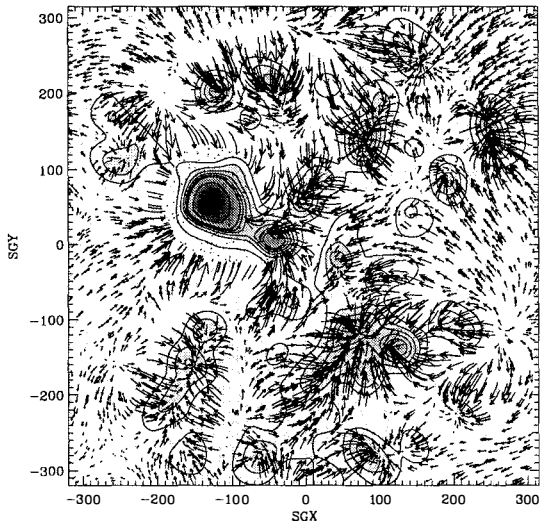


Figure 1: *We show the overdensity field and peculiar motions in the supergalactic plane. Units are in Mpc/h.*

2 Qualitative results

In Fig. 1 we show $\delta_c(\vec{x})$ for a slice of 15 Mpc/h half–width centered on the SG plane in order to show the effect of this procedure, together with the derived velocity field in the plane. See [5] for a list of technical problems, assumptions, checks and refinements to be possibly dealt with, as well as a larger number of figures of the field and flows.

From the flows we derive the picture of a complex pattern, in which a few qualitative conclusions can be drawn (see [5]). Among these, the prediction of an offset of the density peak with the minumum of the peculiar velocity field at the GA position is in a remarkable

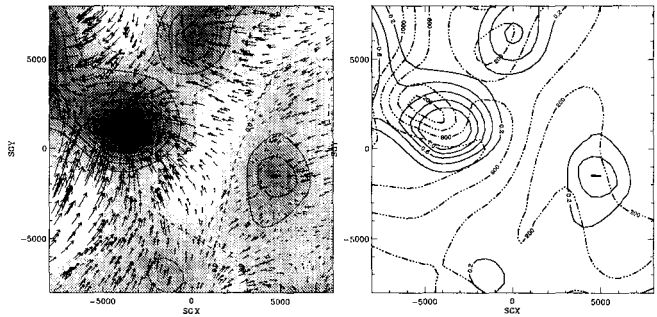


Figure 2: *In the left panel we show an enlargement of the inner region of Fig.2, the one presently seen by catalogs of galaxies. In the right panel we show density isocontours superimposed to peculiar velocities isocountours. Notice the offset at the GA position.*

agreement with the latest results from POTENT applied to the Mark III catalog [2]. It must be noticed that if we force the overdensity field to be zero beyond a depth of 100 Mpc/h, that is with no influence from very large scales, this offset disappears.

3 Estimates of the bias factor

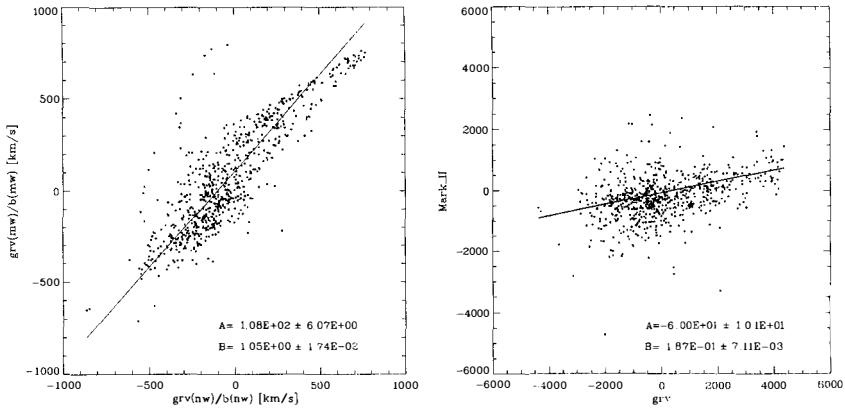


Figure 3: *In the left panel we show the dispersion of the values predicted according to the two different weights at the location of the Mark II galaxies. In the right panel we show the fit for the value of β_c from the average of predictions from the left panel against the Mark II values.*

Now, under the strong hypotheses of: i) validity of linear theory, and ii) simple proportionality of the $\delta_c(\vec{x})$ field and the true mass fluctuation field, $\delta_\rho(\vec{x})$, one would be able to derive the 3D peculiar flows on quite large scales, and in particular the one of the LG. We recover the latter within $\approx 10^o$ [5].

From normalization of the amplitude one can get estimates for β_c, but a better way is likely to be an estimate which is based not on a single point (cf [1]), but on comparison with one of the catalogs of peculiar veocities. At this stage we make a preliminary comparison with the galaxies of the Mark II catalog grouped as in [7].

From a preliminary fit with errors in both variables, we obtain (right panel of Fig. 3) an estimate of $\beta_c = 0.19 \pm 0.01$, which translates into $b_c \Omega_0^{-0.6} = 5.3 \pm 0.20$. Therefore, if one rescales by assuming reasonable but uncertain values for relative biases ($b_{c,o} \equiv 3.5$, $b_{c,I} \equiv 4.5$ [4]), one obtains the estimates of $\Omega_0 \approx 0.5$ if $b_o \equiv 1$, or $\Omega_0 \approx 0.8$ if $b_I \equiv 1$, with uncertainties much larger than the formal ones.

4 Not too large bulk flows on large scales

Even though it furnishes a single point (to the large experimental uncertainties adds the one due to cosmic variance), the motion of a sphere centered on us as a whole wrt the CMB frame is an interesting value, with controversial results which date back to the Rubin–Ford effect. In Fig. 4 we show our preliminary solutions, together with quite recent determinations (the spiral

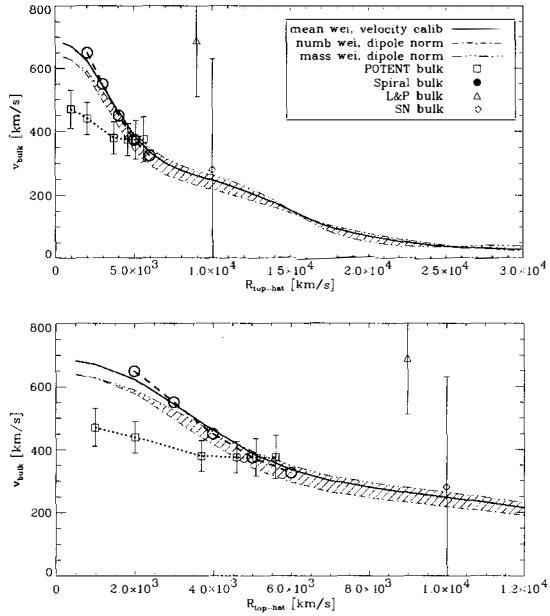


Figure 4: *We show our solutions for the amplitude of the bulk motion in spheres centered on the LG.*

sample results have been presented by Da Costa at this conference). We see that the amplitude of the motion we derive is in good agreement with that from the galaxy samples, while differs from the one derived from clusters [3] (for a depth of 100Mpc/h L&P find 700 ± 180 km/s vs our 250 ± 50 km/s). One must bear in mind, though, problems due to boundary conditions and unsurveyed areas in our model.

References

[1] Branchini, E., & Plionis, M, this volume; Scaramella, R., Vettolani, G., & Zamorani, G., 1994, *Astrophys. J.* **422**, 1

[2] Dekel, A., this volume; also 1994, *Ann. Rev. Astron. Astrophys.* **32**, 371

[3] Lauer, T., & Postman, M., 1994 *Astrophys. J.* **408**, 418

[4] Peacock, J.A., & Dodds, S.J., 1994 *Mon. Not. R. astr. Soc.* **267**, 1020in press.

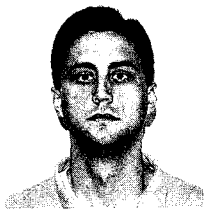
[5] Scaramella, R., 1994, *Astrophys. Lett & Comm.* in press.

[6] Scaramella, R., Zamorani, G., Vettolani, G., & Chincarini, G., 1990, *Astron. J.* **101**, 342

[7] Tormen, G., Moscardini, L., Lucchin, F., & Matarrese, S., 1993 *Astrophys. J.* **411**, 16

A REDSHIFT SURVEY OF A PROMINENT SOUTHERN SUPERCLUSTER CANDIDATE

K. Slinglend [1], D. Batuski [1], C. Balkowski [2],
P. Felenbok [2], S. Maurogordato [2], R. Olowin [3]
[1] *University of Maine, Orono, ME, U.S.A.*
[2] *Observatoire de Meudon - DAEC, Meudon, France.*
[3] *St. Mary's College, Moraga, CA, U.S.A.*



Abstract

Recent analyses of clusters from Abell's catalog and the Abell, Corwin, and Olowin, 1989 (hereafter ACO) catalog of southern rich clusters reveal evidence of three dimensional superclustering on scales of 50-100 h^{-1} Mpc and more (*e.g.*, Batuski and Burns 1985, and Huchra *et al.*, 1990). However, redshifts have been measured for less than 35% of Abell/ACO clusters (and most of these have only one or two galaxies measured – see Struble and Rood 1991).

We have been and are continuing to use MEFOS on the 3.6-m telescope at ESO to observe clusters in a $10° \times 70°$ strip of sky that includes two particularly interesting supercluster candidates (needing only redshift data on clusters in the region to determine the significance of the apparent superclustering). Our sample is limited to richness class $R \geq 1$ clusters, with one or fewer measured redshifts, at high galactic latitude (the limits of Abell's (1958) statistical sample and $|b| > 30°$ for ACO clusters), with $m_{10} \leq 19.0$ (estimated $z < 0.18$).

Our first run of this program took place in August, 1994. We observed 22 clusters in the strip (with 10 or more redshifts per cluster), concentrated on the most prominent of the two supercluster candidates. The results are presented here.

We find a 10x overdensity of Abell/ACO clusters in this region. This supercluster joins three others with similar density enhancements within $z \leq 0.11$ to be explained by theory.

1 Motivation

Abell clusters are excellent tracers of mass on the largest scales. With an average spatial seperation of $\approx 60h^{-1}Mpc$ they are very efficient for mapping scales approaching those measured by the COBE satellite. However, less than one third of the Abell/ACO clusters have measured redshifts. Most of the ones that are measured have only one or two measured redshifts per cluster. This leads to large uncertainties in the cluster redshift because of the possibility of measuring a foreground or background galaxy not associated with the given cluster (projection effects). Our effort here has been to both attempt to quanitfy these projection effects by collecting 10 or more redshifts per cluster and to use the high confidence redshift data to investigate superclusters of the Abell/ACO type.

The particular supercluster candidate (located in the Aquarius region) we investigated in the August, 1994 ESO run is one that was originally identified by Ciardullo *et al.*, 1985. Ciardullo *et al.* identified the supercluster candidate via a single linkage scheme, better known as " friends of friends.". They then measured single redshifts for 20 $R \geq 1$ Abell clusters in this region of sky and found that there was no supercluster, only a chance projection of clusters strung out along the line of sight out to $z \leq 0.2$. However, as pointed out earlier, measuring only a single redshift is dangerous, particularly in region of such high apparent density. We similarly (via percolation) identified a more extended versioon of the same supercluster candidate. Our identification included 34 clusters, 20 of which were originally identified by Ciardullo *et al.*

This region was suggestive of three similar overdensities discovered in the past (*i.e.* Horologium - Lucey *et al.*, 1983, Corona Borealis - Postman *et al.*, 1986, and the Shapley Concentration - Scaramella *et al.*, 1989). If this supercluster indeed proves to be a similarly very high mass overdensity, so that we have four within $z \leq 0.11$, then the theoretical models for the formation of such structure must be able to reproduce it and thus will be even more highly constrained.

2 Cluster Sample

Our entire sample is made up of $R \geq 1$ Abell/ACO clusters within a $10° \times 70°$ strip of sky in the southern hemisphere (see the box drawn in Figure 1). Each point in Figure 1 represents an Abell cluster. This strip was chosen so that it is includes two apparently high mass overdensities. These overdensities (supercluster candidates) were identified using a percolation algorithm based upon the redshifts from the literature (mostly Ciardullo *et al.*) or redshifts estimated from the magnitude of the tenth brightest cluster member. We further restricted our sample to include only those clusters with zero or one previously measured redshift at high galactic latitude (the limits of Abell's (1958) statistical sample and $|b| > 30°$ for ACO clusters). Our distance cut is an approximate one based on the magnitude of the tenth brightest cluster member (m_{10}). We included only those clusters with $m_{10} \leq 19.0$. This corresponds to an estimated $z < 0.18$.

During our first observing run (August, 1994 at ESO), we concentrated on the most dense of the two supercluster candidates. The Aquarius candidate is defined roughly by a box on the sky with the following coordinates: $22.7^h \leq \alpha \leq 23.8^h$, $-17° \leq \delta \leq -27°$ (see upper left of $10° \times 70°$ strip shown in Figure 1).

3 Observations and Data Reduction

The observations took place over five nights beginning August 29, 1994. The observations were under conditions of good seeing ($0.5'' - 2.0''$) and transparency. The instrument used to collect the spectra was the new MEFOS (Meudon-ESO Fiber Optic Spectrograph) mounted on the ESO 3.6m telescope. The instrument was very efficient. We collected approximately 15 redshift-quality spectra within a given cluster field per hour.

The data reduction was performed using modified routines originally written for the reduction of spectra from Steward Observatory's MX spectrograph (routines written by John Hill, Bill Oegerle, David Batuski and Kurt Slinglend). These routines run under the IRAF command language. The redshifts were cross-correlated using the IRAF 'fxcor' cross correlator. The redshifts presented here. The typical error is on the order of 50 km/s.

4 Results

Approximately two hundred (202) high quality redshifts resulted for 14 clusters within the Aquarius supercluster candidate. A histogram of the collected redshifts is shown in Figure 2. The eye is immediately drawn to the major peak with a mean velocity of $\approx 33,500\ km\ s^{-1}$. This peak confirms the existence of a supercluster. There is however a non-negligible amount of noise surrounding the main peak. The noise results from the 1° field of the MEFOS instrument. This field size is about twice a typical Abell diameter at $z = 0.1$. Since all the arms of MEFOS cannot be put very near the center of each field, we have measured many galaxies outside of the Abell radii. This effect does allow us, however, to sample the field galaxy distribution in the surrounding medium. This analysis will be presented in a subsequent paper.

Further evidence for the Aquarius supercluster can be seen in Figure 3. Each stripe represents a mean cluster redshift. From Figure 3, we see there are 10 clusters within $\approx 50\ h^{-3}Mpc^3$ cube centered at $z = 0.108$. This corresponds to an overdensity of ≈ 10. For comparison, the Corona Borealis supercluster has an overdensity of ≈ 20. Also shown in Figure 3 are the clusters measured by Ciardullo *et al.* Only 2 of the 20 clusters measured by Ciardullo fall within the supercluster. However, recall that Ciardullo *et al.* only measured one redshift per cluster in a region of very high density. Thus the cluster redshifts derived have a substantial uncertainty.

5 Conclusion

In September, 1995 we will be reobserving som of the clusters originally measured by Ciardullo *et al.*, collecting 15 or more redshifts per cluster. We will then be able to confirm or reject (with high confidence) the remaining clusters' membership in the Aquarius supercluster. However, even if the clusters measured by Ciardullo *et al.* prove not to be supercluster members, the Aquarius supercluster has already been shown to be an ultra high mass overdensity (10x) similar to Corona Borealis, Horologium, and the Shapley Concentration.

We now have four very large mass overdensities within $z \leq 0.11$. These observations constrain the theoretical models for the formation of such structure and may eventually help to put limits on Ω_o. In the future we plan to compare these results with those from other surveys such as the COBE results, x-ray selected clusters and automatic plate scan selected clusters.

Acknowledgements. This project was partially funded by National Science Foundation Grant AST-9224350 and Sigma Xi, the Scientific Research Society.

References

[1] Batuski and Burns, 1985, *Astrophys. J.* **299**, 5

[2] Ciardullo *et al*, 1985, *Astrophys. J.* **293**, 69

[3] Huchra *et al.*, 1990, *Astrophys. J.* **365**, 66

[4] Lucey *et al.*, 1983, *MNRAS* **203**, 545

[5] Postman *et al.*, 1986, *Astron. J.* **92**, 1238

[6] Scaramella *et al.*, 1989, *Nature* **338**, 562

Figure 1

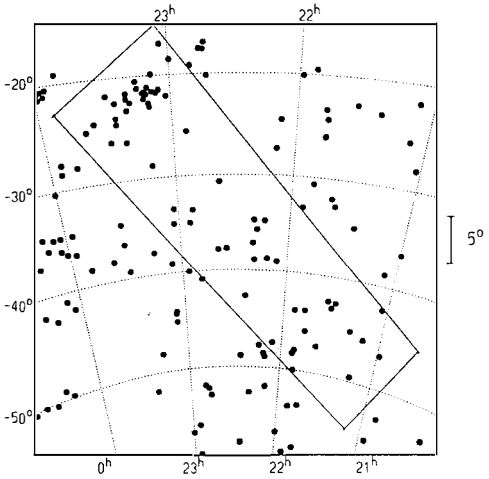


Figure 2

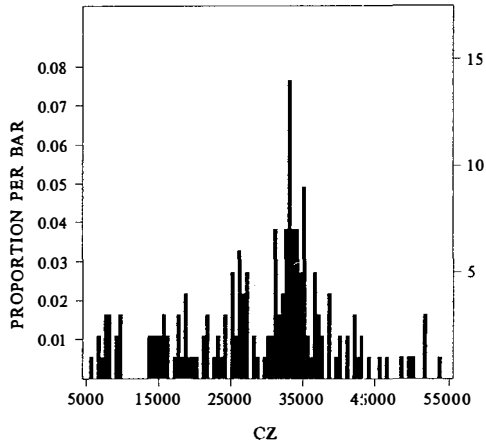
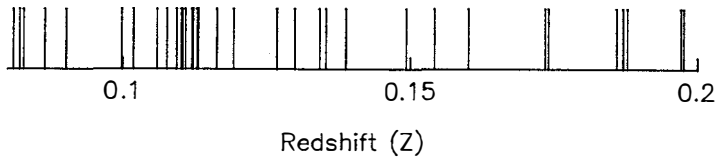
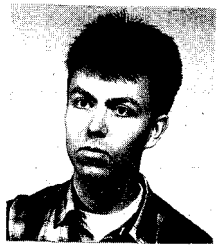


Figure 3



A 140 MPC OSCILLATION OF THE ABELL CLUSTER CORRELATION FUNCTION

Veikko Saar
Tõravere Observatory, EE-2444 Tartu, Estonia



Abstract

We have developed a parameter-independent method to detect local maxima of the two-point correlation function. By applying it to two samples of rich Abell clusters of galaxies with redshift limits $z < 0.08$ and $z < 0.12$ we detect three maxima centered at 150 h^{-1} Mpc, 300 h^{-1} Mpc and 430 h^{-1} Mpc with confidence levels 80% and higher. This sequence of fluctuations has an average interval of 140 h^{-1} Mpc, that can be explained by a power spectrum with a distinct peak at $k = 0.048 \pm 0.005$ h Mpc^{-1}.

The purpose of this work is to investigate the presence of inhomogeneities in 3–dimensional density distributions and to estimate the statistical significance of the result. For detailed description see Saar *et al.* [6].

1 Data

We shall base our analysis on the Abell/ACO catalog of rich clusters of galaxies [1, 2] with updated redshift information [3].

We consider the sample used by Peacock & West [5], but exclude low galactic latitudes to ensure better completeness for higher redshifts. The limiting criteria are: $R \geq 1$, $z < 0.08$, $b > 40°$, $b < -30°$. This selection includes 175 clusters with measured redshifts and 3 clusters with estimated redshifts. We shall also consider a sample with a higher redshift limit $z < 0.12$ that includes 382 measured redshifts and 111 estimated ones, giving about 78% for completeness in redshifts.

The error estimate for clusters with measured redshifts is

$$\sigma_v^2 = \sigma_c^2 + \sigma_g^2/N_z, \quad \sigma_c = 600 \text{ km/s}, \quad \sigma_g = 800 \text{ km/s}, \tag{1}$$

where N_z is the number of galaxies in the particular cluster.

The error in estimated redshifts is much larger. Since the magnitude–redshift relation is determined in the $ln\ z \sim m$ scale, the errors have a normal distribution relative to $ln\ z$ with an rms error

$$\sigma(ln\ z) = 0.27. \tag{2}$$

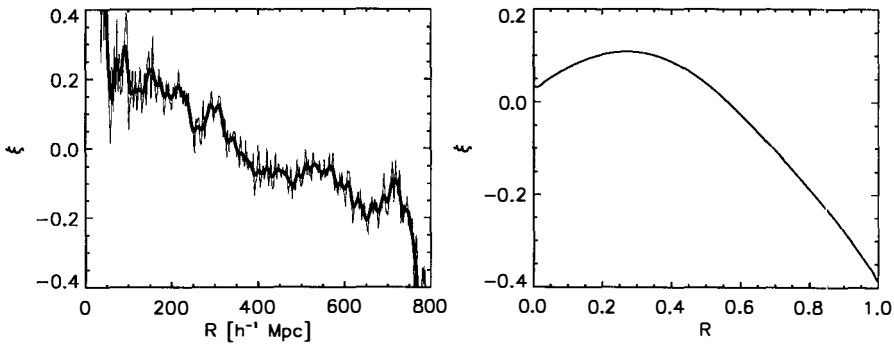


Figure 1: Left: Correlation function of the larger sample. The thin line shows the convolution with a 5 h^{-1} Mpc and the thick line with a 20 h^{-1} Mpc triangular kernel. The dependence of deviations on the smoothing scale is evident. Right: Correlation function of a simulated selection effect within a sphere with diameter $D = 1$. The matter density falls to half its central value at the edges of the sphere.

2 Analysis

We estimate the correlation function as $\xi(r) = dP_{cc}(r)/dP_{rr}(r) - 1$, where dP_{cc} is the probability density of distances of cluster pairs and dP_{rr} is the probability density of a Poisson distribution in the same volume. This gives an expression for the cumulative distribution of distances of cluster pairs $P_{cc}(L)$. Since our data consist of discrete points, we have a sum in an arbitrary interval:

$$\sum_{r=L1}^{r=L2} \Delta P_{cc}(r) = \sum_{r=L1}^{r=L2} (\xi(r) + 1) \Delta P_{rr}(r). \quad (3)$$

The left–hand side of this equation is independent of binning as it just counts all pairs with mutual distances between $L1$ and $L2$. The right–hand side has an additional factor $\xi(r)$. In order to use this equation we have to parametrize the two–point correlation function. As we wish to detect maxima of ξ, we use equation (3) for a limited distance interval and approximate the behavior of ξ in the interval with a parabola. This leaves no binning–dependent terms in the formula.

Our method is robust in the sense that it does not depend on the magnitude of ξ, but only on its local oscillations. This gives us the freedom not to correct for any global trends, such as selection effects (Fig. 1).

Let us consider possible results. We may find no maximum in the selected interval. Secondly, there may be a maximum detected at a very low confidence level (around 50%), in which case it is caused by few clusters, thus being a feature of the particular sample. Thirdly, if a maximum is found with a confidence level near 100%, then it is not sensitive to local variations and should exist in all samples, thus in both of our cluster samples.

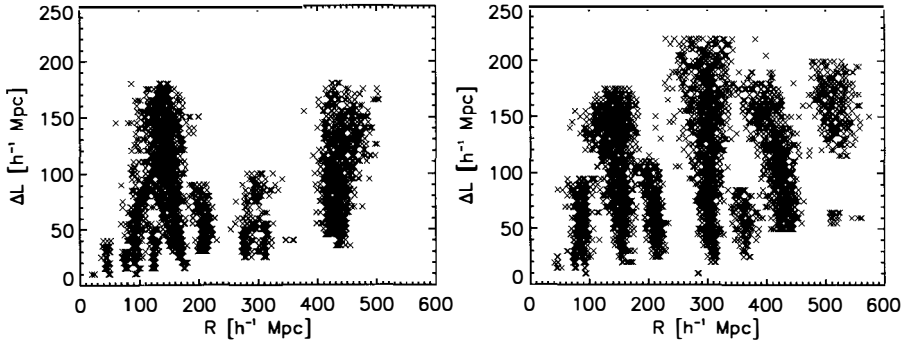


Figure 2: Left: Positions of maxima for intervals with confidence level higher than 50% for the smaller sample, plotted against the width of the interval. Right: Scatter diagram for the larger sample. No maxima were found outside of the ranges of the plot.

The highest confidence levels found were 89% for a maximum centered at 150 h^{-1} Mpc, 94% at 300 h^{-1} Mpc and 83% at 440 h^{-1} Mpc. The maxima extend from intervals close to zero up to certain limits ΔL_{max}, being independent on the width of the search interval.

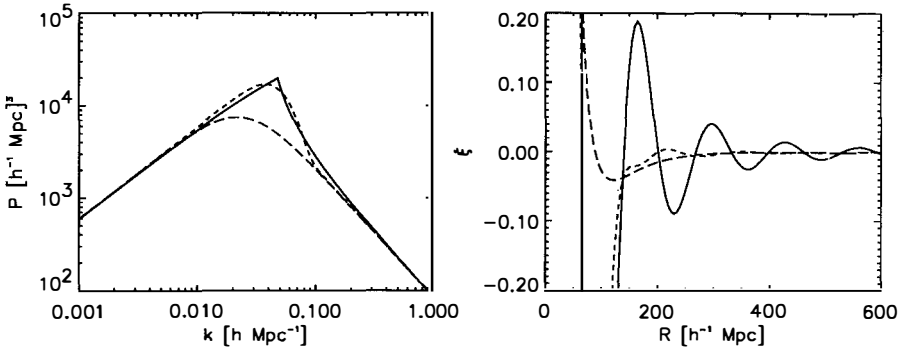


Figure 3: Left: Power spectra. The long-dashed line is the fit of Peacock & West [5], the short-dashed line is for a smooth and the solid line for a sharp maximum at 0.048 h Mpc^{-1}. Right: Correlation functions corresponding to the power spectra. Notice how strong effect the sharpness of the maximum of the power spectrum has on the fluctuations of ξ.

A similar behavior of the two–point correlation function can be predicted by the power spectrum. We take the spectrum used by Peacock & West [5] that does not cause oscillations of ξ, but fluctuations can be produced by using the same spectrum with a sharper maximum. By fixing the small- and large-scale end of the spectrum to match the fit [5], the period of the oscillation is given as $\lambda = 2\pi/k_m$ if the peak is sharp. Smoother maxima give either smaller amplitudes or no oscillations at all. The position of the peak is restricted to $0.043 < k_m < 0.053\ h$ Mpc^{-1} by the data.

3 Conclusions

We have found a sequence of maxima at $110 - 180$, $270 - 330$ and $400 - 450\ h^{-1}$ Mpc, which limits their spacing to the range $\lambda = 140 \pm 30\ h^{-1}$ Mpc. In order to produce the fluctuation amplitude and period of ξ found from the data, the power spectrum must contain a distinct peak at $k_m = 0.048 \pm 0.005\ h$ Mpc^{-1}.

References

[1] Abell G. O., 1958, *Astrophys. J. Suppl. Ser.* **3**, 211

[2] Abell G. O., Corwin H. G., Olowin R. P., 1989, *Astrophys. J. Suppl. Ser.* **70**, 1

[3] Andernach H., Tago E., Stengler–Larrea E., 1995, in The World of Galaxies II, Ap. Lett. & Comm., eds. G. Paturel and C. Petit (New York: Gordon & Breach), in press

[4] Broadhurst T. J., Ellis R. S., Koo D. C., Szalay A. S., 1990, *Nature* **343**, 726

[5] Peacock J. A., West M. J., 1992, *Mon. Not. R. astr. Soc.* **259**, 494

[6] Saar V., Tago E., Einasto J., Einasto M., Andernach H., 1995, *preprint*

A COMPARISON BETWEEN BRIGHT GALAXY AND RICH CLUSTER CORRELATIONS

A. CAPPI[1], C. BENOIST[2], L.N. DA COSTA[3] S. MAUROGORDATO[4]
[1] *Osservatorio Astronomico di Bologna, via Zamboni 33, I-40126 Bologna, Italy*
[2] *DAEC Observatoire de Meudon, Place J.Janssen, F-92195 Meudon Cedex, France*
[3] *IAP, 98 bis bvd Arago, 75014 Paris, France*
[4] *CNRS, DAEC Observatoire de Meudon, Place J.Janssen, F-92195 Meudon Cedex, France*



Abstract

We compare the distributions of very luminous galaxies in the new SSRS2 catalogue and rich clusters. We find that very luminous galaxies ($M \leq -21$) have a significantly stronger correlation function than fainter galaxies, with $r_0 \sim 16\ h^{-1}$ Mpc and zero-point at $\sim 45\ h^{-1}$ Mpc . These values approach the cluster ones. The effect depends on luminosity, and it is not induced by a fractal behaviour or by morphological segregation –the fraction of morphological types is comparable in all the subsamples–. Moreover, these galaxies are not preferentially found in rich clusters. Very luminous galaxies ($L > L_*$) also appear to follow the so-called universal dimensionless correlation function found for clusters and other galaxy systems.

1 Introduction

It is well known that there are significant differences between the galaxy and cluster distributions. The cluster correlation function has a significantly higher amplitude than the galaxy one. Moreover, the correlation function of clusters is positive at larger scales, up to $\sim 50\ h^{-1}$ Mpc. Finally, clusters seem to follow a controversial "dimensionless" correlation function, while galaxies definitely do not follow it. An increasing correlation amplitude with richness was found by Bahcall & Soneira (1983) and Bahcall (1988). Szalay & Schramm (1985) pointed out that the correlation strength increases also with the mean spatial separation of clusters, suggesting the existence of a universal dimensionless correlation function. Bahcall & West (1992) have shown that the scaling relation

$$A_i = r_0^\gamma \sim (0.4 d_i)^{1.8} \tag{1}$$

where $d_i = n^{-1/3}$ is the mean interparticle distance, seems to hold for a number of systems up to superclusters. An interesting point is that, while galaxies –considered as systems with only one member– follow the same richness–amplitude relation of clusters (Bahcall & Soneira 1983; Bahcall & Burgett 1986; Plionis & Borgani 1991), they have a definitely higher amplitude than expected for the dimensionless correlation function. Szalay & Schramm (1985) suggested that the universal

dimensionless correlation function could be due to a fractal distribution, and that the deviation of galaxies from this relation should be explained by gravitational clustering at small scales (see also Luo & Schramm 1992). However, it seems more plausible that the above relation is a consequence of biasing (see Kaiser 1984, Bardeen et al. 1986), where the correlation of more rare and massive systems has an increasing amplitude. CDM simulations by Bahcall & Cen (1992) show that the observed cluster dimensionless correlation function can be best fitted with $\Omega = 0.2$, $h = 0.5$ and $b = 1$, while Mann et al. (1993) find that no model can reproduce the large amplitude of the richness 2 clusters, and Croft & Efstathiou (1994), on the basis of their CDM N–body simulations, claim that the cluster amplitude depends weakly on cluster richness.

As concerning galaxies, after the first claim by Hamilton (1988) of luminosity segregation in the CfA catalogue, there has been no clear evidence for luminosity effects. The general analysis of luminosity and morphology effects in the SSRS2 is presented elsewhere (see Benoist et al., these proceedings). In this talk it will be described some evidence that there is a continuity between the galaxy and cluster distributions, related to an ever–increasing bias: it is probable that the distribution of very luminous galaxies is more similar to that of (poor) clusters than to the distribution of fainter galaxies.

2 Analysis of the subsamples

We used the new magnitude–limited southern sky redshift survey (SSRS2), which includes 3592 galaxies with $m_B(0) \leq 15.5$ (da Costa et al. 1994). We defined different volume–limited samples with a step of 0.5 magnitudes. In each subsample, we selected all galaxies within one magnitude from the absolute limiting magnitude of the subsample. We fixed $H_0 = 100$ and $q_0 = 0.5$. The standard Local Group correction was applied to galaxy velocities. Luminosity distances were computed for the galaxies in the sample, and the knowledge of an *ESO* type T for each galaxy allowed us to apply an appropriate K–correction $K(z, T)$, to calculate the absolute magnitude. A distinct K–correction for 4 different types was applied. For self–consistency, in our correlation analysis we converted all luminosity distances into comoving distances (which are used for clusters).

We estimated the two–point correlation function $\xi(s)$ with the following formula (Hamilton 1994):

$$\xi(s) = \frac{N_{gg} N_{rr}}{N_{gr}^2} - 1 \qquad (2)$$

where N_{cc} is the number of galaxy pairs, N_{rr} the number of random pairs, and N_{cr} the number of galaxy–random pairs. Errors were computed by generating 10 bootstrap catalogs per sample.

Figure 1a shows the correlation length r_0 as a function of the mean interparticle distance $d_i = n^{-1/3}$, where n is the mean density of the subsample. It is apparent that very bright galaxies approach the "universal dimensionless correlation", which is followed remarkably well by subsamples containing galaxies brighter than $M = -20$. The points are systematically above the mean relation, which however was obtained by fitting different systems which show a large scatter (see figure 6 in Bahcall & West 1992). Luminous galaxies follow approximately a relation $r_0 \sim 0.6 d_i$, to be compared to the global fit $r_0 \sim 0.4 d_i$ for the other galaxy systems. The slopes of the galaxy and cluster relations are consistent.

For the SSRS2, da Costa et al. (1994) found a Schechter luminosity function with $M^* = -19.5$; this means that only galaxies in the bright end of the luminosity function, with $L > L^*$, follow the universal relation, while fainter galaxies progressively deviate from it, and seem to approach a minimum amplitude, comparable to that of IRAS galaxies.

Is this behaviour due to a fractal distribution or to the intrinsic difference in luminosity (mass) of these objects? We verified that galaxies within the same luminosity range have comparable correlations, independently of the sample depth; this result rules out a fractal Universe, and confirs the existence of a genuine *luminosity effect*.

The deepest sample containing very bright galaxies ($M \leq -21.0$) shows a cluster–like distribution. For this subsample, we find $r_0 \sim 16 \pm 2\ h^{-1}$ Mpc and a positive signal up to $\sim 45\ h^{-1}$ Mpc. A check

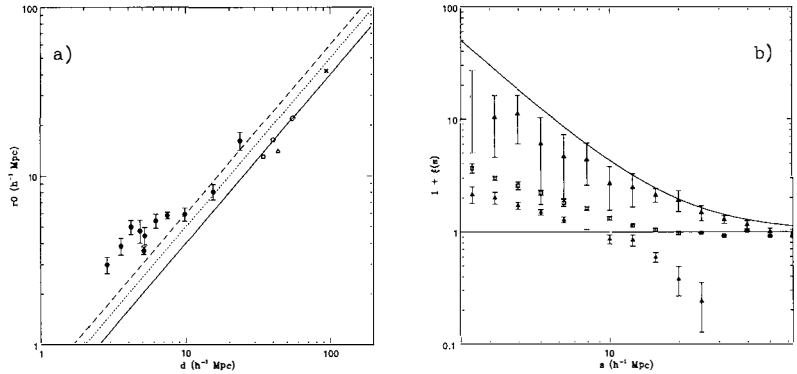


Figure 1: **a)** Correlation length r_0 as a function of the mean interparticle distance $d_i = n^{-1/3}$ for different subsamples of the SSRS2 (filled hexagons with error bars). The other points represent cluster samples of different richness. The relation $A_i \sim (\alpha d_i)^{1.8}$ is also shown; solid line: $\alpha = 0.4$; dotted line: $\alpha = 0.5$; dashed line: $\alpha = 0.6$. **b)** Correlation functions of different volume–limited subsamples. From bottom to top: galaxies with $-17 \leq M \leq -16$, with $-20 \leq M \leq -19$, and with $M < -21$. The solid line represents the best–fit to $R \geq 0$ Abell/ACO clusters ($r_0 = 19.5\ h^{-1}$ Mpc, Cappi & Maurogordato 1992).

with the ACO cluster catalog shows that only 4 out of 133 of these galaxies are found in clusters. Moreover, the morphological mix of these galaxies is very similar to the standard one, with 38% of early type galaxies.

Figure 1b shows the correlation function of different volume–limited subsamples and the fit for $R \geq 0$ ACO clusters. Notice that, while very faint galaxies show a significantly lower amplitude and very luminous galaxies a significantly higher amplitude, samples including more typical galaxies do not have a clear trend; in the figure we show the two extreme samples and one typical intermediate sample, including galaxies around L_*. It is apparent that not only the amplitude of very bright galaxies approaches the cluster one, but also the zero–point increases reaching $\sim 45\ h^{-1}$ Mpc, i.e. a scale comparable to the cluster one. Our results seem to support indirectly the scenario discussed by Bahcall & West (1992) where a richness–dependent correlation reconciles the high amplitude of rich Abell/ACO clusters (see e.g. Postman et al. 1992; Cappi & Maurogordato 1992) with the lower amplitude of poor clusters as in the APM survey (Dalton et al. 1992) and the EDCC survey (Nichol et al. 1992). In any case the correlation length of very bright galaxies ($M \leq 21$), $r_0 = 16 \pm 2\ h^{-1}$ Mpc, should represent a lower limit for the cluster correlation length. Galaxies start to follow the linear relation at a mean interparticle distance of about $10\ h^{-1}$ Mpc, which is half the scale predicted for galaxy systems in the CDM model by Bahcall & Cen which best fits the cluster correlations.

3 Conclusions

We analyzed subsamples of the new SSRS2 including galaxies of different luminosity, comparing their distribution with that of rich galaxy clusters. Our main conclusions are the following.

a) The brightest galaxies ($M \leq -21$) have $r_0 = 16 \pm 2$, thus setting in an unambiguous way a lower limit for the correlation length of rich galaxy clusters, and the zero–point is at $45 h^{-1}$ Mpc, i.e. at a scale comparable to clusters: could it be also the zero–point for the underlying

matter correlation? These bright galaxies have a standard morphological mix and are not found preferentially within rich clusters, so that their correlation does not simply reflect the rich cluster correlation.

b) We found evidence that galaxies with $L > L^*$ follow the universal dimensionless correlation previously found for galaxy clusters. It seems that the same biasing mechanism which is at work for galaxy systems acts on bright ($L > L^*$) galaxies, becoming progressively less effective for lower luminosity galaxies. The mean interparticle distance at which galaxies start to follow the universal scaling relation is $d \sim 10\ h^{-1}$ Mpc. The effect depends on the intrinsic luminosity of galaxies, and *not* on the sample depth.

One should also be aware that, while a useful empirical tool, the $r_0 - d$ relation is only an indirect consequence of the biasing of different classes of objects, characterised by a defined amount of mass within a given radius. A correct comparison between galaxies and clusters would therefore require using a variable different from the mean spatial distance, as discussed by Bernardeau & Schaeffer (1991, 1992).

References

[1] Bahcall, N.A., & Burgett, W.S. 1986, ApJ, 300, L35

[2] Bahcall, N.A., & Cen, R. 1992, ApJ, 398, L81

[3] Bahcall, N.A., & Soneira, R.M. 1983, ApJ, 270, 20

[4] Bardeen, J.M., Bond, J.R., Kaiser, M., & Szalay, A.S. 1986, ApJ, 304, 15

[5] Benoist, C. et al. 1995, these proceedings

[6] Bernardeau, F., & Schaeffer, R. 1991, A&A 250, 23

[7] Bernardeau, F., & Schaeffer, R. 1992, A&A, 255, 1

[8] Cappi, A., & Maurogordato, S. 1992, A&A 259, 423

[9] Croft, R.A.C., & Efstathiou, G. 1994, MNRAS 267, 390

[10] da Costa, L.N., Geller, M.J., Pellegrini, P.S., Latham, D.W., Fairall, A.P., Marzke, R.O., Willmer, C.N.A., Huchra, J.P., Calderon, J.H., Ramella, M., & Kurtz, J. 1994, ApJ 424, L1

[11] Dalton, G.B., Efstathiou, G., Maddox, S.J., & Sutherland, W. 1992, ApJ, 390, L1

[12] Hamilton, A.J.S., 1988, ApJ, 331, L59

[13] Hamilton, A.J.S., 1994, ApJ, 417, 19

[14] Kaiser, N., 1984, ApJ, 284, L9

[15] Luo, X., & Schramm, D.N. 1992, Science, 256, 513

[16] Mann, R.G., Heavens, A.F., & Peacock, J.A. 1993, MNRAS 263, 798

[17] Nichol, R.C., Collins, C.A., Guzzo, L., & Lumsden, S.L. 1992, MNRAS, 255, 21

[18] Plionis, M., & Borgani, S. 1991, MNRAS, 254, 306

[19] Postman, M., Huchra, J.P., & Geller, M.J. 1992, ApJ 384, 407

[20] Szalay, A., & Schramm, D. 1985, Nature, 314, 718

ESTIMATING $\beta \equiv \Omega_o^{0.6}/b$ FROM THE LOCAL GROUP & CLUSTER PECULIAR VELOCITIES

Manolis PLIONIS
International School for Advanced Studies, Via Beirut 2–4, 34014 Trieste, Italy &
National Observatory of Athens, Lofos Nimfon, Thesio, 11810 Athens, Greece



Abstract

Comparing the observed peculiar velocities of the Local Group and of nearby Abell clusters of galaxies with those predicted using linear perturbation theory and the 3-D reconstruction algorithm of Branchini & Plionis (this volume) the value of β can be estimated. I show that the anisotropy that causes the LG motion does not only extend to very large depths ($\sim 160\ h^{-1}$ Mpc) but it is also very coherent, which suggests that the value of $\beta \approx 0.21 \pm 0.015$, obtained from the LG velocity, should not be significantly affected by cosmic variance. Comparing the Abell cluster and QDOT galaxy dipoles in real space their relative biasing factor are estimated to be $b_{cI} \approx 3.5 \pm 0.5$. Finally, using a suitable set of available cluster peculiar velocities I obtain a somewhat lower value of $\beta \approx 0.15 - 0.17$ but with a large uncertainty ($\gtrsim 0.1$) when weighted by the large observational errors. More and better cluster peculiar velocity data are needed to reduce this uncertainty.

1 Introduction

Under the linearity assumption (of gravity and biasing) linear perturbation theory can be used to relate the peculiar velocities of cosmic objects (ex. galaxies and clusters) with their peculiar accelerations, usually estimated by their dipole moments, to determine the cosmological β-parameter [$\beta \equiv \Omega_o^{0.6}/b$; where $b \equiv \frac{\delta N/N}{\delta M/M}$ is the biasing factor]. This relation is:

$$\beta = 4\pi \langle n \rangle \vec{v}/\vec{D} \tag{1}$$

The estimate of $\vec{v}$ is provided in the case of the Local Group by the Doppler-interpreted dipole of the CMB radiation temperature or in the case of other galaxies and clusters by using redshift

independent distance estimates (cf. [1]). The $\vec{D}$ estimate is provided by summing moments of some mass tracer distribution surrounding the source object, taking into account however their selection functions and compensating for possible sky incompleteness. Even so one should be cautious in deducing the value of β from eq.(1) for a number of other reasons:

- Sparse sampling introduces shot-noise that enhances $\vec{D}$, especially at large depths.
- Using one source point (the LG) entails large uncertainties due to cosmic variance.

A detailed analysis, using simulations, showed that the β-parameter estimated on the LG by using high peaks of the density field (clusters) as mass-tracers is very uncertain [6].

On the other hand, the use of many source objects could greatly reduce the latter uncertainty but unfortunately such analyses are usually hampered by the large uncertainty in $\vec{v}$ (due to large uncertainties in their estimated distances) as well as in $\vec{D}$ (due to their surrounding non-symmetric survey volume). See however [2] and [1] for such attempts.

2 β from the LG $\vec{v}$ using the Abell-cluster and QDOT dipoles

Since the most accurately determined value of $\vec{v}$ is that of the LG the above test has been extensively applied to the LG by using many different mass tracer catalogues (see references in [1], [4]). The general result of these studies is that the dipole moment of all these objects is well aligned with that of the CMB, indicating that indeed they trace the underline mass distribution. However, the scale where the dipole apparently converges to its final value differs from catalogue to catalogue with an indication of a strong dependance of the convergence depth, R_{conv}, to the characteristic depth of galaxy catalogue, r^*, with $R_{conv}(r) \approx cr^*$ with $c \approx 1$, which implies a spurious convergence. Only in the cluster dipole case, where $R_{conv} \approx 160\ h^{-1}$ Mpc, we have $c < 1$, probably indicating the true final dipole convergence. The different R_{conv} values could be, among other things, due to: **(a)** redshift-space distortions (***r.s.d.***) coupled with shot-noise effects, **(b)** a distance dependent biasing of the different mass tracers, **(c)** a coherent and large-scale anisotropy generating the LG motion, only parts of which are sampled by the different galaxy dipoles.

The first possibility cannot be the main explanation since in most studies redshift distortions are accounted for (cf. [5], [1], Branchini & Plionis, this volume; hereafter BP). Furthermore, in the cluster case the shot noise effects are minimal since they are volume limited much beyond R_{conv}. The second case lacks, at present, a physical justification while the last case has been shown to be true in [4], where it was found that the differential cluster and QDOT dipoles in large equal volume shells up to R_{conv} point in the general CMB dipole direction, which implies the 'coherence'. In table 1 I present the cluster and QDOT differential dipole directions having included new cluster redshifts and after correcting for redshift-space distortions.

Shell (h^{-1} Mpc)	tracer	#	l	b	$\delta\theta_{cmb}$
0 - 99	cluster/QDOT	47/1181	279°/238°	27°/26°	**4°/34°**
99 - 125	cluster/QDOT	45/235	311°/96°	5°/29°	**41°/121°**
125 - 143	cluster/QDOT	47/106	299°/292°	17°/-10°	**25°/42°**
124 - 157	cluster/QDOT	50/65	266°/259°	22°/32°	**13°/15°**

Table 1: Differential dipole direction after correcting for *r.s.d.* and including in the cluster dipole (1^{st} shell) the effect of the Virgo cluster (see text).

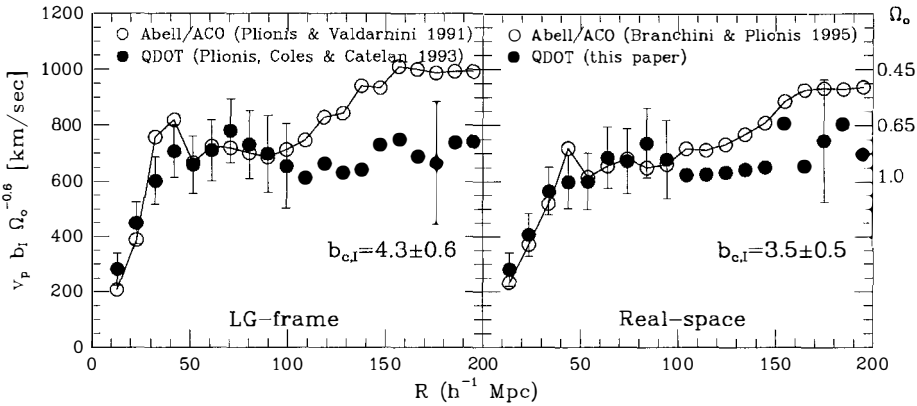


Figure 1: QDOT-galaxy and Abell-cluster dipoles, the latter rescaled by a constant *biasing* factor to *best-fit* each other within the $[10, 100]\ h^{-1}$ Mpc region. **Left panel**: distances in LG frame. **Right panel**: *r.s.d.*-corrected distances. Errorbars are QDOT shot-noise errors (for clarity only few are plotted).

Therefore the estimated value of β obtained from the dipoles of existing galaxy catalogues should be considered strictly an upper limit to the true value. BP using the *r.s.d.*-corrected cluster dipole find $\beta_c \approx 0.21$ with a sampling and cosmic variance uncertainties of $\sim$0.015 and $\sim$0.05 respectively. However, my suspicion is that due to the strong coherence of the anisotropy causing the LG motion the above value of β_c should reflect its true value (within the sampling uncertainty).

It is interesting to compare the QDOT-galaxy and Abell-cluster dipoles within the depths where both have good sampling ($\lesssim$ 100 h^{-1} Mpc due to QDOT selection function) while extending the cluster dipole to shallower depths to include the effects of the Abell-like Virgo cluster (such that the virgocentric infall velocity is $\sim$ 200 km/sec). Thus the lower limit of integration is set to $r \sim 10\ \ h^{-1}$ Mpc. Since both trace the underline mass density field (relatively good alignment of their dipoles with that of the CMB) the only difference between their estimated dipoles should be a constant factor, reflecting their relative biasing parameter, b_{cI}. I plot in figure 1 the QDOT dipole (after subtracting the corresponding shot-noise one) and the rescaled, by the factor shown, Abell-cluster dipole. The agreement of the two dipoles within 100 h^{-1} Mpc is excellent implying that:

(1) Indeed IRAS galaxies and Abell clusters trace both the underline mass distribution.

(2) Linear biasing is valid at least on large ($\gtrsim$ 10 h^{-1} Mpc) scales.

(3) The cluster - IRAS galaxy relative bias is $b_{cI} \approx 3.5$, in agreement with independent studies.

Furthermore, it is evident that although the cluster dipole continues growing for $r > 100$ h^{-1} Mpc the QDOT one flattens out with only weak evidence for a deeper contribution (see also 4^{th} shell in table 1). It has been verified, using simulations [3], that this is due to the QDOT selection function which is such that the QDOT dipole would miss up to a $\sim$ 20% total contribution if such did exist from depths $\sim$ 150 h^{-1} Mpc. The final value of Ω_o from this analysis depends on the unknown biasing factor of the IRAS-galaxy or Abell-cluster distributions with respect to that of the mass. However, with relative biassing of $b_{cI} \approx 3.5$ one would need a value of $b_I \approx 1.3 - 1.4$ to obtain $\Omega_o = 1$.

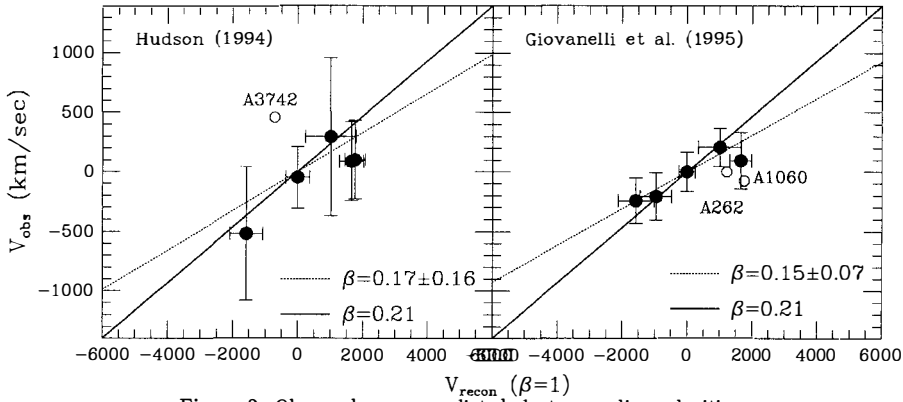


Figure 2: Observed versus predicted cluster peculiar velocities.

3 β from cluster peculiar velocities

Using the reconstruction algorithm described in BP we can relate, using eq.(1), the *r.s.d.*-corrected value of $\vec{D}$ with the observed value of $\vec{v}$ for those clusters for which the latter is available (by means of $D_n - \sigma$ or *T-F* relations) and within the limit of our reconstructed volume $\lesssim 200\ h^{-1}$ Mpc. Due the the large uncertainties especially in $\vec{v}$ a large number of clusters should be used (which presently is not available). In this preliminary analysis we have chosen to exclude clusters that have uncertain peculiar velocities, either due to very discrepant $D_n - \sigma$ and *T-F* distances (ie., A262, A3742) or due to known non-linear effects (ie., Cen30).

In figure 1 the observed $\vec{v}$ is compared with that predicted by eq.(1) for clusters with *T-F* distances taken from the references indicated in the figure. There is a good correlation and the slope gives $\beta \approx 0.15 - 0.17$ which is near although lower than the value found from the LG dipole analysis (see BP). However, the number of available clusters is still too small to put strong constraints on the value of β. Note that although most of the clusters in figure 3 fall on the $\beta = 0.21$ line, the fit is biased to a lower value by Hydra (A1060) (which has 4 Abell neighbours within 30 Mpc) and A1367. If this lower β-value is verified then an $\Omega_o < 1$ model would be probably preferred since the IRAS galaxy biasing value that it implies is $b_I > 1.7$ (see previous section).

References

[1] A. Dekel, *ARA&A* **32** (1994) 99; M.Strauss & J.Willick, *Phys. Reports*, (1995) in press

[2] N. Kaiser et al. *Mon. Not. R. astr. Soc.*, **252** (1991) 1; M. Hudson et al. *Mon. Not. R. astr. Soc.*, submitted

[3] V. Kolokotronis et al. *Mon. Not. R. astr. Soc.*, submitted

[4] M. Plionis and R. Valdarnini *Mon. Not. R. astr. Soc.*, **249** (1991) 46; M. Plionis, P. Coles & P. Catelan *Mon. Not. R. astr. Soc.*, **262** (1993) 465

[5] M. Strauss and M. Davis, *Large Scale Motions in the Universe: A Vatican Study Week* (Princeton Univ. Press, Princeton, 1988), p. 225

[6] P. Tinibrunozzi et al. *Mon. Not. R. astr. Soc.*, submitted

RECONSTRUCTING CLUSTER PECULIAR VELOCITIES WITHIN 20000 Km/s

Enzo BRANCHINI[12] and Manolis PLIONIS[13]
[1] *International School for Advanced Studies, Via Beirut 2-4 34014 Trieste, Italy*
[2] *Queen Mary and Westfield College, Mile End Road, London E1 4NS*
[3] *National Observatory of Athens - Lofos Nimfon, Thesio, 11810, Athens, Greece*



Abstract

Starting from the redshift space distribution of a volume limited sample of Abell+ACO clusters we use a reconstruction procedure to recover their distances and peculiar velocities. The resulting cluster 3-D dipole, as the z-space one, converges at $\sim 170\ h^{-1}$ Mpc and points $\sim 10°$ away from the CMB apex. However, redshift space distortions cause the asymptotic dipole of the z-space cluster distribution to be overestimated with respect to the 3-D one by $\sim 23\%$, leading to a value of $\beta(\equiv \Omega_o^{0.6}/b_c) \approx 0.21$, where b_c is the bias factor of the cluster population with respect to the underlying matter distribution. The resulting cluster velocity field is dominated by a large scale streaming motion along the Perseus Pisces–Great Attractor base-line directed towards the Shapley concentration, in qualitative agreement with the galaxy velocity field on smaller scales. The cluster bulk velocity agrees well with that deduced from the POTENT analysis of galaxy motions at $\sim 60\ h^{-1}$ Mpc; it decreases thereof while pointing in the general direction of the Cosmic Microwave Background (CMB) dipole, in strong disagreement with [3].

1 The Reconstruction Method

We considered the redshift space distribution of the Abell+ACO clusters defined in:
- Abell: $d \leq 250\ h^{-1}$ Mpc, $|b| > 20°$, $m_{10} \leq 17$. N=250 clusters.
- ACO: $d \leq 250\ h^{-1}$ Mpc, $|b| > 20°$, $m_{10} \leq 17$. N=205 clusters.
- Abell+ACO: $d \leq 250\ h^{-1}$ Mpc, $13° < |b| < 20°$, $m_{10} \leq 17$. N=20 clusters.

98% of clusters have measured redshift. For the remaining objects the redshift is estimated using the $m_{10} - z$ relation, of [4], where m_{10} is the magnitude of the tenth brightest galaxy

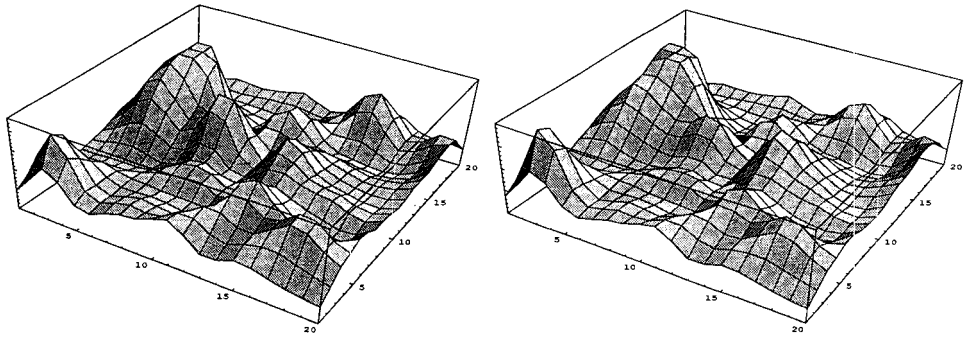


Figure 1: Surface plot visualization of the density field of a slice 8000 km/sec wide centered onto the supergalactic plane both in z space (left panel) and 3-D space (right panel).

in the cluster. We then use a two step procedure to reconstruct the 3-D cluster distribution starting from their observed redshift space positions:

– The first step consists in reconstructing the all sky redshift-space cluster distribution. This is done by generating a population of synthetic objects outside the zone of avoidance (i.e. at $|b| > 20°$) and within 20000 km/s. We impose the synthetic objects to be correlated with the real ones in order to reproduce the observed spatial cluster–cluster correlation while their large scale distribution accounts for galactic absorption, radial selection function and inhomogeneities between the Abell and ACO cluster catalogues. The object distribution within the zone of avoidance is then recovered by randomly cloning the cluster distribution in the nearby galactic strips. The reconstruction within the [20000, 25000] km/s region, where the radial selection function falls below unity, is aimed at providing the boundary conditions for the next step. In this region the synthetic clusters are distributed according to the selection functions but randomly with respect to the real ones to alleviate shot noise effects. The resulting cluster distribution, however, is a considerable improvement over the simple Poissonian one. Finally, the density field beyond 25000 km/s is considered homogeneous and isotropic.

– In the second step we use an iterative technique, similar to [5], to reconstruct the all sky cluster 3-D distribution and their peculiar velocities. The reconstruction algorithm relies on the linear gravitational instability hypothesis and assumes linear biasing. Since the whole reconstruction procedure is based on Monte Carlo techniques, all the analyses described below were performed by averaging over several different realizations of the synthetic cluster population.

2 The Density Field and the Cluster Dipole

In figure 1 we plot a 3-D visualization of the z-space density field (left panel) and the 3-D one (right panel) for a slice of 8000 km/sec wide, centered on the supergalactic plane. It is evident that eliminating the redshift distortions reduces significantly the amplitude of the peaks in z-space with respect to that in the 3-D space. The effect is particularly evident in the Great Attractor region [(X,Y)=(8,11)], while in the Perseus-Pisces region [(X,Y)=(13,10)] the opposite is true, due probably to a negative velocity gradient; increasing towards the LG. Changing the relative amplitude of the Great Attractor and Perseus-Pisces density peaks causes the dipole amplitude to decrease by $\sim$ 23% leading to an overestimate of the β parameter. The

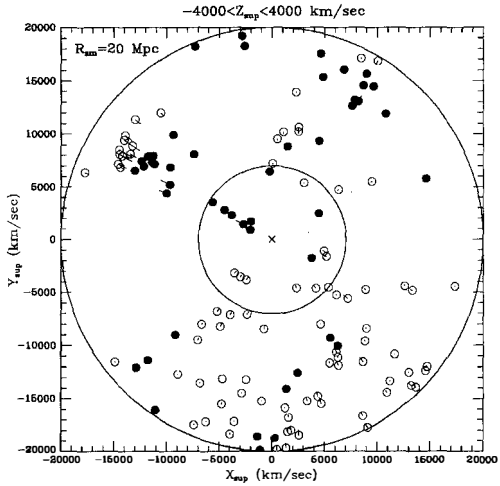


Figure 2: The cluster peculiar velocity field in a $80h^{-1}$ Mpc wide slice projected onto the Supergalactic plane.

direction of the dipole, however, that points $\sim 10°$ away from the CMB apex, does not change appreciably. Comparing the cluster and CMB dipoles we obtain an estimate of β:

$$\beta = 0.21^{+0.07}_{-0.10} \left[\frac{622 - V_{in}\cos\delta\theta}{622 - 180\cos\delta\theta}\right] \quad (1)$$

where $\delta\theta \sim 45°$ is the misalignment angle between the directions of the Virgo cluster and the CMB dipole and V_{in} is the Local Group Virgocentric infall velocity, the introduction of which is necessary because the contribution to the cluster dipole of Virgo is neglected since, due to its proximity, it is not included in the Abell/ACO sample. The quoted uncertainty is dominated by the cosmic variance ($\sim 80\%$). This result is consistent with an $\Omega_o = 1$ universe for $b_c = 4.8$.

3 The Peculiar Velocity Field and the Bulk Flow

We are in the position of exploring the dynamics on scales much larger than those probed by luminous galaxies. Because of the low spatial density, however, galaxy clusters provide a sparse sampling of the cosmic velocity field and does not allow us to characterize the velocity field with a resolution comparable to that obtained from galaxy samples. Nevertheless we are able to visualize large scale features of the linear velocity field since the typical errors of the 1-D cluster peculiar velocities are typically < 150 km/sec.

In Figure 2 we present the cluster peculiar velocity field smoothed using a top hat window of 20 h^{-1} Mpc radius in a slice 8000 km/sec wide projected onto the supergalactic plane. Open and filled dots refer to inflowing and outflowing objects, respectively, while the length of each vector is proportional to the peculiar velocity in the CMB frame. The small circle at the center represents the typical region spanned by dynamical analyses based on galaxy peculiar velocities. The most prominent feature is a large coherent motion in the general direction of the CMB dipole towards the Shapley Concentration $(X, Y) = (-13000, +9000)$ km/s, in qualitative agreement with galaxy studies. This motion does not have a constant amplitude; it is small in

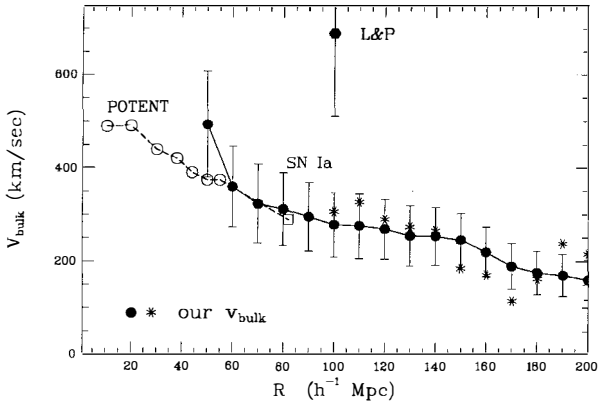


Figure 3: Cumulative bulk flow from clusters (filled dots and starred symbols), POTENT analysis (open dots) and the [3] result (filled exagon).

the Perseus-Pisces region then rises in the Great Attractor zone while dropping on the backside of the Great Attractor. Furthermore, due to our large volume sampled we are able to identify other important features of the large-scale peculiar velocity field such as the prominent infall near the Shapley concentration. We also computed the bulk velocity using two techniques: by estimating the center of mass velocity of the region centered on the LG and also by minimizing the residual velocity of the whole cluster frame. In figure 3 we plot both estimators as filled dots and starred symbols, respectively. Error bars represent 1 σ uncertainties. The two methods provide a consistent estimate of the bulk velocity, well within their errors. Open dots represent the bulk flow obtained by the POTENT reconstruction of the velocity field traced by Mark III galaxies [2]. Although the region where both, the galaxy and cluster bulk velocity estimates, overlap is quite small (between $\sim$ 50 and 60 h^{-1} Mpc), they appear to be consistent with each other. Finally, we point out that the bulk flow at $\sim$ 100 h^{-1} Mpc ([3] sample effective limit) has an amplitude of $\sim$ 250 km/sec, much smaller than that found by [3] ($\sim$ 700 km/sec) and thus in comfortable agreement with most cosmological models.

References

[1] E. Branchini and M. Plionis *Mon. Not. R. astr. Soc*, submitted (1995)

[2] A. Dekel *ARA&A* **32** (1994) 99

[3] T. Lauer and M. Postman *Astrophys. J.*, **408** (1994) 418

[4] M. Plionis and R. Valdarnini *Mon. Not. R. astr. Soc*, **249** (1991) 46

[5] M. Strauss and M. Davis, *Large Scale Motions in the Universe: A Vatican Study Week* (Princeton Univ. Press, Princeton, 1988), P. 225

THE ESO NEARBY ABELL CLUSTERS SURVEY (ENACS): VELOCITY DISPERSION DISTRIBUTION

A. MAZURE [1], P. KATGERT [2], R. DEN HARTOG [2], A. BIVIANO [3], P. DUBATH [4], E. ESCALERA [5], P. FOCARDI [6], D. GERBAL [3,7], G. GIURICIN [8], B. JONES [9], O. LE FEVRE [7], M. MOLES [10], J. PEREA [10], G. RHEE [11]

[1] *LAS, Marseille, F*

[2] *Sterrewacht Leiden, NL*

[3] Institut d'Astrophysique de Paris, F [4] Observatoire de Genève, CH [5] University of Edinburgh, UK [6] University of Bologna, I [7] Observatoire de Meudon, F [8] University of Trieste and SISSA, Trieste, I [9] NORDITA, Copenhagen, D [10] Instituto de Astrofisica de Andalucia, Granada, E [11] University of Nevada, Las Vegas, USA

Abstract

We use a set of 91 clusters observed in the course of the ESO Nearby Abell Cluster Survey (ENACS) and another 37 clusters taken from the literature in order to construct a volume-limited sample of nearby clusters (z <0.08). We define the 3–dimensional Abell richness class R_{3D} and we evaluate the spatial density of clusters with $R_{3D} \geq 1$. For a subset of 43 clusters with N≥10 members and with richness class $R_{3D} \geq 1$ we evaluate the distribution function of the cluster velocity dispersions.

1 Introduction

One of the goals of the ESO Nearby Abell Cluster Survey (ENACS) was to collect redshifts and magnitudes for a complete, volume–limited sample of the 140 R≥1 clusters from the ACO catalogue[1], in a cone around the southern galactic pole defined by $b \leq -30°$ and $\delta \leq 0°$, up to z=0.1 or m_{10}=17. During 35 nights on the ESO 3.6 m we have obtained about 5,500 redshifts in 106 clusters. We observed between 1 and 6 OPTOPUS plates for each cluster, obtaining from a few up to almost 300 redshifts per cluster. R-band magnitudes were obtained from a combination of CCD and photography photometry. We have supplemented our sample with about 1,000 redshifts in 37 clusters collected from the literature.

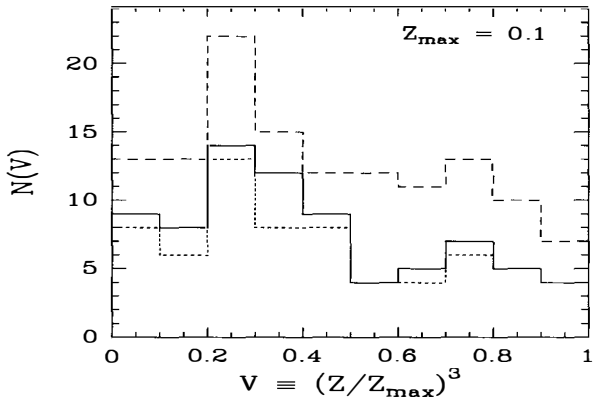


Figure 1: The volume test for uniform sampling. The number of clusters is plotted for 10 concentric shells each with a volume equal to one-tenth the total volume out to z=0.1, which is taken unity. The dashed line represents all clusters in the sample, the solid line the clusters with $N \geq 10$, and the dotted line the clusters with $R_{3D} \geq 1$.

2 A volume-limited sample of clusters

In order to construct a volume–limited sample of clusters we have taken the following steps. First, cluster members must be separated in redshift space from foreground and background galaxies. We have defined the redshift limits on either side of the cluster using the first gap between adjacent galaxies that is larger than 900 km/s; when two galaxies have a velocity difference greater than the chosen gap, they are ascribed to different systems. This value is an optimal value given the aperture and average depth of the individual surveys. For N$\geq$10 systems both N and velocity dispersion σ_V change very little when the gap size is varied by 100 km/s, or when more elaborated schemes, e. g. gaps weighted with N or σ_V are used.

Second, we deal with projection effects along the line of sight by introducing a 3-dimensional equivalent of ACO's richness class, R_{3D}. We find that, on average, $\sim$75% of the observed galaxies is in the main system, while $\sim$25% is in foreground or background. Thus, of the 50 galaxies that are required within [m_3, m_3+2] and 1.5 h^{-1} Mpc around the centre to have a R=1 cluster, 38 objects are on average within the cluster itself. Therefore, we define that $R_{3D} \geq 1$ if the counts of ACO, C_{ACO}, times the fraction of measured redshifts that are in the main system, f_{main}, is $C_{3D} = C_{ACO} \times f_{main} \geq 38$.

Third, we define an optimal depth for the sample. If we divide the volume of the above defined "cone" up to z=0.1 into 10 concentric shells, we find that we sample the clusters with at least 10 members with known redshift up to z=0.08 with a roughly constant spatial density, whereas beyond this limit the density drops by a factor half (see Fig.1). Therefore, we take z=0.08 as the limit of our sample. Of the 58 $N \geq 10$ clusters with $z \leq 0.08$, 43 clusters have $R_{3D} \geq 1$.

Fourth, we have to correct for the incompleteness of this subsample of 43 clusters, by accounting for the clusters with not enough redshifts available to determine C_{3D}. From the C_{ACO} and f_{main} distributions, we estimate that there should be 25 more clusters with $C_{3D} \geq 38$

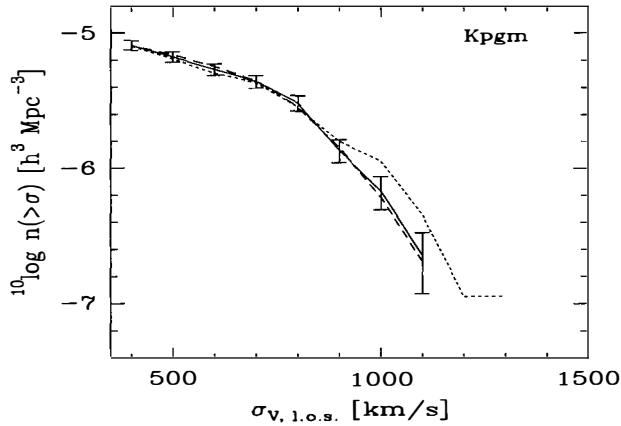


Figure 2: The cumulative distribution of velocity dispersions of clusters. Solid line: $n(>\sigma_V)$ for 77 clusters with $C_{ACO} \geq 50$ and $z \leq 0.1$ (main systems only). Dotted line: idem, but σ_V not corrected for interlopers. Dashed line: $n(>\sigma_V)$ for 43 clusters with $C_{3D} \geq 38$ and $z \leq 0.08$.

in our "cone".

The estimated total number of systems in our "cone" with $C_{3D} \geq 38$ is therefore 68, which yields a co-moving density of $6.5 \times 10^{-6} h^3 Mpc^{-3}$. This number has to be corrected for two effects: (1) incompleteness of the ACO catalogue, which is estimated by comparison with the Edimburgh-Durham Cluster Catalogue[2]; (2) Galactic obscuration[3,4]. Accounting for these two effects brings the estimate of co-moving density of rich clusters to $8.8 \times 10^{-6} h^3 Mpc^{-3}$ in substantial agreement with previous estimates[3,5,6].

3 The Distribution of Velocity Dispersions

We calculate the cluster velocity dispersions σ_V using the robust biweight estimator[7]. For the clusters with N>50 we have removed probable interlopers by applying a new iterative method that uses the combined information of velocities and position[8]. Fig.2 shows the resulting cumulative distribution function of the line-of-sight velocity dispersion for our 43 clusters with z <0.08, $N \geq 10$ members, $R_{3D} \geq 1$. In Fig.3 we compare our distribution with previous results: we find less clusters with large velocity dispersion than previous studies did[9,6]

Our results stress that a fair identification of cluster members considerably reduces the fraction of clusters with high velocity dispersion. Incidentally, compared with the predicted distributions of velocity dispersion which result from cosmological N-body simulations[10] for the standard Ω=1 CDM scenario with various values of the bias parameter b, our results would agree with a high value of b ($b \sim 2.5$).

It can be seen in Fig.3 that in the range $\sigma_V \geq 800$ km s^{-1} our new σ_V-distribution is in perfect agreement with the temperature-distribution[11] of the X-ray emitting intracluster plasma when the isothermal relation T$\propto \sigma_V^2$ is adopted. The disagreement between the two distributions at low σ_V is due to the fact that our sample is complete only for optically rich clusters, and we lack poor clusters and groups, whilst these systems are present in the sample used to derive the temperature distribution.

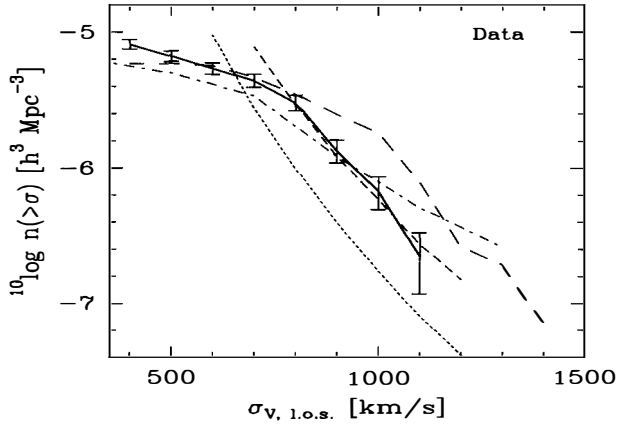


Figure 3: Comparison of the present cumulative distribution of velocity dispersions (solid line) with distributions from the literature: velocity dispersion distributions of Girardi et al.[5] (long-dashed line), and Zabludoff et al.[6] (dashed-dotted line); X-ray emitting gas temperature distributions of Henry & Arnaud[11] (short-dashed line), and Edge et al.[12] (dotted line).

4 References

References

[1] Abell, G.O., Corwin, H.G., Olowin, R.P., 1989, ApJS, 70, 1 (ACO)

[2] Lumsden, S.L., Nichol, R.C., Collins, C.A., Guzzo, L., 1992, MNRAS, 258, 1

[3] Bahcall, N. A. & Soneira, R. M., 1983, ApJ, 270, 20

[4] Postman, M., Huchra, J.P., Geller, M.J., 1986, AJ, 91, 1267

[5] Peacock, J. A. & West, M. J., 1992, MNRAS, 259, 494

[6] Zabludoff, A. I., Geller, M. J., Huchra, J. P., Ramella, M., 1993, AJ, 106, 1301

[7] Beers, T. C., Flynn, K. & Gebhardt, K., 1990, AJ, 100, 32

[8] den Hartog, R. & Katgert, P., 1994, submitted to MNRAS

[9] Girardi M., Biviano A., Giuricin G., Mardirossian F., Mezzetti M., 1993, ApJ, 404, 38

[10] van Kampen, E., 1994, in preparation

[11] Henry, J. P. & Arnaud, K. A., 1991, ApJ, 372, 410

[12] Edge, A. C., Stewart, G. C., Fabian, A., Arnaud, K. A., 1990, MNRAS, 245, 559

SURVEYS OF GALAXY CLUSTERS DETECTED BY ROSAT

Hans Böhringer
Max-Planck-Institut für extraterrestrische Physik, Garching, Germany

Abstract

Clusters of galaxies as the largest well defined objects in the universe are ideal tracers of the large scale structure. The galaxy cluster sample to be used for these cosmological studies is best selected by their detection in X-rays. The ROSAT All Sky Survey is the best basis for such a study. In this contribution we give a brief review of the X-ray properties of clusters, the mass determination of clusters with ROSAT data and the status of redshift survey projects of clusters detected in the ROSAT All Sky Survey.

1 Introduction

Studies of the structure in the large scale matter distribution in the Universe at present have to be based on astronomical observations of visible objects and a theory how the density distribution of these objects is connected to the underlying mass distribution. The traditional and so far most progressed approach is the study of the distribution of galaxies by means of redshift surveys (see e.g. contribution by Vogely). In the nearby Universe the three-dimensional galaxy distribution is known even better from absolute distance indicators independent of the redshifts (see e.g. contribution by Dekel). Also other objects have been used for the study of the large scale structure as for example quasars (see contribution by Andreani) and Lα absorption systems.

The largest clearly defined objects that can be used for this research are clusters of galaxies. They constitute more than mere density enhancements in the galaxy distribution. They are better understood as the largest regions in the Universe that have decoupled from the universal expansion and collapsed to almost dynamical equilibrium objects. They are visualized in X-rays as whole entieties by their intracluster gas and can thus be best characterized by X-ray astronomy as described below (e.g. Sarazin, 1986).

There is an interesting difference in the way the cluster distribution is related to the underlying mass density distribution as compared to galaxies. Clusters of galaxies are formed from the largest density peaks (with a comoving scale of about 5 - 15 Mpc radius) with an amplitude above a certain critical threshold. These density peaks originate from the density fluctuations in the early Universe. In the simplest models these density fluctuations are stochastic and can be described by a Gaussian fluctuation field characterized by a power spectrum. The number density and the spatial distribution of peaks in this field (that later form the clusters we see today) can be statistically calculated if the power spectrum of the Gaussian field is given (see Kaiser 1984, Bardeen *et al.* 1986). Therefore it is possible to relate the observed mass spectrum and the observed spatial correlation function of clusters of galaxies directly to the power spectrum of the density fluctuations in the early Universe. The major simplifications that enters this theory (as it is currently treated in the literature) is the fact that the formation of clusters from the density peaks is approximated by a spherical collapse model. This approximation introduces some uncertainties in particular in the predicted formation times of clusters from the density peaks. As discussed in the contribution by Colafrancesco, the collapse times for a peak with an inhomogeneous density distribution can be much longer than a homogeneous spherical collapse for the same mass and extend of the peak. Apart from this uncertainties due to the simplifications in the theory the mass function and spatial correlation function of galaxy clusters can be directly related to the properties of the underlaying mass distribution in the Universe (e.g. Henry *et al.* 1992, Böhringer and Schindler 1994). The uncertainties introduced by the approximations in the analytical theory can be overcome eventually by studies with N-body simulations which are just about becoming large enough to treat these problems (e.g. contribution by Primack)

The situation is more difficult in the case of the galaxy distribution. The problem of relating the galaxy distribution to the underlaying mass denisty distribution is refered to as the "biasing problem". To obtain an ab intio description of biased galaxy formation one would have to understand how galaxy formation works in dependence on the environment. Since we are still far from such an understanding it is not yet possible to infer the mass distribution from galaxy redshift surveys in an unspeculative way.

Therefore redshift surveys of clusters of galaxies provide a very intertesting complementary way to the galaxy surveys for the study of the large-scale structure of the Universe. X-ray surveys - like in particular the ROSAT All Sky Survey (Trümper 1993) - provide the best basis to obtain a well selected sample of galaxy clusters since clusters are more unambigously recognized as real mass concentrations in X-rays than in the optical. Thus the prospects and first results of cluster surveys based on the ROSAT survey are discussed here. Also the mass determination of clusters using X-ray data is reviewed as the knowledge of the cluster masses is an essential ingredient for the theory on the large scale structure. This is a very brief review that should be considered just as a source of references to some recent work and progress in this field.

2 The Masses of Galaxy Clusters

The masses of clusters of galaxies are currently determined in three ways: from the spatial distribution of the galaxies observed in the optical and their velocity dispersion determined from measured redshifts (e.g. Kent & Gunn 1982), from X-ray data, and from the effect of gravitational lensing (e.g. Kaiser & Squires 1993). Of these the X-ray observations provide currently the most detailed basis for the mass determination. Furthermore X-ray images provide the best account of the dynamical state of the cluster. Clusters are frequently observed to be

in the process of merging of subunits with prominent cases being for example A2256 (Briel *et al.* 1991), Virgo (Böhringer *et al.* 1994), and A3627 (Böhringer *et al.* 1995). In this state the dynamical and hydrostatic equilibrium is very disturbed so that a mass determination based on an equilibrium assumption is not justified. Good X-ray images help to recognize these cases to exclude them from a mass analysis. Knowing the cluster structure one can in fact also analyse these objects quite well if the disturbed part is cut out (see also Schindler 1995).

The X-ray observations provide the information on the density and temperature distribution of the intracluster plasma which are used for the mass analysis. The simultaneous knowledge of the gas density and temperature profile of a spherically symmetric cluster allows to determine the gravitational mass profile of the cluster on the assumption that the gas is in hydrostatic equilibrium. The cluster mass profile is then given by

$$M(r) = -\frac{kT_g(r)\, r^2}{m_h \mu G} \left(\frac{d \log T_g(r)}{dr} + \frac{d \log \rho(r)}{dr} \right) \qquad (1)$$

where $\rho(r)$ and $T_g(r)$ are the density and temperature profile of the gas and the other parameters have their usual meaning.

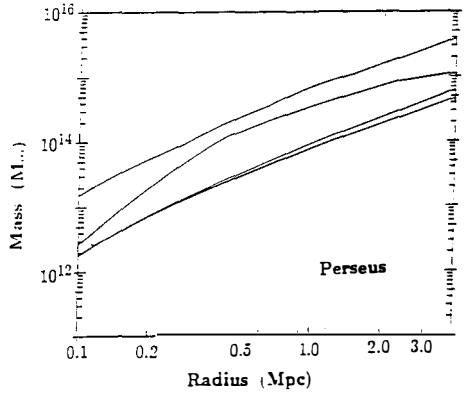


Fig. 1 Integrated radial profiles for the gas and gravitational mass in the Perseus cluster of galaxies as determined from ROSAT X-ray data. The upper two curves indicate the constraint for the gravitational mass profile while the lower two curces bracket the gas mass profile.

The density distribution can be derived with high precission from the X-ray images since the X-ray emission in the ROSAT band is directly proportional to the emission measure with only a very weak dependence on the temperature of the plasma. The major uncertainties are introduced by deviations of the true cluster structure from spherical symmetry with typical uncertainties of the order of 10%. The evaluation of the plasma temperature provides presently the largest problem. The ROSAT observatory has allowed for the first time to determine temperatures as a function of position. But due to the small spectral window the uncertainties in the temperature determinations are quite large, with better quality for low temperature clusters (e.g. David *et al.* 1994). The uncertainties range from about 10% for the lower temperatures around 1 - 2 keV for objects with good spectra to up to a factor of two for the hotter clusters at 8 - 10 keV. The uncertainties in the mass determination is almost proportional to the uncertainties in the temperature (as has been explored by a Monte Carlo mass analysis technique by Neumann & Böhringer, 1995).

The overall accuracy for the mass profile depends then also on the validity of the assumption of hydrostatic equilibrium. Schindler (1995) has explored the influence of deviations from hydrostatic equilibrium on the accuracy of the mass determination from X-ray data by means of N-body/hydrodynamic simulations. She concludes that the errors in the mass results are typically smaller than 15% percent if disturbed clusters or disturbed regions in clusters are avoided. These results and similar conclusions by Evrard (1994) show that the mass analysis by means of X-ray data provides a very robust method.

The high sensitivity and low internal background of the ROSAT observatory allowed for the first time to see the intracluster plasma emission out to large radii. In some nearby clusters the plasma is found to extend out to the virial edge of the cluster. This provides now a means to determine masses for an entire cluster. The Perseus cluster for example, which is the brightest cluster X-ray source in the sky, shows X-ray emission out to about 3 Mpc radius (we use a Hubble constant of 50 km s^{-1} Mpc^{-1} in this section) in the ROSAT All Sky Survey. Resulting curves for the gravitational and gas mass profiles are shown in Fig. 1 for the example of the Perseus cluster. The gas mass is larger than the galaxy mass by more than a factor of 5 (assuming $M/L = 5M_{\odot}/L_{\odot}$ for the galaxies). The gas mass cannot account for the binding mass, however, and the major mass component has to be attributed to "dark matter". The gas density profile has a shallower form than the distribution of the galaxies. The uncertainties in the gravitational mass distribution are too large, however, to decide if the dark matter follows the distribution of the gas or that of the galaxies.

Similar results for the gass mass and gravitational mass were derived from ROSAT data for other nearby clusters (e.g. David *et al.* 1994; Böhringer 1994a). One generally finds that the galaxies contribute about 2 - 7% to the cluster mass, the X-ray emitting gas accounts for about 10 - 30% of the mass, and the remaining part of the infered gravitational mass of clusters has to be attributed to dark matter. Presently more accurate results on the temperature profiles of clusters are becoming available from observations with the Japanese satellite ASCA. The more accurate gravitational mass profiles give gas mass fractions around 20% (Ohashi 1995).

One of the important observational constraints on cosmological models is the mass function of clusters of galaxies. With the possibility to determine cluster masses reliably from X-ray data as described above it would be important to obtain masses for a sample large enough to construct a well defined cluster mass function. This is not yet possible because the number of systems analysed in such detail is still too small, but it should be reachable in the near future from the data in the ROSAT archive and the spectral data now obtained from ASCA.

Bahcall & Cen (1992) have constructed a cluster mass function from known global parameters of clusters like velocity dispersions, X-ray luminosities, and temperatures. We can also make an approach towards the mass function with cluster masses determined from a few ROSAT pointed observations in connection with the previously determined temperature function of clusters.

In a first step we have used the present data for 9 clusters analysed in detail ranging from the small Hickson groups to A2163 to construct a temperature mass relation. The result is shown in Fig. 2. The results for the total mass of the clusters is of course dependent on the radius out to which the mass determination is carried out. The outer radius has to be taken in an objective way, scaled for each cluster in the same way. Considerations of self-similar cluster formation and the assumption that these objects have all formed at the same epoch (quite recently) leads to the relation

$$R_{cut} = M(R_{cut})^{1/3} \qquad (2)$$

Using the result for the Coma cluster with $R_{cut} \sim 3$ Mpc and $M \sim 1.6 \cdot 10^{15}$ $M_{\odot}$ we get

the lower and upper mass limits as shown in the Figure. For most objects the outer radius out to which the X-ray emission was detected is very close to the calculated R_{cut}. Only for HCG42 we had to extrapolate by a factor of about 2.5 out to 0.8 Mpc.

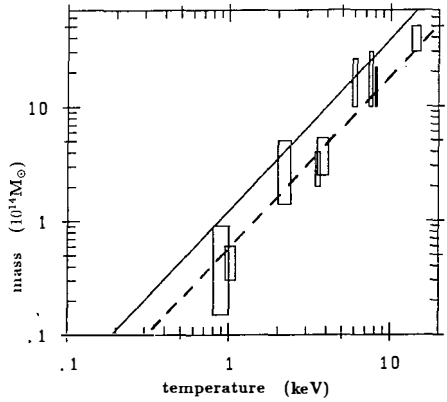


Fig. 2 Temperature mass relation for groups and clusters of galaxies. The upper line shows the relation used in Henry & Arnaud (1991) the lower curve which is a better fit is lower by a factor of 2.

The data shown in Fig. 2 can be fit nicely by a power law relation of the form:

$$M_{15} = h_{50}^{-1} \left(\frac{k\ T}{6.4keV} \right)^{1.5} \tag{3}$$

This would also be expected by a slef-similar model. Henry & Arnaud (1991) used this relation with a proportionality constant of a factor of two higher in their model for the constraints on the primordial power spectrum from their temperature function. Using the temperature function derived by Henry & Arnaud (1991) and Edge *et al.*(1990) we can derive the cluster mass function by means of the above temperature-mass relation. Due to the poor statistics the results have large error bars. Within these error limits the present mass function is completely consistent with the results from Bahcall and Cen (1992).

3 ROSAT Cluster Redshift Surveys

The first processing of the ROSAT All Sky Survey has provided a catalogue of close to 50,000 X-ray sources (Voges *et al.* 1992). About 4000 to 6000 of these sources are expected to be clusters of galaxies. Only about 1300 of these are identified with known Abell clusters (Ebeling *et al.* 1993) when the Sky Survey source list is correlated with the ACO catalogue (Abell, Corwin & Olowin 1989). So most of these cluster are new objects that have to be identified.

Since the detection of clusters in X-rays is the best available observational selection criterion to compile a cluster sample, the ROSAT All Sky Survey provides a good basis to construct a well defined statistical cluster sample for the whole sky - comparable in some way to the construction of the IRAS galaxy catalogue and the subsequent IRAS galaxy redshift surveys.

Several collaborations are currently working on the identification of ROSAT survey clusters and on the measurements of the redshifts of these clusters by means of otpical follow-up observations. The different projects concentrate on different parts of the sky. An overview on the aims and the status of these different projects has recently been given by Böhringer (1994b). Thus they will be described here very briefly.

The two most comprehensive surveys are an ESO key programme to perform a redshift survey of the $\sim$ 700 X-ray brightest clusters in the southern sky (involving groups from MPE Garching, Milano, Bologna, ESO, Liverpool, Edinburgh, Cambridge, NRL Washington, and Saclay) and a complementary redshift survey in the north (involving MPE Garching, CfA Harvard, STScI Baltimore, and ESO). In addition there is a deep cluster survey in the region around the south galactic pole (SGP; conducted by C.A. Collins, R.G. Cruddace, H.T. MacGillivray, A.K. Romer, and a team at MPE Garching), a survey of the X-ray brightest clusters in the north (conducted in a collaboration between IAO Cambridge and MPE Garching), and a deep cluster survey in the region of the north ecliptic pole (involving Hawaii, CfA Harvard, Cambridge, Edinburgh, STScI Baltimore and MPE Garching).

The different identification and redshift survey projects differ in the material that is used to identify the X-ray sources as clusters. In the two southern projects the clusters are identified using three different sources of information. Some clusters are recognized by the fact that they show extended X-ray emission (about 70% of the clearly extended ROSAT survey X-ray sources outside the galactic band are clusters of galaxies and most of the non-cluster sources are readily identified by other obvious nearby objects). Further clusters are found by correlation of the ROSAT source catalogue with the ACO catalogue and a cluster catalogue provided by H.T. MacGillivray which was obtained from an analysis of the COSMOS scans of the UK Schmidt survey. The third search technique searches for local galaxy density enhancements in the object catalogue of the COSMOS data base resulting from the digitization of the UK Schmidt survey by COSMOS at Edinburgh. A major part of the clusters are found by this technique with a sample that highly overlaps with clusters found in the other two identification steps. A statistical analysis of the results of these combined techniques shows that at least 80% of the cluster with an X-ray flux above about $2 \cdot 10^{-12}$ are found by these methods.

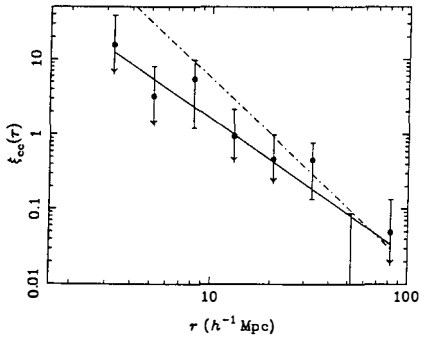


Fig. 3 Correlation function of ROSAT survey clusters of galaxies from the south galactic pole survey (Romer *et al.* 1993).

The first well defined cluster sample from these projects was obtain in the SGP survey with 129 galaxy clusters (Romer *et al.* 1994). The cluster two-point-correlation function obtained from this cluster sample is shown in Fig. 3. The amplitude of the correlation is smaller than

for the samples of northern Abell clusters (Bahcall & Soneira 1983, Postman *et al.* 1992) but comparable to the results from two southern surveys based on cluster samples produced from digitized sky data (Nichol *et al.* 1992, Dalton 1992) and the results for a sample of ROSAT detected ACO clusters (Nichol *et al.* 1993). The difference may be due to projection effets inherent in the Abell cluster catalogue (e.g. Sutherland 1988). To gain a definitive answer on these question larger data samples are necessary.

A larger sample of ROSAT survey clusters of galaxies is currently compiled in the ESO key programme (Böhringer 1994b, Guzzo *et al.*1995). About two thirds of the observing programme has been conducted till now. About 300 new cluster redshifts have been measured and about 200 redshifts for the sample can be obtained from the literature. The final sample should have a size of about 700 clusters. The candidate list prepared prior to the follow-up observations by means of the X-ray properties of the source and the available optical material is still contaminated by objects where the X-ray couterpart is not a cluster of galaxies. This is carefully checked in the spectroscopic follow-up observations and in about 10% of the cases the X-ray source is found not to be a cluster. In most cases it is an AGN.

4 Outlook

Eventaully the southern surveys of ROSAT clusters described above will be combined with the surveys in the north, where also about 300 new cluster redshifts have been determined up to date (Burg *et al.* 1994, Crawford *et al.* 1995). The combined all sky cluster sample will comprise of the order of 1500 X-ray selected clusters. The studies on the large scale structure can then be performed with satisfying significance and statistical measures for the structre can be obtained for scales as large as 1000 Mpc.

5 Acknowledgements

I like to thank my colleagues S. Schindler, D. M. Neumann, W. Voges, L. Guzzo, U.G. Briel, C.A. Collins, R.G. Cruddace, and A.K. Romer for the collaboration in the study of galaxy clusters with ROSAT and in the optical follow-up observations. I especially also like to thank the ROSAT team for providing these beautifully prepared ROSAT data and for the analysis software that makes the data analysis possible.

References

[1] Bahcall, N.A. and Soneira, R.M., 1983, *Astrophys. J.,* 270 20

[2] Bahcall, N.A., and Cen,R., 1992, *Astrophys. J.,* 407 L49

[3] Bardeen, J.M., Bond, J.R., Kaiser, N., and Szalay, A.S., 1986, *Astrophys. J.,* 304 15

[4] Böhringer, H., Briel, U.G., Schwarz, R.A., Voges, W., Hartner, G., and Trümper, J., 1994, *Nature,* 368 828

[5] Böhringer, H., 1994a, in *Cosmological Aspects of X-ray Clusters of Galaxies*, W.C. Seitter (ed.), Kluwer Publ. p. 123

[6] Böhringer H. & Schindler, S. 1992, Proc. of the International School Enrico Fermi, Course CXXII, *Galaxy Formation*, J. Silk and N. Vittorio (eds.), Scieta Italiana di Fisica, North Holland, Amsterdam p. 217

[7] H. Böhringer, 1994, in *Studying the Universe with Clusters of Galaxies*, H. Böhringer and S.C. Schindler (eds.), Proceedings of an astrophysical workshop at Schloß Ringberg, Oct. 10-15, 1993, MPE Report No. 256 93

[8] Böhringer H., Neumann, D.M., Schindler, S. & R.C. Kraan-Korteweg 1995, *Astrophys. J.,* submitted

[9] Burg,R., McLean, B.J.M, Huchra, J.P., Rosati, P., Böhringer, H., Giacconi, R., Voges, W., 1994, in *Studying the Universe with Clusters of Galaxies*, H. Böhringer and S.C. Schindler (eds.), Proceedings of an astrophysical workshop at Schloß Ringberg, Oct. 10-15, 1993, MPE Report No. 256 133

[10] Briel, U.G., Henry, J.P., Schwarz, R.A., Böhringer, H., Ebeling, H., Edge, A.C., Hartner, G., Schindler, S., Trümper, J., and Voges, W., 1991, *Astron. Astrophys.,* 246 L10

[11] C.S. Crawford, A.C. Edge, A.C. Fabian, S.W. Allen, H. Böhringer, H. Ebeling, R.G. McMahon, and W. Voges, 1994, *Mon. Not. R. astr. Soc.,* 274 75

[12] Dalton, G.B., Efstathiou, G., Maddox, S.J., and Sutherland, W., 1992, *Astrophys. J.,* 390 L1

[13] David, L.P., Jones, C., Forman, W., and Daines, S., 1994, *Astrophys. J.,* 428 544

[14] H. Ebeling, W. Voges, H. Böhringer, and A.C. Edge, 1993, *Astron. Astrophys.,* 275 360

[15] Edge, A.C., Stewart, G.C., Fabian, A.C., and Arnaud, K.A., 1990, *Mon. Not. R. astr. Soc.,* 245 599

[16] Evrard, A.E., 1994, in *Clusters of Galaxies*, Proc. of the XIVth Moriond Astrophysics Meeting, Durret, F., Mazure, A., Tran Thanh Van, J. (eds.), Edition Frontiere p. 241

[17] Guzzo, L., et al., 1995, in *Wide-Field Spectroscopy and the Distant Universe*, Maddox, S.J. and Aragon-Salamanca, A. (eds.), World Scientific, Singapore in press

[18] Henry, J.P., and Arnaud, K.A., 1991, *Astrophys. J.,* 372 410

[19] Kaiser, N. & Squires, G., 1993, *Astrophys. J.,* 404 441

[20] Kent, S.M. and Gunn, J.E., 1982, *Astron. J.,* 87 945

[21] Neumann, D.M. & Böhringer, H., 1995, *Astron. Astrophys.,* in press

[22] Nichol, R.C., Briel, U.G., and Henry, J.P., 1994, *Mon. Not. R. astr. Soc.,* 267 771

[23] Nichol, R.C., Collins, C.A., Guzzo, L., and Lumsden, S.L., 1992, *Mon. Not. R. astr. Soc.,* 255 21p

[24] Ohashi, T. 1995, Proc. of the 17th TEXAS Symposium on Relativistic Astrophysics and Cosmology, H. Böhriger, G.E. Morfill, J. Trümper (eds.), New York Academy of Sciences in press

[25] Postman, M., Geller, M.J., and Huchra, J.P., 1992 384 404

[26] Romer, A.K., Collins, C.A., Böhringer, H., Cruddace, R.G., Ebeling, H., MacGillivray, H.T., Voges, W., 1994, *Nature,* 372 75

[27] Schindler, S., 1995, *Astron. Astrophys.,* in press

[28] Trümper, J., 1993, Science 260 1769

[29] Voges, W., Gruber,R., Paul, J., et al., Proc. of Satellite Symposium 3, ESA ISY-3 223

THE SET OF NON-MONOTONOUS CORRELATION FUNCTIONS FOR VERY RICH ABELL CLUSTERS - HISTORY, MODERN RESULTS AND PROJECTS

T.S.FETISSOVA
Astro Space Center, Lebedev Physical Institute,
Profsoyuznaya 84/32, Moscow 117810, Russia

The sample of very rich compact clusters of galaxies consisting of all compact Abell clusters with $R \geq 2$, $0.06 < Z < 0.24$ and $b > 60°$ (the "Shvartsman sample"; the program was initiated by V.F.Shvartsman in 1981, it was otherwise called "The Northern Cone") was first investigated in 1984. The correlation function of this especially deep, complete and homogeneous sample of clusters was shown to have a local maximum $\xi(R)=0.5$ at $R=250$ Mpc ($Ho=50$ km/(s Mpc)).

Now we present new results for correlation functions of a number of larger deep samples consisting of clusters of various richness and analyse their behavior in the range $100 < R < 600$ Mpc. The possibility of using estimated redshifts for a part of clusters in the investigated samples is discussed too.

The upper limit of the inhomogeneity scale of the matter distributionin in the Universe is not yet preciesely determined. We know only the upper limit found from the measurements of fluctuations of the background electromagnetic radiation. This quantity is of major importance for studies of the origin and evolution of the large-scale structure in cosmology. Deep reviews of redshifts of galaxies and clusters of galaxies having purpose to determine Hubble distances and make samples appropriate for statistical computations present one of the most urgent problems in the modern observational cosmology. Up to recent times the maximum reliably established scale of inhomogeneity of luminous matter distribution was used to be taken 40 Mpc, that is, the parameter of clusterization of clusters of galaxies.

The possibility to use the richest clusters of galaxies from Abell catalogue as indicators of large-scale inhomogeneities was suggested by Sokolov and Shvartsman in 1974[1] The objects of this level were expected to give the possibility to solve the problem of maximum scale at which a structure may be perceived. The 6-meter telescope of the North-Caucasian Observatory made possible in our country spectral optical studies testing cosmological hypotheses. An indication to the existence of an inhomogeneity scale 250 Mpc first appeared in 1984[2] as the result of our measurements and gets increasingly more serious confirmations in recent studies independent from one another.

As was published in 1984 [3,4] we've measured 43 new redshifts of richest Abell clusters and together with data of other authors have obtained the complete and very homogeneous sample of compact ("Comp" by Zwicky) and very rich (R≥2 by Abell) clusters of galaxies in the large region near the Northern Pole of the Galaxy ($b > 60^{\circ}$). This program has the name "The Northern Cone".The sample appears to be complete up to z=0.24. In this region there are 50 clusters [5].

The 3-dimensional 2-point elective correlation function for this sample was calculated and showed the excess of pairs of clusters with the mutual distance 250 Mpc (fig.1). The accurate estimations showed that this local maximum of correlation function is statistically significant up to 95%[6].

In the subsequent work [7] we refused the compactness criteria and calculated the correlation function for all clusters with R≥2 in "The Northern Cone" region (fig.2,a). There was the local maximum at 250 Mpc too.

In 1988 we had begun to obtain the analogous sample in the Southern semi-cone ($30^{\circ} < l < 210^{\circ}$, $b < -50^{\circ}$) [8]. A new automatic nonlinear algorithm for measuring redshifts in the faint scanner spectra was developed for this problem. It allowed to measure 23 new cluster's redshifts [7].

The analogous correlation function was calculated for this sample. It should be mentioned that this observational program is not completed as we had only 30 measured redshifts for the sample of 70 clusters. For the other objects we used the estimated

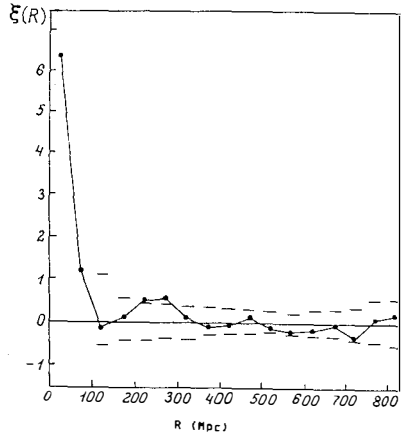


Fig.1. Space correlation function for 50 very rich compact clusters of galaxies (b>60° , 0.06<z<0.24) in "The Northern Cone" region. The dashed lines show the 95% confidence level calculated by special method of simulation [6].

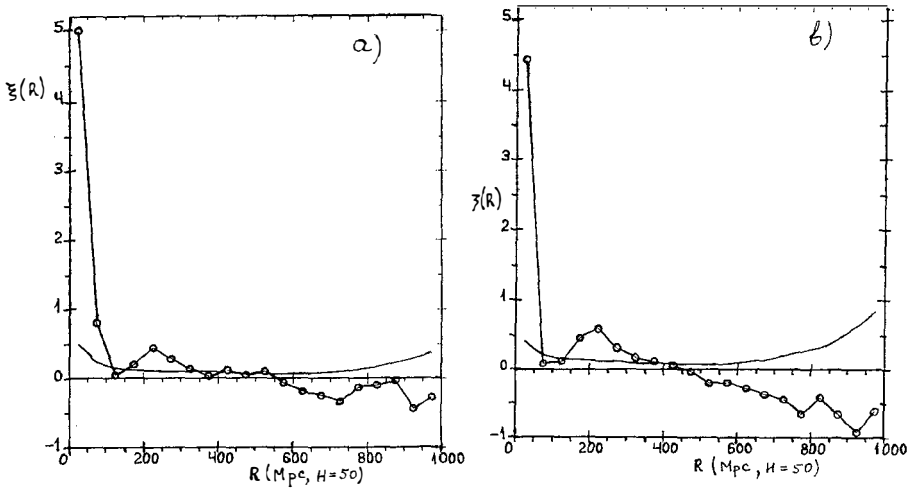


Fig.2. Space correlation function for the sample of

a) 87 clusters with Abell richness 2 and more in "The Northern Cone" region (b>60°, 0.06<z<0.24).63 redshifts are measured, 10 clusters are localized precisely enough. We suppose that the number of "effective" objects is 73. ξ(225 Mpc)=0.44±0.11. Here and in the next figures the level of 1 σ is showen;

b) Space correlation function for the sample of 70 clusters with Abell richness R≥2 in "The Southern Semi-cone" region (b<−60°, 30°<l<210°, 0.06<z<0.24). Only 30 redshifts are measured and about 17 of clusters are localized precisely enough. The number of "effective" objects is 47. ξ(225Mpc)=0.59±0.12.

redshifts. We've discussed this possibility [9] and revealed that 1/3 part of estimated Leir's and van den Bergh's redshifts coincide with the measured ones, 1/3 of them are well enough, but can enlarge our local maximum, and last 1/3 part includes wrong redshifts and increases the total noise of the correlation function. Therefore, we may consider this result as is in a sense qualitative. This semi-qualitative correlation function was calculated and we revealed that the local maximum at 250 Mpc still presented (fig.2,b).It was an encouraging fact because we used the new independent and localized in the opposite direction sample. Using this method we took the next step and calculated correlation functions for the samples which included clusters with R≥1 (fig.3, a and b). There is no doubt about that the local maximum have disappeared.

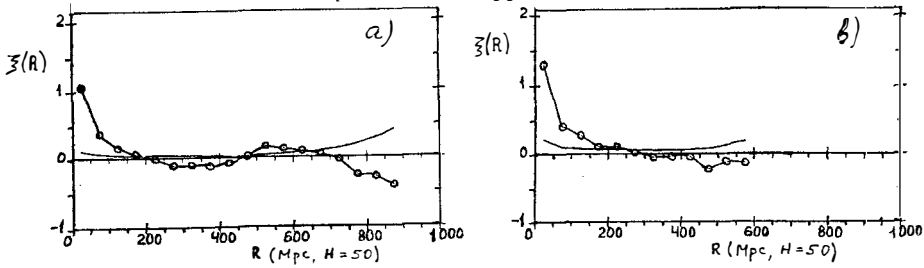


Fig.3. Space correlation function for the samples of
a) 249 clusterswith Abell richness R≥1 in "The Northern Cone" region (b>60°, 0.06<z<<0.1839). 91 redshifts are measured and about 68 clusters are localized well enough. The "effective" number of objects is 159. ξ(225Mpc)=0.01±0.05;
b) 97 clusters with R≥1 in "The Southern Semi-cone" region (b<-60°, 30°<l<210°, 0.06<z<0.1691). 33 redshifts are measured and about 27 clusters are localized precisely enough. The "effective" number of objects is 60.ξ(225Mpc)=0.11±0.07.

The main difficulty now is the lack of precisely measured values of redshifts in the samples. Therefore all redshifts of clusters with R≥1 in the regions b>60°, 0.06<z<0.24 ("The Northern Cone") and b<-60°, 30°<l<210°, 0.06<z<0.24 ("The Southern Semi-cone") should be measured.When we shall have all necessary redshifts we'll obtain the complete and homogeneous samples for subsequent study.

REFERENCES

1. Sokolov D.D., Shvartsman V.F.: 1974, Sov. Phys. JETP, 39, 196.
2. Kopylov A.I., Kuznetsov D.Yu, Fetissova T.S., Shvartsman V.F.:1984,Astron. Tsirk., No. 1347, 1.
3. Kopylov A.I., Fetissova T.S., Shvartsman V.F.: 1984, Astron. Tsirk.,No. 1344, 1,
4. Kopylov A.I. et al. : 1985, Astron. Tsirk., No. 1393, 1.
5. Kopylov A.I.,Kuznetsov D.Yu.,Fetissova T.S.,Shvartsman V.F.: 1988, Collected Articles "Large Scale Structures of the Universe", J.Audouze et.al.(eds.), 129.
6. Kuznetsov D.Yu., Lipovetsky V.A.: 1987, SAO Communications, 53, 92.
7. Fetissova T.S. et al. : 1993, Pis'ma v Astron.J., 19, No. 6, 508.
8. Fetissova T.S.: 1990, SAO Communications, 64, 92.
9. Kuznetsov D.Yu., Fetissova T.S. 1988, Preprint of the Space Research Institute,No.1370,

CLUSTER EVOLUTION AND GRAVITATIONAL INSTABILITY THEORIES

Sergio Colafrancesco
Osservatorio Astronomico di Roma, Monteporzio - Italy

Abstract

We discuss the relevance of clusters of galaxies in probing some aspects of large scale structure scenarios and of gravitational instability theories. We focus on the possible dynamical role of substructure in modifying the overall cluster collapse.

1 X-Ray Clusters and Gravitational Instability Theories

The evolution of density perturbations by gravitational instability is one of the leading models of structure formation in the universe. The evolution of a uniform, spherical perturbation is useful for describing the collapse and virialization of structures like clusters of galaxies in which the role of dissipative processes is not dominant. This model is characterized by the parameter δ_c whose value determines the minimum overdensity threshold ($\delta_c \approx 1.7$) to get a collapsed structure at the cosmic epoch t.

The mass function of this population of cosmic structures contains informations on their dynamical history through the threshold δ_c. In fact, the most rapidly evolving section of the mass function, $N(M,z) \propto exp[-\delta_c^2/2\sigma^2(M,z)]$, depends mostly on the degenerate combination $\delta_c \cdot b$, where b is the usual Lagrangian biasing factor normalizing the variance $\sigma(M,z) = b^{-1}\sigma(M,z)/\sigma(M_o,0)$ of the fluctuation field (Here M_o is a reference mass scale usually taken $\gtrsim 10^{15} M_\odot h^{-1}$, see [1] for a discussion). The exponential decay of the MD reflects the initial conditions of the density fluctuation field in terms of its statistics and of its initial spectrum. In fact, $\sigma(M,z) \sim \int dk k^2 P(k)$ in terms of the spectrum $P(k) = Ak^n T^2(k)$ where the transfer function $T(k)$ depends on how different cosmological scenarios distribute power on the wavenumber space, $k = 2\pi/R$ (here we assume spherical simmetry for wich $M = 4\pi\rho R^3/3$).

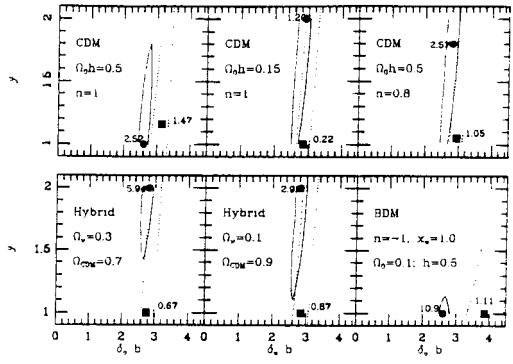


Figure 1: The combined fit to the XRLF and to the XRC

Given that the evolution of a class of cosmic structures can be reasonably followed by a linear analysis – that is the case of clusters of galaxies, as they are the youngest and largest gravitationallly bound structures observed in the universe – the ability to fit the existing data on cluster scales depends mainly on balance between the steepness of the power spectrum (that is determined by global chemistry and by initial condition at early times) and on the amplitude of the combination $b \cdot \delta_c$, representing the efficiency of the selection of collapsing protostructures out of the initial density field at early times.

A detailed analysis of the local X-ray luminosity function (XRLF) [1] shows that $b\delta_c \sim 3$ quite independently of the considered cosmological model (see Fig.1). Constraints on the evolution of X-ray clusters come also from the X-ray counts (XRC): in fact, a strong evolution of the intergalactic medium (IGM) combines with gravitational instability to give the right amount of X-ray clusters at large distances [1].
These results give also insights on the amount of angular anisotropies $\Delta_{rms} \gtrsim 3 \cdot 10^{-6}$ through S-Z effect: considering all the possible uncertainties in the description of the evolution of clusters and their associated IGM, [2] found that the cluster induced anisotropies can contribute realistically $\lesssim 50\%$ of the primary anisotropies on sub-degree angular scales.

2 S.P.Q.R.?

When the initial spectra of the considered cosmological scenarios are normalized to the COBE/DMR amplitude, then values $\delta_c > 1.7$ obtain, quite independently on the assumed theoretical scenario. As $\delta_c = 0.6(3\pi/4)(t_c/t_m)^{2/3}$, according to the uniform spherical model, the previous findings indicate that a delay in cluster collapse time is required by the present data.

Sono Pazzi Questi Romani? ... oops! Let's better say with the Englishmen: *Are These Romans Crazy?* Is the feature of cluster collapse delays a realistic possibility?

To address this question, we propose to go beyond the uniform spherical model for the description of the cluster collapse by studying the dynamical role of substructure during the early stages of cluster formation. To this aim a detailed study of the cluster substructure in the whole phase space is necessary. We evaluated, in fact, the *peculiar velocity probability distribution* $f_{\rm pk}(\vec{v}_{\rm pec} \mid \nu)$ around a peak of given central overdensity $\nu = \delta_0/\sigma$. We consider

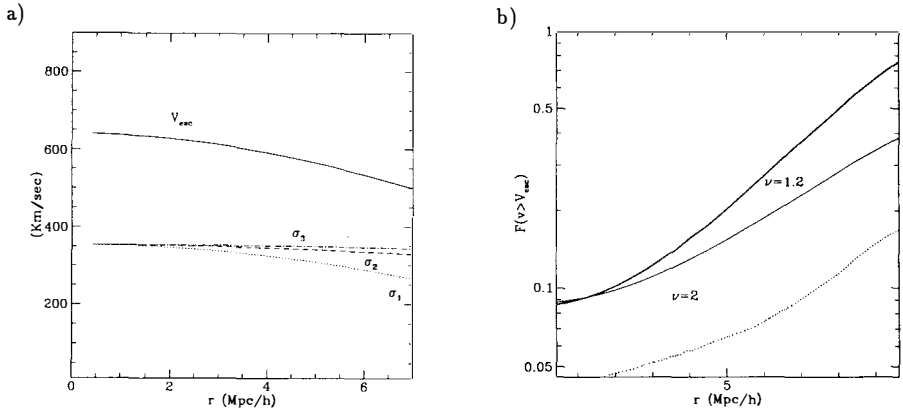


Figure 2: a) Eigenvalues of the velocity correlation tensor for a standard CDM model with $b_8 = 1.1$, a filtering radius $R_f = 5$ Mpc and $\nu = 1.2$.
b) Spatial variation of $F(\mid \vec{v} \mid \geq v_{vesc})$. The thick solid curve is for $b_8 = 1.6$, the other two for $b_8 = 1.1$.

here relatively isolated, high ν density peaks which are nearly spherically symmetric. We show in Fig.2a the eigenvalues $\sigma_i, i = 1, ...3$ of the velocity correlation tensor [3]: these are the components of the peculiar velocity dispersions along the parallel (σ_1) and perpendicular ($\sigma_{2,3}$) w.r.t. the radial direction of a density peak. High ν, i.e. more centrally condensed density peaks have a larger spatial gradient of the velocity dispersion, as one can intuitively expect. It is however interesting to note the considerable difference among the central values of the velocity dispersions: about 100 Km/sec. This effect clearly suggests a broad variance in the magnitude of the expected bulk flows.

From the analysis of the three components of the velocity correlation tensor, we found that peaks show the presence of a nearly isotropic region in the very central regions (at scales $r \approx 0.5 R_f$). Non-radial motions, instead, become dominant in the outer regions of the proto-structures at $r \gtrsim R_f$. As the region of the protostructures that develops infall is found probably at $R \lesssim R_f$, we are lead to the conclusion that in the early stages of the protostructure evolution there is not a coherent infall of matter. This situation might involve a modification of the collapse dynamics of such structures, at least in their early stages.
In the standard CDM scenario the flatness of the power spectrum at high wavenumbers produces an high fraction of clumps on small scales populating the external regions of the clusters. According to the previous results, these clumps can have high velocities (momenta), even larger than the average escape velocity from the structure. As the escape velocity is a measure of the cluster gravitational potential, the frequency of clumps that can be statistically of high momenta (those we call "unbound") is larger in the outer regions of the protostructure. In fact, we evaluated that the fraction of unbound clumps within the filtering radius of the clusters is sensitive (see Fig.2b). We found values

$$F(v > v_{esc}) = \frac{\int_{|\vec{v}| \geq v_{esc}} d^3\vec{v} f_{\rm pk}(\vec{v}, \nu)}{\int d^3\vec{v} f_{\rm pk}(\vec{v}, \nu)} \sim 0.05 \div 0.4 \qquad (1)$$

for quite common peaks, with central heights in the range $\nu \sim 1.2 \div 2$.
These findings indicate that there exist a large fraction of small mass clumps with statistically

high momenta in the peripherical regions, $r \gtrsim R_f$, of the protoclusters. During the collapse of the cluster, and also during the subsequent secondary infall, these high velocity clumps can exchange momentum with the collapsing or infalling clumps and generate a drag force (produced by dynamical friction) onto the collapsing material that acts to delay their collapse time scales [4] [5].

Such considerations support and strengthen the conclusions of our previous work [5] concerning the dynamical effect of small-scale substructure on the collapse of clusters of galaxies. The set of high momentum clumps provides a field of stochastic force generators that intervenes in modifying the equation of motion of the infalling material. In fact, the actual force experienced by an infalling clump of matter, $F = F_o(r) + F_{stoc}(r)$, is the sum of the overall force $F_o(r)$ exerted by the inner mass distribution plus a stochastic component F_{stoc} that depends on the distribution of those clumps, found in the outer parts of the clusters, that can exchange substantial momentum with the infalling clumps still remaining dynamically decoupled from the overall collapse. These stochastic scatterers are those found in a fraction $F(|v| > v_{esc})$.
As a consequence, the eq. of motion of an infalling particle is modified wrt the uniform case by the presence of small scale substructure inducing dynamical friction and it reads:

$$\frac{dv}{dt} = \nabla\phi(r) - \eta v \tag{2}$$

where $\phi(r)$ is the cluster gravitational potential and η is the dynamical friction coefficient (see [4] for details). The collapse time required for the infalling particle to collapse onto the structure is then delayed with respect to the case of a uniform perturbation by the quantity:

$$\frac{t_c(r)}{t_{c0}(r)} = \left[1 + \frac{\eta t_{c0}}{1 - \mu(\delta)}\right] \tag{3}$$

where $\mu(\delta)$ depends non linearly from the average overdensity $\delta(r)$ of the peak (see [5]). This delay effect is predominant in the outer shells of the protocluster.
Because $\delta_c \propto t_c^{2/3}$, the collapse delay experienced by the infalling shells requires that the critical overdensity for the collapse of the perturbation has to be larger than the canonical value $\delta_c \geq \delta_{co} \approx 1.68$ [5]; or, in other words, the shell of cosmic material has to feel a deeper gravitational potential in order to partake the structure collapse.

As a consequence of this result, within overdense regions on the cluster scales, the progenitors of those structures which collapse and virialise by the present time must be among the high peaks of the initial density field. These can be selected out of the initial density field according to the selection function $t(\nu)$ introduced by Colafrancesco et al. [5]
This statistical selection function takes into account the *dynamical biasing* of realistic protostructures out of the structure of the density field at early times. The shape of the function $t(\nu)$ depends on the assumed overdensity threshold for collapse δ_c and on the probability distribution for having a collapsing shell around a density peak. Moreover the function $t(\nu)$ selects peaks of larger height for increasing filtering scale R_f (see Fig.3a). The physical mechanism that we consider to produce the collapse delay of the protoclusters, namely the dynamical friction induced by the presence of small-scale substructure, seems to be different from the one invoked by [6] (see also [7]) to explain the occurrence of "previrialization" of protostructures. Indeed, Peebles suggested (and Evrard and Crone confirmed this result) that the collapse delay is induced by the substructure *external* to a given shell, through tidal torques, while the substructure responsible for the effect we discuss here is *internal* to the collapsing shells and loosely gravitationally bound to them. Both mechanisms act in the same direction, namely they delay the shell collapse, particularly of the outermost ones, although their origin is physically different. A more realistic calculation for the shell collapse time scales should take into account

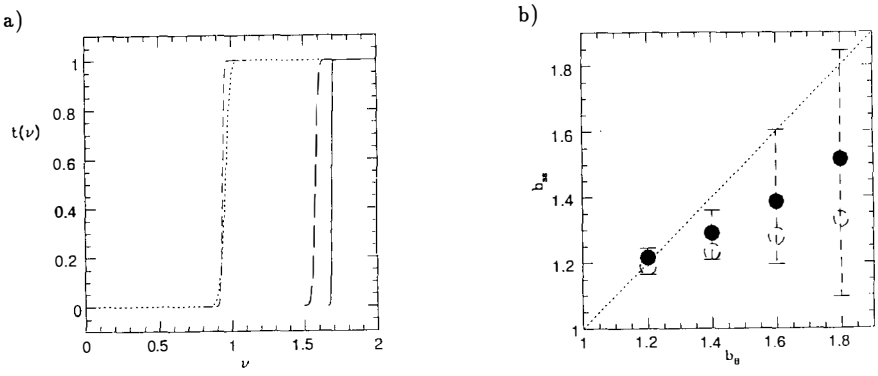


Figure 3: a) The selection function $t(\nu)$ for $R_f = 356$ Kpch^{-1} [$\delta_c = \delta_{c0}$ (*dots*), $\delta_c = 3.51$ *(long-dashed)*] and for $R_f = 500$ Kpch^{-1} [$\delta_c = \delta_{c0}$ (*short-dash*), $\delta_c = 3.51$ *continuous*)].
b) Values of b_{ss} for $R_f = 500h^{-1}$ kpc. *Filled circles*: $\delta_c = \delta_{cf}$, *open circles*: $\delta_c = \delta_{c0}$.

both of these mechanisms: this should clearly result in a collapse delay (and consequentely in gravitational dynamical bias) even larger than the one we derived [5]. In numerical N-body simulations of cluster formation these mechanisms should act together, although we suspect that only very high resolution numerical simulations could be able to disentengle the effects of small-scale substructure with typical mass scales three orders of magnitude lower than that of the typical protostructures which we have considered in this paper.

Based on our selection function, we also derived [5] detailed values for the *dynamical bias*, b_{ss}, on the cluster scales: we found that $b_{ss} \leq b_8$, where b_8 is the value of the biasing level at $8h^{-1}$ Mpc. Depending on the values of δ_c and R_f, we found that $b_{ss}/b_8 \sim 0.5 \div 0.8$ (Fig.3b) for values $b_8 > 1.2$, a set of values indicated by the bulk of the observations on cluster scales. This means that a sensitive fraction of the bias coefficient b_8 required to match the observations of the galaxy and cluster abundances can be accounted for by the non-linear, dynamical effects of substructure during the formation of galaxy clusters.

References

[1] Colafrancesco, S. & Vittorio, N., 1994, *Astrophys. J.*, **422**, 443

[2] Colafrancesco, S., Mazzotta, P., Rephaeli, Y. & Vittorio, N.,1994, *Astrophys. J.*, **433**, 454

[3] Antonuccio-Delogu, V. & Colafrancesco, S., 1995, *Astr. Astrophys.*, submitted

[4] Antonuccio-Delogu, V. & Colafrancesco, S., 1994, *Astrophys. J.*, **427**, 72

[5] Colafrancesco, S., Antonuccio-Delogu, V. & DelPopolo, N., 1995, *Astrophys. J.*, in press

[6] Peebles, P.J.E., 1990, *Astrophys. J.*, **365**, 27

[7] Evrard, A.E., & Crone, M.M., 1992, *Astrophys. J.*, **394**, L1



SESSION VI

COMMON SESSION WITH PARTICLE PHYSICS





A REVIEW OF GRAVITATIONAL MICROLENSING EXPERIMENTS

Christophe MAGNEVILLE
DAPNIA/SPP - CEA/SACLAY
F91191 - GIF-SUR-YVETTE Cedex

Abstract : three experiments are now searching for galatic dark matter in the form of compact objects through gravitational microlensing. All have reported candidate events; We will describe here the gravitational microlensing effect, the specifics of each experiment and discuss their present results.

Resumé : trois experiences recherchent actuellement la matière noire sous forme d'objets compacts au moyen de microlentilles gravitationnelles. Toutes ont observé des événements candidats. Nous décrirons ici l'effet de microlentille gravitationnelle, les spécifications de chaque expérience et nous discuterons de leurs résultats actuels.

THE MICROLENSING EFFECT

The use of the microlensing efect to detect dark matter was first proposed in 1986 by Paczynski. Figures 1 and 2 describe the phenomenon : a halo object D passes very close to the line of sight between the observer O and a distant star S - typically within a thousandth of an arc second.

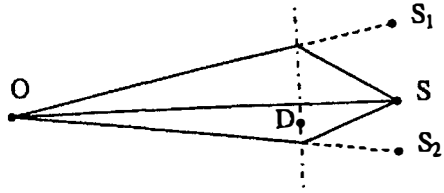


Fig. 1 ; instead of the direct ray going from the star S to the observer O, the deflector D causes the light to follow two distinct optical paths. The observer sees two images S_1 and S_2, usually non separable in the case of microlensing.

In the following, L = OS and x = OD/OS. If the alignment was perfect, the observer would see an Einstein ring of radius R_E, with

$$R_E^2 = \frac{4GML}{c^2} x(1-x) \qquad (1)$$

More generally, the observer receives light through two optical paths, too close to be separated - the separation is also of about 10^{-4} arcsec. But since he received light that was emitted in a larger solid angle than without the deflector, the star appears brighter. It is easy to compute the apparent amplification from the deflection given by general relativity :

$$A = \frac{u^2+2}{u\sqrt{u^2+4}} \qquad (2)$$

where u is the "reduced impact parameter", $d(OS, D)/R_E$ The amplification as a function of u is plotted in fig. 3.

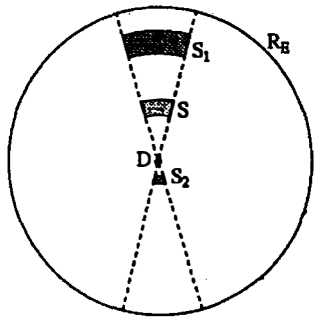


Fig. 2 The microlensing effect as seen in the plane of the deflector. The observer receives light that had been emitted in a larger solid angle in the absence of the deflector. The amplification is in fact simply the ratio of the surfaces $(S_1 + S_2)/S$

Now, since the alignment needs to be so perfect, the effect is going to be sensitive to the movement of the deflector in the halo. If the deflector has a velocity v, which component transverse to the line of sight is $v_\perp$, and its trajectory has a minimum impact parameter u_0, then at any given time, we have

$$u = \sqrt{u_0^2 + \left(\frac{v_\perp}{R_E}(t - t_0)\right)^2}$$

- and the phenomenon is time-dependant. It is convenient to define as $R_E/v_\perp$, the characteristic duration of the phenomenon. For stars in the Large Magellanic Cloud, the average duration is $= 70\,\text{days}\sqrt{M/M_\odot}$. Figure 4 shows typical light curves.

For a given observed light curve, the measurable quantities are the maximum amplification, the duration, and the time of maximum. The amplification gives the impact parameter - which distribution must be flat -, but the duration is a function of the mass of the object, its speed, and its distance from the observer. For any given event, only a most probable mass can thus be computed. This mass is model-dependent, and the distribution around this most probable value is very broad. As statistics increases, it is however possible to perform a moment analysis to compute the moments of the MACHO mass distribution (De Rujula *et al.* 1991).

The probability of the microlensing phenomenon is computed in (Paczynski 1986) for stars in the Large Magellanic Cloud, and more generally in (Griest *et al.* 1991). The idea is that the probability for a given star to be microlensed.

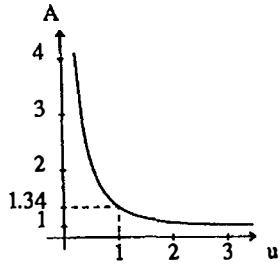


Fig. 3 The amplification as a function of the reduced impact parameter u. A unit impact parameter coresponds to an amplification of 34 %, or 0.3 magnitude.

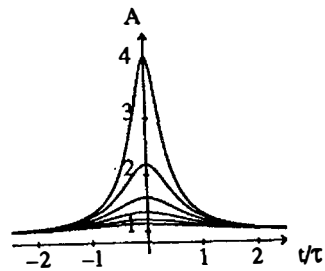


Fig. 4 Some typical light curves. The abscissa is the time in unit of the time required for the deflector to move by an Einstein radius. The various light curves correspond to a reduced minimum impact parameter of 0.25, 0.5, 0.75, 1, 1.25 and 1.5 resp.

at a given instant by more than 34 % is simply the fraction of the sky covered by the Einstein radii of the MACHOs. Since the surface of the Einstein disk is proportional to the mass of the object, the total solid angle fraction - the optical depth - is independant of the mass of the objects. But since the event duration increases with the mass, lighter objects will cause more microlensing events in a given time period. Typically, for stars in the LMC and a "standard" habo, $= 0.5\ 10^{-6}$. It is thus necessary to follow the luminosity of a few million stars.

Some basic properties of the microlensing effect will help to distinguish a signal from the background of variable stars :

- The light curve is symmetric and has a distinctive shape.
- The effect is achromatic, since all photons follow the same geodesic. As most variable stars display colour variations, this is a very powerful criterium.
- The effect is rare enough to be unique for a given star.A long term followup of the candidates is therefore needed.
- The effect is independant of the physical properties of the microlensed star. In particular, the events must trace the spatial repartition of stars, as well as their repartition in the colour-magnitude diagram.

The three experiments

EROS

EROS (Expérience de Recherche d'Objets Sombres) is a French collaboration of astrophysicists and particle physicists. It consists in fact of two experiments. The first one targets high mass objects, and monitors a few millions stars on a time scale of 30 mn.

The plate experiment uses the lm Schmidt telescope at the European Southern Observatory. Each 30 cm x 30 cm plate covers roughly an area of 5° x 5° on the LMC. Two plates are taken each night, one with a blue filter, the other with a red filter. The exposure time is one hour.

The plates are then digitized by the MAMA at the Observatoire de Paris (Berger *et al.* 1991), and each yields 8 108 pixels of 0.7 x 0.7 arcsec2. 56 plates have been taken in 1990-91, 200 in 91-92 and 25 in 92-93.

The photometric analysis is made with a specially developed algorithm, which needs to work well in crowded fields, be automated, and be fast enough to accomodate the huge volume of data.

A reference image is first made by adding the best ten plates in each colour. A catalog of stars is then produced, and the two colours are associated with a pattern matching algorithm.

Then, for each plate, the brightest stars are first identified and matched with the reference catalog, and are also used to determine the PSF. The geometric transformation is then used to impose the position of the stars on the measured image : this saves the star finding process, speeds up the PSF fit, which is then linear, and improves the photometric precision.

About 8 10^6 stars are found on the reference image, but half of them are too faint to be measured accurately enough. Each photometric measurement is then added to the light curves of the stars for further analysis.

The CCD experiment uses a 16-CCD mosaic at the focal plane of a dedicated 40 cm telescope, in the dome of the GPO at La Silla. The CCDs are 576 x 405 pixel Thomson chips. The exposure times are 8 mn in R and 12 mn in B. During the 1991-92 campaign 2500 red and blue exposures have been recorded, and about 6000 during each the following campaigns (1992-93 and 1993-1994). About 10^5 stars are monitored in the bar of the LMC. The photometric algorithm is similar to the one used for the plates.

More details on the EROS experiment can be found in (Aubourg *et al.* 1993a ; Cavalier 1994b ; Queinnec 1994b).

MACHO

The MACHO group is a University of California - CfPA Berkeley - Mount Stromlo Observatory collaboration. It uses a dedicated 50 inch telescope at MSSO, in Australia, with a dual camera system and a dichroic beam splitter, allowing simultaneous exposures in blue and red. Each camera has four 2048 x 2048 CCD, and covers a field of 0.7° x 0.7°. The camera system is described in detail in (Stubbs *et al.* 1993).

The observation strategy targets high-mass objects by surveying many fields : although the exposure time is about 5 mn, the sampling time scale is a day. 82 fields are monitored in the LMC. 21 in the SMC, and 75 in the bulge of the Galaxy. The experiment has started in 1992.

The photometric program, SoDoPhot (Bennett 1994b), is based on DoPhot. As the EROS photometric algorithm does, it uses a template - the best image - to impose the position of stars.

OGLE

The OGLE experiment is a Warsaw-Carnegie collaboration, which observes the Galactic bulge in the Baade's window. It uses a non-dedicated 1 m telescope at Las Campanas Observatory, Chile, equipped with a 2048 x 2048 CCD camera. The data taking has started in 1992 and consists of images taken principally IN I-band and only sparse measurements in V-band. The photometry uses a slighlty modified DoPhot program (Schechter *et al.* 1993).

Results

Once the light curves are built, all the collaborations are searching for a luminosity increase which is unique and achromatic, using roughly the same methods.

The CCD experiment of the EROS collaboration is the only program sensitive to low mass objects, in the range 10^{-7} to 10^{-3} $M_\odot$. No events have been found (Queinnec 1994a ; Queinnec 1994b ; Aubourg *et al.* 1994), while about 10 are expected if the halo is made of stars of less than 10^{-4} $M_\odot$. It is therefore possible to exclude for instance a halo in which more than 30 % of the stars would have such a low mass.

Both the EROS plate experiment and the MACHO experiment are looking for high mass MACHOs in the LMC. The EROS collaboration has reported 2 events (Aubourg *et al.* 1993b ; Cavalier 1994a, Cavalier 1994b), and the MACHO collaboration has reported 3 events (Alcok *et al.* 1993, Bennett 1994a). Table 1 summarizes the characteristics of these events.

Besides, the EROS and MACHO experiments have stars in common. The EROS events happened while MACHO was not yet running, and the MACHO 2 and 3 events are too faint to

be seen by EROS ; but the MACHO 1 event can be seen by EROS, although it has very few blue measurements, and thus was rejected by one of the first cuts in the EROS analysis. By releasing these cuts, EROS has been able to confirm the amplification of MACHO 1.

Table 1 . Characteristics of LMC events. For each event are given the unamplified magnitudes, the maximum amplification, the minimum impact parameter, the duration in days, and the most probable mass for deflectors. A mass ten times higher or lower is just half as probable.

Event	Magnitude		A_{max}	u_0	(days)	M ($M_\odot$)
MACHO 1	R=19.0	V=19.6	7.1	0.14	17.5	0.07
MACHO 2	R=20.4	V=20.7	2.0	0.56	9	0.02
MACHO 3	R=19.1	V=19.4	1.5	0.83	14	0.05
EROS 1	R=18.7	B=19.3	2.5	0.42	26	0.16
EROS 2	R=19.2	B=19.3	3.3	0.31	30	0.20

The efficiency of the experiments is hard do determine, but for both EROS and MACHO, the number of events found seems to be half what would be expected for a halo made of stars just at the ignition threshold.

As far as the Galactic bulge is concerned, the event rate is high enough that information quickly becomes obsolete ... At the time this article is written, the author is aware of 11 events in the OGLE collaboration (Udalski *et al.* 1993), 1994a, 1994b, 1994C) and of more than 30 in the MACHO collaboration (Alcock *et al.* 1994, Ch. Stubbs, priv. comm.), one of which has an amplification by a factor 17.

The bulge rate is at least twice what would be expected for a "minimal disk" (Griest *et al.* 1991), but, according to an analysis performed by the MACHO collaboration on its first four events, would be compatible with a "maximal disk" accounting for most of the velocity at the Sun radius (Alcock *et al.* 1994). On the other hand, the OGLE collaboration claims that its rate cannot be accounted for by any reasonnable disk model, but that "a good case can be made for the lenses to be in the galactic bar, i.e. highly non-axially symmetric galactic bulge" (Paczinsky 1994). More quantitative results should be available soon as the statistics increases.

Conclusion

Gravitational microlensing is a field in which a lot has happened in the previous year. All three collaborations have reported events which are compatible with microlensing.

At the very moment those lines are written, spectra are being taken of a microlensing event that was detected early enough by the MACHO collaboration that the astronomical community has been warned a few days before the maximum. Comparison of spectra at the peak and a few weeks later should, if they are identical, give a very strong weight to the attribution of this event to gravitational microlensing.

Anyway, if the observed light curves are fully compatible with the theory of gravitational microlensing, and if the method has thus proved it was a worthy probe of low-mass star populations, some puzzling discrepancies in the event rates have occured : compared to what is expected from having all the galactic dark matter in a spherical halo, the event rate towards the LMC is half too small, and the one towards the center of the Galaxy is twice too high.

The event rate towards the galactic bugle is high enough for more quantitative results to be available soon. For the LMC, a significant increase in the number of events is required to start doing any statistical analysis.

The MACHO collaboration is planning to continue to run for a few years with the same setup. The EROS collaboration plans to replace its setup with a 1 m dedicated telescope, a dichroid beam splitter and two cameras, each fitted with 8 2948 x 2048 CCDs. The OGLE collaboration should soon have a dedicated 1.27 m telescope, with a 2048 x 2048 CCD, to be expanded later.

References

Ch. Alcock, C.W. Akerlof, R.A. Allsman, T.S. Axelrod, DP. Bennett, S. Chan; K.H. Cook, K.C. Freeman, K. Griest, S.L. Marshall, H.S. Park, H.S. Perlmutter, B.A. Peterson, M.R. Pratt, P.J. Quinn, A.W. Rodgers, C.W. Stubbs, W. Sutherland (1993) : "Possible Gravitational Microlensing of a Star in the Large Magellanic Cloud", in Nature, vol. 365, pp. 621-623

Ch. Alcock, R.A. Allsman, T.S. Axelrod, K.H. Cook, K.C. Freeman, K. Griest, S.L. Marshall, H.S. Perlmutter, B.A. Peterson, M.R. Pratt, P.J. Quinn, A.W. Rodgers, C.W. Stubbs, W. Sutherland (1994) : "Probable Gravitational Microlensing Towards the Galatic Bulge", submitted to Ap. Lett.

E. Aubourg, (1993a) in the Messenger, vol. 72, pp. 20-27

E. Aubourg, P. Bareyre, S. Brehin, M. Gros, M. Lachieze-Rey, B. Laurent, E. Lesquoy, Ch. Magneville, A. Milsztajn, L. Moscoso, F. Queinnec, J. Rich, M. Spiro, L. Vigroux, S. Zylberajch, R. Ansari, F. Cavalier, M. Moniez, J.Ph. Baulieu, R. Ferlet, Ph. Grison, A. Vidal-Nadjar, J. Guibert, O. Moreau, F. Tajahmady, E. Maurice, L. Prévot, C. Gry (1993b) : "Evidence for Gravitational Microlensing by Dark Objects in the Galactic Halo", in Nature, Vol; 365, pp. 623-625

E. Aubourg et al : "Astronomy and Astrophysics, (1995), Vol. 301, pp. 1-5,

D.P. Bennett (1994b) in preparation

J. Berger, J.P. Cordoni, A.M. Fringant, J. Guibert, O. Moreau, H. Reboul, C. Vanderriest (1991) : "MAMA Astrometry and Photometry of 1221 UV-Express Objects in 40 Square Degrees at the North Galactic Pole", in Astm. Astrophys. Suppl. Ser., Vol. 87, pp 389-418

F. Cavalier (1994b) : unpublished Ph. D. Thesis, Saclay preprint DAPNIA/SPP 94-xx

A. De Rujula, P. Jetzer, E. Masso (1991) : "Dark Mass Moments", in Mon. Not. Roy. Ast. Soc., Vol. 250, pp. 348-355

K. Griest, C. Alcock, T.S. Axelrod, D.P. Bennett, K.H. Cook, K.C. Freeman, H.S. Park, S. Perlmutter, B.A. Peterson, P.J. Quinn, A.W. Rodgers, C.W. Stubbs (1991) : "Gravitational Microlensing as a Method of Detecting Disk Dark Matter and Faint Disk Stars", in Ap. J., Vol. 372, pp. L79-L82

B. Paczynski (1986) : "Gravitational Microlensing by the Galactic Halo", in Ap. J., Vol. 304, pp 1-5

B. Paczynski, K.Z. Stanek, A. Udalski, M. Zsymanski, J. Kalyzny, M. Kubiak, M. Mateo, W. Krzeminski (1994) : "Are the OGLE Microlenses in the Galactic Bar ?", submitted to Ap. J. Lett.

F. Queinnec (1994a) : "Results from EROS for Small Mass", talk given at the 14th Mpriond Workshop, 22-29 January, 1994, villars-sur-Ollon, Switzerland.

. F. Queinnec (1994b) : unpublished Ph. D. Thesis, preprint LAL-Orsay 94-xx.

P.L. Schechter, M. Mateo and A. Saha (1993) : "DoPhot. A CCD Photometry Program - Description and Tests", in Pub. Astr. Soc. Pacif., Vol. 105, pp. 1342-1353.

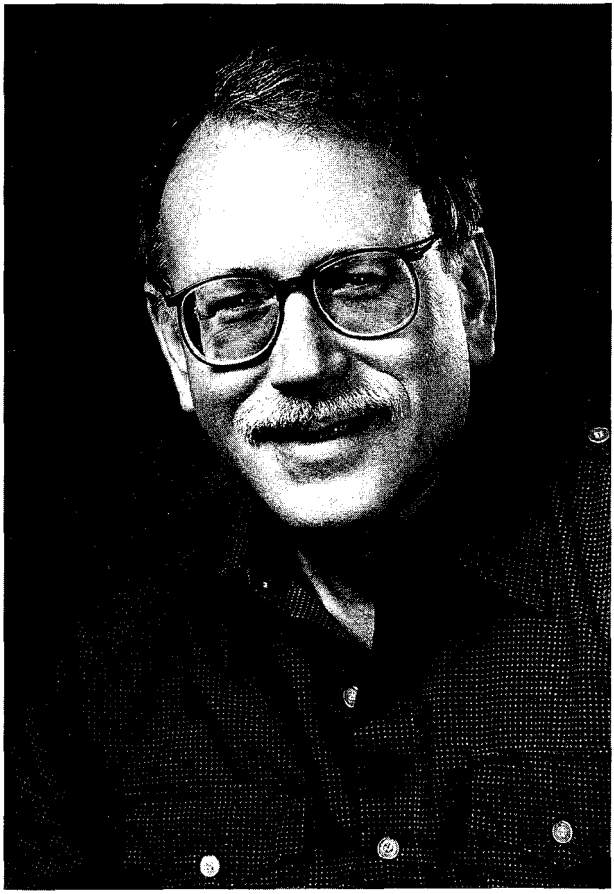
. C. Stubbs, S.L. Marshall, K.H. Cook, R. Hills, J. Noonan, C.W. Akerlof, T.S. Axelrod, D.P. Bennett, K. Dagley, K.C. Freeman, K. Griest, H.S. Park, S. Perlmutter, B.A. Peterson, P.J. Quinn, A.W. Rodgers, C. Sosin, W. Sutherland (1993) : "xx", in SPIE Proc., Vol. 1900, pp. 192-xx.

A. Udalski, M. Szymanski, J. Kaluzny, M. Kubiak, W. Krzeminski, M. Mateo, G.W. Peterson, B. Paczynski (1993) : "The Optical Gravitational Lensing Experiment - Discovery of the 1st Candidate Microlensing Events in the Direction of the Galactic Bulge", in Acta Astronomical, Vol. 43, pp. 289-294.

A. Udalski, M. Szymanski, J. Kaluzny, M. Kubiak, M. Mateo, W. Krzeminski (1994a) : "The Optical Gravitational Lensing Experiment - The Discovery of 3 Further Microlensing Events in the Direction of the Galactic Bulge", in Ap. J., Vol. 426, pp. L69-L72

A. Udalski, M. Szymanski, K.Z. Stanek, J. Kaluzny, M. Kubiak, M. Mateo, W. Krzeminski, B. Paczynski, R. Venkat (1994b) : "The Optical Gravitational Lensing Experiment - the Optical Depth to Gravitational Microlensing in the Firection of the Galactic Bulge", in Acta Astronomica, vol. 44, pp. 165-189

A. Udalski, M. Szymanski, J. Kaluzny, M. Kubiak, M. Mateo, W. Krzeminski, B. Paczynski (1994c) ; "The Optical Gravitational Lensing Experiment - The Early Warning System", preprint astro-ph 9408026.



COLD + HOT DARK MATTER COSMOLOGY

Joel R. Primack[1], Jon Holtzman[2], and Anatoly Klypin[3]
[1]*Santa Cruz Institute for Particle Physics, University of California, Santa Cruz, CA 95064*
[2]*Lowell Observatory, Mars Hill Road, Flagstaff, AZ 86100*
[3]*Department of Astronomy, New Mexico State University, Las Cruces, NM 88001*

Abstract

The Cold + Hot Dark Matter (CHDM) cosmological model appears to require about 5 eV of neutrino mass, in order to produce early enough galaxy formation. These neutrinos would constitute hot dark matter accounting for a fraction $\Omega_\nu = 0.2(0.5/h)^2$ of critical density, where $h \equiv H_0/(100 \text{ km s}^{-1} \text{ Mpc}^{-1})$ is the Hubble parameter. Recent experimental data suggests that this neutrino mass may be divided between two or more species of neutrinos. Here we consider the consequences of such neutrino masses for the formation of galaxies and large scale structure in the universe in cosmological models that are spatially flat and in which most of the dark matter is cold. The linear calculations and N-body simulations that we report here indicate that an $\Omega = 1$ CHDM cosmological model with two neutrinos each of mass $\approx$ 2.4 eV (we will call this model Cν^2DM) agrees well with all available observations. However, we find that this is true only if the Hubble parameter $h \approx 0.5$. We also consider Cold Dark Matter (CDM) models with a cosmological constant Λ and show that evidence for hot dark matter raises serious difficulties for low-Ω ΛCDM models.

1 Introduction

The standard Cold Dark Matter (CDM) cosmological model has too much power on small scales when normalized to COBE. Because of the large velocities of the light neutrinos that make up the hot component of Cold + Hot Dark Matter (CHDM), these neutrinos cluster less on small scales than the cold component of CHDM, thereby producing a lower abundance of clusters and smaller pairwise galaxy velocities in better agreement with observations than standard CDM with the same large-scale normalization. Predictions of a CHDM model with a single massive neutrino species and $\Omega_\nu = 0.3$ (corresponding to $m_\nu \approx 7$ eV for Hubble parameter $h = 0.5$) have been shown [1, 2, 3] to agree well with observations, with the possible exception that galaxies may form too late to account for the observations of quasars and damped Lyα systems [4, 5] at high redshifts $z \gtrsim 3$ [6, 7]. The latter observations can be accommodated [8, 9] if the assumed neutrino mass in CHDM is lowered from $\sim$ 7 eV to $\sim$ 5 eV. Lowering the neutrino mass in CHDM also gives a better account of the Void

Probability Function [10] and of the properties of galaxy groups [3],[11]. With one ~ 5 /eV neutrino COBE-normalized CHDM probably overproduces clusters, as we show below, but this can be avoided if the neutrino mass is shared between two or three species of neutrinos.

As we explain in more detail in §2, current experimental hints regarding neutrino masses suggest that the net neutrino mass of ~ 5 eV required for CHDM is shared among two or three species of neutrinos. In particular, if the deficit of atmospheric ν_μ relative to ν_e is due to $\nu_\mu \to \nu_\tau$ oscillations, then the hot component must involve more than one species of neutrino, since because of the long baseline the ν_μ–ν_τ mass-squared difference must then be rather small, $\sim 10^{-2}$ eV^2. This is consistent with the possible detection of $\bar{\nu}_\mu \to \bar{\nu}_e$ oscillations reported by LSND, which if valid requires neutrino mass in the range relevant for hot dark matter. The theory of r-process nucleosynthesis in type II supernovae that currently seems most promising imposes constraints on neutrino mass and mixing patterns, but an inverted neutrino mass hierarchy with ν_e heaviest meets these constraints.

We will first summarize the experimental hints of neutrino masses from the (a) solar and (b) atmospheric neutrino deficits and from (c) LSND. We also summarize recent work [12] showing that if we take seriously CHDM and all the hints (a-c) of neutrino mass, then the r-process nucleosynthesis constraint leads to an essentially unique pattern of neutrino masses and mixings. Then we will consider in more detail the consequences of such neutrino masses for the formation of galaxies and large scale structure in the universe for cosmological models in which $\Omega = 1$ (or $\Omega + \Omega_\Lambda = 1$, where $\Omega_\Lambda \equiv \Lambda/(3H_0^2)$) in which most of the dark matter is cold. We show that $\Omega_\nu = 0.2$ CHDM with the mass evenly shared between two neutrino species — Cν^2DM — agrees better with observations than the one-neutrino version, better indeed than any other variant of CDM that we have considered. We also discuss other variants of CDM, and show in particular that low-Ω ΛCDM is incompatible with light neutrinos with $m(\nu) \gtrsim 2$ eV. The material presented here is an updated version of that in Ref. [13]; among other things, we now use the latest COBE normalization (corresponding to $Q_{\rm rms-PS} = 20\,\mu$K) for the larger set of cosmological models that we consider.

2 Experimental data on neutrino masses

Evidence for a neutrino mass explanation of the solar ν_e deficit is now fairly convincing, since at least two of the three types of experiments have to be wrong to be compatible with some non-standard solar models [14]. If the solar ν_e deficit is due to MSW $\nu_e \to \nu_\mu$ or $\nu_e \to \nu_s$ neutrino oscillations in the sun, the mass-squared difference between either pair of particles is $\Delta m^2_{ei} \equiv |m(\nu_e)^2 - m(\nu_i)^2| \approx 10^{-5}$ eV^2. (Here ν_s denotes a "sterile" neutrino, one that contributes negligibly to the width of the Z^o. An example is any right-handed neutrino, which would not participate in standard $SU(2) \times U(1)$ electroweak interactions.)

Similarly, evidence for a neutrino mass explanation of the deficit of ν_μ's relative to ν_e's in atmospheric secondary cosmic rays is also increasing, with compatible results from three experiments [15], and especially new information from Kamiokande [16]. The latter includes accelerator confirmation of the ability to separate ν_e and ν_μ events, as well as an independent higher energy data set giving not only a ν_μ/ν_e ratio agreeing with the lower energy data, but also a zenith-angle (hence source-to-detector) dependence compatible with $\nu_\mu \to \nu_e$ or $\nu_\mu \to \nu_\tau$ oscillations with $\Delta m^2_{\mu i} \approx 10^{-2}$ eV^2. Since almost the entire region of $\Delta m^2_{\mu e} - \sin^2 2\theta_{\mu e}$ allowed by the Kamiokande data is excluded by data from the Bugey and Krasnoyarsk reactor neutrino oscillation experiments, $\nu_\mu \to \nu_\tau$ oscillations are favored as an explanation of the atmospheric ν_μ deficit. Moreover, the absolute calculated ν_e and ν_μ fluxes — backed by measurements of μ fluxes —agree with ν_e data but show a ν_μ deficit [17]. (Because the mixing angle $\theta_{\mu i}$ must be large to account for the near 50% deficit of atmospheric ν_μ, $\nu_\mu \to \nu_s$ oscillation is disfavored because such large mixing would populate a fourth neutrino species in the early universe, contrary to Big Bang Nucleosynthesis constraints [18].)

The Liquid Scintillator Neutrino Detector (LSND) experiment at Los Alamos has detected an excess of 9 beam-on events of a type for which the most plausible interpretion appears to be $\bar{\nu}_\mu \to \bar{\nu}_e$ oscillations, with a background of only $\lesssim 2.1 \pm 0.3$ events mimicking a $\bar{\nu}_e$, so the probability that the

excess is a statistical fluke is $< 10^{-3}$ [20]. These events have both a positron track and a correlated γ-ray consistent with $\bar{\nu}_e + p \to e^+ + n$ followed by capture of the neutron by a proton in the mineral oil filling the LSND tank to form a deuteron. If the LSND events are interpreted as $\bar{\nu}_\mu \to \bar{\nu}_e$, the indicated mixing angle is $\sin^2 2\theta_{\mu e} \approx 3 \times 10^{-3}$. There are several ranges of mass-squared difference $\Delta m^2_{\mu e} \equiv |m(\nu_\mu)^2 - m(\nu_e)^2|$ which are compatible with the KARMEN [22] and BNL E776 [23] experiments, $\Delta m^2_{\mu e} \sim 2$, 6, and 10 eV^2, of which $\Delta m^2_{\mu e} \sim 6$ eV^2 appears to be favored, especially if the excess events LSND has detected of the $\nu_\mu \to \nu_e$ type are also considered [21]. If the ν_e mass is relatively small ($\lesssim 1$ eV, as indicated for Majorana neutrino mass from neutrinoless double beta decay experiments), then $\Delta m^2_{\mu e} \sim 6$ eV^2 implies that the ν_μ mass is $\sim 6^{1/2} \approx 2.4$ eV. This and the $\nu_\mu \to \nu_\tau$ explanation of the atmospheric ν_μ deficit then makes $m(\nu_\mu) \approx m(\nu_\tau) \approx 2.4$ eV. It is this scenario for the hot dark matter in a CHDM cosmology which we will show below gives predictions that appear to be in good agreement with astronomical observations.

However, a possibly disturbing consequence of taking all three hints of neutrino mass seriously is that the three incompatible Δm^2 require a minimum of *four* neutrino species, i.e. a sterile neutrino ν_s in addition to ν_e, ν_μ, and ν_τ [19, 12]. The LSND limit $\Delta m^2_{e\mu} > 0.2$ eV^2 implies that atmospheric ν_μ oscillations cannot be to ν_e so they must be $\nu_\mu \to \nu_\tau$; then MSW solar ν_e oscillations cannot be to ν_μ or ν_τ, so they must be $\nu_e \to \nu_s$.

An additional constraint that should perhaps be imposed on neutrino masses and mixings comes from r-process nucleosynthesis [24], which produces all the heavy chemical elements (e.g. gold). The favored site for this process is in a neutrino-heated "hot bubble" well above the neutron star remnant; this model produces the observed abundance of r-process nuclei without any *ad hoc* parameters or dependence on the messy details of the Type II supernova mechanism. However, matter-enhanced (MSW) neutrino oscillations $\nu_m u$ or $\nu_\tau \to \nu_e$ will lead to a hardening of the ν_e spectrum and too much neutron depletion via $\nu_e + n \to e^- + p$ for successful r-process nucleosynthesis for the LSND-suggested neutrino mass $\delta m^2_{e\mu} \approx 6$ eV^2 and $\sin^2 2\theta \approx 3 \times 10^{-3}$ — unless the mass of the ν_e is higher than that of ν_μ and ν_τ, so that no level crossing can occur. (Level crossing and MSW oscillation then will occur for the antineutrinos, but this appears to be consistent with the SN87A neutrino signal [25].) With the r-process constraint leading to an inverted neutrino mass spectrum, taken together with the previous three experimental hints of neutrino mass and the need to have about 5 eV of neutrino mass for CHDM cosmological models, the neutrino masses and mixings are determined essentially uniquely: $m(\nu_e) \approx 2.7$ eV and $m(\nu_\mu) \approx m(\nu_\tau) \approx 1.1$ eV [12]. While it is remarkable that there actually is a consistent solution, we should also keep in mind the liklihood that not all these hints are right. For purposes of the rest of this paper, we will consider CHDM with either one or two massive neutrinos; if the same total mass were shared by three rather than two neutrinos, the cosmological implications would be very similar.

3 Comparison of cosmological model predictions with observations

COBE observations [26] of fluctuations in the microwave background radiation provide an upper limit (since they include possible tensor gravity wave as well as scalar density wave contributions) on the normalization of the spectrum of density fluctuations in models of structure formation in the universe. When COBE normalization is used for the standard Cold Dark Matter (CDM) model [27] in a critical density ($\Omega = 1$) universe with a Zel'dovich primordial power spectrum ($P(k) = Ak^{n_p}$ with $n_p = 1$) as predicted by simple inflationary models, this fits large-scale data but produces too much structure on smaller scales.

We report (quasi-)linear estimates for CDM and CDM variants in the Table. All models in the Table are normalized to COBE [26, 28] except for the two models marked with an asterisk (*). The first two lines of numbers give our estimates of a variety of observational quantities and the uncertainties in them, from large to small scales. The bulk velocity at $r = 50\ h^{-1}$ Mpc is derived from the latest POTENT analysis [29]; the error includes the error from the analysis but not cosmic variance. However, similar constraints come from other data on large scales such as power spectra

that may be less affected by cosmic variance since they probe a larger volume of the universe. We have estimated the current number density of clusters ($N_{\rm clust}$) from comparison of data on the cluster temperature function from X-ray observations with hydrodynamic simulations [30] as well as from number counts of clusters [31]. All recent estimates of the cluster correlation function give fairly large values at 30 h^{-1} Mpc [32]; this also suggests that the zero crossing of the correlation function must exceed $\sim 40\ h^{-1}$ Mpc. The linear estimate of pairwise velocities (σ_v) is not an observed value, since pairwise velocities are strongly influenced by nonlinear evolution. However, from previous experience with N-body simulations for various models, we have found that the results from simulations are about a factor of three or four larger than the linear estimate. The limit we quote here is our estimate of the maximum allowed linear value to match numbers derived from redshift surveys, although the statistics on velocities derived from these surveys may not be very robust [33] since they are heavily influenced by the presence of (relatively rare) clusters [34]. To get a better estimate of pairwise velocities in our preferred Cν^2DM model, we have performed N-body simulations, as discussed below. The final column gives the observed density in cold hydrogen and helium gas at $z = 3.0 - 3.5$ from the latest observations of damped Lyman α systems [5].

The next two lines present predictions from the CDM model, and illustrate its problems. The cluster correlation function at 30 h^{-1} Mpc is smaller than observations indicate regardless of CDM normalization, reflecting the fact that the matter correlation function becomes negative beyond $\sim 40\ h^{-1}$ Mpc. In addition, CDM normalized to COBE produces more than an order of magnitue too many rich clusters (this problem was emphasized by Ref. [35] when the COBE DMR data first became available) and excessive small-scale pairwise velocities. If CDM is normalized to $\sigma_8 = 0.7$ (or equivalently to linear bias $b \equiv \sigma_8^{-1} = 1.43$), the cluster density problem is avoided, but small-scale velocities are still too large [1],[3],[11], and bulk velocities on a scale of 50 h^{-1} Mpc are probably too low. Even biased CDM is able to account for observations of damped Lyα systems, judging from $\Omega_{\rm gas}$, our Press-Schechter estimate of the amount of gas in collapsed halos at redshift $z = 3 - 3.5$.

CDM is attractive because of its simplicity and the existence of well-motivated particle candidates (lightest superpartner particle and axion [37]) for the cold dark matter; moreover, CDM came remarkably close to predicting the COBE signal. So several variations have been tried to patch up the CDM model. Lowering the normalization (introducing a lot of "bias") or "tilting" the primordial spectrum (assuming $n_p \approx 0.7$) improves agreement somewhat with data on intermediate (~ 10 Mpc, e.g. cluster) scales and small ($\sim 1\ h^{-1}$ Mpc, e.g. galaxy pairwise velocity) scales, but leads to serious disagreement with larger-scale (30-100 h^{-1} Mpc) measurements of galaxy bulk velocities and power spectra, and galaxy and cluster correlations. Less tilt will lead to serious overproduction of clusters and large galaxy pairwise velocities — e.g. $n_p = 0.9$ with $h = 0.45$ and no gravity waves, as advocated by Ref. [38], predicts $N_{clust} = 2 \times 10^{-6}$ and $\sigma_v = 279$, both calculated as in the Table.

From the viewpoint of agreeing with observations, the best variants of CDM that have been discussed [39] add either a cosmological constant (ΛCDM) or a little hot (neutrino) dark matter (CHDM). The former assumes $\Omega \approx 0.3$ and adds a cosmological constant Λ such that $\Omega_\Lambda \equiv \Lambda/(3H_0^2) = 1 - \Omega$ to preserve flatness (predicted by inflation) as well as improve agreement with data. ΛCDM works best for a larger Hubble parameter $h \approx 0.7$ favored by many observers. It predicts relatively early galaxy formation since at late times structure formation ceases as the universe goes into inflation caused by the positive cosmological constant.

The problem with CDM is that it has too much power on small scales relative to power at large scales. Since the presence of light neutrinos reduces small scale power (because neutrino free streaming causes neutrino perturbations to damp on smaller scales, and this in turn leads to a slower growth rate for the fluctuations in the cold component of CHDM), including a neutrino component improves the agreement of model predictions with observations.

The first version of CHDM to be studied in detail [1],[2] assumed 60% cold, 30% hot (corresponding to a neutrino of mass $94h^2\Omega_\nu \approx 7$ eV), and 10% baryonic matter, with $\Omega = 1$ and $h = 0.5$. This version of CHDM fits galaxy and larger scale structures in the present-epoch universe quite well. The small-scale velocities in this model are almost small enough [1] to agree with the old result $\sigma(1\ h^{-1}\ \text{Mpc}) = 340$ km s^{-1} from the CfA1 survey [36]. However, this result is now known to be

in error because of the accidental omission of the Virgo cluster [40]; as we mentioned above, this is not a very robust statistic. A direct comparison of galaxy groups in "observed" CDM and CHDM simulations with identically selected CfA1 groups shows that CDM velocities are much too high, even with biasing, while the velocities in the $\Omega_\nu = 0.3$ CHDM model are in reasonable agreement [3],[11]. However, the fraction of galaxies in groups is slightly too high for $\Omega_\nu = 0.3$ CHDM, while it is significantly too low for CDM. Thus agreement is improved for a lower Ω_ν.

CHDM with $\Omega_\nu = 0.3$ has $\Omega_{\rm gas}$ too small [7],[8] to account for the observed damped Lyα absorption systems [4, 5]. This model forms galaxies too late since the large fraction of free-streaming neutrinos washes out small-scale density fluctuations too effectively. But the small-scale power in CHDM models is a very sensitive function of Ω_ν, and lowering the hot fraction to about 20% solves this problem [8]. However, this model (called 1ν in the Table) may have too much power at intermediate scales and overproduces clusters, especially with the new COBE normalization. In order to avoid this, it should probably to be normalized lower — which we might imagine could reflect some tilt and gravity waves — but the danger is that this would result in too little early structure formation (because $\Omega_{\rm gas}$ is exponentially sensitive to the power spectrum).

These CHDM models have placed the needed neutrino mass in one flavor of neutrino, presumably the ν_τ, whereas if the asmospheric ν_μ deficit is due to $\nu_\mu \to \nu_\tau$ oscillations this cannot be correct. If we take the evidence for atmospheric neutrino oscillations *or* the LSND indications seriously, then the ~ 5 eV mass ought to be shared about equally between the ν_μ and ν_τ. Having two neutrinos of 2.4 eV each, which we call the Cν^2DM model, produces an interesting effect: the ratio of the power spectrum for Cν^2DM compared to that for CHDM with the same total neutrino mass in one species is essentially unity at large and small scales, but it has a dip of about 30% centered at $\sim 10\ h^{-1}$ Mpc. The larger neutrino free-streaming length, resulting from a neutrino mass of 2.4 eV instead of twice that, lowers the abundance of clusters and gives better agreement with observations (cf. also Ref. [41]).

The first Cν^2DM line in the Table gives the results for the first-year COBE normalization $Q_{rms-PS} = 17\mu$K, for which all quantities are in good agreement with the astronomical data. The extra free streaming due to the smaller neutrino mass suppresses cluster formation. The small-scale power in this model is nearly identical to that in the 1ν version, so Cν^2 also produces enough $\Omega_{\rm gas}$. Raising the normalization to the COBE two-year value [26, 28] leads to overproduction of clusters — though it is not as bad as for the 1ν version. But this could be counteracted by introducing a little tilt as shown by the next two lines in the Table, which correspond to COBE-normalized [28] chaotic inflation models with inflaton potentials $V(\phi) = m^2\phi^2$ and $\lambda\phi^4$ respectively, which lead to tilts $n = 0.960$, 0.939 with quadrupole tensor-to-scalar power ratios $(T/S)_2 = 0.126$ and 0.255, which are reduced by about 15% for the $\ell = 11$ multipole [42]. These models are in good agreement with observations, except possibly for the small-scale velocities which must be tested by comparing simulations with data. We note that σ_v is a fairly sensitive decreasing function of both Ω_b and Ω_ν, decreasing nearly 10% if Ω_b is increased from 7.5% to 10% *or* if Ω_ν is increased from 20% to 22%.

We are now in the process of analyzing results from new N-body simulations of Cν^2DM (high resolution 800^3 PM mesh in a 50 h^{-1} Mpc box with 256^3 cold and 2×256^3 hot particles). The case simulated was the first of the Cν^2DM ones in the Table, with the lower first-year COBE normalization ($Q = 17$), though as just discussed we expect that the results will not be very different from those for the higher normalization with a little tilt. We find that the hot particles are much more spread out than the cold ones, because the lower amplitude of the fluctuations in the hot component and their higher velocities even at late times (at $z = 0$, $v_{rms} = 75$ km s$^{-1}(m_\nu/2.4{\rm eV})^{-1}$ from the Fermi-Dirac distribution [1]). This implies that the usual growth rates for an $\Omega = 1$ cosmology should be lowered when velocities are estimated at $z = 0$ for $\Omega = 1$ CHDM since the hot component clusters so much less. Projected pairwise velocities can be estimated from the simulation results by placing an "observer" in the box and measuring relative velocities along the line of sight for given projected separation [1]. The dark matter particle pairwise velocity calculated in this way is $\sigma_v({\rm projected, dark\ matter}) = 560$ km s^{-1} at 1 h^{-1} Mpc separation. If we conservatively estimate that the velocity bias (the ratio of the rms velocity of the dark matter halos to that of the dark matter particles [43]) is 0.8, this corresponds

Table 1: Comparison of Models — COBE normalization (except for models marked *): $Q_{\rm rms-ps} = 20\mu$K, or $a_{11} = 7.15$ and $a_8 = 9.5$ [28].

Model	$\Omega_{\rm bar}$ (%)	Ω_ν (%)	N_ν [a]	m_ν [a]	σ_8 [b]	V [c] 50Mpc	$N_{\rm clust}$ [d] (10^{-7})	ξ_{cc} [e] 30Mpc	r [f] $\xi=0$	σ_v [g] 1Mpc	$\Omega_{\rm gas}$ [h] (10^{-3})
OBSERVATIONS						335	4.0	0.30	> 40	< 200	3.0
uncertainties						80	2.0	0.15			1.0
CDM models, h=0.5 ($t_0 = 13.0$ Gy)											
COBE (Q_{20})	7.5	0	0	0.00	1.28	422	100.	0.12	36	479	39
biased*	7.5	0	0	0.00	0.70	231	1.2	0.08	36	262	14
CHDM models, h=0.5 ($t_0 = 13.0$ Gy)											
KHPR (Q_{20})	10.0	30	1	7.04	0.78	425	16.	0.40	51	117	2.4
1ν (Q_{20})	7.5	20	1	4.69	0.89	423	27.	0.30	52	184	12.
Cν^2DM (Q_{17}*)	7.5	20	2	2.35	0.67	347	2.4	0.35	70	144	4.6
Cν^2DM (a_{11})	7.5	20	2	2.35	0.78	408	11.	0.38	70	169	11.
Cν^2DM$_{n0.96}$	7.5	20	2	2.35	0.69	374	3.7	0.39	71	142	5.5
Cν^2DM$_{n0.94}$	7.5	20	2	2.35	0.63	350	1.5	0.39	72	128	3.3
ΛCDM/ΛCHDM models, $h = 0.7$, $\Omega_0 = 0.3$, and $\Omega_\Lambda = 0.7$ ($t_0 = 13.5$ Gy)											
ΛCDM (a_8)	2.6	0	0	0.00	1.13	362	3.7	0.26	125	71	21.
ΛCHDM (a_8)	2.6	5.3	1	2.44	0.69	342	0.08	0.43	135	29	0.0004
ΛCDM/ΛCHDM models, $h = 0.6$, $\Omega_0 = 0.5$, and $\Omega_\Lambda = 0.5$ ($t_0 = 13.5$ Gy)											
ΛCDM (a_8)	3.5	0	0	0.00	1.25	403	22.	0.29	66	167	27.
ΛCHDM (a_8)	3.5	7.2	1	2.43	0.86	390	3.2	0.50	100	80	3.5

[a] N_ν is the number of ν species with mass. If $N_\nu \geq 1$, each species has the same mass m_ν.
[b] $(\Delta M/M)_{\rm rms}$ for $R_{\rm top-hat} = 8h^{-1}$ Mpc.
[c] Bulk velocity in top-hat sphere of radius $50h^{-1}$ Mpc.
[d] Number density of clusters $N(>M)$ in units of $10^{-7}\,h^3$Mpc^{-3} above the mass $M = 10^{15}h^{-1}M_\odot$, calculated using Press-Schechter approximation with gaussian filter and $\delta_c = 1.50$.
[e] The cluster-cluster correlation function amplitude at $30h^{-1}$ Mpc, computed using linear theory [39: HP93] and assuming a unit bias factor for the dynamical contribution.
[f] Zero crossing ($\xi(r) = 0$) of the correlation function in units of h^{-1} Mpc.
[g] Linear estimate of pairwise velocity at $r = 1h^{-1}$ Mpc: $\sigma_v^2 = 2H_0^2\,\Omega^{1.2}\int dk\,P(k)(1 - \sin kr)/kr$.
[h] Mean density of collapsed baryons at $z = 3$–3.5 in units of 10^{-3} of critical density, calculated using $\Omega_{\rm gas} = (\Omega_b/\Omega_c)\,{\rm erfc}(\delta_c/\sqrt{2}\sigma)$, with $\delta_c = 1.4$ [8], and σ computed for mass $5 \times 10^{10}h^{-1}M_\odot$ using gaussian smoothing and assuming all gas is neutral. Since some gas may be ionized or removed by star formation, $\Omega_{\rm gas}$ for the various models should be at least as high as the observations.

to 450 km s^{-1} for galaxies, consistent with current observations (and, as expected, about a factor of 3 larger than the linear estimate in the Table). As already mentioned, the Void Probability Function from these simulations is in excellent agreement with the PPS and CfA2 data [10].

It is remarkable that, with the experimentally suggested neutrino masses, only cosmological models with $h \approx 0.5$ match observations. As we discussed in Ref. [13], for $h = 0.7$ — favored by many observers — CDM ($\mathrm{CDM}_{0.7}$) is an even worse fit to the data than for $h = 0.5$ because the larger h makes matter-dominance ($\propto \Omega h^2$) occur earlier and thus moves the bend in the CDM spectrum to smaller scales, giving more intermediate and small scale power for a given large scale normalization. Adding two 2.4 eV neutrinos only slightly improves the situation, because this only gives $\Omega_\nu \sim 0.1$ for $h = 0.7$, so the spectrum is not modified very much. Of course, with large h, $\Omega = 1$ models also lead to too short a time since the big bang: $t_0 = 2/(3H_0) = 6.52\,\mathrm{Gy}/h = 9.3$ Gy for $h = 0.7$.

A larger age is obtained for an open universe; in order to be consistent with inflation, we assume a positive cosmological constant. The maximum value of Λ allowed by the COBE data is $\Omega_\Lambda \equiv \Lambda/(3H_0^2) \approx 0.78$ [44], and the maximum allowed by quasar lensing statistics is $\Omega_\Lambda \approx 0.7$ [45]. For a flat ($k = 0$) universe with $\Omega_\Lambda = 0.7$ and $\Omega = 0.3$, $h = 0.7$ corresponds to $t_0 = 13.5$ Gy. ΛCDM with these parameters is a good fit [46] to the data. However, this model becomes much worse if even one neutrino of 2.4 eV is added, seriously underproducing clusters and Ω_{gas} because of the excessive fraction of hot dark matter suppressing small-scale structure. Consequently, low-Ω_0 models have serious problems if any neutrinos have significant mass. Raising Ω_0 to 0.5 gives enough cold dark matter to counteract the poisoning of structure formation by a single neutrino species of 2.44 eV mass, but this model must have a lower Hubble parameter to be consistent with $t_0 \geq 13$ Gy ($h \geq 62.5$ for $\Omega_0 = 0.5$).

A similar situation occurs for $\Omega = 1$ Cν^2DM with $h = 0.4$, for which $\Omega_\nu = 0.32$ with two 2.4 eV neutrinos. (Recall that for given $m(\nu)$, Ω_ν scales as h^{-2} since critical density is $\propto h^2$.) Because the bend in the CDM spectrum moves to larger scales as h decreases, there is less intermediate and small scale power for given large scale normalization; adding hot dark matter further decreases small scale power. We find that even with only one 2.4 eV neutrino, there is just not enough power to generate the observed number of clusters or high-redshift objects.

4 Conclusions

Ever since the early 1980s there have been hints [47] that features on small and large scales may require a hybrid scenario in which there are two different kinds of dark matter. Preliminary studies of the CHDM scenario were carried out in 1984 [48] and it was first worked out in detail only in the last two years [1],[2],[3] with one massive neutrino. We have shown here that the Cν^2DM model, with Hubble parameter $h = 0.5$ and both neutrinos having a mass of 2.4 eV as suggested by ongoing experiments, gives a remarkably good account of all presently available astronomical data. New data on CMB, large scale structure, and structure formation will severely test this highly predictive model. Results expected soon from ν-oscillation experiments will clarify whether indeed $m(\nu_\mu) \approx m(\nu_\tau) \approx$ 2.4 eV. The Table shows the implications of such neutrino masses for a variety of popular CDM-type cosmological models. If even just the ν_μ has a mass of 2.4 eV, as suggested by preliminary results from the LSND experiment, flat low-Ω CDM models are disfavored.

ACKNOWLEDGEMENTS. We have benefited from conversations with S. Bonometto, S. Borgani, D. Caldwell, A. Dekel, S. Faber, G. Fuller, R. Nolthenius, and Y.-Z. Qian. This research was supported by NSF grants at UCSC and NMSU and by a DOE grant at UCSB. The simulations were done on the Convex C-3880 at NCSA.

References

[1] A. Klypin, J. Holtzman, J.R. Primack, and E. Regős, *Astrophys. J.* **416**, 1-16 (1993).

[2] M. Davis, F. Summers, and D. Schlegel, *Nature* **359**, 393 (1992); D. Schlegel, M. Davis, F. Summers, and J.A. Holtzman, *Astroph. J.* **427**, 512 (1994). Y.P. Jing, H.J. Mo, G. Börner, and L.Z. Fang, *Astron. Astroph.* **284**, 703 (1994).

[3] Nolthenius, R., Klypin, A., & Primack, J.R. *Astrophys. J. Letters* **422**, L45-48 (1994).

[4] K.M. Lanzetta, *Publ. Astron. Soc. Pacific* **105**, 1063 (1993); K.M. Lanzetta, A. Wolfe, D.A. Turnshek, Preprint (1993).

[5] L. Storrie-Lombardi, R.G. McMahon, M.J. Irwin, and C. Hazard, in *Proc. ESO Workshop on QSO Absorption Lines*, in press (1995).

[6] M.G. Haehnelt, *Mon. Not. Roy. Astron. Soc.* **265**, 727 (1993). D.Yu. Pogosyan and A.A. Starobinsky, *ibid.* **265**, 507 (1993). A.R. Liddle and D. Lyth, *ibid.* **265**, 379 (1993).

[7] H.J. Mo and J. Miralda-Escude, *Astroph. J.* **430**, L25 (1994); G. Kauffmann and S. Charlot, *Astroph. J.* **430**, L97 (1994); C.P. Ma and E. Bertschinger, *Astroph. J.* **434**, L5 (1994).

[8] A. Klypin, S. Borgani, J. Holtzman, J.R. Primack, *Astrophys. J.*, **444**, 1 (1995).

[9] C.-P. Ma, in *Dark Matter* Proc. 5th Ann. Astrophys. Conf. in Maryland, October 1994, eds. Stephen S. Holt and Charles L. Bennett (American Institute of Physics, 1995), in press.

[10] S. Ghigna, S. Borgani, S. Bonometto, L. Guzzo, A. Klypin, J.R. Primack, R. Giovanelli, and M. Haynes, *Astroph. J. Lett.* (1994). We have found the VPF predicted from our new $C\nu^2$DM simulations to be in excellent agreement with observations (work in prep.).

[11] R. Nolthenius, A. Klypin, J.R. Primack, *Astrophys. J.* in press (1995).

[12] George M. Fuller, Joel R. Primack, and Yong-Zhong Qian, Preprint astro-ph/9502081, *Phys. Rev.* in press (1995).

[13] Joel R. Primack, Jon Holtzman, Anatoly Klypin, and David O. Caldwell, *Phys. Rev. Lett.*, **74**, 2160-2163 (1995).

[14] J.N. Bahcall, at Neutrino94, in *Nucl. Phys. B*, Proc. Supp. **38**, 98 (1995); V. Berezinzky, G. Forentini, and M. Lissia, *Phys. Lett. B* **341**, 38 (1994); P.I. Krastev and A.Yu. Smirnov, *Phys. Lett. B* **338**, 282; S.P. Rosen, *27th Int. Conf. on High Energy Phys.*, Glasgow (1994); N. Hata and P. Langacker, *Phys. Rev. D* **50**, 632 (1994).

[15] K.S. Hirata et al., *Phys. Lett.* **B280**, 146 (1992); R. Becker-Szendy et al., *Phys. Rev.* **D46**, 3720 (1992); P.J. Litchfield, in *Proc. Int. Europhys. Conf. on High Energy Phys.*, eds. J. Carr and M. Perrottel (Ed. Frontières, Gif-sur-Yvette, France, 1993).

[16] Fukuda, Y. et al., *Phys. Lett. B* **335**, 237 (1994). K. Inoue, at Moriond'95.

[17] G. Barr, T.K.Gaisser, and T. Stanev, *Phys. Rev. D* **39**, 3532 (1989); W. Frati et al., *Phys. Rev. D* **48**, 1140 (1993); D.H. Perkins, *Astropart. Phys.* **2**, 249 (1994).

[18] Z. Shi, D.N. Schramm, B.D. Fields, *Phys. Rev. D* **48**, 2563 (1993), and refs. therein.

[19] D.O. Caldwell, in *Perspectives in Neutrinos, Atomic Physics, and Gravitation*, ed. J. Tran Thanh Van et al. (Ed. Frontieres, Gif-sur-Yvette, France, 1993). D.O. Caldwell, and R. Mohapatra, *Phys. Rev. D* **48**, 3259 (1993). J.T.Peltoniemi and J.W.F. Valle, *Nucl. Phys. B* **406**, 409 (1993).

[20] C. Athanassopoulos et al. (LSND), rev. preprint submitted to *Phys. Rev. Lett.* (June 9, 1995). Also I. Stancu, Moriond'95.

[21] D.O. Caldwell, in *Trends in Astro-particle Physics* Stockholm, 1994, eds. L. Bergstrom, P. Carlson, P.O. Hulth and N. Snellman, *Nucl. Phys. B*, Proc. Suppl. (in press).

[22] G. Drexlin, *Prog. in Part. and Nucl. Phys.* **32** (in press, 1994); J. Kleinfeller, Moriond95.

[23] L. Borodovsky et al., *Phys. Rev. Lett.* **68**, 274 (1992).

[24] Y.-Z. Qian et al., *Phys. Rev. Lett.* **71**, 1965 (1993); Y.-Z. Qian, Ph.D. thesis, UCSD (1993).

[25] Y.-Z. Qian and G. M. Fuller, *Phys. Rev. D*, in press (1995).

[26] K.M. Gorski et al., *Astrophys. J. Lett.* **430**, L89 (1994); C.L. Bennett et al., *Astrophys. J.* (in press, 1994); E.F. Bunn, D. Scott, and M. White, *Astrophys. J.* **441**, L9 (1995); R. Stompor et al., *Mon. Not. Roy. Astr. Soc.* (in press, 1995).

[27] G.R. Blumenthal, S.M. Faber, J.R. Primack, and M. Rees, *Nature* (1984); M. Davis, G. Efstathiou, C. Frenk, and S.D.M. White, *Nature* (1992); J.P. Ostriker, *Ann. Rev. Astron. Astrophys.* **31**, 689 (1993).

[28] We actually normalize the models not to $Q_{\rm rms-PS} = 20$ but rather to the "pivot points" $a_{11} = 7.15$ for the Cν^2DM models, or $a_8 = 9.5$ for the ΛCDM models, as recommended by Stompor et al., Ref. [26].

[29] A. Dekel, *Ann. Rev. Astron. Astroph.* **32**, 371 (1994) and private communications.

[30] G. Bryan et al., *Astroph. J.* **37**, L5 (1994).

[31] We have increased the cluster masses in N. Bahcall and R. Cen, *Astroph. J.* **408**, L77 (1993) by a factor of 1.4; the results are then in rough agreement with those of A. Biviano et al., *Astroph. J.* **411**, L13 (1993) and S.D.M. White, J.F. Navarro, A.E. Evrard, and C.S. Frenk, *Nature* **366**, 429 (1993).

[32] See e.g. S. Olivier, J. Primack, G.R. Blumenthal, and A. Dekel, *Astroph. J.* **408**, 17 (1993); A. Klypin and G. Rhee, *Astroph. J.* **428**, 399 (1994); and refs. therein.

[33] H.J. Mo, Y.P. Jing, and G. Börner, *Mon. Not. Roy. Astron. Soc.* **264**, 825 (1994); W.H. Zurek, P.J. Quinn, J.K. Salmon, and M.S. Warren, *Astroph. J.* **431**, 559 (1994). Cf. also Refs. [3] and [40].

[34] R. O. Marzke et al., CfA preprint (1995).

[35] G. Efstathiou, J.R. Bond, S.D.M. White, *Mon. Not. Roy. Astron. Soc.* **258**, P1 (1992).

[36] M. Davis, P.J.E. Peebles, *Astrophys. J.* **267**, 465 (1983).

[37] See e.g. J.R. Primack, D. Seckel, and B. Sadoulet, *Ann. Rev. Nucl. Part. Sci.* **38**, 751 (1988).

[38] D. Scott, J. Silk, and M. White, *Science*, **268**, 829 (1995).

[39] J. Holtzman, *Astroph. J. Suppl.* **81**, 1 (1989); J. Holtzman and J.R. Primack, *Astroph. J.* **405**, 428 (1993). A.R. Liddle and D.H. Lyth, *Phys. Rep.* **231**, 1 (1993).

[40] R. Somerville, J.R. Primack, R. Nolthenius, and M. Davis, in prep. (1995).

[41] D. Pogosyan and A.A. Starobinsky, in Large-Scale Structure in the Universe, eds. J.P.Miicket, S.Gottlöeber, V. Müller, (World Scientific, 1995), in press.

[42] M. S. Turner, *Phys. Rev. D*, **48**, 3502 (1993); M. S. Turner, M. White, and J. E. Lidsey, *Phys. Rev. D*, **48**, 4613 (1993).

[43] R.G. Carlberg and H.M.P. Couchman, *Astroph. J.* **340**, 47 (1989).

[44] E. Bunn & N. Sugiyama, preprint astro-ph/9407069 (1994).

[45] D. Maoz and H.-W. Rix, *Astroph. J.* **416**, 425 (1993). C. Kochanek, *Astroph. J.* **419**, 12 (1993), UCLA Conference, ed. D. Cline (1995), in press, and private communication.

[46] G. Efstathiou, W.J. Sutherland, S.J. Maddox, *Nature* **348**, 705 (1990); R. Cen, N.Y. Gnedin, and J.P. Ostriker, *Astroph. J.* **417**, 387 (1993).

[47] A. Dekel, *Astron. Astrophys.* **101**, 79-87 (1981); Dekel, A. *Astroph. J.* **284**, 445-456 (1984).

[48] See the historical references in Ref. [1].

SOLAR NEUTRINO PROBLEM, 1995

V. Berezinsky [1]
[1] *INFN, Laboratori Nazionali del Gran Sasso, 67010 Assergi (AQ), Italy*



Abstract

The status of the Solar Neutrino Problem (SNP), as it is seen in 1995, is reviewed. Basically, there are two principal solutions to the SNP: (i) with *standard neutrino* (neutrino of SM of electroweak interactions) and (ii) with *nonstandard neutrino* (neutrino beyond the SM). Actually, one can distinguish three solar-neutrino problems: the deficit of ^8B-neutrinos, the deficit of ^7Be-neutrinos and the Homestake/Kamiokande conflict. The first problem probably can be solved with small correlated changes of nuclear cross-sections and the change of central temperature of the Sun. The deficit of ^7Be- neutrinos looks like the key problem. The Homestake/Kamiokande conflict strongly disfavors or excludes the standard neutrino (nuclear/astrophysical solution to the SNP). MSW conversion gives most plausible explanation to the SNP.

1 Introduction

The Solar Neutrino Problem (SNP) is a deficit of neutrino fluxes detected in all four solar-neutrino experiments [1],[2], [3],[4]. The data, as reported in 1995, are listed in Table 1 and compared with calculations of Bahcall and Pinnsoneault [5] for the Standard Solar Model (SSM).

Table 1: The solar-neutrino data of 1995 compared with the SSM prediction [5]

	DATA	SSM [5]	DATA/SSM
GALLEX (SNU)	$79 \pm 10 \pm 6$	132	0.598 ± 0.088
SAGE (SNU)	$69 \pm 10^{+5}_{-7}$	132	0.532 ± 0.088
KAMIOKANDE ($10^6\ cm^{-2}s^{-1}$)	$2.75^{+0.20}_{-0.18} \pm 0.41$	5.69	0.484 ± 0.079
HOMESTAKE (SNU)	$2.55 \pm 0.17 \pm 0.18$	8.0	0.319 ± 0.031

The solar neutrino spectrum is characterized by three most important components. (see Table 2).

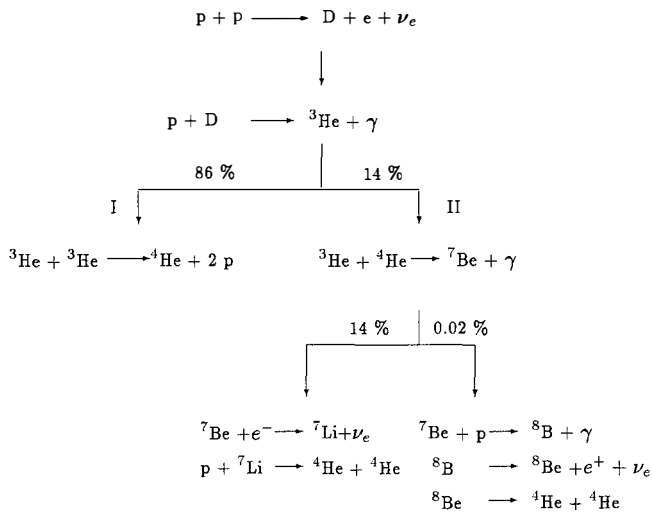
(i) The most energetic part of the spectrum is presented by boron neutrinos from ${}^8B \rightarrow {}^8Be + e^+ + \nu_e$ decay. The maximum energy of neutrinos in this spectrum is $E_{\nu,max} \approx 14\ MeV$. Kamiokande, which has the highest threshold of neutrino detection ($E_\nu^{th} \approx 7\ MeV$ since 1991) detects only boron neutrinos.

(ii) Beryllyum neutrinos (${}^7Be + e^- \rightarrow {}^7Li + \nu_e$) are monoenergetic ($E_\nu = 0.862\ MeV$). Predicted flux of Be-neutrinos depends weakly on the solar model and is $(4.2 - 4.9) \cdot 10^9\ cm^{-2}s^{-1}$. Homestake detects both boron and beryllium neutrinos: ${}^8B$-neutrinos provide about 80% of the total signal and ${}^7Be$-neutrinos - about 15%

(iii) The low-energy part of the solar-neutrino specrum is presented by pp- neutrinos ($p + p \rightarrow {}^2H + e^+ + \nu_e$) with maximum energy $E_\nu^{max} = 0.42\ MeV$. These neutrinos greatly overnumber the flux of other neutrinos ($6.1 \cdot 10^{10}\ cm^{-2}s^{-1}$). The flux is determined practically only by solar luminsity and therefore is very reliably predicted. GALLEX and SAGE measure mostly pp-neutrinos (about 60% of the total signal) with some contribution of ${}^7Be$ and ${}^8B$ neutrinos (about 25% and 10%, respectively).

From Table 1 one can see that the suppression factor, DATA/SSM, is ~ 0.5 within 1σ for the first three experiments, while for the Homestake detector it is ~ 0.3. It is easy to understand that it creates a problem for nuclear/astrophysical solution to SNP. Indeed, since the nuclear/astrophysical factors cannot change the shape of ${}^8B$-neutrino spectrum, the suppression factor for boron neutrino signal in Homestake should be the same (~ 0.5) as in Kamiokande.

Table 2: Nuclear reactions in the Sun (pp-chain)



Of course ^7Be-neutrinos can be suppressed more strongly, but their contribution to the total signal in the Homestake detector is small ($\sim$ 15%). The incompatibility of the Homestake and Kamiokande results was first understood by Bahcall and Bethe [6].

The disrepancy between predicted and observed neutrino fluxes, as given in Table 1, is a severe problem. The SSM is the most elaborated stellar model. The modern status of the SSM is described in ref's [7],[8]. The calculations use input parameters such as the solar mass, solar radius, surface chemical composition and nuclear reaction rates, and are normalized by the value of luminosity, $L_\odot$, and by data of helioseismology, (see ref.[8] for a detailed analysis).

There are at least 11 recently published calculations [5,9-20] for the SSM as it is described above. In all these works the physics included is the same. The slight difference in the results is caused by the different input parameters, most notably by the opacity of the Sun. The calculated parameter which is most important for the solar neutrino fluxes

is the central temperature. It varies by $\pm 1\%$ in the above cited calculations. The results are summarized in ref.[20] as $T_c = (15.55 \pm 0.15) \cdot 10^6 K$.

The numerial predictions of the SSM are questioned by uncertainties most notably in the rate of nuclear reactions [7],[10] and in the opacity coefficients [7],[8]. They can be also influenced by collective effects in plasma [21].

There are actually three solar-neutrino problems.

The Homestake/Kamiokande conflict, mentioned above, will be described in some detail in Section 2. This is the most serious problem for the case of the standard neutrino (the nuclear/astrophysical solution to the SNP). If both experiments are correct and $\nu^{37}Cl$-cross-section is not overestimated, neutrino is not standard. The Homestake/Kamiokande problem is analyzed in refs.[6], [10], [22], [23]. An interesting discussion of the adjacent problem, the ratio of beryllium and boron neutrino fluxes, is given in ref.[24].

Boron-neutrino deficit is a second solar-neutrino problem. For the last 25 years the Homestake results were interpreted as deficit of ^8B-neutrinos. As described in Section 3, it could be that ^8B- neutrino problem will be solved by the small correlated changes in the nuclear cross-sections combined with very small ($\sim 1 - 2\%$) reduction of the central temperature of the Sun.

The third solar-neutrino problem, the *deficit of* ^7Be*-neutrinos* is discussed in Section 4. At present it looks like the essence of the solar-neutrino problem. The significant contribution to understanding of this problem is given in refs.[25]-[28]. The direct detection of ^7Be-neutrinos will be performed by BOREXINO [29] at Gran Sasso.

The three solar-neutrino problems, as they discussed above, were recently reviewed in refs. [23], [30].

It is worth to emphasize the role of gallium experiments in understanding of Be-neutrino problem. In fact, the gallium results alone limit the beryllium neutrino flux below the prediction of the SSM [31], [32]. However, if to subtract from the gallium counting rate the contribution due to ^8B- neutrinos (taken, for example, from the Kamiokande data) and the contribution due to pp-neutrinos (from the solar-luminosity sum rule) then no place is left for ^7Be-neutrino flux [33]. For more detailed analysis see ref.[27].

One can conclude therefore that the case of the standard neutrino (the astrophysical solution to the SNP) is strongly disfavored.

The other solution is given by the nonstandard neutrino: MSW conversion [34], vacuum oscillations [35](for the state-of-the-art description see [36]), resonant spin-flavor precession [37], and matter enhanced transition induced by flavor-chaging neutral currents [38]. The most accurate description of all solar-neutrino data is given by the small-mixing angle MSW conversion. This topic is reviewed by A.Smirnov in these Proceedings.

We shall not touch here the description of the experiments. A reader can find it in the recent review [39].

2 Homestake/Kamiokande conflict or a problem of Be/B neutrino ratio

It can be rigorously proved that the case of the standard neutrinos (a nuclear/astrophysical solution) is excluded or strongly disfavored if the Homestake and Kamiokande results are correct within the cited the statistical and systematic errors.

The point is that the suppression of SSM flux for the Homestake detector (data/SSM = 0.32) is stronger than for Kamiokande (data/SSM = 0.48). However, Homestake detects the same boron neutrinos as Kamiokande, and additionally Be-neutrinos. This argument was first considered quantitatively by Bahcall and Bethe [6]. Using the known relative efficiencies of the two detectors, they found that the counting rate due to boron neutrinos in the Homestake detector calculated from the Kamiokande date to be 3.0 ± 0.49 SNU. It has to be compared with the total counting rate, 2.55 ± 0.25 SNU, which includes Be-neutrinos, *pep*-neutrinos etc. For this latter contribution the authors suggested to use the SSM calculations, since SSM uncertainties for Be- and *pep*-neutrinos are considerably smaller than for B-neutrinos. The two above-mentioned sources give 1.4 SNU and therefore the total counting rate should be 4.40 ± 0.49 SNU, to be compared with 2.55 ± 0.25 SNU observed. Note that we updated here the data used in ref.[6].

In refs.[10],[22] the Homestake/Kamiokande problem was analyzed using the graph $\phi_\nu(^7Be) - \phi_\nu(^8B)$, where ϕ_ν is the neutrino flux at the Earth. It is demonstrated that two regions allowed by Kamiokande and Homestake, respectively, do not intersect each other. The separation of two regions is the smallest at the zero ^7Be- neutrino flux, however, even here they do not intersect each other at $90\% CL$.

In ref.[23] the Homestake/Kamiokande problem is analyzed analytically in terms of two ratios: $R_{Be} \equiv \phi_\nu(Be)/\phi_\nu^{SSM}(Be)$ and $R_B \equiv \phi_\nu(B)/\phi_\nu^S SM(B)$. It is shown that independently of the choice of the SSM model

$$R_{Be}/R_B < -1.08 \pm 0.48$$

The uncertainties in nuclear cross-sections do not affect this proof. The temperature solution (low T_c) is strongly excluded.

The analysis described above implies that an astrophysical solution to the Homestake-Kamiokande conflict needs unphysically low Be-neutrino flux.

The only way to avoid the Homestake/Kamiokande contradiction is to assume that $\nu^{37}Cl$ cross-section is overestimated (however, according to ref.[7] it is clear that it is not the case) or that at least one of the two experiments (Homestake and Kamiokande) has uknown large systematic error.

3 Boron neutrino problem

This problem is clearly seen from Table 1 as neutrino deficit in the Kamiokande detector, which measures only boron neutrinos. The neutrino deficit in the Homestake detector also shows the suppression of the boron neutrino flux, because about 80% of the total

signal in this detector is provided by the boron neutrinos. The boron neutrino problem was recognized during the last 25 years due to the Homestake results.

Two recently discussed effects can resolve this problem.

The first one is the new measurements of $p + {}^7Be \rightarrow {}^8B + e^+ + \nu_e$ cross-section. As one can see from Table 2, the boron neutrino flux is proportional to this cross-section or to the astrophysical S-factor, $S_{17}(0)$, which conventionally characterizes [7] this cross-section. Recently this factor was found from the inverse process, the dissociation of ${}^8B$-nuclei in the Coulomb field of ${}^{208}Pb$: ${}^8B + {}^{208}Pb \rightarrow {}^{208}Pb + {}^7Be + p$. These measurements [40] result in the value of S-factor $S_{17}(0) = 16.7 \pm 2\ eV \cdot b$ to be compared with $S_{17}(0) = 22.4 \pm 2.1\ eV \cdot b$ used by Bahcall and Pinsonneault [5]. This value of $S_{17}(0)$ coincides with the lowest value from the previous measurements and, if true, can lower the predicted flux by a factor 1.3, which alone is still insufficient to resolve the boron neutrino problem (see Table 1).

The second phenomenon is the collective processes in the dense plasma [21].

Collective effects imply the influence of plasma on the elementary processes (e.g. on scattering). The major effect is the change of opacity. According to ref.[21] there are three main effects: the Doppler effect in the Raman resonance, the collective effects in the bremsstrahlung and degeneration of electrons. All these effects can diminish the local opacity in solar core by 18%. In principle it should result in decreasing of T_c. However, at present we have only the indication of the new plasma effects, which must be incorporated in the calculations of solar opacity and the solar models. Note that helioseismological data confirm the existing SSM models at $r \geq 0.2 R_\odot$.

To bring the Kamiokande flux into agreement with theoretical prediction one needs, beyond the factor 1.3 due to the low value of $S_{17}(0)$, to diminish the central temperature T_c only by 2.5%. It can be achieved by lowering the opacity in the solar core due to e.g. the collective plasma effects or due to slight increase of the heavy element abundancies. The increase of ${}^3He + {}^3He$ cross-section, S_{33}, or decrease of ${}^3He + {}^4He$ -cross-section, S_{34}, (see Table 2) can also facilate this task.

We therefore conclude that the prediction for boron neutrino flux can be brought into agreement with the Kamiokande observations by the price of small correlated changes of the cross-sections and the central temperature. At present this possibility should be still considered as the speculative one.

4 Beryllium-neutrino problem

We have at least a realistic hope that the boron-neutrino problem can be solved within the nuclear/astrophysical solution.

In several works [25]-[28] it was recently realized that the essence of the solar neutrino problem is a deficit of beryllium neutrinos.

We saw already this problem in Section 2: the Homestake/Kamiokande conflict demands too low Be/B neutrino ratio.

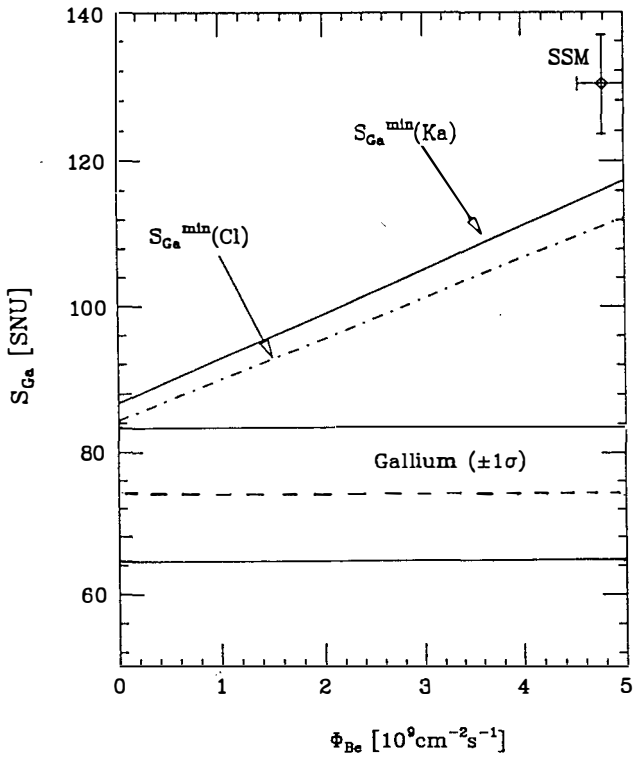


Fig.1 The gallium signal S_{Ga} as a function of ^7Be- neutrino flux (from [27]). Curves $S_{Ga}^{min}(Cl)$ and $S_{Ga}^{min}(Ka)$ give the gallium signal with the minimum boron neutrino contribution evaluated from the Homestake and Kamokande experiments, respectively. The predicted signal is above the observed one (74 ± 9 SNU) even when $\phi_\nu(Be) = 0$.

The model-independent lower limit for the gallium experiment gives another insight into the problem [33]. To obtain this limit let us assume zero beryllium neutrino flux $\phi_\nu(Be) = 0$. The flux of pp-neutrinos can be found from the solar luminosity sum rule. We obtain $\phi(pp) = 6.48 \cdot 10^{10}\ cm^{-2}s^{-1}$ or 76.5 SNU for a gallium detector. The flux of ^8B-neutrino as given by the Kamiokande experiment is $(2.75 \pm 0.26 \pm 0.35) \cdot 10^6\ cm^{-2}s^{-1}$. The 1σ lower limit (statistical error only) corresponds to $2.49 \cdot 10^6\ cm^{-2}s^{-1}$ or 6.0 SNU for the gallium experiments. If we neglect all other neutrino sources we obtain in sum 82.5 SNU. To compare this (unrealistically low) lower limit with observational data we use the latest data of GALLEX [1] ($79 \pm 10 \pm 7$ SNU) and SAGE [2] ($69 \pm 10 \pm \frac{5}{7}$ SNU). If we take the average and sum the errors quadratically we obtain 74 ± 9 SNU, i.e. 1σ below the very stringent lower limit obtained above. We then conclude that the results of the gallium experiments combined with the lower limit of Kamiokande leaves no place for beryllium neutrinos.

The upper limits for beryllium neutrino fluxes were obtained in ref's [25] and [26] from gallium experiments and Kamiokande. In terms of the signal in the gallium detectors they are found to be 19 SNU at 95% CL [25] and 5.1 SNU at 68% CL [26]. These figures are to be compared with $31 - 36$ SNU predicted by the most SSM. If one takes the Homestake data instead of Kamiokande, almost the same cotradiction arises [27]. This result is illustrated by Fig.1 from the work [27]. We updated this graph averaging the fluxes of GALLEX and SAGE.

5 Low neutrino-flux models.

Reducing the $S_{17}(0)$ and slightly changing the other cross-sections or the temperature, one can bring the prediction for the ^8B- neutrino flux into agreement with observations (the Kamiokande data). Two models with low ^8B-neutrino flux have been recently elaborated.

Let us start with the Shi and Schramm (SS) model [41]. This is the SSM model with two input parameters modified as $S_{17} = 20.2\ eV$ and heavy element abundance $Z = 0.015$. The low Z provides the lower central temperature T_c. Actually, this aim can be accomlished due to the collective plasma effects. The ^8B-neutrino flux is predicted to be $3 \cdot 10^6\ cm^{-2}s^{-1}$, in a good agreement with the Kamiokande data $(2.75 \pm 0.45) \cdot 10^6\ cm^{-2}s^{-1}$.

Dar and Shaviv [42] introduced in their model (DS) the following new elements: (i) they calculated $S_{17}(0)$ from the Filippone et al data and found this value as low as $17\ eV \cdot b$, (ii) they evaluated also $S_{34}(0)$ for $^3He(\alpha,\gamma)^7Be$ reaction and found it to be $0.45\ keV \cdot b$, which is considerably lower than the Bahcall-Pinsonneault value $0.533\ keV \cdot b$, (iii) they used the updated value of the solar luminosity, $L_\odot = 3.826(8) \cdot 10^{33}\ erg/s$, (iv)they reconsidered the screening effects for the nuclear reactions and (v) they included into stellar evolution code the diffusion of *all* chemical elements and started the evolution calculations from the pre-main sequence stage. Actually, only items (i) - (iii) are relevant to neutrino fluxes. In fact, the item (v) was already included in the Kovetz-Shaviv [9] model and did not give much difference in comparison with the other SM calculations. The item (iv), as the authors mentioned, give the minor effect. The same is true for the

item (iii),which was already taken into account in some other calculations. Therefore, the main impact on the neutrino fluxes is caused by diminishing of S_{17} and S_{34}.

The comparison of the low neutrino-flux models (SS and DS) with the two standard models (BP [5] and TL [11]) and with the observational data is given in Table 3.

Table 3: Comparison of the low neutrino-flux models with the Standard Solar models and experimental data.

	BP	TL	SS(93)	DS(94)	experim. data
pp(E10)	6.00	6.02	6.1	6.04	
$^7Be(E9)$	4.89	4.33	3.9	4.30	$< 2.1(95\%CL)$
$^8B(E6)$	5.69	4.43	3.0	2.77	2.75 ± 0.45 (Kamiokande)
$^{13}N(E8)$	4.92	3.83	—	0.747	
$^{15}O(E8)$	4.26	3.15	—	0.217	
Homestake (SNU)	8.0 ± 3.0	6.4 ± 1.4	4.5	4.2	2.55 ± 0.25
GALLEX (SNU)	132^{+21}_{-17}	127 ± 7	114	109	$79 \pm 10 \pm 6$
SAGE (SNU)	132^{+21}_{-17}	127 ± 7	114	109	$69 \pm 10 \pm 6$
$T_c(10^7\ K)$	1.559	1.549	1.545	1.571	
$S_{17}\ eV \cdot b$	24	21	20.2	17	
$S_{34}\ keV \cdot b$	0.533	—	—	0.45	
$S_{33}\ MeV \cdot b$	5.0	—	5.6	5.6	

The first column in Table 3 gives the list of physical quantities and of experiments, the second column gives the predictions of the Bahcall and Pinsonneault model [5], the third column refers to the Turck-Chiese and Lopes model [11], in the fourth and fifth columns the predictions of the low-flux models (Shi and Schramm [41] and Dar and Shaviv [42]) are listed and the last column gives the experimental data. The neutrino fluxes (pp, Be etc) are given in units $cm^{-2}s^{-1}$ with the orders of magnitude indicated in the first column.

One can see that in both low neutrino-flux models the predicted ^8B- neutrino flux is in good agreement with the observations (Kamiokande). In accordance with the general demonstration given in Section 2, both models contradict the Homestake data. As we already know from Section 2 the only way to avoid this confict in the framework of an astrophysical solution is to assume that one of the two experiments (or both) has the large systematic error. This point is clearly recognized by Shi and Schramm [41]. Dar and Shaviv [42] claim that the discrepancy of their model with the Homestake data is not significant, if one takes the Homestake data after 1986. But actually even in this case

their predicted flux (4.2 SNU) is 4.1σ higher than the the flux 2.78 ± 0.35 SNU measured for the same period [4]. For the case of the flux, averaged over 1970 - 1993, it is 6.6σ higher.

We conclude therefore that both low neutrino-flux models are in contradiction with the Homestake observations as they must be according to the general demonstration given in Sections 2 and 4.

The second neutrino problem, i.e. the deficit of ^7Be-neutrinos, is also present in the low-flux models. It can be seen from the comparison of the predicted ^7Be-neutrino flux ($3.9 \cdot 10^9$ $cm^{-2}s^{-1}$ and $4.30 \cdot 10^9$ $cm^{-2}s^{-1}$ for the SS and DS models, respectively) with the model-independent upper limits($2.4 \cdot 10^9$ $cm^{-2}s^{-1}(95\%CL)$ and $2.1 \cdot 10^9$ $cm^{-2}s^{-1}(95\%CL)$ according to refs. [25] and [26], respectively). The deficit of ^7Be-neutrinos is also reflected by too high prediction for the counting rate in the gallium experiments (114 SNU and 109 SNU for the SS and DS models, respectively).

Thus the models confirm the model-independent conclusions of the Sections 2 - 4:
(i) Boron-neutrino problem can be solved by the price of the small correlated changes of the input parameters.
(ii) The Homestake/Kamiokande conflict and the deficit of ^7Be neutrinos are not solved by these models, in accordance with the model-independent analysis.

6 MSW solution for the models with low ^8B-neutrino flux

Assuming the SSM for neutrino production, the MSW conversion describes well all solar neutrino experiments. Howevere, it seems plausible that SSM will be modified as described above, with the boron neutrino flux reduced.

Does MSW solution exist for such the models?

What are parameters of this solution (Δm^2 and $sin^2 2\theta$) for the models with low ^8B-neutrino flux?

The refs.[43] and [44] address these questions. Fig 2 (from ref.[44]) illustrates how the allowed regions in $\Delta m^2 - \sin^2 2\theta$-plot transform with variation of ^8B-neutrino flux.

The numbers in Fig.2 give the ratio ζ of ^8B neutrino flux to that in the SSM [5].

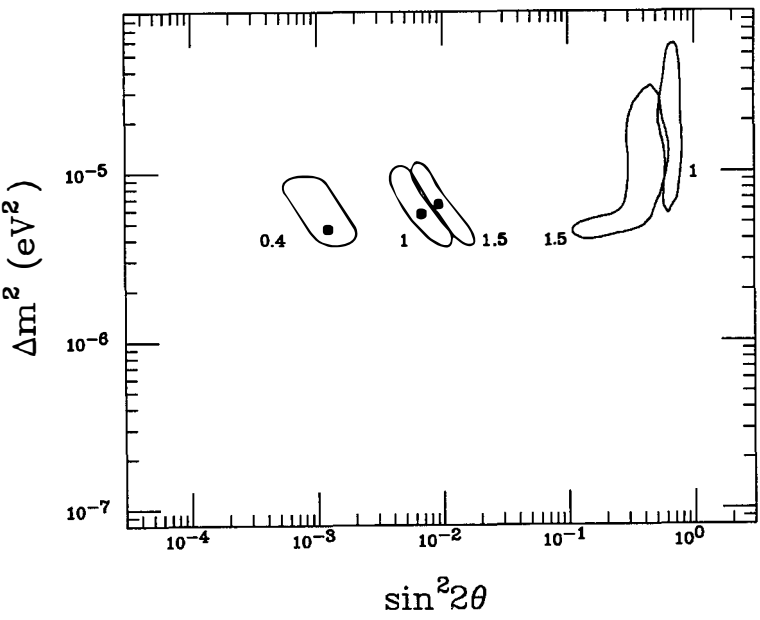


Fig.2 The $\Delta m^2 - \sin^2 2\theta$ plot for SSM [5] with the boron neutrino flux varied (from [44]).
The original boron neutrino flux in this model corresponds to the ratio $\zeta = 1$. The flux reduced by factor $\zeta = 0.4$ is marked in Fig.2 by number 0.4. The region marked by number 1.5 corresponds to the boron flux increased by factor $\zeta = 1.5$. The confidence regions are defined as $\chi^2 = 7.82$.

The following conclusions can be derived from this picture.

(i) MSW solution exists for a large range of ratios ζ.

(ii) The *small angle* MSW solution shifts to the smaller mixing angles when the boron-neutrino flux becomes smaller (ζ decreases).

(iii) Increasing the boron neutrino flux results in appearance of large allowed region for the *large-angle* MSW solution, while the decreasing results in disappearance of this solution.

(iv) Δm^2 remains practically unchanged with the variation of the boron neutrino flux.

These models can have rather pessimistic predictions for the nearest-future solar neu-

trino experiments, SNO and Superkamiokande. In the models with the small mixing angles, $sin^2 2\theta \leq 1 \cdot 10^{-3}$, the MSW conversion of ν_e-neutrinos occurs most effectively at energy $E_\nu < 5\ MeV$, i.e. below the threshold energy for SNO and Superkamiokande. Therefore, the distortion of the boron-neutrino spectrum, as well as anomalous NC/CC-ratio, are the small effects for these detectors.

7 Conclusions

The low p^7Be- cross-section and reduced core opacity (due to collective plasma effects) can diminish the flux of ^8B- neutrinos to the level of the Kamiokande observations. Thus, the 25 year-old problem of the ^8B- neutrino deficit can dissappear. Instead we face now the problem of low $\phi_\nu(Be)/\phi_\nu(B)$- ratio or Be- neutrino deficit. This problem is mainly created by the ratio of the Homestake to Kamiokande counting rates and is supported by the deficit of the ^7Be- neutrinos in the gallium experiments. If the Homestake and Kamiokande data are correct within the given statistical and systematic errors and if the $\nu_e + ^{37}Cl \rightarrow ^{37}Ar + e$- cross-section is not overestimated, a nuclear/astrophysical solution to the $\phi_\nu(Be)/\phi_\nu(B)$ problem is excluded. It means the existence of the *nonstandard* neutrino, i.e. with properties outside the SM of electroweak interactions.

If one belives that one of these experiments is wrong, we are still left with the conflict (though statistically less significant) between the gallium experiments and the remaining experiment. This comparison results in very small lower limit for ^7Be-neutrinos: $\phi_\nu(Be) < 2.6 \cdot 10^9\ cm^{-2}s^{-1}(95\%CL)$ [25] and $\phi_\nu(Be) < 2.1 \cdot 10^9\ cm^{-2}s^{-1}(95\%CL)$ [26]. These limits are to be compared with the SSM prediction $4.89 \cdot 10^9\ cm^{-2}s^{-1}$.

The deficit of the beryllium neutrinos looks now as the essence of the solar neutrino problem. SNO and Superkamiokande have too high energy threshold ($5\ MeV$) for detection of beryllium neutrinos. BOREXINO [29], recently approved at Gran Sasso, will detect the beryllium neutrinos even in the case of the full conversion of electron neutrinos into muon or tau neutrinos. This is possible due to NC scattering of these neutrinos off the electrons. From the future projects HELLAZ [45] is extremely efficient detector of ^7Be neutrinos. Like BOREXINO it will exploit νe-scattering. The signature of ^7Be-neutrinos in this project is their energy, which is supposed to be known due to precise measurements of the energy of the recoil electron and its scattering angle.

In conclusion, a nuclear/astrophysical solution to the Solar Neutrino Problem is strongly disfavored, while the MSW solution can explain the results of all four neutrino experiments, even if the prediction for ^8B neutrino flux is considerably changed.

8 Acknowledgements

I am very grateful to J.Bahcall, E.Bellotti, G.Fiorentini, M.Lissia, T.Kirsten, S.Mikheyev and A.Smirnov for very helpful discussions.
It is a great pleasure for me to thank Charling Tao and Tran Thanh Van for kind invitation to the Moriond meeting and for hospitslity.

References

[1] P.Anselman et al (GALLEX collaboration), Phys.Lett **327B**, 377 (1994)

[2] J.N.Abdurashitov et al (SAGE collaboration), Talk at 27th Int. Conf. on High Energy Physics, Glasgow 20-27 July 1994.

[3] K.Inoue, Talk at XXX Rencontres de Moriond, March 12-18, 1995.

[4] B.T.Cleveland et al (Homestake), Nuclear Phys.B (Proc.Suppl.) **39**, 47, 1995.

[5] J.N. Bahcall and M. Pinsonneault, Rev. Mod. Phys. **64**, 885, 1992.

[6] J.N. Bahcall and H.A. Bethe, Phys. Rev. Lett. **65**, 2233 1990.

[7] J.N. Bahcall, Neutrino Astrophysics, Cambridge Univ. Press, Cambridge, 1989.

[8] S. Turck-Chieze, W. Däppen, E. Fossat, J. Provost, E. Schatzmann and D. Vignaud, Phys. Rep. **230**, 57 ,1993.

[9] A.Kovetz and G.Shaviv Ap.J. **426**, 787, (1994).

[10] V.Castellani, S.Degl'Innocenti, F.Fiorentini, Astron. Astrophys. **271**, 601, 1993.

[11] S.Turck-Chiese and I.Lopes, Ap.J. **408**, 347 (1993).

[12] G.Berthomieu et al, Astron.Astroph.**268**, 775 (1993).

[13] D.B.Güinter et al, Ap.J. **387**, 372 (1992).

[14] J.Christiansen-Dalsgaard, Geophys. Astrophys. Fluid.Dyn. **62**, 123 (1992).

[15] B.Ahrens, M.Stix and M.Thorn, Astron.Astroph. **264**, 673 (1992)

[16] J.A.Guzik and A.N.Cox, Ap.J.Lett. **381**, 331 (1991).

[17] C.R.Proffitt and A.N.Cox, Ap.J.**380**, 238 (1991).

[18] I.J.Sackman, A.I.Boothroyd and W.A.Fowler, Ap.J.**360**, 727 (1990).

[19] Y.Lebreton and W.Däppen, *in* Seismology of the Sun and the Sun-like Stars (ed. V.Domingo and E.J.Rolfe), European Space Agency, Noordwijk, 1988.

[20] J.N.Bahcall, Phys.Rev.Lett. **71**, 2369 (1993).

[21] V. Tsytovich, in*"Solar Neutrino Problem"*, eds V.Berezinsky and E.Fiorini, vol.1,p.238, 1994.

[22] N.Hata, S.Bludman and P.Langacker, Phys.Rev.**D 49**, 3622, (1994).

[23] V.Berezinsky, Comm.Nucl.Part.Phys.**21**, 249, (1994).

[24] R.S.Raghavan, Preprint ATT Bell Labs, 11121-94086-38M, (1994).

[25] J.Bahcall, Phys.Lett **338 B**, 276, (1994).

[26] S.Degl'Innocenti, G.Fiorentini ans M.Lissia, Preprint INFNFE-10-94,(1994)

[27] V.Castellani et al, Phys. Rev.D **50**,4749, (1994).

[28] W.Kwong and S.P.Rosen, Phys.Rev.Lett **73**, 369, (1994)

[29] C.Arpesella et al, "Borexino at Gran Sasso"(Proposal), ed. by G.Bellini and R.Raghavan, INFN, Univ.of Milan, 1991;
E.Bellotti, Nucl.Phys. B (Proc. Suppl)**38**, 90, (1995).

[30] T.Kirsten, Invited talk at 17th TEXAS Symposium on Relativistic Astrophysics, Munich, 1994, to be published in Ann. N.Y. Academy of Sciences (1995),

[31] T.Kirsten, Invited talk at Int. Conf. "Neutrino-95", Nucl.Phys.B(Proc.Suppl) **38**, 68, (1995).

[32] W.Hampel, Talk at Int. Symp. "Nuclei in Cosmos", Gran Sasso, 1994 (to be published in the Proceedings).

[33] V.Berezinsky, Int. Workshop "Neutrino Telescopes" ed. M.Baldo Ceolin, Venice, Febr. 22-24 1994, p.239, (1994).

[34] S.P.Mikheyev and A.Yu.Smirnov, Yadern. Fiz., **42**, 1441, (1985);
L.Wolfenstein, Phys.Rev. **D17**, 2369, (1978).

[35] B.Pontecorvo, Zh.Eksp.Theor.Fiz. **33**, 549, (1953).

[36] P.I.Krastev and S.T.Petcov, Preprint SISSA 4/94/EP.

[37] E.Kh.Akhmedov, Phys.Lett.**213B**, 64, (1988);
C.S.Lim and W.Marciano, Phys.Rev.**D37**, 1368, (1988).

[38] S.P.Mikheyev and A.Yu.Smirnov, Proc. of Weak and Electromagnetic Interactions in Nuclei (Heidelberg 1986), ed. H.V.Klapdor, 710, (1987),
M.Guzzo, A.Masiero and S.T.Petcov, Phys.Lett. **260 B**, 154, (1991);
E.Roulet, Phys.Rev. **D 44**, R935, (1991).

[39] T.J.Bowles and V.N.Gavrin, Annu.Rev.Nucl.Part.Sci. **43**, 117, (1993).

[40] T.Motobayashi et al, Phys.Rev.Lett.**73**, 2680, (1994)

[41] X.Shi and D.N.Schramm, Part World **3**, 149, (1993)
D.N.Schramm and X.Shi, Nucl.Phys. B (Proc.Suppl.) **35**, 321, (1994)
X.Shi, D.N.Schramm and D.S.Dearborn, Phys.Rev. D**50**, 2414, (1994)

[42] A.Dar and G.Shaviv, Preprint Technion, Ph-94-5, (1994)
G.Shaviv Nucl.Phys. B (Proc.Suppl.) **38**, 81, (1995).

[43] P.I.Krastev and A.Yu.Smirnov, Phys.Lett.**338 B**, 282, (1994).

[44] V.Berezinsky, G.Fiorentini, M.Lissia, Phys.Lett. **341 B**, 38, (1994).

[45] T.Ypsilantis et al Preprint LPC-92-31
G.Bonvicini, Nucl.Phys.B (Proc.Suppl.) **35**, 438, 1994.



THE RUSSIAN-AMERICAN GALLIUM SOLAR NEUTRINO EXPERIMENT

S.R. Elliott [1], J.N. Abdurashitov[2], T.J. Bowles[3], M.L. Cherry[4], B.T. Cleveland[5], T. Daily[5], R Davis, Jr.[5], V.N. Gavrin[2], V.V. Gorbatschev[2], A.O. Gusev[2], A.V. Kalikhov[2],N.G. Khairnasov[2], T.V. Knodel[2], V.N. Kornoukhov[2], K. Lande[5], C.K. Lee[5], I.N. Mirmov[2], J.S. Nico[3], A.M. Pshukov[2], A.M Shalagin[2], A.A. Shikhin[2], W.A. Teasdale[3], E.P. Veretenkin[2], V.M. Vermul[2], D.L. Wark[3,*], P.W. Wildenhain[5], J.F. Wilkerson[1], and G.T. Zatsepin[2]

[1]University of Washington, Seattle, WA 98195 USA
[2]Institute for Nuclear Research, Russian Academy of Sciences, Moscow 1173122, Russia
[3]Los Alamos National Laboratory, Los Alamos, NM 87545 USA
[4]Louisiana State University, Baton Rouge, LA 70803 USA
[5]University of Pennsylvania, Philadelphia, PA 19104 USA

presented by S. R. Elliott

The Russian-American Gallium solar neutrino Experiment (SAGE) is described. The solar neutrino flux measured by 31 extractions through October, 1993 is presented. The result of $69 \pm 10^{+5}_{-7}$ SNU is to be compared with a standard solar model prediction of 132 SNU. The status of a ^{51}Cr neutrino source irradiation to test the overall operation of the experiment is also presented.

Introduction

The solar neutrino problem (SNP) has persisted for nearly 30 years. However its character has changed significantly. Originally the problem was defined by a discrepancy between an absolute capture rate measurement and an absolute capture rate calculation; i.e. the Cl experiment result of 2.55 ± 0.25 SNU[1] differed from the standard solar model (SSM) calculations of 8.0 ± 1.0 SNU[2] and 6.4 ± 1.4 SNU[3] (where 1 SNU = 10^{-36} interactions/atom/sec). A large number of astrophysical and particle physics solutions were proposed to resolve this discrepancy[4]. Recently, however, results from the Kamiokande[5], SAGE[6], and GALLEX[7] collaborations have significantly influenced the interpretation of the SNP solution.

Thus, at the present time we have four experiments, three of which have different energy thresholds, and therefore each experiment has different sensitivity to the various components of the solar neutrino flux. The Kamiokande experiment is predominantly sensitive to the high-energy ^{8}B neutrinos. The Cl experiment also detects ^{8}B but in addition ^{7}Be neutrinos. Finally, the gallium experiments are sensitive to all three major solar neutrino components: ^{8}B, ^{7}Be, and the low energy pp neutrinos. As a consequence, the problem can be analyzed in a nearly model-independent way that requires minimal input from the SSM. Using only neutrino spectral shapes and neutrino-target cross sections as input assumptions, the experimental signals can be expressed as linear combinations of the three neutrino type fluxes with only small corrections for the minor neutrino components. Solving these expressions for the fluxes, results in a very small ^{7}Be neutrino flux although the ^{8}B neutrino flux is appreciable. Since the stellar formation of ^{8}B requires the presence of ^{7}Be, this result is a contradiction which forms the basis for a more modern statement of the SNP. It is a contradiction which is difficult to resolve without invoking non-standard-model particle physics as discussed by several authors[8,9,10,11,12]. This manuscript describes the status of the Russian-American Gallium Experiment.

SAGE Operation

SAGE is a radiochemical experiment based on the inverse beta decay reaction on ^{71}Ga. The low energy threshold of this reaction (233 keV) provides sensitivity to pp neutrinos. The laboratory is in a deep underground cavity (4800 m.w.e.) at the Baksan Neutrino Observatory in the Caucusus Mountains in southern Russia. Data acquisition began in 1989 with backgrounds reduced sufficiently to provide sensitivity to solar neutrinos by early 1990. A second phase of the experiment (SAGE II) began in September 1992 after a number of improvements.

The experiment presently uses 55 tons of gallium contained in 8 chemical reactors. At the beginning of an exposure to solar neutrinos, approximately 700 μgm of natural Ge

in the form of a Ge-Ga alloy is added to the Ga in roughly equal parts to each reactor. At the end of the exposure, typically 30 days, the Ge carrier and any ^{71}Ge produced by solar neutrinos are chemically extracted. From the extractant, the gas germane (GeH_4) is synthesized, mixed with Xe in a 20%:80% ratio, and used to fill a 0.75-cm^3 cylindrical proportional counter. The extraction and synthesis chemistry have been described previously[6].

^{71}Ge decays via electron capture and is detected in the proportional counter by the Auger electrons or X rays produced during the electron shell relaxation. Not only do the ^{71}Ge events possess a characteristic energy (10.4-keV K peak, 1.2-keV L peak) but their pointlike ionization produces a fast risetime in contrast to the extended ionization of common background processes. Thus the energy and risetime of each event is measured providing a strong signal/background ratio improvement. The ^{71}Ge candidate events, selected by risetime and energy, are then analyzed using a maximum likelihood procedure[13] assuming an exponential decay superimposed on a constant-rate background.

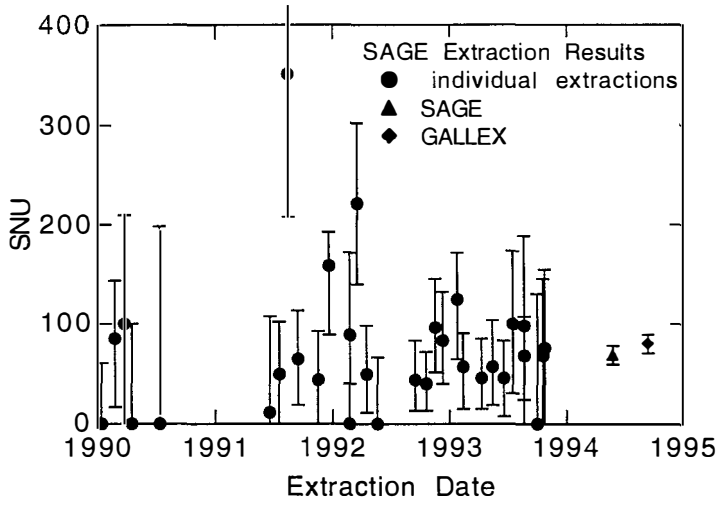


Figure 1: The individual extraction results. Also shown are the combined fits of the SAGE and GALLEX data[7].

The Data

Data taken up to May 1992 is referred to as SAGE I and is discussed in detail in Ref. [6]. SAGE II began in September 1992 and data analyzed similarly to SAGE I including

extractions through October 1993 are presented in Table 1. Improvements in the electronic noise and ambient radioactivity significantly reduced the background and hence the K-peak-candidate count rate in SAGE II (0.036 cpd) is much lower than SAGE I (0.103 cpd). Results from 31 extractions from SAGE I and II are shown graphically in Fig. 1. A combined fit to all data, requiring that the signal be the same for each extraction but allowing the background to be different, yields a result of $69 \pm 10^{+5}_{-7}$ SNU. (Here the former uncertainty is due to statistics and the latter is due to systematic effects.) This result is derived holding the ^{71}Ge half-life constant. If this parameter is allowed to float, the best fit gives 12 ± 3 days in good agreement with the known half-life of 11.43 days. Fig. 2a shows the energy distribution of the fast events for SAGE II for times early in counting when ^{71}Ge should be present. Fig. 2b displays a similar spectrum but for events occuring at long times when the ^{71}Ge has all decayed away. The K and L peaks are clear in Fig. 2a and are missing in Fig. 2b just as one expects.

We have considered a number of systematic uncertainties to this result which were summarized for the SAGE I data in Ref. [6]. We take those values as the preliminary estimates of the corresponding values for SAGE II.

Table 1: The summary of the individual run results. The exposure date is the Ge-71 half-life weighted average of the exposure period (See Ref. [4] pg 316).

exposure date	mass Ga	best fit SNU	68% CL SNU
1992.696	55.600 t	43	12-83
1992.786	55.482 t	39	12-71
1992.868	55.377 t	96	50-145
1992.942	55.263 t	83	40-132
1993.067	55.136 t	125	65-172
1993.112	55.026 t	56	14-80
1993.277	48.220 t	46	15-85
1993.363	48.171 t	57	19-104
1993.454	54.656 t	45	8-83
1993.536	40.441 t	101	30-174
1993.630	40.358 t	69	25-109
1993.628	14.090 t	99	0-190
1993.746	14.055 t	0	0-130
1993.797	14.100 t	69	0-147
1993.809	14.021 t	76	0-155

The ^{51}Cr Experiment

During the winter of 1994-1995, a number of extractions were done on a sample of Ga which contained a neutrino source at its center. To make the source, 513 gms of Cr metal enriched to 92% in ^{50}Cr, were irradiated in the fall of 1994 at the fast breeder reactor BN-350 in Kazakhstan. The activated Cr was then contained within a tungsten cylinder

and installed in a chemical reactor containing 13 tons of Ga. Normally, the reactors used for storing the Ga during solar neutrinos exposures have a large stirring mechanism used during the extractions. The reactor used for the ^{51}Cr runs had its stirring mechanism removed to permit room for additional Ga. At the end of each exposure, the Ga was transferred from this special reactor to two normal reactors which contained stirring mechanisms where the extraction chemistry could be performed. Prior to the ^{51}Cr experiment, several solar neutrino runs were made with gallium in this special reactor and no difficulties were observed.

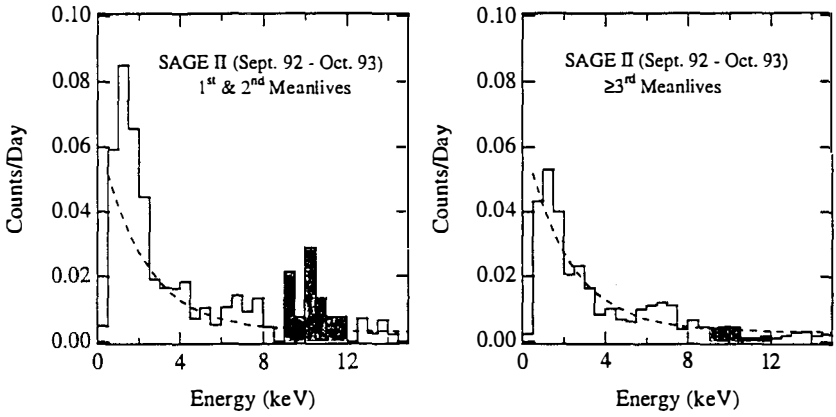


Figure 2: The energy spectrum of the SAGE II data. The left (right) figure shows the spectrum at early (late) times. The shaded areas indicate the K-peak region.

On December 26, 1994, the source was initially placed in the Ga test reactor. Preliminary estimates of the activity from calorimetry indicate a source strength of 510 kCi at that time. At this strength, the expected production rate in 13 tons of metallic Ga is 15 ^{71}Ge atoms per day compared to the 0.3 ^{71}Ge atoms/day produced by solar neutrinos. The first 5 exposures had durations chosen to produce roughly equal signal rates (~15 counts in the K peak) and an additional 3 extractions with 1 month exposures were also done. The counting of the samples from these extractions will continue throughout the summer of 1995.

Summary

The results of the first 31 extractions from the SAGE experiment yields a result of $69 \pm 10^{+5}_{-7}$ SNU. This includes analysis of the ^{71}Ge K-peak-only data from SAGE I and SAGE II through October 1993. The solar neutrino data from SAGE II extends until January 1995 and a waveform analysis of the proportional counter signals from this data should provide sensitivity to the L peak. The ^{51}Cr experiment extractions are completed and will check the experimental operation.

Acknowledgments

The SAGE collaboration wishes to thank A. E. Chudakov, G. T. Garvey, M. A. Markov, V. A. Matveev, J. M. Moss, S. P. Rosen, V. A. Rubakov, and A. N. Tavkhelidze for their continued interest in out work and for stimulating discussions. We are also grateful to J. N. Bahcall, R. G. H. Robertson, A. Yu. Smirnov, and many members of the GALLEX collaboration for useful discussions. We acknowledge the support of the Russian Academy of Sciences, the Institute for Nuclear Research of the Russian Academy of Sciences, the Russian Ministry of Science and Technology, the Russian Foundation of Fundamental Research, the Division of Nuclear Physics of the Department of Energy, and the National Science Foundation.

References

* present address: Department of Particle and Nuclear Physics, Oxford University, Keble Road, Oxford OX1 3RH, UK.

1) B. T. Cleveland *et al.*, Nucl. Phys. (proceed. supl.) **B38**, 47 (1995).
2) J. N. Bahcall and M. H. Pinsonneault, Rev. Mod. Phys. **64**, 885 (1992).
3) S. Trck-Chieze and I. Lopes, Astrophys. J. **408**, 347 (1993).
4) J. N. Bahcall Neutrino Astrophysics (Cambridge U.P., Cambridge, 1989).
5) Y. Suzuki, Nucl. Phys. (proceed. supl.) **B38**, 54 (1995).
6) J. N. Abdurashitov *et al.*, Phys. Lett. **B328**, 234 (1994).
7) P. Anselmann *et al.*, Phys. Lett. **B327**, 377 (1994).
8) J. N. Bahcall, Phys. Lett. **B338**, 276 (1994).
9) V. Berezinsky, Comm. Nucl. Part. Phys. **21**, 249 (1994).
10) S. Parke, Phys. Rev. Lett. **74**, 839 (1995).
11) N. Hata, S. Bludman, and P. Langacker, Phys. Rev. **D49**, 3622 (1994).
12) V. Castellani et al., Phys. Rev. **D50**, 4749 (1994).
13) B. T. Cleveland, Nucl. Instrum. Methods **214**, 451 (1983).

RECENT RESULTS FROM THE GALLEX EXPERIMENT

Charling Tao
LPC Collège de France, Paris, France.
CEA, DAPNIA/SPP, CE Saclay, France.

Abstract

The GALLEX collaboration has performed an experiment with an intense neutrino source. The main features of this experiment are reported in this paper. The results establish that the GALLEX experiment has no unforeseen problem at the level 1.04 ± 0.12, (ratio of measured number of events to expected number of events) thus confirming a solar neutrino deficit in the gallium experiments.

The radiochemical GALLEX experiment is the first one to have detected the primary pp neutrinos [4] from the most abundant and best predicted of the solar neutrino branches. The results of GALLEX [1] show a deficit of solar neutrinos : $77.1\ ^{+9.6}_{-10.1}$ SNU, (combined 3 years of solar runs), compared to the standard solar model (SSM) predictions of 123 SNU [2] to 132 SNU [3], as in all other solar neutrino experiments [5, 6, 7].

Since the consequences of these results are crucial for particle and astrophysics, it is very important to place the trustworthiness of the experimental techniques beyond any reasonable doubt. The most straightforward check is to expose these experiments to neutrino sources with known activity levels and appropriate energy, under conditions nearly identical to those used in solar exposures . GALLEX has performed the first experiment of this kind and its preliminary results are reported here with details to be found in [8] and references therein.

1 Fabrication of the ^{51}Cr source.

^{51}Cr is produced by neutron capture on ^{50}Cr ; its half-life is 27.706 ± 0.007 days [8]. ^{51}Cr decays by electron capture with a Q-value of 751 keV to the ground state of ^{51}V (90 14 %

branching ratio [8]) and to the first excited state (9.86 ± 0.05 %), which deexcites to the ground state with emission of a 320 keV γ ray. Aside from the low intensity internal bremsstrahlung, the neutrino spectrum consists of four monoenergetic lines (746keV (81 %), 751 keV (9 %), 426 keV (9 %) and 431 keV (1 %)).

Natural chromium consists of 4 stable isotopes. The low natural abundance of ^{50}Cr (4.35 %) along with the high cross-section of ^{53}Cr makes it technically impossible to reach with natural chromium, the activity level, $\approx$ 50 PBq required for a neutrino source experiment. The Kurchatov Institute in Moscow could provide us with chromium, enriched in ^{50}Cr (about 40 %) and depleted in ^{53}Cr (about 1 %) in the form of solid chromium trioxide, CrO_3 , 40 kg were delivered to Saclay between 1992 and 1994. Severe specifications were asked and met for possible impurities in the enriched chromium, of the order of ppm for Na, La, Sc, Sb, Co, Ag, Th, As, Tb and of ppb for Ga, Fe, Zn, Cd, Br, Te and U.

Since CrO_3 is thermally unstable, it is unacceptable as a target for irradiation in a nuclear reactor. We have transformed it into metallic chromium by electrolysis and broken the metal into irregular chips of $\approx 1\,mm^3$ volume, outgassed under vacuum to remove the large quantities of hydrogen that had been absorbed during electrolysis, so that $\approx$36 kg of product could be placed in the nuclear reactor.

Siloé, located at the "Centre d'études nucléaires de Grenoble" (France) and operated by CEA (Commissariat à l'énergie atomique), is a swimming pool reactor, with 35 MW thermal power. The dedicated core for the chromium irradiation was specially built and arranged in a checker-board configuration for our purpose.

The chromium chips were placed in 12 special irradiator containers that were constructed of zircalloy so as to be as transparent to neutrons as possible; two irradiator containers were placed in each of the six crenels. The chromium was exposed to an average perturbed neutron flux of 5.2×10^{13} n/(cm^2.s), with large variations around this mean value that depended on the positions of the irradiator containers in the reactor. The irradiation started at 10 am on May 27, 1994, and lasted without any interruption to end-of-bombardment (EOB = t_0), June 20 at 6 am.

The irradiated material was unloaded in a hot cell at Siloé. The chromium chips were then placed in a sealed stainless-steel container and inserted into a tungsten shield (8.5 cm wall thickness) for biological protection. Very sensitive measurements showed that the external dose at any position on the surface of the tungsten shield was less than 7 μSv/h [9], well below the maximum 200 μSv/h-level allowed by the safety authorities. Gamma-ray spectroscopy outside the shield showed activation of impurities in the chromium of Na, Sc, Cu, As, Ag, and Sb at levels that are orders of magnitude lower than specified [9].

2 Measurement of the source activity.

The amount of irradiated chromium composing the neutrino source within the tungsten shield was 35530 ± 10 g. The activity of this source was determined by three fully independent methods, as described below.

a) The ionization chamber technique. 31 samples were taken in the hot cell to be measured after careful mixing of the contents of each irradiator. The activity of each very active sample (about 2 TBq/g) was measured via the 320 keV γ ray, using an ionization chamber which was calibrated with a standard ^{51}Cr source [10]. As cross checks, some of these samples were totally dissolved, diluted, and aliquots taken, which were then assayed by gamma-ray spectroscopy, using Ge crystals calibrated with other absolute ^{51}Cr standard sources. The results of these different absolute γ-ray measurements are consistent.

The variance of the 31 individual results is consistent with the assumption that the total of all these samples is representative of the full 35.53 kg of chromium. The average specific activity of the 31 metal samples is 1.71 ± 0.04 TBq/g [10] and, consequently, the total activity of the source is 60.8 ± 1.4 PBq at EOB.

b) Calorimetry. The calorimetric method has the advantage that, since it measures the activity of the total source, it does not depend on our ability to take representative samples. Immediately after insertion of the source into the tungsten shield, the total thermal power of the source was determined by placing the source-plus-shield configuration in a thermally shielded vacuum vessel and measuring the rate of the ensuing temperature increase. By comparing the measured rate with that in similar measurements where known amounts of thermal power were supplied by a resistance heater to 35.5 kg of chromium metal, we deduce a source power of 385 ± 13 W at EOB. The mean energy release of ^{51}Cr is known to be 36.51 ± 0.16 keV per decay [8], emitted in the form of 320 keV γ-rays (9.86 % abundance), X-rays, and Auger electrons. Due to the very low rate of impurities in the chromium, the amount of energy deposited in the calorimeter by these contaminants is negligible. Thus we deduce that the source neutrino activity is 65.9 ± 3.0 PBq at EOB [11].

c) Neutronics and gamma-scanning. The knowledge of the neutron flux and of the relevant capture cross-section for producing ^{51}Cr provides another method for evaluating the final activity of the source. The relative energy spectrum of the neutrons, as a function of the position in the median plane of the reactor, is found by numerically solving the neutron transport equation for the Siloé configuration described in [12]. An on-line neutron measurement in one crenel gives the overall normalization. The axial neutron-flux distribution is deduced from the activity measured in the irradiator containers, as a function of the height above the median plane. The value of the source activity deduced from these neutron measurements is 64.4 ± 5.2 PBq at EOB [12].

Gamma-ray scanning of the 320 keV γ ray, measured in half of the irradiators in the reactor pool, yields the total source activity in a more or less independent way : the result is 64.0 ± 5.2 PBq at EOB [12].

d) Mean value of the ^{51}Cr source activity. The agreement between the results of the independent methods discussed above allows us to take a weighted average of their values. The resulting mean activity of the ^{51}Cr source at EOB in Siloé is $A_0(t_0) = 61.9 \pm 1.2$ PBq (1.67 ± 0.03 MCi), stated with a one-σ error.

3 The Source experiment.

For the transport between Grenoble and Gran Sasso, the source inside its sealed tungsten shield was placed in a special certified container used for transport of radioactive material.

The total time from EOB to the introduction of the source into the reentrant tube in the GALLEX target tank at Gran Sasso was 3.69 days, equivalent to an 8.8 % decrease of activity.

To avoid any heat transfer from the source to the gallium solution, which could change the kinetics of the germanium desorption [8], a copper thermal shield, cooled with tap water (60 l/h), was placed between the source and the wall of the reentrant tube. The ^{51}Cr neutrino source was inserted in its final position, in the A-tank, on June 23, 1994 at 10:36 pm. It was removed on October 10 at 2 pm and returned to Grenoble.

The experimental conditions were kept exactly as in the solar runs, except that the collection of the ^{71}Ge produced by the decaying ^{51}Cr was optimized by doing shorter exposures. That is, the duration of each source exposure was selected so that about the same number of ^{71}Ge atoms was desorbed in each run; in particular, the first desorption was done 3.35 days after the

insertion of the source, while the last 5 exposures each lasted about 2 weeks. Data taking, counting procedures in these runs and the ^{71}Ge data analysis were performed exactly as for our solar runs [1, 4].

However, the maximum likelihood fit to the time sequence of counter events of a given exposure has been modified to depend on three terms : a_{Cr}, $a_{\odot}$ and b. a_{Cr} characterizes the production of ^{71}Ge by the source (which decays with the ^{51}Cr half-life) and is proportional to the activity $\bar{A}_0$ at EOB, now treated as an unknown that is determined from the fit. $a_{\odot}$ characterizes the production of ^{71}Ge by the Sun and by side reactions [4], and is treated as a constant input term; this production rate (0.78 ± 0.11 ^{71}Ge atoms per day) is taken from solar exposures [1]. b is the constant background during the counting. Only a_{Cr} and b are fitted.

The standard counting period in GALLEX of 6 months per run but the present results have a requirement of a 3-month minimum counting period per run and only the first 7 runs were included in this analysis.

The energy spectra of the events within the rise-time windows give clear L and K-peaks with a decay time well fitted by the known 11.43-day half-life of ^{71}Ge and a constant background. (If the half-life is treated as a free parameter, the result is $T_{1/2} = 12.4 \pm 1.5$ days.) The number of observed events attributed to the ^{71}Ge in these runs is 154, with 138 events attributed to neutrinos from the ^{51}Cr source and 16 to neutrinos from the Sun.

Figure 1 presents the time dependence of these results during the course of the source experiment. The results for each run are plotted at the time that the exposure to the source neutrinos began. The horizontal lines show the duration of each exposure. The fitted half-life of the ^{51}Cr obtained with the maximum likelihood method from these ^{71}Ge data is 24.4 ± 7.1 days. The curve in figure 1 is the number of ^{71}Ge atoms produced per day predicted from the measured A_0 value of the source, 61.9 PBq, assuming the known half-life of ^{51}Cr plus the known 0.78 ^{71}Ge atoms per day produced by solar neutrinos and side reactions.

From the global analysis of the first 7 source exposures, we deduce a mean initial source strength $\bar{A}_0 = 64.1 \pm 6.6$ (statistical) $\pm$ 3.3 (systematic), i.e. 64.1 ± 7.4 after adding quadratically the statistical and systematic error. This value is to be compared with the directly measured ^{51}Cr source strength, $A_0 = 61.9 \pm 1.2$ PBq. The ratio of these values is $R = 1.04 \pm 0.12$, where the quoted error includes the experimental errors in ^{71}Ge counting and in the source activity determinations, but does not include errors in the neutrino-absorption cross-sections.

4 Conclusions

The 40 % deficit of the solar neutrino flux observed by GALLEX, as compared to the SSM prediction, cannot be attributed to experimental artifacts. In fact, this source experiment directly demonstrates the validity of the basic principles of the radiochemical methods used in our solar neutrino detector : that on the order of ten radioactive atoms produced by neutrino capture can be removed from tons of target material, purified and counted quantitatively. No unknown systematic effects take place at a level ≥ 10 %. Because of the similarity of the neutrino energy spectra from ^{51}Cr and from the solar ^{7}Be branch, this experimental result also means that GALLEX is able to detect ^{7}Be neutrinos with close to full efficiency.

After the ^{51}Cr source was removed from the GALLEX target, solar neutrino exposures recommenced on October 12, 1994. Another source experiment is planned in the autumn of 1995 to get statistical errors at the level of 4 years of GALLEX solar neutrinos.

Acknowledgements. It is a pleasure to thank all members of the GALLEX collaboration for

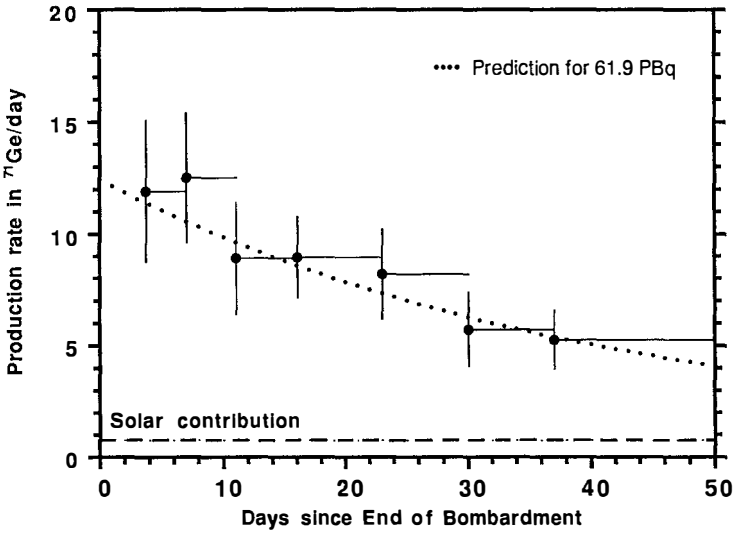


Figure 1: *Number of ^{71}Ge atoms produced per day during the course of the source experiment (first 7 runs only). The points for each run are plotted at the beginning of each exposure, with the horizontal lines showing the duration of the exposures. The predicted curve (dotted line), which decreases with the known half-life of ^{51}Cr, is based on the relationship between the directly measured source strength and the 0.189 ^{71}Ge production rate per day. The curve also includes the constant 0.78/day production rate due to solar neutrinos and side reactions (dashed line).*

their contributions. My Saclay colleagues, M. Cribier, J. Rich, M. Spiro and D. Vignaud have offered me throughout these years support, friendship and stimulating discussions for which I am most grateful.

References

[1] GALLEX Collaboration, P. Anselmann et al., Phys. Lett.(1995) to appear soon.
GALLEX Collaboration, P. Anselmann et al., Phys. Lett. B327 (1994) 377

[2] S. Turck-Chièze and I. Lopes, Ap. J. 408 (1993) 347

[3] J. N. Bahcall and M. H. Pinsonneault, Rev. Mod. Phys. 64 (1992) 885

[4] GALLEX Collaboration, P. Anselmann et al., Phys. Lett. B285 (1992) 376, Phys. Lett. B314 (1993) 445

[5] R. Davis, Prog. Part. Nucl. Phys. 32 (1994) 13

[6] K. S. Hirata et al., Phys. Rev. D44 (1991) 2241, Y. Suzuki, Nucl. Phys. B (Proc. Suppl.) 35 (1994) 407

[7] J. N. Abdurashitov et al., Phys. Lett. B328 (1994) 234

[8] P. Anselmann et al., Phys. Lett. B342 (1995) 440.

[9] E. Bellotti et al., "Measurements of the gamma and neutron activity outside the GALLEX neutrino source", GALLEX internal note GX-63, to be submitted to Nucl. Instr. and Methods [1]

[10] M. Cribier and J. Gorry, "Measurements of the ^{51}Cr source activity with the ionization chamber technique", GALLEX internal note GX-64, November 1994 [1]

[11] Saclay group, "Calorimetric measurements of the ^{51}Cr source activity", GALLEX internal note GX-58, October 1994 [1]

[12] A. Bevilacqua, "Production de la source de chrome de GALLEX et détermination de l'activité", GALLEX internal note GX-59, September 1994 [1]

[1] GALLEX internal notes are available on request by email at gallexcoord@vaxgs.lngs.infn.it.

DISCOVERY PHYSICS AT THE LARGE HADRON COLLIDER

Nick Ellis
PPE Division, CERN, Geneva, Switzerland

Abstract

The Large Hadron Collider (LHC) has recently been approved as the next major particle accelerator for CERN, the European organisation for particle physics research. LHC will collider counter-rotating, high-intensity beams of protons, with a centre-of-mass energy available for producing new kinds of particles an order of magnitude higher than at today's highest-energy machine, and with three orders of magnitude higher interaction rate. LHC will also be used to produce ultra-high energy collisions between pairs of lead ions and, at a later stage, between electrons and protons. This paper, presented in a joint session with astrophysicists, briefly describes the LHC machine and the particle detectors that will be used with it, before discussing some examples of physics studies that will be performed. Emphasis will be placed on topics that relate to cosmology: Searches for Higgs bosons, searches for Supersymmetric particles and CP violation.

The Large Hadron Collider (LHC)

LHC will produce ultra-high-energy collisions between counter-rotating beams of particles. It will collide beams of protons at a centre-of-mass energy $\sqrt{s}$ = 14 TeV, compared to 1.8 TeV at today's highest energy machine, the "Tevatron" proton–antiproton collider at Fermilab in the USA. The LHC luminosity (interaction rate for a process of a given cross-section) will be much higher than at the Tevatron, $L \approx 10^{34}$ cm^{-2}s^{-1} compared to $L \approx 10^{31}$ cm^{-2}s^{-1}. Roughly speaking, the high energy allows one to produce new, heavy particles, while the high luminosity gives access to rare (i.e. low cross-section) processes. LHC will also collide beams of lead ions with a centre-of-mass energy $\sqrt{s}$ = 6 TeV per nucleon.

LHC will use existing CERN infrastructure — the 27-km circumference LEP tunnel which will accommodate the new accelerator and the present accelerator complex which will be used as an injector (i.e. will accelerate the particles up to high energy before they are transferred into the LHC and accelerated to ultra-high energy). At a later stage, the presence of the existing electron–positron collider (LEP) and LHC in the same tunnel will make possible very-high-energy electron–proton collisions.

The LHC Machine

The use of the existing CERN infrastructure brings about a dramatic cost saving compared to creating a totally new facility. However, the need to fit within the existing 27-km circumference LEP tunnel is a significant constraint. To reach the desired ultra-high beam energies, very powerful dipole magnets are required to guide the particle beams in circular orbits. The solution that has been adopted uses 9 Tesla, twin-aperture dipole magnets (opposite polarity is required for guiding the counter-rotating beams). The machine will contain about 1300 of these dipole magnets, each 13 m long.

A very significant effort has been undertaken to develop the large superconducting magnets. The superconducting coils will be cooled to 1.9 K using superfluid helium. Prototype magnets already exist and have been tested up to the nominal field strength.

In December 1994, the LHC project was approved by the CERN council. The start of physics is scheduled for 2004. Depending on the level on contributions to the project from states that are not members of CERN, full energy may not be achieved until 2007 (if no such contributions are received).

The LHC Detectors

There will be several detectors for LHC — two general purpose experiments called ATLAS and CMS, a heavy-ion experiment called ALICE, and a number of smaller

experiments optimised for more specific studies. An example of a specialised experiment is LHC-B which will study B-physics (i.e. study particles containing bottom-quarks).

General-purpose experiments

Technical proposals for the two general-purpose experiments were presented in December 1994 [1, 2]. In fact, the word "experiment" is misleading — "laboratory" or "facility" might be more appropriate. Each of ATLAS and CMS will be built, operated and exploited by a team of ≈1500 scientists and engineers. Each "experiment" will carry out a very broad programme of physics — the work will be divided between a large number of analysis groups studying different aspects of the data.

The experiments will have to deal with very challenging experimental conditions [3]. The total interaction rate between pairs of protons will be ~10^9 Hz, with each interaction producing on average about 30 charged particles in the region covered by the detectors. The high interaction rate and the complex final states require novel detectors with short response times and fine segmentation. With very large numbers of sensor channels sampled at very high rate (typically 40 MHz due to the bunch structure of the accelerator), very sophisticated data-collection and data-selection systems are needed.

ATLAS and CMS will be built from a number of components that measure different aspects of the final state of the interaction. Working out from the interaction point, one performs measurements as follows: The momenta of charged particles are determined by measuring the particle trajectories in a solenoidal magnetic field (the radius of curvature is inversely proportional to momentum). The energies of particles that interact via the electromagnetic interaction (electrons and photons, where the latter may come from $\pi^0 \rightarrow \gamma\gamma$ decays) are then measured in "electromagnetic" calorimeters. Much of the energy from hadrons (particles that interact via the strong interaction such as protons, neutrons, and $\pi^{\pm}$ and $K^{\pm}$ mesons) is not contained in the electromagnetic calorimeters, but is measured in "hadronic" calorimeters. The calorimeters represent very effective shielding, absorbing almost all the particles. However, high-momentum muons escape and their trajectories are measured beyond the calorimetry.

Of course, neutrinos and possibly other weakly interacting particles escape without detection. However, one may infer their presence and estimate their energies from the resulting momentum imbalance.

Heavy-ion experiment

Although the ALICE detector is similar to ATLAS and CMS at the level of the above discussion, the experimental challenges are somewhat different. For Pb–Pb collisions the beams will be much less intense and the interaction rate, ≈3000 Hz, will be much lower than in the proton–proton case. However, each head-on collision between lead ions will produce a very large number of particles (~2000–8000). Because of the low interaction rate, detectors with a relatively slow response time can be used. This allows one to adopt solutions optimised to handle the complexity of the final state.

Overview of LHC Physics

Before discussing some examples of physics studies that one will perform at LHC, it is perhaps worth recalling the principal features of the Standard Model of particle physics (SM) [4] and its weaknesses. This will demonstrate the fundamental importance of some of the studies that are to be performed at LHC.

According to the SM, the basic constituents of matter are the spin-1/2 fundamental fermions, the quarks which come in six flavours (up, down; charm, strange; top, bottom) and the leptons (electron, electron-neutrino; muon, muon-neutrino; tau, tau-neutrino). The forces between these particles (excluding gravity which is not significant at the particle level) are mediated by spin-1 gauge bosons: the photon (electromagnetic interaction), the W and Z bosons (weak interaction), and the gluons (strong interaction). Different kinds of charges are associated with the different gauge bosons: electric charge for the photon, weak isospin and hypercharge for the W and Z, and colour for the gluons. All of the above particles are known to exist. Ordinary matter is composed of these constituents — for example, the proton and neutron are bound three-quark states.

The SM treats the electromagnetic and weak interactions as different aspects of the same "electro-weak" force — the "weak" force only appears to be relatively weak at low energies because the W and Z bosons are massive (~ 90 GeV) whereas the photon is massless — if one were to perform experiments at sufficiently high energies, the force strengths would be similar.

A critical ingredient of the SM is the way in which the particle masses are generated. Early attempts to introduce explicit mass terms failed because such theories could not be renormalized and lacked predictive power. The solution (due to work by Glashow, Weinberg and Salam, and by 't Hooft), the so-called Higgs mechanism, was to introduce a scalar (i.e. spin-0) field that has a non-zero vacuum expectation value and which interacts with the other particles. The mass of a given particle depends on how it couples to the scalar field. The SM has made remarkably accurate predictions that

have subsequently been checked through precision measurements, for example at LEP.

A consequence of the way in which particle masses are introduced in the SM is the presence of one or more spin-0 particles called Higgs bosons. In the Minimal Standard Model (MSM), there is a single, electrically neutral Higgs boson. However, many scenarios for extensions to the SM, for example Supersymmetry (see below), require several Higgs particles some of which are charged.

The Higgs mechanism is absolutely essential to the SM and it is of paramount importance to test its validity experimentally by searching for the predicted Higgs bosons. The Higgs is not just another particle — if it exists, it is a completely new object playing a unique role in nature and responsible for particle masses. Furthermore, Higgs fields associated with physics at very high energy scales would be of cosmological importance. While scalar fields could be responsible for inflation [5], no fundamental scalar particle has yet been observed.

The SM has excellent predictive power and is self consistent. However, it has a number of weaknesses (apart from the fact that the Higgs boson has not yet been seen). There are strong reasons for believing that the SM is incomplete — many parameters have to be derived from experiment, notably all the fermion masses and the parameters that describe flavour mixing and CP violation in the weak interaction which are related to the couplings of fermions to the Higgs field.

We don't understand why there are three generations of particles (e.g. electron, muon and tau) and we don't really understand CP violation (i.e. asymmetries between the behaviour of matter and antimatter particles). These two issues may be coupled: existing measurements of CP violation can be parametrized in the SM through the matrix that describes the weak-interaction eigenstates in terms of the quark-mass eigenstates. Future studies of CP violation, in particular those related to bottom quarks that can be performed at LHC, will test this parametrization and may provide clues to a deeper underlying origin of CP violation. It is worth noting that CP violation is one of the essential ingredients for baryogenesis (A. D. Sakharov, 1967) — the observed universe is composed of matter rather than antimatter.

Motivated by the success of unifying the electromagnetic and weak forces and other considerations, many physicists are considering Grand Unified Theories (GUTs) in which the strong force is also "unified". Extrapolations of the coupling constants from low-energy measurements to the GUTs energy scale appear to be more consistent with unification in the case of Supersymmetric (SUSY) models than in the MSM. SUSY is a symmetry between bosons and fermions — for each normal particle there is a SUSY partner with the same quantum numbers, but with different

spin: The quarks and leptons have spin-0 partners, whereas the photon, W, Z and gluons have spin-1/2 counterparts. It is often assumed that there is a conserved quantum number called R-parity associated with SUSY; in this case the lightest SUSY particle is stable and is a dark-matter candidate.

Independent of any theoretical prejudices, experimenters should clearly search for new spin-1 particles associated with new forces, for compositeness (substructure within quarks for example), for leptoquarks and other exotica, and, of course, for unexpected phenomena.

In addition to the searches for new particles and new phenomena described above, many measurements can be made relating to the known particles. These include studies of the top quark (mass measurement and searches for rare decay modes), the bottom-quark (study of CP violation and flavour oscillations, and searches for rare decays) and more general studies of particle production.

A final aspect of LHC physics that should be mentioned relates to heavy-ion collisions in which very high energy densities will be achieved. It is thought that under these conditions a phase transition will occur, producing a new state of matter — the quark–gluon plasma. In normal matter the quarks and gluons appear in tightly bound states (e.g. protons and neutrons); in the quark–gluon plasma, the quarks and gluons would behave as free particles. Hence, the LHC heavy-ion programme will study strong-interaction thermodynamics at extreme energy densities. Such conditions would have occurred in the early universe (at times ~ 10^{-5} s).

Some Examples of Physics Studies

In the following, some examples of physics studies that will be performed at LHC are briefly described. Much more detail can be found in the ATLAS and CMS Technical Proposals [1, 2].

Higgs Boson Searches

As stated above, in the MSM there is just one Higgs boson which is neutral. Its mass is poorly constrained, but for a given mass the production and decay properties are predicted. For relatively small masses ($m_H < 700$ GeV), the dominant production process is from gluon–gluon fusion via a top-quark loop; for higher masses W and Z fusion become important. Higgs bosons may also be produced in association with W and Z bosons — the cross-section is relatively small, but the additional signature of a W or Z gives relatively less background.

The most promising decay modes in which to search for the SM Higgs depend on the mass. In the mass range 80–150 GeV, the decay $H \rightarrow \gamma\gamma$ is promising. By using photons, one can avoid hadronic backgrounds (the photon does not "feel" the strong

interaction). Photons have the experimental advantages that they can be cleanly identified and their energy and direction can be measured with precision. In the mass range under consideration, the Higgs has a small (~ MeV) natural width (i.e. it has a relatively long lifetime).

In principle the measurement is very simple: One selects events with two high-energy photons and one plots the number of events as a function of the invariant mass of the photon pair. A signal will then appear as a peak with a width determined by the detector resolution. However, there are large backgrounds — the cross-section for producing jet pairs is much larger than that for jet–photon pairs which is in turn much larger than that for photon pairs. (Jets are the manifestation of quarks or gluons which "hadronize" and are observed as a collection of approximately collinear particles). One therefore needs a detector with excellent performance for distinguishing photons from jets (a jet-rejection factor of more than 1000 is needed, with high photon efficiency).

Having eliminated the jet-related backgrounds, the rate of $H \rightarrow \gamma\gamma$ production is still small compared to other sources of photon pairs. Hence, one is looking for a small signal on top of a large background. Although the Higgs search in the $H \rightarrow \gamma\gamma$ channel will not be easy, detailed studies by ATLAS and CMS show that it is possible and that each experiment would be able to make a statistically significant measurement after a single year of data collection at the design luminosity of LHC. For example, for a mass of 120 GeV, ATLAS would expect to see a six-standard-deviation effect.

For Higgs masses above about 120 GeV, $H \rightarrow ZZ^*$ decays may be seen (the "star" indicates that one of the Z bosons is virtual), where the Z and Z* decay to electron or muon pairs. Note that for $m_H > 2\, m_W$, decays into vector boson pairs dominate. The two-Z final state gives a very clean experimental signature — the electrons and muons are identified with little background from misidentified hadrons, and their momenta can be measured with precision. The dominant background is from continuum ZZ^* and $Z\gamma^*$ production, but this becomes small (about 10%) for $m_H > 2\, m_Z$. For masses between about 120 GeV and 600 GeV, ATLAS and CMS would each expect to observe a very significant signal after a single year of running at design luminosity.

ATLAS and CMS have performed detailed studies to establish the feasibility of discovering the Higgs bosons in theories beyond the SM — typically these theories have several Higgs bosons some of which are charged and some of which are neutral. A particularly interesting case is the Minimal Supersymmetric Standard Model. Here it has been shown that, by considering a variety of decay modes of the different

Higgs particles, one would be able to detect at least one Higgs decay channel for almost any choice of the free parameters of the theory.

Supersymmetry (SUSY)

As mentioned above, in SUSY one expects a complete spectrum of partners for all the normal particles. The SUSY partners of the quarks and gluons — so called squarks and gluinos — carry colour charge and are produced with large cross-sections at LHC (via the strong interaction). The key to discovering SUSY is missing transverse energy combined with large numbers of leptons and/or jets produced in cascade decays of heavy SUSY particles — assuming R-parity conservation the lightest SUSY particle (LSP) is non-interacting and behaves like a neutrino from the point of view of the experiment; as mentioned above, the LSP is a dark-matter candidate. Studies have shown that ATLAS and CMS will be sensitive to squarks and gluinos with masses up to at least 1–2 TeV.

CP violation

The violation of CP symmetry means that antimatter particles behave differently from their matter counterparts. It is one of the essential ingredients for baryogenesis as mentioned above — it is probably required to explain why the universe in which we live is made of only of matter (and not antimatter). Up to now, the only evidence for CP violation in particle physics has come from precision studies of the neutral kaon system.

In the SM, CP violation can be parametrized as a phase angle in the matrix that expresses the eigenstates of the weak interaction in terms of the quark-mass eigenstates. Based on this parametrization, one expects to see CP-violation effects also in the neutral-B systems B_d^0 (quark content $\bar{b}d$) and B_s^0 (quark content $\bar{b}s$). One will check if the measurements are consistent with the SM. If they are, one will measure the relevant parameters of the model. If not, one may have a handle on new physics.

As an example, consider the decay $B_d^0 \to J/\psi\, K_S^0$. The J/ψ is a $c\bar{c}$ bound state, and, assuming CP symmetry, the K_S^0 is the CP-even combination of $\bar{s}d$ and $\bar{d}s$, so that the final state does not carry any flavour quantum number or charge. Any difference in the decay rate of B_d^0 and its antiparticle $\bar{B}_d^0$ to this final state is therefore direct evidence for CP violation in the bottom-quark system.

At LHC, $b\bar{b}$ pairs are produced via the strong interaction which respects bottom-flavour conservation. Experimentally, one will determine whether a B_d^0 or $\bar{B}_d^0$ was produced by looking at the decay of the second bottom-quark in the event. For example, one can use the charge-sign of the muon from a semileptonic decay of the

bottom quark: $pp \rightarrow b\bar{b}$; $b \rightarrow B^- \rightarrow \mu^- \nu X$; $\bar{b} \rightarrow B_d^0 \rightarrow J/\psi\, K_S^0$. CP violation would be seen as an asymmetry in the observed rate between μ^- and μ^+ "tags".

Similar studies will be made using the decays $B_d^0 \rightarrow \pi^+\pi^-$ and $B_s^0 \rightarrow J/\psi\phi$, where only a very small asymmetry is expected in the SM in the latter case, making it an interesting channel in which to search for non-SM sources of CP violation. B_s^0 mesons will not be produced at e^+e^- "B-factories" operating with a centre-of-mass energy at the $\Upsilon(4S)$ mass, but will be copiously produced at LHC.

Conclusions

The LHC presents great challenges and opportunities. The challenges include performing a broad range of precision measurements under the difficult experimental conditions of a hadron collider, constructing detector systems of unprecedented size and complexity, and building an accelerator with a novel design of superconducting magnet cooled with superfluid helium. In this short paper it has been possible to indicate only a few of the opportunities that exist for new physics studies. One will be able to perform investigations of fundamental importance such as trying to understand the origin of mass, searching for entirely new types of particle, new forces and a new phase of matter (the quark–gluon plasma), and studying CP violation in the bottom-quark sector. The possibility of Pb–Pb and electron–proton, as well as proton–proton collisions, makes for a very broad physics programme.

As briefly discussed above, many detailed studies have already been made of a wide variety of physics processes that may occur at LHC. However, with an order of magnitude higher energy and a thousand times higher luminosity than at today's most powerful machine, the LHC will explore new territory — one should also be ready for surprises.

Acknowledgements

I would like to thank my colleagues in the LHC collaborations for their help in preparing this talk, in particular Daniel Froidevaux and Peter Jenni. I would like to thank Belen Gavela for helpful discussions and for her comments on this manuscript. I would also like to thank the organisers and my fellow participants, both from the particle-physics and astrophysics communities, for the very pleasant atmosphere at the conference.

References

[1] ATLAS Technical Proposal, CERN/LHCC/94–43.

[2] CMS Technical Proposal, CERN/LHCC/94–38.

[3] See for example, N. Ellis and T.S. Virdee, Annu. Rev. Nucl. Part. Sci., 44 (1994) 609–653.

[4] See for example, F. Halzen and A. D. Martin, Quarks and Leptons, Wiley, 1984.

[5] A.D. Dolgov, M.V. Sazhin and Ya. B. Zeldovich, Basics of Modern Cosmology, Editions Frontières, Gif-sur-Yvette, France, 1990.

SOLAR NEUTRINOS AND LEPTON MIXING

A. Yu. Smirnov
International Centre for Theoretical Physics, I-34100, Trieste, Italy and
Institute for Nuclear Research, RAS, 107 370 Moscow, Russia

ABSTRACT

With latest experimental data the solar neutrino problem enters new phase when crucial aspects of the problem can be formulated in the (solar) model independent way. Original neutrino fluxes can be considered as free parameters to be found from the solar neutrino experiments. Resonance flavour conversion gives the best fit of all experimental results. Already existing data allow to constraint both neutrino parameters and original neutrino fluxes. The reconciliation of the solution of the solar neutrino problem with other neutrino mass hints (atmospheric neutrino problem, hot dark matter etc.) may require the existence of new very light fermion. Supersymmetry can provide a framework within which the desired properties of such a light fermion follow naturally. The existence of the fermion can be related to axion physics, mechanism of μ-term generation etc..

1. Introduction.

There are three phases in understanding of the solar neutrino problem:

1. *Theory without experiment.* The problem was predicted by B. Pontecorvo: Even before the first Homestake results he suggested that neutrino oscillations can influence the solar neutrino fluxes, diminishing the detected signals.

2. *Theory and Experiment.* During more than 20 years we had one experiment and one model. Namely, Davis's experiment and Bahcall's predictions of neutrino fluxes in the Standard Solar Model (SSM). The problem was formulated as the smallness of the Homestake signal in comparison with Bahcall's prediction.

3. *Experiment without theory.* Results (now rather precise) from Homestake[1], Kamiokande[2], SAGE[3] and GALLEX[4] experiments as well as calibration of Kamiokande and recent GALLEX experiment with ^{51}Cr source allow one to formulate the problem in almost solar model independent way.

There is some hope that forthcoming experiments SuperKamiokande and SNO will resolve the problem (at least establish, finally, whether the astrophysics or neutrino properties are responsible for the observable deficit) without referring to the predictions of the specific solar models.

In this paper we summarize essential points of this third phase and consider some implications of the data to the lepton mixing.

2. Solar Neutrino Problem without Solar Neutrino Model.

In spite of serious progress in the solar modeling and very good agreement of SSM and helioseismological data, the predicted solar neutrino fluxes still have rather large uncertainties. Mainly, they are related to the nuclear cross-sections (first of all, for the reaction $p + ^7 Be \to ^8 B + \gamma$) and probably to some plasma effects which have not yet been properly taken into account. These uncertainties will hardly be fixed before new experiments on solar neutrinos start to operate. In this connection it is instructive to use as much as possible model independent approach to the problem, and try to resolve it using solar neutrino data only. Main points of the approach are the following[5-18].

1. Only general notion is used about the solar neutrinos: the composition, the energy spectra of components, but not the absolute values of fluxes. These absolute values are considered as *free parameters to be found from the solar neutrino experiments.* In particular, the boron neutrino flux can be written as

$$\Phi_B = f_B \cdot \Phi_B^{SSM}, \tag{1}$$

where f_B is free parameter, and Φ_B^{SSM} is the flux in the reference SSM[19]. Similarly, parameters f_i $(i = Be, pp, NO)$ for other important fluxes can be introduced.

2. One confronts the data from different experiments immediately.

3. The normalization of the solar neutrino flux is used which follows from the solar luminosity

at the condition of thermal equilibrium of the Sun.

In fact, present experimental situation makes the analysis of data to be very simple. There are two key point in this analysis.

Kamiokande versus Homestake[5-16]. Boron neutrino flux measured by Kamiokande gives the contribution to Ar-production rate $Q^B_{Ar} = 3.00 \pm 0.45$ SNU [1] which exceeds the total signal observed by Homestake: $Q^B_{Ar} = 2.55 \pm 0.25$ SNU. This means that the contributions of all other fluxes to Q_{Ar}, and in particular, of the Beryllium neutrinos should be strongly suppressed.

Gallium Experiment Results versus Solar Luminosity[7,20,17]. The luminosity of the Sun allows one to estimate the pp- neutrino flux and consequently its contribution to Ge-production rate: $Q^{pp}_{Ge} \approx 71$ SNU. This value plus small (~ 5 SNU) contribution of boron neutrinos coincide within 1σ with total signal observed by GALLEX and SAGE. Consequently, gallium results can be reproduced if the beryllium neutrino flux as well as all other fluxes of the intermediate energies are strongly suppressed.

Thus both these points indicate on strong suppression of the ^{7}Be- neutrino line. Statistical analysis gives $f_{Be} < 0.4$ (2σ) (for more detail see[13,14,15]).

It follows from the above consideration that the data fix uniquely values of fluxes which give the *best fit*[17]:

1. Boron neutrino flux should be $\approx 0.4\Phi^{SSM}_B$.
2. Beryllium neutrino flux as well as other fluxes of the intermediate energies (pep, N, O) give negligible contributions to the signals.
3. There is little or no suppression of the pp-flux.

Moreover, to reproduce central values of signals one should suggest that there is an additional flux which contributes to the Kamiokande signal, $\Delta\Phi_B \approx 0.09\Phi^{SSM}_B$, but does not contribute to the Ar-production rate. Any deviation from this picture gives worser fit. Thus the energy dependence of the suppression factor $P(E)$ can be represented as

$$P(E) \sim \begin{cases} 0.9 - 1 & E < 0.5 \text{ MeV} \\ \sim 0 & E \sim 0.7 - 1.5 \text{ MeV} \\ 0.4 - 1 & E > 7 \text{ MeV} . \end{cases} \qquad (2)$$

Large uncertainty of the suppression in high energy region is related to the uncertainty in the original boron neutrino flux. Kamiokande admits a mild distortion of the recoil electron spectrum.

Evidently the astrophysics can not reproduce such a picture[5,6,8-15]. Typically one gets more strong suppression of the boron neutrino flux than the beryllium neutrino flux.

[1] In this estimation it was suggested that the contribution to the Kamiokande follows from the electron neutrinos only.

3. Neutrino parameters and neutrino fluxes

There are several recent studies of the particle physics solutions of the solar neutrino problem for unfixed values of original fluxes[16,17,18,21,22].

Long length vacuum oscillations can reasonably reproduce the desired suppression factor. For $\Delta m^2 > 7 \cdot 10^{-11}$ eV^2 the pp-neutrino flux is in the region of averaged oscillations, where $P = 1 - 0.5 \sin^2 2\theta$, the Beryllium neutrinos are in the fastly oscillating region of the $P(E)$ (so that one expects an appreciable time variations of the Be-neutrino flux due to annual change of distance between the Sun and the Earth). Boron neutrinos are in the first (high energy) minimum of $P(E)$. This allows one to reach the inequality $P_{pp} > P_B > B_{Be}$ implied by (2). However, there is an obvious relation between maximal suppression of the Be-line and the suppression of pp-neutrinos: $P_{Be,min} = 2P_{pp} - 1$, and due to this the best fit configuration (2) can not be realized.

With diminishing f_B the needed suppression of B-neutrino flux due to the oscillations becomes weaker. Therefore for fixed values of Δm^2 the allowed regions of parameters shift to smaller $\sin^2 2\theta$ [21,22]. In particular, for $f_B = 0.7$, the region is at $\sin^2 2\theta < 0.7$ thus satisfying the potential bound from SN87A[23]. For $f_B \sim 0.4$ the mixing can be as small as $\sin^2 2\theta < 0.5 - 0.6$. Moreover, for $f_B = 0.5$ the allowed region appears at $\Delta m^2 \sim 5 \cdot 10^{-12}$ eV^2 which corresponds to a position of the Be-neutrino line in the first high energy minimum of P. Depending on neutrino parameters and f_B, f_{Be} ... one can get a variety of distortions of the boron neutrino energy spectrum.

Being excluded at $f_B = 1$, the oscillations into sterile neutrino are allowed for $f_B < 0.7$[22].

Resonance flavour conversion can precisely reproduce the desired energy dependence of the suppression factor (2). In the region of small mixing angles:

$$P_{pp} \sim 1, \quad P_{Be} \sim 0, \quad P_B \sim exp(-E_{na}/E), \tag{3}$$

where $E_{na} \equiv \Delta m^2 l_n \sin^2 2\theta$ An additional contribution to Kamiokande $\Delta f \approx 0.09$ follows from scattering of the converted ν_μ (ν_τ) on electrons due to the neutral currents. As the result: $R_{\nu e} \sim f_B[P_B + 1/6(1 - P_B)]$. With diminishing f_B the desired suppression due to conversion relaxes, and therefore $\sin^2 2\theta$ decreases according to (3)[17,18]. At $\Delta m^2 = 6 \cdot 10^{-6}$ eV^2 the best fit of the data for flavour mixing corresponds to[17]

f_B	0.4	0.5	0.75	1.0	1.5	2.0
$\sin^2 2\theta$	$1.0 \cdot 10^{-3}$	$1.8 \cdot 10^{-3}$	$4.3 \cdot 10^{-3}$	$6.2 \cdot 10^{-3}$	$9 \cdot 10^{-3}$	10^{-2}

(4)

(For $f_B \sim 0.38$ the best fit is at $\Delta m^2 = 4 \cdot 10^{-6}$ eV^2). The decrease of f_{Be} gives an additional shift of the allowed region to smaller values of $\sin^2 2\theta$. A consistent description of the data has been found for[17]

$$f_B \sim 0.4 - 2.0.$$

(see (4) and table in (5)). For unfixed values of the original fluxes, f_B, f_{Be} ..., the allowed region of neutrino parameters is controlled immediately by Gallium data and by the "double

ratio"[17]. Namely, the mass squared difference

$$\Delta m^2 = (6 \pm 2) \cdot 10^{-6} \mathrm{eV}^2, \tag{5}$$

is restricted essentially by results from Gallium experiments which imply that the adiabatic edge of the suppression pit is in between the end point of the pp-neutrino spectrum and the Be-line. This bound does not depend on mixing angle in a wide region of θ. (For sterile neutrinos the bound is approximately the same). For fixed Δm^2 the mixing $\sin^2 2\theta$ is determined by the "double ratio"

$$R_{H/K} \equiv \frac{R_{Ar}}{R_{\nu_e}},$$

where $R_{Ar} \equiv Q_{Ar}^{obs}/Q_{Ar}^{SSM}$ and $R_{\nu_e} \equiv \Phi_B^{obs}/\Phi_B^{SSM}$ are the suppressions of signals in Cl–Ar and Kamiokande experiments, respectively. Here Q_{Ar}^{SSM}, Φ_B^{SSM} are the predictions in the reference model[19] and Q_{Ar}^{obs}, Φ_B^{obs} are the observable signals. The ratio $R_{H/K}$ depends very weakly on the solar model. It has however different behaviour for the conversion into active and into sterile neutrinos. For $\Delta m^2 = 6 \cdot 10^{-6}$ eV^2 we get

$\sin^2 2\theta$	$2 \cdot 10^{-3}$	$5 \cdot 10^{-3}$	10^{-2}	$2 \cdot 10^{-2}$
$R_{H/K}^a$	0.75	0.64	0.56	0.21
$R_{H/K}^s$	0.77	0.74	0.72	0.69 .

(6)

The experimental value is $R_{H/K} = 0.65 \pm 0.11$. In the case of active neutrinos $R_{H/K}$ drops quickly when $\sin^2 2\theta$ becomes larger than 10^{-2}. The reason is that the Kamiokande signal is dominated by NC scattering of ν_μ and ν_τ and $R_{\nu e} \to 1/6$, whereas R_{Ar} is strongly suppressed. Central value of $R_{H/K}$ can be achieved at $\sin^2 2\theta = 5 \cdot 10^{-6}$ and $f_B \approx 1.1$.

In the case of conversion into sterile neutrinos there is no NC effect for ν_s and the suppression of both Homestake and Kamiokande signals strengthen with θ increase simultaneously. As the result one has weak dependence of $R_{H/K}^s$ on mixing angle. However, for large $\sin^2 2\theta_{es}$ the original flux of Boron neutrinos should be large (to compensate for a strong suppression effect). If we restrict $\Phi_B \leq 1.5 \Phi_B^{SSM}$, then the bound on the mixing angle becomes: $\sin^2 2\theta_{es} < 1.5 \cdot 10^{-2}$.

For very small mixing solution: $f_B \sim 0.5$, $\sin^2 2\theta_{es} \sim 10^{-3}$, all the effects of conversion in the high energy part of the boron neutrino spectrum ($E > 5-6$ MeV) become very weak. In particular, the distortion of the energy spectrum disappears, and the ratio $(CC/NC)^{exp}/(CC/NC)^{th}$ approaches 1. Thus studying just this part of spectrum it will be difficult to identify the solution (e.g., to distinguish the conversion and the astrophysical effects).

Recent calculations in SSM with diffusion of heavy elements give larger boron neutrino flux[24], so that even with 25% decrease of nuclear cross-section and 2% decrease of central temperature of the Sun one still needs an appreciable conversion effect. This gives a hope that the problem can be resolved by SuperKamiokande/SNO experiments.

With increase of f_B the fit of the data in the large mixing domain becomes better[17]. Here the Kamiokande signal can be explained essentially by NC effect and the mixing can be relatively small. Be- neutrinos are sufficiently suppressed and suppression of the pp-neutrinos is rather weak. For $f_B = 2$ the values $\sin^2 2\theta = 0.2 - 0.3$ become allowed. The corresponding

mass squared difference is $\Delta m^2 = 6 \cdot 10^{-6} - 10^{-4}$ eV^2.

4. Lepton mixing: pattern, implications

Let us consider possible implications of the solar neutrino data to the lepton mixing. The scale of masses

$$m_2 = (2-3) \cdot 10^{-3}\text{eV} \tag{7}$$

needed for solar neutrinos can be obtained by the see-saw mechanism with the mass of the RH neutrino component in the intermediate range: $M \sim 10^{11}$ GeV. The common observation is that M_R can be related to the scale of the Peccei-Quinn symmetry breaking or to SUSY breaking in the hidden sector etc.. The desired mixing is consistent with the following relation

$$\theta_{e\mu} = \sqrt{\frac{m_e}{m_\mu}} - e^{i\phi}\theta_\nu, \tag{8}$$

where θ_ν comes from diagonalization of neutrino mass matrix. The relation (8) may follow from Fritzsch ansatz in the context of the see-saw mechanism. There are however two cautions. In many models the angle θ_ν is very small, and from (8) one finds $\sin^2 2\theta_{e\mu} \approx 4(m_e/m_\mu) \approx 2 \cdot 10^{-2}$ which is too large (see table in (6)). For very small mixing solution, $\sin^2 2\theta_{e\mu} \sim 10^{-3}$, one needs strong cancellation of contributions in (8).

Is the solution of the solar neutrino problem compatible with explanations of other neutrino anomalies like deficit of the atmospheric ν_μ- flux, possible signal of the $\bar{\nu}_\mu - \bar{\nu}_\tau$ oscillations, existence of the hot component of dark matter? Here the key words are the "pattern" and the "scenarios" of neutrino masses and mixing. Let us outline two possibilities.

1. Standard scenario of neutrino masses and mixing.

(i). Neutrino masses are generated by the see-saw mechanism with masses of the RH components $M_R = 10^{11} - 10^{12}$ GeV. This scale can originate from Grand Unification scale, M_{GU}, and the Planck scale, M_{Pl}, as $M_R \sim M_{GU}^2/M_{Pl}$.

(ii) Second mass, m_2, is in the range (7), so that the resonance flavour conversion $\nu_e \to \nu_\mu$ solves the solar neutrino problem.

(iii) The third neutrino (at $m^D \sim 50$ GeV and $M = 10^{12}$ GeV) has the mass about 5 eV. It composes the desired hot component of dark matter.

(iv) The decays of the RH neutrinos with mass 10^{12} GeV can produce the lepton asymmetry of the Universe which can be transformed in to the baryon asymmetry during the electroweak phase transition[25].

(v) Large Yukawa coupling of neutrino from the third generation, e.g. $Y_\nu \sim Y_{top}$, give appreciable renormalization effects in the region of momenta $M_R - M_{GU}$. The $b-\tau$ mass ratio increases by $(10-15)\%$ in the SUSY. In turn this disfavours the $b-\tau$ mass unification for low values of $\tan\beta$ [26,27].

(vi) Simplest schemes with quark - lepton symmetry lead to mixing angle for the e and τ generations: $\theta_{e\tau} \sim (0.3-3)V_{ub}$ which is close the bound from the nucleosynthesis of heavy elements (r-processes) in the inner part of the supernova: $\sin^2 2\theta_{e\tau} < 10^{-5}$ ($m_3 > 2$ eV)[28].
(vii) For $\mu - \tau$ mixings one expects [29] $\theta_{\mu\tau} \sim kV_{cb}\eta$, where $k = 1/3 - 3$ and $\eta \sim 1$ is the renormalization factor. For $m_3 > 3$ eV some part of expected region of mixing angles is already excluded by FNAL 531. Large part of the region can be studied by CHORUS and NOMAD. The rest (especially $m_3 < 2$ eV) will be covered by E 803.
(viii) The depth of $\bar{\nu}_\mu - \bar{\nu}_e$ oscillations with $\Delta m^2 \approx m_3$ turns out to be $4|U_{3\mu}|^2|U_{3e}|^2 \approx 4|\theta_{e\tau}|^2|\theta_{\mu\tau}|^2$. The existing experimental data give the bound on this depth: $< 10^{-3}$ [30] which is too small to explain the LSND result.

The standard scenario does not solve the atmospheric neutrino problem. One can sacrifice the HDM suggesting that some other particles are responsible for the structure formation in the Universe, or consider strongly degenerate neutrino spectrum which has a potential problem with neutrinoless double beta decay. In both cases no appreciable effects in KARMEN/LSND experiments are expected.

2. Neutrinos and light singlet fermion

More safed way to accommodate all the anomalies is to introduce one new neutrino state[31-37]. As follows from LEP bound on the number of neutrino species this state should be sterile (singlet of standard group). Taking into account also strong bound on parameters of oscillations into sterile neutrino from Primordial Nucleosynthesis one can write the following "scenario" [31-35]:

(i) Sterile neutrino has the mass $m_S \sim (2-3)\cdot 10^{-3}$ eV and mixes with ν_e, so that the resonance conversion $\nu_e - \nu_s$ solves the solar neutrino problem;
(ii)The masses of ν_μ and ν_τ are in the range 2 - 3 eV, they supply the desired hot component of the DM;
(iii) ν_μ and ν_τ form the pseudo Dirac neutrino with large (maximal) mixing and the oscillations $\nu_\mu - \nu_\tau$ explain the atmospheric neutrino problem;
(iv) ν_e is very light: $m_1 < 2\cdot 10^{-3}$ eV. The $\bar{\nu}_\mu - \bar{\nu}_e$ mixing can be strong enough to explain the LSND result.
(v) Production of heavy elements in supernova via "r-processes" is problematic for this scenario.

What is the origin of sterile neutrino? Of course, the RH neutrino components are natural candidates. However in this case the see-saw mechanism does not operate. Another possibility is that singlet fermion S exists beyond the standard see-saw structure[36]. Its appearance is motivated by some reasons not related to the neutrino physics. And moreover, this scalar can be family blind. The lightness of S is nontrivial since standard model symmetry does not protect S from acquiring the mass $m_s \gg m_W$.

We suggest[36] (see also[37]) that S mixes with active neutrinos via interactions with RH neutrino components only. So that in the basis (S, ν_e, N) the mass matrix has the following form

$$\mathcal{M} = \begin{pmatrix} 0 & 0 & m_{es} \\ 0 & 0 & m_e \\ m_{es} & m_e & M_e \end{pmatrix}. \tag{9}$$

Diagonalization gives one massless and one light state with mass $m_1 \simeq -(m_e^2 + m_{es}^2)/M_e$. The ν_e–S mixing angle is determined by $\tan\theta_{es} = m_e/m_{es}$. This mechanism allows one to generate simultaneously the mass and mixing without introduction of very small mass scale. Taking for m_e the typical Dirac mass of the first generation: $m_e \sim (1-5)$ MeV, and suggesting that $\nu_e \to S$ conversion explains the solar neutrino problem, we find $m_{es} = \frac{m_e}{\tan\theta_{es}} \simeq (0.02 - 0.3)$ GeV[36].

How the scale $0.1 - 1$ GeV appears in singlet sector? One possibility is the supersymmetry endowed by some spontaneously broken global symmetry, e.g. $U(1)_G$ in the simplest case. Spontaneous violation of $U(1)_G$ results in goldstone boson, and in the supersymmetric limit corresponding superpartner (fermion) is massless. Supersymmetry breaking parametrized by soft breaking terms leads in general to the S-mass which can be as big as $O(m_{3/2})$. That is the supersymmetry alone can not protect very small mass scales, and one needs some additional care to further suppress m_S.

One possibility is the based on R-symmetry ($G \equiv R$) spontaneously broken up to the R-parity[36]. The R-parity conservation requires for the fermion S to be a component of singlet superfield which has no VEV. This allows one to construct a simple model in which the properties (mass and mixing) of S follow from the conservation of R-symmetry. S is mixed with RH neutrinos by the interaction with additional singlet field y which can acquire VEV radiatively after soft SUSY breaking. The model can naturally incorporate the spontaneous violation of Peccei-Quinn symmetry or/and lepton number. The fields involved can spontaneously generate the μ-term. Approximate horizontal (family) $U(1)^h$ symmetry can provide simultaneous explanations for the predominant coupling of S to the first generation (thus satisfying the Nucleosynthesis bound) and for the pseudo-Dirac structure of ν_μ–ν_τ needed in solving the atmospheric neutrino and hot dark matter problem. Breaking of $U(1)^h$ can be arranged in such a way that the parameters of $\bar{\nu}_\mu \to \bar{\nu}_e$ oscillations are in the region of sensitivity of KARMEN and LSND experiments.

Conclusion

After top quark discovery the neutrinos are the only known fermions with unknown masses. There is some hope that things are comming to a head and in 2 - 3 years we will know the answer.

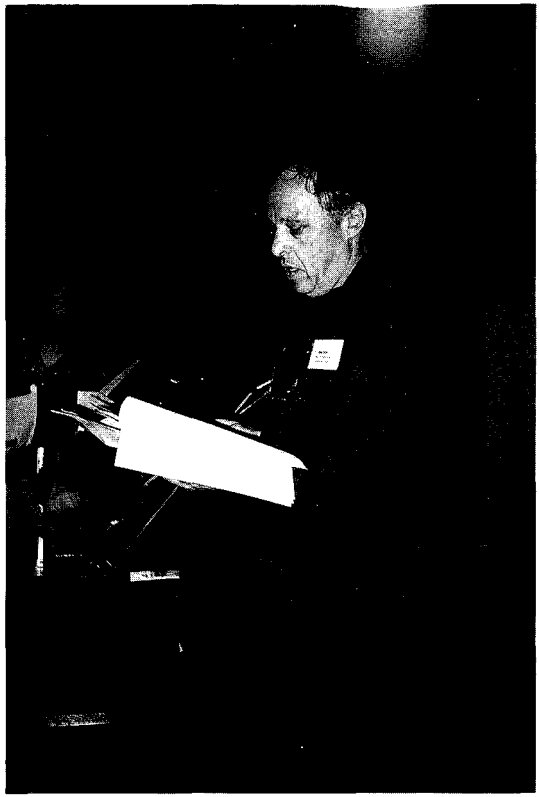
REFERENCES

1. K. Lande, Nucl. Phys. B38 (Proc. Suppl.) (1995) 47.
2. K. Inoe, these Proceedings.
3. S. Eliott, these Proceedings.

4. C. Tao, these Proceedings.
5. I. Barabanov, (1988) unpublished
6. J. N. Bahcall and H. A. Bethe, Phys. Rev. Lett., 65 (1990) 2233; Phys. Rev. D47 (1993) 1298.
7. M. Spiro and D. Vignaud, Phys. Lett. B 242 (1990) 279.
8. V. Castellani, S. Degl'Innocenti and G. Fiorentini, Phys. Lett. B 303 (1993) 68: Astron. Astroph. 271 (1993) 601.
9. H. Hata, S. Bludman and P. Langacker, Phys. Rev. D 49 (1994) 3622.
10. V. S. Berezinsky, Comm Nucl. Part. Phys. 21 (1994) 249.
11. A. Yu. Smirnov, Report DOE/ER/40561-136 -INT94-13-01.
12. W. Kwong and S. P. Rosen, Phys. Rev. Lett., 73 (1994) 369.
13. S. Parke, Phys. Rev. Lett. 74 (1995) 839.
14. S. Degl'Innocenti, G. Fiorentini and M. Lissia, Ferrara preprint INFNFE-10-94.
15. V. S. Berezinsky, these Proceedings.
16. N. Hata and P. Langacker, Phys. Rev. D 50 (1994) 632; Report UPR -0625T, hep-ph/9409372.
17. S. P. Krastev and A. Yu. Smirnov Phys. Lett. B 338 (1994) 282.
18. V. S. Berezinsky G. Fiorentini and M. Lissia, Phys. Lett., B 341 (1994) 38.
19. J. N. Bahcall and M. H. Pinsonneault, Rev. Mod. Phys. 60 (1989) 297.
20. A. Dar and G. Shaviv, Report Technion-Ph-94-5 (1994).
21. Z. G. Berezhiani and A. Rossi, Phys. Rev. D51 (1995) 5229.
22. P. I. Krastev and S. P. Petcov, report SISSA-9/95/EP.
23. A. Yu. Smirnov, D. N. Spergel and J. N. Bahcall, Phys. Rev. D49 (1994) 1389.
24. C. R. Proffitt, Astrophys. J. 425 (1994) 849; A. Kovetz, G. Shaviv, Astrophys. J. 426 (1994) 787; J. N. Bahcall and M. H. Pinsonneault, IASSNS-AST 95/24.
25. M. Fukugita and T. Yanagida, Phys. Lett., B174 (1986) 45.
26. F. Vissani and A. Yu. Smirnov, Phys. Lett., B 341 (1994) 173.
27. A. Brignole, H. Murayama and R. Rattazzi, Phys. Lett. B335 (1994) 345.
28. Y. -Z. Qian et al., Phys. Rev. Lett., 71 (1993) 1965.
29. S. Dimopoulos, L. J. Hall and S Raby, Phys. Rev. D47 (1993) R3697.
30. K. S. Babu, J.C. Pati and F. Wilczek, Preprint IASSNS-HEP 95/37.
31. D. O. Caldwell and R. N. Mohapatra, Phys. Rev. D48 (1993) 3259.
32. J. Peltoniemi and J. W. F. Valle, Nucl. Phys. B406 (1993) 409.
33. J. Peltoniemi, D. Tommasini, and J. W. F. Valle, Phys. Lett. B298 (1993) 383;
34. J. T. Peltoniemi, Mod. Phys. Lett. A8 (1993) 3593.
35. J. R. Primack, J. Holtzman, A. Klypin, and D. O. Caldwell, Phys. Rev. Lett. 74 (1995) 2160; and references therein.
36. E. J. Chun, A. S. Joshipura and A. Yu. Smirnov, IC/95/76, PRL-TH/95-7, hep-ph/9505275.
37. E. Ma and P. Roy, preprint UCRHEP-T145 (hep-ph/9504342).

SESSION VII

THE COSMIC MICROWAVE BACKGROUND RADIATION



RECENT RESULTS ON THE COSMIC MICROWAVE BACKGROUND

Joseph Silk
Departments of Astronomy and Physics, and Center for Particle Astrophysics
University of California, Berkeley, U.S.A.

Abstract

I review recent detections of angular anisotropies in the cosmic microwave background, including results on large and intermediate angular scales. Reconstruction of the primordial matter fluctuation power spectrum is the desired goal, and progress is being made: there already is overlap between CMB fluctuations and deep galaxy redshift surveys on scales of $\sim 100 - 300$Mpc. The mainstream model is that of inflationary cold dark matter with a slight twist (a 20% admixture of hot dark matter, introduction of a cosmological constant with $\Omega \approx 0.3$ in a flat universe, or even an inflationary open model), designed to account for the excess of large-scale power required by the deep surveys. A more bizarre possibility is discussed, notably that of an open baryon dark matter-dominated universe. Such a model leads to unique, and imminently testable, predictions.

1 Introduction

The past two years have seen a remarkable flurry of observations of temperature anisotropies in the cosmic microwave background. The angular scales of detections of possible intrinsic fluctuations range from those mapped by the COBE DMR all-sky experiment down to subdegree scales. There is still large uncertainty about systematic errors that include atmospheric galactic and extragalactic foregrounds as well as experimental noise. However the largest angular scale results appear to be relatively free of contamination, and present a reasonably unambiguous measurement of intrinsic fluctuations. The level of $\delta T/T$ on large angular scales translates directly to a value of the primordial density fluctuation amplitude at the epoch of last scattering of matter and radiation. Hence we finally have a normalization of the primordial density fluctuation spectrum.

This enables one, in the context of specific models for the primordial fluctuation power spectrum $P_{mat}(k)$, to make detailed predictions about large-scale structure in the present-day universe. At present, I shall argue in this talk, the models are still poorly constrained. There are several attractive cosmological models that are consistent with all of the data on both $\delta T/T$ and on large-scale structure, provided that one is willing to add parameters to the simplest models. The parameters are plausible, and eventually, as the observational data improves, should be directly measureable.

2 Constraints from the COBE DMR Results

The two-year DMR data, after galaxy subtraction, can be combined, using the two highest frequency channels and an optimal eigenmode analysis, to give the radiation power spectrum[1]. The temperature fluctuation signal is expanded in spherical harmonics, with coefficient a_{lm}, and averaged over azimuthal angle as appropriate for a statistically isotropic universe. The temperature correlation function is expanded as a Fourier power series, with coefficient

$$c_l \equiv \Sigma |a_{lm}|^2.$$

The contribution to the rms temperature fluctuations $(\delta T/T)^2_{rms}$ per logarithmic decade in l is $l(l+1)c_l$. Theoretical models specify a_{lm}, generally as a gaussian distribution. One therefore expects a "cosmic" variance in the c_l 's, given by a χ^2 distribution, with $2l+1$ degrees of freedom, corresponding to observations by a set of $2l+1$ independent observers. The observed data also has a cosmic variance, due to sampling independent patches of the sky. The first $10l$'s contain a cosmic signal[2]. For purely gravitational potential fluctuations described by $P_{mat}(k) \propto k^n$ this should correspond to $n = 1$. Forcing a power-law fit yields $n = 1 \pm$ with a normalization to the quadrupole coefficient of the c_l's, $Q_{rms} = 20\mu$ K.

No model in fact predicts a constant index power-law representation for the c_l's. The simplest scale invariant inflationary theory for $\Omega = 1$ cold dark matter has an index that is about 0.95 at low l but steepens to ~ 1.1 above the $l \approx 9$ pivot point for constant total power in the COBE data. The low quadrupole at the high $l = 3, 4$ points means that steep spectra, $n \approx 1.5$, fit about as well as CDM. The CDM model rises partly because there is not precise scale invariance, as progressively larger scales leave the horizon when the inflation potential is slowly rolling over, and partly because of the onset of the adiabatic oscillation/doppler scattering peak.

Attempts to fit inflationary ($\Omega = 1$) CDM may be summarized in terms of the amplitude $\sigma(M)$ of density fluctuations averaged over a sphere of radius $8h^{-1}Mpc$, conventionally defined as σ_8. One finds[3] that the canonical CDM model, with $h = 0.5, \Omega_B = 0.05$, and primordial ($n = 1$) scale-invariant fluctuations, requires $\sigma_8 = 1.4$. This produces an order of magnitude too many galaxy clusters.

If $\Omega = 1$, there are at least four possibilities for reducing σ_8 to a more acceptable value[4]. Lowering H_0 to 30 $\mathrm{km s^{-1} Mpc^{-1}}$ results in $\sigma_8 = 0.7$. Increasing the neutrino density by a factor of 3 has a similar effect, via the relevant quantity that determines the spectral shape, namely the ratio of horizon scale at the epoch of matter-radiation equality to a length scale given by the galaxy or cluster correlation length. This comparison determines the quantity $\Omega h\,(g_\star)^{-1/2}$. One can achieve an effective increase in the number of relativistic species $g_\star$ if, say, one of the two neutrino species had a mass of $\gtrsim 1$ keV and underwent early decay into light neutrinos. One can thereby add an admixture of about 20 percent of hot dark matter. Finally, one can tilt the primordial spectrum. Reducing n lowers σ_8. Addition of a tensor mode according to the generalized inflationary potential prescription $T/S = 7(1-n)$ means that only a modest

degree of tilt is required, to $n \approx 0.9$ in order to reduce σ_8 to 0.8. The corresponding 70 percent tensor contribution would primarily affect the largest angular scale anisotropies above $\sim 2°$. Fluctuations on smaller angular scales are redshifted away on scales below the horizon at last scattering, since they entered the horizon during radiation domination. By contrast, scalar fluctuations maintain their amplitudes on sub-last scattering horizon scales became of the self-gravity of the density fluctuations in the cold dark matter.

Once σ_8 is in the range $0.5 - 0.8$, one has to examine in detail large-scale structure observations on scales below $\sim 10 - 20\ h^{-1}$ Mpc to find a suitable discriminant[5]. Not all measures agree. For example, the void probability function is consistent with $\Omega = 1$. The galaxy and cluster correlation functions appear to require lower Ω_{CDM} if $h \gtrsim 0.5$. However one runs into the uncertain issues of galaxy and cluster selection, relative to the dark matter. These measurements depend on the uncertain ratio of mass-to-light (or degree of biasing) as a function of scale. Determinations of the matter power spectrum that are bias-dependent involve direct measurements of galaxy velocities.

Pairwise velocities of galaxies also favor a lower Ω_{CDM} on scales of $\lesssim 1\ h^{-1}$ Mpc, although one has now to confront objections of sample bias with respect to clusters and effects of extended halos. A more promising technique is the study of large-scale bulk flows, utilizing direct distance determinations via Tully-Fisher or fundamental plane correlations to infer galaxy peculiar velocities. The microwave background fluctuations on degree and subdegree scales offer a potentially promising means of directly measuring $P_{mat}(k)$.

3 Intermediate Angular Scale $\delta T/T$

The horizon scale at last scattering, approximately equal to $2\Omega^{1/2}[(1 + z_{LS})/1000]^{-1/2}$, demarcates the divide between large-scale, acausal inflationary fluctuations and smaller-scale causal fluctuations that dominate $\delta T/T$ at the last scattering epoch. If $\Omega < 1$, the gravitational potential fluctuations decay slowly, and the passage of CMB photons through time-varying potentials induces additional large angular scale fluctuations. Within the last scattering horizon, gravity acts to cause fluctuations to respond by inducing bulk motions. This causes Doppler fluctuations on degree scales. Even larger, however, are the rarefactions and compressions associated with fluctuations in the sound wave regime, that span scales up to that of the sound horizon at last scattering. The sound and light horizons are almost identical, since the sound velocity is close to c, approximately equal in fact to $[3(1 + z_{eq})/(1 + z_{LS})]^{-1/2}c$. On scales smaller than about 10 or 20 percent of the last scattering horizon, the oscillations are damped out by photon diffusion. The various effects add in quadrature to give the relic spectrum of $\delta T/T$ fluctuations.

Prior to recombination, subhorizon fluctuations oscillate like gigantic sound waves of scale up to the sound horizon scale. An inflationary origin requires fluctuations of a given comoving wavelength to have the same phase. At the epoch of last scattering, the first two or three adiabatic compression peaks leave an imprint on the CMB anisotropy[6]. Doppler peaks are 90 degrees out of phase with the adiabatic compression peak. Potentially detectable fluctuations consist of the first three peaks, the second being mostly Doppler in origin. Fluctuations at succcessively smaller wavelengths are smoothed by radiative diffusion.

Detection of the peaks requires sensitivity at a level of $10 - 20\mu$ K, feasible with the new generation of experiments. This interpretation of the peaks leads to an intuitive understanding of the variation in peak amplitude when parameters such as Ω_B, h and Ω are varied. For example, increasing Ω_B enhances the first and third peaks which amplify as a higher radiation density can be compressed. Since an increase in Ω_B actually decreases the sound speed, the second peak decreases as Ω_B is increased. Variation of h introduces a similar but opposite

scaling, since the controlling parameter is $\Omega_B h^2$. Variation of Ω has the most intriguing effect on the peaks: their location changes due to the curvature of space, thereby affecting the horizon-scale photon trajectories from the Ω–insensitive epoch of last scattering. Reduction of Ω shifts the peaks to smaller scales, by a factor of about $\Omega^{1/2}$. This has an especially notable effect at arc-minute scales, where ground-based interferometers at centimeter wavelengths, such as the AT or the VLA, and millimeter wavelength bolometer arrays, such as SUZIE and SCUBA, should soon be making significant inroads on the current limits.

The present data is already suggestive of the existence of an adiabatic peak[4]. A weighted average of the degree-scale data finds that at degree scales the measured $\delta T/T$ is at least a factor of 2 larger than at COBE scales (to 95 percent confidence). An immediate implication of this result is that any early reionization of the universe subsequent to the primary last scattering epoch at $z \sim 1000$ could at most have resulted in a optical depth of no more than unity. Any larger optical depth would have erased or smoothed the degree-scale fluctuations to an unacceptably low level.

4 Confrontation with the matter power spectrum from galaxy surveys

The CMB detection of anisotropies effectively measures, for a given model, the matter power spectrum at $z \sim 1000$ on large comoving scales, to about $100h^{-1}$Mpc. Deep, well-sampled, galaxy redshift surveys are begining to probe the power spectrum of luminous matter to a similar depth[7]. Measurements of galaxy peculiar velocity fields address, to a more restricted depth, the underlying matter power spectrum[8].

The galaxy redshift surveys probe the power spectrum at $z \sim 0$. However, several corrections need to be applied to the data, that introduce considerable uncertainty, when a comparison is made with the CMB-derived power spectrum. The measured fluctuations probe the quasi-linear regime, $(\delta\rho/\rho)_{rms}$ having unit amplitude in the galaxy counts over spheres of radius $8h^{-1}$ Mpc. The galaxy measurements are generally performed in redshift space, and conversion to physical coordinate space requires knowledge of the underlying peculiar velocity field. Numerical simulations have been useful in tacking these corrections. A potentially more serious problem however is that the inhomogeneties on large scales of the underlying galaxy distribution inevitably affects the measurement statistics. A survey to ~ 100 Mpc depth may not be deep enough to provide a fair sample of the universe. Moreover, estimation of the uncertainties in derived parameters, when the background is inhomogeneous, results in non-Gaussian error statistics that must be simulated for every data set. This makes it difficult to compare with the CMB results, which, if foreground corrections are not an issue, should be well-described by gaussian statistics.

Nevertheless comparisons have been performed of the COBE-normalized power spectrum. CMB reconstruction has been performed on $\geq 100h^{-1}$ Mpcscales and galaxy survey reconstruction applied over $\sim 10 - 200h^{-1}$Mpc scales. The comparison is sensitive to Ω, since the differential growth of fluctuations between $z \sim 1000$ and $z \sim 0$ decreases as Ω is lowered. Lowering Ω turns out to improve the fit with the different data sets, as the shape of the power spectrum, essentially the ratio of power at $100h^{-1}$Mpc to $8h^{-1}$Mpc, appears to favour a low density universe. The best fit CDM model is described by comparing the shape parameter, defined to be Ωh, equal to 0.25, with the power spectrum peak that is determined by the dimensionless ratio of horizon scale at matter-radiation equality ($\propto (\Omega h^2)^{-1}$) to the normalization scale ($\propto h^{-1}$). Models that fit the data equally well have $\Omega \approx 0.3$, with or without a cosmological constant. Introduction of Λ in order to flatten the universe has the advantage of

allowing a slightly higher value of the age and hence Hubble constant. The MDM (cold plus hot dark matter) model does not fare as well, but the introduction of a 20% hot admixture reduces the small-scale power sufficiently that an adequate fit to the power spectrum is attained even if $\Omega = 1$. In all of these models, the fluctuation spectral index must be carefully adjusted. A slight deviation from unity to $n = 0.9$ or 0.95, with the corresponding introduction of a modest tensor component, is necessary to fine-tune the model into agreement with the data.

It is perhaps not surprising to find that even the $\Omega = 1$ CDM model can be revived with judicious choice of parameters[5]. With $n \approx 0.9$ and $h \approx 0.45$, σ_8 can be reduced to 0.75 and the shape of the power spectrum can be fit with comparable accuracy to the rival CDM models. Eventually, as observations of the galaxy distribution are pushed to $z \sim 1$ and as the adiabatic peaks in the CMB power spectrum are mapped, it will be possible to distinguish between the alternative models.

5 Exotic Models

The motivations for inflation, resulting in Ω=1, and CDM, an aftermath of SUSY, come from applications of particle physics to the very early universe. Poll the astronomerss, however, and there is little doubt that the preferred universe would be quite different. All local, and therefore, at least until now, the best sampled and studied, data, to $\sim 10h^{-1}$Mpc, favour a low density universe. The only type of matter hitherto observed, and most notably, the only type of halo dark matter actually detected, is baryonic.

Unfortunately, the open baryonic universe not only requires careful adjustment of several parameters, but lacks any quantitative theory for the origin and initial spectrum of the primordial density fluctuations. This makes it remarkably ugly, as theories go, but this does not provide a sufficiently compelling reason for rejecting it. The baryonic dark matter (BDM) universe, having a non-inflationary origin, should generically possess non-gaussian primordial density fluctuations, although there is no prescription for the non-gaussianity. This does mean, however, that both degree-scale temperature fluctuations in the CMB and density fluctuations on scales of $\sim$ 100 Mpc, where the predicted power of the BDM model peaks, should be non-gaussian. The initial fluctuations in the BDM model must be primordial entropy fluctuations; CMB anisotropies rule out a baryon-dominated universe with adiabatic fluctuations. The BDM model power spectrum peak corresponds to the maximum sound horizon or Jeans mass, at a scale of $\sim$ 100Mpc.

One unappealing consequence is that if the universe did not undergo early reionization, unacceptably large degree-scale CMB temperature fluctuations are generated, once the power spectrum is constrained to fit the galaxy survey data over $(\sim 10 - 100)h^{-1}$ Mpc. If the same power law fluctuation spectrum that is required by the galaxy data ($n_{eff} \approx -1$) continues to larger scales, thereby determining the primordial entropy fluctuation spectrum, one can COBE-normalize the BDM model. On COBE scales, the predicted microwave background fluctuations have[9] $n_{eff} \approx 2$, to be compared with the inflationary $n \approx 1$ predictions. This is due to the imprint of the curvature of the universe. The entropy fluctuations also result in growth since equivalence, since they induce curvature fluctuations at horizon-crossing. in the matter-dominated era, generating the predicted peaks in the power spectrum at the corresponding length scales. On larger scales, the surviving density fluctuations have $n_{eff} \approx 4$, corresponding to Poisson fluctuations.

Early reionization leads to further difficulties for the BDM model. The optical depth τ to the primary last scattering surface must exceed unity. However in this case a significant spectral distortion of the CMB is generated by passage through the ionized intergalactic medium, if

reionization occurred at $z \geq 500$, that exceeds the COBE FIRAS limit on the Compton y-parameter, $y \equiv \int (kT/m_e c^2) d\tau \leq 3 \times 10^{-4}$.

There are two possible parameters that can be adjusted to revive the BDM model[10]. One can effectively reduce the degree-scale fluctuations either by introducing a cosmological constant or by modifying the initial entropy fluctuation spectrum from a constant power law spectrum index $n_{eff} \approx -1$. With Λ, one is in effect returning to an inflationary universe, although with primordial entropy rather than adiabatic fluctuations. The lack of any theory for these initial conditions is not a severe drawback to the model, because there is so much uncertainty in the inflationary models that one cannot guarantee that adiabatic fluctuations of magnitude $\sim 10^{-5}$ are inevitable. Indeed, the COBE normalizaton is usually used to specify the initial amplitude of fluctuations and thereby constrain the inflaton potential.

The BDM models do have an interesting prediction for the model power spectrum. Baryon-dominance results in the survival of residual acoustic oscillations (also called Sakharov oscillations). These are potentially detectable in well-sampled deep survey of galaxys, as discrete features on scales of $\sim 100h^{-1}$Mpcin the matter power spectrum. Acoustic oscillations are also found in low density, low H_0 CDM models, where the baryon fraction can exceed ~ 10 percent. There are also interesting consequences for the CMB temperature fluctuations. Whether or not the initial fluctuations were non-gaussian, it is likely that secondary ionization is highly inhomogeneous in such a model, and therefore imprints a non-gaussian distribution of fluctuations onto the CMB.

Consider the following not implausible sequence of events. The first Jeans mass objects to form in a BDM model have masses $\sim 10^5 M_\odot$ at $z \sim 1000$. They may form as late as $z \sim 100$ and still have provided substantial reheating, and in particular, reionization and appreciable optical depth to electron scattering. Early formation of subgalactic mass objects is inevitable in the BDM model. The extrapolated power spectrum implies that $\delta\rho/\rho$ diverges as approximately $M^{-1/3}$. Whether these final objects fragment into many stars or collapse into supermassive objects, they are likely to produce substantial amounts of ionizing radiation. If star formation is their destiny, then a massive star-dominated initial mass function is often considered to be a likely, if not inevitable, outcome. This is not so much for theoretical arguments, which are ambivalent on this issue, but for more pragmatic reasons. These are most notably the origin of the metallicities of the oldest stars, where an r-process signature is seen, and the heavy element enrichment of the intracluster medium in galaxy clusters, where there is both an enhanced ratio of iron abundance to visible light from associated galaxies and a type II supernova yield signature.

The first generation of these objects to have formed must have constituted relatively rare events. Suppose for example that they were the 3σ tail of a gaussian distribution (although it is by no means evident that the BDM model has gaussian-distributed fluctuations in the absence of any theory). Then as much as ~ 1 percent of the baryons would have collapsed The ionizing radiation interacts with the surronding neutral gas to produce HII regions surrounded by partially ionized transition layers. The photons are sufficiently hard that the transition layer has a significant extent. Wherever the ionization of hydrogen is elevated above the freeze-out value remaining from recombination, one may expect there to be substantial formation of molecular hydrogen, via formation of H^- molecules. The H_2 enhances the gas cooling rate. Much of the intergalactic medium is scheduled to collapse in a hierarchical clustering gravitational instability model, but enhanced H_2 cooling accelerates this process locally. One may expect the regions surrounding the first objects to be triggered into further collapse and star formation. A related effect is the fragmentation of the swept-up shells if the cumulative effects of many supernovae drive a wind.

The net result is inhomogeneous, and in particular, non-gaussian, reionization of the in-

tergalactic medium. The H_2 formation only occurs at $z \leq 100$, so that this provides a natural bound to the redshift of reionization, and to a scattering optical depth of order unity. The relevent angular scale for the patchy reionization is the horizon size at $z \sim 100$, or $\sim 3(\Omega/0.2)^{1/2}(100/z)^{1/2}$ degrees.

Acknowledgements. I am grateful to E. Bunn, W. Hu, D. Scott, N. Sugiyama, M. Tegmark and M. White for many stimulating discussions of the work described here.

References

[1] Bunn, E., 1995, *PhD Thesis*, University of California, Berkeley

[2] Gorski, K. M. *et al.* 1994, *Astrophys. J.*, **430**, L89.

[3] White, M. and Bunn, E. 1995, *Astrophys. J.*, in press.

[4] Scott, D., Silk, J. and White, M. 1994, *Science*, **268**, 829.

[5] White, M., Scott, D., Silk, J. and Davis, M. 1994, *MNRAS*, in press.

[6] Hu, W. and Sugiyama, N. 1994, *Phys. Rev.*, **51**, 2599.

[7] Efstathiou, G. 1995, in the proceedings of the 1993 Les Houches Summer School on Theoretical Physics *Cosmology and Large-Scale Structure*, eds. R. Schaeffer, J. Silk, M. Spiro and J. Saint-Justin (Elsevier: Dordrecht), in press.

[8] Strauss, M. and Willick, J. 1995, preprint.

[9] Sugiyama, N. and Silk, J. 1994, *Phys. Rev. Lett.*, **73**, 509.

[10] Hu, W. and Sugiyama, N. 1994, *Astrophys. J.*, in press.

ANISOTROPIES OF THE MICROWAVE BACKGROUND RADIATION AND THE LARGE-SCALE STRUCTURE OF THE UNIVERSE

George Efstathiou
Astrophysics, University of Oxford, England.

Abstract

I review recent observations of anisotropies in the microwave background and the large-scale clustering of galaxies. The observations are compatible with scale-invariant cold dark matter (CDM) models, but cannot yet distinguish between variants such as a vacuum dominated CDM model or a critical-density universe made up of a mixture of hot and cold dark matter. I discuss future projects that might resolve these problems, in particular the ESA COBRAS/SAMBA proposal to map microwave background anisotropies and the galaxy redshift surveys to be undertaken by the Anglo-Australian Observatory and the Sloan Digital Sky Survey.

1 Introduction

The discovery of anisotropies in the microwave background radiation by the COBE team[51] is probably the most important development in cosmology since the detection of the background radiation by Penzias and Wilson in 1965[48]. At long last, we have direct experimental evidence for small irregularities in the early Universe that are very likely the product of exotic physical processes operating at extraordinarily high energies of more that 10^{15}GeV. Observations of the microwave background radiation are one of the few ways in which we can test inflationary models of the early Universe (see [33]) and could set useful limits on the existence of topological defects such as cosmic strings and textures[12].

The temperature irregularities are almost certainly the imprints of small fluctuations that have grown by gravitational instability to form the structure that we see in the Universe today.

By linking observations of the microwave background with observations of galaxy clustering and peculiar velocity fields we can hope to construct a consistent theory of the origin of structure and perhaps gain important clues as to the nature of the dark matter in the Universe. Since the COBE discovery, there has been a flood of papers investigating constraint on various models, for example, cold dark matter (CDM) models and a plethora of variants, including mixtures of CDM and massive neutrinos, CDM models with non-scale invariant spectra, low-density models, and so on (see the review by White, Scott and Silk [60]). In this short article, I will be less concerned about which specific model provides the best fit to the data, but will instead concentrate on the quality of the observations and how they might be improved in the next few years. I discuss microwave background anisotropies in Section 2 and observations of galaxy clustering in Section 3. A much more detailed discussion of observations of large-scale structure can be found in my Les Houches lectures[18]. I will not discuss observations of peculiar velocity fields; see the article by Dekel in these proceedings and ref [53].

2 Microwave Background Anisotropies

2.1 Theoretical predictions

The temperature pattern on the celestial sphere can be expanded in spherical harmonics

$$\frac{\Delta T}{T} = \sum_{\ell,m} a_\ell^m Y_\ell^m(\theta,\phi). \tag{1}$$

This expansion is natural if we have complete sky coverage, and if the fluctuations are Gaussian, each a_ℓ^m coefficient in (1) is statistically independent with variance,

$$C_\ell = \langle |a_\ell^m|^2 \rangle. \tag{2}$$

The coefficients C_ℓ define the power spectrum of the temperature anisotropies. From the theoretical point of view, this is the most important statistic to measure in the first instance since it provides a complete statistical description of the anisotropies if the initial fluctuations are Gaussian.

The mean-square temperature anisotropy expected in a given experiment can be written in terms of the power spectrum C_ℓ,

$$\left(\frac{\Delta T}{T}\right)^2_{rms} = \tfrac{1}{4\pi}\sum_\ell (2\ell+1) C_\ell F_\ell^2 \approx \tfrac{1}{2\pi}\int \ell^2 C_\ell F_\ell^2 \, d\ln\ell, \tag{3}$$

where the specific experimental details concerning the scanning pattern and beam widths have been absorbed into the *filter function* F_ℓ. For example, for an experiment with a single Gaussian beam width of dispersion θ_s, $F_\ell^2 = \exp(-\ell(\ell+1)\theta_s^2)$ and so the experiment is sensitive only to multipoles $\ell \lesssim 1/\theta_s$. Filter functions for a number of recent experiments are given by White and Srednicki[59]. The integral in equation (3) shows why theorists usually plot $\ell^2 C_\ell$ against the logarithm of ℓ, since one can immediately see the contribution to $(\Delta T/T)_{rms}$ in any given range of multipoles from the area enclosed by the theoretical curves. Some examples are shown in Figure 1. The curves with a peak at $\ell \sim 200$ show computations of the scalar component of C_ℓ for $\Omega = 1$ CDM models with scale invariant adiabatic initial fluctuations for several values of the baryon density Ω_b. The curves have been computed assuming a Hubble constant[1] $h = 0.5$ using the techniques described by Bond and Efstathiou[8] and have been normalized to match

[1]Where the h is the Hubble constant in units of 100 km s^{-1} Mpc^{-1}

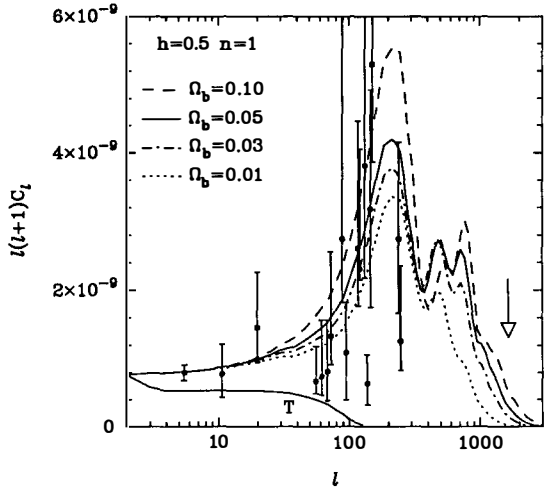


Figure 1. The curves show power spectra of the microwave background anisotropies, C_ℓ, for scale invariant CDM models with $\Omega = 1$, $h = 0.5$, for several values of the baryon density Ω_b. The curves with a peak at $\ell \sim 200$ show the scalar mode contribution, and the curve labelled T shows the tensor mode power spectrum. The tensor mode contribution is independent of Ω_b and has been normalized arbitrarily to match the scalar quadrupole amplitude. The points with error bars show the (approximate) results from a number of recent experiments (see refs [6] and [60] for details). The point with the small error bar at $\ell \approx 5$ shows the two-year COBE results (*e.g.* ref [24]).

the COBE observations. The curve labelled T shows the radiation power spectrum arising from tensor perturbations (*i.e.* gravitational waves) predicted in some inflationary models (see refs [1], [13], [16] and [34]), arbitrarily normalized to match the scalar mode quadrupole amplitude C_2 (this component will be discussed further below). All of the curves have been computed assuming that recombination occurs at $z \sim 1000$ in the usual way[47] with no subsequent reionization of the intergalactic medium.

At multipoles $\ell \lesssim 100$ (corresponding to angular scales $\theta \sim \pi/\ell \lesssim 2°$) the power spectra are very nearly flat. On these angular scales, the temperature anisotropies arise from the Sachs-Wolfe effect[50], *i.e.* from the gravitational potential fluctuations at the surface of last scattering. If we assume a spatially flat universe with $\Omega = 1$, it is straighforward to relate the power-spectrum of present day density irregularities, $P(k)$, to the amplitude of the temperature anisotropies; for a power law spectrum $P(k) = Bk^n$, the result is

$$C_\ell = \frac{B}{16}\left(\frac{H_0}{c}\right)^{n+3} \frac{\Gamma(3-n)}{\Gamma^2\left(\frac{4-n}{2}\right)} \frac{\Gamma\left(\ell+\left(\frac{n-1}{2}\right)\right)}{\Gamma\left(\ell+\left(\frac{5-n}{2}\right)\right)}. \tag{4}$$

Thus, for a scale invariant spectrum ($n = +1$), $C_\ell \propto 1/[\ell(\ell+1)]$, *i.e.* the temperature pattern is scaleinvariant in two-dimensions (*cf* equation 3). Measurements of the temperature anisotropies on large angular scales can therefore constrain the amplitude B and spectral index n of the mass fluctuations (subject to certain assumptions concerning the geometry and matter content of the Universe, see Section 2.3).

2.2 Experimental results

The latest (two-year) maps from COBE have been analysed by a number of groups to estimate the best fitting spectral index n and amplitude in equation (3) (usually characterised by the *rms* quadrupole amplitude $Q_{rms} = T_0(5C_2/4\pi)^{1/2}$, where $T_0 = 2.735K$ is the mean temperature of the microwave background[42]. Some representative results (with 1σ errors) are as follows: $n = 1.10 \pm 0.32$, $Q_{rms}^{n=1} = 19.9 \pm 1.6\mu K$ (ref [24]); $n = 1.27 \pm 0.22$, $Q_{rms}^{n=1} = 20.4 \pm 2.1\mu K$ (ref [6]); $n = 1.30^{+0.24}_{-0.37}$, $Q_{rms}^{n=1} = 21.1 \pm 1.5\mu K$ (ref [11]). The results are somewhat dependent on exactly which set of COBE maps are used and whether or not the COBE quadrupole is included in the fits. (I have listed numbers including the quadrupole, which may be affected by the Galaxy; removing the quadrupole decreases the spectral index by about $\delta n \approx 0.2$, and increases Q_{rms} by about $1\mu K$). The amplitudes $Q_{rms}^{n=1}$ listed here are fits assuming $n = 1$ in equation (3). Averaging these results gives $Q_{rms}^{n=1} = 20.5 \pm 1.7\mu K$; I use this number to normalize the theoretical predictions in subsequent sections. The COBE maps are consistent with a scale invariant spectrum, $n = +1$, within rather large errors, and also with Bond's analysis[6] of the Far-Infrared Survey[23] at a frequency $\nu = 170$GHz, which gives $n = 1.6^{+0.7}_{-0.8}$, $Q_{rms}^{n=1} = 20.2 \pm 4.9\mu K$. The COBE maps are also consistent with the higher sensitivity maps of the Tenerife experiment[58] at frequencies $\nu = 10$, 15 and 32.5GHz. Thus, there is very good evidence that the large-angle anisotropies are independent of frequency over the range 10 – 170GHz, as expected if they are caused by primordial fluctuations.

On angular scales $\theta \lesssim 1^\circ\Omega_0^{1/2}(z_R/1000)^{1/2}$ (the angle subtended by the Hubble radius ct at the redshift of recombination, z_R), we expect to see 'acoustic' peaks in the power spectrum as shown in Figure 1 (provided the intergalactic medium is not subsequently reionized at high redshifts). A number of ground based and balloon borne experiments on angular scales $\theta \sim 1^\circ$ have been carried out over the last few years, most of which have detected fluctuations. These are shown schematically by the points in Figure 1 (see ref [60]) and are discussed further by Silk in these proceedings. The error bars on these intermediate angle experiments are still quite large, and there is a real possibility that some of the signal is caused by foreground contamination (free-free and synchrotron radiation at frequencies $\nu \lesssim 30GHz$ and Galactic dust at $\nu \gtrsim 100GHz$), but taken at face value the results suggest that the power spectrum is rising at multipoles $\ell \gtrsim 100$.

Figure 2 shows how power-spectra such as those plotted in Figure 1 translate into maps of the temperature fluctuations. The upper figure shows a realization of an $\Omega_b = 0.05$, $h = 0.5$, CDM model at the angular resolution of COBE, with approximately the same noise as the two-year maps. The lower figure shows how this realization of sky would look at an angular resolution of 30arcmin in the absence of noise. Evidently, the model predicts a large amount of small scale structure, with prominent hot and cold spots of width of $\sim 1^\circ$–2°, *i.e.* angular scales corresponding to the first peak in the power spectrum. A real map such as this is a theorists dream, which could perhaps be fulfilled in the next decade (see Section 2.4).

2.3 Some Cosmological Implications

Figure 3 shows an updated version of a diagram from ref [22] summarizing some of the constraints on CDM-like models from COBE and observations of large-scale structure. We assume

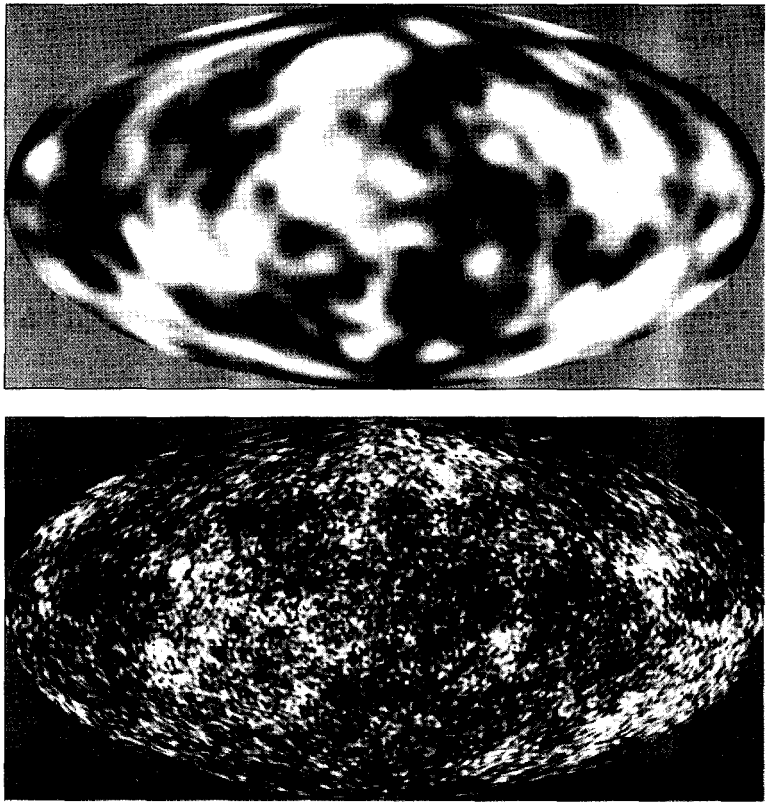


Figure 2. Simulated maps of the background radiation anisotropies expected in an $\Omega = 1$ CDM model. The input power spectrum is plotted as the solid line in Figure 1. The upper picture shows a simulated COBE map with a resolution of 7° together with random noise as in the COBE two-year data. The lower panel shows the same realization of the sky, but at an angular resolution of 30′ and without random noise.

that the mass fluctuations at the present day are characterised by the power spectrum

$$P(k) = Bk/(1 + [ak + (bk)^{3/2} + (ck)^2]^\nu)^{-2/\nu}, \qquad (5)$$
$$a = (6.4/\Gamma)h^{-1}\mathrm{Mpc}, \quad b = (3.0/\Gamma)h^{-1}\mathrm{Mpc}, \quad c = (1.7/\Gamma)h^{-1}\mathrm{Mpc}\ , \quad \nu = 1.13.$$

Equation (5) is accurate to a few precent for spatially flat universes in which baryons make a negligible contribution to the total mass density[7]. The parameter $\Gamma = \Omega_0 h$ defines a useful sequence of models with varying amounts of large-scale power. In the standard version of the

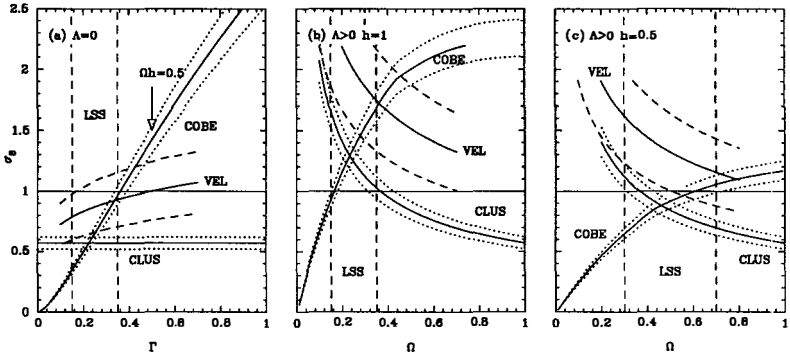


Figure 3. Constraints on the amplitude of the mass fluctuations in spheres of radius $8h^{-1}$ Mpc for spatially flat CDM-like models ($\Omega_0 = 1$ in (a), and low density models with a non-zero cosmogical constant with $h = 1$ and $h = 0.5$ in (b) and (c) respectively). The lines labelled COBE show the one-sigma range allowed by the two-year maps. The vertical lines labelled LSS show the range of Γ values implied by observations of galaxy clustering (see Section 3). The lines labelled CLUS, show the limits on σ_8 implied by the abundances and masses of rich clusters of galaxies, and the lines labelled VEL show approximate constraints from observations of large-scale peculiar velocity fields.

CDM model[4,15], $\Omega_0 = 1$ and $h \approx 0.5$, thus $\Gamma \approx 0.5$. We will see in Section 3 that observations of large scale galaxy clustering are better fitted by equation (3) with Γ in the range 0.15–0.35 (shown by the dashed lines labelled LSS in Figure 3).

Figure 3 shows various constraints on the *rms* amplitude of the mass fluctuations averaged in spheres of radius $8h^{-1}$Mpc, σ_8, as a function of Γ for spatially flat CDM-like models. The curves labelled COBE shows the limits implied by the two-year COBE results (computed from equation (4) and its generalization to models with non-zero cosmological constant[32]). The lines labelled VEL show approximate 1σ ranges on σ_8 implied by galaxy peculiar velocities and the density field of IRAS galaxies (see ref [22] for further details). The lines labelled CLUS show the constraint $\sigma_8 \approx (0.57 \pm 0.05)\Omega_0^{-0.56}$ derived from the abundances and masses of rich clusters[61]. This figure illustrates two important points. Firstly, the standard CDM model ($\Omega = 1$, $h \approx 0.5$, shown by the arrow in Figure 3a) requires $\sigma_8 \approx 1.4 \pm 0.1$ (*cf* ref [11]); this is higher than inferred from observations of galaxy clustering $(\sigma_8)_{gal} \approx 0.95 \pm 0.05$ (ref [40]) and may be difficult to reconcile with the masses of typical Abell clusters[61]. Secondly, the various constraints roughly overlap in each of the panels if $\Gamma \approx 0.3$; thus a wide class of cosmological models are consistent with the observations provided that the power spectrum has more power at large scales than the standard $\Gamma = 0.5$ CDM model. Constraints on low-density CDM models and mixed dark models implied by the microwave background anisotropies are discussed in refs [25], [26] and [52].

In computing the COBE constraints in Figure 3, the contributions to the temperature anisotropies from tensor modes have been neglected. For a wide class of models of inflation, the

ratio of tensor to scalar components is related to the spectral index n_s of the scalar perturbations by the relation[13]

$$C_2^T/C_2^S \approx 7(1 - n_s + \delta), \tag{6}$$

where the term δ depends on the shape of the inflaton potential and is usually negligible unless the potential is finely tuned, *e.g.* by having an inflexion point, see ref [5]). Figure 4 shows the COBE constraints on σ_8 as a function of spectral index assuming equation (6) with $\delta = 0$ and $\Omega_0 = 1$; these curves are computed from numerical computations of the radiation power-spectra. Notice that σ_8 is a strong function of the spectral index n_s and that values as low as 0.5 can be obtained with a modest tilt in the spectrum. It is perhaps possible that a CDM model with a spectral index in the range 0.8–0.9 and $\Gamma \approx 0.4$ (as in Figure 4b), and no additional components, might be compatible with the various observational constraints plotted in Figure 3.

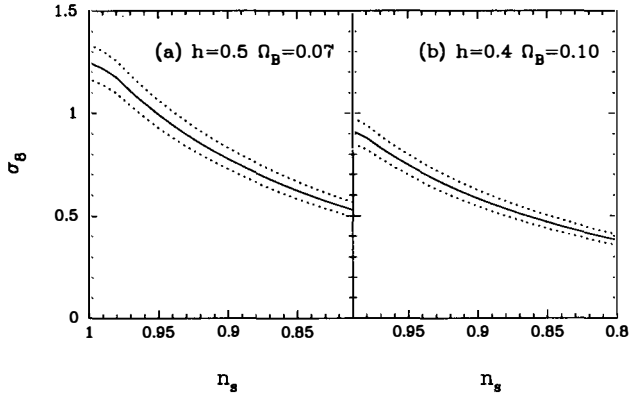


Figure 4. COBE constraints on σ_8 for $\Omega_0 = 1$ CDM dominated universes with tilted spectra (spectral index n_s) and a ratio of tensor to scalar modes given by equation (6). The dashed lines show the 1σ ranges allowed by the two-year COBE data.

2.4 Prospects for the future

Evidently one of the most important goals in microwave background research over the next few years is to determine the radiation power spectrum to high accuracy up to multipoles $\ell \gtrsim 1000$. The best prospects for achieving this are from long duration balloon flights[36], ground based interferometry[44], or from a new space mission. Proposals for satellites to study microwave background anistropies are under consideration by NASA and ESA, and offer the best prospects of producing high sensitivity maps over a wide frequency range and over a large area of sky. For example, the ESA COBRAS/SAMBA proposal[41] aims to map the background anisotropies over $\sim 95\%$ of the sky with a resolution of between $5'$ and $30'$ with a sensitivity of a few $\times 10^{-6}$ per pixel over much of the frequency range 30–900GHz. Such an experiment would be capable of producing a map of the microwave sky similar to that shown in the lower panel of Figure 2 in regions free of Galactic foregrounds. It is difficult to estimate the likely contamination by foregrounds at the level of few μK and at a resolution of a few arcminutes

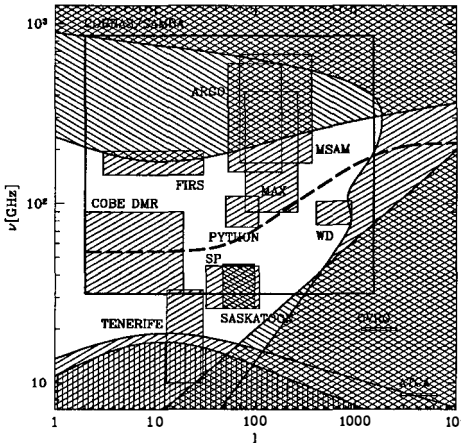


Figure 5. Microwave background experiments plotted in the ν–ℓ plane. The boxes show roughly the range of frequencies and multipoles probed by various experiments, including the proposed COBRAS/SAMBA satellite. The shaded regions show, roughly, where various foregrounds cause *rms* fluctuations that exceed those of COBE normalized scale-invariant fluctuations for a typical 'clean' region of the sky. They correspond to Galactic dust (top), free-free emission (lower left), synchrotron emission (lower left, vertically shaded), radio point sources (lower right) and COBRAS/SAMBA instrumental noise and beam dilution (right). The heavy dashed line shows the frequency where the total foreground contribution to each multipole is minimised. (From ref [57]).

(see the article by Bouchet in these proceedings), but there are several reasons for optimism (see ref [57]): (i) From the low-frequency 408MHz maps[28] and the IRAS 100μ maps[43], we find that the power-spectra of the Galactic emissions decrease as $C_\ell \propto \ell^{-3}$, thus the relative contribution of Galactic foregrounds to intrinsic signal is likely to decrease rapidly with increasing multipole if the primordial signal has a power spectrum similar to the curves shown in Figure 1; (ii) With a multifrequency experiment, it is possible to design an optimal Wiener filter in the frequency-multipole plane that can accurately separate between frequency dependent foregrounds and primordial anisotropies; (iii) extrapolating from the 100μm IRAS maps with the dust model of Reach *et al* [49], we find that in the cleanest 20% of sky (with 100μm emission of $\lesssim$1MJy/sr), Galactic dust is likely to contribute $\Delta T/T \lesssim 2 \times 10^{-6}$ at frequencies of $\sim$ 125GHz. At these frequencies it may be possible to recover the power spectrum of primordial anisotropies to an accuracy of a few percent, without any foreground subtraction at all. Some of these results are indicated schematically in Figure 5. This indicates that experiments at frequencies of $\sim$ 100GHz are likely to be least affected by Galactic foregrounds and point sources over a wide range of multipoles.

From the theoretical point of view there are, of course, a large number of questions that could be answered by projects such as COBRAS/SAMBA. For example:

• Are the acoustic peaks really present in the power-spectrum or is there evidence that the integalactic medium was reionized at high redshifts? (The experimental results plotted in Figure 1 already suggest not).

• Is there any evidence for a gravitational wave contribution to the background anisotropies?
• The shape of the radiation power spectrum depends on the form of the primordial fluctuation spectrum, Ω_b, h, Λ, the geometry of the Universe *etc* (see *e.g.* refs [8], [29] and [31]) and so it should be possible to set constraints on these parameters. However, note that it is possible to construct models with different cosmological parameters that have very nearly the same background radiation power spectra[10] and so other observational constraints are required to remove the degeneracies.
• Is there any evidence of non-Gaussian features suggestive of topological defects?
• Multifrequency observations with a precision of a few μK should allow a detection of the Sunyaev-Zeldovich effect[62] in large numbers of clusters of galaxies and lead to useful contraints on the evolution of structure[9].

3 Observations of Galaxy Clustering

3.1 $P(k)$ from the APM Galaxy Survey

The APM Galaxy Survey[37,38] is the largest uniform galaxy catalogue, consisting of over 2 million galaxies in the Southern sky. The angular correlation function $w(\theta)$ measured from the APM Survey provides a useful constraint on large-scale galaxy clustering and has been discussed extensively in the literature (see *e.g.* refs [39], [17] and [18]). Recently, Baugh and Efstathiou[2,3] have shown how measurements of either the angular correlation function or the two-dimensional power-spectrum can be inverted to recover the three-dimensional power spectrum $P(k)$ of the galaxy distribution in *real space*. The points in Figure 6 show estimates of $P(k)$ from ref [2]. These estimates were derived by inverting the angular correlation function measured for APM galaxies in the magnitude range $17 < b_J < 20$ (with a median redshift of ≈ 0.13). The error bars are derived from the scatter from $P(k)$ determined from 4 separate zones of the survey of roughly equal area. Note that systematic errors probably become larger than the random errors at wavenumbers $k \lesssim 0.05h\mathrm{Mpc}^{-1}$, and that uncertainties in the cosmological model, the redshift distribution of the APM galaxies, and the evolution of $P(k)$ introduce an additional uncertainty of about 10-20% in the overall normalization of $P(k)$ (see ref [2] for a discussion of these points). The curves in Figure 6a show the family of CDM power spectra defined by equation (5) arbitrarily normalized to $\sigma_8 = 1$. Evidently, the power spectrum of the standard $\Gamma = 0.5$ CDM model is a poor fit to the observations, which are better described by equation (5) with $\Gamma \approx 0.3$.

In Figure 6b we compare the APM power spectrum to the power spectra of the mass distributions determined from N-body simulations of three CDM-like models: standard CDM (SCDM) *i.e.* $\Omega = 1$, $h = 0.5$; a low density spatially flat model (LCDM) with $\Omega = 0.2$ and $h = 1$; a mixed dark matter (MDM) model with $h = 0.5$ in which CDM contributes $\Omega_{CDM} = 0.6$, light neutrinos contribute $\Omega_\nu = 0.3$ and baryons contribute $\Omega_b = 0.1$. The MDM and SCDM simulations are as described in ref [14]; for each of these models we ran an ensemble of 10 simulations each containing 10^6 particles within a cubical computational box of length $300h^{-1}$Mpc using the P^{3}M N-body code[20]. The LCDM curves in Figure 6b were derived from an ensemble of 10 simulations each containing 4×10^6 particles within a box of length $600h^{-1}$Mpc. The models were evolved to approximately match the amplitude of microwave background anisotropies determined from the first year COBE maps[51] ignoring any contributions to the anisotropies from gravitational waves; thus σ_8 for the mass fluctuations is equal to unity for the LCDM and SCDM models, and is 0.67 for the MDM model. The two-year COBE results summarized in the previous Section require larger values of σ_8 (by about 20–30%)

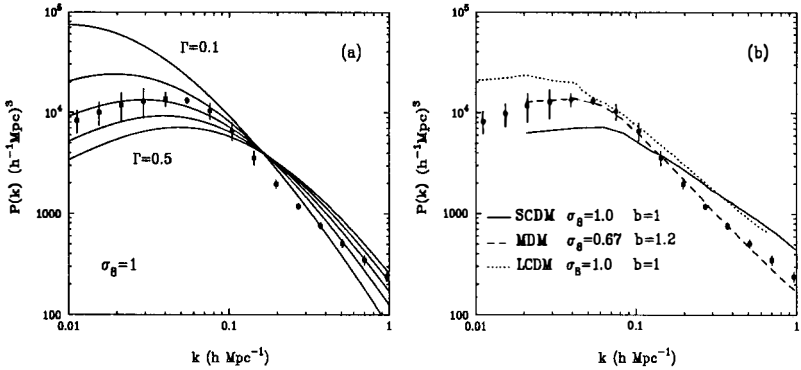


Figure 6. The points show estimates of the three-dimensional power spectrum of the galaxy distribution derived from the APM Galaxy Survey[2]. The error bars show 1σ errors derived by dividing the survey into four zones of roughly equal area. The curves in Figure 6a show the CDM linear power spectrum of equ (5) normalized to $\sigma_8 = 1$ for $\Gamma = 0.1$, 0.2, 0.3, 0.4 and 0.5 (top to bottom). The curves in Figure 6b show the power spectra of the mass fluctuations measured from (approximately) COBE normalized N-body simulations of three CDM-like models as described in the text.

but this small difference is unimportant in most of the discussion that follows.

Each of the curves in Figure 6b shows the mean of the power spectra of the mass distributions, $P_m(k)$, estimated from the simulations. For the MDM model, we have arbitarily multiplied $P_m(k)$ by a constant b^2, with $b = 1.2$, to match the observations on large scales, *i.e.* we have introduced a linear biasing factor in relating mass fluctuations to fluctuations in the galaxy distribution. Figure 6b illustrates the following points:

- The SCDM curve has a similar shape to the linear theory power spectrum plotted in Figure 6a over almost the entire range of wavenumbers plotted in the figure ($k \lesssim 0.3h$ Mpc^{-1}). To reconcile the SCDM curve with the APM data would require substantial scale-dependent biasing, with galaxies strongly biased relative to the mass distribution at wavenumbers $k \lesssim 0.1h$ Mpc^{-1} and strongly antibiased at larger wavenumbers.
- The LCDM model provides a good match to the observations at wavenumbers $k \lesssim 0.1h$ Mpc^{-1} but lies above the data points at larger wavenumbers. Evidently antibiasing is required on spatial scales $\lesssim 5h^{-1}$Mpc if this model is to match the clustering of the galaxy distribution (*cf* ref [21]).
- The MDM model provides a satisfactory fit to the observations over the entire range of wavenumbers plotted in the figure. The small degree of biasing, $b \sim 1.2$, assumed in Figure 6b is not significant, because it lies within the uncertainties of the observational estimates of $P(k)$ and is of the same order as the difference in normalizations implied by the first-year and two-year COBE maps.

3.2 Comparison with $P(k)$ from redshift surveys

In this subsection we compare the APM power spectrum with the power spectra estimated from galaxy redshift surveys. For a more detailed discussion of the surveys, the methods used to estimate $P(k)$, and references to previous work, see my review article[18]. Figure 7 shows the APM power spectrum together with estimates of $P(k)$ for IRAS and optically selected galaxies. The open circles show $P(k)$ from a reanalysis of the 1.2Jy and QDOT IRAS surveys[54]. The open triangles show $P(k)$ for the optically selected CfA-2 survey[45]; these are derived from a volume limited subset of the CfA-2 survey consisting of 1509 galaxies to a coordinate distance of $101h^{-1}$Mpc. The open crosses show $P(k)$ for the Stromlo-APM redshift survey[35], a 1-in-20 randomly selected subset of APM galaxies with $b_J < 17.15$.

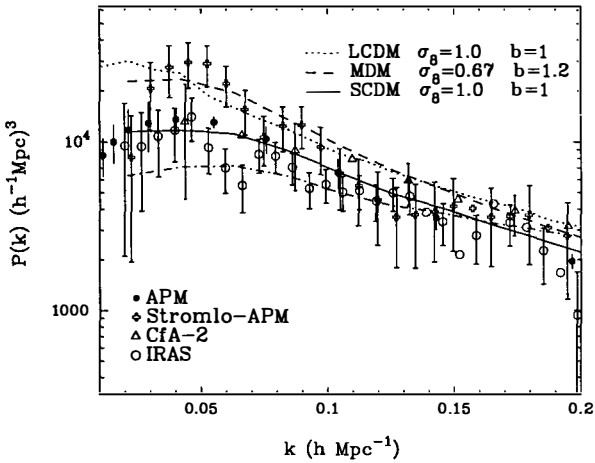


Figure 7. Power spectra of galaxies estimated from the APM Galaxy Survey and from various redshift surveys. The filled circles show the real-space estimates of $P(k)$ derived from the APM Survey, as plotted in Figure 6. The other points show estimates of $P(k)$ in *redshift-space* derived from various redshift surveys: the combined 1.2Jy and QDOT surveys of IRAS galaxies[54]; the CfA-2 survey[45]; the Stromlo-APM survey[55]. The Stromlo-APM and IRAS estimates are for flux limited samples while the CfA-2 estimates are for a volume limited sample as described in the text. The error bars on the points show 1σ error estimates. The solid, dotted and dashed lines show *redshift-space* estimates of $P(k)$ for the three ensembles of simulation plotted in Figure 6b. The dot-dashed curve shows $P(k)$ in *real-space* for the SCDM model illustrating how the power-spectrum is affected by redshift-space distortions.

The three uppermost lines show estimates of $P(k)$ in redshift-space derived from the three ensembles of N-body simulations described in the previous subsection. We make the following remarks concerning this figure:

• Galaxy peculiar motions introduce distortions between the true clustering pattern and that seen in redshift surveys. On small scales, the distortions cause groups and clusters to be elongated along the line-of-sight (so called 'fingers of God'). On large scales, where the mass

fluctuations are linear, we expect to see clusters elongated perpendicular to the line-of-sight, leading to an overall boost in the amplitude of the power-spectrum, $P_s(k)$, measured in redshift-space relative to that measured in real-space, $P_r(k)$,

$$P_s(k) \approx \left(1 + \frac{2}{3}\frac{\Omega^{0.6}}{b} + \frac{1}{5}\frac{\Omega^{1.2}}{b^2}\right) P_r(k), \quad (7)$$

(see ref [30]), where we have assumed a linear biasing factor b to relate fluctuations in the galaxy density field to those of the mass distribution $(\delta\rho/\rho)_{\rm gal} = b(\delta\rho/\rho)_{\rm mass}$. Redshift-space distortions can be measured by searching for anisotropies in the power-spectrum or two-point correlation function (see Hamilton's article in these proceedings and references therein).

- Peculiar motions cause significant differences in the shape of the power-spectra measured in redshift- and real-space (*cf* the SCDM curves plotted in Figure 7). It is important, therefore, that estimates of $P(k)$ derived from redshift surveys are compared with theoretical predictions *in redshift-space*.
- The IRAS power spectrum lies below the real-space estimates of $P(k)$ derived from the APM survey by a factor of ~ 1.5. The effect is relatively small, and is consistent with an analysis of the cell-count variances of IRAS and the Stromlo-APM redshift surveys[19].
- The CfA-2 and Stromlo-APM power spectra agree well at wavenumbers $k \gtrsim 0.1h{\rm Mpc}^{-1}$. At lower wavenumbers the Stromlo-APM estimates are higher than the CfA estimates by about a factor of two; however, the errors on both estimates at such low wavenumbers are large
- The redshift-space power spectra derived for the MDM and LCDM models are compatible with the CfA-2 and Stromlo-APM estimates, within the large observational errors. The SCDM curve is broadly consistent with the shapes of the power-spectra estimated from the IRAS and CfA-2 surveys, though it lies low compared to the Stromlo-APM estimates at wavenumbers $k \lesssim 0.1h{\rm Mpc}^{-1}$.
- The scatter in the estimates of $P(k)$ from various redshift surveys is evidently large and it is clear from Figure 7 that the observations cannot yet differentiate reliably between different CDM-like models [2].

3.3 Prospects for the future

Despite the large amount of effort invested in galaxy redshift surveys, the results of the previous subsection shows that much more work needs to be done. Fortunately, two large galaxy surveys are about to begin which should lead to a substantial improvement in our understanding of large-scale structure in the Universe within the next few years. The Sloan Digital Sky Survey[27] aims to produce a multicolour deep CCD survey over π steradians of the sky and redshifts for 10^6 galaxies. A consortium of UK and Australian astronomers is planning to measure redshifts of $\sim 250,000$ galaxies within the next two to three years using the 2-degree field (2dF) fibre-positioning system at the Anglo Australian Telescope[56]. As an example of what we might expect, Figure 8 shows the galaxy distribution in a 2° wide declination slice from a simulation of the APM Galaxy Survey to a magnitude limit of $b_J = 19.5$. The picture contains 31,000 galaxies and it should be possible to measure redshifts for all galaxies in a strip like this in about 9 nights using the 2dF system.

Some of the key problems that these surveys will help answer are as follows:

- The large volumes in the new surveys should lead to much improved measures of the power spectrum of galaxy clustering. It may be possible to detect the turn-over of the power spectrum to the scale invariant form at $k \lesssim 0.05h^{-1}$Mpc predicted in CDM-like models.

[2]Despite some claims to the contrary, *e.g.* refs [46], [45].

• The present generation of redshift surveys is already leading to useful measurements of redshift space anisotropies on large-scales (see Hamilton's article in these proceedings). The new surveys should give a very precise determination of $\Omega^{0.6}/b$ via equation (7) and may even allow us to determine whether the bias parameter varies with scale.
• There are some tentative indications that optically luminous galaxies are more strongly clustered than less luminous galaxies[45] and that IRAS galaxies are more weakly clustered than optically selected galaxies (Figure 7). Determining the clustering properties of galaxies of different morphological types and luminosities is surely amongst the most important goals of the new redshift surveys. It would be interesting to know, for example, whether faint galaxies inhabit low density regions, whether galaxies in filaments and walls have properties that are systematically different to those of other galaxies, Such observations are likely to provide strong constraints on the physical processes relevant to galaxy formation.

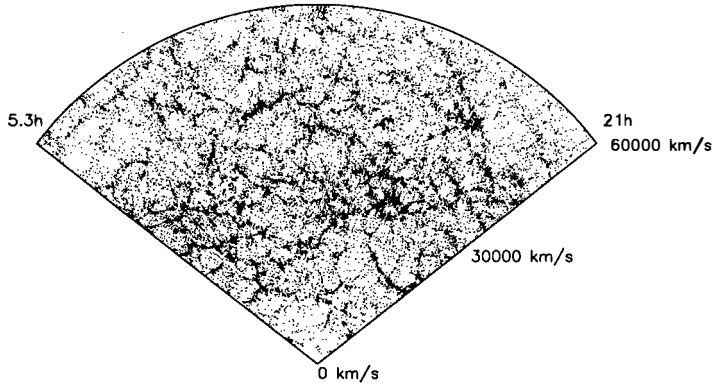


Figure 8. A numerical simulation of a 2° wide declination slice in a redshift survey limited at $b_J = 19.5$. The simulation is of a spatially flat CDM model (equation 5) with $\Omega = 0.2$, $h = 1$ and $\sigma_8 = 1$.

• The simulated map in Figure 8 shows the now familiar pattern of interconnecting filaments, walls and voids. Attempts to quantify the morphological appearance of the galaxy distribution have met with fairly limited success, although there is a large literature on the subject. There is a need to develop new statistics of galaxy clustering and to link these with the predictions of models of galaxy formation.
• The new surveys should lead to improved dynamical mass determinations for groups and clusters and may resolve some of the controversial points concerning the spatial distribution of rich clusters (see ref [18]).

4 Conclusions

The new projects described in Sections 2.4 and 3.3 offer a real prospect of establishing a close link between fluctuations in the early universe and large-scale structure at the present day. As things stand, we have some tentative indications in support of the CDM-like models described

here, for example, the determination of a spectral index close to unity from the COBE maps, the indications of an acoustic peak in the power spectrum of the radiation anisotropies and the shape of the power spectrum of the galaxy distribution. However, the observations are not yet precise enough to distinguish between various CDM-like models such as the vacuum dominated and mixed dark matter models plotted in Figure 7. Improved observations, especially of the microwave background anisotropies, should resolve many of the remaining ambiguities and provide sensitive tests of other models of structure formation (*e.g.* cosmic strings and textures) that have not been discussed here.

Acknowledgements I would like to thank various collaborators who have contributed to the work described here, especially Carlton Baugh, Dick Bond, Gavin Dalton, Steve Maddox, Will Sutherland, Helen Tadros and Max Tegmark. I thank the UK Particle and Astrophysics Reseach Council for the award of a Senior Fellowship.

REFERENCES

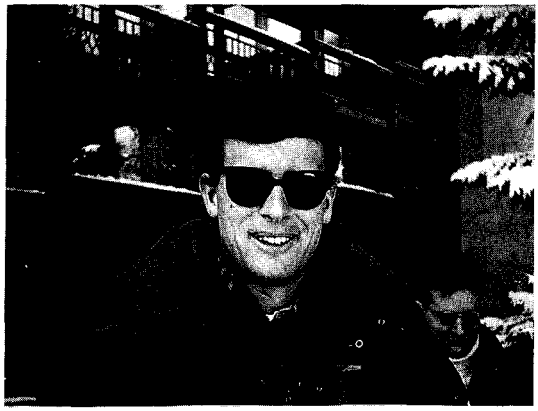
[1] Abbott L.F., Wise M., 1984, Nucl. Phys. **B244**, 541.
[2] Baugh C.M., Efstathiou G., 1993, MNRAS, **265**, 145.
[3] Baugh C.M., Efstathiou G., 1994, MNRAS, **267**, 323.
[4] Blumenthal G.R., Faber S.M., Primack J.R., Rees M.J., 1984, Nature, **311**, 517.
[5] Bond J.R., 1995, *Les Houches Lectures*, ed. R. Schaefer, Elsevier Science Publishers, Netherlands, in press.
[6] Bond J.R., 1995, PRL, **74**, 4369.
[7] Bond J.R., Efstathiou G., 1984, ApJ, **285**, L45.
[8] Bond J.R., Efstathiou G., 1987, MNRAS, **226**, 655.
[9] Bond J.R., Myers S., 1993, in *The Evolution of Galaxies and Their Environments*, Proceedings of the Third Teton Summer School, eds M. Shull, H. Thronson, NASA Conference Publications **3190**, p21.
[10] Bond J.R., Crittenden R., Davis R.L., Efstathiou G., Steinhardt P.J., 1994, PRL, **72**, 13.
[11] Bunn E.F., Scott D., White M., 1995, ApJ, **441**, L9.
[12] Coulson D., Ferreira P. Graham P., Turok N., 1994, Nature, **368**, 27.
[13] Crittenden R., Bond J.R., Davis R.L., Steinhardt P.L., 1993, PRL, **71**, 324.
[14] Dalton G.B., Croft R.A.C., Efstathiou G., Sutherland W.J., Maddox S.J., 1994, MNRAS, **271**, L47.
[15] Davis M., Efstathiou G., Frenk C.S., White, S.D.M., 1985, ApJ, **292**, 371.
[16] Davis R.L., Hodges H.M., Smoot G.F., Steinhardt P.J., Turner M.S., PRL, **69**, 1856.
[17] Efstathiou G., 1993, *Proc Natl Acad Sci. USA*, **90**, 4859.
[18] Efstathiou G, 1995, *Les Houches Lectures*, ed. R. Schaefer, Elsevier Science Publishers, Netherlands, in press.
[19] Efstathiou G., 1995, MNRAS, in press.
[20] Efstathiou G., Davis M., Frenk C.S., White S.D.M., 1985, ApJ, **292**, 371.
[21] Efstathiou G., Sutherland W.J., Maddox S.J., 1990, Nature, **348**, 705.
[22] Efstathiou G., Bond J.R., White S.D.M., 1992, MNRAS, **258**, 1p.
[23] Ganga K., *et al* 1993, ApJ, **410**, L57.
[24] Gorski K.M., Hinshaw G., Banday A.J., Bennett C.L., Wright E.L., Kogut A., Smoot G.F., Lubin P., 1994, ApJ, **430**, L89.
[25] Gorski K.M., Ratra B., Sugiyama N., Banday A.J., 1995, ApJ, **444**, 262.
[26] Gorski K.M., Stompor R., Banday A.J., 1995, preprint astro-ph/9502033.

[27] Gunn, J., Weinberg D., 1995, in *Wide Field Spectroscopy and the Distant Universe*, eds. S.J. Maddox & A. Aragón-Salamanca, World Scientific Publishing Co., Singapore, p3.
[28] Haslam C.G.T. *et al* 1982, A&A Supp., **47**, 1.
[29] Hu W., Sugiyama N., 1995, ApJ, **444**, 489.
[30] Kaiser, N., 1987, MNRAS, **227**, 1.
[31] Kamionkowski M., Spergel D.N., 1994, ApJ., **431**, 1.
[32] Kofman L.A., Starobinsky A.A., 1985, Sov. Astron. Lett., **11**, 271.
[33] Kolb E.W., Turner M.S., 1990, *The Early Universe*, Addison-Wesley Publishing Company.
[34] Lidsey J.E., Coles P., 1992, MNRAS, **258**, 57p.
[35] Loveday J., Peterson, B.A, Efstathiou G., Maddox S.J., 1992, ApJ, **390**, 338.
[36] Lubin P.M., 1995, in *Extragalactic Background Radiations*, eds D. Calzetti, M. Livio, P. Madau, Cambridge University Press, Cambridge, p191.
[37] Maddox S.J., Sutherland W.J., Efstathiou G., Loveday J., 1990, MNRAS, **243**, 692.
[38] Maddox S.J., Efstathiou G., Sutherland W.J., 1990, MNRAS, **246**, 433.
[39] Maddox S.J., Efstathiou G., Sutherland W.J., Loveday J., 1990, MNRAS, **242**, 43p.
[40] Maddox S.J., Efstathiou G., Sutherland W.J., 1995, MNRAS, submitted.
[41] Mandolesi N., *et al* 1995, Astrophys Lett. & Comm., in press.
[42] Mather J.C., *et al* 1990, ApJ, **354**, L37.
[43] Neugebauer G., *et al* 1984, ApJ, **278**, L1.
[44] O'Sullivan C., *et al* 1995, MNRAS, **274**, 861.
[45] Park C., Vogeley M.S., Geller M.J., Huchra J.P., 1994, ApJ, **431**, 569.
[46] Peacock J.A., Dodds S.J., 1994, MNRAS, **267**, 1020.
[47] Peebles P.J.E., 1968, ApJ, **153**, 1.
[48] Penzias A.A., Wilson, R.W., 1965, ApJ, **142**, 419.
[49] Reach W.T., *et al* 1995, preprint astro-ph/9505056.
[50] Sachs R.K., Wolfe A.M., 1967, ApJ, **147**, 73.
[51] Smoot G.F. *et al* 1992, ApJ, **396**, L1.
[52] Stompor R., Gorski K.M., Banday A.J., 1995, preprint, astro-ph/9502035.
[53] Strauss M.A., Willick J.A., 1995, Physics Reports, in press.
[54] Tadros H., Efstathiou G., 1995a, MNRAS, in press, astro-ph/9507050
[55] Tadros H., Efstathiou G., 1995b, in preparation.
[56] Taylor K., 1995, in *Wide Field Spectroscopy and the Distant Universe*, eds. S.J. Maddox & A. Aragón-Salamanca, World Scientific Publishing Co., Singapore, p25.
[57] Tegmark M., Efstathiou G., 1995, MNRAS, submitted, astro-ph/9507009
[58] Watson R.A. *et al* 1994, Nature, **357**, 660.
[59] White M., Srednicki, M, 1995, ApJ, **443**, 6.
[60] White M., Scott D., Silk J., 1994, ARAA, **32**, 319.
[61] White S.D.M., Efstathiou G., Frenk C.S., 1993, MNRAS, **262**, 1023.
[62] Zeldovich Ya B., Sunyaev R.A., 1969, Ap. Space Sci., **4**, 301.



SESSION VIII

THE DEEP UNIVERSE



Evolution of galaxies and clustering from the Canada-France Redshift Survey

O. Le Fèvre [1], S.J. Lilly [2], D. Crampton [3], F. Hammer [1], D,. Hudon [2], D. Schade [2], L. Tresse [1]
[1] *DAEC, Observatoire de Paris-Meudon, 92195 Meudon Cedex, France.*
[2] *Astronomy Dept., University of Toronto, Toronto, Ontario, Canada.*
[3] *Dominion Astrophysical Observatory, National Research Council of Canada, Victoria, Canada*

Abstract

The Canada-France Redshift Survey (CFRS) sample contains 591 galaxies with secure redshift in the range $0 < z < 1.2$. We discuss here several results: (1) the luminosity function of blue galaxies evolves with epoch, equivalent to a brightening of $\sim$1 mag. by $z\sim$ 0.8, or a density change by a factor ~ 3, while for redder galaxies it is consistent with no-evolution; (2) HST imaging of a small sample of 32 CFRS galaxies with $z > 0.5$ shows that the luminosity of discs is higher than the local value by $\sim$1.2 mag. by $z\sim$0.7; (3) the amplitude of the two-point correlation function on scales $\sim 1h^{-1}$ Mpc is evolving with epoch, implying a clustering growth, $0 \leq \epsilon \leq 2$, faster than if the clustering was evolving with bound units of constant physical size.

1 Presentation of the Survey

The Canada-France Redshift Survey started from the merger of Canadian and French programs ([1]; [2]), prompted by the commissioning of the Multi-Object-Spectrograph at the CFHT in mid-1992. The goal of acquiring spectra for a sample of 1000 objects selected solely from the apparent magnitude $17.5 \leq I_{AB} \leq 22.5$ was defined ([3]). The scientific aims of the project were: *(i)* to define the galaxy population from the epoch-dependent luminosity function in rest-frame B-band, *(ii)* to determine the evolution of the small scale clustering properties of the galaxy population, *(iii)* to relate the faint field galaxy population to the radio sources revealed in the deepest VLA images, *(iv)* to allow construction of well defined samples of galaxies for SED, morphology, and kinematics studies.

Five high galactic latitude fields have been selected. The survey is based on deep photometry in the I band, supplemented by B, V and K' photometry for most fields ([3]). The spectroscopy of 1010 objects was conducted with the MOS-SIS spectrograph at CFHT, and completed in about 20 nights of observations thanks to the high multiplexing gain of the instrument ([4]). Great care has been taken to reduce the spectra and measure redshifts, with 3 independant data reduction. The final photometric catalogs contain more than 6000 galaxies, while the spectroscopic sample contains 1010 objects as follows: 200 stars, 591 galaxies with secure redshifts in the range $0 \leq z \leq 1.3$, 6 QSOs, 146 objects with uncertain or unknown redshifts, and 67 objects affected by observational problems placed in a supplemental list. Details of the data reduction and spectroscopic catalogs are given in papers CFRS-II to CFRS-V ([4][5][6][7]). Faint μJy radio-sources identifications are analyzed in Hammer et al. ([8]).

The mean redshift of the CFRS is z=0.56, with ≈350 galaxies with redshifts above z=0.5, considerably increasing the total number of galaxies ever identified at such redshifts.

2 The evolution of the luminosity function

The trivariate luminosity function of galaxies $\Phi(M, color, z)$ shows unambiguously that the population evolves, with strong differences as a function of color ([9]). The luminosity function of red galaxies shows very little change over $0 < z < 1$, consistent with no change at all with redshift over 2/3 of the age of the universe ($\Omega = 1$). A change of at most a few tens of a magnitude or ≈30% in density is allowed by the data. The blue galaxies show definite evolution for $z > 0.5$. At $0.5 \leq z \leq 0.75$, the luminosity function appears to have brightened by ∼1 magnitude, though it is not possible to disentangle luminosity from number density evolution. At higher redshifts, the evolution appears to saturate at the brightest magnitudes but continues at the fainter levels with a steepening of the luminosity function. At low redshifts, $z < 0.2$, a significant excess relative to the Loveday et al. ([10]) local luminosity function is seen around $M_{AB}(B) \sim -18$, similar to what is found in the local CfA survey ([11]). This population may represent the descendants of the blue population seen at higher redshifts. Given that the evolution is seen within a single well defined sample, we regard it as secure evidence for changes in the galaxy population, and believe that the no-evolution hypothesis ([12]) cannot be valid.

3 Luminosity vs. number density evolution: impact of HST imaging

The clear evolution of the luminosity function with epoch can be produced by either luminosity evolution of the galaxies or by number density evolution, or a combination of both. Luminosity evolution is expected from evolving stellar populations, while number density evolution can be produced by, e.g., widespread merging. The phenomena at play would have to last over timescales of several Gy to produce the evolution with epoch seen in the CFRS.

Both these effects can be investigated from imaging with the Hubble Space Telescope. Figure 1 shows the images of two galaxies in the CFRS observed with F814W during cycle 4. One can see the exquisite resolution and amount of details observed in these galaxies at more that half the age of the universe. Quantitative analysis of the images obtained with HST has been performed on 32 galaxies with secure redshifts $0.5 < z < 1.2$, using 2D image fitting. It shows that *(i)* the mean rest frame central surface brightness is $\mu_B(AB) = 20.2 \pm 0.25$, or 1.2 magnitudes brighter than the local Freeman value ([14]), *(ii)* 30% of the galaxies show irregularity or clear signs of interaction/mergers, *(iii)* 30% have blue compact components mostly in peculiar/asymmetric galaxies. These results are discussed in more detail in Schade et al. ([13]).

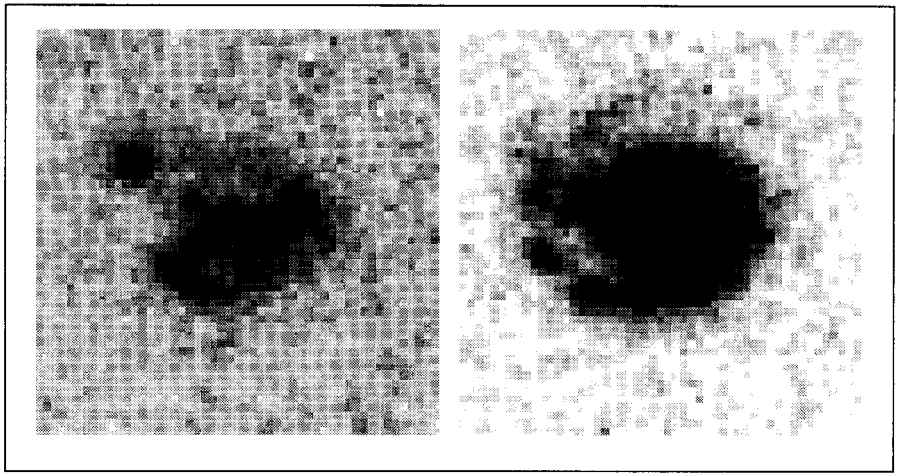


Figure 1: HST images of CFRS galaxies at z=0.602 (right) and z=0.989 (left), 6000sec. obtained in the F814W filter (I band). Image size is 5"x5".

4 Evolution of the clustering since z~1

It is expected that the clustering of galaxies must change with epoch in an expanding universe where structures evolve under the action of gravity. As a consequence, the two-point correlation function $\xi(r)$ should change with cosmic epoch, but the exact form of this evolution is at present poorly known. To account for the redshift accuracy from the low resolution CFRS spectra, we have computed the projected correlation function (see [15] for details)

$$\omega(r_p) = \frac{c}{H_0 \times (1+z)^2 \times (1+2q_0 z)^{1/2}} \int_{-\delta z}^{+\delta z} \xi(r_p, \pi) dz$$

with

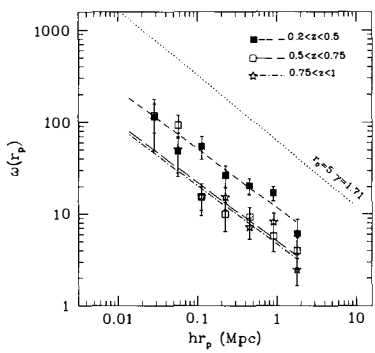
$$1 + \xi(r_p, \pi) = \frac{DD(r_p, \pi)}{DR(r_p, \pi)}$$

Owing to the peculiar catalog geometry ([4]), the random catalog has been constructed from the positions of CFRS galaxies but the redshifts have been selected at random, so as to follow the observed redshift distribution. Figure 2 shows $\omega(rp)$ computed for 3 redshift bins, while Figure 3 shows the correlation length $r_0(z)$ measured from power-law fits of $\omega(r_p)$, with $r_0(z)$ parametrized as

$$r_0(z) = r_0(0) \times (1+z)^{-(3+\epsilon)/\gamma}$$

We find that the clustering must grow faster, $0 \leq \epsilon \leq 2$, than if the clustering was evolving with bound gravitational units keeping a fixed physical size ([15]).

The auto-correlation of pair separations and power spectrum analysis do not find significant periodic patterns in the distribution of galaxies along the lines of sight, contrary to what was found by Broadhurst et al. ([16]). The two densest structures identified from the picket-fence redshift distribution correspond to a sheet of galaxies at z~0.985 ([17]), and a moderately rich cluster of galaxies at z=0.78 ([15]).



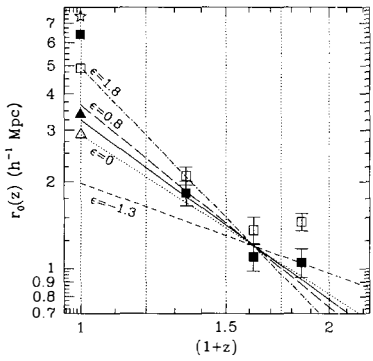


Figure 2 (left): 2–point correlation function $\omega(rp)$ computed in 3 redshift bins.
Figure 3 (right): evolution of the correlation length with redshift for $q_0 = 0.5$ ($q_0 = 0$ open squares). Symbols at z=0 represent the range of r_0 found locally ([18]).

References

[1] Tresse, L., Hammer, F., Le Fèvre, O., Proust, D., 1995, *Astr. Astrophys.* **277**, 53
[2] Lilly, S.J., 1993, *Astrophys. J.* **411**, 501
[3] Lilly, S.J., Le Fèvre, O., Crampton, D., Hammer, F., Tresse, L., 1995a, Ap.J., *CFRS–I, in press.*
[4] Le Fèvre, O., Crampton, D., Hammer, F., Lilly, S.J., Tresse, L., 1995a, Ap.J., *CFRS–II, in press.*
[5] Lilly, S.J., Hammer, F., Le Fèvre, O., Crampton, D., 1995c, Ap.J., *CFRS–III, in press.*
[6] Hammer, F., Crampton, D., Le Fèvre, O., Lilly, S.J., 1995, Ap.J., *CFRS–IV, in press.*
[7] Crampton, D., Le Fèvre, O., Lilly, S.J., Hammer, F., 1995, Ap.J., *CFRS–V, in press.*
[8] Hammer, F., Crampton, D., Lilly, S.J., O. Le Fèvre, T. Kenet, 1995, MNRAS, *CFRS-VII, in press.*
[9] Lilly, S.J., Tresse, L., Hammer, F., Crampton, D., Le Fèvre, O., 1995b, Ap.J., *CFRS–VI, in press*
[10] Loveday, J., Peterson, B.A., Efstathiou, G., Maddox, S.J., 1992, *Astrophys. J.* **390**, 338
[11] Marzke, R.O., Geller, M.J., Huchra, J.P., Corwin, H., 1994, *in press.*
[12] Koo, D.C., Gronwall, C., Bruzual A.G., 1993, *Astrophys. J.* **415**, L21
[13] Schade, D.J., Lilly, S.J., Crampton, D., Hammer, F., Le Fèvre, O., Tresse, L., 1995, Ap.J.Lett., *in press.*
[14] Freeman, K., 1970, *Astrophys. J.* **160**, 811.
[15] Le Fèvre, O., Hudon, D., Lilly, S.J., Crampton, D., Hammer, F., Tresse, L., 1995, *preprint.*
[16] Broadhurst, T.J., Ellis, R.S., Koo, D.C., Szalay, A.S., 1990, Nature, **343**, 726.
[17] Le Fèvre, O., Crampton, D., Hammer, F., Lilly, S.J., Tresse, L., 1994, *Astrophys. J.* **423**, L89
[18] Loveday, J., Maddox, S.J., Efstathiou, G., Peterson, B.A., 1995, *Astrophys. J.* **442**, 457.

THE ANGULAR CORRELATION FUNCTION OF FAINT FIELD GALAXIES

A. Campos [1], G. Yepes [2], M. Carlson [3], A.A. Klypin [3], M. Moles [4] and H. Joergensen [5]
[1] *Dept. of Physics, University of Durham, UK.*
[2] *Dept. Fisica Teorica, Univ. Autonoma de Madrid, Spain.*
[3] *Dept. of Astronomy, New Mexico State Univ., US.*
[4] *Instituto de Astrofisica de Andalucia, Spain*
[5] *Copenhagen Observatory, Denmark*

Abstract

In order to check the existence of strong large-scale clustering in the distribution of galaxies, we are building-up a new catalog of galaxies using CCD images. This catalog will allow us to measure the angular correlation function of galaxies over the same range of metric separations as the APM and about four magnitudes deeper. Preliminar results seem to indicate a flattening of the slope of the correlation at short scales with depth. We also detect a signal at ~ 1 deg., that we conservatively place as an upper limit to the correlation at those scales until new data becomes available.

1 Introduction

The angular correlation function of galaxies $\omega(\theta)$ measures the clustering of galaxies as seen in the plane of the sky. It is just the projection of its spatial equivalent, the two-point correlation function $\xi(r)$, which is directly related to the power spectrum of density fluctuations that characterizes the growth of structure in the Universe.
Estimation of $\omega(\theta)$ from the APM photographic survey revealed the existence of strong clustering of galaxies beyond $\sim 10h^{-1}$ Mpc [1]. The clustering of galaxies at large scales poses a severe observational constraint for cosmological models. Actually the APM data rules out one of the most popular models, the cold dark matter model with $\Omega = 1$ (i.e. flat Universe). Because the precise measurement of $\omega(\theta)$ is a crucial observational test in cosmology, the reliability of the

APM results has been intensely debated [2]
The measurement of $\omega(\theta)$ down to faint magnitudes can be used as a probe of the redshift distribution $N(z)$ of the objects, together with clustering evolution. In recent work it has been shown [3] that $\omega(\theta)$ can be approximately fitted by a power-law at short scales, with an amplitude that decreases faster than expected in non-evolving models. With regards to the slope there is some controversy. Whereas some authors can fit the *canonical* slope (~ 0.8) to their data, even to faint limits [4] [5], others claim to find a flattening with depth [6] [7].

2 The Catalog

We are building-up a new CCD catalog to measure $\omega(\theta)$ for faint galaxies. To date, we have 64 CCD fields in the northern hemisphere and 27 in the south, observed using the 2.5m INT telescope at La Palma Obs. and the 1.5m telescope at La Silla Obs. respectively. In what follows we will refer to the data in the northern hemisphere.
The CCD fields have a field of view of about $\sim 11' \times 11'$ each, and are distributed over an area of about $\sim 10^o \times 8^o$. Angular distance between contigous fields is approx. 0.8 deg.
Observations are being carried out in the R filter. We used FOCAS to automatically identify the galaxies in the fields and compute the magnitudes. Our number counts are consistent with counts previously published by other authors down to $R \sim 23$. For the slice $R = 22.5$ -- 23 we calculate to have a completeness of about $\sim 80\%$.
Weather conditions were excellent. Seeing was stable, around 1″ during the observing runs. The internal photometric consistency computed using the standard stars is better than $\sim 0.03-0.04$ mag. Also we checked that the number of galaxies in each of the individual fields was not correlated with the estimated brightness of the sky, seeing, night of observation or air mass.

3 The angular correlation function

We estimate $\omega(\theta)$ using the direct pair-counting method proposed by [8]: $\omega(\theta) = (DD - 2DR + RR)/RR$, where DD, DR and RR are the number of data-data, data-random and random-random pairs at an angular separation θ.

3.1 Short Scales

In Figure 1 (left panel) we show results for short scales. Solid lines are best fits to the data, whereas dashed lines correspond to the "classical" slope $\delta = -0.8$. The computation of $\omega(\theta)$ was made using the whole catalog.
At short scales only inter-frame pairs are considered, while the average density of galaxies is calculated using all the frames. As these are distributed over a large area $\sim 10^o \times 8^o$ deg., there is no need for an integral constraint correction, because this will be negligible.
In the Figure we see that there is a clear flattening of the slope of the correlation function with depth. The observed flattening has to be taken with caution, because it could partially but due to spureous signal introduced by field-to-field variations. Notice however that we estimate these to be small, due to the excellent observing conditions.
To check whether we do actually detect a flatening of the slope with the depth, we have

estimated $\omega(\theta)$ for the 64 individual fields, and taken the average. The correction for integral constraint was made in a self-consistent way. We first computed the integral $I = 1/\Omega^2 \times \int \theta^{-\delta} d\Omega_1 d\Omega_2$ using the slope fitted to the observed correlation function and for the geometry of one individual field. Then we calculated the amplitude A by fitting the relation: $\omega(\theta) = A \times (\theta^{-\delta} - I)$. The correlation function was then corrected by adding to it the quantity $A \times I$. A new value for the slope was then fitted, which was used to compute a new integral correction. This procedure was repeated until convergence was reached, tipically in 4-5 steps.

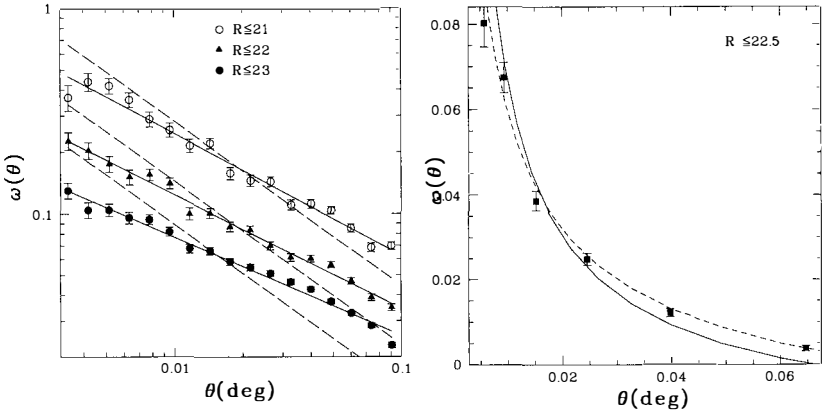


Figure 1 Observed angular correlation function for different depths. Errorbars correspond to 1σ poissonian errors. Lines are different fits as explained in the text.

By using this approach to the integral constraint correction, an slope flatter than $\delta = -0.8$ was also fitted to the correlation function computed using the individual fields, i.e. $\delta = -0.66$ for $R \leq 21.5$, $\delta = -0.6$ for $R \leq 22$ and $\delta = -0.55$ for $R \leq 22.5$. In Figure 1 (right panel) we plot the observed correlation function (linear plot) and the closest fitting functions of the form $A \times (\theta^{-\delta} - I)$ for $R \leq 22.5$. The solid line correspond to $\delta = -0.8$, and the dashed line to $\delta = -0.55$, as fitted using the iterative process to correct for the integral constraint.

3.2 Large Scales

In Figure 2 we show $\omega(\theta)$ for $R \leq 22$ (for both inter-frame and intra-frame scales) together with the slices of the APM scaled to match the amplitude of our data at short scales ($\sim 1'$). The APM slices were first fitted using a two power-law $\xi(r)$ with slopes -1.66 and -3. Then we used the full relativistic Limber formula to compute the shifts in $\log(\omega)$ and $\log(\theta)$, assuming a Schechter-like luminosity function with $M_* = -19.8$ and $\alpha = -1$ as well as clustering stable in physical coordinates. The shape of $\omega(\theta)$ is not much sensitive to galaxy evolution, opposite to the amplitude that can vary quite drastically with it. As we are mainly concerned about the ratio of power from short to large scales, to check the scale of the break, we did not include luminosity evolution.

In order to simulate the effect of field-to-field variations in the zero-point of the photometry on our results, we added a random shift to the zero point of the fields between -0.15 and 0.15 mag, and computed $\omega(\theta)$ for the resulting sample. This procedure was repeated 50 times. The average result and standard deviation for the 50 realizations are shown in Figure 3. Taking

into account that we formally have 0.03-0.04 mag of internal consistency, together with the fact that the majority of the images were taken at nearly the same air mass ($\sim$ 1) under stable, good seeing conditions, the error bars shown in the Figure at large scales provide a reasonable indication of the actual error (or even an upper limit). At short scales, we see that field-to-field variations, as expected, introduce some small spureous signal in $\omega(\theta)$.
Our preliminar results show an indication of a signal at 1 degree separation, which is consistent with APM results re-scaled to the depth of our catalog. The correlation function at 0.6-0.8 deg. degrees appears to be negative, and positive for 0.8-1.7 deg. These results will be confirmed by a more detailed analysis. At this stage, we conservatively treat the results as an upper limit.

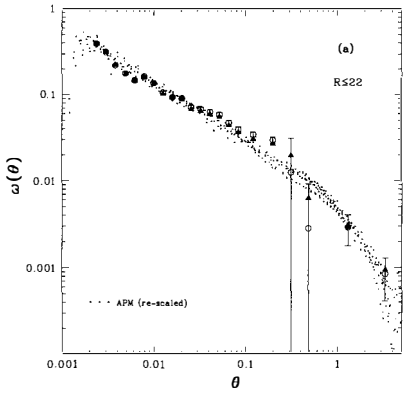


Figure 2 Angular correlation function for $R \leq 22$ galaxies (solid triangles). It is also shown the average result and standard deviation from 50 artificial data sets built-up by adding a random shift between -0.15 and 0.15 to the photometric zero-point of the CCD fields. Results for the slices of the APM scaled to fit the amplitude of our data at short scales (see the text) are shown as well.

References

[1] Maddox, S.J., Efstathiou, G., Sutherland, W.J. & Loveday, J. 1990, MNRAS 246 433.

[2] Fong, R., Hale-Sutton, D. & Shanks, T. 1992, MNRAS 257 650.

[3] Roche, N., Shanks, T., Metcalfe, N. & Fong, R. 1993, MNRAS 263 360.

[4] Couch, W.J., Jercevic, J.S. & Boyle, B.J. 1995, MNRAS in press.

[5] Brainerd, T.G., Smail, I. & Mould, J. 1995, ApJ in press.

[6] Neuschaefer, L.W. & Windhorst, R.A. 1995, ApJ 439 14.

[7] Pritchet, C.J. & Infante, L. 1992, ApJ Lett 399 L35.

[8] Landy, S.D. & Szalay, A.S. 1993, ApJ 412, 64.

MORPHOLOGICAL NUMBER-COUNTS FROM ULTRADEEP HST IMAGES

S. P. Driver, R. A. Windhorst
Arizona State University, Tempe, USA



Abstract

We discuss the observations leading to the Faint Blue Galaxy problem and the uncertainties upon which faint galaxy models are based. Using deep Hubble Space Telescope (HST) imaging with the Wide Field Planetary Camera (WFPC2), we show how morphological information has been used to shed new light on the problem. Initial results indicate that the giant galaxies (ellipticals and early-type spirals), are well fit by *no-evolution* standard models down to $m_I \sim 24.5$ ($z \sim 0.8$). The data also show that the faint blue galaxies have late-type/irregular morphologies and cannot be adequately modelled until better constraints are placed on the local space density for this class of galaxies.

1 Faint Galaxy Number-counts

One of the most basic astronomical observations is to simply count the number of galaxies in a given direction as a function of apparent magnitude and use these observations to help understand the nature of our Universe. The advantages of such a simple observation, is that good statistical data can be obtained over a large magnitude range. Figure 1 shows some of the *number-count* data, obtained by many groups over a wide range of magnitude. The original contention [21], was that data such as these would allow a direct measurement of the cosmological parameters (Ω, q_o, Λ) — the idea being that the departure of the number-counts from a purely Euclidean slope of 0.6 is attributable to the geometry of the Universe. The lines shown in Figure 1, reflect the predicted number-counts based on the best non-evolving standard models and it is clear that the models and the data strongly disagree at progressively fainter magnitudes. This discrepancy gives rise to the fairly long standing Faint Blue Galaxy (FBG) problem [23], [2], [24], discussed in the next section. In this article, we briefly outline the current state of the observations, the uncertainties that go into generating a faint galaxy model, and how the latest HST images, obtained with the WFPC2, now allow us to use morphological information to simplify the problem.

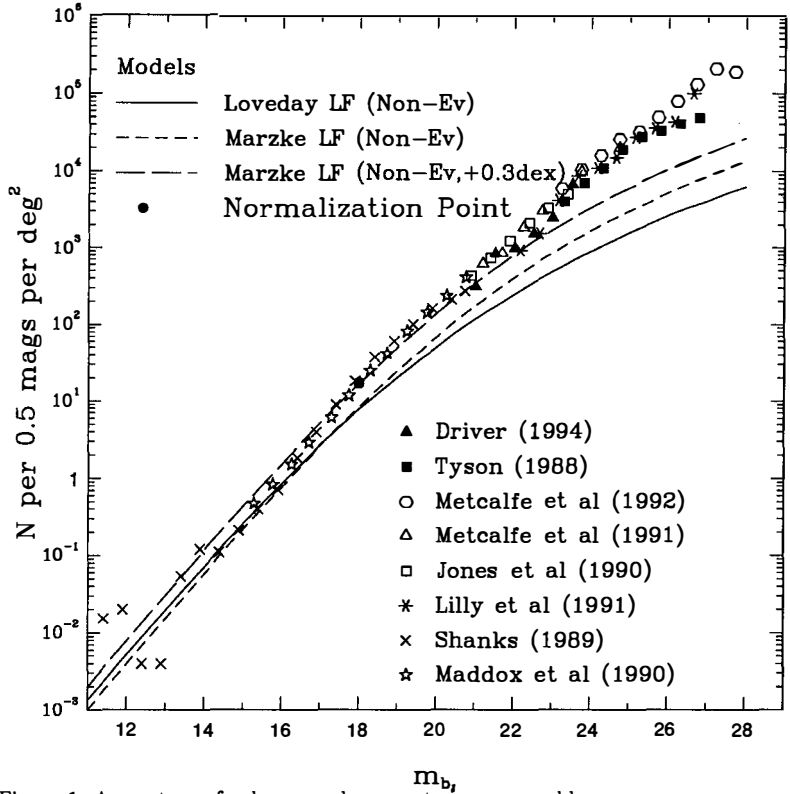


Figure 1: A montage of galaxy number-counts as measured by numerous groups over the past decade. The model lines show various predictions from the standard no-evolution models.

1.1 Observations

1.1.1 Number-counts Figure 1 shows the observed B-band number-counts, counts at longer optical and infra-red wavelengths follow shallower slopes at comparative magnitudes and come closer to matching the model predictions [24]. In fact the more recent deep K-band counts, [4], [16], lie close to the current standard model expectations. Essentially this simply states that the galaxies responsible for the faint excess in the B-band must be blue.

1.1.2 Colours The review article by Koo & Kron [24] contains an excellent diagram (see their Figure 2) of the colour-magnitude trend, from which two distinct pieces of information can be drawn. Firstly, the *mean* galaxy $(b_J - r_F)$ colour shifts towards the blue at fainter magnitudes (as we know it must from the number-counts in these bands), and secondly, the colour distribution broadens significantly at fainter magnitudes. This broadening is greater than the photometric errors at faint magnitudes, and would seem to imply that the observed galaxy population at faint magnitudes is *more diverse* than that observed locally in a magnitude limited sample. The mean observed colours of faint field galaxies in $(B - R)$, $(B - V)$ and $(V - R)$ have also been shown [8] to be consistent with the observed colours of late-type spirals and irregulars.

1.1.3 Redshift surveys The ideal data set required to fully resolve the FBG problem is a large, complete and well defined redshift survey to faint magnitudes. Unfortunately measuring redshifts for faint field galaxies is a particularly time-consuming process and current resources restrict the measurement of redshifts to galaxies brighter than $m_b < 24$, where the problem is less distinct (c.f. Fig. 1). The redshift surveys that have been made, e.g. [2] [17], all point to a redshift distribution whose shape is consistent with that expected from the current standard no-evolution models, but of course inconsistent in terms of absolute numbers. In total, these surveys represent only a few hundred galaxies with incompleteness limits in the range 70-90 %. While it may seem unlikely that the missing galaxies are mostly at high or low-z, the possibility cannot be ruled out, as the selection biases are poorly defined, and are likely to be a strong function of spectral range sampling, surface brightness and epoch[1].

1.1.4 Normalisation More worrisome perhaps, than the discrepancies between faint galaxy models and faint galaxy observations, is the apparent discrepancy between models and observations at relatively bright magnitudes ($m_b \sim 18$ mag). The solid line, in Figure 1, shows the current conventional model, based on a standard flat cosmology ($\Omega = 1, q_o = 0.5$) and the Mt. Stromlo-APM luminosity function (LF) [25]. And, at $m_b \sim 18$ mag ($z \sim 0.1$), there is already a discrepancy of a factor of two (0.3 dex) between the model and the galaxy counts. This discrepancy has been known for some time and is normally explained away in terms of a large local inhomogeneity [31], significant local evolution [26], incompleteness in the local surveys due to surface brightness and visibility constraints, [35] [5] [13], and/or systematic magnitude errors in the local surveys [28]. However, it is still unclear as to which effect(s) are responsible. Although, recent UKIRT observations, from which the local K-band LF has been derived [18], find a *higher* local normalisation suggesting that the previous local surveys have indeed suffered from high incompleteness.

1.2 Faint Galaxy Models

Despite the original aim of faint galaxy counts, the model predictions depend more critically on knowledge of the local LF [23] and any evolutionary processes [33], than on the cosmological parameters (Ω & Λ)[2]. To understand these dependancies, Figure 2 shows the inner workings of a typical faint galaxy model [7]. The thick line represents a prediction of the galaxy number-counts, based on knowledge of the local LF, k-corrections, a standard flat cosmology and no-evolution. Each of the dashed lines represents the contribution to the total counts from a narrow luminosity class. Immediately apparent are the effects of cosmology, most notably the k-corrections, which cause the departure of the individual lines from the Euclidean slope of 0.6. Hence at faint magnitudes the intrinsically more luminous (and therefore more distant) galaxies are effected more severely, and so the predicted counts at progressively fainter magnitudes depend more and more heavily on the contribution from the lower luminosity classes. Furthermore, at fainter magnitudes no one single luminosity class dominates the total counts, explaining perhaps the apparent diversity seen in the colour distribution and low correlation amplitude. Note that steepening the local LF has the effect of decreasing the distance between the dashed lines on Figure 2, so exascerbating this dependancy. Likewise evolutionary effects may cause an independent steepening or flattening of each line, dependent on the level and type of evolution for that luminosity class. All in all, the number of potential unknowns is extremely large.

[1] A galaxy undergoing a recent starburst is likely to exhibit larger equivalent widths in the characteristic spectral lines and so be rendered more readily detectable.

[2] For $\Lambda = 0$ models, the predicted number-counts are relatively *insensitive* to the matter density [12].

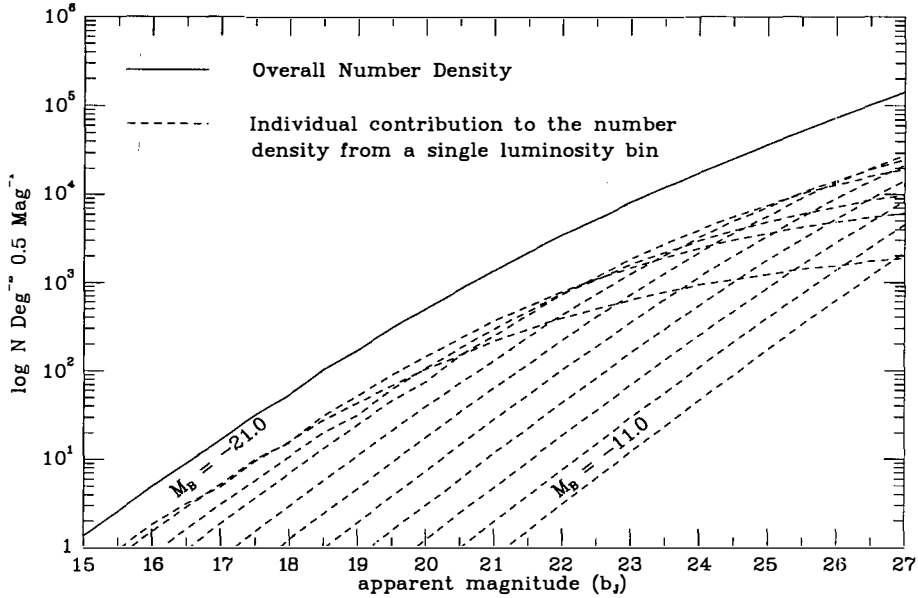


Figure 2: The "inner workings" of a faint galaxy model. The solid line shows the total prediction and the dashed lines show the contribution from each intrinsic luminosity interval.

1.2.1 The Cosmological Parameters Adopting an open $\Lambda = 0$ Universe (*i.e.* low q_o) reduces the decrease of the comoving volume element such that slightly higher counts are predicted at fainter magnitudes. However the gain is small, relative to the FBG problem (typically a factor of 2 at $m_b \sim 24$ compared to the deficit of 10 [12]). Alternatively adopting a large positive Λ will increase the predicted numbers sufficiently, to begin reconciling the models with the data - however such a solution over-predicts the number-counts at longer observed wavebands [12] [15] [6].

1.2.2 The Local Luminosity Function A more basic dependency of faint galaxy models is upon the true local space density of galaxies [8]. Various groups, [13], [29], have postulated that surface brightness selection effects in the local surveys may have led to an underestimation of the slope of the true Schechter function (SFn) [30], which is typically used to describe the local space density of galaxies. A more subtle problem, however, is the inadequacy of using a single SFn to describe a wide range of luminosity and morphological types. One must be wary of extrapolating the bright end of a SFn to faint intrinsic luminosities, where the available local data is scarce. In particular, SFn's are incapable of following a sudden change or discontinuity in the local luminosity distribution.

To illustrate these points, Figure 3 shows the data from the Mt. Stromlo-APM survey [25] in which $\sim$ 1800 galaxies were used to define a single global field SFn. The four insets represent four alternative luminosity functions. Models (a) and (b) are typical SFn representations, with differing slope parameters, while models (c) and (d) are Schechter-like functions, where an intial flat SFn is allowed to exhibit a discontinuous change in slope at some intermediate magnitude (intended to correspond to the giant/dwarf luminosity boundary at $M_{b_J} \sim -18$, [1]).

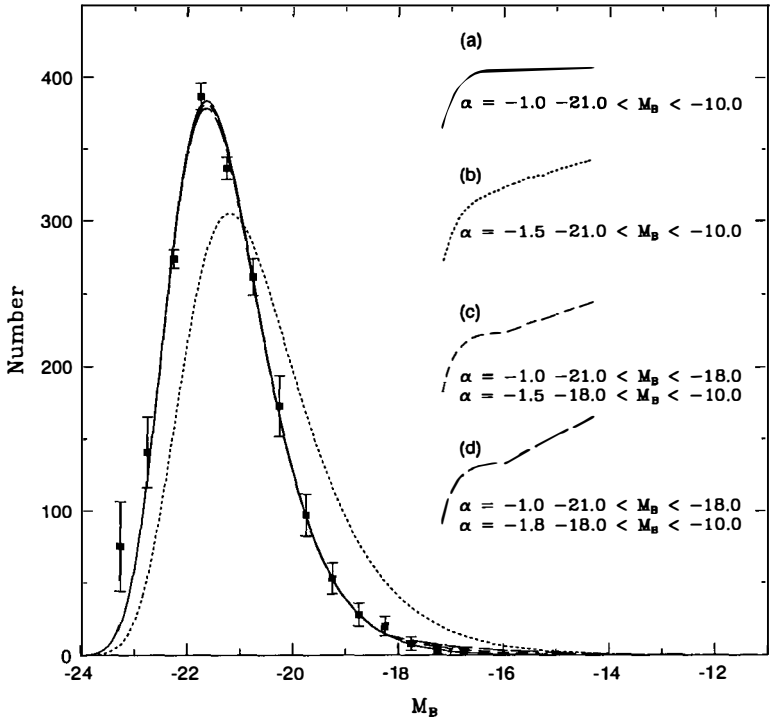


Figure 3: The observed Magnitude distribution of galaxies in a magnitude limited sample compared to four alternate LFs.

When these models are represented as they would be observed in a magnitude limited sample, *i.e.* in real numbers unadjusted for volume, models (a), (c) and (d) are indistinguishable. And, while the Mt. Stromlo-APM data can conclusively rule out a global SFn with a slope of $\alpha = -1.5$, it cannot rule out a turn up in the field luminosity function at luminosities fainter than $M_{b_J} \sim -18.0$. In reality this merely states that the local space density of low luminosity systems (dwarfs, irregulars etc) is extremely poorly constrained. One reason to perhaps suspect that the true luminosity distribution may indeed turn up, at fainter magnitudes, is from observations of clusters, where measurements of the luminosity distribution are more reliable. For example an upturn in the cluster LF has been noted in Coma, [20] [32], Virgo, [22], A963, [9], as well as various local groups [14], although some clusters show no such effect. In reality it is simply clear that there are no strong constraints, to date, as to the slope of the faint end of the field LF and, as already stated in §1.2, the predicted galaxy number-counts at faint magnitudes are critically dependant on knowing this faint end slope.

1.2.3 Evolution ? The more conventional explanation for the observed excess has always been to invoke some kind of luminosity evolution, [2] [33], and more recently merger evolution, fading dwarfs or other somewhat more imaginative scenarios. Clearly the Universe did not form with the current local galaxy population in place, and therefore some evolutionary process(es) must have occurred between the decoupling era and today. The question is when and by what mechanism. Typically luminosity evolution models are based on an initial star-burst,

after which the galaxies luminosity decays typically exponentially with time. The resulting galaxy luminosities vary typically as $(1+z)^{\gamma}$ and merger models normally follow the form luminosity $\propto (1+z)^{-\gamma}$ and number density $\propto (1+z)^{\delta}$. With reasonable values of γ and δ, the evolutionary effects far overshadow the discrepancy between low and high q_o models. However with the current variety of locally observed galaxy types it is unlikely that any single evolutionary scenario is responsible, or if so, then galaxy evolution is most definitely not coeval or ubiquitous and any single evolutionary model is likely to fail.

2 Galaxy Morphology using the Hubble Space Telescope

As outlined in the previous section, the number of unknowns upon which the typical faint galaxy model is based are very large. Given these uncertainties, it seems hardly surprising that the models and observations are not well matched. Additional observational constraints are required to help simplify the problem at hand. Since the refurbishment of the HST, detailed images of faint field galaxies at 0.1″ resolution have now be obtained. Typically previous ground-based images have been limited by atmospheric seeing to a resolution of 0.8″ and normally worse in the case of multiple stacked images taken over an appreciable time-span. The HST offers a factor of almost 100 increase in the number of independently sampled pixels, and so allows morphological details to be seen down to the faintest detectable magnitudes. Indeed, the effects of cosmology assist in the sense that the angular diameter of a fixed object varies little beyond redshifts $z > 0.5$, such that it is an objects apparent surface brightness which limits the ability to discern morphology, rather than telescope resolution.

With morphological information, it becomes possible to simplify the modelling process. For example, galaxies of a similar type are more likely to have evolved via a similar evolutionary mechanism, and so it would seem more realistic to adopt a separate evolutionary model for each type. The local LF is also better established for galaxies of certain type, e.g. ellipticals and early-type spirals. Ultimately, morphological segregation allows each morphological type to be modelled independently, so reducing the complexity of each individual model.

2.1 The HST Morphological Number Counts

Recently four morphological surveys of faint field galaxies have been made from the HST Medium Deep Survey (MDS): CRGINOW [3], DWG [10], DWOKGR [11] and GES [19]. The CRGINOW survey is based on the entire WF/PC data-set (11,500 galaxies) and the morphological typing is automated to distinguish between disk and bulge systems. The WF/PC data covers the range $18 < m_I < 21$. The other three WFPC2 surveys (each containing between 150 and 300 galaxies) extend this range to $m_I < 24.5$, based on eyeball classifications, typically made by a number of independent observers and using both the image data and the objects major-axis surface brightness profiles. Various consistency checks suggest that the morphological accuracy is ~ 1 Hubble-type, hence the three WFPC2 studies classify galaxies into three broad classes, E/S0's (bulges), Sabc's (bulge-disks) and Sd/Irr's (disks and asymmetrical systems).

Figure 5 shows the morphological number-counts for (a) all types, (b) E/S0s, (c) Sabc's and (d) Sd/Irrs. The counts for all types, agree well with groundbased counts and show the usual trend of a steep slope. The dotted and dashed lines in Fig. 5a illustrate the conventional no-evolution models which show the usual underprediction of the galaxy counts at fainter magnitudes. The other three panels in Figure 5 represent the new morphological number counts, as revealed by MDS studies of WF/PC and WFPC2 data.

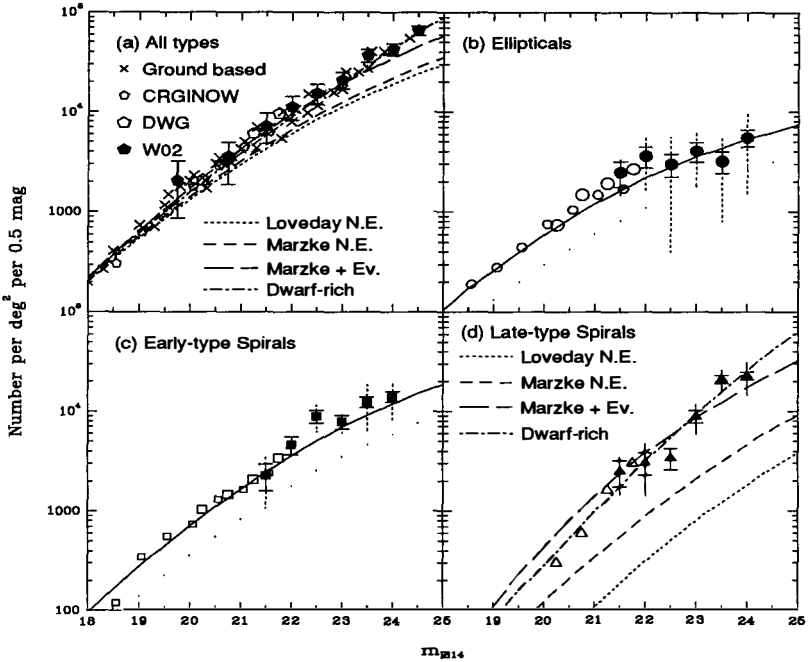


Figure 4: Morphological galaxy counts from HST WFPC2 images

2.2 Modelling the Morphological Number-counts

For each of the morphological groupings shown in Figure 5b, c & d we show the predictions from the standard best fit no-evolution models. These models assume a standard flat cosmology and the local LFs as derived by MGHC [27], all re-normalised by the same factor of 2 for the reasons outlined in §1.1.4. For simplicity, no-evolution is incorporated into the models and the models do not include any isophotal selection effects. From comparisons between the predictions of these basic models and the morphological counts, we can see that:
(i) Elliptical and S0s appear to follow closely the prediction based on a standard flat cosmology, no-evolution and a flat re-normalised luminosity function.
(ii) Early-type spirals similarly appear to follow the predicted number-counts for this type.
(iii) The Late-type Spirals and Irregulars are severly under-predicted by the models based on either the Loveday *et al* LF [25], or the Marzke *et al.* LF [27].

The primary conclusion is clear: *it is the late-type/Irregular population which is responsible for the faint blue galaxy excess*, and this is fully consistent with the earlier discussion that it is the properties of these types of galaxies of which we are most uncertain. The second conclusion is more unexpected in that, *the elliptical and early-spirals are remarkably well fit by the standard no-evolution models.* This implies that little or no evolution has occurred in these populations out to $m_I \sim 24.25$ (or $z \leq 0.8$), and that the standard cosmological model cannot be grossly incorrect. In fact, the possibility now exists to return to the initial aim of faint galaxy number-counts and start using morphological galaxy counts, of E/SO's say, to constrain cosmological models, and in particular Λ. This exciting prospect is not discussed further here but see [12] for more details.

Two more subtle points are also borne out with regards to LF normalisation. The first is that the individual LFs have each been re-normalised by the same amount, the fact that despite this both the E/SO and Sabc models match their respective counts, argues against an evolutionary or incompleteness explanation to the normalisation problem — as such solutions would be expected to effect these types to different degrees. The second point is that the shape of the E/SO and Sabc curves closely follow the shape of the counts, regardless of normalisation. Hence, if significant local luminosity or number evolution had occurred, then it would have to switch off, over the regime shown in Figure 5, for the shape of the counts to remain consistent with the no-evolution predictions. Both of these points are somewhat tentative, but argue for a large local inhomogeneity or a systematic zero point error explaining to the normalisation problem.

Finally, concentrating on the late-type Irregular population alone, we can attempt to determine how best the models can be reconciled with the observations. If these systems are genuine late-type spirals and Irregulars, their intrinsic luminosities are likely to be low, and hence their corresponding redshifts will also be low, ruling out any cosmological effects. Briefly we can consider the two extremes: (a) a non-evolving solution, and (b) an evolving solution based on the conventional Mt. Stromlo-APM LF.

2.2.1 A Dwarf Dominated Model To reconcile the predicted number-counts to the observations of Sd/Irr's alone without evolution requires increasing the normalisation of the late-type LF by a factor of 5 and increasing the Schechter slope to $\alpha = -1.8$ (dashed line on Fig. 5d, [8]). Such an increase has been shown to be inconsistent [7] with the faint redshift surveys, e.g. [17], which find little or no evidence for a low-z bump in the redshift distribution at faint magnitudes.

2.2.2 An Evolving Standard-Dwarf Model Conversely we can consider the level of evolution required to reconcile the observations to the predictions by adopting some simple parmaterisation of the luminosity evolution of dwarf galaxies, assuming the conventional flat faint end slope [25]. For example, if we assume a ubiquitous starburst at $z = 0.5$ in the entire population, afterwhich the luminosity decays exponentially with time [29], we find that 2 magnitudes of evolution is required in the entire dwarf population to match the observations ([11], large dashed line on Figure 5d). Although alternative evolutionary scenarios are possible, such as merging, the level of evolution required is extraordinarily high.

3 Conclusions

The faint blue galaxy problem, which has been with us for almost two decades, has been "morphologically resolved" due to the superb quality of the WFPC2 data from the refurbished Hubble Space Telescope. By segregating the faint galaxy number-counts into three broad morphological types (E/S0, Sabc, Sd/Irr), a significant step forward in the observational constraints has been made. The independent elliptical and early-type spiral number-counts follow closely the predictions of the non-evolving standard model, based on a standard flat cosmology and knowledge of the local space densities of these types. No significant luminosity or merger evolution is required to reconcile these observations with the models and, assuming no cosmic conspiracy, this places the end of the epoch of giant galaxy formation to $z \geq 0.8$.

As a side product, it may now become possible to constrain cosmological models using these morphological number-counts, although clearly a far larger statistical sample is required, as is

spectroscopic confirmation of the morphological typing. The principle remaining problem then, is the required renormalisation of the models at relatively bright magnitudes.

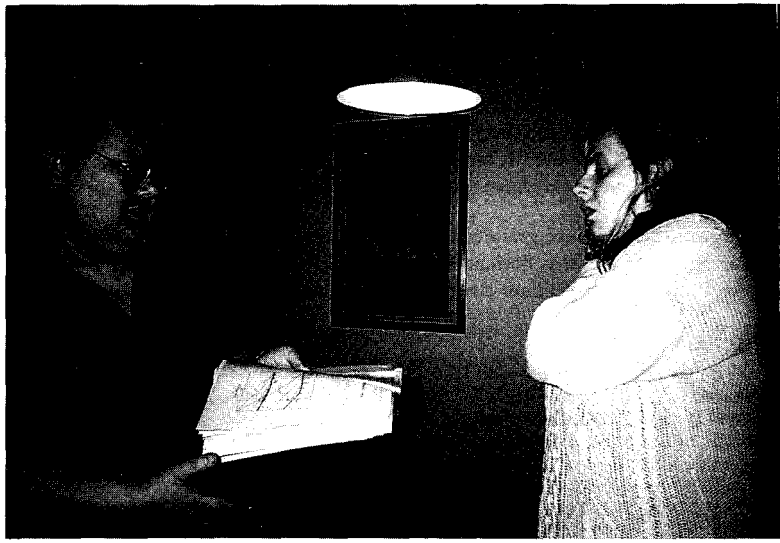
The morphological types responsible for the faint blue excess have been shown to be systems consistent with late-type/Irregular morphologies. Their observed number-counts disagree with model predictions for this type by a factor of 10 ! However, it is precisely this population for which the local properties (e.g. local space density and star-forming mechanisms) are poorly understood, so that the FBG problem is simply a reflection of this fact. Neither steepening the local faint end slope of the LF, nor evolution of a flat faint-end can alone provide viable solutions. However a combination of these two effects can provide a plausible solution [29].

In summation the faint blue galaxy excess has been isolated, the morphologies determined, but the balance between star-bursts, mergers and/or a steep faint end slope is unclear, and liable to remain so until improvements have been made in our knowledge of the local late-population.

Acknowledgements. We are grateful to the other Medium Deep Survey team members and in particular Richard Griffiths, Stefano Casertano, Eric Ostrander and Karl Glazebrook and also to Steve Phillipps and William Keel for informative discussions.

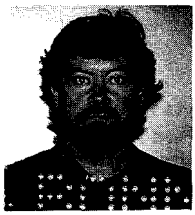
References

[1] Bingelli B., Sandage A., Tammann G.A., 1988, *Ann. Rev. in Astron. & Astrophys.* **26**, 509
[2] Broadhurst T.J., Ellis R.S., Shanks T., 1988, *Mon. Not. R. astr. Soc.* **235**, 827
[3] Casertano S. *et al.*, 1995, *Astrophys. J.* **in press**
[4] Cowie L.L. *et al.*, 1994, *Astrophys. J.* **434**, 114
[5] Disney M.J., 1976, *Nature* **263**, 573
[6] Djorgovski S., *et al*, 1995, *Astrophys. J. Letters.* **438**, L13
[7] Driver S.P., 1994, PhD Thesis, Univ. of Wales
[8] Driver S.P. *et al.*, 1994, *Mon. Not. R. astr. Soc.* **266**, 155
[9] Driver S.P. *et al.*, 1994, *Mon. Not. R. astr. Soc.* **268**, 393
[10] Driver S.P., Windhorst R.A., Griffiths R.E., 1995 *Astrophys. J.* **in press**
[11] Driver S.P. *et al.*, 1995, *Astrophys. J. Letters.* **in press**
[12] Driver S.P., Phillipps S., Bristow P.D., Windhorst R.A., 1995, *Mon. Not. R. astr. Soc.* **sub.**
[13] Ferguson H., McGaugh S.S., 1995, *Astrophys. J.* ,, 440470
[14] Ferguson H., Sandage A., 1991, *Astron. J.* **96**, 1620
[15] Gardner J.P., Cowie L.L., Wainscoat R.J., 1993, *Astrophys. J. Letters.* **415**, L9
[16] Glazebrook K., Peacock J., Collins C., Miller L., 1994, *Mon. Not. R. astr. Soc.* **266**, 65
[17] Glazebrook K. *et al.*, 1995, *Mon. Not. R. astr. Soc.* **273**, 157
[18] Glazebrook K., Peacock J., Miller L., Collins C.A., 1995, *Mon. Not. R. astr. Soc.* **in press**
[19] Glazebrook K., Ellis R.S., Santiago B., 1995, *Mon. Not. R. astr. Soc.* **sub.**
[20] Godwin J.G., Peach J.V., 1982, *Mon. Not. R. astr. Soc.* **200**, 733
[21] Hubble E, 1936, in *The Realm of the Nebulae*, Yale Univ. Press
[22] Impey C., Bothun G., Malin D.F., 1988 *Astrophys. J.* **330**, 634
[23] Kron R.G., 1982, Vistas in Astronomy, 26 37
[24] Koo D.C., Kron R.G., 1992, *Ann. Rev. in Astron. & Astrophys.* **30**, 613
[25] Loveday J., Peterson B.A., Efstathiou G., Maddox S.J., 1992, *Astrophys. J.* **390**, 338
[26] Maddox S.J. *et al.*, 1990, *Mon. Not. R. astr. Soc.* **243**, 692
[27] Marzke R., Geller M.J., Huchra J.P., Corwin Jr H.G., 1994, *Astron. J.* **108**, 437
[28] Metcalfe N. Fong D., Shanks T., 1995, *Mon. Not. R. astr. Soc.* **in press**
[29] Phillipps S., Driver S.P., 1995, *Mon. Not. R. astr. Soc.* **in press**
[30] Schechter P., 1976, *Astrophys. J.* **203**, 297
[31] Shanks T., 1989, in *The Extra-Galactic Background Light*, eds Bowyer S.C., Leinert C., pub Kluwer Academic Publishers
[32] Thompson L.A., Gregory S.A., 1993, *Astrophys. J.* **106**, 2197
[33] Tinsley B.M., 1977, *Astrophys. J.* **216**, 349
[34] Windhorst R.A., Keel W.C., 1995, *Astrophys. J. Letters.* **sub.**
[35] Zwicky F., 1957, in *Morphological Astronomy*, Springer-Verlag



EVOLUTION OF THE GALAXY PAIR RATE

L. Infante, P. Universidad Católica de Chile
R. Carlberg, University of Toronto, Canada
C.J. Pritchet, University of Victoria, Canada



Abstract

To study the merger rate with redshift faint galaxy pairs (with separations $< 20h^{-1}kpc$) have been selected from Canada-France-Hawaii (CFHT) and ESO New-Technology-Telescope (NTT) images in the V band. We have carried out observations of fields near the North Galactic Pole (NGP) and the South Galactic Pole (SGP). In this paper we report on the results obtained from the NGP data. An statistical comparison is performed between close pairs and the field galaxy population. Redshifts of 14 galaxies ($V \leq 22.5$, $< z >= 0.36$) in close pairs ($\theta < 6$ arcsec) and 38 field galaxies ($< z >= 0.42$) have been used in the analysis. We find that, (a) the similarity of the two redshift distributions, $\Delta z \leq 0.1$, limits any differential luminosity enhancement of close pairs to less than half a magnitude. (b)The pairs are somewhat bluer than the field and have nearly twice the average [O II] detection rate of the field, but the differences are not statistically significant. (c) Physical pairs comprise about 7% of the faint galaxies in our survey fields. The same physical separation applied to local galaxies finds only 2.6% in pairs.

1 Introduction

Faint galaxies are much more numerous than predicted by no-evolution models[1] ($10\times$ at $m_B = 25$). This observation seems to demand strong luminosity evolution in the faint galaxy population; yet the redshift distributions n(z) of faint galaxies are remarkably consistent with no-evolution predictions, with a surprisingly low median redshift of $z \simeq 0.3$ at $m_B \simeq 21 - 22.5$ [2-4]. The observed redshift distributions predict, using a straightforward calculation with little model dependency, angular correlation amplitudes that are about a factor of 2 higher than those observed over a wide range from $20 < m_B < 24$. The factor of 2 excess in the counts N(m), and the correlation deficiency, can be neatly resolved by introducing a "new", weakly clustered population at the surprisingly low redshifts of $0.2 < z < 1$[5,6]. However, some form of luminosity-dependent evolution must be invoked to brighten invisible low-L galaxies at $z = 0$ to $\sim L^*$ at $z \simeq 0.3$, yet maintain the no-evolution shape of n(z)[2-4].

An alternate method for generating larger numbers of galaxies in the past is to invoke mergers. The merger rate is expected to possess a strong redshift dependence[7], varying roughly as roughly as $(1+z)^m$, where $m \sim 4.5\Omega^{0.4}$. A growing body of observational evidence supports

a higher rate of dynamical interactions in the past[2,3,8–14], including close pairs[8] $m \simeq 4$, cluster bluing[9] $m \approx 5$, faint galaxy $n(z)$[2,3,10] $m \approx 5$, IRAS counts[11] $m \approx 3$, QSOs[12,13] $m \approx 6$, and IRAS z's[14] $m = 6.7 \pm 2.3$. but almost all such evidence is indirectly connected to merging and is limited to small samples of objects. "Passive" mergers (in which total L is conserved) by themselves do not help the excess galaxy problem[4]. However, mergers may be expected to induce star formation and make galaxies brighter and bluer[15], and hence provide some of the evolution required to explain the observations.

In this paper we seek a deeper understanding of the nature of galaxies at intermediate z. Specifically, we obtain an independent redshift survey of galaxies at faint magnitudes. We compute $\omega(\theta)$ at small separations, $\theta < 6''$. And, we evaluate the role of mergers in galaxy evolution at intermediate z.

2 Observations

The NGP observations were carried out in March 1992 with the CFHT using the Marlin multi-object imaging spectrograph with a Ford 1024^2 CCD. Imaging observations were acquired on 7, $6' \times 6'$ fields in Johnson V and Kron-Cousin I filters. Masks for the MOS plates were produced by assigning slits to galaxies in pairs and filled with field objects at $V < 22$. Magnitudes were obtained for 1062 objects of which 2/3 were classified as galaxies. The photometric errors are ~ 0.1 at $V = 22.5$ and $I = 22$. For more details see Carlberg *et al.* (1994)[16].

3 Results

53 redshifts of galaxies drawn from a $V \leq 22.5$ photometric sample of $\simeq 300$ galaxies were measured, 14 of which correspond to galaxies in close pairs. Pairs are defined as objects closer than $6''$ on the sky. The pairs are compared to a sample of nearby pairs assembled from the UGC catalog with the same projected physical separation.

A first result of this study is that the mean redshift of the pair population is very similar to the mean redshift of the field galaxies at the same magnitude limit. This limits the differential luminosity evolution between the field and pairs to less than ~ 0.5 mag difference. The small magnitude difference implies that if an average pair has interaction induced star formation, it only adds 13% more stellar mass on the average. Integrated over the lifetime of the galaxy this could account for the entire stellar mass, but as an upper limit, given the observational constraints we have derived.

A second result is that the rise of the fraction of galaxies in close physical pairs implies that the merger rate–redshift relation is $(1+z)^{3.4 \pm 1.0}$ over the interval $0 < z < 0.4$. This result is somewhat shallower than that of Zepf and Koo[8]; however it should be more reliable because uncertainties concerning the redshift distribution of the pairs have been removed. When combined with theoretical modeling of the expected merger rate-redshift relation, our observations have two important implications. If all of these galaxies do merge, then the average mass at $z \simeq 0.4$ is reduced by 32%, and by a factor of ~ 2.7 at redshift 1 (the latter result depending significantly on the accuracy of the model used for the extrapolation). Secondly, the slope of the merger-rate redshift relation indicates $\Omega \simeq 1.1 \pm 0.55$. The combination of model dependencies and large random error makes this density estimate less than compelling.

A third result is an excess correlation at projected separations of $< 20h^{-1}$ kpc. The strong correlation at $r \lesssim 20h^{-1}$ kpc could be either a local bound population, or the result of a luminosity enhancement of intrinsically faint galaxies in close pairs.

There are several limitations inherent in this study. A larger photometric and redshift sample would allow a conclusive check of the color differences between field and pairs, which are expected to be in the range of 10%, because the field is so much bluer than observed locally. In this study there is no conclusive direct indicator that mergers have taken place, or will take place, other than the (difficult to quantify) distortion morphology; nor is there any direct indication that pairs have excess star formation rates. The relative rate of merging is established to within an accuracy of a factor of two, but the absolute rate is still poorly known, and the impact of merging on the mass function hinges upon an integral over the absolute rate.

Mora data have been collected at the South Galactic Pole with the ESO NTT to increase the number of pairs. Reductions and analysis of these data are in progress.

This work was supported in part by FONDECYT grant #1930570.

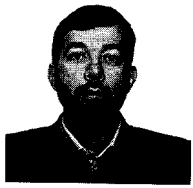
References

[1] Maddox *et al.* 1990, MNRAS, **247**,1P
[2] Colless, Ellis, Taylor, and Hook 1990, MNRAS, **244**, 408.
[3] Broadhurst, Ellis and Shanks 1988, MNRAS, **235**, 827.
[4] Lilly, Cowie, and Gardner 1991, ApJ, **369**, 79.
[5] Efstathiou, Bernstein, Katz, Tyson and Guhathakurta, 1991, ApJ, **380**, L47
[6] Infante and Pritchet 1994, ApJ, **439**, 565
[7] Carlberg 1990, ApJ, **359**, L1.
[8] Zepf and Koo 1989, ApJ, **337**, 34.
[9] Butcher and Oemler 1984, ApJ, **285**, 426.
[10] Koo and Kron 1987, in IAU 124, p. 383.
[11] Lonsdale *et al.* 1990, ApJ, **358**, 60.
[12] Schmidt and Green 1983, ApJ, **269**, 357.
[13] Boyle, Shanks and Peterson 1988, MNRAS, **235**, 935.
[14] Saunders *et al.* 1990, MNRAS, **242**, 318.
[15] Larson and Tinsley 1978, ApJ, **219**, 46.
[16] Carlberg, Pritchet and Infante, 1994, ApJ, **435**, 540



CLUSTERING PROPERTIES OF THE LYα CLOUDS

S. Cristiani [1], S. D'Odorico[2], V. D'Odorico[1], A. Fontana [3], E. Giallongo [3] and S. Savaglio[4]
[1] *Dipartimento di Astronomia dell'Università, Padova, Italy.*
[2] *European Southern Observatory, Garching, Germany.*
[3] *Osservatorio Astronomico di Roma, Monteporzio, Italy.*
[4] *Dipartimento di Fisica dell'Università, Cosenza, Italy*



Abstract

The spectra of the QSOs PKS2126-158 ($z_{em} = 3.27$) and Q0055-269 ($z_{em} = 3.66$) have been observed at high resolution ($2.2 - 2.7 \times 10^4$). Significant clustering, with $\xi \simeq 1$ at $\Delta v = 100$ km s^{-1}, is detected in both cases for lines with $\log N_{HI} \geq 13.8$. A similar result is obtained analysing the data available in the literature for Q0014+81. An anticlustering signal is also detected on scales $\Delta v \sim 600$ km s^{-1}. Two voids of size ~ 2000 km s^{-1} are found in the spectrum of Q0055-269 with a probability of 2×10^{-4}.

1 Clustering properties of the Ly$_\alpha$ lines

No clustering in the velocity space has been detected so far for Ly$_\alpha$ lines on scales $300 < \Delta v < 30000$ km s^{-1} ([11], [12], [15]). Their spatial distribution is different from that of the metal-line systems selected by means of the CIV doublet, that are known to cluster on scales at least up to 600 km s^{-1} ([13]). Preliminary results at high resolution seem to indicate weak clustering on smaller scales ($\Delta v = 50 - 300$ km s^{-1}, [14], [1]).

Although clustering is expected to decrease with redshift, from an empirical point of view it is attractive to push the observations towards high redshifts: the larger the density of lines, the better the chances of detecting a clustering signal. For this reason we have chosen two relatively high-z QSOs, PKS216-158 ($z_{em} = 3.27$) and Q0055-269 ($z_{em} = 3.66$), to be observed at ESO La Silla with the NTT telescope and the EMMI instrument in the echelle mode ([2], [5] and unpublished observations). The weighted mean of the flux-calibrated spectra have a resolution $R \sim 27000$ and $R \sim 22000$ for PKS2126 and Q0055, respectively. The signal-to-noise ratio per

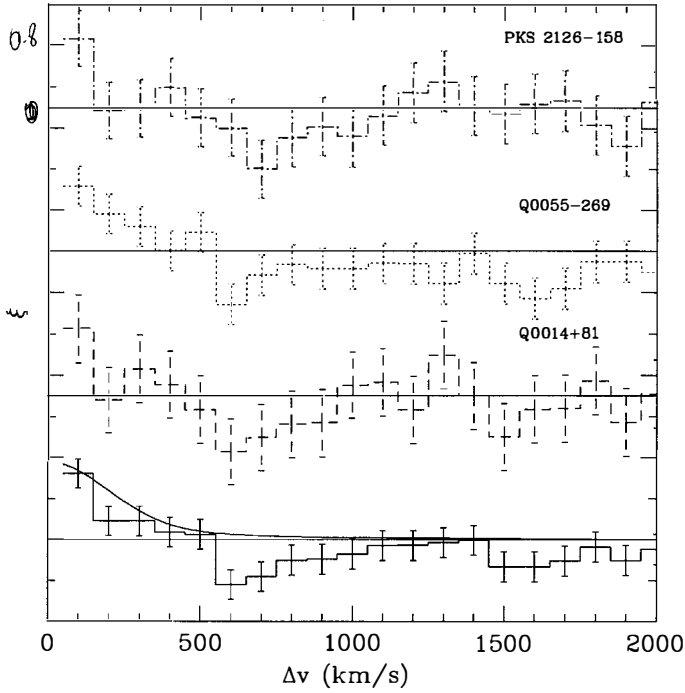


Figure 1: Two-point correlation function of the Lyman–α lines: PKS2126-158 (dot-dashed line), Q0055-269 (dotted line), Q0014+81 (dashed line) and weighted mean of the three (continuous line). For each histogram the horizontal continuous line defines the zero level. The distance between two tick marks on the y-axis corresponds to 0.5 units. The continuous curve superimposed to the lowest histogram is the model described in Sec. 2 computed from eq. (2) with $\gamma = 1.77$, $\sigma = 150$ km s^{-1}, $r_{cl} = 110$ kpc and $r_o = 280$ kpc at $z = 3$.

resolution element at the continuum level ranges from $S/N \sim 10$ to 40 in the region between Ly$_\alpha$ and Ly$_\beta$. Column densities and Doppler widths of the Ly$_\alpha$ lines and metal-line systems have been derived by a fitting procedure ([6]). The statistical distribution of the Doppler parameter for the Ly$_\alpha$ lines is peaked at $b \simeq 23$ km s^{-1}. The column density distribution is described by a power-law with a break or cutoff at $\log N_{HI} \simeq 14.5$. A featureless distribution is rejected with a probability of $> 99.9\%$.

We have computed the two-point correlation function in the velocity space for PKS2126-158, Q0055-269 and Q0014+81 ([10]) as:

$$\xi(v, \Delta v) = \frac{N_{obs}(v, \Delta v)}{N_{exp}(v, \Delta v)} - 1 \qquad (1)$$

where N_{obs} is the observed number of line pairs with velocity separations between v and $v + \Delta v$ and N_{exp} is the number of pairs expected from a random distribution in redshift. In our line sample N_{exp} has been obtained averaging 1000 numerical simulations generated according to

the cosmological distribution $\propto (1+z)^{\gamma}$, derived from the maximum likelihood analysis of the real line sample in the appropriate interval of column density and redshift. In this way it is possible to correct for incomplete wavelength coverage due to gaps in the spectra or occultation of weak lines by strong complexes. The region within 8 Mpc from the quasar has been excluded because of the proximity effect. No velocity splittings $\Delta v < 25$ km s^{-1} were included because of the intrinsic line blending due to the typical widths of the Ly$_\alpha$ lines. The 1σ deviation from a random distribution has been estimated as $N_{exp}^{-1/2}$, a good approximation in the case of weak clustering $\xi \leq 1$. The resulting correlation function of the Ly$_\alpha$ lines shows a weak but significant signal for all three QSOs on scales $\Delta v \sim 100$ km/s. Exploring the variations of the correlation as a function of the column density, an increase appears as the column density threshold is raised. The maximum significant signal is obtained for lines with $\log N_{HI} \gtrsim 13.8$, for which the measured correlation functions are $\xi_{2126} = 0.83 \pm 0.34$ ($\log N_{HI} \geq 13.85$) $\xi_{0055} = 0.79 \pm 0.24$ ($\log N_{HI} \geq 13.85$), $\xi_{0014} = 0.81 \pm 0.41$ ($\log N_{HI} \geq 14.1$), for $\Delta v = 100$ km s^{-1} (Fig. 1). When computing ξ for lines in the range $\log N_{HI} < 13.6$ (including in the simulated spectra gaps due to lines with $\log N_{HI} > 13.8$), no significant clustering is observed.

The correlation found for the Ly$_\alpha$ cloud positions is less pronounced than for metal-line absorption systems or galaxies, but consistent with a scenario of gravitationally induced correlations, as expected in models where gravitation is an important confining agent ([8]). The correlation found would imply, in the standard CDM framework, that the Ly$_\alpha$ clouds responsible for the weakest absorption are abundant in underdense regions.

Significant anticlustering is detected at scales $\Delta v \sim 600$ km s^{-1} (Fig.1). Possible origins for this phenomenon are inhomogeneities in the UV ionizing background and variations in the baryon to dark matter ratio due to reionization processes (see Bouchet, this meeting).

2 The dimensions of the Ly$_\alpha$ clouds

At small velocity differences the three-dimensional spatial autocorrelation function ξ_r and the redshift autocorrelation function are related by the convolution ([7]):

$$\xi_v = \int_0^\infty H dr\ \xi(r)\ P(v \mid r) \propto \int_{r_{cl}}^\infty \frac{H dr}{\sigma} \left(\frac{r}{r_o}\right)^{-\gamma} \left[e^{-\frac{(Hr-v)^2}{2\sigma^2}} + e^{-\frac{(Hr+v)^2}{2\sigma^2}}\right] \qquad (2)$$

where a Gaussian distribution of the peculiar motions with respect to the Hubble flow is assumed together with a power-law spatial correlation function of the galaxy-type.

At small velocity splittings, the redshift correlation scale r_o depends mainly on the cloud sizes r_{cl} and on the velocity dispersion. Although these quantities are poorly known, it is instructive to derive constraints on the cloud sizes and velocity dispersions from the observed correlation. Assuming an index $\gamma = 1.77$ for the power-law spatial correlation function, the fit shown in Fig.1 provides upper limits on the cloud sizes as a function of the velocity dispersion and of the appropriate correlation scale. We obtain $r_{cl} \sim 100 - 190$ kpc for $\sigma_v = 50 - 160$ km s^{-1}, and $r_o \sim 245 - 420$ kpc, respectively. In the former case a good fit to the overall shape of the observed correlation function requires a very low value $\gamma = 1.1$. For $\sigma_v > 200$ km s^{-1} the redshift correlation function becomes too flat and very steep γ values are needed (e.g. $\sigma_v = 300$ km s^{-1} requires $\gamma = 4$).

3 Voids in the Ly$_\alpha$ forest

Voids in the Ly$_\alpha$ forest also provide a test for models of the large-scale structure and of the homogeneity of the UV ionizing flux. Searches for megaparsec-sized voids have produced a

couple of claims ([3], [4]), but uncertainties in the line statistics strongly influence the probability estimate ([9]). High resolution data, less affected by blending effects, are ideal in this respect.

We have searched for gaps in a sample of Ly_α lines of Q0055-269 limited, to ensure statistical completeness and accuracy in the deblending, to $\log N_{HI} \geq 13.3$ and $b \leq 30$ km s^{-1}. Two regions devoid of such lines have been found, centered respectively at $\lambda \sim 5000, 5206$ Å, with sizes $\Delta v \sim 2009, 2046$ km s^{-1} (i.e. ~ 20 Mpc). To establish the random probability of observing such gaps, a set of 50000 spectra have been simulated with the observed number ($N = 178$) of redshifts randomly generated in the same interval of the data (excluding the region within 8 Mpc from the quasar) according to the cosmological distribution. The probability of getting a gap larger than the maximum observed one is then $\simeq 0.02$. The 2046 km s^{-1} gap is significant only to 2.2σ level, but the joint probability for the presence of the two observed gaps in the same spectrum is $\simeq 2 \times 10^{-4}$. Even if underdense regions are statistically significant in our spectrum, the filling factor is less than 10%.

References

[1] Chernomordik, V., 1995, ApJ, 440, 431

[2] Cristiani, S., D'Odorico, S., Fontana, A., Giallongo, E. & Savaglio, S. 1995, MNRAS, 273, 1016

[3] Crotts, A. P. S. 1989, ApJ, 336, 550

[4] Dobrzycki, A., & Bechtold, J. 1991, ApJ, 377, L69

[5] Giallongo, E., Cristiani, S., Fontana, A., & Trevese, D. 1993, ApJ, 416, 137

[6] Fontana, A., Ballester, P. 1995, ESO Messenger, 80

[7] Heisler, J., Hogan, C. J., & White, S. D. M. 1989, ApJ, 347, 52

[8] Mo, H. J., Miralda-Escudé, J., & Rees, M. J. 1993, MNRAS, 264, 705

[9] Ostriker, J. P., Bajtlik, S., & Duncan, R. C. 1988, ApJ, 327, L35

[10] Rauch, M., Carswell, R. F., Chaffee, F. H., Foltz, C. B., Webb, J. K., Weymann, R. J., Bechtold, J., & Green, R. F. 1992, ApJ, 390, 387

[11] Sargent, W. L. W., Young, P. J., Boksenberg, A., & Tytler, D. 1980, ApJS 42, 41

[12] Sargent, W. L. W., Young, P. J., & Schneider, D. P. 1982, ApJ, 256, 374

[13] Sargent, W. L. W., Boksenberg, A., & Steidel, C. C. 1988, ApJS, 68, 539

[14] Webb, J. K. 1987, in IAU Symposium 124, Observational Cosmology, ed. A. Hewett, G. Burbidge, & L. Z. Fang (Dordrecht: Reidel), 803

[15] Webb, J. K., & Barcons, X. 1991, MNRAS, 250, 270

LYMAN ALPHA FOREST CLUSTERING USING CELL COUNTS STATISTICS

François R. Bouchet[1], and Avery Meiksin[2]
[1] *Institut d'Astrophysique de Paris, CNRS, Paris, France.*
[2] *University of Chicago, Department of Astronomy & Astrophysics, Chicago, USA.*

Abstract

We present a novel technique for calculating Lyα forest correlations based on cell counts. It is applied to the line lists from 7 QSOs observed at high resolution ($\Delta v < 25\,\mathrm{km\,s^{-1}}$). Two spectra (Q0055−259 and Q0014+813) appear to be sufficiently free of biases to obtain meaningful estimates. We find for both positive correlations, with a maximum of $0.5-1$, on the scale of $0.5-3h^{-1}$ Mpc (comoving), or $100-600\,\mathrm{km\,s^{-1}}$, which is consistent with the primordial power spectrum inferred from optically-selected galaxy surveys. Strong evidence for anti-correlation on the scale of $3-6h^{-1}$ Mpc is also found. If this first detection of anti-correlations is physical, additional factors to gravity may play a role in determining the clustering of the Lyα forest on comoving scales $> 3h^{-1}$ Mpc.

Attempts to search for correlations in the Lyα forest have generally led to inconclusive results (e.g., Webb 1986; Rauch et al. 1992). Recently, the results of a high spectral resolution observation of Q0055–269 by Cristiani et al. (1995) has produced the strongest evidence yet for clustering in the Lyα forest. They report an amplitude of ~ 0.5 on the scale of a few hundred kilometers per second (see also Cristiani, this volume). Here we describe a novel method whose results confirm earlier findings, and provide the first evidence for anti-correlations at larger scales.

A homogeneous and isotropic statistical point process may be completely described by the correlation functions of the system. The distribution functions of the neighbor counts (NPDF) is an equivalent description, related to the former through a set of infinite sums (White 1979). In particular, the two-point correlation function $\xi(s)$, where s is a measure of the separation of the objects, may be expressed as the sum over the NPDF, P_N, the distribution probabilities of finding the $N+1$ nearest neighbors a distance s from a given point: $n\,[1+\xi(s)]\;ds = n\sum_{N=0}^{\infty} P_N(s)ds$ where n is the number density of objects per unit separation s. For a Poisson

process, the NPDF is $\hat{P}_N(s) = \mu^N \exp(-\mu)/N!$, where $\mu = ns$. It is convenient to multiply the previous equation by the density of objects, integrate over all space, and subtract off the Poisson contribution, to relate the integral of the two-point function to the cumulative distributions C_N of neighbor counts. Denoting by dN/dz the density of absorbers per unit redshift, and by Z the redshift integration range, the result is

$$\int_Z dz \left(\frac{dN}{dz}\right)^2 \frac{dz}{ds} \int_{s_{\min}}^{s} ds' \xi(s') = \sum_{N=0}^{\infty} \left[C_N(s) - \hat{C}_N(s)\right], \qquad (1)$$

where $\hat{C}_N(s)$ is the cumulative distribution of neighbor counts expected for a Poisson process, $\hat{C}_N(s) = \int_Z dz \left(\frac{dN}{dz}\right)^2 \int_{s_{\min}}^{s} ds' \frac{dz}{ds'} \hat{P}_N(s')$. This form has the useful feature that the maximum difference between $C_N(s)$ and $\hat{C}_N(s)$ (normalized to unity for $s \to \infty$), is the Kolmogorov-Smirnov measure of distance between the two distributions. It provides a direct estimate for the probability that the statistics of the distribution are non-Poissonian. The minimum separation $s_{\min}$ in eqs.(1) accounts for the finite resolution of the QSO spectra, set according to the minimum resolvable absorption line separation as defined by the observers. This procedure indeed results in a matching between the observed and predicted cell size distributions for small separations. To extract the correlation function from its integral, we neglect any dependence on redshift, since the Lyα forest in a given QSO is measured only over a small redshift interval. The integrals may then be reversed in eq.(1), yielding an integral of $\xi(s)$ only over s. The correlation function is then obtained by computing a smoothed derivative of the integral, using the kernel $M_4(x) = 2/3 - x^2 + |x|^3/2$ for $0 \le x \le 1$, $(2 - |x|)^3/6$ for $1 \le x \le 2$, and 0 for $x \ge 2$, where $x = s/h$, and h is the smoothing length (e.g., Monaghan 1985). We checked on realistic test problems that this approach converges (from above) to the correct correlation function as the density of lines is increased.

We estimated the correlation functions for the Lyα forests measured in 7 QSOs observed at high resolution ($< 25\,\mathrm{km\,s^{-1}}$), over the redshift range $2 < z < 4$. The results for two of these, Q0055–269 at $z = 3.66$ (Cristiani et al. 1995), and Q0014+813 at $z = 3.38$ (Rauch et al. 1992), are shown in Figure 1a. The correlation functions are computed as a function of comoving separation r_c, for $H_0 = 100h\,\mathrm{km\,s^{-1}\,Mpc^{-1}}$. The conversion to velocity separation is given by $\Delta v \simeq 200 \Delta r_c$. Only systems with reported column densities exceeding $10^{13.75}\,\mathrm{cm^{-2}}$ are included. Because metal systems show positive correlations (e.g., Young et al. 1982), we exclude from consideration the lines within $\pm 500\,\mathrm{km\,s^{-1}}$ (in the local rest frame) of the metal systems quoted by the observers[1]. To avoid the proximity effect (Murdoch et al. 1986), we also exclude the region within $7000\,\mathrm{km\,s^{-1}}$ of the QSO redshift. The smoothing length used to extract $\xi(s)$ from its integral is $50\,\mathrm{km\,s^{-1}}$. The results quoted below for the integral of $\xi(s)$ are independent of this choice.

In agreement with Cristiani et al. , we find evidence for positive correlations on scales up to $3h^{-1}$ Mpc, or $\sim 600\,\mathrm{km\,s^{-1}}$, with $\xi \simeq 0.5 - 1$ on the scale of $0.5h^{-1}$ Mpc. The integrated correlation function between 0.5 and 1.5 h^{-1} Mpc is 1.02, and between 0.5 and 3 h^{-1} Mpc is 1.46. The number density of lines found is consistent with an average density of $dN/dz = 4.96(1+z)^{2.46}$, where the exponent is adopted from the analysis of Press et al. (1993). Generating 1000 Monte Carlo simulations with this line density, we find that the probabilities of obtaining values as large as those measured in these two intervals are 0.3% and 5.7%, respectively. We

[1]We also check for possible contamination by C IV doublets misindentified as Lyα lines in the spectra of Q0055–269 and Q0014+813, for systems with an inferred H I column density exceeding $10^{13.3}\,\mathrm{cm^{-2}}$. We find only one candidate C IV system, at $z = 2.5642$ in the spectrum of Q0055–269, but with quoted H I column densities smaller than $10^{13.75}\,\mathrm{cm^{-2}}$.

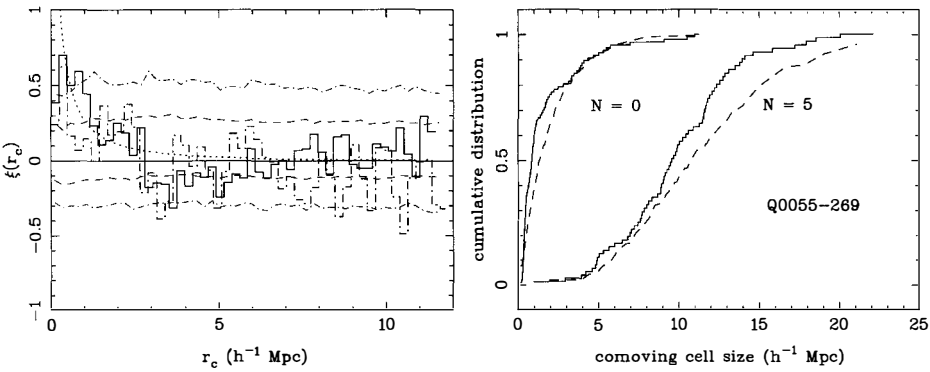


Figure 1: (a) Cell count estimate of $\xi(r_c)$, for Q0055−269 (*solid*), and Q0014+813 (*dot-dashed*). The error ranges shown are the 1σ and 2σ variances for the corresponding Poisson distribution. The correlation function for unbiased $\Omega = 1$ CDM with $h = 0.5$ and $\sigma_8 = 1$ (assuming linear growth, $\xi \propto (1+z)^{-2}$, *dotted line*) is consistent with the clustering of galaxies on scales smaller than $20h^{-1}$ Mpc. (b) Distribution of cell sizes for $N = 0$ (gaps) and $N = 5$ neighbors, compared with the expectations for a random distribution of lines, for Q0055−269.

also find evidence for anticorrelation on the scale of $3 - 6h^{-1}$ Mpc. The integrated correlation function over this range is −0.83, with a Poisson probability for a value this low of 0.6%.

An even stronger measure of the deviation from a Poisson distribution for the absorber positions is provided by the distribution of cell sizes for different cell counts. We show the measured and predicted cell size distributions for cell counts $N = 0$ (gaps) and $N = 5$ in Figure 1b. The estimated distribution is based on assuming a minimum separation of 14 km s^{-1}, the reported resolution of the spectrum. The measured distribution matches the predicted for small and large separations. The maximum difference between the measured and predicted gap distribution is 0.222. The KS probability of obtaining so large a difference is 1.4×10^{-4}. The void distribution yields weaker evidence for clustering in the range $13.3 < \log N_{\rm HI} < 13.8$, with a KS probability of 7.0% for the distribution to be Poisson. Marginal evidence is found for a non-Poisson distribution over the range $13.3 < \log N_{\rm HI} < 13.6$, with a KS probability that the void distribution is Poisson of 11%. The pair count estimate of Cristiani et al. yielded no evidence for clustering in this range.

Positive, somewhat weaker, correlations over the same scale are found for the forest measured in Q0014+813 as well, although the level of significance is much smaller. The integrated correlation function over the range $0.5 - 3h^{-1}$ Mpc is 0.97, the probability for which we find to be 17%, adopting a line density of $5.05(1+z)^{2.46}$ to match the observed number of lines in this QSO. Intriguingly, negative correlations are again found over the range $3 - 6h^{-1}$ Mpc. The integrated correlation function over this range is -0.41, with a probability of 13% for obtaining so low a value. The KS test applied to the void distribution provides stronger evidence for clustering, rejecting a Poisson distribution at the 97.6% confidence level.

We have measured the correlation functions of the Lyα forest in 5 additional QSOs with spectra observed at better than 25 km s^{-1} resolution, Q2126−158 (Giallongo et al. 1993), Q1946+7658 (Fan & Tytler 1994), Q2206−199N (Pettini et al. 1990; Rauch et al. 1993), Q1100−264 (Carswell et al. 1991), and Q1331+170 (Kulkarni et al. 1995). We do not claim a detection of physical correlations in these spectra, however. While strong, highly significant correlations are

found, with a typical amplitude of $2 - 3$ at a comoving separation of $0.5 - 1h^{-1}$ Mpc, we find large positive and negative excursions at larger separations which greatly exceed the random expectations. While these excursions may in principle be revealing large-scale inhomogeneities in the Lyα forest, we suspect they represent instead the interplay between the varying level of noise across the spectra and the algorithms employed to detect and measure the individual absorption features. Reobserving these spectra at higher signal-to-noise, with comparable or improved resolution, is required to decide the reality of the correlations. In one additional case examined, Q1442+101 at $z = 3.54$ (Frye et al. 1994), the correlations found may directly be attributed to the line-finding algorithm.

In summary, for comoving separations less than $3h^{-1}$ Mpc, remarkably good agreement is found between the measurements and the expected correlations deduced using the measured galaxy power spectrum,suggesting that the Lyα forest originates from the same primordial density fluctuations as do the galaxies. If the anticorrelations on larger scales are physical, they suggest non-gravitational effects are at work on scales exceeding $3h^{-1}$ Mpc. A plausible candidate for modifying the correlation function is the UV photoionizing background.

References

Carswell, R. F., Lanzetta, K. M., Parnell, H. C., & Webb, J. K. 1991, *Astrophys. J.* **371**, 36

Cristiani, S., d'Odorico, S., Fontana, A., Giallongo, E., & Savaglio, S. 1995 (preprint)

da Costa, L. N., Vogeley, M. S., Geller, M. J., Huchra, J. P., & Park, C. 1995, *Astrophys. J.* (in press)

Frye, B. L., Bechtold, J., Moustakas, L. A., & Dobrzycki, A. 1993, *MNRAS* **263**, 575

Giallongo, E., Cristiani, S., Fontana, A., & Trèvese, D. 1993, *Astrophys. J.* **416**, 137

Kulkarni, V. P., Huang, K., Green, R. F., Bechtold, J., Welty, D. E., & York, D. G. 1995, *Astrophys. J.* (in press)

Monaghan, J. J. 1985, Comp. Phys. Rep., **3**, 71

Murdoch, H. S., Hunstead, R. W., Pettini, M., & Blades, J. C. 1986, *Astrophys. J.* **309**, 19

Pettini, M., Hunstead, R. W., Smith, L., & Mar, D. P. 1990, *MNRAS* **246**, 545

Press, W. H., Rybicki, G. B., & Schneider, D. P. 1993, *Astrophys. J.* **414**, 64

Rauch, M., Carswell, R. F., Chaffee, F. H., Foltz, C. B., Webb, J. K., Weymann, R. J., Bechtold, J., & Green, R. F. 1992, *Astrophys. J.* **390**, 387

Rauch, M., Carswell, R. F., Webb, J. K., and Weymann, R. J. 1993, *MNRAS* **260**, 589

Webb, J. K. 1986, in IAU Symposium 124, Observational Cosmology, ed. A. Hewitt, G. Burbidge, and Li-Zh. Fang (Dordrecht: Reidel), p. 803

White, S. D. M. 1979, *MNRAS* **186**, 145

Young, P., Sargent, W. L. W., and Boksenberg, A. 1982, *Astrophys. J. Suppl. Ser.* **48**, 455

QUASARS AND LARGE SCALE STRUCTURE OF THE UNIVERSE

V.N.Lukash
Astro Space Centre of Lebedev Physical Institute,
Profsoyuznaya 84/32 , 117810 Moscow, Russia

The majority of bright distant quasars ($z \gtrsim 1$) may form in massive mergers appearing in compact galaxy groups in/and young clusters. The expected tests are (i) large correlation signal for medium-z QSOs ($1 < z < 2$) and (ii) direct search for quasar groups (QGs) indicating positions of distant pre-superclusters which later will evolve to the "systems" like the local Great Attractor or Shapley concentration. We discuss large QGs with more than ten members within regions $\leq l_{LS} \sim 100-150\,h^{-1}Mpc$, tracing the enhanced density regions at $z \lesssim 2$. These early large scale structures (i) provide a natural way to "bias" the distribution of Abell clusters, and (ii) suggest that the spectrum of primordial density perturbations is nearly flat at scales encompassing both cluster and GAs, $l = \pi k^{-1} \in (10.100)h^{-1}Mpc : \Delta_k^2 \sim k^3 P(k) \sim k^\gamma, \gamma = 1^{+0.6}_{-0.4}$.

Current discussion on the cosmological models of large scale structure (LSS) formation is strongly stimulated by recent observational progress. Today, we have few independent evidences for existence of large scale structures up to a typical scale $l_{LS} \cong 100 - 150h^{-1}Mpc$. The most important data come from the Great Attractor ($z \leq 0.03$), distributions of clusters of galaxies ($z \leq 0.1$) and pencil beam galactic surveys ($z \leq 0.3$). It is now on agenda to test ever deeper tracers, e.g., radiogalaxies and active galactic nuclei (AGNs), quasars (QSOs), absorption (L_α, CIV) and emission (21 cm) clouds, X-ray clusters and others, to make sure how far these large structures extend in the past. The result would allow direct dynamical reconstruction of the primordial spectrum of density perturbations within scales $10 - 100h^{-1}Mpc$. Together with $\Delta T/T(\Theta \geq 1^o)$ measurements this could certainly solve the problem of the primordial spectrum in the whole range of large scales.

Here, let me concentrate on the relationship between quasar groups and enhanced density regions that are called distant Great Attractors (GAs)[1]. As for the local GA, by distant GA we understand a patch of enhanced total density, scaled in any dimension from larger than richest cluster size and up to $\sim l_{LS}$ (and further, if any). The opposite construction is void (Great Repulsor), a patch of decreased total density. Both notions - GAs and voids - are quasilinear systems still expanding with the Universe (the density variation may consist $\sim 10 - 30\%$ on scale $\sim 100h^{-1}Mpc$) which differ them drastically from the objects just collapsed or collapsing at least in one direction – galactic clusters, filaments and walls – the latter direction size being $\lesssim 10h^{-1}Mpc$.

There are two principal steps on the way to relate distant QGs and GAs:

* Clusters, where they are concentrated (the superclusters), trace the mass density enhancements;

* Clusters of distant clusters contain (at least some) QGs.

The first point is confimed today in the nearby region where peculiar velocity measurements are done, and by the alignment of the cluster dipole with microwave background dipole . As for the second point, there are few observational indications (I stress here only two of them):

1) The QSO correlation functions at different redshifts and comparison with clusters' and galaxies' correlation functions.

2) Direct investigations of the environments of nearby QSOs.

The QSO correlation function displaying strong QSO clustering at $r \leq 10h^{-1}$ Mpc, a weaker clumping at $\sim 20 - 100h^{-1}Mpc$ and the absence of correlations for $r > 150h^{-1}Mpc$, evolves explicitely growing to smaller redshifts: for $z \Rightarrow 0$ it looks like the distribution of galaxies whereas for $z > 2$ the QSOs seem to be

randomly distributed. According to [2,3], $\xi_{qq} \sim (1+z)^{-a}$, with $a \sim 2-3$. Having analysed 8 homogeneous surveys of QSOs we found that the main contribution to q-q correlation signal comes from medium-z quasars with the correlation radius $\sim 10\,h^{-1}\,Mpc$ $(1 < z < 2)$[4]. When approximating it by $z = 0$ due to the linear perturbation law ($\xi_{qq} \sim (1+z)^{-2}$), the correlation function for those QSOs would correspond by now to that of the reach clusters of galaxies. As the nearby QSOs ($z < 1$) are distributed much more like galaxies than like clusters, they seem to be a different population which is more closely connected to poor environments like loose groups of galaxies (whereas the bright distant quasars mostly form in compact groups in preclusters). One of the principal tests here could be a clear detection of the decay of ξ_{qq} beyond $z > 2$.

Today's observations display that QSOs at $z > 0.5$ are frequently associated with rich clusters and compact groups, while those at $z < 0.5$ seem to be found in sparse poor systems like loose galactic groups. It gives us a guess that quasars may form in merging and intercting galaxies originating in galaxy concentrations (the density enhancements). These merging effects generate instability processes in host galaxies resulting in the gas infall and accreation material supply (to a massive black hole) enough for the QSO burning. Regarding bright distant quasars ($z \gtrsim 1$) such conditions can really exist in young clusters which are in process of the first contraflows' origin, i.e., well before the cluster virialization and X-ray gas appearing. Taking into account that the first violent crossings (caustics of LSS forming) of the cosmic primordial medium must certainly arrise in the central regions of young preclusters at $z \sim 2.5$, we may relate this epoch with the quasar peak existing at redshifts $z \sim 2-3$. Of course,not every QSO we do associate with collapsing compact groups in young clusters (there were few generations of QSOs depending on the environmental physical conditions which provided due to merging activity for the galactic matter infall and formation of the accreating gas disk). The smaller masses collapsed earlier and could not ensure intensive galaxy interactions, while the larger LSS masses collapsed later in the medium with a much smaller fraction of the gas (transfering to stars) already totally ionized.

If so, then at least two topics are on the agenda:

* It is possible to find distant GAs by groups (and even pairs) of QSOs in scale of few tens of Mpc ($l_{GA} \lesssim 100 h^{-1} Mpc$).

* Relationship between the epochs of first generation of caustics in preclusters ($z \sim 2-3$) and in GAs ($z \sim 0$) prompts the true model of LSS formation.

The QSO test for GA search proposed in the first topic can be successfully used at $0.5 \leq z \leq 3.5$, where large QSO number densities are observed.

Today we have information on eleven QGs with more than ten members in a group and the number density enhancement (relative to the background QSO density) more than factor of two [5]. The most famous in the list is the group at $z = 1.1$ consisting of 25 QSOs within $\sim 60h^{-1}Mpc$[6]. All QGs are found for $z < 2$ and not seen at larger redshifts (though the spatial number density of QSOs grows sharply up to $z \sim 2.5$), the typical QG-sizes are about supercluster scales ($\sim l_{LS}$).

If the formation epochs of clusters and GAs are really "separated" by the interval $\Delta z \sim 2.5$ ("subcluster formation" proceeds in a broad interval centered at $z^*_{CL} \sim 2.5$, while "cluster formation" goes on nearly now) we have the following simple estimate for the spectrum of Gaussian density perturbations $\delta \equiv \delta\rho/\rho$ within the dynamical scale range $l = \pi k^{-1} \in 10 - 100h^{-1}Mpc$:

$$\Delta^2_k \sim k^\gamma, \quad \gamma = 1^{+0.6}_{-0.4} \tag{1}$$
$$\delta^2 = (1+z)^{-2} \int \frac{dk}{k} \Delta^2_k,$$

where δ^2 is the variance. It predicts the correlation function of the dynamical mass $\xi(r) \sim r^{-\gamma}$, which means that clusters are clumped in regions overdensed by GA-scale perturbations. By now, the perturbations on supercluster scale seem to be clearly outlined (according to eq.(1) $\delta_{GA} \sim \delta_{LS} \sim 0.2$) when the dynamical scale ($\delta_D \sim \delta_{Cl} \sim 1$) is closed to $10h^{-1}Mpc$) (which is the scale of largest clusters and the width of the walls and filaments of LSS network).

Such a flat spectra bring about the following conclusions.

(i) Clusters today should be most developed and concentrated in central parts of GAs (clusters trace the mass in dense regions), while sparse young clusters may be found nearby or inside voids.

(ii) If the majority of bright QSOs broadly peaked at $z \sim 2 - 3$ is formed in preclusters in GA-locations then the mean separation between QSOs at $z \sim 2.5$ should correlate with l_{LS} which is actually in good agreement with observations.

(iii) The Gaussian flat spectra (1) create by $z < 1$ a great variety of coherent structures (the hierarchies of walls, filaments, voids and GAs) produced by broadscale (in $l \in 10 - 100h^{-1}Mpc$) perturbations with close initial amplitudes.

(iv) Since galaxies form before clusters,their first generation is not modulated by GA-perturbations. However, merging and generating processes for galaxies going most active in rich environments (the dense regions), lead to the successive generation of large galaxies (which give birth to bright QSOs) namely at GA locations. The test could be a search of dwarf galaxies in voids.

(v) Obviously, spectra (1) are more flat than that in standard CDM (the latter anticipates $\Delta_k^2 \sim k^{2-3}$ in the scale range). As the COBE $\Delta T/T$ detection indicate consistency with Zeldovich-Harrison (ZH) spectrum at very large scale ($\Delta_k^2 \sim k^4, l \sim 1000h^{-1}Mpc$) then the turn from the flat part (1) to ZH asymptotic should happen at supercluster scale $\sim 150h^{-1}Mpc$, which can obviously be the real feature of the primordial spectrum (contrary to the case of galaxy clusters to be the consequence of current dynamical time).

Summarising, we can say that available data back the following conjectures.

* QGs may be good tracers of enhanced matter density regions (distant GAs), they render in sizes up to $l_{GA} \sim 100 - 150h^{-1}Mpc$ and extend by $z_{LS} \sim 2$.

* Majority of distant QSOs ($1 \lesssim z \lesssim 3$) can be created in massive merges forming in collapsing compact groups in precluster clumps.

Both points are selfconsistent if and only if QSOs belonging to QGs were born not far before the time where given QG is observed, which is also consistent with a relatively short lifetime of medium and bright QSOs. It means that very distant QSOs at $z > z_{LS}$ appear more or less random in space (GA perturbations are small yet). On the contrary, the medium-z QSOs stemming at $z < z_{LS}$ originate already in groups (the formation time of galaxy clusters is strongly modulated by GA-scale perturbations). Note in this connection that late QSOs ($z < 1$) form in poor environments as their formation is delayed. The evolutionary epoch of compact groups is mainly over by now, so, the remnants of the distant QSOs may be hidden in large E-galaxies, while the collapsing time of loose groups and young clusters today is comparable with the Hubble time.

Certainly, both points lead to obvious conclusion that the part of the primordial spectrum between the dynamical scale ($\sim 10h^{-1}Mpc$) and the coherence length ($\sim 100 - 150h^{-1}Mpc$) is nearly flat (see eq. (1)).

This work has been supported in part by Russian Foundation for Fundamental Research (code 93-02-2929) and International Sience Foundation (grant MEZ300).

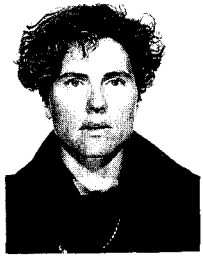
References

[1] Komberg B.V., Lukash V.N., 1994, *MNRAS* **269**, 277
[2] Iovino A., Shaver P.A., Cristiani S., 1991, in *The Space Distribution of Quasars*, Crampton D.*et al.*, eds., ASP Conf. Series, **21**, 202
[3] Mo H.J., Fang L.Z., 1993 *ApJ* **410**, 493
[4] Komberg B.V., Kravtsov A.V., Lukash V.N.,1994, *Astronomy Astrophys.* **286**, L19
[5] Komberg B.V., Kravtsov A.V., Lukash V.N.,1995, *submited to MNRAS*
[6] Crampton D., Cowley A.P., Hartwick F.D.A., 1989, *ApJ* **345**, 59



THE CLUSTERING OF QUASARS

P. Andreani, S. Cristiani & F. La Franca
Dipartimento di Astronomia dell'Università, Padova, Italy.



Abstract

We have investigated the spatial distribution of quasars and its relationship with redshift by using the two-point correlation function, the variance of cell counts and the conditional density as a function of redshift. By comparing our results with those found by other authors we conclude that quasars have a correlation function with amplitude similar to or greater than that of galaxies, but the issue of its evolution still needs to be settled. We discuss how this can be achieved by adding new observations and comparing real data with survey simulations.

1 Introduction

As widely discussed in this meeting the investigation of the large scale structure of the universe and its connection with the primordial density fluctuations, which in the gravitational instability picture gave origin to it, represents one of the major problems in modern cosmology. In order to tackle this, we have still to face two fundamental problems: on the one hand, we lack a theoretical picture relating the present day distribution of matter with the primordial fluctuations. There are actually first attempts to determine the evolution of the mass two-point correlation function from the linear regime to the present-day one ([14] [21], [19], [17] and Jain, this meeting), but the fundamental question of its relationship with the galaxy two-point correlation function needs still a deep understanding of the bias mechanism. On the other hand, we do not have any knowledge of the distribution of objects at high redshift since the available galaxy catalogs provide the determination of galaxy clustering only at relatively low redshifts. However, this problem can be soon challenged by studying quasars and their relationship with galaxies. From an observational point of view there are in fact two novelties: (1) the rapid growth of quasar surveys, which will help in assessing the statistical significance of QSO distribution and (2) the investigation of QSO's environments, which will relate QSOs with galaxies (see Boyle, this meeting).

2 The Quasar two-point correlation function

QSO clustering has been investigated by several authors and a detailed study of this effect at scales $r \leq 150\ h^{-1}$ Mpc ([24], [22], [1], [12] [2]) has been possible only with the availability of complete and faint quasar samples with *high* surface density, while previous attempts failed ([20]; [25], [7], [5], [11], [6]). The quasar two-point correlation function (CF) shows a shape and an amplitude, within the errorbars, similar to those of the galaxy CF: parametrizing the CF with the usual power-law model, $\xi(r) = (\frac{r}{r_0})^{\gamma}$, provides an amplitude r_0 in the range $6 \div 10\ h^{-1}$ Mpc. The same conclusion but with a higher S/N ratio is also found by using the conditional density, Γ, i.e. the mean density about a given object ([2]). This function is better suited for samples without a definite mean density and gives a less ambiguous and more robust description of the distribution.

3 The variance of Quasar counts

An independent way of establishing the clustering strength of objects is the measurement of the variance σ^2 of counts in cells. The variance is related to the spatial CF by a volume average and with respect to the CF yields a more reliable evaluation of the clustering amplitude at the scale of the cell–size.

The analysis has been carried out in the redshift range $1.0 \div 2.2$ for cells of volume V_u. A maximum likelihood analysis gives estimates of $\sigma^2(\ell)$ ($\ell \equiv V_u^{1/3}$) for $\ell =$ 40, 60, 80 and 100 h^{-1} Mpc: $\sigma^2(\ell) = 0.46^{+0.27}_{-0.27}$, $0.18^{+0.14}_{-0.15}$, $0.05^{+0.14}_{-0.05}$ and $0.12^{+0.13}_{-0.12}$, respectively, where the 70% confidence ranges account for both sampling errors and statistical fluctuations in the counts (see [4] for details). This allows a comparison of QSO clustering on large scales with analogous data obtained both for optical and IRAS galaxies: QSOs seem to be more clustered than these galaxies by a biasing factor $b_{QSO}/b_{gal} \sim 1.4 - 2.3$.

4 The evolution of QSO clustering

The increasing number of complete samples permits now to study not only the global quasar clustering with high statistical significance but also its cosmic evolution. At present seemingly contradictory results have been supported: Iovino et al. ([13]), Mo & Fang ([18]) and Komberg et al. ([15]) claim evidence for an evolving two-point correlation function with redshift in comoving coordinates, $\xi(z) \propto (1+z)^{-(2 \div 3)}$, while Andreani & Cristiani ([3]) and Shanks & Boyle ([23]) do not find such an effect and suggest that a stable clustering, $\xi(z) \sim const$, in comoving coordinates is consistent with the data. Probably this discrepancy can be reconciled once poor statistics and the partial knowledge of the selection effects affecting the samples will be better taken into account.

5 New data and the simulation of surveys

In order to address issues to the evolution of clustering we have pursued our investigation twofold: on the one hand we have enlarged our sample by including the deepest fields of the HBQS survey (*Homogenous Bright Quasar Survey*, [9]) covering a large connected area; on the other hand we have followed an inverse approach by building mock samples and comparing them with the real ones.

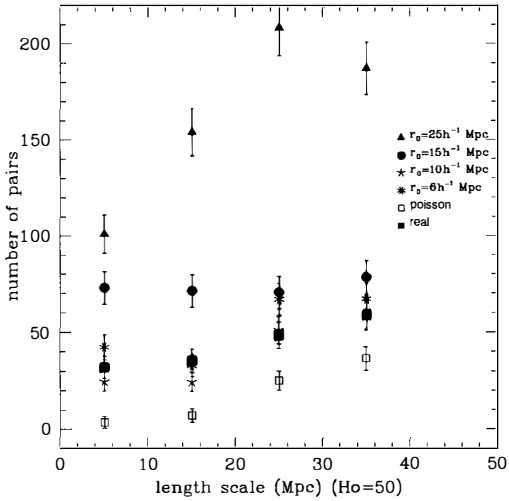


Figure 1: The qso pairs in shells of depth of 10 Mpc centred at 5, 15, 25 and 35 Mpc. Real data are shown as filled squares, the poissonian distribution as open squares. The other symbols refer to simulations corresponding to different clustering models, whose clustering amplitudes, r_0, are listed in the upper right corner.

The mock surveys have been constructed as follows: (a) absolute magnitudes and redshifts are randomly extracted from a probability distribution function given by the adopted quasar luminosity function ([10], [16]). (b) The evolution with redshift is given by a simple pure luminosity evolution model: the luminosity function is assumed to translate towards brighter magnitudes with redshift with a law $M_B = M_B^\star - 2.5k\log(1+z)$. (c) Angular position of each object is found according to a clustering model, built by parametrizing the correlation function of quasars as usual, $\xi(r) = (\frac{r}{r_0})^{-\gamma}$, and assigning to each object a probability of being clustered found by a weighted volume average of this function. (d) The absolute magnitude is converted into apparent magnitude by taking account of the k-corrections (as in [8]) and to this photometric errors are randomly assigned. (e) Finally these mock catalogs are 'convolved' with the observation selection function given by the limiting fluxes, area, magnitudes, and selection criteria for candidates of each survey. We consider only objects with absolute B magnitude $M_B \leq -23$ in a flat universe ($\Omega = 1$) with H_o=50 km/s/Mpc and $q_o = 0.5$. Results from 1000 simulations of each survey are added and the redshift distribution is then compared with the real one. A Kolmogorov-Smirnov test gives always a very high probability (always >0.20) that the two distributions are drawn from the same population. Finally we compute the number of pairs in shells of depth of 10 Mpc between 0 and 40 Mpc for the simulated surveys and the real ones. Errors on the simulated pairs are negligible, while those for the real ones are obtained with bootstrapping techniques. Figure 1 shows the number of pairs in the real case (filled squares) and those resulting from simulations. The real qso pairs undoubtedly lie above those expected from a poissonian distribution and exclude most of the selected models but those with $r_0 \sim 6 \div 10$ h^{-1} Mpc. This approach is being used also for investigating the evolution with redshift. While issues to the evolution of qso-pairs can be properly addressed with the present

data, their statistical significance is not enough to distinguish the most common hypotheses of the kind of clustering evolution (stable clustering, linear evolution, collapsing). To this aim we are completing a sample of 600 quasars selected over an area of 25 deg^2 with $B \leq 20.5$. This large connected and deep area will soon show unambigously the kind of evolution at the 95% confidence level. In fact, in the hypothesis of one of the milder clustering evolution in which $\xi(r) = \xi(r)(1+z)^{-1.2}$ (stable clustering), we would expect 67 pair at low redshift against 43 at high redshift.

References

[1] Anderson N., Kunth D., Sargent W.L.W., 1988, AJ **95**, 644

[2] Andreani P., Cristiani S., La Franca F., 1991 MNRAS **253**, 527

[3] Andreani P. & Cristiani S. 1992, ApJ **398**, L13

[4] Andreani P., Cristiani S., Lucchin F., Matarrese S., Moscardini L., 1994, ApJ **430**, 458

[5] Clowes R.G. 1986, MNRAS **218**, 139

[6] Clowes R.G., Iovino A. & Shaver P. 1987, MNRAS, **227**, 921

[7] Chu Y.Q. & Zhu X.F. 1983, ApJ **267**, 4

[8] Cristiani S. & Vio R. 1990, A&A **227**, 385

[9] Cristiani S., La Franca F., Andreani P., Gemmo A., et al., 1995, A&AS in press

[10] Cristiani S. & La Franca F., 1994, in *Wide-Field Spectroscopy and the Distant Universe*, eds. S.J. Maddox & A. Aragón-Salamanca (World Scientific: Singapore)

[11] Drinkwater M. 1986, in *Quasar*, eds G. Svarup & V.K. Kapahi, Reidel,p.503

[12] Iovino A. & Shaver P., 1988, ApJ **330**, L13

[13] Iovino A., Shaver P., Cristiani, 1991, in *the Space Distribution of Quasars*, ASP Conference Series, vol. 21, p.202, ed. D. Crampton

[14] Hamilton A.J.S., Kumar P., Lu E. & A. Matthews, 1991, ApJ **374** L1

[15] Komberg B.V., Kravtsov A.V. & Lukash V.N., 1994, A&A **286**, L19

[16] La Franca F. et al., 1995, in preparation

[17] Mo H.J., Jain B. and White S.D.M. 1995, MNRAS, submitted

[18] Mo H.J. & Fang L.Z. 1993, ApJ **410**, 493

[19] Nityananda R. & Padmanabhan T., 1994, MNRAS **271**, 976

[20] Osmer P.S. 1981, ApJ **247**, 762

[21] Peacock J.A. & Dodds S.J. 1994 MNRAS **267**, 1020

[22] Shanks T., Fong R., Boyle B.J., Peterson B.A., 1987, MNRAS **227**, 739

[23] Shanks T., & Boyle B.J., 1994, MNRAS **271**, 753

[24] Shaver P. 1984, A&A **136**, L9

[25] Webster A., 1982, MNRAS **199**, 683

GRAVITATIONAL LENSING OF QUASAR 0957+561 AND THE DETERMINATION OF H_0

George Rhee[1], Gary Bernstein[2], Tony Tyson[3] and Phil Fischer[3]
1. Department of Physics
University of Nevada, Las Vegas
Las Vegas NV 89154-4002
2. Department of Astronomy, University of Michigan
3. AT&T Bell Labs



ABSTRACT

We present results of a deep imaging study of the cluster lensing the double quasar 0957+561. Using data obtained at KPNO and CFHT we have detected distortions in the lensed blue background galaxy population. From these arclet distortions we have constructed a map of the mass density in the field of the double QSO. We use this map to provide constraints on the mass concentrations responsible for the lensing. Using these constraints in conjunction with mass models and the known time delay between the A and B images we place limits on the value of the Hubble constant.

INTRODUCTION

The double quasar 0957+561 was the first discovered instance of multiple imaging via gravitational lensing and has been observed in the radio, optical, infrared and X-ray. It is the only gravitational lens system for which the magnification matrix and the time delay between the two images are well constrained. This is at present the only system for which one can follow the suggestion of Refsdal (1966) to derive the Hubble constant from the time delay between multiple images. Unfortunately the lens geometry cannot be explained using only the galaxy G1 found between the quasar images. The galaxy cluster surrounding G1 is an important deflector as well and this complication has so far precluded construction of a unique, satisfactory model of the lens, reducing the accuracy of the derived Hubble constant. To address this problem have obtained deep images of the system at CFHT. The cluster is sufficiently massive to cause distortions on distant background galaxy images. We have used a mass map derived from lensing distortions to improve the accuracy of the cluster center location and place new limits on H_0.

THE TIME DELAY

To derive the Hubble constant using the double quasar one must measure the difference in the light travel time along the paths from the source to the observer. This has been done in the radio and optical by monitoring the two quasar images. Vanderriest et al. (1989) obtain a value of 415 ± 20 days based on optical data. Schild (1991) obtains a value of 404 ± 10 days also based on optical monitoring. Press et al. (1992) using a global χ^2 statistic obtain a value 536 ± 12 days using the same optical data. They emphasize that smooth interpolation followed by cross correlation is an unreliable technique. From radio monitoring studies Lehar et al. (1991) conclude that the time delay is 513 ± 40 days. We conclude that the true value of the time delay lies between 415 and 540 days.

THE LENS PROPERTIES

The galaxy principally responsible for the lensing (G1) lies between the two quasars about 1″ north of the B image. It has a redshift of 0.36. Bernstein et al. (1993) have published photometry of this galaxy. They find that the surface brightness profile is well fit by a power law with index $n = -1.94 \pm 0.06$. The profile is also well fit by a de Vaucouleurs law with $R_e = 4.5 \pm 0.65''$. The central surface brightness is $I_e = 23.7 \pm 0.1$ R mag arcsec $^{-2}$. The position angle of the galaxy may twist slightly about a mean value of 55° . The I_e and R_e values quoted above are typical for brightest cluster member ellipticals or cD's. Applying the

Faber-Jackson relation to these data one infers a velocity dispersion for G1 of $\sim 400\,\mathrm{km\,s^{-1}}$. From spectroscopic observations Rhee (1991) derives a velocity dispersion 300 ± 50 $\mathrm{km\,s^{-1}}$ for G1. This is somewhat less than predicted from the Faber Jackson relation but it is known that brightest cluster ellipticals tend to have lower velocity dispersions than the Faber-Jackson law would suggest.

MODELS OF THE MASS DISTRIBUTION

Based on the observations described above we have derived models for the galaxy and cluster lensing the double quasar. We model the galaxy mass to have the profile $\Sigma_0(r) = 0.033(r/3)^n$ in the range $0.3'' \leq r \leq 30''$, the power law index is allowed the following range $-1.9 \leq n \leq -0.5$. There are 4 free parameters for the galaxy model: the velocity dispersion, the ellipticity, the galaxy position angle and the power law index. The cluster is modeled to first order in the ellipticity as an expansion of an elliptical pseudo-isothermal sphere.

$$\phi_c = b_c(s_c^2 + r^2)^{\frac{1}{2}} + \frac{\gamma}{3} b_c r^2 (s_c^2 + r^2)^{-\frac{1}{2}} \cos 2(\theta - \theta_\gamma)$$

The 6 free parameters are: the cluster velocity dispersion, the cluster core radius, the cluster ellipticity, the cluster position angle the distance between the cluster center and the galaxy center and the position angle of the line joining the cluster center to the galaxy center. The cluster maps show that the cluster potential is not perfectly smooth. This can be taken into account by adding a shear component to the two components listed above. The shear component has two parameters the magnitude of the shear and its position angle. The effect of the shear may be taken as some indication of the changes in the models that would result from the addition of lumps to the mass distribution.

THE OBSERVATIONS

The observations were made with FOCAM and the SAIC CCD at CFHT in January 1994. We obtained a 3 hour integration in B band and a 4 hour integration in I-band. Sky flats of high precision were secured from dithered exposures on a control field. By inverting the estimated shear field inferred from the observed shapes and orientations of background galaxies we have obtained a map of the surface mass density of the matter lensing Q0957+561.

CONSTRAINTS ON THE MASS MODELS

From the map of the mass distribution we can locate the center of the cluster relative to the lensing galaxy. This is a key parameter for the determination of H_0. We measure the cluster center position to be at a distance (r_c) of 9 arcseconds from the lensing galaxy in the direction

$\theta_c = 193°$. In a recent study Dahle et al. (1994) using deep images obtained with the Nordic Optical Telescope find $r_c = 6$ arcseconds and $\theta_c = 123°$. The uncertainties associated with these numbers are ~3 arcseconds in the distance and ~ 30° for the position angle.

CONCLUSION

From the constraints on two of the parameters of our model of the cluster and galaxy lensing Q0957+561 we can infer limits on the Hubble constant. Using the distortion of background galaxies we have derived a map of the mass distribution lensing the QSO. We have used this map to locate the position of the cluster lensing the QSO. The two parameters are the position angle of the vector joining the first ranked galaxy (G1) to cluster center, and the length of this vector. By limiting the range in values that these two parameters can have we eliminate all models except those having H_0 less than 70 km/s/Mpc.

ACKNOWLEDGEMENTS

George Rhee acknowledges travel support from the UNLV Physics department Bigelow fund and acomodation support from an EEC grant.

REFERENCES

Bernstein, G.M., Tyson, J.A., & Kochanek, C.S. 1993, AJ, 105, 81ϑ

Dahle, H., Maddox, S.J., and Lilje, P.B. 1994, ApJL, in press

Lehar, J., Hewitt, J.N., & Roberts, D.H., 1989, in Gravitational Lenses, ed. J.M. Moran, J.N. Hewitt, & K.Y. lo (Berlin: Springer)

Refsdal, S. 1966, MNRAS, 132, 101

Rhee, G. 1991, Nature, 350, 211

Press, W.H., Rybicki, G.B., & Hewitt, J.N. 1992, ApJ, 385, 416

Schild, R., AJ, 1990, 100, 1771

Vanderriest, C., Schneider, J., Herpe, G., Chevreton, M., Moles, M., and Wlerick, G. 1989, A&A, 215, 1

The Environments of $z < 0.3$ QSOs

B.J. Boyle [1], R.J.Smith[2], S.J. Maddox[1]
[1] *Royal Greenwich Observatory, Cambridge, UK.*
[2] *Institute of Astronomy, Cambridge, UK.*

Abstract

Based on a cross-correlation analysis of X-ray selected QSOs with faint ($B_J < 20.5$) galaxies, we find a 5σ galaxy excess around low-redshift ($z < 0.3$) QSOs with an amplitude identical to that of the galaxy angular correlation function. The similarity between QSO-galaxy clustering and galaxy-galaxy clustering suggests that QSOs are unbiased with respect to galaxies and make useful tracers of large-scale structure in the Universe.

1 Introduction

The clustering of QSOs can, in principle, place useful constraints on the form and evolution of structure in the Universe [11], particularly at redshifts ($z > 0.3$) and scales ($> 100h^{-1}$ Mpc) which can not directly be probed with galaxies. However, existing studies of QSO clustering are limited to relatively small samples of QSOs ([1], [7], [11]) typically containing less than 1500 objects. Although most of these studies agree that QSOs exhibit significant clustering at small scales ($< 20h^{-1}$ Mpc) with a mean correlation length $r_0 \sim 6h^{-1}$ Mpc, there is little concencus over the evolution with redshift in the strength of this clustering or in the strength of clustering at larger scales ($> 20h^{-1}$ Mpc). This is primarily due to the lack of observational data. Fortunately, with the imminent availability of wide-field multi-object spectrographs such as the 2dF [14] and Sloane Digitial Sky Survey [5], significantly larger QSO surveys should be forthcoming within the next 2-3 years. For example, there is a current proposal to conduct a QSO survey on the AAT 2dF (P.I.s Boyle and Shanks) which will yield spectra for 30000 $B_J < 21$ UVX-selected QSOs in 40 nights of telescope time. With such a survey it will be possible to measure *directly* the evolution of clustering with redshift, thereby placing limits on galaxy formation models and the value of Ω_0. The survey will also provide an accurate estimate of the strength of QSO clustering at large scales ($> 20h^{-1}$ Mpc), yielding important information

on the index of the primordial fluctation power spectrum, n, as well as providing a potential measure of q_0 and Λ_0 [11].

However, QSOs can only be used as reliable probes of large-scale structure if it is understood how they are distributed with respect to galaxies. Existing deep CCD surveys ([2], [4]) indicate that radio-quiet QSOs (which comprise over 95% of the QSO population) inhabit normal galaxy environments over a wide range in redshifts ($0.3 < z < 1.5$). This is in marked contrast to radio-loud QSOs, whose environments undergo strong evolution over the range $0.3 < z < 0.6$ [4] and appear to inhabit rich clusters at higher redshifts [8]. Unfortunately, results on QSO environments at these redshifts are drawn primarily from deep CCD imaging studies and are thus highly dependent on the correction applied to convert *observed* galaxy excess on the sky to *physical* galaxy clustering at the redshift of the QSO. For all but the lowest redshifts ($z \sim 0.3$), this involves an uncertain extrapolation of the galaxy luminosity function and its evolution with redshift. To obtain a more accurate estimate of the environments of QSOs, we have therefore carried out out an investigation of the environments of the lowest redshift ($z < 0.3$) QSOs, using QSO and galaxy samples which have recently become availiable. Full details of this work are to be published in [12].

2 Data

We cross-correlated the positions of 169 X-ray selected $z < 0.3$ QSOs identified in the *Einstein* Medium Sensitivity Survey (EMSS, [13]) with the positions of $B_J < 20.5$ galaxies detected from the APM galaxy survey [10] and from the APM Sky Catalogues [6]. The $z < 0.3$ QSOs are predominantly ($> 96\%$) radio-quiet [3] and lie in the absolute magnitude range $-24 < M_B < -21$. From these data-sets we derived the QSO-galaxy cross-correlation function $w_{qg}(\theta)$ as follows:

$$w_{qg}(\theta) = \frac{N_{QG}}{N_{QR}} - 1, \qquad (1)$$

where N_{QG} is the number of galaxies found at a given separation (θ) and N_{QR} is the number of random points expected in the same annulus. Fortuitously, the redshift distribution of the QSO sample is identical to that of $B_J < 20.5$ galaxies, and thus (since both samples have identical projection effects) the amplitude of $w_{qg}(\theta)$ can be directly compared to that of the $B_J < 20.5$ galaxy angular correlation function, $w_{gg}(\theta)$, in order to estimate the relative strength of QSO and galaxy environments.

3 Results

In figure 1 we plot the pair-weighted $w_{qg}(\theta)$ obtained from all $z < 0.3$ QSOs in the sample. The positive detection of clustering at small scales (< 4arcmin) is significant at the 4.7σ level (728 independent QSO-galaxy pairs found, 610 pairs expected). Errors bars in figure 1 are based on the rms spread in $w_{qg}(\theta)$ over 5 independent sub-samples. Based on χ^2 fits, the ratio between $w_{qg}(\theta)$ and $w_{gg}(\theta)$ is given by:

$$w_{qg}(\theta)/w_{gg}(\theta) = 1.0^{+0.7}_{-0.4} \qquad (2)$$

where the errors represent the 95% confidence interval. We find no signficant detection of galaxy clustering around a 'control' sample of 154 $z > 0.3$ QSOs selected from the EMSS, indicating that the observed correlation is not an artefact of the data-sets used. Splitting the QSO sample into Northern and Southern fields (for which different galaxy catalogues were used) or into low

($M_B > -22$) and high ($M_B < -22$) luminosity ranges also revealed no significant difference between either sets of sub-samples.

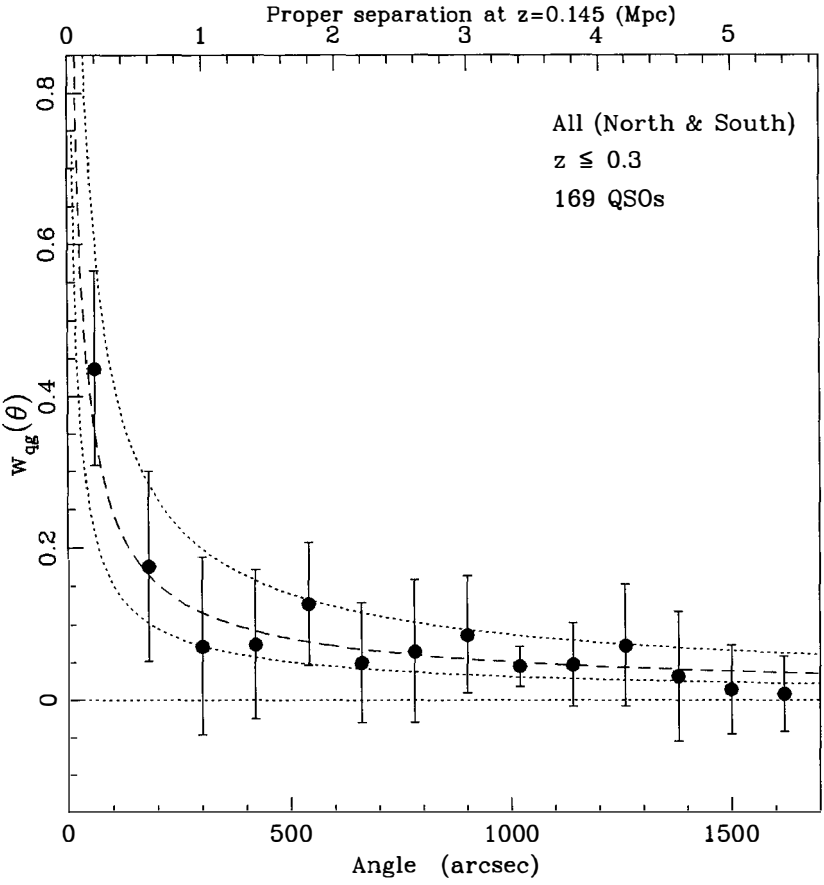


Figure 1 The QSO-galaxy angular cross-correlation function, $w_{qg}(\theta)$, for 169 $z \leq 0.3$ EMSS QSOs and the APM $B_J \leq 20.5$ galaxies. The dashed curve is the angular $B_J < 20.5$ mag galaxy auto-correlation function, $w_{gg}(\theta)$, derived from the APM galaxy survey [9]. The dotted lines indicate the $\pm 2\sigma$ limits for the fit of $w_{gg}(\theta)$ to $w_{qg}(\theta)$.

4 Discussion

From the observed agreement between the amplitudes of $w_{qg}(\theta)$ and $w_{gg}(\theta)$ we conclude that low luminosity ($M_B > -24$) QSOs randomly sample the galaxy distribution at low redshifts ($z < 0.3$). Coupled with previous results ([2], [4]) this implies that radio-quiet QSOs undergo

no appreciable change in their environment over a wide range of redshifts ($0 < z < 1.5$) or luminosities ($-27 < M_B < -22$). This suggests that radio-quiet QSOs are as unbiased a tracer of mass in the Universe as galaxies, but have the further advantages of sparse sampling and high luminosity. The agreement between the QSO-galaxy and galaxy-galaxy correlation functions also implies that both QSOs and galaxies are likely to have similar correlation lengths at the present epoch. This is consistent with the observed comoving correlation length of QSOs at $z \sim 1.5$ (which is also the same as that of present day galaxies) only if the QSO correlation length is constant in comoving separation [11]. Although care must be taken in interpreting this result (the comoving separations over which the correlation lengths are derived – ≤ 2 Mpc for the low redshift QSO-galaxy correlation function and ≤ 10 Mpc for the high redshift QSO-QSO correlation function – could correspond to different non-linear and linear evolutionary regimes), it is clear that the study of QSO environments at low/intermediate redshifts provides a useful additional constraint on the evolution of structure in the Universe.

Acknowledgements. RJS acknowledges the receipt of a PPARC studentship.

References

[1] Andreani P., Cristiani S., 1992, *Astrophys. J.* **398**, L13

[2] Boyle B.J., Couch W.J., 1993, *Mon. Not. R. astr. Soc.* **264**, 604

[3] Della Ceca R., Zamorani G., Maccacaro T., Wolter A., Griffiths R., Stocke J.T., Setti G., 1994, *Astrophys. J.* **430**, 533

[4] Ellingson E., Yee H.K.C., Green R.F., 1991, *Astrophys. J.* **371**, 49

[5] Gunn J., Weinberg D., 1995, in *Wide-field Spectroscopy and the Distant Universe*, p.3, eds Maddox & Aragon-Salamanca, World Scientific.

[6] Irwin M.J., Maddox S.J., McMahon R.G., 1994, *Spectrum*, **2**, 14

[7] Iovino A., Shaver P.A., Cristiani S., 1991, in *ASP Conf. Ser. Vol. 21, The Space Distribution of Quasars* p.202, ed Crampton, Astron. Soc. Pacif.

[8] Hintzen P., Romanishin W., Valdes F., 1991, *Astrophys. J.* **366**, 7

[9] Maddox S.J., Efstathiou G., Sutherland W.J., Loveday J., 1990, *Mon. Not. R. astr. Soc.* **242**, 43P

[10] Maddox S.J., Sutherland W.J., Efstathiou G., Loveday J., 1990, *Mon. Not. R. astr. Soc.* **243**, 692

[11] Shanks T., Boyle B.J., 1994, *Mon. Not. R. astr. Soc.* **271**, 753

[12] Smith R.J., Boyle B.J., Maddox, S.J., 1995, *Mon. Not. R. astr. Soc.* submitted

[13] Stocke J.T., Morris S.L., Gioia I.M., Maccacaro T., Schild R., Wolter A., Fleming T.A., Henry J.P., 1991, *Astrophys. J. Suppl. Ser.* **76**, 813

[14] Taylor K. 1995, in *Wide-field Spectroscopy and the Distant Universe*, p.15, eds Maddox & Aragon-Salamanca, World Scientific.

LARGE GROUPS OF QUASARS

Matthew J. Graham [1], Roger G. Clowes [1], Luis E. Campusano [2]
[1] *Centre for Astrophysics, University of Central Lancashire, Preston, UK.*
[2] *Departamento de Astronomía, Universidad de Chile, Santiago, Chile.*



Abstract

We have developed a general method using the minimal spanning tree (MST) for finding large groups in quasar surveys and assessing their statistical significance. We have applied our technique to six surveys, three of them with claims of large groups. The three known groups are recovered and also we find a new grouping of ten quasars at $z \sim 1.9$ and a grouping of seven Seyfert galaxies at $z \sim 0.19$. The former grouping has dimensions of $\sim 120 \times 90 \times 20h^{-3}$ Mpc^3 and the latter has dimensions of $\sim 60 \times 30 \times 10h^{-3}$ Mpc^3. We also present an update of the Clowes & Campusano group of quasars discovered in 1991 [3].

1 Introduction

Large groups of quasars are important components of the early Universe. Three are known at present: Webster [1], Crampton, Cowley & Hartwick [2] and Clowes & Campusano [3]. The latter group appears to be the largest at $\sim 200h^{-1}$ Mpc. The rôle of these groups in the overall structure of the early Universe is unknown, but higher redshift counterparts of the 'Great Wall' or the 'Great Attractor' are two possibilities [4]. Whatever their nature, the frequency and properties of these groups at intermediate redshifts $z \leq 2.0$ can provide important observational constraints on models of the formation and development of structure at early epochs: for example, Komberg & Lukash [4] have suggested such groups require more power on large scales than is consistent with the standard CDM model. It has also been proposed that all quasar clustering, even on small scales ($< 10h^{-1}$ Mpc), is localised in such groups [2].

It is entirely possible that large groups of quasars have been missed in previous analyses of quasar catalogues because of the low power of commonly used statistical methods, e.g. power spectrum analysis (PSA) or the two-point correlation function, at scales approaching the survey

dimensions. In this paper we describe a test based on the minimal spanning tree (MST) to find candidates for quasar groups and assign a statistical significance to them. We also present an update on the quasar group discovered by Clowes & Campusano [3].

2 Method

The minimal spanning tree is a geometric construct, which has found many applications in biology, chemistry and physics. It was introduced into astronomy by Barrow et al. [6] and has been used to find and quantify intrinsic patterns in the galaxy distribution by several authors.

The basis of our selection method for finding quasar group candidates is separation – removing from the MST any edges whose lengths exceed some limit. We separate the MST for a data set at increasing limits. At each separation limit, we calculate the total number of connected structures present. We use as the critical separation limit the separation limit that gives the greatest number of disjoint pieces. We rank each of the structures present at the critical separation limit by the median length of their component edges. The first-ranked or dominant connected structure in ascending order is considered a candidate for a quasar group.

Having determined suitable candidates for quasar groups, we next ascertain which are statistically significant. We use the normalized mean, m, and normalized standard deviation, σ, of the edge-lengths of the MST of the group candidate to characterize the corresponding distribution. This method was developed in two dimensions by [11] and [12, 13]; we have extended it to three dimensions. Normalisation ensures that different distributions can be compared, regardless of the density or area of the surveys.

Frequently, there are other quasars at the same redshift as a candidate structure which the MST does not pick out as belonging to the candidate. In such cases, we have considered the distribution of all quasars in the redshift bin containing the candidate structure. In this way, we avoid the posterior bias that would result from considering the candidate alone. The candidate alone, however, allows an estimate of a minimum characteristic size for the assumed group based on its extent in the survey.

In the asymptotic limit, the values of (m, σ) for a variety of well-characterized distributions converge on specific localized regions of the m–σ plane: in particular, uniform random distributions correspond to a single, fixed point. Other locations correspond to distributions that are: (i) clustered; (ii) possessing a concentration gradient; (iii) quasi-periodic; and (iv) highly-ordered. However, for small samples, far from the asymptotic limit, a uniform random distribution corresponds to a spread of positions in the m–σ plane. Significance levels can be obtained from this spread. As the size of the sample tends to infinity, the spread tends to zero and its centroid converges toward the asymptotic location.

We calculate m and σ for the 2D and 3D MSTs of the group candidate and then compare these values with the distribution of m and σ obtained from randomly generated MSTs, having the same number of points and lying in the same area or volume as the candidate group.

Full details of the method are presented in [5].

3 Results

We have so far applied our group finding procedure to six surveys: [3, 10], [2], [14], [15], [16, 17] and [18]. The first three are known to contain quasar groups; the other three were chosen as having uniform angular coverage. In analysing the Clowes & Campusano data set, we have used the full updated sample of 117 quasars [10]. Of these, 15 are now seen to belong to the

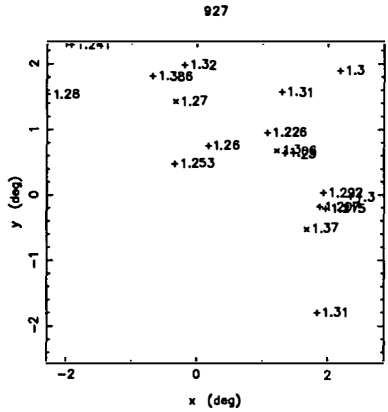


Figure 1: Sky distribution of the Clowes & Campusano group members. There are 15 quasars from our survey (+ symbols) and 3 more from other sources (× symbols). The redshifts are shown with the points; all are accurate to at least two decimal places (the plotting software truncates final zeros). The coordinates are degrees east and north of the field centre.

quasar group, which lies in the range $1.2 \leq z < 1.4$. The sky distribution of these 15 quasars within the survey area, together with an additional three quasars known from other sources, is shown in Fig. 1.

In determining the significance of the candidate, we are assuming a quasar group will be in the cluster region of the m–σ diagram. For each survey, 3000 random MSTs were generated, except for [2] where 10 000 were generated to put an upper limit on the significance level. The results of the 2D and 3D m–σ tests for the six surveys are summarized in Table 1. The significance levels given are the levels at which the null hypothesis that the quasars are randomly distributed can be rejected.

Table 1: This summarizes the results of 2D and 3D m–σ tests carried out on quasar group candidates detected in the host surveys. The number of objects refers to the number of quasars in the redshift range. The number of objects in the candidate is given in parentheses. Significance is determined by the number of random MSTs with $m \leq m_S$ and $\sigma \leq \sigma_S$, where m_S and σ_S are the values of m and σ for the candidate groups.

Host survey	No. of objects	Redshift range	2D MST sig. (%)	3D MST sig. (%)	Minimum size (h^{-3} Mpc^3)
Clowes & Campusano [3]	15 (6)	$1.2 \leq z < 1.4$	2.57	1.56	$150 \times 100 \times 60$
Crampton et al. [2]	23 (11)	$1.0 \leq z < 1.2$	0.42	< 0.01	$60 \times 45 \times 15$
Osmer & Smith [14]	6 (4)	$0.0 \leq z < 1.0$	0.63	0.37	$95 \times 30 \times 15$
Osmer & Hewett [15]	17 (6)	$1.8 \leq z < 2.0$	0.57	5.03	
(Sample 2 – inhomogeneous)	21 (10)	$1.8 \leq z < 2.0$	2.27	8.00	$120 \times 90 \times 20$
Cristiani et al. [16, 17]	21 (7)	$0.0 \leq z < 0.5$	37.40	0.57	$60 \times 30 \times 10$
Hawkins & Véron [18]	10 (5)	$0.7 \leq z < 0.9$	44.27	31.80	

4 Conclusions

We have developed a technique for finding candidates for quasar groups using the minimal spanning tree. We have applied it to six surveys. We have recovered the three previously claimed quasar groups and have found a candidate for a quasar group, consisting of at least ten quasars at $z \sim 1.9$, in [15], and a grouping of seven Seyfert galaxies at $z \sim 0.19$ in [16, 17]. We have also presented an update of a previously known quasar group.

Acknowledgements. LEC was funded partly by grant 985/93 from the Fondo Nacional de Desarrollo Científico y Tecnológico, Chile. MJG acknowledges receipt of an EC grant to attend this conference.

References

[1] Webster A., 1982, *Mon. Not. R. astr. Soc.* **199**, 683

[2] Crampton D., Cowley A.P., Hartwick F.D.A., 1989, *Astrophys. J.* **345**, 59

[3] Clowes R.G., Campusano L.E., 1991, *Mon. Not. R. astr. Soc.* **249**, 218

[4] Komberg B.V., Lukash V.N., 1994, *Mon. Not. R. astr. Soc.* **269**, 277

[5] Graham M.J., Clowes R.G., Campusano L.E., 1995, *Mon. Not. R. astr. Soc.* in press

[6] Barrow J.D., Bhavsar S.P., Sonoda D.H., 1985, *Mon. Not. R. astr. Soc.* **216**, 17

[7] Bhavsar S.P., Ling E.N., 1988, *Astrophys. J.* **331**, L63

[8] Einasto M., Einasto J., Tago E., Dalton G.B., Andernach H., 1994, *Mon. Not. R. astr. Soc.* **269**, 301

[9] Osmer P.S., 1981, *Astrophys. J.* **247**, 762

[10] Clowes R.G., Campusano L.E., Graham M.J., 1995, in *Proceedings of the 35th Herstmonceux Conference*, World Scientific Publishing, in press

[11] Hoffman R., Jain A.K., 1983, *Patt. Rec. Lett. A* **1**, 175

[12] Dussert C., Rasigni M., Palmari J., Rasigni G., Llebaria A., Marty F., 1986, *J. Theor. Biol.* **125**, 317

[13] Dussert C., Rasigni M., Llebaria A., 1988, *J. Theor. Biol.* **135**, 295

[14] Osmer P.S., Smith M.G., 1980, *Astrophys. J. Suppl. Ser.* **42**, 333

[15] Osmer P.S., Hewett P.C., 1991, *Astrophys. J. Suppl. Ser.* **75**, 273

[16] Cristiani S., Barbieri C., Iovino A., La Franca F., Nota A., 1989, *Astr. Astrophys. Suppl. Ser.* **77**, 161

[17] La Franca F., Cristiani S., Barbieri C., 1992, *Astron. J.* **103**, 1062

[18] Hawkins M.R.S., Véron P., 1993, *Mon. Not. R. astr. Soc.* **260**, 202

SESSION IX

DARK MATTER

THE NATURE OF DARK MATTER: THE CASE FOR NONBARYONIC DARK MATTER

Bernard Sadoulet
Center for Particle Astrophysics, University of California at Berkeley,
Lawrence Berkeley National Laboratory, Berkeley, CA 94720 U.S.A.

Abstract

We attempt to summarize the hints we currently have from observational cosmology on the nature of the dark matter in the universe: what can we learn from the current estimates of the mean density, and what can we learn from our comparison of the large scale structure and the comic microwave background? Both sets of observations point to a nonbaryonic component.



I. Introduction

There is mounting evidence that at least 90% of the mass in the universe is "dark." By dark we mean that it is does not emit or absorb any kind of electromagnetic radiation and is only seen by its gravitational effect on visible objects. But we do not yet know the exact amount, or the nature, of this obviously major component of the physical universe. This fundamental puzzle constitutes the "dark matter problem" which dates back to Zwicky[1], and has been often reviewed in the past[2]. Its solution touches central issues in cosmology and astrophysics, and probably also involves particle physics.

Three types of evidence are leading to the conclusion that dark matter exists. The rotation velocities[3] of luminous objects around spiral galaxies indicate at least 10 times as much mass as seen in stars. Studies of the velocities of globular clusters[4] around elliptical galaxies lead to a mass to light ratio (M/L) of 15, while the extended x-ray emission[5] observed around them implies even larger values (>70). Clusters of galaxies exhibit even larger amounts of dark matter (M/L>100), as evidenced by three types of observations: the large dispersion velocities of the galaxies, the temperature of x-ray gases present in the center of many clusters[6], and the mapping of mass distribution through gravitational lensing[7]. It is highly significant that these three different methods indicate similar values for the depth of potential wells of the clusters.

If there is a wide consensus on the existence of dark matter, there is a lot of controversy about its abundance and even more about its nature. A fundamental question is to understand whether dark matter is made of ordinary baryonic matter or whether it has to be something totally new: a nonbaryonic substance somehow formed in the hot Big Bang.

In the talks at the Workshop, we attempted to gather the various pieces of evidence on the nature of dark matter, from cosmology, physics of the early universe, and observation of massive compact halo objects. The space limitations lead us to focus in this written version on the two major arguments for nonbaryonic dark matter: the value of Ω and the magnitude of the temperature fluctuations observed by COBE in the cosmic microwave background. In section II, we will summarize the current attempts to measure the average mass density of the universe and evaluate their consequences. In section III we will describe indications coming from the observations of the large scale structure of galaxies and their comparison with the measurements.

II. The Average Mass Density and the Nature of Dark Matter

The average mass density in the universe is a critical element in the investigation of the nature of dark matter. We believe that we know the average density of baryons in the universe, and if the measured total density were to be significantly higher, it would

be clear evidence that the dark matter is predominantly nonbaryonic. Measuring densities in units of the critical density

$$\rho_c = \frac{3H^2}{8\pi G}, \tag{1}$$

where H is the Hubble expansion parameter, we can compare the amount of baryons in the universe

$$\Omega_b = \frac{\rho_b}{\rho_c}, \tag{2}$$

to the total average density measured by

$$\Omega = \frac{\rho}{\rho_c} \ . \tag{3}$$

Our confidence in our knowledge of the number of baryons in the universe is based on the success of the standard scenario of (homogeneous) nucleosynthesis in accounting for the observational determinations of the primordial abundance of light elements (helium 4, deuterium, helium 3 and lithium 7)[8]. The limits on the baryonic density Ω_b by the most recent analyses of the primordial abundances are surprisingly narrow:

$$0.01 \leq \Omega_b h^2 \leq 0.015, \tag{4}$$

where h is the Hubble expansion parameter in the usual units of 100 km/s/Mpc. If we assume a lower limit for the Hubble constant of 40 km/s/Mpc, we obtain an upper limit for Ω_b of 0.1. What then are the current experimental estimates of the value of Ω? We can classify the current methods into three categories: inventories, dynamical methods and cosmological tests. We will take them in turn.

Inventories

The basic idea of an inventory is to measure the mass of individual components, such as galaxy clusters, and sum them appropriately to get the average density. Usually the mass M is deduced from the dispersion velocities through the virial theorem, and converted into a mass to light ratio M/L which allows us to compute the mass density from the luminosity distribution of the considered objects:

$$\rho = \left\langle \frac{M}{L} \frac{dL}{dV} \right\rangle \approx \left\langle \frac{M}{L} \right\rangle \left\langle \frac{dL}{dV} \right\rangle, \tag{5}$$

where L is the absolute luminosity of the objects, dL/dV is the luminosity volume density and $\langle\rangle$ denotes an average taken on all the objects considered. In applying the method it is, however, difficult to know where the system being considered stops. For instance, at large distances from the center of spiral galaxies we are running out of objects to measure, and galaxies far from the cluster core fade in the field. Figures 1 and 2 give the

estimates obtained for Ω with such methods, for spiral galaxies and clusters of galaxies corresponding to M/L of 30h and 225h respectively. They are drawn for two values of the Hubble constant, H = 50 km/s/Mpc and H = 80 km/s/Mpc respectively. The values obtained are much smaller than 1, which would correspond to M/L of 1500h. None of the known objects have such high mass to light ratio. However, it should be noted that the virial theorem is only sensitive to inhomogeneities of the mass distribution, and that such methods can only give a lower limit of Ω.

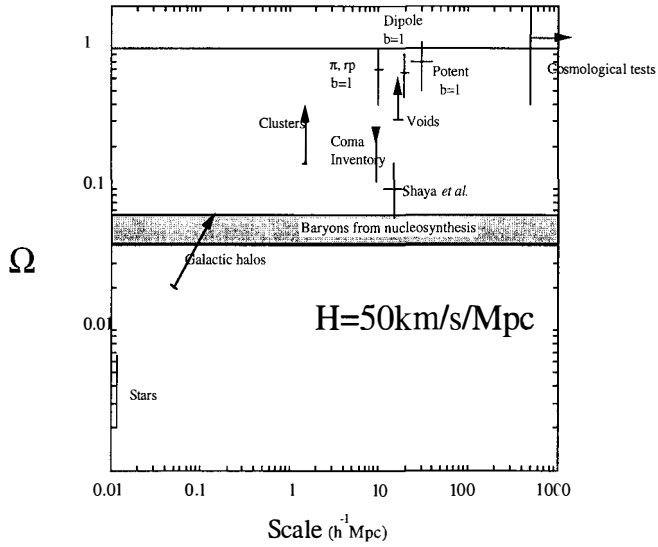


Figure 1. Effective Ω as function of scale for a Hubble constant of 50 km/s/Mpc.

Recently, S. White and coworkers[9] have proposed a method which, combined with primordial nucleosynthesis, gives an upper limit for Ω. Consider, for instance, the Coma cluster. The mass in baryons M_b can be bound from below by summing the mass in stars and in the intracluster gas deduced from the x-ray luminosity. The total mass M_t can be obtained either from the virial velocities of galaxies or the x-ray temperature. We can then get the ratio M_b/M_t for the cluster. This can be transformed into a lower limit of M_b/M_t for the whole universe, if we can reliably estimate the baryon enhancement which occurred in the cluster collapse. For objects as large as Coma, this correction appears never to be large in the various models they consider (at most 40%). They finally obtain

$$\left(\frac{M_b}{M_t}\right) \geq 0.015 + 0.08h^{-\frac{3}{2}}. \qquad (6)$$

Combining with the upper limit for Ω_b given above, we get the upper limit

$$\Omega \leq \frac{0.015}{h^2\left(0.015 + 0.08h^{\frac{3}{2}}\right)}, \tag{7}$$

which is 0.3 for $h = 0.5$ and 0.2 for $h = 0.8$. These estimates are indicated in Figures 1 and 2. Note that this method has been criticized on two grounds: the x-ray measurements of the total mass tend to give lower values of the total mass than gravitational lensing observation and the baryon enhancement given by the models used by the authors may be too low.

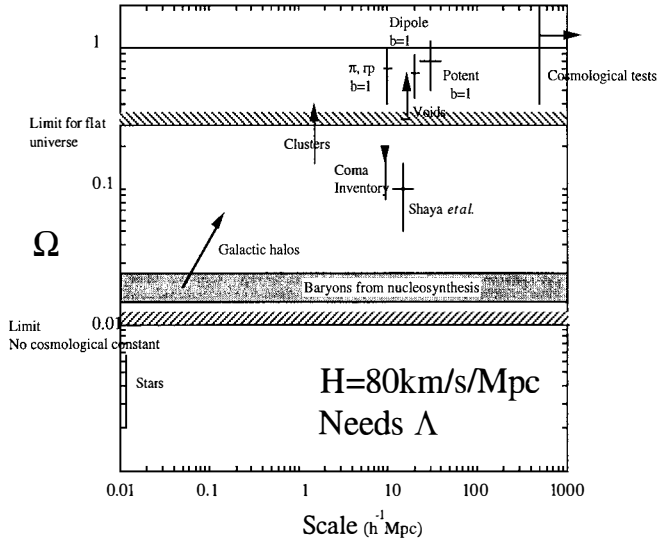


Figure 2. Effective Ω as function of scale for a Hubble constant of 80 km/s/Mpc.

Dynamical Methods

Attempts to apply the virial theorem on even larger scale structure are prevented by the fact that the systems are not stationary, with structure still clearly forming. Not only do we observe on the large scale a complex distribution of galaxies[10] with voids, filaments, bubbles and the like, not typical of a virialized system, but velocity flows coherent on large scales can be deduced from the comparison of the distance and redshift of (relatively close-by) galaxies[11], or reconstructed[12] from the density of galaxies detected in the infrared by the IRAS satellite.

As the time that structure takes to form is sensitive to the underlying averaged

density, one can attempt to use the large scale distribution of galaxies and the associated velocity flows to estimate Ω. Basically, one writes the equations:

observed velocities = acceleration (due to density inhomogeneities) × time of formation,

or

observed inhomogeneities = rate of variation (due to peculiar velocities) × time.

In the linear regime[13], these equations become

$$\vec{v} = G\rho_b \vec{\nabla} \int d^3x' \frac{\frac{\delta\rho}{\rho_b}}{|x-x'|} \times \frac{2f}{3H\Omega} = \frac{Hf}{4\pi} \vec{\nabla} \int d^3x' \frac{\frac{\delta\rho}{\rho_b}}{|x-x'|} \tag{8}$$

$$\text{and } \frac{\delta\rho}{\rho_b} = -\vec{\nabla}.\vec{v} \times \frac{1}{Hf} \text{ with } f \approx \Omega^{0.6}. \tag{9}$$

Unfortunately we do not have access to the mass density fluctuation $\delta\rho/\rho$, but only the object density contrast $\delta n/n$ in the number of galaxies, and we have numerous indications that light does not trace mass. It is usually assumed that the two densities are related by

$$\frac{\delta n}{n} = b\frac{\delta\rho}{\rho_b}, \tag{10}$$

where b is the "biasing parameter" which is usually taken as constant (but does not need to be!). In the linear regime, we can then only obtain the value of $\beta = \Omega^{0.6}/b$ and not the value of Ω!

This method has been applied in three ways, depending on the way peculiar velocities are measured:

• We can compare the measured value of our peculiar velocity with respect to the cosmic microwave background to that obtained from summing the acceleration due to observed density inhomogeneities[12].

• The radial components of the peculiar velocity field can be measured from the comparison of the measured redshifts with absolute distance indicators. The three dimensional velocity field can then be reconstructed[14] through the natural assumption of zero vorticity ($\vec{\nabla} \times \vec{v} = 0$), as any initial vorticity would be erased by the Hubble expansion. This allows us to compare the observed density fluctuations to those predicted by the divergence of the velocity field. The results obtained with this procedure, which is called "POTENT," has recently been reviewed by A. Dekel[15].

• Finally we can study the velocity correlations[16] around clusters of galaxies. We can plot the relative radial velocity π as a function of the perpendicular distance r_p. Close to a cluster center, virial velocities will generate a distribution elongated in the radial direction. At larger distance we observe a flattening of the distribution in the radial (π) direction because the pull of gravity decreases the redshift dispersion. As before, the growth of this structure is dependent on the time available and therefore of $f(\Omega)$.

The three methods give very similar results:

$$0.5 \leq \beta \leq 1.2, \tag{11}$$

which means that if the bias parameter b is greater than 1, Ω is greater than 0.3. This is reassuring, as the distance indicator indicators used in the second method were *a priori* suspect. We have entered these results in Figures 1 and 2 assuming $b = 1$. We should, however, note a recent calculation by Shaya, Peebles and Tully[17] which gives

$$\Omega = 0.1 \pm 0.04. \tag{12}$$

It is still too early to pin down the origin of this discrepancy. We should note also that although it is unlikely that $b < 1$, there is no strong theoretical basis for any value of b. So far, the only dynamical method result independent of b, is obtained from the void distribution[18], which again points to $\Omega \geq 0.3$!

Cosmological Tests

A potentially powerful set of methods relies on a direct determination of the geometry of the universe by measuring quantities sensitive to this geometry. For instance, the variation of the apparent luminosity of a "standard candle" (i.e., a constant absolute luminosity object) as a function of redshift would tell us about potential deviation from the $1/r^2$ law which is only valid in a flat space, or the change with redshift of the volume element traced by the density of galaxies would be a direct indication of spatial curvature. These cosmological tests directly address the question of the value of Ω (and Λ), but they require that one be able to differentiate between the variation due to cosmology and the evolution of the objects.

This problem has so far plagued the first type of measurement. For instance, in the classical test of Sandage and coworkers[19] using the brightest galaxy in a cluster as a standard candle, the luminosity evolution dominated cosmological effect. In recent years, a new idea has been developed: Type Ia supernovae appear to be reasonable standard candles "locally," they can be efficiently searched for[20] at intermediate redshifts (0.5), and they are probably the best hope to perform this luminosity test. The main problem appears to be the need for a very large amount of telescope time for photometric and spectroscopic follow-up.

The volume variation test was first attempted on radio galaxies, counting their number as a function of luminosity, but they evolve too rapidly with redshift. Recent attempts[21] to use the K band to measure the number density of optical galaxies as a function of luminosity gave ambiguous results, as the overall picture is complicated by mergers and "local" dwarf star-forming galaxies.

The real way to do the volume test would be to directly measure the counts as a function of redshift, and not rely on luminosity which is not simply related to redshift. This approach was pioneered by Loh and Spillar[22], but their heroic attempt has been criticized on many grounds[23] and is not reliable. With the operation of the Keck 10-m

telescope, it will soon be possible to do this measurement in a much more convincing way with a suitable multi-slit spectrograph. For instance, the DEIMOS spectrograph now under construction at Lick would allow the measurement not only of the color and redshift of the object, but also its mass through the measurement of the internal velocity dispersion. This should be a powerful method to detect merging, gravitational lensing and luminosity evolution, and should provide a much more reliable determination of the geometry.

We should finally comment on the constraints from the determinations of the Hubble Constant H_O. Over the last few years, a number of methods (Tully-Fisher, surface brightness fluctuations, planetary nebulae and supernova photosphere methods) seem to converge[24] to a value of

$$H_O \approx 80 \text{ km/s/Mpc.} \tag{13}$$

The recent determination of H_O with the measurement of Cepheids by the Hubble Space Telescope in M100 is similarly high. Although physical methods[24] tend to give lower values, we may have to face a fairly high value, such as that chosen to draw Figure 2. This leads to a number of problems with the age of the universe which none of us would accept to be below 12 billion years. As shown by the lower hatched line, without a cosmological constant, this imposes an upper limit of Ω of 1% which is grossly in contradiction with observations. We would therefore be led to introducing a cosmological constant. The upper hatched line in Figure 2 indicates the corresponding upper limit for the case of a flat universe ($\Omega_\Lambda + \Omega = 1$).

In conclusion, as shown in Figures 1 and 2, there are now many indications that Ω is greater than the values obtained from primordial nucleosynthesis and this independently from the value of the Hubble constant. Although these estimates stem mostly from the study of velocity flows at large scale and may be subject to large systematics (including the value of the bias parameters), they are based on substantively different methods and seem difficult to totally discount. We may be close to reaching a point where we do no have to appeal to the naturalness of $\Omega = 1$ or to inflation to justify the existence of dark matter. It is interesting to note that a powerful new generation of cosmological tests may soon be available, allowing us to pin down the geometry of the universe. It may also be the case that our scenario of primordial nucleosynthesis is wrong. However, it has been so far remarkably stable.

III. The Formation of Structure and Dark Matter

A different line of argument based on the distribution of mass and the large scale structure that we observe in the universe may lead to similar conclusions that at least the major part of dark matter is not made of baryons. The formation of structure is certainly due, at least in part, to gravitational collapse of density fluctuations, and since

dark matter is gravitationally dominant, its nature imprints characteristic features on the observed universe[25]. It has been known for some time that the mere fact that the 2.7K cosmic microwave background is so smooth and the large scale structure is so clumpy is difficult to understand without the presence of nonbaryonic dark matter. If the background photons tell us about the baryonic density fluctuations at time of recombination, without dark matter there is simply not enough time to grow the large fluctuations observed today. With nonbaryonic dark matter, this is much easier. Before protons and electrons recombine into hydrogen, they are prevented from growing density fluctuations by their coupling to photons, which diffuse easily through the medium. Dark matter density fluctuations, on the contrary, can grow since they are uncoupled to photons. After recombination, the baryons fall into the potential wells prepared by dark matter, and there is enough time then to form the structure observed today.

This argument has recently become much more precise with the detection by the COBE satellite of anisotropies[26] in the temperature of the cosmic microwave background. Figure 3 displays the power spectrum of density fluctuations of galaxies as observed[27] by IRAS as a function of the spatial frequency. How can we place the COBE measurement on the same graph? If we make the assumption that the dark matter is predominantly nonbaryonic and that gravitational waves do not play an important role, we can relate the $<(\Delta T/T)^2>$ measured at the various angular scales to the spectral power density $P(k) = <(\delta\rho/\rho)^2>$ at the redshift of recombination $z \approx 1000$. If we make in addition the assumption that the universe is close to being flat (with or without a small cosmological constant), we can then extrapolate to the current epoque, and obtain the upper lozenge at the top left of the plot. It is striking that we can draw a smooth curve passing both through the IRAS points and the extrapolated COBE result. This is the best evidence obtained so far for large scale structure to have indeed originated from primordial density fluctuations. It is also a good indication for the nonbaryonic character of dark matter; had we assumed the dominance of baryonic dark matter our extrapolation to the current epoque would have been much lower. Only somewhat contrived models (e.g., the so-called "isocurvature" scenarios[28]) with a large number of parameters are then able to link the microwave fluctuations and the large scale structure observations. In contrast, the qualitative features of the full spectrum are obtained by the very simple cold dark matter model displayed in the figure[29]. But it is clear that this first approximation fails in detail, in particular as it predicts too much power on small scales. This can be fixed, for instance by adding a 5 eV neutrino as in the Cold + Hot Dark Matter model[30], but before such a massive neutrino is detected it is difficult to say in the laboratory whether we are just adding an arbitrary parameter or describing reality. There are a number of other ways to fix the problem[31].

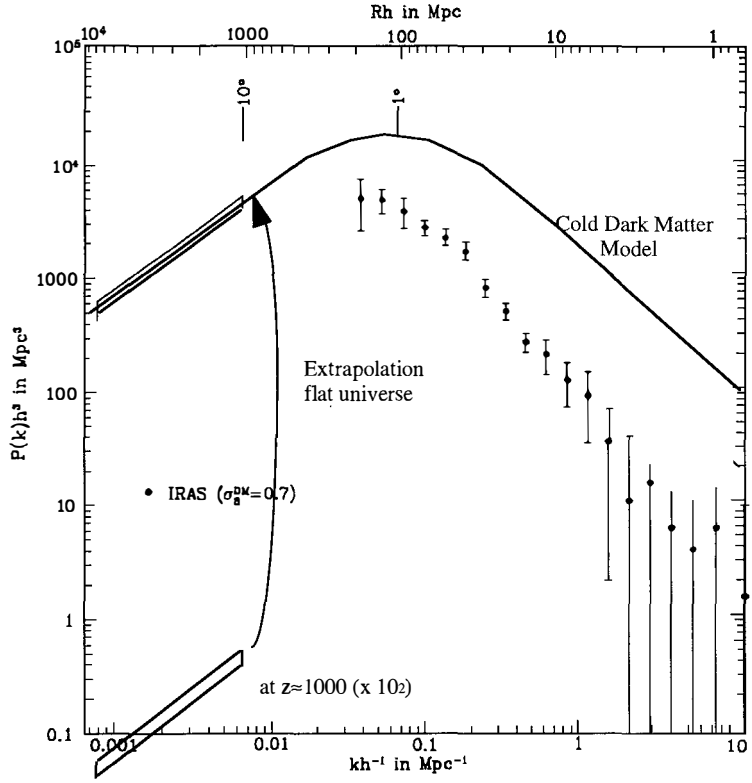


Figure 3. Comparison of the power spectrum of density fluctuations observed at large scales with extrapolation of density fluctuations inferred from the COBE measurement of the comic microwave background temperature fluctuations. This graph assumes adiabatic fluctuations and nonbaryonic dark matter.

IV. Conclusions

Deciphering the nature of dark matter is one of the most fundamental scientific problems of our time, and it is particularly important to decide if it is baryonic or nonbaryonic. There is growing evidence from cosmological observations that a major fraction of it should be nonbaryonic. We have recalled here the main two arguments: the apparent large value of Ω obtained from velocity flows at large scale and the order of magnitude of the temperature fluctuations observed in the cosmic microwave background. There is good hope that in the coming years these arguments will become very solid (or disappear!). However, nothing will replace the direct detection of dark matter!

Acknowledgments

It is a pleasure to acknowledge numerous exchanges on these matters with the members of the Center for Particle Astrophysics, (in particular, M. Davis, J. Primack, J. Silk and M. White), and with the participants of the workshop (in particular, A. Dekel and G. Efstathiou) .

This work was supported by the Center for Particle Astrophysics, a National Science Foundation Science and Technology Center operated by the University of California under Cooperative Agreement no. AST-912005 and by the Department of Energy under the contract DE-AC03-76SF00098.

References

1. F. Zwicky, *Helv. Phys. Acta* **6** (1933) 110.
2. S.M. Faber and J.S. Gallagher, *Ann. Rev. Astron. Ap.* **17** (1979) 135; V. Trimble, "Existence and Nature of Dark Matter in the Universe," *Ann. Rev. Astron. Ap.* **25** (1987) 245.
3. See, e.g., A. Bosma, *Ap. J.* **86** (1981) 1825.
4. See, e.g., J.R. Mould, J.B. Oke and J.M. Nemec, *Ap. J.* **92** (1987) 153.
5. Fabian *et al.*, *MNRAS* **221** (1986) 1049.
6. D. Fabricant and P. Gorenstein, *Ap. J.* **267** (1984) 535; C. Jones and W. Forman, *Ap. J.* **276** (1984) 38.
7. See, e.g., J.A. Tyson, F. Valdes, R.A. Wenk *et al.*, *Ap. J.* **349** (1990) 2; Maoz *et al.*, *Ap. J.* **394** (1992) 51; B. Fort *et al.*, *Ap. J. Lett.* **399** (1992) L125.
8. J. Yang *et al.*, "Primordial Nucleosynthesis: A Critical Comparison of Theory and Observation," *Ap. J.* **281** (1984) 493; see the recent reviews by K.A Olive, D.N. Schramm, G. Steigman and T. Walker, *Phys. Lett.* **B426** (1990); D. Denegri, B. Sadoulet and M. Spiro, "The Number of Neutrinos Species," *Rev. of Modern Physics* **62** (1990) 1. For a recent review, see K.A. Olive, "The Quark Hadron Transition in Cosmology and Astrophysics," *Science* **251** (1991) 1194.
9. S.D.M. White *et al.*, "The Baryon Content of Galaxy Clusters: A Challenge to Cosmological Orthodoxy," *Nature* **366** (1993) 429.
10. J. Huchra and M. Geller, *Science* **246** (1989) 891.
11. A. Dressler, S.M. Faber, D. Burstein *et al.*, "Spectroscopy and Photometry of Elliptical Galaxies: A Large Streaming Motion in the Local Universe," *Ap. J. Lett.* **313** (1987) L37; A. Dressler, D. Lynden-Bell, D. Burstein *et al.*, *Ap. J.* **313** (1987) 42.
12. M.A. Strauss and M. Davis, "A Redshift Survey of IRAS Galaxies," in *Proceedings of IAU Symposium No. 130, Large Scale Structure of the Universe*, Balaton, Hungary, June 1987; M. Davis, M.A. Strauss and A. Yahil, "A Redshift Survey of Iras Galaxies: III Reconstruction of the Velocity and Density Fields," *UCB/SUNY/Cal Tech*, (July 1990); W. Saunders *et al.*, "The Density Field of the Local Universe," *Nature* **349** (1991) 32.
13. P.J.E. Peebles, "The Large Scale Structure of the Universe," Princeton University Press, section 14 (1980).
14. E. Bertschinger and A. Dekel, *Ap. J. Lett.* **336** (1990) 15; A. Dekel, E. Bertschinger and S.M. Faber, *Ap. J.* **364** (1990).
15. (1994) 371.
16. M. Davis, private communication.

17. P.J.E. Peebles, seminar at the Berkeley Astronomy Department, March 1995.
18. A. Dekel, in this volume.
19. A. Sandage, *Physics Today* **34** (1970).
20. H.U. Norgaard-Nielsen *et al.*, *Nature* **339** (1989) 523; S. Perlmutter *et al.*, *Ap. J. Lett.* **440** (1995) L41.
21. L.L. Cowie, "Galaxy Formation and Evolution," *Physica Scripta* (1990).
22. E. Loh and Spillar, *Ap. J.* **303** (1986) 154; *Ap. J. Lett.* **307** (1988) L1; E. Loh, *Ap. J.* **329** (1988) 24.
23. See, e.g., Caditz and Petrosian, *Ap. J. Lett.* **337** (1989) L65; Bahcall and Tremaine, *Ap. J. Lett.* **326** (1988) L1; Omote and Yoshida, *Ap. J.* **361** (1990) 27.
24. M. Fukugita, C.J. Hogan and P.J.E. Peebles, "The Cosmic Distance Scales and the Hubble Constant," *Nature* **366** (1993) 309; W.L. Freedman *et al.*, "Distance to the Virgo Cluster Galaxy M100 from Hubble Space Telescope Observations of Cepheids," *Nature* **371** (1994) 757.
25. See, e.g., J.R. Primack, "Dark Matter, Galaxies, and Large Scale Structure in the Universe," lectures presented at the International School of Physics "Enrico Fermi," Varenna, Italy, June 26–July 6, 1984, *SLAC-PUB-3387* (1984).
26. G. Smoot, C. Bennett, A. Kogut, E. Wright *et al.*, "Structure in the COBE DMR First Year Maps," *Ap. J. Lett.* **396** (1992) L1.
27. K. Fisher, M. Davis, M.A. Strauss, A. Yahil *et al.*, "The Power Spectrum of IRAS Galaxies," *Ap. J.* **389** (1992) 188.
28. P.J.E. Peebles, *Nature* **327** (1987) 210.
29. S.D.M. White *et al.*, *Ap. J.* **313** (1987) 505; C.S. Frenk *et al.*, *Ap. J.* **351** (1990) 10.
30. M. Davis, F. Summers and D. Schlegel, *Nature* **359** (1992) 393; A. Klypin, J. Holtzman, J.R. Primack and E. Reg, *Ap. J.* **416** (1993) 1; Y.P. Jing *et al.*, *Astron. Ap.* **284** (1994) 703; C.P. Ma and E. Bertschinger, *Ap. J.* **434** (1994) L5. See also J.R. Primack, in these proceedings.
31. See, e.g., the review by D. Scott, J. Silk and M. White, *Science* **268** (1995) 829.

CAN DARK MATTER BE FULLY BARYONIC ?

J.-M. Alimi, & A. Serna
Laboratoire d'Astrophysique Extragalactique et de Cosmologie (CNRS, URA173), Observatoire de Paris-Meudon, Meudon CEDEX 92195, France

Abstract

The most natural alternatives to General Relativity are scalar-tensor theories, which contain the metric tensor $g_{\mu\nu}$ and an additional scalar field Φ. This class of theories arise currently in primordial cosmology (inflation), and particle physics (Kaluza-Klein, supersymmetric, low-energy limit of superstrings, theories). We have deduced the light element production and analyzed all possible cosmological models in scalar-tensor theories compatible with solar-systems experiments, binary pulsar dynamics... We then succeeded for the first time in constructing a class of scalar-tensor models which predicts right primordial light elements abundances allowing the Universe closure only by baryons. Such predictions have been obtained because the speed-up factor (ratio between the theory Hubble parameter to that obtained in General Relativity) in such class of theories has a non-monotonous time evolution during primordial nucleosynthesis. These theories have also important consequences on inflation and large-scale structure formation.

1 Introduction

In the standard picture of Big Bang nucleosynthesis the yields of light elements only agree with their inferred primordial abundances if the baryonic density parameter, Ω_b, is smaller than 0.1. In the opposite, the dynamical analysis of systems with different sizes, as spiral galaxies, galaxy clusters or cosmic velocity fields..., suggests an observational estimation of the total density parameter, Ω_0, larger than 0.1. Two possibilities can be then considered to solve such apparent contradiction. The first one consists to introduce a non-baryonic dark matter component. This hypothesis has been extensively studied in the literature [1]. However, up to now, there is not a clear observational evidence of detection of such component. The second possibility consists to modify explicitly the primordial nucleosynthesis process (PNP) by

introducing for example decaying particles, or by considering inhomogeneities in the neutron-proton primordial density field, or more exotic procedures. It has been shown that when these scenarios are made to fit the observed abundances accurately, the resulting conclusions on the allowed contribution of baryons to the critical density, remains approximatively the same as in the standard homogeneous case [2]. All these methods have not been then largely succesfull. We propose a different approach. A reformulation of the dark matter problem in the framework of scalar-tensor gravity theories.

2 Scalar-tensor Gravity Theories: Fundamental Motivations and Physical Constraints

The Einstein Equivalence Principle generates a whole class of theories (called metric theories) describing gravitational interaction. The distinction among these theories lies in the number and type (tensorial, vectorial, scalar) of additional gravitational fields, other than the metric tensor $g_{\mu\nu}$, they contain. From a theoretical point of view, the most natural alternatives to General Relativity (GR) are scalar-tensor theories, which contain an additional scalar field, ϕ, the relative importance of which is determined by an arbitrary coupling function $\omega(\phi)$ [3, 4, 5]. GR corresponds to the case where the field $\Phi = \text{const.} = 1$ implying an infinite $\omega(\Phi)$. Brans-Dicke's theory is defined by a constant $\omega(\Phi)$. Many other scalar-tensor theories have been proposed in the literature [6].

In recent years, scalar-tensor theories have received a renewed interest specially in cosmology [7], because it provides a natural (non-fine-tuned) way to restore the original ideas of inflation while avoiding the cosmological difficulties coming from the vacuum-dominated exponential expansion obtained in GR. Scalar-tensor theories also arise in current theoretical attempts at deepening the connection between gravitation and the other interactions. For example, in modern revivals of the Kaluza-Klein theory and in supersymmetric theories with extra dimensions, one or several scalar fields arise in the compactification of these extra dimensions [8]. Furthermore, scalar-tensor theories may also appear as a low-energy limit of superstring theories [9].

Scalar-tensor theories are not however physically interesting at all epochs. We know that GR allows to reproduce very accurately the solar-system and the binary pulsar dynamics. The present behavior of scalar-tensor theories is then constrained to be extremely close to that implied by GR. The physical conditions in the early universe and the subsequent cosmological evolution in scalar-tensor theories can be nevertheless very different from the usual ones. Since a wide class of these theories exhibit an attractive mechanism towards Einstein's theory [10], they can be compatible with present solar-system experiments in spite of their very different predictions at early times. We will show here that a class of these theories is able to reproduce the right light element abundances with an allowed baryon density range much larger than that permitted by GR. How such result is it possible ?

3 Primordial Nucleosynthesis and Cosmological Models in the Scalar-Tensor Gravity Theories

The introduction of a scalar field Φ can modify the expansion rate in the early universe. Consequently, the n/p ratio at the beginning of primordial nucleosynthesis (PN) as well as the PNP itself can be modified. In order to evaluate the implications of such modifications on the light element production, it is first necessary to compute precisely the resulting cosmological models.

We consider an homogeneous and isotropic universe. The line-element has then a Robertson-Walker form and the energy-momentum tensor corresponds to a perfect fluid. The field equations are then

$$\begin{aligned} \frac{8\pi}{3\phi}\rho &= \frac{c^2 k}{R_0^2 a^2} + \frac{\dot{a}^2}{a^2} - \frac{\omega}{6}\frac{\dot{\phi}^2}{\phi^2} + \frac{\dot{a}\dot{\phi}}{a\phi} \\ \ddot{\phi} + 3\frac{\dot{a}}{a}\dot{\phi} &= \frac{1}{(3+2\omega)}[8\pi(\rho - 3P/c^2) - \omega'\dot{\phi}^2] \end{aligned} \tag{1}$$

where $k = 0, \pm 1$, ρ and P are the energy-mass density and pressure, respectively, $a \equiv R/R_0$ is the dimensionless scale factor and dots mean time derivatives.

It is convenient to consider the speed-up factor, $\xi \equiv H/H^{FRW}$, where $H \equiv \dot{a}/a$ is the Hubble parameter, while H^{FRW} is that predicted by GR at the same temperature. Since we are only interested on viable scalar-tensor cosmological models, that is, those which are compatible with present solar-system experiments but where the early evolution of the Universe is distinguishable from that obtained in GR, the present value of ξ is normalized so that $\xi \to 1$.

Analytical asymptotic solutions of all possible scalar-tensor cosmological models converging towards GR have been obtained and discussed elsewhere [11]. By specifying $\omega(\Phi)$ as a Taylor series, we have then numerically computed the cosmological models at any time. Four main classes of theories have been found (Fig. 1). The first and the second class correspond to singular models with a monotonous speed-up factor $\xi(T) \equiv H/H^{FRW}$ faster or slower, respectively, than in GR. Non-singular models or models with a critical temperature where $3 + 2\omega = 0$ constitute the third class. Finally, the last class corresponds to models with a non-monotonous $\xi(T)$ function. It is defined, for instance by the following coupling function $\omega(\Phi)$.

$$3 + 2\omega(\Phi) = \frac{3}{\lambda^2}[(\Phi - 1) + k] \tag{2}$$

with a positive present value of the coupling function ω_0 and a present Φ value greater than unity, the parameters λ and k satisfying $\lambda^2/k > 1$.

The Ω_b constraints obtained in the first three classes of theories do not differ considerably from that found in GR.

Theories with a non-monotonous evolution of the speed-up factor ξ (see Fig. 1) have an initial phase where the expansion of the universe is slower than in GR, but it later becomes faster than in the standard cosmology. Figs. 2 show the light element abundances as a function of ω_0 and η_{10} in the theory defined by $\lambda^2 = 3/2$ and $k = 1/2$. For the very high ω_0 values, the maximum ξ value is reached much before the PNP (Fig. 1d). Consequently the speed-up factor is greater than unity during nucleosynthesis and the resulting bounds on ω_0, ξ_{10} and η_{10} are then equal to those found for theories of class-1. However, we can also see from these figures that each element has another allowed interval for not so high values of ω_0. Simultaneously right primordial abundances in this last interval can be obtained for high η_{10} values. The achievement of such high η_{10} values in the framework of these theories can be explained as follows. In a class-4 theory distinguishable from GR, the expansion rate of the universe at the beginning of nucleosynthesis is slower than in GR. As in class-2 theories (those with an expansion rate slower than in GR), the tendency to have a smaller production of ^{4}He can be balanced by considering high η_{10} values. The upper bound on η_{10} is then constrained by the D/H abundance. However, differently from class-2 theories, the expansion rate of the universe becomes faster than in GR during the PNP. The D burning is then much less effective because it occurs in a shorter time and, consequently, high η_{10} values are allowed.

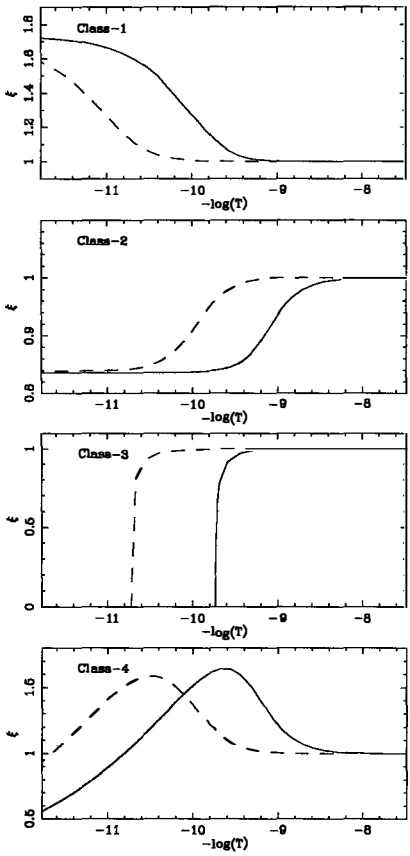


Figure 1: Expansion rate $\xi = H/H^{FRW}$ as a function of T for different types of cosmological models. Solid lines correspond to ω_0 values smaller than those of dashed-lines.

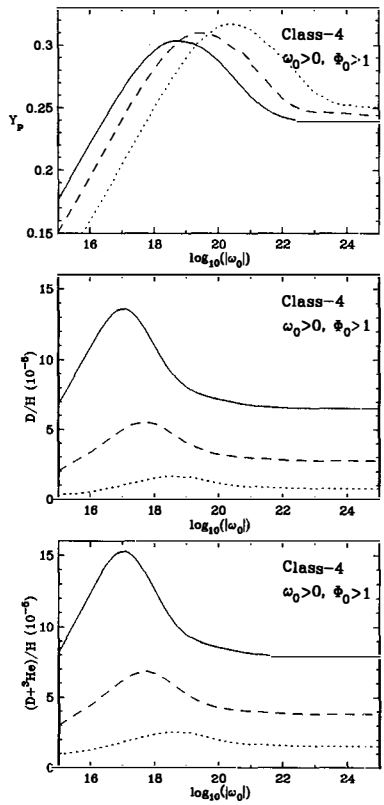


Figure 2: Primordial abundances of a) ^{4}He, b) D/H, and c) (D+^{3}He)/H, as a function of ω_0. The theory shown in this figure is defined by $\omega_0 > 0, \Phi_0 > 1, k = 1/2, \lambda^2 = 3/2$. Solid line corresponds to $\eta_{10} = 3$, dashed line to $\eta_{10} = 5$, and dotted line to $\eta_{10} = 10$.

In order to obtain the largest η_{10} value allowed in the framework of this class of models, we must then analyze those theories with the highest ξ value during the PNP, but with $\xi_{10} < 1$ at the beginning of PN. We have performed such an analysis in terms of λ and k. We have found that, in fact, the allowed Ω_{b0} value is considerably increased with respect to that obtained in other classes of scalar-tensor theories. However, the ω_0 lower-bound is smaller as the allowed Ω_{b0} is higher. The upper bound on the baryon contribution to the density parameter is then determined by the compatibility with solar-system experiments which requires $\omega_0 > 500$ and leads to right primordial abundances with $\eta_{10} \leq 58.7$, that is

$$0.01 \leq \Omega_{b0} \leq 1.38 \tag{3}$$

The above result does not signify that Ω_{b0} values equal or greater than unity are only possible for rather low values of ω_0. For instance, for $\lambda^2 = 0.1$ and $k = 10^{-5}$, we can always find some interval of ω_0 greater than 10^7 allowing nevertheless for η_{10} values in the range $2.8 \leq \eta_{10} \leq 56.5$. The resulting permitted interval for Ω_{b0} is then $0.01 \leq \Omega_{b0} \leq 1.33$. Closure of the universe by baryons is then possible in the framework of this class of scalar-tensor theories even when a standard composition of the universe is used [13]. The ω_0 values needed to allow for $\Omega_{b0} \geq 1$ are very high and, consequently, this class of theories are at present close enough to GR to ensure compatibility with post-Newtonian experiments. On the contrary, they are very different from GR at early times implying expansion rates of the universe which can be several hundred faster (when $\xi = \xi_{max}$) than in the FRW cosmology.

4 Conclusion

We have succeeded in constructing a class of scalar-tensor models which, for the first time, predict the right primordial light element abundances (Helium, Deuterium, and Lithium [13]) while being effectively different from GR during the primordial nucleosynthesis process. This class of scalar-tensor models allows the Universe closure only with baryons. Inflation models in these theories and their consequences on the primordial fluctuation spectrum as well as on the large-scale structure formation are open questions. The study of these question is forthcoming.

A similar analysis for class-1, class-2 and class-3 scalar-tensor theories [11, 12] implies, in the opposite, that the right primordial abundances are only obtained in the limit where these theories are almost undistinguishable from GR from the beginning of the PNP to the present. Consequently, we get then similar constraint on Ω_{b0} than in GR (Table 1).

Table 1. Baryonic Density and Scalar-Tensor Theory.

GR	Class-1	Class-2	Class-3	Class-4
$2.8 \leq \eta_{10} \leq 3.7$	$2.8 \leq \eta_{10} \leq 3.7$	$2.8 \leq \eta_{10} \leq 8.4$	$2.8 \leq \eta_{10} \leq 8.4$	$2.8 \leq \eta_{10} \leq 58.7$
$0.01 \leq \Omega_{b0} \leq 0.09$	$0.01 \leq \Omega_{b0} \leq 0.09$	$0.01 \leq \Omega_{b0} \leq 0.19$	$0.01 \leq \Omega_{b0} \leq 0.19$	$0.01 \leq \Omega_{b0} \leq 1.4$
$\omega_0 = \infty$	$\omega_0 \geq 10^{20}$	$\omega_0 \geq 10^{20}$	$\omega_0 \geq 10^{20}$	$\omega_0 \geq 500$

References

[1] P.J.E. Peebles, Principles of Physical Cosmology, *Princeton University Press* (1993).

[2] D.N. Schramm, Physica Scripta **T36**, 22 (1991).

[3] P. G. Bergmann, Int J. Theor. Phys. **1**, 25 (1968).

[4] R. V. Wagoner, Phys. Rev. D **1**, 3209 (1970).

[5] K. Nordtvedt, Astrophys. J. **161**, 1059 (1970).

[6] C. M. Will; Phys. Reports **113**, 345 (1984); C. M. Will, Theory and Experiment in Gravitational Physics, *Cambridge University Press* (1993).

[7] D. La and P. J. Steinhardt, Phys. Rev. Lett. **62**, 376 (1989); E. W. Weinberg, Phys. Rev. D **40**, 3950 (1989); D. La, P. J. Steinhardt, and E. Bertschinger, Phys. Lett. B **231**, 231 (1989); F. S. Accetta and J. J. Trester, Phys. Rev. D **39**, 2854 (1989); P. J. Steinhardt and F. S. Accetta, Phys. Rev. Lett. **64**, 2740 (1990); J. D. Barrow and K. Maeda, Nucl. Phys. B **341**, 294 (1990); A. R. Liddle and D. Wands, Mon. Not. R. Astron. Soc. **253**, 637 (1991); A. R. Liddle and D. Wands, Phys. Rev. D **45**, 2665 (1992).

[8] P. Jordan, Nature **164**, 637 (1949); E. W. Kolb, M. J. Perry, and T. P. Walker, Phys. Rev. D **33**, 869 (1986); E. Vayonakis, Phys. Lett. B **213**, 419 (1988); A. A. Coley, Astron. Astrophys. **233**, 305 (1990).

[9] T. Damour, in Gravitation and Quantizations, Proceedings of LVIIth Les Houches Summer Scholl, edited by B. Julia and J. Zinn-Justin (North-Holland, Amsterdam).

[10] P. J. Steinhardt and F. S. Accetta, Phys. Rev. Lett. **64**, 2740 (1990); J. D. Barrow and K. Maeda, Nucl. Phys. B **341**, 294 (1990); J. D. Bekenstein and A. Meisels, Phys. Rev. D **18**, 4378 (1978); J. García-Bellido and M. Quirós, Phys. Lett. B **243**, 45 (1990); T. Damour and K. Nordtvedt, Phys. Rev. D **48**, 3436 (1993).

[11] A. Serna, & J.-M. Alimi, *submitted to Phys. Rev. D* (1995a).

[12] A. Serna, & J.-M. Alimi, *submitted to Phys. Rev. D* (1995b).

[13] J.-M. Alimi & A. Serna, *submitted to Nature* (1995).

SEARCHES FOR NON BARYONIC DARK MATTER: THE CASE FOR WIMPs

R. Bernabei
Dipartimento di Fisica, II Università di Roma
INFN sezione di Roma2, Roma, Italia

ABSTRACT

A review on particle Dark Matter searches deep underground is presented. Most of the experimental results are reviewed.

1. Introduction

Many experimental observations suggest the existence of non luminous matter (Dark Matter) in our Universe, such as the behaviour of the galaxy dispersion velocities and the rotational curves in spiral galaxies [1,2,3], the rotation of the Large Magellanic Cloud around our Galaxy faster than expected from the gravitational attraction of visible matter [4], the study of the kinetic energies of the X-ray emitting gases surrounding elliptical galaxies [5] and the measured hot intergalactic plasma velocity distribution in clusters of galaxies, not consistent with the luminous matter distribution [6]. They suggest the possibility that $\Omega \approx 1$ as foreseen by the inflationary theories - proposed to avoid any fine tuning in the big bang initial conditions - instead of the value $\Omega \approx 0.007$ [7] derived from the photometric measurements. In addition, also recent experimental results [8,9,10] seem to support the standard cosmological models in the inflationary scenario. From nucleosynthesis - considering the initial amount of light elements (^{4}He,^{3}He,^{7}Li) - the baryonic Dark Matter is constrained to be $\Omega_b \approx 0.05 \pm 0.03$ [11,12], while preliminary results from the searches for MACHOs (Massive Compact Halo Objects) by microlensing effect exclude at 90% C.L. that they may constitute more than $\approx$ 10-20% of the Dark Matter in the galactic halo [13].

Non baryonic Dark Matter - "hot" and "cold" - are needed to account for the structure formation in the Universe. The "hot" Dark Matter is formed by particles relativistic at decoupling time with masses less than $\approx$ 100 eV (light neutrinos), while the latter ones are relic particles non relativistic at temperatures greater than 10^4 K with masses from few GeV to 10^{19} GeV (Weakly Interacting Massive Particles, WIMPs, such as cosmions, heavy neutrinos and SUSY particles as f.i. the lightest supersymmetric particle, named neutralino: χ, stable in the Minimal Supersymmetric Standard Model) or axions[1]. Finally, an interpretation of COBE measurements

---

[1] The axions are light bosons which could solve the CP violation in strong interactions [14,15,16] and close the Universe, if their mass would be in the range 10^{-2} - 10^{-5} eV.

suggests the possibility of a mixed Dark Matter composed by: 69% "cold", 30% "hot" and 1% baryonic Dark Matter [17]. Notice that if a neutrino mass of $\approx$ 2.5 eV (i.e. in the range of cosmological interest) will be confirmed by LSND experiment [18], this would be consistent with the mixed Dark Matter model supporting "hot" Dark Matter at level of $\approx$ 20%.

2. The WIMPs

To survive up to now the relic WIMPs must have an annihilation rate lower than the expansion rate of the Universe; therefore, their cross section on ordinary matter should be of the order of the weak interaction cross sections. The WIMPs are considered to form a dissipationless gas trapped in the gravitational field of Galaxy with a quasi-maxwellian velocity distribution. The expected flux is: $\varphi_{WIMPs} = n_0 \times \langle\beta c\rangle \approx 10^7 \times \left(\frac{1\ GeV}{M_W}\right)$[part/cm^2/s], where n_0 is the total density generally assumed equal to ρ_{halo}/M_W[2]. An annual modulation of the flux - and consequently of the measured rate - is expected due to the Earth velocity motion around the Sun on a plane at γ (60^0) respect to the Galactic one.

WIMPs can be detected both by direct and indirect methods. In the first case, their elastic interaction on target nuclei is detected by the recoiling nucleus signal or, in case of inelastic scattering, also by the successive disexcitation gammas. In the other case, the flux of secondary particles - mainly gammas and neutrinos - produced by the WIMP annihilation in the Sun, in the Earth or in the halo could be detected.

3. Direct detection by WIMPs-nucleus elastic scattering

In the direct search of WIMPs-nucleus elastic scattering the measured quantity is the recoil energy of a nucleus of mass M_N on which a WIMP - of M_W mass and β velocity - impinges. Taking into account the WIMP velocity distribution, the expected nuclear recoil spectrum can be written as: $\frac{dR}{dE_R} = \frac{R_0}{\langle E_M\rangle} F^2(E_R) I(E_R)$, where R_0 is the total rate; $\langle E_M\rangle = \frac{2 m_{red}^2 \langle\beta^2\rangle}{M_N}$, with m_{red} WIMP-nucleus reduced mass; $F(E_R)$ denotes a form factor due to the finite size of the nucleus and $I(E_R)$ is a kinetic

---

[2] Notice that - due to the large uncertainty in the ρ_{halo} determination - slightly different values are sometimes considered by different authors: the cautelative choice 0.3 GeVcm^{-3} has to be recommended. Furthermore, it has to be rescaled when the calculated $\Omega_W h^2$ would be less than a model dependent value, $\delta_{lim} = (\Omega_W h^2)_{min}$, corresponding to large annihilation cross section.

factor: $I(E_R) = \frac{<\beta^2>}{<\beta>} \int_{\beta_{min}(E_R)}^{\beta_{max}} \frac{g(\beta)}{\beta} d\beta$, where $\beta_{min}(E_R) = \sqrt{\frac{M_N E_R}{2m_{red}^2}}$ β_{max} is the maximal WIMP velocity in the halo (i.e. the Galaxy escape velocity) evaluated in the Earth reference frame[3] and $g(\beta) = \int f(\beta)\, \beta^2\, d\Omega$ is the WIMP velocity distribution averaged over the solid angle. From these relations a quasi exponential behaviour of the rate can be derived[4], whose mean energy is in the range few keV to some tens keV.

The total rate can be written as $R_0 = n_0 <\beta c> \sigma (\frac{6.022 \times 10^{26}}{A})$ /kg/s, where σ is the WIMP-nucleus cross section and A is the atomic number. If the WIMP-nucleus elastic scattering occurs through a coherent interaction (as in case of Dirac neutrino and sneutrino), the dominant effect would be the coherent sum of the scattering amplitudes on all the nucleons: $\sigma \propto A^2$, giving a strong enhancement of the cross section, reduced in case of heavy nuclei or high experimental energy threshold by the nuclear form factor $F(E_R)$ [19,20,21,22]. In this case $R_{0(coherent)} \approx$ 10-1000 cpd/kg. In case only the spin dependent interaction (as in case of Majorana neutrino and photino) would be present, the cross section would be different from zero if a non-zero spin target-nucleus is considered and it would be propotional to $C\lambda^2 J(J+1)$ with J total nuclear spin, $\lambda^2 J(J+1)$ spin factor and C squared adronic matrix element for the WIMP-nucleon interaction[5], giving $R_{0(axial)} \approx$ 0.1-1 cpd/kg or less.

To study the eventual presence of a Dark Matter signal the theoretical calculated recoil energy spectrum has to be compared with the experimental one for various M_W, deriving an exclusion plot in the plane (M_W, σ). The use of different target-detectors could help - in principle - to distinguish Dark Matter signals from background, while information on the nature of the signal can be also obtained by comparing the results on a zero spin and a non-zero spin nucleus [23]. A definitive confirmation of the presence and origin of a signal would be given by the annual modulation of the rate; a large detector is needed to point out this $\approx$ 10% effect. Recently, it has been suggested [24] to consider the signature coming from a diurnal modulation of the Dark Matter signal; but this effect strongly depends on σ, M_W and the latitude of the experimental site. Another WIMP signature would be the detection of the recoil nucleus direction related to the Earth's galactic motion [25,26]. Finally,

[3] Notice that here, for semplicity, the assumption β_{max} equal to a constant value is done. This is a good approximation in case β_{max} is assumed to be 800 km/s/c with $\beta_{esc} \approx$ 610 km/s/c.

[4] a pure exponential behaviour would be obtained in case Earth's velocity is assumed to be zero.

[5] In ref. (20) the spin factors for several nuclei have been calculated.

we recall here that the possibility to distinguish nuclear recoil from electromagnetic background has to be considered only an effective method for electromagnetic background rejection; in fact, signals from fast neutrons and end-range alphas cannot be distinguished from those induced by recoil nuclei scattered by a WIMP and their contribution cannot be evaluated in reliable manner.

3.1. Status of the experiments

The main problem when developing detectors devoted to the direct particle Dark Matter search is the needed extreme background reduction; detailed discussions can be found in ref. [27]. As a preliminary step, the quenching factors (ratio between the ionization or scintillation or heat - depending on the used detector type - detected for a nuclear recoil and for an electron of same energy) have to be measured by neutron elastic collision experiments [28]; this quantity is necessary to properly evaluate the recoil energy, E_R, being generally the detectors calibrated with γ sources. Often in case of a single type of target nucleus the Lindhard theory [29,30] substitutes the experimental determination.

In table I the main features of various experiments are summarized. We have to remark that present germanium results profit of $\approx$ 20 years of developments, while scintillators have been used for this application only recently and therefore large efforts are still needed and possible to find effective methods for the internal background extreme reduction. Notice that large mass detectors to look for annual modulation and/or very low rate candidates could be easily built in case of scintillators. Also a large set of target nuclei are available, many of them suitable for axially coupled candidate search. Measurements with calcium fluoride crystals are in progress in Kamioka mine and R&D on liquid xenon are performed by the UK collaboration; the BPRS collaboration started a new R&D on CaF_2(Eu) low activity crystals, while the DAMA group is performing measurements with an improved low activity LXe detector using Kr-free xenon enriched in ^{129}Xe at 99.5%. Regarding the NaI(Tl) experiments, the BPRS collaboration has pointed out the feasibility of a pulse shape analysis in NaI(Tl) even at very low energy [28] quantitatively developing a detailed pulse shape analysis between the signal (nuclear recoils) and the background. Measurements of nuclear Na and I recoils have been performed by exposing a small NaI(Tl) crystal in a neutron beam. As an exercise, the method has been applied to a set of data corresponding to 20 days with a 7 kg crystal building a profile - by 2 keV energy bin between 6 and 16 keV- by adding all the pulse shape recorded by a waveform recorder. Comparing the experimental profiles with the reference ones from pure recoils and pure electrons pulses, the maximum Na recoil percentage, α, which could be allowed in the data at 90 % confidence level, has been evaluated with a likelihood method. Rejection factors $1/\alpha$ ranging from around 3

in the 6-8 keV bin to 20 in the 14-16 keV bin have been obtained for the considered data.

Table 1
Some features of experiments performed with ionizing detectors and scintillators [28,30-38].

Detector	Laboratory	Collab.	Rate near threshold (cpd/kg/keV)	threshold (kee[6])
Ge up to 1 kg(1987, 1991)	Homestake	Avignone/ Drukier et al.	≈ 2	4
Ge 0.9 kg (1988)	Oroville	UCSB/UCB/ LBL	≈ 3	3
Ge 0.8 kg (1991)	S.Gotthard	Caltech/PSI/ Neuchatel	≈ 3	2
Ge 0.234 kg (1993)	Canfrac	Zaragoza/ PNL/USC	≈ 8	≈2
Ge 2.9 kg (1994)	LNGS	Heidelberg/ Moscow	0.2	12
Si 4x17 g (1990)	Oroville	UCSB/UCB/ LBL/Saclay	≈ 60	1.1
NaI 0.76 kg (1992) 7 kg	LNGS/ LSM/ Mentogou	BPRS[7]	≈ 7 ≈ 1 - ≈ 3[7a]	≈ 4 ≈ 4
NaI 3x10.7 kg (1993)	Canfranc	Zaragoza,PNL, USC	≈ 8	≈ 6
NaI 36.5 kg (1993) (+ active anticoinc.)	Kamioka	Osaka	≈ 6	≈ 5
NaI 1 kg (1994)	Boulby	UK coll.	≈ 7	≈ 4
CaF_2(Eu) 0.37 kg (1993)	LNGS/ LSM/ Mentogou	BPRS	≈ 15	≈ 4
LXe 6.5 kg (preliminary test)	LNGS	DAMA	≈ 10	≈ 8

[6] kee means keV electron equivalent.

[7] Only the BPRS and UK collaborations are performing new developments on low activity crystals: the other results on NaI(Tl) have been obtained using detectors built years ago for other purpose.

[7a] depending on the crystal (4 × 7kg crystals are available) and on the nearby materials and shielding in the considered measurement.

The UK collaboration has also suggested to use pure NaI at LN_2 temperature, discriminating recoil nuclei from electromagnetic background by comparing the wavelength of the emitted scintillation light [40]. Finally, an Italian/CERN/USA collaboration [41] has proposed a LXe detector with proportional scintillation to discriminate nuclear recoils from electromagnetic background by comparing the ionization and light signals. Large efforts are in progress to obtain the ultimate low rate for such detectors. Notice that sometimes, various background subtraction techniques are used and they have to be properly evaluated when comparing the different results. Furthermore, also slightly different astrophysical and nuclear physics parameters have been used and, therefore, also the homogenity in the calculations has to be checked before comparing published exclusion plots.

Other detectors now widely developed for Dark Matter and $\beta\beta$ decay experiments are the bolometers.

Table 2

Main activities on bolometers [42-47].

Detector	Laboratory	Collab.	Threshold (kee[8])
Ge (60 g)+ ionization	Stanford shallow site	CFPA	3 (24 mK)
LiF (100g), NaF (30g), CaF_2(Eu)(2g)+scintillation[9]; TeO_2(334 g) and $CdWO_4$(60g) for $\beta\beta$ exp.	LNGS	Milano	- (25 mK)
Ge (7 g)+ionization Al_2O_3 (24 g -> ~25 cpd/kg/keV at 16 keV)	LSM	CEA/IN_2P_3/INSU	1.7 (34 mK) 2. (60 mK)
Al_2O_3 (31 g)	Munich	MPI-Munich/Garching	0.3 (15 mK)
LiF (2.8 g)	Kamioka	Tokyo	≈4 (12 mK)

These detectors offer very low energy threshold - in principle - and high energy resolution. However, only small masses can be used up to now and the microphonic problems could significatively limit the reach able energy threshold,

[8] In case of bolometers generally the quenching factor is assumed equal to 1, however, f.i. the role of defects eventually present in the crystal could require some experimental verifications. Furthermore in case of heat/ionization or heat/scintillation detectors the quoted values would be generally referred to kee unity.

[9] For dark matter experiments with this kind of technique, some limitations have to be overcomed 43,48).

while the background induced by the dilution refrigerator could be not negligible. It has been pointed out the possibility to reject the electromagnetic background comparing the bolometric signal with the ionization one using a germanium crystal [42] (more recently it has been also suggested to compare it with the light response in a $CaF_2(Eu)$ detector [43], but the threshold in that case will be fixed by the ionization (or scintillation) signal and the discrimination would be - at very low energy - statistical more than event by event. Various projects are in progress and table 2 summarizes the main activities on bolometers.

Many other detectors have been proposed for the direct search of Dark Matter deep underground such as a low activity high pressure gaseous Time Projection Chamber, TPC, of 1 m^3 of xenon or CF_4 - by product of an experiment for the neutrino magnetic moment measurement [49], optically imaged low pressure TPC [50], xenon superheated "bubble chamber" in which only recoils can be detected [51], analysis by atomic force microscope of the tracks induced in mica by WIMPs since the Earth formation [52] and superconducting detectors both in form of granules or disks [53,54]. These and many other ideas are still in development.

4.WIMPs-nucleus inelastic scattering

Regarding the direct detection by WIMP-nucleus inelastic scattering which produces low-lying excited nuclear states [55,56], we just recall that these processes can be identified by observing the emission of a decay photon in the 10-100 keV energy range, but the expected rates are very low [56] (rates less than $\approx 2\times10^{-3}$ cpd/kg). A first measurement of this type has been performed by [55] using $\approx$ 620 kg NaI(Tl) looking for the 57.6 keV line from the disexcitation of ^{127}I following a WIMP inelastic scattering. But because the experimental rate is extremely high compared to the one expected for WIMP-nucleus inelastic scattering, the contribution of standard contaminants around 57.6 keV has been extrapolated by MonteCarlo calculation and subtracted from the experimental spectrum together with an assumed continuous background. This procedure quotes a subtracted rate of $< 9.79 \times 10^{-2}$ cpd/kg at 2 σ C.L. from a measured rate of $\approx$ 600 cpd/kg in the interesting energy region; that suggests a global percentage error from the evaluated spectrum, the experimental one and the subtraction procedure better than $\approx$ 1/5000.

5. WIMP indirect detection

It has been pointed out that big bang particles could be a promising source of high energy neutrinos, gamma's, antiprotons and positrons via Dark Matter particles annihilation within the Earth, the Sun or the Galactic halo [57]. The best signature could come from ν_μ interacting in the rock below the detector and producing "up-

going" muons to be distinguished from those due to the atmospheric neutrino interactions. The expected μ flux depends on the WIMP annihilation rate in the considered body. In case of Sun a "steady state" between the capture and annihilation processes can be reached and the μ flux could be proportional to the elastic scattering cross sections on the nuclei. Therefore, an upper limit on the effective WIMP elastic scattering cross section could be derived and compared with the limits obtained in the direct searches.In case of Earth a similar interpretation would be less safe, because the capture rates are much lower and a steady state may or may not have been reached. Evaluation of expected up-going muon fluxes from relic χ-χ annihilation in the Earth and in the Sun - detectable in a neutrino telescope - can be found in ref. [58]. Notice that a significant uncertainty in this kind of measurements could arise, in particular, from the evaluation of the atmospheric neutrino contribution; this would limit also the sensitivity reachable by these indirect search experiments increasing only with the square root of the exposure.

As we mentioned at the beginning, the annihilation of Dark Matter particles could also produce antimatter particles and gamma's. In particular, some calculations on high energy γ produced by χ-χ annihilation [59] estimate expected fluxes of the order of 10^{-7} - 10^{-8} $cm^{-2}s^{-1}$ for γ's energy larger than 300 MeV.

5.1 Experiments on indirect detection searches

The detectors used for WIMP indirect detection should have extremely large exposure (= area $\times$ time); therefore, they are much more expensive than those for direct searches. However, in general they have more physical goals than the indirect search for particle Dark Matter alone. Various underground detectors have collected data in the last years [60,61]; the most stringent constraints have been provided by the Kamiokande experiment [61]. New experimental set-ups are now ready to take data or in project [62] both underground (SUPERKAMIOKANDE, SNO) and underwater - water of seas or of lakes - (DUMAND,LAKE-BAIKAL, AMANDA, NESTOR).

We recall here in particular the Kamiokande detector (Kamiokande-I and its upgraded phase, Kamiokande-II); it is an imaging water Cherenkov detector located 2700 m.w.e. underground in the Kamioka mine. In Kamiokande-I, 2340 tons of purified water in a cylindrical steel tank were viewed by 1000×20" photomultipliers covering 20% of the tank surface [63]. In Kamiokande-II, the inner detector - reduced to be 2140 tons with 948 photomultipliers - was surrounded by an anticounter with $\approx$ 1.5 m thick water viewed by 123×20" photomultipliers [64]. Kamiokande gave results on different arguments such as solar neutrinos, heavy neutrinos search [65] and searches for neutralino Dark Matter both for masses less and higher than the W boson [61]. In fact, from the measured up-going muon flux: $(2.04\pm0.13)\times10^{-13}$ $cm^{-2}s^{-}$

$^{1}sr^{-1}$ (averaged over zenith angles between 90^{0} and 180^{0}) and the expected model dependent contribution from atmospheric neutrinos[10]: 1.92×10^{-13} $cm^{-2}s^{-1}sr^{-1}$, the upper limit for muons produced by $\chi\chi$ annihilation was evaluated to be 4.0×10^{-14} $cm^{-2}s^{-1}$ in 770 m^2y, in case they come from the Earth's centre, and to be 6.6×10^{-14} $cm^{-2}s^{-1}$ in 215 m^2y, in case they come from the Sun. From these data, several constraints on the χ parameter space (μ, M_2) have been derived in ref. [61].

We will notice, however, that this kind of results depends on several parameters and assumptions, significantly more than in the direct detection case; we just recall as an example the calculation of the atmospheric neutrino background that can result in quite different numbers [61,69] and the assumption that neutrino species remain unchanged from production to detection (if neutrino oscillation would account f.i. for the solar neutrinos, the measured up-going muon flux from χ-χ annihilation will be either reduced or enhanced [70] by this effect).

6. Conclusions

We can conclude that the particle Dark Matter search is a very stimulating challenge. Significant steps towards a better knowledge of the problem have been recently done, but efforts are still needed in several fields to solve this puzzle. The direct and indirect searches are complementary and could both profit by comparing the interpretation of the respective results. Several years are still needed before large surface underwater detectors for indirect searches would be operative and also to improve as much as possible the sensitivity of the direct detection experiments, in the meantime final clarifications on baryonic and "hot" possible candidates could be obtained. An eventual discovery of supersymmetric particles at accelerator experiments will definitely push this search accrediting the existence of the more interesting particle Dark Matter candidates and constraining the predictive models.

References

1) Zwicky F., Helv. Phys. Acta 6 (1933), 110.
2) Einasto J. et al., Nature 250 (1974), 309.
3) Ostriker J.P., Peebles P.J.E. and Yahil A, Ap. J. Lett. 193 (1974), L1.
4) Fich M. and Tremaine S., Ann. Rev. Astron. Astrop. 29 (1991), 409.
5) Trimble V., Ann. Rev. Astron. Astrop. 25 (1987), 425.
6) Bird et al., Ap. J. 404 (1993), 81.
7) Trimble V., Contemp. Phys. 19 (1988), 373.
8) Wright E. et al., Ap. J. 396 (1992), L13.
9) Smooth G. et al., Ap. J. 396 (1992), L1.
10) Dekel A. et al., Ap. J. 405 (1993), 437.

[10] using the atmospheric neutrino fluxes calculated by [66], the charged current cross sections using the quark distribution in [67] and the formula for muon energy loss in [68].

11) Olive K. and Schramm D. W., Nature 360 (1992),434.
12) Schramm D. W., FERMILAB conf. 93/022-A.
13) Moscoso L., DAPNIA/SPP94-34 (1994); C. Magneville, these Proceedings.
14) Peccei R. D. and Quinn H., Phys. Rev. Lett. 38(1977), 1440 and Phys. Rev. D16 (1977), 1791.
15) Turner M.S., Phys. Rev. D33 (1986), 889.
16) Sikivie P., Phys. Rev. D32 (1985), 2988 and in "The dark side of the Universe", World Sc. Pub. (1994), 141.
17) Taylor A. N. and Rowan-Robinson M., Nature 359 (1992), 396.
18) D.O. Caldweell, talk given at Moriond, Villar sur Ollon, jan 1995.
19) A. Bottino et al., Phys. Lett. B295 (1992), 330.
20) Ellis J. and Flores R.A, Phys. Lett. B263 (1991), 259 and references therein.
21) Engel J., Phys. Lett. B264 (1991), 114.
22) Engel J. et al.,Phys. Lett. B275(1992),119; Ressel M.T. et al.,UCRL-JC-114085 (1993).
23) Belli P. et al., in "The dark side of the Universe", World Sc. Pub. (1994), 257.
24) Collar J. I. et al., Phys. Rev. D47 (1993), 5238.
25) Gerbier G. et al., Nuclear Phys. B13 (1990), 207 and Besida O., in "The dark side of the Universe", World Sc. Pub. (1994), 277.
26) Belli P. et al., Nuovo Cim. **C15** (1992), 475.
27) Gaillard-Lecanu E. et al., in "The dark side of the Universe", World Sc.Pub. (1994), 194; C. Bacci et al., Nuclear Phys. B35 (1994), 159; L. Mosca, DAPNIA/SPP 94-12; Heusser G., MPI H-V26-93; C. Arpesella, in "The dark side of the Universe", World Sc.Pub. (1994), 164.
28) Gerbier G. et al., Phys. Rev. D 42 (1990), 3211; Gerbier G. et al., in proc. Rencontres de Moriond, Ed. Frontieres 1991; C. Bacci et al., in "Particle Astrophysics, Atomic Physics and Gravitation", Frontieres ed. (1995),157; C.Bacci et al., SIF atti Conferenze Vol. 47 (1995),121; C. Bacci et al., Nuclear Phys. B 35 (1994), 165; P. Belli et al., in "Particle Astrophysics, Atomic Physics and Gravitation", Frontieres ed. (1995),161; R. Bernabei et al., ROM2F/94/56 to appear on Nucl. Phys. B, Proc. Supp.; C. Bacci et al., ROM2F-95/08 (1995) to be presented at ICRC95; Fushimi K. et al, Phys. Rev. C47 (1993) R425;T.J. Sumner et al., in the Moriond Proc., jan. 1994; Davies G. J. et al, Phys. Lett. B322 (1994), 159; Quenby et al., pre-print Imperial College/astrop. group-001 (1994); Bacci C. et al., LNGS-93/83 and Astrop. Phys. 2 (1994), 117.
29) J. Lindhard et al., Mat-Fys. Medd. 33 (1963) 10.
30) P. Belli et al., Nucl. Instr. & Meth. A336 (1993), 336.
31) Ahlen S.P. et al., Phys. Lett. B195 (1987), 603
32) Caldwell D.O. et al., Phys. Rev. Lett. 61 (1988) 510.
33) Caldwell D. O. et al., Phys. Rev. Lett. 65 (1990), 1305.
34) Reusser D. et al., Phys. Lett. B255 (1991), 143.
35) Bacci C. et al., Phys. Lett. B293 (1992), 460;
36) Drukier A. K. et al., Nucl. Phys. B (Proc. suppl.) 28A (1992).
37) Sarsa M.L. et al., Nuclear Phys. B (Proc. suppl.) 35 (1994), 154.
38) Beck et al., in "The dark side of the Universe", World Sc. Pub. (1994), 184.
39) Ellis J. et al., Phys. Lett. B212 (1988), 375.
40) Spooner N.J.C. and Smith P.F., Phys. Lett. B314 (1994), 430.
41) Benetti P. et al., Proc. of the JCLRD conf., Tokyo, 1992.
42) T. Shutt et al., Phys. Rev. Lett. 29 (1992) 3425 and Phys. Rev. Lett. 29 (1992), 3531 and in "The dark side of the Universe", World Sc. Pub. (1994),243; see also D. Akerib, these Proceedings.

43) A. Alessandrello et al., Nuclear Phys. B 28A (1992), 233; A. Alessandrello et al., in "The dark side of the Universe", World Sc. Pub. (1994), 253.
44) N. Coron et al., Nuclear Phys. B (Proc. suppl.) 35 (1994), 169.
45) Forster G. et al, to appear in the Proc. of the Moriond rencontre, jan. 1994.
46) Minowa M. et al., Nucl.Instr & Meth. A327 (1993), 612.
47) see also M. de Jesus, these Proceedings.
48) P. Belli et al, Nucl. Instr. & Meth. A357 (1995), 329.
49) Vuilleumier J.L.,in "The dark side of the Universe", World Sc. Pub. (1994), 281.
50) K.N. Buckland et al., Phys. Rev. Lett. 73 (1994), 1067.
51) Zacek V., pre-print ROM2F/93/20 (1993).
52) Price B., talk given at II Rome University, june 1994.
53) "Low temperature detectors for neutrinos and Dark Matter", ed.Frontieres (1990).
54) Carelli P. et al., in "The dark side of the Universe", World Sc. Pub. (1994), 2490.
55) Fushimi K. et al, Nucl. Phys. B35 (1994), 400.
56) Ellis J. et al., Phys. Lett. B212 (1988), 375.
57) Berezinsky V.S., LNGS-92/42; Mac Gibbon J.H. and Branderberger R.H., Nucl. Phys. B331 (1990), 153; Frampton P.H. and Glashow G.L., Phys. Rev. Lett. 44 (1980), 1481; Silk J. et al., Phys. Rev. Lett. 55 (1985), 257; Krauss L.M., Phys. Rev. D33 (1986), 2079; Gaisser T.K. et al., Phys. Rev. D34 (1986), 2206; Gelmini G. B. et al., Nucl. Phys. B351 (1991), 623; Bottino A. et al., Phys. Lett. B265 (1991), 57; Kamionkowski M., Phys. Rev. D44 (1991),3021; Press W.H. and Spergel D. N., Ap. J. 296 (1985), 679; Gould A., Ap. J. 321 (1987), 571.
58) Bottino A. et al., Astrop. Phys. 3 (1995), 65; Bottino A. et al., DFTT-10/91 and Phys. Lett. B265 (1991), 57.
59) Berezinsky V. et al., pre-print LNGS 94/90 (1994).
60) Losecco J.M. et al., Phys. Lett. B188 (1987), 388; L. Moscoso, Proc. on *Neutrino telescopes*, ed. M. Baldo Ceolin (1988); Berger C. et al., Z. Phys. C48 (1990), 221; Aglietta M. et al., Nucl. Phys. B35 (1994), 254; Douglas G.M. et al., Nucl. Phys. B35 (1994), 235; Ruddick K., Nucl. Phys. B35 (1994), 246.
61) Mori M. et al., Phys. Lett. B270 (1991), 89; Mori M. et al, Phys. Lett. B 287 (1992), 217; Mori M. et al., Phys. Rev. D48 (1993), 5505.
62) Stanev T., Nucl. Phys. B35 (1994), 185; Belolaptikov I.A. et al. , Nucl. Phys. B35 (1994), 290; Bouchta A. (AMANDA coll.),Proc. *Neutrino Telescopes*, ed. Baldo Ceolin (1994), 561; Anassontzis E. et al., Nucl. Phys. B35 (1994), 294.
63) Arisaka K. et al., J. Phys. Soc. Jpn. 54 (1985), 3213.
64) Hirata K.S. et al., Phys. Rev. D38 (1988), 448.
65) Mori M. et al, Phys. Lett. B 289 (1992), 463.
66) Volkova V. L. Yad. Fiz. 31 (1980), 784 [Sov. J. Nucl. Phys. 31 (1980), 1510].
67) Eichten E. et al., Rev. Mod. Phys. 56 (1984), 579 and 58 (1986) 1065.
68) Lohmann W. et al., pre-print CERN n. 85-03 (1985).
69) Ryazhskaya O.G., LNGS 94/110, 1994; Gaisser T.K. and Stanev T., Phys. Rev. D30 (1984), 985; Mitsui K. et al., Il Nuovo Cim. 9C (1986), 995; Oyama Y. et al., Phys. Rev. D39 (1989), 1481.
70) Ellis et al, Phys. Lett. B294 (1992), 229.



SEARCHING FOR WIMPS: THE CFPA CRYOGENIC DARK MATTER EXPERIMENT

Daniel S. Akerib
for the CDMS Collaboration[1]
Center for Particle Astrophysics
University of California, Berkeley, California, USA



Abstract

Our group, the CDMS Collaboration, will soon begin the first phase of an experiment to search for WIMPs, or weakly-interacting massive particles, in the galactic halo using terrestrial detectors. This generic class of hypothetical particles, whose properties are similar to those predicted by extensions of the standard model of particle physics, could comprise the cold component of non-baryonic dark matter. I will describe our experiment, which is based on cooled germanium detectors in a shielded low-background cryostat.

1 Introduction

Observations of stars and galaxies over a large range of distance scales indicate the presence of significant amounts of dark matter that is unseen except for its gravitational effects. There is general consensus that a significant amount of the dark matter, on the order of the critical density, is comprised of a non-baryonic "cold" component. We are building an experiment to search for direct evidence of one of the hypothesized types of cold dark matter known as WIMPs, or weakly-interacting massive particles. These particles, which could arise from supersymmetric effects in the early universe, would have undergone gravitational clustering on a wide range of distance scales. They could also make up a significant fraction of the dark matter in our own galactic halo and be detected via elastic scattering in terrestrial detectors. Typical event rates are in the range from 1–0.001 events per kilogram of detector per day with deposited energies as low as 1 keV — a considerable experimental challenge.

2 Relic WIMPs

WIMPs are a generic class of particles that would have existed in thermal and chemical equilibrium with the hot plasma of the early universe. For any particle species to survive in significant number as the universe cools (in the absence of a particle-anti-particle asymmetry), its cross section must be so weak that its annihilation rate is low compared to the expansion rate when the temperature is high compared to the particle mass. Otherwise, by the time it decouples from the plasma, its thermal abundance will be a negligible fraction of the energy density. Since the freeze-out temperature and cross section are related, the hypothesis of a cosmologically significant freeze-out density is used to constrain the cross section. A critical density of WIMPs along with the observed expansion rate corresponds to cross sections on the weak scale for masses in the 10–1000 GeV/c^2 range, suggesting that supersymmetry (SUSY) or other extensions to the standard model may provide the dark matter. Also, for this range of mass and cross section the freeze-out temperature is such that the particles would be non-relativistic at the time that the universe becomses matter dominated, the criterion for *cold* dark matter.

The elastic cross section for WIMP-nucleon scattering can be calculated for a given relic density, target nucleon, and set of SUSY parameters. The event rate in an Earth-based detector is estimated as a function of WIMP mass by assuming that the WIMPs saturate the galactic halo, or some fraction thereof. The nucleon recoil energy spectrum is estimated by assuming that the WIMPs have virialized and have a Maxwellian distribution with a typical halo velocity. The result is a rate from 1–0.001 events/kg/day and recoil energies as low as a keV.

3 The CDMS Experiment

The first generation of experiments to set limits on WIMPs were largely based on germanium detectors originally designed to search for double beta decay [2][3]. Although these experiments ruled out a Dirac neutrino down to a mass of 10 GeV/c^2, significant progress is prevented by photon backgrounds from ambient radioactivity that are difficult to further reduce. A new round of experiments is getting underway employing a variety of technologies and approaches to overcome this problem [4]. Some experiments search in regions of parameter space where signal rates are higher, while others employ techniques to directly suppress background. It may also be possible to exploit intrinsic modulations in the direction or time-structure of the signal to enhance sensitivity.

Our collaboration, the Cryogenic Dark Matter Search (CDMS), which is coordinated by UC Berkeley's Center for Particle Astrophysics, emphasizes detectors with intrinsic background rejection. We have developed detectors with phonon-mediated signals using both neutron-transmutation-doped (NTD) germanium thermistors and superconducting transition-edge sensors (TES) mounted on short cylindrical crystals of germanium and silicon [5]. In addition to the phonon signal, we measure a charge signal by collecting the electron-hole pairs generated by the scaterring event. Since WIMPs produce nuclear recoils and photons produce more-ionizing electron recoils, a comparison of the energy into the two channels allows us to discriminate between signal and background on an event-by-event basis.

Our best detector to date is a 62-g germanium device with NTD thermistor readout. It has FWHM energy resolutions (at threshold) of 500 eV in phonons and 1200 eV in charge. Measured energy spectra using photon and neutron test particles indicate that we reject about 99% of the photon-induced electron recoils, while maintaining high efficiency for the neutron-induced nuclear recoils. Based on this technology we are building six 165-g germanium detectors for the initial astrophysics run of the experiment.

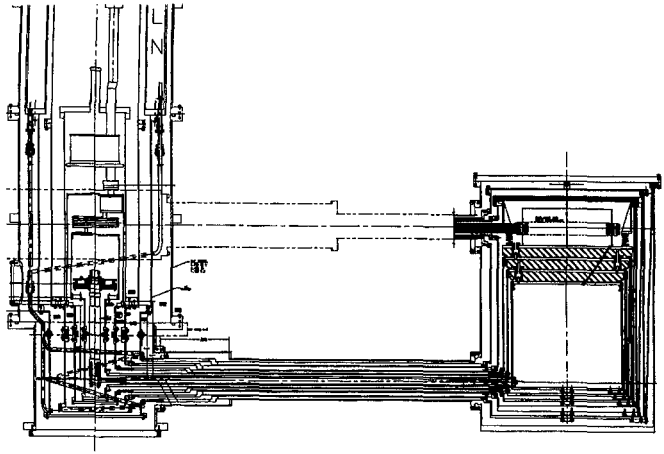


Figure 1: The cryostat for the CDMS Experiment. The detector volume of one cubic foot (left) has been cooled to a temperature below 10 mK through the lower set of copper stems that connect it to a commercial dilution refrigerator (right). The upper set of stems carries the detector wiring out to room temperature. This design allows us to isolate and shield the detector volume.

The thermal signal requires that we operate the detectors at a temperature of about 20 mK. While this can be done in a commercial dilution refrigerator, we have the additional requirement of extremely low radioactive background. We have therefore built a custom cryostat from pre-screened low-activity materials that is cooled by a modified commercial refrigerator, as shown in figure 1. The detector volume is at the end of a meter-long extension which allows it to be surrounded by a shield (not shown). At the time of this writing, we have successfully installed and cooled the cryostat at a nearby underground site at Stanford University for the first phase of the experiment. Over the coming months we plan to install and operate the 1 kilogram of germanium detectors described above. Future runs at Stanford will take advantage of ongoing detector development with the TES readout on silicon and germanium. We will also make detectors from a 500-g boule of isotopically enriched ^{73}Ge which will have higher sensitivity for WIMPs that scatter via axial-vector couplings.

Although the Stanford site is not very deep, we chose it for the first phase od the experiment because the convenient access facilitates debugging of the complex technologies we are using. However, since the site has an overburden of only 17 meters of water equivalent we have the added complication of neutron production from cosmic ray muons. Since the neutrons lead to nuclear recoils, as do the WIMPs, we slow most of them down to sub-threshold recoil energies with polyethylene moderator [6]. We achieve further rejection with a plastic scintillator box that surrounds the cryostat and provides a veto signal for any events in coincidence with a passing muon. Also, since our apparatus consists of closely-spaced stacks of short cylindrical detectors, many neutrons will scatter in more than one of them and can thus be rejected. According to estimates of the background rates based on both measurements and simulations, we expect to make substantial gains in sensitivity over previous experiments, even at this depth (see figure 2).

Eventually, even as our detectors improve, backgrounds will cause us to reach a point of diminishing returns. Therefore, we plan to continue the experiment at a very deep site. Since the absence of cosmic ray muons will virtually eliminate the neutron background we will

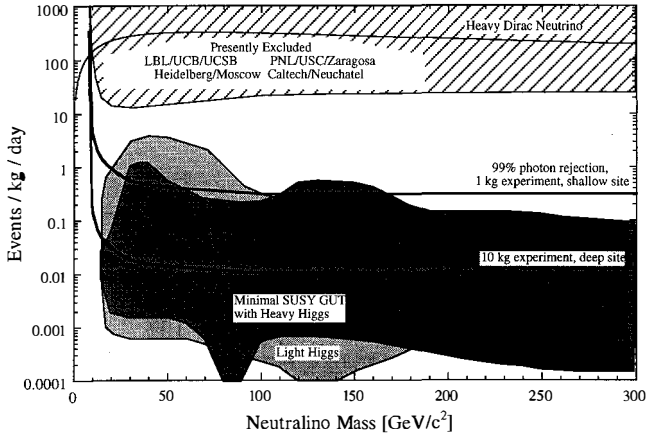


Figure 2: The event rate per kilogram of germanium versus the mass of the neutralino. The hatched region has been excluded by previous searches. The shaded regions show the range of event rates for SUSY models that predict a cosmologically significant relic density [7]. The thick solid lines show the anticipated sensitivity for the first and second phases of the CDMS Experiment.

should allow us to boost the total detector mass to 10 kg. When combined with a year of running time and an anticipated reduction in cosmogenically-induced photon activity we hope to reach a sensitivity of about 0.01 events/kg/day, as illustrated in figure 2.

Acknowledgements. This work was supported by the Center for Particle Astrophysics, an NSF Science and Technology Center operated by the University of California, Berkeley, under Cooperative Agreement No. ADT-8809616, and by the Department of Energy under contracts DE-AC03-76SF00098, DE-FG03-90ER40569, and DE-FG03-91ER40618.

References

[1] The members of the Cryogenic Dark Matter Search are D.S. Akerib, P.D. Barnes, Jr., D. Bauer, P.L. Brink, B. Cabrera, D.O. Caldwell, B. Chugg, R.M. Clarke, A.K. Cummings, A. Da Silva, A. Davies, R.C. Diaz, B.L. Dougherty, J. Emes, S.R. Golwala, D. Hale, E.E. Haller, K.D. Irwin, V. Kuzminov, A. Lu, S.W. Nam, M.J. Penn, V. Novikov, B.V. Pritychenko, F. Queinnec, R.R. Ross, B. Sadoulet, D.N. Seitz, T. Shutt, A. Smith, G. Smith, A.H. Sonnenschein, W.K. Stockwell, J.D. Taylor, R. Therrien, T. Turnbull, S. White, R.C. Wolgast, S. Yellin, and B.A. Young.

[2] D.O. Cladwell *et al.*, Phys. Rev. Lett. **61**, 510 (1988).

[3] D. Reusser *et al.*, Phys. Lett. B **255**, 143 (1991).

[4] R. Bernabei, these proceedings.

[5] P.D. Barnes, Jr. *et al.*, J. Low Temp. Phys. **93**, 791 (1993).

[6] A. Da Silva *et al.*, Nucl. Instrum. Meth. **A354**, 553 (1995).

[7] K. Griest, private communication.

Axions: Dark Matter and the Strong CP Problem

Leslie J Rosenberg
Massachusetts Institute of Technology
Dept. of Physics and Laboratory for Nuclear Science
Cambridge, MA 02139, USA



Abstract

The axion, a hypothetical elementary particle, was proposed originally as a solution to the strong CP problem in QCD. It was later recognized that axions would be a good candidate for dark matter. New, very sensitive searches are underway to detect axions forming our galactic halo.

1 Overview

In a by now classic set of observations, rotation speeds of stars in galaxies as a function of distance from the galactic center show a universal feature: the speed is approximately constant for distances outside the luminous core of the galaxy. This "flat rotation curve," and other observations, imply the existence of large halos of nonluminous matter surrounding galaxies. The density of this dark matter at our position in the galaxy is approximately 0.3 GeV/cm^3, this value uncertain by perhaps a factor of two. Discovering the identity of dark matter is one of the most exciting challenges confronting science today. It seems plausible from the success of models of nucleosynthesis in explaining the abundance of light isotopes, and of cosmological inflation in explaining the near flatness and homogeneity of the present universe, that most dark matter is non-baryonic. The leading non-baryonic dark matter candidates are neutrinos, weakly interacting massive particles (such as the lightest supersymmetric particle), primordial black holes, and axions. Axions are "cold dark matter," whereas neutrinos are "hot dark matter." Generally speaking, studies of large scale structure and galaxy formation favor substantial amounts of cold dark matter over hot. If the dark matter is a mixture of the two, the cold component dominates galactic halos.

The existence of the axion is natural from a particle physics view as it would explain why, contrary to expectations, strong interactions conserve P and CP. This "strong CP problem"

is solved by the presence of the axion,[1] a prediction of an elegant solution, Peccei-Quinn symmetry, to the strong CP problem of QCD. The resulting axion mass is a free parameter, with plausible range from 10^{-12}eV to 1MeV. Current limits on the axion mass from astrophysical and cosmological considerations constrain the mass to the three decade window 1-1000μeV. Laboratory experiments are underway to probe the first decade of allowed mass.

2 What's the Strong CP Problem, and what's an Axion

QCD, the theory of the strong interactions, has an impressive string of successes. Its non-Abelian nature is experimentally established. Decay rates and quantum statistics support the notion of color. Cross sections and branching ratios are in accord with perturbative predictions. There is, however, a loose end, the strong CP problem. The essential non-Abelian nature of the theory introduces QCD effects that violate CP. This CP violation surfaces as, say, an electric dipole moment to the neutron. However, no moment is found, with present bounds billions of times less than the expected level. The source of CP violating effects can be traced to the QCD vacuum. Skipping considerable detail, the reasoning behind this assertion is as follows: The QCD vacuum is the lowest energy gluon field configuration. In QCD, there are many degenerate vacuua, each labeled by winding number n, and gauge transformations can change one winding number vacuum into another.

Now, suppose a particular gauge transformation T_1 acting on a n vacuum turns it into a $n+1$ vacuum. This violates gauge invariance in much the way that a beach ball acted on by T_1 is turned into a bagel, as sketched in figure 1. In order to preserve our cherished gauge invariance, we construct a gauge invariant vacuum by a Bloch-wave-like superposition of vacuua, like so:

$$|\Theta\rangle = \sum_n e^{-in\Theta}|n\rangle \quad . \tag{1}$$

Such a vacuum, the Θ vacuum, is gauge invariant. Indeed it's easy to show that T_1 acting on the Θ vacuum is, up to a phase, the original vacuum. This Θ vacuum surfaces as a new effective non-perturbative term in the QCD Lagrangian proportional to $\bar{\Theta}G\tilde{G}$, with G the gluon field strength, $\tilde{G}$ its dual, M the quark mass matrix, and $\bar{\Theta} = \Theta + \arg\det M$. The $\bar{\Theta}$ factor contains contributions from the QCD vacuum and phases from the quark mass matrix. The $G\tilde{G}$ term in the Lagrangian is a total derivative, and does not contribute to the classical equations of motion or perturbative effects. However, the term is explicitly CP violating, and can contribute non-perturbative CP violating effects.

One such observable is the electric dipole moment of a spinning, spherically symmetric pétanque ball. From symmetry, the dipole moment must align or anti-align with the spin axis—for definiteness, we'll consider the aligned case. This spinning ball, as seen in a parity inverting mirror (P), still has spin and dipole axis aligned. Now, following the P mirror, look at the system in a charge conjugation inverting mirror (C); the spin and electric dipole axis are now anti-aligned and CP is then explicitly violated. The orientations of electric dipole and spin axes of the pétanque ball seen in P and C mirrors are shown in figure 2. Notice that unless CP is violated, the electric dipole moment of a spinning ball must vanish. In fact, very little research has been done on the CP properties of pétanque balls; the spinning neutron is studied, instead.

With a $\bar{\Theta}$ of order 1, the neutron in this way would acquire a CP violating electric dipole moment[2] of order 10^{-15}e-cm. The current limits are approaching 10^{-25}e-cm.[3], and these experiments in the context of the Θ vacuum limits $\bar{\Theta}$ to less than 10^{-10}. In a nutshell, this immeasurably small value of $\bar{\Theta}$ is the strong CP problem. Of course, a parameter equal to zero

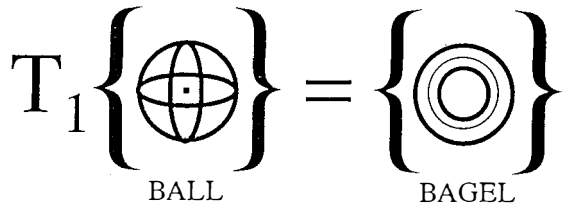


Figure 1: The gauge transformation T_1 can violate gauge invariance by turning a pétanque ball into a bagel.

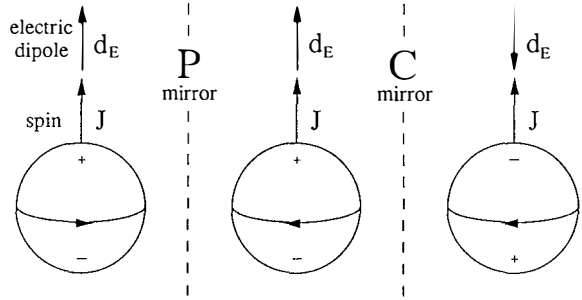


Figure 2: The electric dipole and spin axes of a spinning pétanque ball, and the axes seen in parity (P), then charge conjugation (C) mirrors.

is no cause for alarm. After all, the neutrino mass may very well be zero, with no one losing much sleep over it. However, the immeasurably small $\bar{\Theta}$ is a greater worry. Recall that $\bar{\Theta}$ contains contributions from QCD (through the Θ vacuum) and weak interactions (through the quark mass matrix). It is likely the weak contribution is non-zero, so the Θ vacuum contribution appears with opposite sign and almost precisely cancels. The two contributions, one from QCD and one from weak interactions, are independent. The zero in the strong CP problem is more than a simple zero, it is the near perfect cancellation of two independent finite effects There are ways to evade this problem,[4] among them: Unlikely as it seems, perhaps a u- or d-quark is massless, so a chiral rotation can make $\bar{\Theta}$ zero. Lowest order current algebra mass relations forbid a massless light quark, but the issue of whether or not the effective quark mass is zero from higher order corrections is controversial. Perhaps $\bar{\Theta}$ of zero, forcing CP conservation, is a new tree level symmetry of QCD—dubbed soft CP—although no one has yet advanced a workable model. To me, the most compelling solution is the one invoking the axion.

Now we can ask what axions are and what they have to do with the Strong CP Problem. To make the connection, let's consider a game of pool, in particular a gedanken pool table and pool room. Now, when playing pool, it's nice to have a level playing surface; the usual way of achieving this is to turn leg adjusters until the table is level, an operation we call "fine tuning." This fine tuning has limitations. Move the table to another room, and you must repeat the adjustment. If the room settles, you must repeat the adjustment. Basically, fine tuning works only for one particular location at one particular time. Wouldn't it be nice if the table adjusts itself? We can achieve this through the mechanism shown in figure 3. Here, the table rotates around a pivot point, a long pendulum arm is rigidly connected to the table, and θ is the tilt angle. Further, the room where the table goes has a switch on the wall that turns on gravity—it's a rather unusual room. Now, with gravity switched off, we push the table into the room. Without gravity, there is no preferred direction and θ is arbitrary. Now, switch gravity on, and the table starts to oscillate. Notice the oscillation is symmetric about $\theta = 0$ and there is energy stored in oscillations. What have we done? We have turned θ into a field. In doing so, the classical value of the field is driven to zero in a dynamical way, and the phonon-like field quanta are axions.

Enough with the pool table. The accepted way of introducing axions is to start with the idea of Peccei and Quinn.[5] They showed that by a slight extension of the standard model Higgs sector, the combined electroweak and QCD theories have a global U(1) symmetry, dubbed the Peccei-Quinn symmetry. At the scale f_{PQ}, the axion appears as the Goldstone boson of this spontaneously broken $U(1)_{PQ}$ symmetry.[6] I prefer to think of the axion in terms of pétanque balls and pool tables.

3 Properties of the Axion

In the last section, we saw how axions emerged as a consequence of the complicated QCD vacuum. This section continues with a discussion of how the axion couples to ordinary matter and radiation. The mass of the axion is substantially unconstrained by theory. The axion mass and the PQ symmetry breaking scale f_{PQ} are related through

$$m_a = \frac{\sqrt{z}}{1+z}\frac{f_\pi m_\pi}{f_{PQ}/N} \quad , \tag{2}$$

where z is the ratio of u- and d-quark masses (presumed near 0.5), and N is the color anomaly of the PQ symmetry, related to the coupling of axions to color. The anomaly N is model dependent, axion couple to color differently in different models in much the same way that the

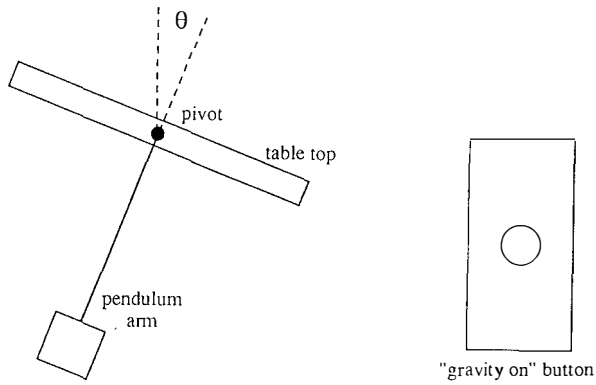


Figure 3: A gedanken pool table and pool room. The pool table rotates around a pivot point and is rigidly connected to a pendulum arm. When you switch on gravity, the table oscillates. The mean value of the angle is zero, and the quanta of oscillations are axions. Pool table analogy thanks to Pierre Sikivie.

relation between the vacuum expectation value of the axion field and the vacuum angle $\bar{\Theta}$ is model dependent (the theoretical constant is closely related in both cases). The axion can be considered to have effective couplings with normal matter and radiation, with coupling constants $g_{a\gamma\gamma}$, g_{aee}, g_{app}, etc., for the axion coupling to photons, electrons and protons. Since the elementary axion couplings are model dependent, these effective couplings are model dependent as well. For instance, the effective two photon coupling constant is

$$g_{a\gamma\gamma} = \frac{\alpha/2\pi}{f_{PQ}/N}(E/N - 2(4+z)/3(1+z) \quad , \tag{3}$$

with E is the electromagnetic anomaly, related to the coupling of axions to charged leptons, and the factor containing the ratio z of light quark masses $2(4+z)/3(1+z)$ is approximately 2. The tree level coupling of axions to color is fundamental to the role of axions in solving the strong CP problem. A tree level coupling of the axions to charged leptons is optional, here different theories call for different couplings. The extreme cases are axions with no tree level coupling to electrons (termed hadronic axions[7]), and axions where all the tree level quark and electron couplings are of the same strength (these are axions in a simple GUTs scenario and are termed DFSZ axions[8]). Note that even in hadronic axion models, there is an effective electron coupling through the anomalies. The effective coupling constants of axions with normal matter and radiation all depend in a Higgs-like way on $1/f_{PQ}$, so the larger the axion mass, the stronger the couplings. When the axion is very light, the couplings are very weak, and the axion is hard to detect. Such axions are termed invisible axions. The current round of axion searches looks for these invisible axions through their coupling with two photons. This coupling has strength

$g_{a\gamma\gamma}$, resulting in two photon lifetime

$$\tau = 7 \times 10^{24}\text{sec}\frac{(m_a/\text{eV})^{-5}}{\{E/N - 2(4+z)/3(1+z)\}/0.7} \quad . \tag{4}$$

There is nothing forbidding the anomaly ratio E/N from having the special value such that the axion has effectively infinite two photon lifetime. However, the E/N ratio in the simple DFSZ GUTs models has value 8/3, and there is no reason to think dynamics would drive E/N to the special infinite lifetime value.

4 Astrophysical and Laboratory Constraints on the Axion Mass

The original axion, rooted in symmetry breaking in the standard model $SU(2) \times U(1)$, called for f_{PQ} to be the 250GeV weak scale, leading to axions with masses near 10keV. Such axions couple relatively strongly and were quickly ruled out by accelerator experiments, e.g., $K \to \pi + a$ followed possibly by the axion decay into two electrons.[9] Non-observation of such decays constrain the axion mass to less than 10keV, and effectively rules out the original axion. However, at least in retrospect, there is no particularly good reason to believe the PQ symmetry breaking should be at the weak scale, and the search continues for invisible axions, those with f_{PQ} much larger than 250GeV. Through their effects on stellar dynamics and cosmological evolution, mass constraints can be placed on even invisible axions.

4.1 Axions and Stellar Dynamics

The evolution of a star is throttled by the rate at which thermal energy is dissipated. Electromagnetic interactions regulate photon energy transport, with the interaction length of nuclear reaction photons at the center of the sun on the order of centimeters; these photons bounce around the sun for millions of years before they escape. The electromagnetic interactions are, in this context, quite strong. On the other hand, invisible axions as well as neutrinos efficiently transport energy out of the star, thereby accelerating the star's evolution.

From the age and nuclear epoch of the sun, and models of solar dynamics, it is unlikely that axions at this moment could remove more than about half of the liberated nuclear energy, constraining the DFSZ axion mass to less than about 1eV.[10] The count of red giants in a population of stars thereby goes down, and these considerations result in a red giant constraint on the hadronic axion mass of a few eV or so.[11] A sufficiently massive DFSZ axion will prevent the helium from reaching the helium burning temperature, and such considerations constrain DFSZ axions to masses less than about 10^{-2}eV. Also, as for the solar limit, these limits do not apply to axion masses greater than the core temperature near 10keV.

4.2 Axions and Supernovae

In 1987, a nearby star in the LMC exploded as a supernova. Dubbed SN1987A, this event had enormous implications for particle and astrophysics. The impulsive release of the approximately 10^{53} ergs of gravitational binding energy eventually appeared as neutrinos with characteristic temperature of around 10MeV. However, the neutrinos released in the core have a relatively short path length; it takes many scatterings before a neutrino can escape. The supernova cooling is throttled by the relatively strong neutrino interactions. The Kamiokande and IMB detectors together recorded 19 neutrinos spread over about 10 seconds, a result consistent with our understanding of Type II supernovae dynamics and the number of light neutrino flavors.

An axion would efficiently transport energy out of the explosion, and reduce the spread in neutrino arrival times. The nucleons in the core have an effective coupling to axions, and since for this process, the electromagnetic anomaly does not directly enter, the DFSZ and hadronic axions couple to nucleons with similar strength. A detailed calculation[12] predicts that for axions of mass near 10^{-3}eV, the axion and neutrino energy transport out of the core are about equal. These calculation begins to break down near axion mass so large that they no longer escape without extensive rescattering. Briefly, effects of multiple scattering begin near axion mass 20×10^{-3}eV, and by 2eV, the relatively strongly interacting axions transport less power out of the core than any one neutrino species. These considerations constrain the axion mass to below 10^{-3}eV or above 2eV.

5 Production of Relic Axions

The laboratory and astrophysics bounds—essentially upper bounds—on the axion mass involve creation and detection of new axions. If axions are the dark matter, they must be a relic of the early universe. We know of only a few ways in which substantial numbers of such relic axions are created. These production mechanisms, coupled with the requirement that axions not severely overclose the universe, result in lower bounds on the axion mass. The mass range between the upper and lower bounds is the axion window mentioned in the introduction.

5.1 Relic Axions: Thermal Production

It the near thermal equilibrium of the early universe, axions were created and destroyed in particle interactions. For example, axions participated in Primakoff-like processes involving quarks or nucleons $\gamma + N \leftrightarrow a + N$. The important scales in thermal processes are the reaction rates involving axions and the expansion rate of the universe. For low reaction rates, axions freeze out of equilibrium and their overall density is then fixed in any comoving volume—this scenario is familiar from relic neutrino production. From considerations of this sort, we find that for axions to freeze out at closure density, the axion mass must be greater than about 10eV (with factors of two uncertainty arising from the Hubble constant).[13] Such relatively heavy axions are already excluded by astrophysical bounds, so it is unlikely that thermal axions comprise a substantial component of dark matter.

5.2 Relic Axions: Misalignment Production

In our Θ vacuum picture of QCD, CP conservation is a consequence of the $\bar{\Theta}$ parameter being driven to a classical value corresponding to the potential minimum as a consequence of the axion acquiring mass. Recall, however, that the axion did not start out with mass—it acquired mass near the temperature Λ_{QCD}—so the $U_{PQ}(1)$ angle parameter has arbitrary value in early times. We say the initial value is misaligned with its present value. This is the mechanism of misalignment production.[14] The quanta form a Bose condensate, and the axions have an extraordinarily tiny velocity dispersion. Misalignment axions are cold dark matter. The present density of misalignment axions is[15]

$$\Omega_a = 0.85 \times 10^{\pm 0.4} (\Lambda_{QCD}/200\text{MeV})^{-0.7} \times (m_a/10^{-5}\text{eV})^{-1.18}/h^2 \quad , \tag{5}$$

where the Hubble factor h arises from the expansion driven damping, and the QCD scale arises from the temperature where mass appears. This prediction for the present axion density

assumes an initial misalignment angle of $\pi\sqrt{3}$—the RMS angle of the interval $-\pi$ to π. This is reasonable as, without inflation, the initial misalignment angle was a composite of independent individual misalignment angles from a great number of causally disconnected volumes. With these assumptions and canonical values for the Hubble and QCD scales, axions with mass near 10^{-5}eV have closure density, and axions with substantially lower mass would severely overclose the universe. This misalignment axion production mechanism therefore provides a lower limit to the axion mass. Should inflation have occurred after axions first appear at the PQ symmetry breaking scale, there is just one initial misalignment angle corresponding to the angle in our pre-inflation volume. Here, the statistics of many causally disconnected volumes cannot be invoked, and one is forced to the weaker argument that a misalignment angle very near zero is unlikely. The axions are produced with a momentum dispersion related to the inverse of the initial Hubble length. Today, the momentum is reduced by the ratio of 2.7K to the temperature of the universe when axions acquired mass. Dividing by mass gives the present axion velocity dispersion of $10^{-22}(m_a/\mathrm{eV})^{-0.82}c$. Indeed, this is very cold dark matter.

5.3 Relic Axions: String Decay

Recall that the axion is the Goldstone boson of a spontaneously broken global U(1) symmetry. Such broken symmetries have strings as solutions to the equation of motion. Strings are nearly one-dimensional objects, either closed loops or infinitely long, arising from the mismatch between the arbitrary choice of broken vacuum in neighboring volumes.[16] Assuming no inflation or that inflation occurred before the breaking of PQ symmetry, a network of strings develop carrying appreciable energy. These strings interact, and in doing so form loops. These loops evaporate via axion radiation, and these radiated axions could form a substantial component of dark matter.[17] However, uncertainties in the radiation rate remain large. Also unresolved is the question of the phase space structure of string axions; the issue here is how their primordial velocity spectrum compares to a thermal distribution.

5.4 Relic Axions: Phase Space Structure

Our galactic structure is due to gravitational relaxation processes acting on the more uniform distribution of primordial matter. Axions, whether string or misalignment produced, are subject to these same gravitational forces, and relax with normal matter into something resembling an isothermal dark matter halo around our galaxy. There are large deviations from a thermal distribution in that the highest energy particles have discrete values of velocity. The phase space structure of radial infall axions in a halo are shown in upper figure 4, where the radial coordinate is distance from the center of the galaxy.[18] The energy spectrum of axions at our radius from the center of the galaxy is shown in lower figure 4. The isothermal peak is to the left, and the newer infall peaks are off to the right. Perhaps 10% of the axions are in the first infall peak, a narrow structure with fractional width narrower than 10^{-19}.

5.5 Relic Axions: Summary

Thermal axions would probably not contribute greatly to closure density. However, axions from misalignment or strings could be significant. Many uncertainties remain, most notably the issue of the velocity spectrum of string axions. There are additional uncertainties coming from Λ_{QCD} and the Hubble constant. The summary of the various laboratory, astrophysical and cosmological constraints on axion mass are shown in figure 5.

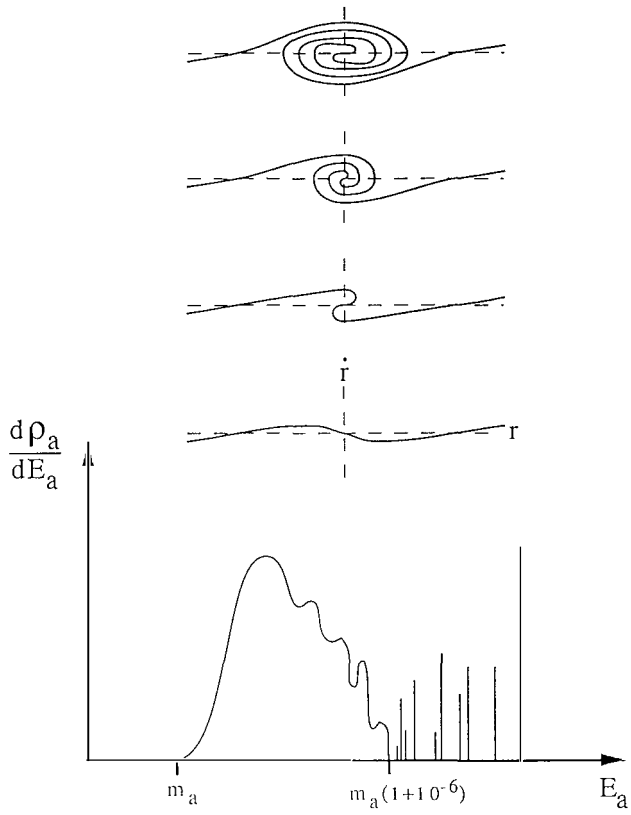


Figure 4: upper: Phase space of axions. The distance coordinate is the distance from the center of the galaxy. lower: Energy spectrum of axions near Earth.

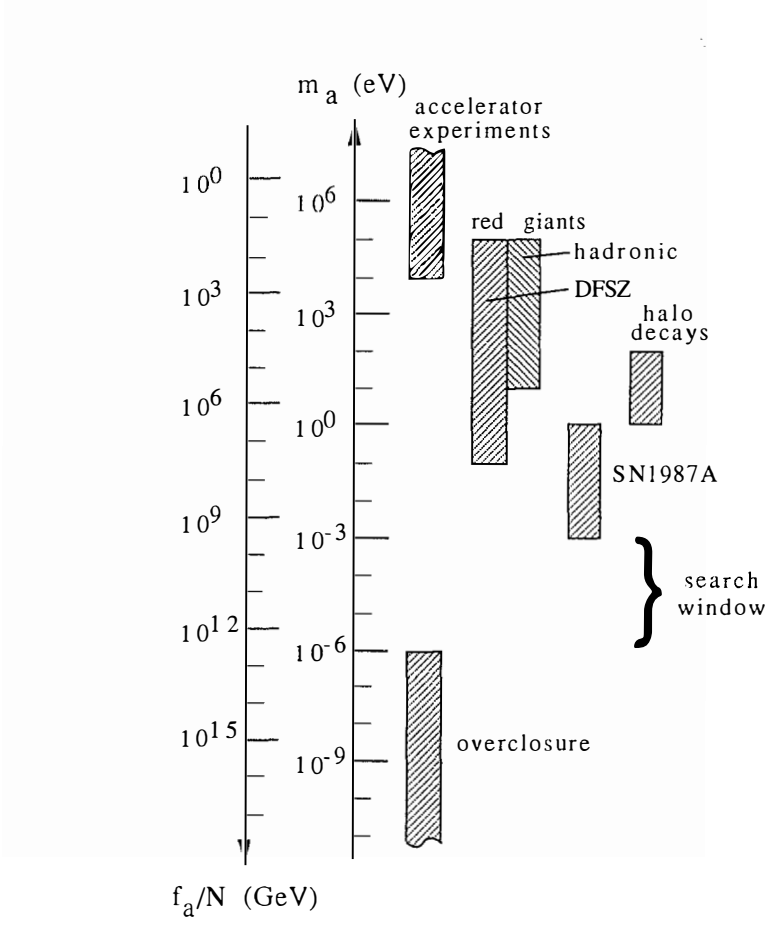


Figure 5: Laboratory, astrophysical and cosmological constraints on the axion mass.

6 Detection of Relic Axions: Sikivie-Type Detectors

The hypothesis that the halo of our galaxy is made of axions can be tested by finding resonant conversion of halo axions to photons in a magnetic field. This is the most mature of the various techniques of axion detection, and is the focus of this section. Space limitations prohibit mention of other clever detection schemes, and I apologize for their absence. In resonant conversion, a tunable high Q cryogenic cavity is placed within the bore of a superconducting solenoid, and the frequency of the lowest TM mode is slowly changed until excess power is detected from resonant axion—photon conversion.[19] The excess power is

$$P = 4 \cdot 10^{-26}\mathrm{Watt} \left(\frac{V}{0.22\mathrm{m}^3}\right) \left(\frac{B_0}{10\mathrm{Tesla}}\right)^2 \times C_{nl} \left(\frac{g_\gamma}{0.97}\right)^2 \left(\frac{\rho_a}{0.5 \cdot 10^{24}\mathrm{g/cm}^3}\right) \times \left(\frac{m_a}{2\pi\mathrm{GHz}}\right) \min(Q_L, Q_a) \tag{6}$$

with V the volume of the cavity, B_0 the effective magnetic field strength, C a mode-dependent form factor of order 0.5, ρ_a the density of galactic halo axions at the earth, m_a the axion mass, Q_L the loaded quality factor of the cavity and $Q_a \sim 10^6$ the "quality factor" of the galactic halo axions, *i.e.*, the ratio of their energy to their energy spread. Finally, g_γ is the coupling strength of the axion with two photons. The value $g_\gamma \sim 0.36$ is predicted for DFSZ axions, and the value is 0.97 for a model of hadronic axions. This is a tiny amount of power; consider that with the nominal value of constants in the above expression, the black body radiation in the appropriate Q_a bandwidth emitted from the 1K cavity is ten times larger than the power from axion conversions.

There is a semi-classical way to derive this expression for the conversion power of axions in the cavity,[20] where a correspondence is made between effective Lagrangians describing coupling the axion to two photons in the cavity and a LRC equivalent circuit. The axion interaction Lagrangian density is $\mathcal{L} = -(g_{a\gamma\gamma}/4\pi)a\vec{E} \cdot \vec{B}$, where $\vec{E}$ and $\vec{B}$ are electromagnetic fields in the cavity. In this density, the axion field (a) has large de Broglie wavelength relative to the cavity size, and can therefore be treated as spatially constant. Assume the cavity is a right circular cylinder of volume V, and take for B an externally applied magnetic field B_0 along the cavity axis. The integral of $\vec{B}_0 \cdot \vec{E}$ over the cavity volume depends on the configuration of $\vec{E}$, that is, on the $\vec{E}$ fields of that particular cavity mode. By expanding the E fields into normal·cavity modes $\vec{E} = \sum_i E_i\hat{e}$ with normalization $\int \hat{e}_i \cdot \hat{e}_i = V$, we can define a form factor $G_i = 1/V \int \hat{e}_i \cdot \hat{z}dV$, where we have taken the cavity axis and constant B field along the z-direction. The resonant behavior for a particular mode of the cavity may be represented by a series driven LRC equivalent circuit, with interaction Lagrangian $L = \mathcal{E}q$, where $\mathcal{E}$ is the driving EMF, and q the charge on the capacitor. We make the correspondence between the cavity and equivalent circuit by equating the cavity energy $(1/8\pi) \int \vec{E}_i \cdot \vec{E}_i dV$ and equivalent circuit energy $(1/2C)q^2$, and equating the cavity and equivalent circuit interaction Lagrangians, resulting in EMF

$$\mathcal{E} = \frac{-g_{a\gamma\gamma}}{\sqrt{4\pi}} B_0 G_i (V/C)^{1/2} a \quad . \tag{7}$$

At resonance, the power from axion conversions is

$$P_0 = \mathcal{E}^2/R = \frac{g_{a\gamma\gamma}^2}{4\pi} B_0^2 G_i^2 \frac{V}{RC} \langle a^2 \rangle \quad , \tag{8}$$

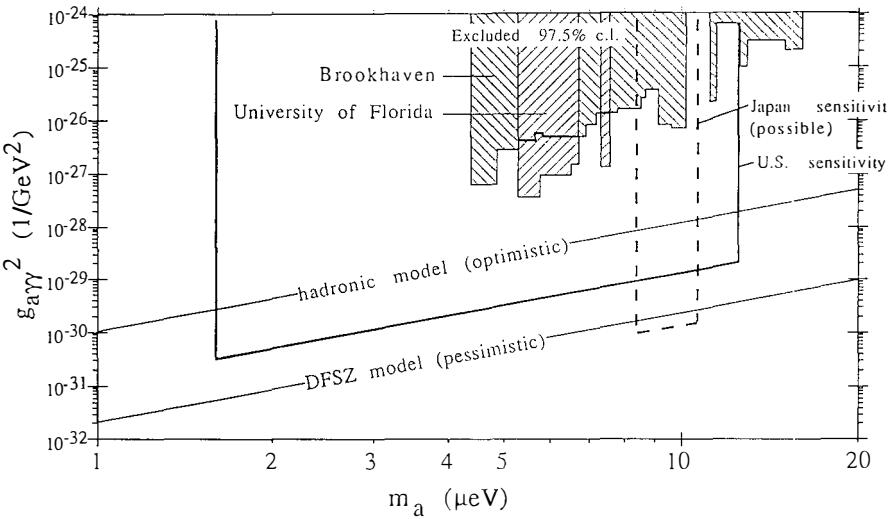


Figure 6: Exclusion regions in the axion mass versus coupling constant plane obtained by the pilot cavity experiments. Also shown are the coupling constants expected in a range (DFSZ and hadronic) of axion models. The area extending into the KSVZ (hadronic axion) region is the expected sensitivity of the U.S. experiment. The narrow region extending into the DFSZ region is the possible sensitivity of the Japanese experiment.

where $\langle a^2 \rangle$ is the axion density divided by m_a^2. With the cavity resonant frequency ω tuned to the axion energy E_a, and the cavity Q given in the LRC representation as $1/\omega RC$, we are done. The power generated in the cavity from axion to photon conversions is

$$P_0 = \frac{g_{a\gamma\gamma}^2}{4\pi} B_0^2 G_i^2 V Q \omega \langle \rho_a \rangle / m_a^2 \quad . \tag{9}$$

In the appropriate units, this is exactly the same result arrived at from field-theoretic arguments.

Pilot experiments (also called First Generation Experiments) have been carried out using relatively small volume magnets and—by current standards—noisy amplifiers, at Brookhaven National Laboratory (BNL) and at the University of Florida (UF). These experiments had $B_0^2 V$ values of 0.36 and 0.45 $T^2 m^3$, respectively. Figure 6 shows the regions in the coupling-squared versus mass plane eliminated by these searches, compared with the predicted coupling constants. The pilot experiments have demonstrated the principle of axion detection and have shown that reasonable sensitivity can be achieved over a wide range of frequencies. However, much larger systems are needed for sensitivity to plausible axion models.

A second-generation axion search, to be operated at the Lawrence Livermore National Laboratory, is now under construction in the U.S. The spokespersons are Leslie J Rosenberg

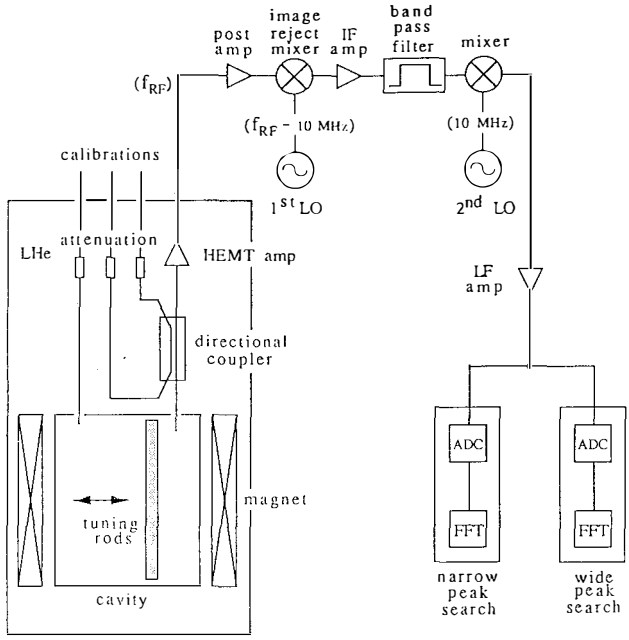


Figure 7: Sketch of the U.S. axion search experiment.

(MIT) and Karl van Bibber (LLNL).[21] The capability of this experiment to either detect axions (with s/n of 4) or exclude them (at the 97.7% C.L.) is shown in figure 6 as the region extending into KSVZ (hadronic) axion couplings. The key goals of the experiment are: (1) To achieve a power sensitivity which is conservatively a factor of 40 improvement (and probably closer to a factor of 100) over the pilot experiments. This is to be achieved by a combination of scaling up in magnet volume, and improving the noise temperature of state-of-the-art microwave amplifiers. (2) To search the mass range $1.5\mu eV < m_a < 12.6\mu eV$. This is to be achieved through filling the magnet volume with multiple cavities.

A sketch of the U.S. experiment is shown in figure 7. The experiment will utilize a superconducting magnet with a central field of 8.5T. The volume for the cavities will have an inner diameter of 50 cm, and a length of 100 cm. Hence, $B_0^2 V = 12 T^2 m^3$, approximately a factor 25 over the pilot experiments. The experimental volume will be separated from the magnet cryostat by a cold-vacuum wall. The magnet will be operated at 4.2K, and it will be possible to exchange cavity arrays and electronics in the experimental volume whilst the magnet is energized, and more importantly the temperature of the cavity arrays will be independent of that of the magnet. Initially, the cavity will be operated at about 1.5K, about the noise temperature of the best microwave amplifiers available today in the UHF through S-bands (0.5 through 3GHz). The expected total noise temperature of 3K (physical plus electronic) yields another factor 1.6 in improved sensitivity over the pilot experiments.

In the U.S. experiment, for the first time, arrays of multiple cavities will be used to extend the mass search range. Tuning is accomplished by moving dielectric or metallic rods within the cavity, and in this way the experiment will cover the range $1.5\mu eV < m_a < 12.6\mu eV$. It will start taking data in late 1994, and run for approximately three years.

Also, the possible narrow peaks in the halo axion phase space are exploited to increase the experiment sensitivity. How this works is as follows: The ultimate signal to noise ratio is given by SNR $= (P_s/T_n)\sqrt{t/B}$, with P_s and T_n the signal power and noise temperature coming out of the receiver electronics, and t and B the signal integration time and bandwidth. The integration time is about 100s, and for isothermal halo axions, the bandwidth is of order 1kHz. Now consider a narrow line of width 10^{-2} (this is actually a rather modest width compared to the intrinsic phase space width of the first infall peak) containing a fraction f_1 of the halo axions. The signal to noise ratio in this narrower bandwidth is better by the factor $f_a\sqrt{10^5} = 300 f_1$. In the U.S. experiment, there are separate processing paths for the isothermal and narrow peak searches.

Another second generation axion search, to be operated at Kyoto, is now under construction in Japan. The spokesperson is Seishi Matsuki (Kyoto). It is similar to the U.S. design, except for its dilution refrigerator and Rydberg atom beam system. Two useful properties of Rydberg atoms in states of principal quantum number n near 100 are:[22] (1) The interval between energy levels is very small, for example, $\Delta E_{100} \sim 3 \times 10^{-6}$eV $\sim$ 7GHz $\sim 2 \times 10^{-1}$cm^{-1}. (2) The electric dipole transition moment between $\Delta n = 1$ states is very large, for example, the absorption cross section with $n = 100$ can approach 1cm^2. This suggests that Rydberg atoms can be used as sensitive microwave photon counters.

The Japanese design of a Rydberg atom microwave single photon counter is shown in figure 8. Here, atoms in the ground state are sent through a detection cavity. Just before entering the cavity, atoms are excited by a laser, where the $n \rightarrow n+1$ transition is fine-tuned to the conversion cavity microwave frequency by a weak external magnetic field. Rydberg atoms that have absorbed a microwave photon are the only ones ionized,[23] and the electrons are counted.

The conversion cavity, a right circular cylinder 7 cm diameter and 80 cm long, is threaded by a 7T magnetic field, and the tuning range is 2.4GHz $\pm$ 10-20%. Extrapolating from their earlier experience with Rydberg counting, they hope for a sensitivity below the DFSZ model over a narrow mass range for a year of operation, as shown by the lower excluded region in figure 6.

7 Conclusions

The axion, first proposed in the late 1970's as a solution to the strong CP problem, also answers the question of the nature of dark matter. If anything, the case for the existence of axions has grown stronger over time. Interest in axions has tracked the rising interest in topological defects, and axionic strings could have important cosmological consequences. The suggestion has been made that perhaps MACHOS—Jupiter mass objects—form not only the baryonic component of dark matter, but all the dark matter, or maybe all the dark matter in our galactic halo. However, early hints are that MACHO dark matter is not dominant, even in our own halo. This, and the recent negative Hubble telescope search for substantial dark matter in the form of low mass stars, weakens the case for baryons as the primary dark matter. The measurements of the microwave background quadrupole anisotropy tells us that while pure cold dark matter—for example, axions—is not a perfect fit, hot dark matter is a horrific fit. The following point is contentious, but I believe the anisotropy data tells us that dark matter is substantially cold. The present window of allowed axion mass—10^{-6} to 10^{-3}eV—has been

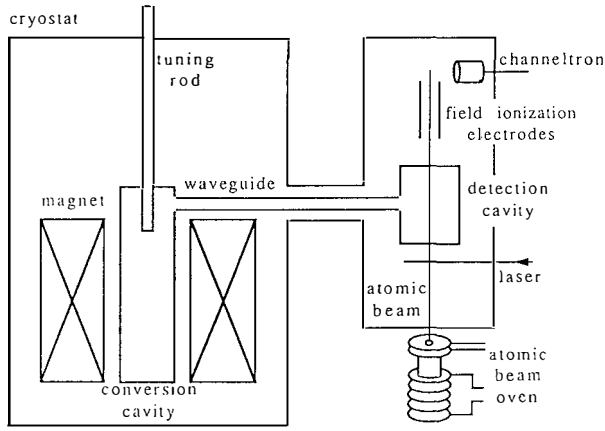


Figure 8: Sketch of the Japanese axion search experiment based on Rydberg atom microwave photon counting. In the actual experiment, the detection and conversion cavities are directly coupled.

under intense scrutiny for years and has survived substantially unscathed. It is intriguing that misalignment axions in this window have about the right mass to close the universe. Sikivie-type RF cavity experiments are underway to probe this window with reasonable sensitivity, and other experiments are in the proposal stage. It looks promising for axions: (1) they are on firm theoretical ground; (2) the data calls for substantial amounts of non-baryonic dark matter, even in our own halo; (3) the data hints a substantial component of dark matter is cold, say, in the form of axions; (4) experiments are underway to look for these halo axions.

Acknowledgements. I thank Pierre Sikivie and Michael Turner for providing their patient teachings. I also thank my colleagues at LBL, Florida, FNAL, Livermore, and MIT for their good ideas and suggestions. Finally, I thank MIT for allowing me the freedom to search for axions.

References

[1] R.D. Peccei, reviews the axion and the strong CP problem in, C. Jarlskog ,"CP Violation", World Scientific, Singapore (1989) 503.

[2] Because of the CPT theorem, I am sometimes careless in noting the distinction between T and CP violation. To get it right, see Robert G. Sachs, "The Physics of Time Reversal", University of Chicago Press (1987).

[3] Altarev et al., Phys.Lett. B276 242.

[4] For example, see T.Cheng and L.Li, "Gauge Theory of Elementary Particle Physics," Oxford University Press, New York (1984).

[5] R.D.Peccei and H.R.Quinn, Phys.Rev. D16 (1977) 1791.

[6] S.Weinberg, Phys.Rev.Lett. 40 (1978) 223; F.Wilczek, Phys.Rev.Lett. 39 (1978) 1304.

[7] J.Kim, Phys.Rev.Lett. 43(1979)103; M.Shifman, A.Vainshtein and V.Zakharov, Nucl.Phys. B166 (1980) 493.

[8] M.Dine, W.Fischler and M.Srednicki, Phys.Lett. B104 (1981) 199; A.Zhitnitsky, Sov.J.Nucl.Phys. 31 (1980) 260.

[9] Y.Asano et al., Phys.Lett. 107B (1981) 159-162.

[10] J.Frieman, S.Dimopoulos and M.Turner, Phys.Rev. D36 (1987) 2201.

[11] G.Raffelt and D.Dearborn, Phys.Rev. D36 (1987) 2211.

[12] R.Brinkmann and M.Turner, Phys.Rev. D38 (1988) 2338.

[13] M.Turner, Phys.Rev.Lett. 59 (1987) 2489.

[14] J.Preskill, M.Wise and F.Wilczek, Phys.Lett. B120 (1983) 127; L.Abbott and P.Sikivie, Phys.Lett. B120 (1983) 133; M.Dine and W.Fischler, Phys.Lett. B120 (1983) 137.

[15] M.Turner, Phys.Rev. D33 (1986) 889.

[16] H.Nelson and P.Oleson, Nucl.Phys. B61 (1973) 45; A.Vilenkin, Phys.Rep. 121 (1985) 263.

[17] R.Davis, Phys.Lett. B180 (1986) 225.

[18] P.Sikivie and J.R.Isper, Phys.Lett. B291 (1992) 288.

[19] P. Sikivie, Phys. Rev. Lett. 51 (1983) 1415.

[20] J.Rogers, University of Rochester, thesis, Department of Physics preprint UR-1021 (1987).

[21] The collaboration includes scientists from MIT, University of Florida, University of California at Berkeley, University of Chicago, Lawrence Livermore National Laboratory, Lawrence Berkeley Laboratory, and Fermi National Accelerator Laboratory.

[22] For a review of Rydberg atoms, see T.Gallagher, "Rydberg Atoms," Cambridge University Press, Cambridge (1994).

[23] The potential of the Rydberg electron in an external electric field "leans over", so that above a critical value of n, the atom spontaneously ionizes when passing the ionization electrodes.

THE EDELWEISS* EXPERIMENT: A STATUS REPORT

Dominique Yvon
for the EDELWEISS collaboration

*Experience pour DEtecter Les WIMPs En Site Souterrain

A. de Bellefon[1], L. Berger[2], I. Berkès[3], C. Bobin[3], D. Broszkiewicz[1], B. Chambon[3], M. Chapellier[5], G. Chardin[4], Ph. Charvin[6], V. Chazal[3], N. Coron[8], M. De Jesus[3], D. Drain[3], L. Dumoulin[2], Y. Giraud-Héraud[1], C. Goldbach[7], J. Leblanc[8], Y. Messous[3], X. F. Navick[5], G. Nollez[7], C. Pastor[3], P. Pari[5], I. Prostakov[4], M. C. Perillo -Isaac[1], D. Yvon[4].

[1]LPC Collège de France, 11 place Marcelin Berthelot, F-75231 Paris cedex 05, France.
[2]CSNSM, Bat 108, F-91405 Orsay Campus, France.
[3]Institut de Physique Nucléaire de Lyon, Université C. Bernard Lyon I & IN2P3, F-69622 Villeurbanne Cedex, France.
[4]CEA-CE Saclay, DAPNIA/Service de Physique des Particules, Bat 141, F-91191 Gif-sur-Yvette cedex
[5]CEA-CE Saclay, DRECAM/SPEC, Orme des merisiers, F-91191 Gif-sur-Yvette cedex
6Laboratoire Souterrain de Modane, 90 rue de Polset, F-73500 Modane, France.
[7]Institut d'Astrophysique de Paris, CNRS, 98[bis] Bd. Arago, F-75014 Paris, France.
[8]Institut d'Astrophysique Spatiale, Université Paris XI, F-91405 Orsay Cedex, France.

Abstract

We ran a 1.5 keV threshold, 24g bolometer, deep underground, in a selected environment for low radioactivity. The experimental setup is quickly described. Preliminary analysis based on 125 hours of effective running time exhibits a 10 fold improvement in the event rate at energy between 10 and 20 keV relative to the previous attempt in 1991. However, the event rate is still two orders of magnitude higher than the best detectors at these energies. We are currently working at identifying the origin of the radioactive contaminants and developing new detectors.

The "Dark Matter problem" has been extensively discussed in the literature[9]. Some elementary particles could account for a large fraction of the unseen mass. An active field in particle physics is the search for supersymetric particles. The Lightest Supersymetric Particle (LSP), if the R-parity is conserved, is a good candidate for Dark Matter. More generally, the constraint from nucleosynthesis together with the observed value of matter density suggest that Weakly Interacting Massive Particles (WIMPs) would account to part of, if not all, the Dark Matter of the Universe. Goodman and Witten [3] proposed to detect WIMPs through their elastic scattering on nuclei. Several attempts have been conducted already [4]. The main challenges of these experiments consist in achieving a low ($\leq$keV) detection threshold and very low background radioactivity.
The EDELWEISS experiment has been designed as a prototype experiment for WIMPs detection using Bolometers. This is the first bolometer experiment with this physics goal installed in a deep underground site: the Modane Underground Laboratory under a rock

shielding of 4800 meter water equivalent depth. The motivation for using bolometers for WIMP detection is double:
First, bolometer detectors are the detectors with the lowest threshold. Since the energy distribution of nucleus recoil is close of an exponential shape, the lower detection threshold is the more efficient.
Second, bolometer detectors are the only known detectors to measure ionisation and heat [7] or heat and light produced by a few keV nucleus recoil. Atomic models predict [5], and measurements have shown [6] that nucleus recoils ionise and scintillate less than electrons of the same kinetic energy. This allows an event by event or a statistical identification of electron and γ interactions, which constitute the main source of radioactive background.
We are now tackling the issues of bolometer experiments. Currently, our main effort is to get rid of parasitic events (microphonics, electromagnetic pulses), selecting low radioactive materials and developing more sensitive bolometers.

1. Experimental set up:

a) The dilution refrigerator.
We built a dilution refrigerator from carefully selected low radioactivity materials. Its base temperature is 35 mK. The available volume is a cylinder of 80 mm diameter and 300 mm height. Fall this year, the cryostat should be upgraded to a base temperature of 10 mK and an available diameter of 90 mm, 300 mm height. An automated gas handling system was developed to run this refrigerator. It allows monitoring the experiment over Internet, and greatly simplify the cooling and the maintenance of the cryostat.

b) The low radioactivity shield.
The refrigerator was placed inside a low radioactivity "outer shield" consisting of 10 to 15 cm of low radioactivity lead and of 10 cm of copper. A 5 cm thick selected iron layer covers this structure for mechanical sustainment.
In the cold part of the cryostat, an internal shield at a temperature of 4 K is made from archaeological lead, between 2 to 5 cm thick. An additional 9 cm archaeological lead shield at 55 mK is blocking the line of sight toward the dilution unit. This shield is designed to provide a 4π steradian shield to the detector.

c) The detector
We have used a 24 g sapphire bolometer with NTD Ge thermometer described in [1]. In running conditions, we got a typical detector sensitivity of 260nV/keV with an impedance of 700 kΩ at zero bias. We tried to run the bolometer with higher sensor impedance. Although the bolometer sensitivity was increased up to 800 nV/keV, the increase in microphonic noise did not improved the energy threshold.

d) The low noise readout system.
We have designed a flexible and dismountable wiring and electronic readout system. Emphasis in the design was put on achieving optimal electronic noise (no ground loops, careful shielding), and reduced sensitivity to microphonics. The preamplifier system was designed according to Ref.[8]. We achieved a noise level close to the thermodynamic limit ($\approx$2 nV.Hz$^{-1/2}$ in running conditions), although most events close to the threshold are due to microphonics. Up to six signal channels can be implemented in this set-up. With the above detector, we observed a 0.9 keV (FWHM) baseline width and ran the detector with an electronic threshold less than 2 keV.

e) Energy calibration.
Due to the 4π archaeological lead shield and to cryogenic constraint, it is difficult to insert a γ source close enough to the detector and get a low energy calibration. thus we placed a ^{60}Co γ source, which provides 1.173 MeV and 1.333 MeV lines, inside the "outer shield" close to the detector. γ went through the 4K shield and we registered the Compton spectrum. Previous measurement showed that the detector response was linear to few %

up to 1 MeV[1]. Fitting the observed spectrum to the montecarlo predicted spectrum allow a calibration better than 5%, dominated by the systematics on linearity and simulations.

2. Preliminary results.

The present results are based on an effective running time of 125 hours. Event shape using a Le Croy 6810 wave shape recorder and time were recorded. Analysis of shape of events showed that a significant fraction of events come from artefacts due to microphonics and electromagnetic noises that we did not completely succeed to shield from. These spurious triggers display different shapes from events due to radioactive background. Off line, we fitted the events' to a template, allowing time shift of events relative to the template. The template was built using low energy Compton events from ^{60}Co calibration runs. A simple cut on the fit residual while retaining 100% of the Compton interaction events allows a complete elimination of the electromagnetic noise events above 5 keV. Further analysis is going on.
After normalisation we get the preliminary spectrum plotted on figure (1).
Above 16 keV, we measured a event rate of 25 events/kg/keV/day. Below 16 keV the event rate rises rapidly. We believe that the event rate is artificially high due to the lack of containment (small size) of the detector. Thus the high energy γ interactions are shifted toward smaller energy. Taking these results into account, we are able to place an exclusion plot for Weakly Interacting Massive Particles figure (2).

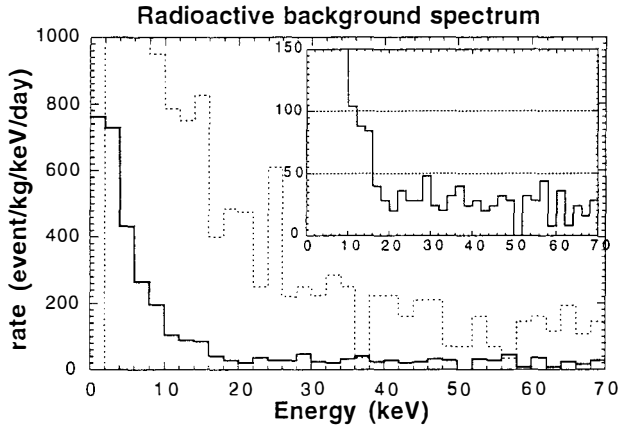


Figure 1: *Radioactive background spectrum normalised to event rate in events/kg/keV/day. Dashed line: result of the 1991 attempt [2], solid line: this experiment. An average event rate of 25 events/kg/keV/day above 16 keV is observed. The insert shows more accuratly the radioactive background at energies above 15 keV.*

3. Future Plans:

We are now measuring the radioactive contaminants of our setup using a 100 cm^3 germanium diode running at 77K inside the cryostat.

We are also developing massive bolometers, using thin films thermal sensors, and involving simultaneous measurements of ionisation and heat signals. Simultaneous measurement of light and heat signals is also being investigated. Our current program

includes the measurement of a 1 kg sapphire bolometer and 70 g Ge diodes with simultaneous detection of heat and ionisation signals. These measurements are expected to be completed by mid 1996.

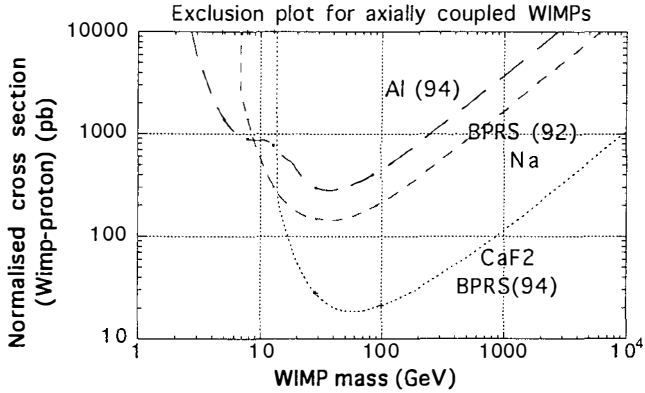


Figure 2: *Exclusion plot in the hypothesis of an axially coupled WIMP, extracted from the background spectrum shown on fig(1). This experiment is labelled as Al(94). For comparison, we plotted the best previous results extracted from [10]. Courtesy of C. Tao and G. Gerbier.*

Acknowledgements.
It is a pleasure to thank the technical support of the collaboration for their help. In this respect, special thanks are due to JP. Soirat (DAPNIA/SPP), Ph. Forget, G. Guerrier (DRECAM/SPEC), JP. Hadjout (IPNL) and M. Martin (IAP). It is also a pleasure to acknowledge useful discussions with J.L Bret and A. Benoît (CRTBT), P. Garoche (URA2), and JP. Torre (IAS) for technical advice of cryogenic environment. F. et Ph. Hubert (CENBG) have been of great help for low radioactivity measurements.

References

[1] P. de Marcillac et al., 1992, in Low Temperature Detectors for Neutrinos and Dark Matter IV, ec. Booth N. E. and Salmon G. L., (Editions Frontière, Gif sur Yvette, 1992), p. 81)
[2] N. Coron et al., Astron. Astrophys. 278 (1993) L31.
[3] M.W. Goodman and E. Witten, Phys. Rev. D31 (1985) 3059.
[4] For a review talk about direct detection of WIMPs, L. Mosca, Proc. of Rencontres de Moriond on Particle Astrophysics, Atomic Physics and Gravitation, (Editions Frontière, Gif sur Yvette, 1994).and references therein.
[5] J. Lindhard, V. Nielsen, M. Scharff, and P. V. Thomsen, Mat. Fys. Medd. K. Dan. Vidensk. Selsk. 33, (1963) 10
[6] C. Chasman et al., Phys. Rev. Lett. **21**, 1430 (1968) and references therein; G. Gerbier et al., Phys. Rev. A**45**, (1992) 2104; A. R. Sattler, F. L. Vook, and J. M. Palms, Phys. Rev. **143,** 588 (1966)
[7] T. Shutt et al., Phys. Rev. Lett. **69**, 24 (1992); N. Spooner et al., Phys. Lett. B **273**, 333 (1991); B. L. Dougherty et al., J. Low Temp. Phys 93 365 (1993)
[8] D. Yvon et al., submitted to Nuclear Instrument and Methods A.
[9] For a review talk on the Dark Matter porblem and the candidates, see B. Sadoulet, these proceedings and references herein.
[10] C. Bacci et al, Astroparticle Physics **2,** 117 (1994).

GIANT LUMINOUS ARCS

François Hammer[1], Isabella Gioia[2], Olivier Le Fèvre[1], Gerry Luppino[2]

[1] *DAEC, Observatoire de Meudon, France*

[2] *Institute of Astronomy, University of Hawaii, USA*

Abstract

Since 80s, clusters of galaxies were not believed to be enough massive and compact to reach their lensing critical density, i.e. to provide strong lensing events by their own. In 1981, a filament structure in A370 was reported[1], and has been identified 5 years latter to the so-called giant luminous arc[2], simultaneously with a similar structure in Cl2244-02[3]. The first lensing models [4] were quickly made and reproduced well the arcs, providing a strong support that arcs are images of background galaxies gravitationally distorted by cluster core masses. The definitive proof came from the redshift measurement of the A370 arc, which yielded a value almost twice the cluster redshift [5]. Arc studies are now very numerous, most of them intending to estimate the amount and the distribution of the dark matter component in clusters, and more than 40 giant luminous arcs have been already discovered. In this short paper, we summarize the main results concerning the giant luminous arcs (defined as having R<22.5 and axis ratio l/w > 10) including the new constraints derived on the dark matter density profile within the cluster cores, and the new insights well below 1 kpc scale of the morphology of faint distant galaxies.

1 What can be derived from arc observations.

Mass estimation of the lensing cluster core can be fairly accurate when it is based on the observation of a large arc (l/w > 10) with a known redshift, although some estimations can be affected by the presence of cluster substructures. They lead to M/L values ranging from 100 to 300 with uncertainties as low as 10% for the best configurations [6].

For images having a large axis ratio (l/w >> 1) one[7] can establish the relationship between the observed arc width (w) and the source diameter (d) as w = 1/2 d (1 - K(arc))$^{-1}$, where K(arc) is the lensing matter term at the arc location, which is proportional to the local mass surface density. For a very compact density profile (point mass), K(arc)=0, providing w = 1/2 d, for a singular isothermal sphere, K(arc)=0.5 and w=d while for an isothermal profile

with a core (with radius $\approx$ arc impact parameter), K(arc) $\approx$ 0.75, w=2d. Since most of the giant luminous arcs are generally unresolved from the ground (w < 0"5), either the arc sources are very compact, or the matter term K(arc) should be not very larger than 0.5. From the observations of faint galaxy sizes, it seems rather conservative to estimate that the core radius of the most of the arc clusters cannot be significantly higher than the observed arc radius, which range from 50 to 150 kpc.

The former relationship provides a fundamental uncertainty to our knowledge of the magnification factor (ratio of the arc luminosity to the source luminosity), which can be expressed as

$$Amp = 1/4(l/w)(1 - K(arc))^{-2}, \quad (1)$$

and also strongly depends on the lens density profile. Distant rich clusters of galaxies were often claimed to be gravitational "telescopes" allowing redshift measurement of galaxies otherwise too faint, but we still have a poor knowledge of the accurate powers of such "telescopes". It prevents us to draw an Hubble diagram for the arc sources, in order, for example, to go beyond the magnitude limit of current spectroscopic surveys.

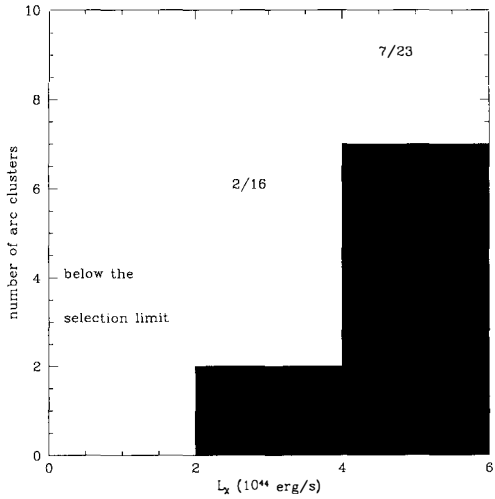
2 Statistics of luminous arcs.

The previous relationships show that modelling of arcs in clusters can be generally done assuming a large variety of cluster density profiles. An interesting possibility to constrain the cluster mass density profile from arc modelling has been done in Cl 2137-23 [8], assuming that several images of the same source are lying at different impact parameters (including the so-called radial arc). Another alternative would be to measure redshifts of several arcs at different impact parameters in the same cluster.

Since the magnification probabilities depend so strongly on the lens density profile, solid constraints on the latter can be derived through arc statistic studies. Wu and Hammer [9] have developped a statistical model, assuming that lensing clusters follow the X-ray luminosity function and that arc sources follow a Schechter luminosity function scaled on the density of faint galaxies from deep spectroscopic surveys. In order to compare the results to the observations, the generated arcs have been limited by their magnitude and by their axis ratio. The predicted distribution for arc cluster and source redshifts is in good agreement with the available data as well as for the X-ray luminosity distribution of arc clusters. Recall that most, if not all, of the arc clusters are X-ray luminous. Several mass density profiles have been tested through that model, resulting to the expectation of one giant luminous arc per three ($L_X > 410^{44}$ erg/s) clusters, if latter have density profile following singular isothermal sphere, and ten times less giant luminous arcs, if lensing clusters have $\approx$ 200 kpc core radii. Indeed, in the last case, the predicted number of giant luminous arcs over the whole sky would drop to 12, much less than the number of already known arcs!

In order to have an observational data basis directly comparable to the theoretical expectations, a systematic survey of a complete sample of clusters have been done [10]. Target clusters (39 clusters with $L_X > 2\ 10^{44}$ erg/s and z >0.15) have been selected from the Einstein Medium Survey Catalog, and have been imaged in two colors (V and I or B and R) at a moderate depth at C.F.H.T. and U.H.22' (20mn exposure time in each filter at C.F.H.T., $\mu(V) < 25.3$ and $\mu(I) < 25.2$) with good seeing conditions (0".5 < FWHM < 1"). Recall that the luminosity function assumed for lensing clusters in the Wu and Hammer's work have been derived from the EMSS catalog. 14 luminous arcs (R < 22.5 and l/w > 4) have been detected including 8 giant luminous arcs (l/w> 10). The arcs have been identified by eye by two independent groups, and one can not expect a large contamination by cluster edge-on spiral galaxies [11].In

Figure 1

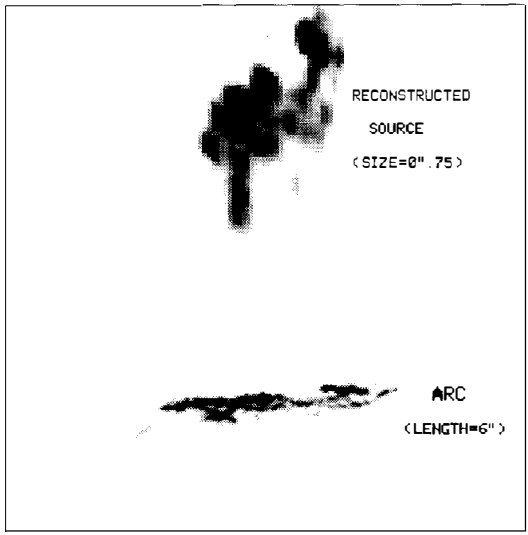


such a double limited sample (in flux and in axis ratio), no bias should be expected against arcs having intermediate axis ratio ($4 < l/w < 10$) since at a given magnitude, the smaller arcs should have brighter surface brightnesses. Figure 1 shows the number of arc clusters in function of the cluster X-ray luminosity. 7 of the 23 very luminous clusters ($L_X > 4\ 10^{44}$ erg/s) have an arc or more in their core, which is consistent with the prediction of Wu and Hammer, if cluster mass density profiles have very small or null core radii. Conversely, the 16 moderately luminous X-ray clusters ($2\ 10^{44} < L_X < 4\ 10^{44}$ erg/s) only show 2 arcs in their cores. One can interpret Figure 1 as revealing that only very powerful X-ray clusters have reached the lensing critical density, i.e. they have much more compact mass density profiles (or small core radii) than the other ones.

Another test of the cluster density profile can be provided by examining the distribution of their axis ratio, which also depends on the density profile, since the fraction of arcs having large arc axis ratio increases for decreasing cluster core radii[6]. 8 of the 12 arcs detected in the sample of the 23 very luminous clusters have an axis ratio larger than 10, which is marginally consistent with a singular isothermal sphere density profile for lensing clusters, but highly inconsistent with the presence of core radii larger than $\approx$ 50 kpc (probability of rejection $\approx$ 0.9996 [6]). It is also interesting to notice that the 2 arcs detected in the 16 intermediately powerful X-ray clusters have small axis ratio ($l/w < 10$).

3 Giant arcs as magnified galaxies and new HST observations.

Magnification factor along the arc length can easily reach values larger than 10. It results that one can resolve details ten times smaller than if the source was not magnified. For example, it has been suggested [12] that the patchy appearance of the Cl2244-02 arc is the result of intrinsic source structures (arms and bulge of a nearly face-on galaxy), convolved by the spatial resolution (FWHM $\approx$ 0"6, the arc width is not resolved from the ground).
The cluster MS0440+0204 has been observed by the HST in October 1994, with a total inte-



gration time of 6 hours in a broad band filter centered on 7000A. Several arcs in this cluster were already identified from the ground[13], and the HST image strikingly reveals the circular symmetry of their distribution around the cluster core. MS0440+0204 deserves further studies but already appears to be an almost ideal lens, for which it would be easy, from a minimum of assumptions, to derive the density profile (indeed the core radius appears to be very small). On this image, the 14 arcs all have their widths spatially resolved (pixel size of WFPC2 = 0".1), and several of them show structures and compact or unresolved sources. One should notice that when a spatially unresolved source is found in an arc, it implies an intrinsic size smaller than 0".1/(Amp(1-K)), which can be as small as 0".01 in most cases. Such very compact sources have then intrinsic sizes smaller than 120 pc if the surrounding galaxy lies at z=1, and could be compact HII regions for example. Figure 2 shows a tentative of source reconstruction for one arc detected around the MS0440+0204 core, assuming a singular isothermal density profile for the cluster, and a magnification factor of 9 for the arc. The arc length is 6", the reconstructed pixel size is 0".011, and the reconstructed source size 0".75. Most of the reconstructed sources have irregular morphologies, although one could identify arm-like structures in some of them. More definitive results are in progress.

4 Summary.

There are several tens of giant luminous arcs which are now discovered, and more than one hundred are expected. Their modelling can provide fairly good estimation of the projected masses in rich cluster cores, and the derived M/L ratio are ranging from 100 to 300. Their statistical properties (number occurence, axis ratio distribution) lead to a dark matter component much more concentrated to the cluster center than the X-ray gas or the galaxy distribution. The first survey of a complete sample of X-ray clusters has led to the discovery of 14 luminous arcs, most of them lying in the brightest X-ray clusters. It results that only Lx > 4 10^{44} erg/s clusters have reached the critical lensing density and have core radii likely smaller than 50 kpc,

while less luminous clusters are either less massive or less compact.
First results from a new HST image of MS0440+0204 are presented. Not less than 14 arcs are found in the core of this very rich cluster, which appears by many aspects, to be an ideal lens. First source reconstruction technics are experienced from this high quality data, and reveals the internal structure of background sources, i.e. on faint distant galaxies. These galaxies, otherwise barely resolved from the ground, shows arm-like structures and compact sources (HII regions ?) as small as 120 kpc, if the source is lying at z=1.

References

[1] Hoag, A., 1981, B.A.A.S., 13, 799
[2] Soucail, G.,*et al.* A& A, 172, L14
[3] Lynds, R., Petrosian, V., 1986, B.A.A.S., 18, 1014
[4] Hammer, F., 1987, in Bergeron et al, eds., 3rd IAP Astrophys. Meeting on High Redshift Objects, Edts Frontières, Gif sur Yvette, P. 467
[5] Soucail, G.,*et al.* 1988, A& A, 191, L19
[6] Hammer, F.,*et al.* 1993, in the 31st Liege Int. Astrophys. Coll. on Gravitational Lenses, Institut d'Astrophysique, Eds J. Surdej et al, P. 609
[7] Hammer, F., 1991, ApJ, 383, 66
[8] Mellier, Y., Fort, B., Kneib, J.P., 1993, ApJ, 407, 33
[9] Wu, X.P., Hammer, F., 1993, MNRAS, 262, 187
[10] Luppino, G.,*et al.* 1995, ApJ, submitted
[11] Le Fèvre, O.,*et al.* 1994, ApJ, 422, L5
[12] Hammer, F., Rigaut, F., 1989, A& A, 226, 45
[13] Luppino, G.,*et al.* 1993, ApJ, 416, 444

SESSION X

NEW WINDOWS

GRAVITATIONAL WAVES AND COSMOLOGY

Thibault Damour[1,2]
[1] *Institut des Hautes Etudes Scientifiques, 35, route de Chartres, 91440 Bures-sur-Yvette, France,*
[2] *DARC-Observatoire de Paris-CNRS, 92195 Meudon Cedex, France*

Abstract

After a brief presentation of gravitational-wave research, one discusses the potential impact of gravitational wave observations on cosmology.

1 Gravitational Waves

The concept of gravitational wave ("onde gravifique") was introduced (in a sketchy form) by Poincaré [1], [2], [3] within the context of Lorentz-invariant theories of the gravitational interaction. However, it is only within the context of general relativity that Einstein [4], [5] introduced a full-fledged mathematical description of linearized gravitational waves. His main result was that there exists a coordinate system in which a gravitational wave is described by a transverse, traceless symmetric tensor $h_{ij}^{TT}(t,x)$ propagating with the velocity of light. He also worked out the total energy flux radiated in gravitational waves at infinity in the case when the forces responsible for the motion of the gravitational-wave source are *non gravitational* (e.g. an elastically vibrating crystal). His result (called Einstein's "quadrupole formula") reads

$$\left(\frac{dE}{dt}\right)_{radiated} = \frac{G}{5c^5}\,\frac{d^3I_{ij}}{dt^3}\,\frac{d^3I_{ij}}{dt^3}\,, \tag{1}$$

where

$$I_{ij}(t) = \int d^3x\,\frac{T^{00}(t,x)}{c^2}\,(x^ix^j - \frac{1}{3}\,x^2\delta^{ij}) \tag{2}$$

denotes the quadrupole moment of the mass-energy distribution of the source. This initial breakthrough was followed by a long period of conceptual and technical confusion which lasted from 1918 up to 1956. Some of the reasons at the basis of this confusion were: (i) the lack

of a clear understanding of the *physical effects* of a gravitational wave, (ii) the mathematical difficulty to control non linear effects in the generation and propagation of gravitational waves, and (iii) the absence of exact, time-dependent solutions of general relativity with bounded sources. Though important advances were made during this period by Landau and Lifshitz [6] and Fock [7] (who proved that the validity of the quadrupole formula (1), (2) extended to *self-gravitating* sources such as binary stars), our understanding of gravitational waves was still incomplete, and there were even lingering doubts about their physical reality. [Note that doubts are still expressed [8], [9], though they are unfounded [10], [11].]

The modern (conceptually and technically clearer) era of gravitational-wave research started in 1956 with Pirani's [12] conceptual understanding of the physical effects induced by a passing gravitational wave (see also [13]). Pirani understood that a gravitational wave of dimensionless amplitude $h_{ij}^{TT}(t,x)$ (corresponding to a ripple of spacetime curvature $R_{oioj}(t,x) = -\frac{1}{2}\, c^{-2}\partial^2 h_{ij}^{TT}/\partial t^2$) would locally induce the relative fluctuation $\delta L/L = \frac{1}{2}\, h_{ij}^{TT} \nu^i \nu^j$ in the measured distance L separating two free test masses oriented in the direction $\boldsymbol{\nu}$. [Because of the transversality of h_{ij}^{TT} note that δL vanishes if the direction $\boldsymbol{\nu}$ coincides with the direction of propagation $\mathbf{n}$.] This soon led Weber to inventing and constructing the first gravitational-wave detectors [14]. Subsequent important dates are: (i) Weber's claim, in 1969 [15], of an actual detection of gravitational waves, and (ii) Taylor's announcement, in December 1978 [16], of the observation of a decay of the orbital period of the binary pulsar PSR1913+16 [17] which agreed with the value one would heuristically expect from the energy loss (1). Weber's claim was not confirmed, but gave an enormous boost to the experimental effort toward the detection of gravitational waves and to theoretical thinking about possible astrophysical sources. On the other hand, Taylor's announcement was confirmed and refined by further observations. It also had an enormous impact on the theoretical work on gravitational waves. At present, the agreement to 0.35% between the observation of the orbital period change of PSR1913+16 [18], [19], and the theory of the motion of binary systems of strongly-self-gravitating bodies, including the effects generated by the finite velocity of propagation of gravity [20], [21], [22], firmly establishes the reality of gravitational radiation. Contrary to what is often stated, this agreement is a *direct* experimental confirmation that the gravitational interaction propagates with the velocity of light between the two neutron stars making up the binary pulsar PSR1913+16. Recently, an independent experimental confirmation was brought by the observational data on the binary pulsar PSR1534+12, [23], which also give us our first confirmations of the strong-field regime of general relativity [24].

The present status of the experimental effort toward the direct detection of gravitational waves is the following:

(i) some groups pursue Weber's concept of solid, *resonating* detectors. The modern versions of this concept aim at taking advantage of noise reduction at cryogenic [down to milli-Kelvin!] temperatures [Baton-Rouge, Rome-Frascati-CERN, Trento, Perth] and of spherical shapes [Leiden]. Though such cryogenic resonant detectors might usefully complement interferometric ones when searching for a stochastic background of gravitational waves [25], they do not seem competitive for detecting the other types of gravitational waves.

ii) the main experimental effort is directed toward constructing large *interferometric* detectors of gravitational waves. Two ground-based projects have been approved and are under construction: the North-American LIGO project (two 4km-size interferometers) and the Franco-Italian VIRGO project (one 3km-size interferometer). The LIGO/VIRGO projects represents a network of three detectors which will start taking data at the turn of the century. [Note that a network of three detectors is an absolute minimum for being able to measure the direction of incidence of the gravitational waves and therefore for starting to do any gravitational-wave astronomy.] Other projects [Germany-Great-Britain, Japan, Australia] might usefully join the

LIGO/VIRGO network in the future. Recently, the European Space Agency has approved the concept of a space-based interferometric detector of gravitational waves as Cornerstone Mission No.7 in the Horizon 2000 Plus programme. Such a detector (which might operate sometime after 2016) will crucially complement the ground-based detectors in opening the low-freqency window $10^{-4} - 10^{-1}$ Hz. [The LIGO-VIRGO network will observe in the higher-frequency window $10 - 10^4$ Hz.]

Let us finally mention that the dimensionless amplitude $h_{ij}^{TT}(t,x)$ of a gravitational wave is related, to lowest order, to the motion of the source by

$$h_{ij}^{TT}(t,x) \simeq \frac{2G}{c^4 r} P_{ijk\ell}(n) \left\{ \frac{d^2}{dt^2} I_{k\ell}\left(t - \frac{r}{c}\right) \right\} \tag{3}$$

where $P_{ijk\ell}(n) = (\delta_{ik} - n_i n_k)(\delta_{j\ell} - n_j n_\ell) - \frac{1}{2}(\delta_{ij} - n_i n_j)(\delta_{k\ell} - n_k n_\ell)$ is the transverse-traceless projection operator onto the plane orthogonal to the local direction of propagation $n \equiv x/r$, and where $I_{ij}(t)$ is the quadrupole moment of the source, equation (2). Recent theoretical work has allowed one to improve very much on the lowest-order (Einstein-Landau-Lifshitz-Fock) result (3) by taking into account higher multipoles [26] and nonlinear effects in the generation and propagation of gravitational waves [27], [28], [29], [30]. As we shall see below such theoretical refinements may be of essential help in deciphering the information contained in some sources of gravitational (inspiralling binaries). On the other hand, many astrophysical sources are not amenable to an analytical treatment and the computation of their gravitational radiation must be done by sophisticated numerical methods (such as spectral methods [31]). To have in mind rough estimates, let us note that equation (3) implies a gravitational wave amplitude $h \sim |h_{ij}^{TT}|$ of order

$$h \sim \frac{G}{c^4} \frac{E_{kin}^{non\ spher}}{r} \sim 10^{-20} \left(\frac{E_{kin}^{non\ spher}}{M_\odot c^2}\right) \left(\frac{10 Mpc}{r}\right), \tag{4}$$

where $E_{kin}^{non\ spher}$ denotes the *non spherical* part of the kinetic energy of the source (i.e. more precisely the trace-free part of the kinetic energy tensor $K_{ij} = \int d^3x c^{-2} T^{00} v^i v^j$ which appears as a contribution to $d^2 I_{ij}/dt^2$). By comparison, the LIGO/VIRGO first-generation detectors will have a sensitivity corresponding to featureless (wide-band) bursts of amplitude $h \sim 10^{-21}$, i.e. more precisely, to a spectral density for relative length fluctuations $\tilde{h} \sim 3 \times 10^{-23}\, Hz^{-1/2}$. [Remember that, as understood by Pirani, a gravitational wave of amplitude h_{ij}^{TT} induces fractional changes in the length of each arm of an interferometer of $\delta L/L = \frac{1}{2} h_{ij}^{TT} \nu^i \nu^j$.] Virgo-cluster events happening several times per year (gravitational collapses) will have $r \sim 10$ Mpc but a kinetic energy $E_{kin}^{non\ spher}$ so small compared to $M_\odot c^2$ that the corresponding featureless burst of gravitational waves, with an amplitude on Earth $h \ll 10^{-21}$, will not be detectable by LIGO/VIRGO [31]. At the present time, the most secure sources for LIGO/VIRGO are coalescing binary neutron stars with $r \sim 100$ Mpc, $E_{kin}^{non\ spher} \sim E_{kin} \lesssim 0.1 M_\odot c^2$ which should generate several times per year gravitational of amplitude $h \sim 10^{-23}$. Such waves should be detectable by LIGO/VIRGO because they are emitted as a mathematically well predicted, quasi-periodic wave packet (whose last several thousands cycles will pass through the detector's bandwidth), thereby allowing matched-filter methods to dig deeply into the wide-band noise.

To complete the present very brief introduction to gravitational-wave research we urge the reader to consult more detailed reviews [32], [33], [34], [35], [36] and/or recent topical books [37], [38].

2 Astronomy and Cosmology from Gravitational Wave Observations

Let us first recall that the main reasons one has to develop gravitational-wave observatories are:

(i) to detect, for the first time, passing gravitational waves and to verify the predictions of general relativity concerning their structure, their propagation and their generation in strong-field regions, and

(ii) to open a new, much more transparent "window" on the universe which is a priori likely to create a revolution in our view of the universe comparable to or greater than that which resulted from opening, say, the radio or X windows.

The anticipations we can make now, by extrapolating from the "orthogonal" information deduced from the various electromagnetic and neutrinic windows, will probably pale in comparison with the unexpected results future gravitational-wave observatories will bring. Let us, however, briefly discuss these anticipations. (We refer to references [35]-[38] for more detailed presentations.)

2.1 Galactic and Virgo-cluster astronomies

It is not likely that the LIGO/VIRGO observatory will see sources in our Galaxy or even in the Virgo cluster. However, space-based giant interferometers (such as the LISA project; a constellation of three pairs of satellites in heliocentric orbit, separated by $\sim 5 \times 10^6$ km) should detect many galactic binary systems made of compact objects: neutron-star-neutron-star systems, as well as, possibly, systems containing white dwarfs or black holes. Such observations would give important information about the evolution of binary systems. On the other hand, one does not expect to observe sources in the Virgo-cluster, except in the case where strong non-axisymmetric instabilities set in during the collapse of the core of a star or in the dynamics of a newly born neutron star [31].

2.2 Extragalactic astronomy and cosmology

Here, one can anticipate with confidence that gravitational-wave observations will bring important cosmological information. First, a cosmologically very interesting type of sources are coalescing compact binary systems, i.e. the last minutes of the evolution of systems of two neutron stars, or two black holes, or one neutron star and one black hole. As is observationally confirmed in the cases of PSR1913+16 and PSR1534+12, gravitational radiation damping leads to a slow contraction of the binary orbit. After some time ($\sim$ 300 million years in the case of PSR1913+16), the two neutron stars will end up quite close to each other (say a few hundred kilometers), at which stage the system will undergo a very rapid evolution consisting of a fast inspiral motion followed by tidal disruption of the less massive neutron star and coalescence of all the matter into one fast-rotating central object (neutron star or black hole). As pointed out by Schutz [39], the last minutes of the inspiral motion (corresponding to orbital frequencies sliding from 5 Hz up to $\sim 10^3$ Hz) give us a very clean tool for measuring cosmologically interesting quantities. Indeed, to lowest order (i.e. when using equations (1) and (3)), the quasi-periodic gravitational wave emitted by an inspiralling binary can be analytically computed and its amplitude is found to depend: on several angles, on the combination $m_\bullet \equiv [m_1 m_2/(m_1+m_2)^2]^{3/5}(m_1+m_2)$ of the two masses, on the (instantaneous) gravitational-wave frequency f and on the distance r at which the source is located. On the other hand, the rate of change of the (upward sliding) gravitational wave frequency is a mathematically

well-defined function of m_0, r and f. [The fact that the same combination of masses m_0 enters both the amplitude h and df/dt is simply due to the fact that df/dt is driven, via the radiation reaction on the orbit, by the gravitational radiation losses which are proportional to $(dh/dt)^2$.] Observation of the gravitational-wave inspiral signals in at least three detectors allows one to measure (modulo a two-fold ambiguity) all the unknown angles, as well as the astrophysically important mass combination m_0, *and the distance* r. This is a very rare example where observations done on Earth will give us a direct, absolute measurement (in light seconds) of the distance separating us from an astrophysical system located several hundred megaparsecs away. Current estimates suggest that LIGO/VIRGO should see several events per year from coalescences happening within a radius $r \sim 200$ Mpc. The angular position on the sky should be determined by gravitational wave observations to a few degrees, which should be enough for pinpointing a cluster of galaxies probably hosting the galaxy containing the coalescing binary. Combining the gravitational-wave measurement of the distance r, and an optical measurement of the redshift z of the cluster of galaxies will give us access to Hubble's constant H_0 to better than 10% [39]. Moreover, if coalescing binaries are the origin of gamma-ray bursts, the correlation between the two will allow one to lower the signal-over-noise confidence threshold and to observe farther, more numerous, systems (as well as to obtain a rich information on the precursors of gamma-ray bursters) [40]. When LIGO/VIRGO is in its more advanced configuration (with improved sensitivity), it will become possible to detect inspiralling neutron-star/black-hole systems at cosmological redshifts $z \gtrsim 1$. [If the number density of such systems is comparable to that of the double neutron-star systems, one should observe several events per day!] There the strategy to get cosmologically significant information would be different, as the angular measurements will become too imprecise to usefully locate the source on the sky. First, one must go beyond the lowest-order formula (3) and include the analytically computable higher-order contributions to the gravitational-wave signal emitted by an inspiralling binary. Thanks to the theoretical generation formalism developed in Refs. [27]-[30], it has been recently possible to work out analytically the fractional corrections to the "quadrupole" formula (3) up to the order $(v/c)^4$ [40]. Such a theoretical accuracy is important for modelling with precision the evolution in time of the phase of the gravitational wave signal [41] and thereby to measure not only the mass combination m_0 appearing at lowest order, but the symmetric mass ratio $m_1 m_2/(m_1 + m_2)^2$ entering higher orders. As a consequence, gravitational wave observations of inspiralling binary systems will give access separately to the distance r and to the two masses m_1 and m_2. Actually, in the case of cosmologically distant binaries, one measures the luminosity distance r_{lum} and the "redshifted" masses $(1+z)m_1$, $(1+z)m_2$. If one *assumes* (in agreement with current data) that the physical mass m_1 of the neutron star is equal to $1.4 M_\odot$ within a small dispersion, the gravitational-wave measurement of $(1+z)m_1$ will give us access to the redshift z. Therefore, after one year of data one will be able to plot about thousand measurements of z versus r_{lum}. This plot has a rich cosmological content, and could allow one to measure H_0 to 1 km/s/Mpc, and, more interestingly, to measure the deceleration parameter q_0 and the dimensionless cosmological constant λ_0 to a few tens of percent [42], [43].

Another type of gravitational-wave observations which could have an important impact on cosmology is the search for a stochastic background of gravitational radiation. Correlating data from two separate interferometers, e.g. the two LIGO ones, or, better (because of a smaller separation) the VIRGO detector and another interferometer in Europe, can allow one to detect a stochastic background whose contribution to the closure density $\Omega_{GW}(f) \equiv f(d\rho_{GW}/df)/\rho_{critical}$ is as small as a few times 10^{-10} for $f \sim 100$ Hz [44]. Such a measurement would not constrain inflationary models (for which $\Omega_{GW}^{inf} \sim (H_{inf}/m_{Planck})^2 \Omega_{rad} < 10^{-14}$), but would give a crucial

test of cosmic string scenarios of galaxy formation which predict [45], [46]

$$\Omega_{GW}^{local strings} > 10^{-2} G\mu/c^2 > 0.5 \times 10^{-8} . \quad (5)$$

In conclusion, I hope I have convinced the reader that gravitational-wave observations will open exciting possibilities for cosmology.

References

[1] Poincaré H., (5 juin 1905), *C.R. Acad. Sc. Paris*, **140**, p.1504-1508.

[2] Poincaré H., 1906, *Rend. Circ. Matem. Palermo*, **21**, p.129-176.

[3] Poincaré H., 1908, *Revue Générale des Sciences pures et appliquées*, **19**, p.386-402.

[4] Einstein A., 1916, *Preuss. Akad. Wiss. Sitzber.* (Berlin), p.688.

[5] Einstein A., 1918, *Preuss. Akad. Wiss. Sitzber.* (Berlin), p.154.

[6] Landau L.D. and Lifshitz E.M., (Nauka, Moscow, 1941), *Teoriya Polya*, (Theory of Fields).

[7] Fock V.A., (Fizmatgiz, Moscow, 1955), *Teoriya prostranstva vremeni i tyagoteniya*; see (Pergamon, London, 1959), *Theory of Space, Time and Gravitation.*

[8] Bonnor W.B., 1994, *Class. Quantum Grav.*, **11**, p.2007.

[9] Chown M., (17 September 1994), *New Scientist*, **143**, No. 1943, p.15.

[10] Damour T., 1995, *Class. Quantum Grav.*, **12**, p.725.

[11] Chown M., (14 January 1995), *New Scientist*, p.16.

[12] Pirani F.A.E., 1956, *Acta Phys. Polonica*, **15**, p.389.

[13] Bondi H., 1957, *Nature*, **179**, p.1072.

[14] Weber J., 1960, *Phys. Rev.*, **117**, p.306.

[15] Weber J., 1969, *Phys. Rev. Lett.*, **22**, p.1320.

[16] Taylor J.H., Fowler L.A. and McCulloch P.M., 1979, *Nature*, **277**, p.437.

[17] Hulse R.A. and Taylor J.H., 1975, *Astrophys. J. (Lett.)*, **195**, p.L51.

[18] Taylor J.H. and Weisberg J.M., 1989, *Astrophys. J.*, **345**, p.434.

[19] Taylor J.H., 1992, *Phil. Trans. R. Soc. London* A, **341**, p.117; 1993 *Class. Quant. Grav.*, **10**, p.S167.

[20] Damour T. and Deruelle N., 1981, *Phys. Lett.* A, **87**, p.81; Damour T., 1982, *C.R. Acad. Sci. Paris*, **294**, p.1335.

[21] Damour T., 1983, *Phys. Rev. Lett.*, **51**, p.1019; in *Gravitational Radiation*, edited by N. Deruelle and T. Piran, (North-Holland, Amsterdam, 1983), p.59-144.

[22] Damour T. and Deruelle N., 1986, *Ann. Inst. H. Poincaré*, **44**, p.263.

[23] Wolszczan A. and Taylor J.H., to be published, (quoted in J.H. Taylor, 1994, *Rev. Mod. Phys.*, **66**, p.711).

[24] Taylor J.H., Wolszczan A., Damour T. and Weisberg J.M., 1992, *Nature*, **355**, p.132.

[25] Astone P., Lobo J.A. and Schutz B.F., 1994, *Class. Quantum. Grav.*, **11**, p.2093.

[26] Damour T. and Iyer B.R., 1991, *Phys. Rev.* D, **43**, p.3259.

[27] Blanchet L. and Damour T., 1989, *Ann. Inst. H. Poincaré*, (Physique Théorique), **50**, p.377.

[28] Damour T. and Iyer B.R., 1991, *Ann. Inst. H. Poincaré*, (Physique Théorique), **54**, p.115.

[29] Blanchet L. and Damour T., 1992, *Phys. Rev.* D, **46**, p.4304.

[30] Blanchet L., 1995, *Phys. Rev.* D, **51**, p.2559.

[31] Bonazzola S. and Marck J.A., 1993, *Astron. Astrophys.*, **267**, p.623.

[32] Thorne K.S., *Gravitational Radiation*, in *300 Years of Gravitation*, edited by S.W. Hawking and W. Israel (Cambridge University Press, Cambridge, 1987), p.330-458.

[33] Damour T., *An introduction to the theory of gravitational radiation*, in *Gravitation in Astrophysics*, edited by B. Carter and J.B. Hartle, (Plenum Press, New York, 1987), p.3-62.

[34] Giazotto A., 1989, *Phys. Rep.*, **182**, p.365.

[35] Schutz B.F., 1989, *Class. Quantum Grav.*, **6**, p.1761; 1993, **10**, p.S135; in *General Relativity and Gravitation 1992, Proc. 13th Int. Conf. on General Relativity and Gravitation*, edited by R.H. Gleiser, C.N. Kozameh and O.M. Moreschi (Institute of Physics, Bristol, 1993); in *Frontiers of Astrophysics*, edited by Per B. Lilje and Per Maltby (Inst. Theor. Astrophys., Univ. of Oslo, 1995), p.45-68.

[36] Bonazzola S. and Marck J.A., 1994, *Astrophysical sources of gravitational radiation*, Annu. Rev. Nucl. Part. Sci., **45**, p.655-717.

[37] Blair D.G., editor, *The Detection of Gravitational Waves*, (Cambridge University Press, Cambridge, 1991).

[38] Schutz B.F., editor, *Gravitational Wave Data Analysis*, (Kluwer, Dordrecht, 1989).

[39] Schutz B.F., 1986, *Nature*, **323**, p.310; Krolak A. and Schutz B.F., 1987, *Gen. Rel. Grav.*, **19**, p.1163; 1989, *Class. Quantum Grav.*, **6**, p.1761.

[40] Piran T., to be published.

[41] Blanchet L., Damour T., Iyer B.R., Will C.M. and Wiseman A.G., (1 May 1995), *Phys. Rev. Lett.*; Blanchet L., Damour T. and Iyer B.R., 1995, *Phys. Rev.* D, to appear.

[42] Cutler C. et al., 1993, *Phys. Rev. Lett.*, **70**, p.2984.

[43] Markovic D.M., 1993, *Phys. Rev.*, **D48**, p.4738.

[44] Flanagan E., *Phys. Rev.* D, in press.

[45] Bouchet F.R. and Bennett D.P., 1990, *Phys. Rev.*, **D41**, p.720.

[46] Vilenkin A. and Shellard E.P.S., *Cosmic Strings and other Topological Defects*, (Cambridge University Press, Cambridge, 1994).

Scale Relativity and Structuration of the Universe.

Laurent Nottale
C.N.R.S., DAEC, Observatoire de Paris-Meudon

Abstract. Some cosmological consequences of the principle of scale relativity are briefly considered in this contribution. General linear scale-laws satisfying the above principle take the form of the Lorentz group. This allows one to solve the horizon/causality problem without inflation, and implies that the fractal dimension of structures in the universe must vary with scale, in a way that depends on the value of the cosmological constant. This theory explains the observed value of the exponent of the correlation function, $\gamma = 1.8$, predicts that γ must decrease for increasing scales, and accounts for the transition to uniformity at large scales. It allows a measurement of the cosmological constant that agrees with an independant estimate from the vacuum energy density.

The principle of scale relativity is an extension of Einstein's principle of relativity that takes into account the transformation of reference systems not only under space-time displacements (as in motion relativity), but also under dilations of space-time resolutions (scale laws). When applied to the cosmological domain, the theory of scale relativity leads to several new proposals and predictions.

In scale relativity, we first substitute to the "Galilean-like" laws of dilation $ln\rho'' = ln\rho + ln\rho'$ the more general Lorentzian law [1,2]:

$$ln\rho'' = \frac{ln\rho + ln\rho'}{1 + ln\rho\, ln\rho' / \mathbb{C}^2} \quad . \tag{1}$$

Under this form the scale relativity symmetry remains unbroken. Such a law corresponds, at the present epoch, only to the null mass limit. It is expected to apply in a universal way during the very first instants of the universe. This law assumes that, at very high energy, no static scale and no space or time unit can be defined, so that only pure contractions and dilations have physical meaning. (One could object that the Planck scale can always be used as unit, but, as we shall recall hereafter, it plays a special role in scale relativity). In Eq. 1, there appears a universal purely numerical constant $C = ln\mathbb{K}$. As we shall see, the value of $\mathbb{K}$ is of the order of 5×10^{60}: its emergence yields an explanation to the Eddington-Dirac large number "coincidences" [3].

Now, pure scale relativity is broken in microphysics by the mass of elementary particles, i.e., by the emergence of their de Broglie length:

$$\lambda_{dB} = \hbar / mv \tag{2}$$

and in macrophysics by the emergence of static structures (galaxies, groups, cluster cores) of typical sizes:

$$\lambda_g \approx \frac{1}{3} Gm / \langle v^2 \rangle \quad . \tag{3}$$

The effect of these two symmetry breakings is to separate the scale axis into three domains, a quantum (scale-dependent), a classical (scale-independent) and a cosmological (scale-dependent) domain (see Fig. 1).

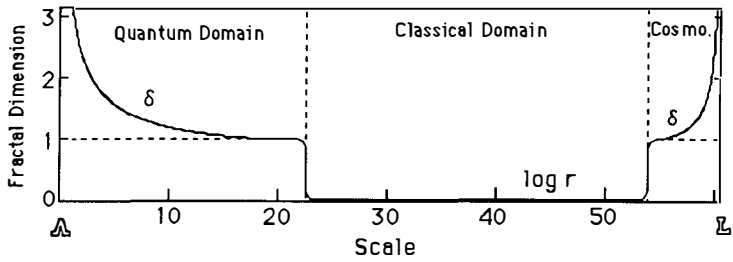


Figure 1. Variation of the fractal dimension in the three, quantum, classical and cosmological domains of the present era, in terms of logarithm of resolution, in the case of scale-relativistic (Lorentzian) scale laws.

The consequence is that, in the two scale-dependent domains, the static scales can be taken as reference, so that one do not deal any longer with pure dilation laws, but with new laws involving dimensioned space and time intervals:

$$ln(\lambda''/\lambda) = \frac{ln(\lambda'/\lambda) + ln\rho}{1 + ln(\lambda'/\lambda)\, ln\rho / ln^2(\mathbb{R}/\lambda)} \tag{4}$$

In this new dilation law, the symmetry breaking has substituted a length-time scale that is invariant under dilations to the invariant dilation of Eq. 1. In the microphysical domain, this scale is naturally identified with

the Planck scale, $\ell = (\hbar G/c^3)^{1/2}$, that now becomes impassable and plays the physical role that was previously devoted to the zero point [1,2]. In the cosmological domain, the invariant scale is identidied with the scale of the cosmological constant , $\mathcal{L} = \Lambda^{-1/2}$ [4].

We shall in this contribution briefly consider the various consequences and predictions of the new theory in the cosmological domain. A more detailed account can be found in Refs. [3,4].

Horizon / causality problem:

In the theory of scale relativity, the standard laws of dilations currently used up to now are shown to be low energy (i.e., large length-time scale) approximations of more general laws that take a Lorentzian form (see Eq. 1). One can indeed demonstrate [1,2] that the general solution to the special relativity problem (i.e., find the laws of transformation of coordinates that are linear and satisfy the principle of relativity) is the Lorentz group. This result, which was known to apply to motion laws [2,5], applies also to scale laws (i.e., contraction and dilations of resolutions).

The horizon / causality problem is simply solved in this framework without needing an inflation phase, thanks to the new role played by the Planck lenth-time scale. It is identified with a limiting scale, invariant under dilations. This implies a causal connection of all points of the universe at the Planck epoch. The light cones flare when $t \to \ell/c$ and finally always cross themselves (see Fig. 2 and Ref. 4]).

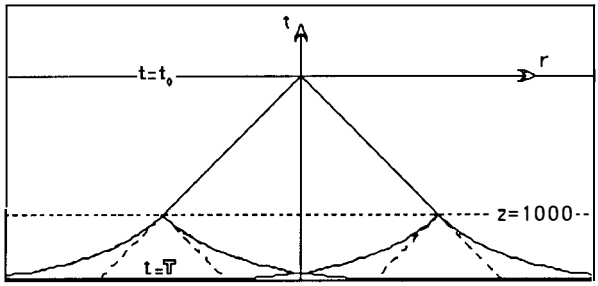


Figure 2. Illustration of the flare of light cones in scale-relativity, allowing causal connection of any couple of points in the universe (from Fig.7.1 of Ref[4]).

Cosmological constant and vacuum energy density.

One of the most difficult open questions in present cosmology is the problem of the vacuum energy density and its manifestation as an effective cosmological constant [6,7]. Scale relativity solves this problem and connect it to Dirac's large number hypothesis.

The first step toward our solution consists in considering the vacuum as fractal, (i.e., explicitly scale dependent). As a consequence, the Planck value of the vacuum energy density (that gave rise to the 10^{120} discrepancy with observational limits) is relevant only at the Planck scale, and becomes irrelevant at the cosmological scale. We expect the vacuum energy density to be solution of a scale (renormalisation group-like) differential equation [2,3,8]:

$$d\rho/d\ln r = \Gamma(\rho) = a + b\,\rho + O(\rho^2) , \qquad (5)$$

where ρ has been normalized to its Planck value, so that it is always <1, allowing the Taylor expansion of $\Gamma(\rho)$. This equation is solved as:

$$\rho = \rho_c \, [1 + (r_o/r)^{-b}] \, . \tag{6}$$

We recover the well known combination of a fractal, power law behavior at small scales (here), and of scale-independence at large scale, with a fractal/non-fractal transition about some scale r_o that comes out as an integration constant [2, 8-10].

The second step toward a solution is to realize that, when considering the various field contributions to the vacuum density, we may always chose $\langle E \rangle = 0$ (i.e., renormalize the energy density of the vacuum). But consider now the gravitational self-energy of vacuum fluctuations [11]. It writes:

$$E_g = \frac{G}{c^4} \frac{\langle E^2 \rangle}{r} \, . \tag{7}$$

The Heisenberg relations prevent from making $\langle E^2 \rangle = 0$, so that this gravitational self-energy *cannot* vanish. With $\langle E^2 \rangle^{1/2} = \hbar c / r$, we obtain the asymptotic high energy behavior:

$$\rho_g = \rho_P \left(\frac{\mathbb{A}}{r}\right)^6 \, , \tag{8}$$

where ρ_P is the Planck energy density. From this equation we can make the identification $-b = 6$. We are now able to demonstrate one of Dirac's large number relations, and to write it in terms of invariant quantities (i.e., we do not need varying constants to implement it in this form).

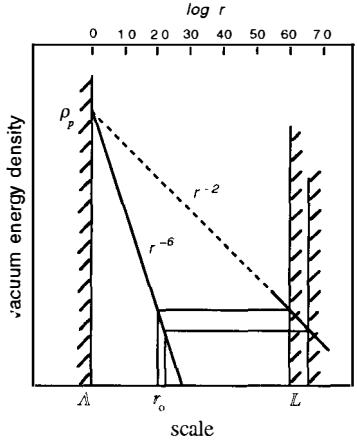


Figure 3. Variation of the gravitational self-energy density of vacuum fluctuations from the Planck length-scale to the cosmological scale $\mathbb{L} = \Lambda^{-1/2}$ (see text).

Indeed, introducing our maximal scale-relativistic length scale $\mathbb{L} = \Lambda^{-1/2}$, we get the relation:

$$\mathbb{K} = \mathbb{L} / \mathbb{A} = (r_o/\mathbb{A})^3 = (m_P/m_o)^3 \, , \tag{9}$$

where r_o is the Compton length of the typical particle mass m_o. Then the power 3 in Dirac's relation is understood as coming from the power 6 of the gravitational self-energy of vacuum fluctuations and of the power 2 that relies the invariant impassable scale $\mathbb{L}$ to the cosmological constant,following the relation $\Lambda = 1/\mathbb{L}^2$ (see Fig. 3).

Now a complete solution to the problem would be reached only provided the transition scale r_o be known. Consider the possible range for the cosmological constant: Ω_Λ is observationnally upper bounded by $\Omega_\Lambda < 1$.

Concerning lower bounds, one may remark that any value smaller than ≈ 0.01 would be indistinguishable from zero, since it would loose any effect on the determination of the comological evolution. It is remarkable that the corresponding range for $\mathbb{K}$, $3 \times 10^{60} - 3 \times 10^{61}$, yields a very small range for m_o, namely 40 – 85 MeV. This short interval is known to contain several important scales of particle physics: the classical radius of the electron, that yields the e^+e^- annihilation cross section at the energy of the electron mass and corresponds to an energy 70.02 MeV; the effective mass of quarks in the lightest meson, $m_{\pi/2}$ = 69.78 MeV; the QCD scale for 6 quark flavours, Λ_{QCD} = 66±10 MeV; the diameter of nucleons, that corresponds to an energy 2 x 64 MeV. Then we can make the conjecture that the present value of the cosmological constant has been fixed at the end of the quark-hadron transition, so that the transition scale r_o is nothing but this particular scale (Fig. 3). Along such lines, we get:

$$\mathbb{K} = (5.3 \pm 2)\, 10^{60} , \tag{10}$$

corresponding to $\Lambda = 1.36\ 10^{-56}$ cm^{-2} and to $\Omega_\Lambda = 0.36\ h^{-2}$. Such a value of Λ would solve the age problem. Indeed the age of the universe becomes larger than 13 Gyr (in agreement with globular clusters) provided $h < 0.75$ in the flat case ($\Omega_{tot} = 1$), and $h < 0.85$ if $\Omega_{tot} < 1$.

Note that all the above calculation is made in the framework of Galilean scale laws. The passage to Lorentzian laws would change only the domain of very high erergies, and thus would not affect our result, since it depends essentially on what happens at scale r_o.

Slope of the autocorrelation function.

It has been observed for long that the autocorrelation functions of various classes of extragalactic objects (from galaxies to superclusters) were characterized by a power law variation in function of scale, with an apparently universel index γ =1.8, smaller than the value $\gamma = 2$ expected from the simplest models of hierarchical formation.

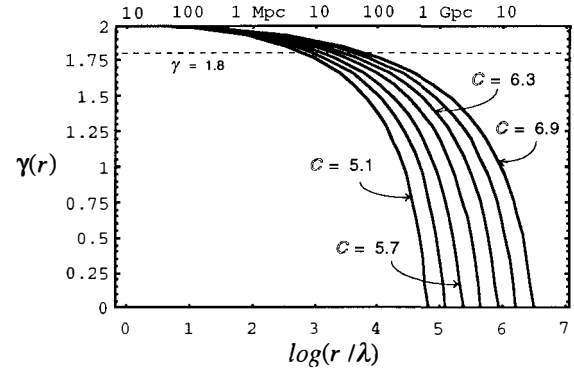


Figure 4. Variation with scale of the power of the galaxy-galaxy autocorrelation function in scale-relativity, for various values of the constant $C = log(\mathbb{L}/\lambda)$.

The theory of scale relativity brings a simple solution to this problem. The value $\gamma = 2$ is nothing but what is expected in the framework of Galilean scale laws: it is the manifestation of a fractal dimension $\delta = 3 - \gamma = 1$. In scale relativity, one must jump to Lorentzian laws at large scales in order to ensure scale-covariance. The fractal dimension now becomes itself scale-varying and depends on the cosmological constant $\Lambda = 1/\mathbb{L}^2$ as [4]:

$$\delta = \delta(r) = \frac{1}{\sqrt{1 - ln^2(r/\lambda_g) / ln^2(r/\mathbb{L})}} , \qquad (11)$$

where λ_g is the typical static radius of the objects considered (10 kpc for giant galaxies, 100 to 300 kpc for clusters...). Several consequences and new predictions arise from this formula.

First we expect $\gamma = 2$ at small scales. Several observations confirm this prediction: the flat rotation curves of galaxies imply halos in which mass varies as $M(r)=r^{\delta}$, with $\delta = 1$; Vader and Sandage [12] have found an autocorrelation of dwarf galaxies at small scales (10–200 kpc) caracterized by a power $\gamma \approx 2.2$; the analysis of the CfA survey by Davies and Peebles [13] shows that, apart from fluctuations coming from deconvolution, the average γ is 2 between 10 and 300 kpc, while it reaches its value 1.8 only between 1 and 10 Mpc (see their Fig. 3).

We predict a value of 1.8 at a scale of ≈10 Mpc. Conversely, this becomes a direct measurement of the cosmological constant. We have indeed plotted in Fig. 4 the function $\gamma(r) = 3 - \delta(r)$ for various values of $\mathbb{C} = log(\mathbb{L}/\lambda_g)$, from $\mathbb{C} = 5.1$ (i.e., $\mathbb{K} = 2.3 \times 10^{60}$) to $\mathbb{C} = 6.9$ ($\mathbb{K} = 1.4 \times 10^{62}$). The best fit of the observed value of γ(1.8 at 10 Mpc) is obtained for $\mathbb{C} = 5.4$–5.7, i.e., $\mathbb{L} = 2.5$–5 Gpc, $\mathbb{K} = 4.4$–9.3×10^{60}, $\Lambda = 1.9$–0.18×10^{-56} (i.e. $\Omega_\Lambda = 0.77$–0.18 for $H_0 = 80$ km.s^{-1}.Mpc^{-1}): these values are in good agreement with our previous estimate from the vacuum energy density. This new determination is expected to be highly improved in the near future. Indeed we predict a fast variation of γ at large scales: it must fall to a value of 1.4–1.5 at a scale of 100 Mpc for galaxies. Some recent results [14] seem to confirm such a prediction.

The transition to uniformity ($\gamma = 0$, $\delta = 3$) is reached only at very large scales (> 1 Gpc). This seems to be confirmed by the recent suggestion that the COBE map remains characterized by a low fractal dimension $\delta = 1.43 \pm 0.07$. [15].

References.

1. Nottale, L., 1992, *International Journal of Modern Physics,* A**7**, 4899-4936.
2. Nottale, L., 1993, *Fractal Space-Time and Microphysics: Towards a Theory of Scale Relativity.* (World Scientific, London).
3. Nottale, L., 1995, in preparation.
4. Nottale, L., 1993, *Fractal Space-Time and Microphysics,* (World Scientific), Chapt. 7.1.
5. Levy-Leblond, J.M., 1976, *American Journal of Physics* **44**, 271-277.
6. Weinberg, S., 1989, *Rev. Mod. Phys.* **61**, 1.
7. Carroll, S.M., Press, W.H., & Turner, E.L., 1992, *Ann. Rev. Astron. Astrophys.* **30**, 499.
8. Nottale, L., 1994, *Chaos, Solitons and Fractals*, **4**, 361-388.
9. Nottale, L., 1995, *Chaos, Solitons and Fractals*, **6**, 401-413.
10. Nottale, L., 1995, in *Relativity in General,* proceedings of Relativity Meeting '93 (ed. J. Diaz Alonso and M. Lorente Paramo), Editions Frontières, p. 121-132.
11. Zeldovich, Ya. B, 1967, *Pis'ma Zh. Eksp. Teor. Fiz.* **6**, 883 [*JETP Lett.* **6**, 316].
12. Vader, J.P., Sandage, A., 1991, *Astrophys. J. Lett.* **379**, L1.
13. Davis, M., Peebles, P.J.E., 1983, *Astrophys. J.* **267**, 465.
14. Campos, A., this meeting.
15. De Gouveia Dal Pino, E.M., *et al.*, 1995, *Astrophys. J. Lett.* **442**, L45.

Résumé. Quelques conséquences du principe de relativité d'échelle en cosmologie sont considérées dans cette contribution. La forme générale des lois d'échelle linéaires qui satisfont à ce principe est celle du groupe de Lorentz. Ceci permet de résoudre le problème de l'horizon sans faire appel à l'inflation, et implique que la dimension fractale des grandes structures doit varier en fonction de l'échelle, d'une manière qui dépend de la valeur de la constante cosmologique. Cette théorie explique la valeur $\gamma = 1.8$ de la puissance de la fonction d'autocorrélation, prédit que γ doit décroître quand l'échelle croît et rend compte de la transition à l'uniformité. Enfin elle permet d'obtenir une mesure de la constante cosmologique en accord avec une estimation indépendante à partir de la densité d'énergie du vide.

SESSION XI

NEW AND FUTURE PROJECTS



TWO NEW RADIO PROJECTS: FORT AND SKAI

Wim van Driel
Nançay Radio Astronomy Observatory, USN, Observatoire de Paris, France.

Abstract

There are two new radio astronomical projects which are clearly of interest for future studies of large-scale structures in the Universe. One, the FORT project, is the upgrade of the Nançay decimetric radio telescope, the third largest instrument operating at decimetric wavelengths with the effective collecting surface of a 94 m diameter dish. In 1998 the telescope will have a new, optimized focal system, including a Gregorian mirror system. It will then be available for, e.g., sensitive long-term 21-cm H I line surveys of large samples of galaxies. A possible key project will be the observation of about 5000 to 7000 galaxies in order to improve our knowledge of the Tully-Fisher relation. Systematic searches for galaxies hidden behind the Milky Way are another type of survey for which the Nançay telescope is well-suited. The other, the ambitious "Square Kilometer Array" or SKAI project, concerns planning the next generation decimetric/metric wavelength radio telescope with a collective surface of a square kilometer. This array is expected to be a hundred times more sensitive than the largest presently operating radio telescopes. There are in principle several options for its technical realisation, but the application of phased-array techniques seems the best suited at present, also from a budgetary point of view. This giant instrument will obviously revolutionize the use of radio telescopes for cosmological studies and be of interest to a large community of astronomers which at present do not yet use radio data, since it will allow, e.g., the detection of H I in normal spiral galaxies out to a redshift of 3 and of OH megamasers out to $z \sim 8$.

1 FORT – Science with the renovated Nançay radio telescope

The decimetric radio telescope of the Nançay Radio Astronomy Observatory of the Paris Observatory was put into operation 30 years ago and is the third largest working instrument of its kind with the equivalent collecting area of a 94 m diameter dish. It is a transit instrument consisting of a fixed spherical mirror (300 m long and 35 m high) and a tiltable flat mirror of 200×40 m, with a receiver carriage movable along a 90 m long track, which permits a one hour long tracking for any source North of declination -39°. Due to its elongated geometry, its beam size at 21-cm wavelength is about $4' \times 22'$ ($\alpha \times \delta$).

Its exceptionally long f/D ratio allows the use of simple "Hoghorn" receiver feeds, designed 25 years ago for operation at 9, 18 and 21 cm wavelength, tuned to the CH, OH and H I spectral lines, respectively. These are no longer competetive in terms of efficiency and system temperature, however. In order to keep the Nançay radio telescope at a good international level, the performance of its receiver system needs to be upgraded to actual technological standards.

Thus, the telescope is presently being refurbished with a completely new optimised receiver system in the so-called FORT project, a French acronym for "Optimised Focus for the Radio Telescope". The new focal design consists of a Gregorian two-mirror focal system and two interchangeable corrugated horns, providing an optimum illumination of the telescope surface, minimum sensitivity to unwanted outside interfering radiation and equal sensitivity in horizontal and vertical polarization. It was designed using specially developped software at the CSIRO Division of Radiophysics in Australia, where also a 1:20 scale model was built of the chosen design, which was then tested to be in full accordance with the calculations and to meet the required specifications ([1],[2]).

After completion of the FORT project, foreseen for mid-1998, the telescope will be able to operate in the entire 8.5-30 cm wavelength domain, where it will be about 2.5 times more sensitive in the 21-cm H I line compared to its present performance; its expected increase in sensitivity at 9 cm will be even a factor of 10.

Its increased sensitivity will also make the telescope more susceptible to radio interference. Fortunately, it is among the best-protected radio telescopes in this respect (as found during a recent survey of radio observatory sites) due to its location inside a dense, extended forest in a rural region in the heart of France and due to the fact that its feed system is located close to the ground. Thus, its susceptibility to radio interference is 20 to 30 dB lower than that of a more conventional radio telescope in a flat, open field.

To make the best use of the scientific potential of the renovated Nançay radio telescope, it is our intention to dedicate a considerable portion of the available observing time to long-duration key projects, like large 21-cm H I line surveys of galaxies.

One of the proposed key projects is of clear interest to studies of large scale structures in the Universe. In this project, accurate H I line profiles would be measured of well over a thousand galaxies per year, in order to improve our understanding of the crucial Tully-Fisher relation used for galactic distance determinations. The present knowledge of this relation is flawed by several biases, of which the Malmquist bias appears to be the most severe and fundamental. In order to minimize these biases, systematic 21-cm line observations are needed of galaxies which are relatively distant (out to $v_{rad} \lesssim 10{,}000$ km/s), in terms of regular H I line observations which are severly restricted by strong radar interference at larger redshifts, outside the strictly protected bands reserved for radio astronomy.

The completion of 21-cm H I line observations of all galaxies down to an apparent (blue) diameter of 1 arcmin would require the observation of about 5000 to 7000 objects out to a, still protected and unpolluted, radial velocity of about 10,000 km/s. Thus, the total H I line database available for a study of the Tully-Fisher relation would then encompass some 15,000 objects. Such a long-term project would be even more valuable if one could obtain observations at complementary wavelengths, such as near-infrared imaging, since the Tully-Fisher shows the smallest intrinsic scatter at near-infrared wavelengths and there the galactic diameters could be determined in a more homogeneous way, less impeded by Galactic or internal dust absorption. Near-infrared sky surveys presently under way, like DENIS, could provide such data for very large galaxy samples. Such a Tully-Fisher key project could well be accompanied by even deeper H I line observations in and around certain groups and clusters.

Systematic searches for galaxies, both far and near, hidden behind the dusty plane of the Milky Way, are another type of large project well-suited to the Nançay radio telescope and of

clear interest to studies of the distribution and motions of matter, both luminous and dark, in the Universe. Such searches (see, e.g., Kraan-Korteweg *et al.*, this Volume) could be made using target selections based on data obtained in other wavelength domains (optical, near-infrared) or through so-called blind H I line surveys where one simply scans through a section of the sky at radio wavelengths.

2 SKAI – planning the next generation radio telescope

The sensitivity of many types of detectors used in science progresses in an exponential manner with time. This is also true for radio telescopes: on a plot of the sensitivity of new radio telescopes as function of time, from the 1930's equipment of Reber to the VLA of the 1980's, one notices a clear linear relation. If one wishes to continue this "law" of technological progress, then radio astronomers should have access to a telescope with an about hundred times better sensitivity by the year 2010.

In fact, the feasability of such a next generation very large radio telescope, referred to as the "Square Kilometer Array Interferometer", or SKAI, is actually being studied by astronomers from a number of countries interested in astronomical observations in the decimetric/metric wavelength range. Such an ambitious project needs to be conceived in an international context, since its expected total construction cost is about 100 to 200 million US dollars. The International Union of Radio Science (URSI) has therefore created a Large Telescope Working Group to study this project.

The goal of designing SKAI is actually twofold: not only should this instrument allow observations with truly unprecedented sensitivity, it should also put radio astronomy back at the forefront of technological development in radio wave detection. Seen the various constraints, both scientific and economic, the challenge is thus not only to design a state-of-the-art radio telescope with a collecting surface of about 1 square kilometer (i.e., 150 times the surface of the Nançay telescope) which can operate at frequencies of about 0.2–2 GHz, but to do this for a cost of a mere 100 $ per square meter.

Note, that the SKAI should not be thought of as a single very large telescope of about 1 km×1 km dimensions, but rather like a collection of smaller elements of a few hundred meters diameter at most, seen the largest angular size of the objects one might want to observe with it (like galaxies), dispersed over an area of several tens of kilometers on a side, with outriggers at a few hundred kilometers distance, in order to provide the long baselines required for high resolution studies.

There are, in principle, several fundamentally different options to build such a huge radio astronomical interferometer. If one thinks of adapting already proven designs, one could consider buiding either (A.) an array of Arecibo-style fixed spherical transit telescopes of several hundred meters diameter each, with less stringent surface accuracy and suspended feed platform stability requirements. This design can only be implemented succesfully, though, in a large region with suitable Karst formations in which the necessary spherical depressions can be found. Or one could consider (B.) a series of paraboloids of small or large diameter (like the minimum-cost design 45 m dishes of India's new Giant Meter wavelength Radio Telescope, the GMRT). The main concern here is the mechanical reliability of a low-cost pointing and tracking system. At present it is not clear yet, though, if these designs can be built, and later maintained, within the envisioned budget.

The solution seems to lie in the application of new technologies, not used before in radio astronomy: the multi-beam synthesis techniques already applied in certain types of radars and sonars and for medical scanning devices.

The novelty of this possible concept for SKAI is immediately clear if one pictures the completed instrument: the Square Kilometer Array will resemble neither a collection of giant holes in the ground covered with mesh (à la Arecibo) nor a posy of metal sunflowers turning their heads towards cosmic sources (like Westerbork or the VLA). Instead, I jokingly referred to the about 300 m diameter basic elements of the interferometer as "hi-tech parking lots" for a good reason: they will consist of a collection of about ten thousand flat, rubber-covered tiles of about 1 square meter surface each, placed flat on the ground without any movable parts or receivers hanging some distance above it. The tiles will be packed with numerous dipole receivers, possibly of different sizes in order to allow good detection characteristics over the large wavelength range requested for scientific reasons.

Another critical issue in the planning of this ultrasensitive radio telescope is its capability for dealing with radio interference at the frequencies used, both ground-based and space-based. Radio interference outside the strictly protected, but rather restricted, bands available for radio astronomy is already a major nuisance at the actual sensitivity levels. Observing with a hundred times more sensitive radio telescope will require an active strategy for dealing with interference, as the presently used passive techniques will no longer be adequate. An advantage of the proposed phased beam technique is the capability of generation patterns of azimuths along the horizon at which the telescope will not be sensitive for unwanted incoming radiation, such as interference. In this manner known fixed sources, like radars, can be blanked out. The huge increase in sensitivity will cause the clear detection of many weak interference signals, which now merely add to the background noise, but this in it itself also offers the possible means for real-time recognition and filtering, as the interference signals (like distant radar pulses) are often different in nature from real noise and therefore recognisable by dedicated software if the sampling rate of the observations is high enough.

The science one can envision doing with a radio telescope one hundred times more sensitive than the actually available largest ones can only be described in superlative terms. Its capabilities will undoubtedly be very attractive for research projects of communities of astronomers which are not yet presently using radio telescopes on a regular basis. Its implications for, e.g., cosmology and studies of large scale structures in the Universe are profound: imagine, if you will, a telescope capable of determining a hugely redshifted "21-cm" H I line profile of a normal spiral galaxy at a redshift of 3, or of the OH line megamaser emission of an ultraluminous galaxy at $z \sim 8$. The use of state-of-the-art broad-band correlators with a very large radial velocity coverage will allow the measurement of accurate line profiles of multitudes of galaxies within reasonable integration times.

The future of the SKAI project is not clear at present, however. It needs the concerted will and effort of a number of countries to make it become reality. If new technologies need to be applied, a few years of initial research and development are thought to be necessary to establish the feasability and the actual building costs of the instrument. If the project proceeds as hoped, the Array can be expected to be operational by the year 2010.

References

[1] Granet C. 1995, New multi-reflector feed system for the Nançay radio telescope, Ph.D. thesis, Université d'Orléans, France

[2] Granet C., James G.L., Pezzani J. 1995, A new feed system for the Nançay radio telescope, in Proc. JINA (Journées Internationales de Nice sur les Antennes), 8-10 Nov. 1994

THE COBRAS/SAMBA CMB PROJECT

François R. Bouchet[1], Richard Gispert[2], and Jean-Lou Puget[2]
[1] *Institut d'Astrophysique de Paris, CNRS, Paris, France.*
[2] *Institut d'Astrophysique Spatiale, Orsay, France.*

Abstract

COBRAS/SAMBA is a second generation satelitte dedicated to mapping at high resolution and sensitivity the anisotropies of the Cosmic Microwave Background (CMB). This mission is in the assessment study phase (A) at ESA, with a decision expected mid 1996, for a launch around 2003.

1 Small scale anisotropies of the Cosmic Microwave Background

A central problem in cosmology is the building and testing of a full and detailed theory for the formation of (large-scale) structures in the Universe. It is widely believed that the observed structures today grew by gravitational instability out of very small density perturbations. Such perturbations should have left imprints as small temperature anisotropies in the cosmic microwave background (CMB) radiation.

The COBE satellite has opened up a new era by reporting the first detection of such temperature anisotropies. However, COBE was limited by poor sensitivity, and restricted to angular scales greater than 7 degrees, much more extended than the precursors of any of the structures observed in the Universe today. As a result, these measurements are compatible with a wide range of cosmological theories. On the other hand, high precision measurements at the degree scale will be extremely discriminating, allowing strong constraints on large scale structure formation theories, the ionization history, the cosmological parameters (such as the Hubble and cosmological constants, or the type and amount of dark matter), and very early Universe particle theories. These goals could be met by producing nearly full-sky maps of the background anisotropies with a sensitivity of $\frac{\Delta T}{T} \sim 10^{-6}$ on scales from 10 arc minutes to tens of degrees.

More precisely, the statistics of the background anisotropies, if Gaussian, would favor inflationary models, whereas non-Gaussian fluctuations would rather favor models in which irregularities are generated by topological defects such as strings, monopoles and textures. The

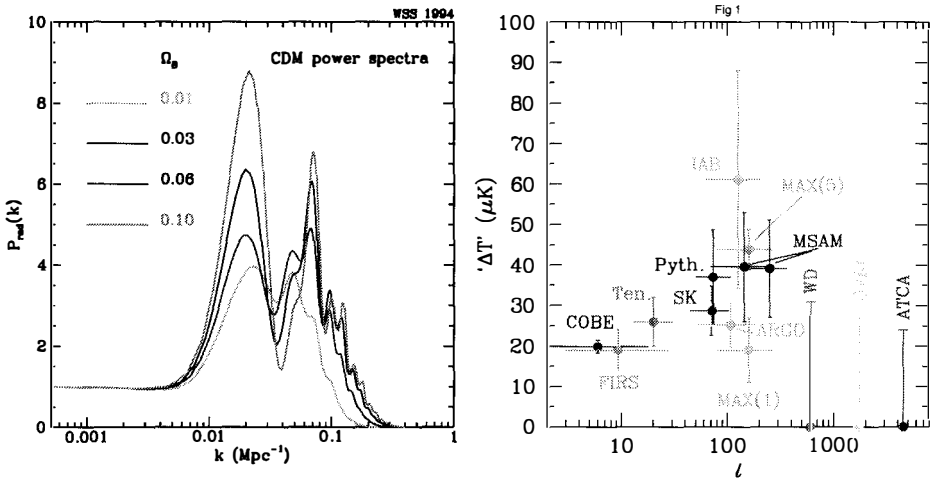


Figure 1: (a) Variation with the baryonic content of the Universe of the power spectrum for a CDM model(b) Currrent state of the CMB measurements. Both plots are courtesy of the Berkeley CMB group.

shape of the primordial fluctuation spectrum, according to most theories of the origin of the fluctuations in the Universe corresponds to potential fluctuations $\delta\phi$ which should be independent of the scale of the irregularities (λ). Even a few percent deviation from this prediction would have extremely important consequences for the inflationary models. These models also predict a specific ratio of tensor (generated by gravitational waves) vs. scalar anisotropies depending notably on the scale of the fluctuations. The best way to learn about the reionization history of the universe would be through the small-scale anisotropies which may be partly erased if the inter-galactic medium was re-ionized at high redshift. These small scale anisotropies depend also on the baryon density (see fig. 1.a), the nature of the dark matter, and the geome--try of the Universe (and of course on the initial spectrum of irregularities). Observations of the structure of the CMB on scales down to $10'$ will resolve structures comparable in scale to clusters of galaxies ($\sim 10h^{-1}$Mpc[1]) and so allow a much more direct link between observations of galaxy clustering, galaxy peculiar velocities and temperature anisotropies. Additionally, the detection of at least 1000 rich clusters[2] by the Sunyaev-Zeldovich effect[4], in combination with X-ray observations would constrain the evolution of rich clusters of galaxies and provide another handle on H_0. Finally, the Doppler effect on the same clusters might provide a unique measurement of their peculiar velocity dispersion.

[1] h is Hubble's constant in units of 100 km s^{-1}Mpc^{-1}.

[2] assuming a photon noise limited space experiment.

2 Model of the Galactic Foregrounds

The final accuracy of the measurements of the cosmological anisotropies will rely on the ability to separate these fluctuations from those coming from the galactic background and from unresolved extra galactic sources. It is thus crucial to know the expected contribution of these foregrounds, in order to predict the expected fraction of the sky for which no "cleaning" would be necessary. Here we describe our model for the galactic emission to do this.

2.1 Dust emission

The spectrum of the dust emission in the wavelength range of interest has been measured by the FIRAS instrument aboard COBE with a 7 degree beam (Wright et al. 1991, Reach et al. 1995). Several ballon experiments have detected the dust emission at high galactic latitude in a few photometric bands with angular resolution from 30 arc minute to 1 degree (Fischer et al. 1995, Page et al. 1990, De Bernardis 1990, Andreani 1990, Meinhold and Lubin 1991, Cheng et al. 1994...). The average spectrum at high latitude exhibits a cold component and can be modeled[7] with a dust at 21.3 K, with an emissivity ν^α of spectral index $\alpha = 1.28$. We used the DIRBE data at 240μ as a spatial template, and the average spectrum above to predict the long wavelenth behaviour of the dust.

This is a worst case because it assumes that the "cold component" is all interstellar and is present wherever dust emission is detected at 240μ. Indeed, the decomposition in two components with two temperatures (and $\alpha = 2$) in the paper by Reach et al. (1995) shows that the properties of this cold component are variable; the ratio of the optical depth of the cold to warm component increases at high latitudes. It is likely that part of this cold component is in fact extragalactic. In that case it is also a foreground to the CMB, but with quite different properties in term of inhomogeneities. The interstellar cold component is then concentrated in the higher column density lines of sight of the ISM, the more diffuse phase having an emissivity law with $\alpha = 2$. This reduces the contribution at long wavelength by a significant factor (2.7 for 1mm, 5.8 at 3mm) as compared to our pessimistic modelisation.

We checked that the power spectrum of the DIRBE fluctuations is decreasing like the 3^{rd} power of the spatial frequency, ℓ, in agreement with the determination of Gautier et al. (198?) who used instead the 100μ IRAS data down to a resolution of 4 arc minutes.

2.2 Free-free emission emission

The ionized gas in the interstellar medium can be traced in several ways, e.g. through its H_α emission (Reynolds 1992), the NII fine structure line at 205μ, the FIRAS data, or pulsar dispersion measures.

The NII measurements lead to a somewhat higher emission measure than the H_α, the latter observations being biased toward low column density regions. Taking this into account, Bennet et al. (1992) deduce an average brightness of the free-free emission at the galactic pole of 7 μK at 53 GHz. The power spectrum of the very limited available data from Reynolds appears very similar to the ℓ^{-3} one of the dust. Furthermore, this H_α data shows a part correlated with the HI clouds traced by their 21 cm emission line.

We make the hypothesis that all the ionised Hydrogen of the ISM is associated with dust, as suggested by the observations of individual ionised regions. We can thus use the DIRBE 240

[7]This corresponds to the region B4 with $37 < b < 53$ and $-53 < b < -37$ in the PhD thesis of Barnes. It is also compatible with the analysis of Reach et al. 95, who find $T = 22.2$, $\alpha = 1.12$ between 30 and 60 degrees, and $T = 20.7$, $\alpha = 1.36$ between -30 and -60 degrees.

micron map as a spatial template for the dust *and* the free-free emissions correlated with HI. In addition, we model the part uncorrelated with HI by using the same template but north/south inverted; this second, uncorrelatred, component accounts for 5% of the total gaz and 50% of the free-free emission. The spectrum of the free-free emission is modeled as $I_\nu \propto \nu^{-0.16}$, and normalised to give 7 μK at 53 GHz for a dust emission of $\simeq$ 2 MJy/sr at 240μ.

2.3 Synchrotron emission

We use a spectral index of $\alpha = -0.7$ to extrapolate at higher frequency the spatial template provided by the full sky map at 408 MHz of Haslam et al. (1970). We found that the power spectrum of that map at high latitude is roughly $\propto \ell^{-1.5}$. Since it is somewhat shallower than -2, its integral in a restricted range of angular scales is dominated by the small scale limit, contrary to the case of dust and free-free distributions.

2.4 Characterisation of the fluctuations

By using the model outlined above, one can generate at any desired frequency full sky maps with (for instance) a 1 degree FWHM resolution for the dust, free-free, and synchrotron emissions, and for their sum. We found convenient to express all the emissions in equivalent thermodynamical temperature fluctuations.

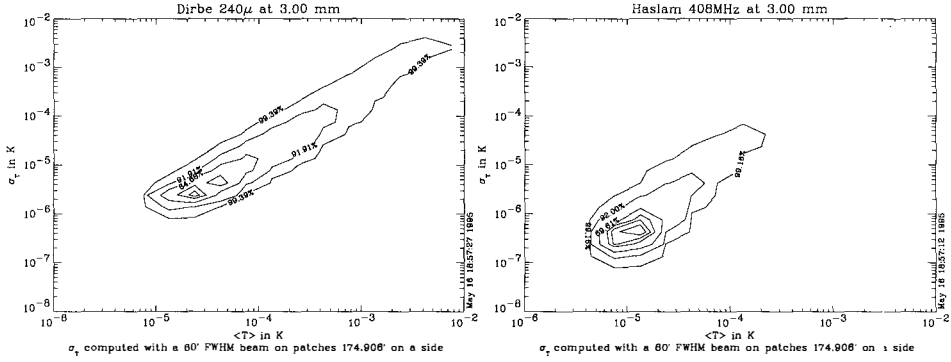


Figure 2: Temperatures distribution at 3mm for (a) "Dust+Free-Free" (b) "Synchrotron".

In order to obtain *local* estimates of the level of fluctuations at intermediate angular scales of the various components, we compute the *rms* fluctuation of the maps over square patches with 3 degrees on a side (i.e. containing about 10 beams of 1 degree FWHM). Since this amounts to restrict the contribution to the variance to a range ℓ ($\delta\ell$, comparable to ℓ), we are in effect measuring the local variations of the normalisation of the angular power-spectrum. As shown in figure 2, at 3mm, 70% of the patches for the synchrotron have a mean temperature less than 2×10^{-5}, and fluctuations σ_T about 20 times smaller. For the dust, 65% of the patches have a mean temperature less than 2×10^{-4}, and fluctuations σ_T about 10 times smaller. This figures provide direct graphical evidence that a large fraction of the sky will have low levels of pollution.

The figure 3 gives the fraction of the sky for which the *rms* fluctuations of the foregrounds (integrated over a restricted range in ℓ) and of their total contribution are less than a given

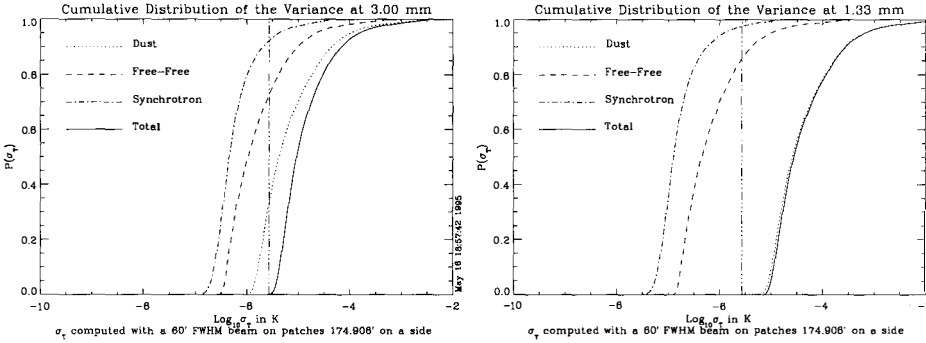


Figure 3: Foreground fluctuations in 3 degree patches for a 1 degree FWHM gaussian beam (a) at 3mm (b) at 1mm.

value. In the 1 to 3 degree resolution range, the *rms* total for the best half of the sky is $1. \times 10^{-5}$ at 3mm and 3×10^{-5} at 1.3mm. For a CDM case, the coresponding CMB fluctuations would be of order $3. \times 10^{-5}$. Note that while at 1.3 mm the fluctuations come only from the dust, at 3mm the free-free part is substancial.

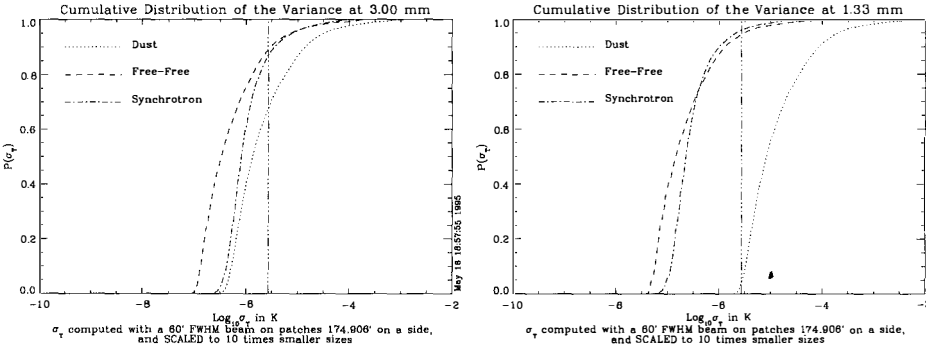


Figure 4: Foreground fluctuations scaled to 18 arc minutes patches. with a 6 arc minutes FWHM beam (a) at 3mm (b) at 1mm.

We can furthermore use the knowledge of the slope of the power spectra of the components to estimate the results of such measurements on smaller angular scales. Indeed, measurements with a 6 arc minute beam over 18 arc minute patches should be $10^{-1/2}$ smaller (dust and free-free) and $10^{1/4}$ larger (synchrotron) than the previous ones on 10 times larger scales. The figure 4.b shows such plots scaled to 10 time smaller sizes, i.e. patches of 18 arc minute for a 6 arc minute FWHM beam. In that case, the foreground gets smoother (half of the sky is with *rms* fluctuations smaller than 10^{-6} at 3mm, and $3. \times 10^{-6}$ at 1.3mm). CMB fluctuations in the CDM case would still be of order $3. \times 10^{-5}$. At 3mm, the contribution to the fluctuations from synchrotron and dust emission are comparable.

2.5 Consequences

This shows that the scientifically important small scales (structure of the "Doppler" peaks past the first one[8]) can be reached more easily at high frequency (for a given telescope size). Indeed, by working at low frequency, the foreground is dominated by the free-free that cannot be taken out because it is measurable only at longer wavelengths where the resolution is not as good. On the contrary, the dust emission gets smoother at small scales and it can be measured with a better angular resolution at higher frequency. A correction with only a 20% accuracy, which is relatively easy brings the dust contribution below the free free one, even at 3 mm.

About the extragalactic background due to early galaxies: it is possible (and even likely!) that the fluctuations due to distant galaxies dominate over those coming from the galactic dust distribution in the low cirrus regions. It is important, both for the measurement of the small scales primordial fluctuations and because of its own cosmological interest, to extract properly this component. The only way to separate it is to have enough channels at high frequency because the spectrum of high redshift galaxies is rising with frequency. Nevertheless this spectrum has to be flatter than the spectrum of the local dust because the 300μ to 1mm range is closer to the maximum of the redshifted dust emission. The statistics of the fluctuations will be an important tool which requires the coverage of a fairly large fraction of the sky. From that point of view the rise of the curves in the figures is steep meaning that the "good sky" is a large fraction of the total.

3 Mission concept

Measuring the cosmological background anisotropies with an accuracy better than a part in a million on scales down to ten arc minutes is a very ambitious goal. Within 10 years, balloon-borne experiments are likely to have located the first Doppler peak and measured it's amplitude with 10-30% accuracy. Their main limitation comes form the short duration of exposures available, the atmospheric effects, and difficulties in controling foregrounds contamination and systematics. On the other hand, although difficult, the goal above is achievable in the coming decade with a dedicated satellite experiment using the best detectors available today.

Indeed, the European Space Agency is studying a mission (COBRAS-SAMBA) which is aimed at the measurements described above[9]. This mission will be up for selection in the spring of 1996 to become the third medium-size mission of the Horizon 2000 plan. This concept results from the work of the ESA Science Team[10].

The payload will be passively cooled; preliminary thermal models indicate that the focal plane assembly will reach an average temperature of $\sim$100 K, while the telescope optical surfaces will stabilize at $\sim$120 K. These temperatures, in addition to the absence of the atmospheric noise and heat load due to the chosen orbit, insure that the conditions for a low and stable background are met.

[8] In the case of CMB fluctuations produced by topological defects like cosmic strings, the angular resolution is even more crucial, for their signature stands out all the more clearly than one goes to smaller scales.

[9] A less ambitious version is studied by the French Space Agency (CNES) in collaboration with laboratories in UK, Italy and USA. It relies only on bolometers cooled to 100 mK with the same technique as in COBRAS-SAMBA mission and plans to include only 5 wavelengths channels. It is based on a 80-cm telescope placed in a polar sun-synchronous orbit.

[10] The COBRAS/SAMBA Science Team which carried the study was : M. Bersanelli, C. Cesarsky, L. Danese, G. Efstathiou, M. Griffin, J.-M. Lamarre, M. Mandolesi, H.U. Norgaard-Nielsen, O. Pace, E. Pagana, J.-L. Puget, J. Tauber and S. Volonté. Requests for copies of the relevant report can be obtained from S. Volonté, ESA HQ, 8-10 rue Mario Nikis, PARIS CEDEX 15, FRANCE.

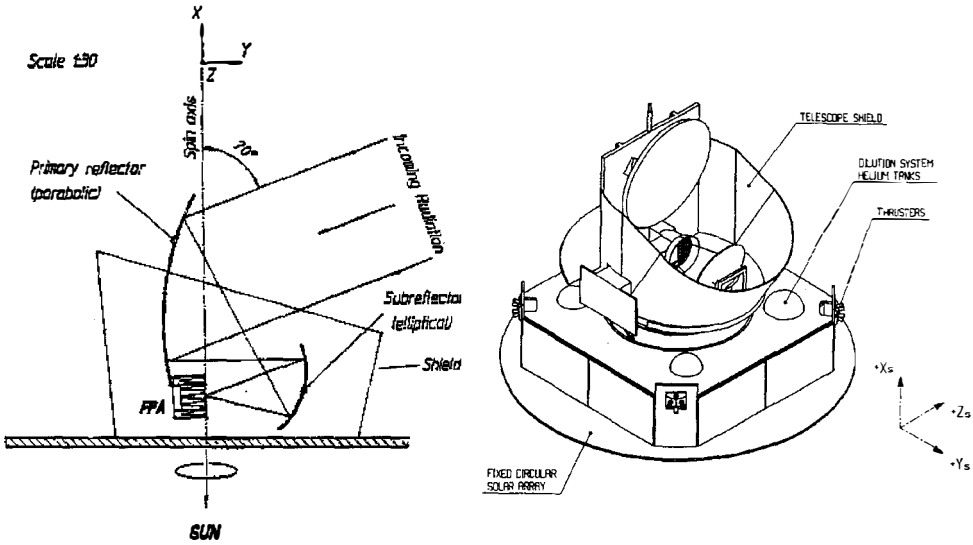


Figure 5: (a) Cross-sectional sketch of the model payload. Shown are the largest flared shield, the telescope and the focal plane assembly. (b) 3D view of the model payload.

An off-axis 1.5 meter gregorian telescope provides the necessary angular resolution and collecting area to meet the objectives of the mission. The separation of the different components of the foreground emissions requires a broad frequency coverage. The proposed mission will incorporate nine frequency bands provided by five arrays of bolometers at high frequency and four arrays of passively cooled tuned radio detectors at low frequency. The 56 bolometers require cooling to $\sim$0.1 K, which will be achieved with an active system similar to the one foreseen for the ESA cornerstone mission FIRST. It combines active coolers reaching 4 K with a dilution refrigeration system working at zero gravity, both being developed and space-qualified in Europe. The refrigeration system will include two pressurized tanks of ^{3}He and ^{4}He, giving an operational lifetime of at least two years.

On the low frequency side, HEMT (High Electron Mobility Transistors) amplifiers give the required sensitivity to detect temperature anisotropies of the cosmological background at all angular scales larger than 0°.5. The frequency and angular coverage will provide good overlap with the COBE-DMR maps.

The frequency band at which the foreground emission is the lowest ($\sim$130 GHz) will be covered by both the tuned radio receivers and the bolometers. The fact that the tuned radio detectors are passively cooled insures that the low frequency channels can be operated for a duration limited only by spacecraft consumables.

COBRAS-SAMBA will be placed into a halo orbit around the L2 Lagrangian point of the Earth-Sun system. This location is much more favorable than a low-earth orbit, or even the L5 orbit in terms of observing efficiency, since the Earth and Moon would always be located behind the telescope, and straylight would not be a significant issue. The L2 orbit is also very favorable from the point of view of passive cooling and thermal stability.

The requirement of coverage of a large fraction of the sky is obtained by offsetting the optical axis of the telescope by 70° with respect to the spin axis of the satellite directed along

the line joining the satellite and the Sun. In this nominal position, the optical axis scans a circle of diameter 60° , centered on a point in the ecliptic plane in the anti-Sun direction. In one year, the observed circle sweeps the whole ecliptic. To increase the sky coverage, the spacecraft rotation axis will be moved away from the ecliptic plane by up to $\pm 15°$.

Center Frequency	31.5	53	90	125	150	217	353	545	857
Detector Type	HEMT radiometer arrays				Bolometer arrays				
Det. Temperature	~100 K				0.1-0.15 K				
Cooling needed	Passive				Cryocooler+Dilution system				
Number of Detectors♣	4	14	26	12	8	12	12	12	12
Angular Resolution	30	30	30	30	10.5	7.5	4.5	4.5	4.5
Bandwidth ($\frac{\Delta\nu}{\nu}$)	0.15	0.15	0.15	0.15	0.35	0.35	0.35	0.35	0.35
$\frac{\Delta T}{T}$ Sensitivity◇	6.5	4.0	3.5	8.5	2.1	2.2	13.2	99.3	$> 10^3$
$\frac{\Delta T}{T}$ Sensitivity♡	2.2	1.3	1.2	2.8	0.7	0.7	4.4	33	7600

♣ For the HEMTS, each dual-polarization horn supports two receivers (detectors).

◇ 1σ sensitivity for a 2 years mission, over 90% of the sky.

♡ 1σ sensitivity for a 2 years mission, over 2% of the sky with deep integration.

Table I: Payload Characteristics. Frequencies are in GHz, angular resolutions in arc minute, $\Delta T/T$ Sensitivity in 10^{-6} units.

The coverage of the sky is not uniform in terms of integration time per pixel. However, the motion of the spin axis can be chosen in such a way as to give deeper integrations in chosen parts of the sky. The regions of lowest galactic emission are of particular interest for the anisotropy measurement, and many of them will be observable during the mission. Table I shows the estimated average sensitivities per pixel at the end of the two year baseline mission, for each frequency channel, assuming an observing strategy as sketched above. The pixel size for each channel is also given in Table I.

As this brief summary of the mission concept shows, a high precision determination of the small scale anisotropies of the CMB is now within reach.

References

Andreani 1990,

Barnes, W.J., 1994, PhD thesis at the University of Chicago

Bennet, C.L. et al., 1992, *Astrophys. J.* **397**, L7

Cheng E.S. et al., 1994, *Astrophys. J.* **422**, L37

De Bernardis P. 1990,

Fischer M. et al., 1995,

Gautier, T.N., Boulanger F., Perault M., & Puget J.-L. 1992, *Astron. J.* **344**, 35

Haslam C.G.T., Quigley M.J.S., Salter C.J., 1970, *MNRAS* **147**, 405

Meinhold, P. and Lubin P.1991, *Astrophys. J.* **370**, L11

Page L.A., Cheng E.S., & Meyer, S.S., 1990, *Astrophys. J.* **355**, L1

Reach W., et al., 1995, ApJ, in press.

Reynolds, 1992, *Astrophys. J.* **392**, L35

Wright E.L. et al. 1991, *Astrophys. J.* **381**, 200

Survey Spectrographs for Cosmology at the ESO–VLT

O. Le Fèvre [1], P. Vettolani [2]
[1] *DAEC, Observatoire de Paris-Meudon, 92195 Meudon Cedex, France.*
[2] *IRA–CNR, via Gobetti 101, 40129 Bologna, Italy.*

Abstract

Wide field multi-object spectrographs aimed toward large cosmology surveys are being designed for the ESO-VLT second generation of instruments. The spectrograph(s) should ideally cover the wavelength range 5500–1.8μm, over a wide field 16'x16', with multiplexing gains of more than 500. Imaging spectrograph designs with high throughput are being explored together with OH-suppressor designs for the near-IR. Such instrument(s) are crucialy needed for the VLT to participate at the forefront of the mapping of the distant universe and improve substantialy our knowledge of large scale structure and galaxy evolution toward the epoch of structure and galaxy formation. The main scientific thrust is to provide large (> several times 10^4) samples of L_* galaxies up to large look-back times, covering the redshift range $0.3 \leq z \leq\sim 2.5$ (or more).

1 Background

Understanding the structure and evolution of our universe is a fundamental quest in modern cosmology. Major theoretical and observational efforts are being dedicated to the study of the evolution of galaxies and large scale structure.

Mapping of the local universe has reached an industrial age, and projects like the Center for Astrophysics survey [1], the Southern Sky Redshift survey [2], the Las Campanas redshift survey [3], the ESO slice project [4] are providing astronomers today with a map of the universe out to ~200Mpc. Even larger and deeper surveys such as the 2dF Galaxy Redshift Survey, the Sloan Digital Sky Survey [5], are about to begin and should provide an unprecedented view of large slices through the universe out to redshifts ~0.3 within the next few years.

However, we need to explore a wide range in look back time to trace the evolution history of our universe from the very early epoch mapped by COBE to the present as mapped by the local surveys. Going further than $z \sim 0.3$, only a few large scale surveys have explored the universe of

normal galaxies to larger redshifts, the current limit reached being $z \sim 1$ [6][7][8]. The Canada-France Redshift Survey has identified more than 350 galaxies above z=0.5 and up to z=1.3, and has allowed to present for the first time the evolution of the luminosity function and of the two-point correlation function, from an epoch when the universe was 40% of its present age [9][6]. The redshift information is crucial to direct pointed HST observations providing detailled morphological information, to give us an increasingly clearer picture of galaxy evolution out to $z \sim 1$. These surveys have been conducted in pencil-beams, crossing large galaxy over-densities out to z$\sim$1 [10], but do not sample adequately the largest structures on scales $\sim$100Mpc.

At redshifts larger than $\sim$0.3, the advent of 8m+ class telescopes will undoubtedly revolutionnize observational cosmology. Samples of $\sim 10^5$ galaxies brighter than $\sim 0.1 - 0.3 L_*$ could be obtained through dedicated visible-light instrumentation at z$\sim$1. Moreover, the technology of near-IR arrays is following a fast development pace and allows to apply visible-light observing techniques, such as multi-object spectroscopy, to the 1–1.8μm domain, where much of the spectral energy and spectral line information is redshifted for redshifts above z$\sim$1. These arrays will allow to gather samples of several$\times 10^4 L_*$ galaxies up to redshifts well in excess of 2, and expand our knowledge of galaxy and large scale structure evolution to look-back times $\sim$15% the age of the universe or less.

Most 8m+ telescope projects have identified very distant galaxies as a priority target, as examplified by new results from the Keck telescope [8]. The first generation of VLT instruments will allow spectacular results on single-objet observations. However, the instruments being currently built will not have the adequate capabilities to provide the large statistical samples that are needed to map the universe at very large redshifts. Following the users propositions sollicited by an ESO working group, and the recommandations of the ESO Science and Technical Committee, ESO is therefore investigating the possibility to build survey spectrographs with a strong aim at cosmology. Preliminary studies are underway to identify the best suited designs.

2 Science Goals

The main science goals are oriented toward the understanding of the evolution of galaxies and large scale structure from a look back time $\sim$20% the age of the universe ($0 \leq z \leq \sim 2.5$). The main science drivers are:

1. **Evolution of galaxies**. The goals are (1) measure the evolution of the galaxy luminosity function, as a function of time, galaxy type and local environment (field vs. clusters) and evaluate the respective contributions of number density evolution and luminosity evolution, (2) characterize the spectrophotometric evolution, (3) create samples of galaxies which can serve as a basis for morphological studies with high spatial resolution imaging (HST, adaptive optics).

2. **Evolution of large scale structures**. The goals are (1) obtain accurate maps of large volumes of the distant universe at different epochs, (2) quantify the evolution of the clustering of galaxies, via e.g. the two point correlation function, on scales up to several$\times$100 Mpc, (3) characterize the evolution and dynamics of clusters of galaxies.

3. **Identification and distribution of very high-redshift QSOs**. The goals are (1) measure the evolution of the luminosity function, (2) search for very high redshift QSOs.

In order to achieve these goals, the aim is to be able to gather large samples of galaxies to map the universe and to address galaxy evolution through solid statistical analysis. This

leads to *(1)* increase the size of existing samples of galaxies at z$\sim$0.5–1 by several orders of magnitude, on order 10^5, through a combination of a deeper probing of the luminosity function to fainter objects and a wider angular coverage to cover scales of several$\times$100 Mpc, *(2)* build a large sample, on order 10^4, of normal galaxies at $z \gg 1$ over scales $\sim$100Mpc, *(3)* construct a sample of clusters (or proto-clusters) of galaxies at $z \gg 1$, *(4)* construct a sample of very high redshift QSOs. The large numbers of galaxies in these samples would allow to study the time evolution of galaxies and large scale structures in a multivariate parameter space (luminosity, color/star formation, environment).

3 Proposed Instrument Concepts

The science goals have several implications for the instrument design. The field must be wide, so that coupled with large detectors, the multi-object unit will allow to obtain simultaneously the spectra of as many objects as possible. The wavelength coverage must be from $\sim$ 5000 to $\sim$ 1.8μm to allow to observe the 3700–4350 region, rich in spectral information for redshift measurement as well as for line diagnostics, for the redshift range $0.3 \leq z \leq\sim 3$. The spectral domain up to 1μm is clearly for redshifts <1, unless Lyα emission is indeed present in galaxies at z$\geq$ 2.5, while above 1μm is for redshifts >1, the complementarity visible – near-IR is then critical for the science goals to cover a look-back time interval as wide as possible. Spectral resolution must allow to measure redshifts to an accuracy of $\sim$150 km/s. The instrument must allow to identify $\sim 0.2L_*$ galaxies below $z \sim 1$, and $\sim 0.5L_*$ galaxies at $z \sim 2$. Considering that galaxies show $\sim$1 magnitude of evolution by $z = 0.8$ [11], we need to reach down to $M_B \sim -20$ at z$\sim$1, this corresponds roughly to a galaxy with I=22.5 in the visible. This is easily within the reach of multi-slit spectrographs on the VLT, as shown by the CFRS [12].

Extrapolating the evolution seen at lower redshifts out to z$\sim$2, with, say another 0.75 mag of evolution, a reasonable assumption since stellar populations are still expected to evolve, one would need to reach $M_B = -21.5$ to observe $\sim 0.5L_*$ galaxies, corresponding approximately to J=21.75. This implies to be able to subtract the sky background to an accuracy of 0.15% in the J band, comparable to what is acheived in the I band with multi-slit spectrographs [12].

We are therefore investigating the following instrument concepts:

1. Wide Field Imaging Spectrograph (WFIS). This instrument concept was proposed by Delabre et al. [13] for the 0.35–1μm domain. Expanding the field to 4x8'x8' seems possible and would allow to obtain simultaneous spectra of more than 500 galaxies.

2. Near InfraRed Multi-Object Spectrograph (NIRMOS). This is based on the same design as above, with an optical train optimized for the range 1–1.8μm. Current IR arrays allow to cover a field 4x5'x5', and will allow to obtain simultaneous spectra of more than 200 galaxies.

3. Visible InfraRed Multi-Object Spectrograph (VIRMOS). The same 4 channel design would be optimized for 0.5–1.8μm, the detector/camera unit being exchanged for visible or IR observations. The multiplexing gains would be the same as above.

4. OH suppressor, multi-fiber spectrograph for the near-IR. The multiplexing unit would consist in a fiber positionner with $\sim$100 fibers for simultaneous observations.

The specifications of the first two concepts are detailled in Table I.

A feasibility study has been contracted by ESO: the above concepts are being examined in details by a consortium of French and Italian Institutes (O. Le Fèvre P.I., P. Vettolani, co-P.I.,

M. Cappacioli, D. Maccagni, A. Mazure, J.P. Picat, co-Is). It is expected that the optimum concept(s) will be presented to ESO in 1996, as a pre-requisite for ESO to commit itself to build the survey spectrographs needed for the VLT to work at the forefront of observational cosmology.

Table I: specifications for WFIS and NIRMOS

Specification	WFIS	NIRMOS
Wavelength range	5000–1μm	1–1.8μm
Field	$4 \times 8' \times 8'$	$4 \times 5' \times 5'$
Pixel scale	0.23"	0.3"
Detectors	4 CCDs 2048×4096 15μm pixels	4 HgCdTe 1024^2 18.5μm pixels
Resolving Power	200–2000	200–2000
Number of slits	Unrestricted Practical Max. 500	Unrestricted Practical Max. 200

References

[1] CFA
[2] DaCosta, L., this volume
[3] Lin, H., Kirshner, R.P., Shectman, S.A., Landy, S.D., Oemler, A., Tucker, D.L., Schechter, P.L., this volume
[4] Zucca, N., this volume
[5] Vogeley, M.S., this volume
[6] Le Fèvre, O., Lilly, S.J., Crampton, D., Hammer, F., Hudon, D., Schade, D., Tresse, L., this volume
[7] Glazebrook, K., Ellis, R., Colless, M., Broadhurst, T., Allington-Smith, J., Tanvir, N., 1995, MNRAS, 273, 157
[8] Cowie, L.L., Hu, E.M., Songaila, A., 1995, Nature, preprint
[9] Lilly, S.J., Tresse, L., Hammer, F., Crampton, D., Le Fèvre, O., 1995b, Ap.J., *CFRS–VI*, in press, Dec.10 issue
[10] Le Fèvre, O., Crampton, D., Hammer, F., Lilly, S.J., Tresse, L., 1994, Ap.J., 424, L14
[11] Schade, D., Lilly, S.J., Crampton, D., Hammer, F., Le Fèvre, O., Tresse, L., 1995, Ap.J., *CFRS–IX*, in press, Sept.1 issue
[12] Le Fèvre, O., Crampton, D., Hammer, F., Lilly, S.J., Tresse, L., 1995a, Ap.J., *CFRS–II*, in press, Dec.10 issue
[13] Delabre, B., D'Odorico, S., Vettolani, S., Proc. SPIE, 2198, 414

POSTER PAPERS

STRUCTURES OF GALAXY CLUSTERS WITH CENTRAL DOMINANT GALAXIES

F.W. BAIER [1], H. WIPPER [1], H.T. MACGILLIVRAY [2]
[1] *WIP – Group "Galaxy Clusters", University Potsdam, An der Sternwarte 16, 14482 Potsdam, Germany*
[2] *Royal Observatory, Blackford Hill, Edinburgh, Edinburgh EH9 3HJ, Scotland*



Abstract

The structures of 27 galaxy clusters with central dominant galaxies are investigated. The data from automatic scans of UK Schmidt plates obtained in the Royal Observatory Edinburgh are used for this investigation.

1 Introduction

Normally it is assumed that both the intracluster medium and galaxy number densities are related to the potential well of galaxy clusters in a similar way (Slezak et al. 1994). Traditionally the assumption of a hydrostatic equilibrium of both the hot intracluster gas and the galaxies with the binding cluster potential is made (Wu 1994, Lubin and Bahcall 1993).

There is a growing number of arguments against these assumptions. According to Wu (1994) it is very likely that even a large percentage of galaxy clusters with strong X-ray emission is still in a nonvirialized cosmodynamical state. This result is confirmed by growing evidence for subclustering in clusters.

It is not the aim of our investigation to support the general knowledge of the existence of such substructures in clusters. Rather we accept the necessity to compare the optical and X-ray structures in as many clusters as possible in order to discuss the coupling of gas and galaxies. In this connection we would like to provide new informations for the optical structures of 27 clusters with central dominant galaxies.

2 Results

The investigated clusters are given in the Table 1.

Table 1. Investigated galaxy clusters

Cluster	z	BM–Type	RS–Type	Cluster	z	BM–Type	RS–Type
A 0014	0.0640	III:	C:, E(cD)	A 1631	0.0508	I	C, S0/a
A 0085	0.0556	I	cD, cD	A 1644	0.0449	II	cD, cD
A 0119	0.0440	II–III	C:, gE	A 1650	0.0845	I–II	cD, cDsp
A 0151	0.0526	II:	cD, cDs	A 1651	0.0825	I–II	cD, cD
A 0279	0.0797	I–II	cD, cD	A 1836	0.0363	II:	I, S/S0
A 0358	0.0576	–	C:, E	A 1837	0.0376	I–II	cD, cD
A 0496	0.0320	I:	cD, cD	A 2400	0.0881	II:	F, cD
A 0644	0.0704	III:	cD, cD	A 2559	0.0796	I–II	cD, cDp
A 0754	0.0528	I–II	cD, cDs	A 2670	0.0749	I–II	cD, cD
A 0912	0.0888	–	cD, cDp	A 3112	0.0703	I	
A 0957	0.0431	I–II	L, E/S0	A 3380	0.0567	I–II	
A 0978	0.0527	II:	F, cD	A 3667	0.0530	I–II	
A 1139	0.0383	I:	I, E/S0	S 0084	0.11	I	
A 1308	0.0481	II–III	cD, cDp				

Among the investigated clusters we found a high percentage of double and multiple cluster structures. Insofar our result is in agreement with the conclusion from former investigations that substructures seem to be an essential property of most galaxy clusters (Geller and Beers 1982, Baier 1983, Bird 1994, 1995). Therefore, we consider the evolution from multiple and double clusters via flat clusters to concentrated clusters as the normal way of cluster evolution. Most observed clusters seem to be relatively unevolved objects. We cannot accept the conclusion by Girardi et al. (1995) that galaxy clusters are satisfactorily described by isothermal models.

A detailed discussion of the optical structures of these clusters is given in Baier et al. (1995).

References

[1] Baier, F.W.: 1983, Astron. Nachr. **304**, 211
[2] Baier, F.W., Wipper, H., and MacGillivray, H.T.: 1995, Astron. Astrophys. submitted
[3] Bird, C.M.: 1994, Astron. J. **107**, 1637
[4] Bird, C.M.: 1995, Preprint, Department of Physics, University of Cansas
[5] Geller, M.J., and Beers, T.C.: 1982, Publ. Astron. Soc. Pacific **94**, 421
[6] Girardi, M., Biviano, A., Giuricin, G., Mardirossian, F., and Mezzetti, M.: 1995, Astrophys. J. **438**, 527
[7] Lubin, L.M., and Bahcall, N.A.: 1993, Astrophys. J. **415**, L17
[8] Slezak, E., Durret, F., and Gerbal, D.: 1994, Astron. J. **108**, 1996
[9] Wu, X.-P.: 1994, Astrophys. J. **436**, L 115

THE SIGNIFICANCE OF ORIENTATIONS OF GALAXY CLUSTERS

F.W. BAIER, H. WIPPER
WIP - Group "Galaxy Clusters", University Potsdam
An der Sternwarte 16, 14482 Potsdam
Germany



Abstract

The orientations of central dominant galaxies and their host clusters for 201 galaxy clusters of different morphological types are considered. We found great uncertainties of cluster orientations mainly because of the influence of substructures. Despite of these uncertainties there seems to be a tendency to a general alignment between central dominant galaxies and clusters.

1 Alignments between CDGs and COGs

Orientations of clusters of galaxies (COGs) and of their central dominant galaxies (CDGs) were discussed in a large number of papers. Many discussions were connected with the consideration of alignments between orientations of COGs and their CDGs. Evidence for such an alignment effect was detected by Sastry (1968), Carter and Metcalfe (1980), Binggeli (1982), Struble and Peebles (1985), Rhee and Katgert (1987), Struble (1988, investigation of bright binaries in clusters), and Rhee and Latour (1991). Tucker and Peterson (1988) found only marginal evidence for such alignments.

There is strong evidence that CDGs are formed by cannibalism in poor clusters. These poor clusters are assumed to merge and to build up rich clusters. Mostly the investigations of alignment effects were confined to pronounced cD galaxies and to rather regular and concentrated rich clusters, i.e. clusters of BM-types I and I-II, which should be in a more relaxed state. The very high degree of substructure in many rich clusters which are in an early stage of dynamical

evolution is considered as the result of recent cluster merging. The existence of substructures should produce more amorphous and less defined global cluster structures. This should reduce any alignment effect. In order to investigate the power of this effect we discussed the question of alignments between CDGs and COGs of quite different structure types and with CDGs of the morphological types cD, gE, E, and S0. For a sample of 201 clusters we present the correlation between the orientations of the CDGs and the corresponding COGs in Figure 1 as well as the distribution of the differences between both orientations in Figure 2.

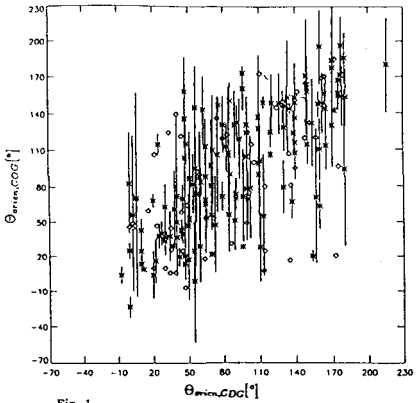


Fig. 1.
Correlation between the position angles of the CDGs ($\theta_{prim,CDG}$) and the position angles of the corresponding clusters ($\theta_{prim,COG}$).

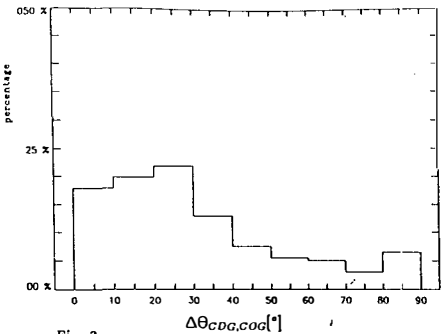


Fig. 2.
Frequency distribution of the differences between the position angle of the CDG and the corresponding COG ($\Delta\theta_{CDG,COG}$).

2 Conclusion

Despite of the extension of the cluster sample to less evolved clusters we find a confirmation for the general alignment of CDGs with their parent clusters. But there are considerable differences between cluster orientations determined by different authors and with different methods. From the investigation of a selected sample of COGs we conclude that the existence of substructures can destroy perfectly any alignment in concrete clusters. On the other side our result shows that nevertheless a general alignment effect seems to survive. For a detailed discussion we refer to Baier and Wipper (1995).

References

[1] Baier, F.W., and Wipper, H.: 1995, Astron. Nachr. submitted
[2] Binggeli, B.: 1982, Astron. Astrophys. **107**, 338
[3] Carter, D., and Metcalfe, N.: 1980, Mon. Not. R. Astr. Soc. **191**, 325
[4] Rhee, G.R.F.N., and Katgert, P.: 1987, Astron. Astrophys. **183**, 217
[5] Rhee, G.R.F.N., and Latour, H.J.: 1991, Astron. Astrophys. **243**, 38
[6] Sastry, G.N.: 1968, Publ. Astron. Soc. Pac. **108**, 1996
[7] Struble, M.F., and Peebles, P.J.E.: 1985, Astron. J. **90**, 582
[8] Struble, M.F.: 1988, Astron. J. **96**, 1534
[9] Tucker, G.S., and Peterson, 1988, Astron. J. **95**, 298

ANALYSIS OF THE 1.936 Jy IRAS SURVEY THROUGH THE SCALING FORMALISM

Rosa Domínguez-Tenreiro
María de los Ángeles Gómez-Flechoso
Gustavo Yepes
Dpto. Física Teórica, C-XI, UAM, 28049 Madrid, Spain

Abstract

We present the results of the scaling analysis of the IRAS 1.936 Jy redshift catalog. Clustering differences between northern and southern IRAS galaxies have been detected, and also between galaxies which occupy other different locations in the volume sampled by the survey. This implies that this volume cannot be considered as a fair sample extracted from a hypothetical universal galaxy distribution. No depth effect has been found. Moreover, IRAS galaxies do not exhibit IR luminosity segregation, except at small scale in the denser areas of some subvolumes. Finally, the comparison of the clustering properties of IRAS and optically selected galaxies has revealed that they are different, both in regions of moderate and low density. This implies that the differences are not dominated by galaxies which belong to the cores of rich galaxy clusters, undersampled by the IRAS catalog.

1. Introduction

The statistical analysis of the galaxy distribution in catalogs is of key importance to test theoretical models which try to explain the processes of large scale structure formation. Moreover, it allows us to infer the properties of the large scale galaxy distribution. The most popular tool to describe galaxy distributions is the two-point correlation function [1]. However, it is well known that two distributions of points can have comparable two-point correlations and have, nevertheless, very different clustering properties [1,2]. So, it seems convenient to complement the statistical analysis of galaxy catalogs using other statistical descriptors.

Here we present the results of the analysis of the 1.936 IRAS survey [3] by means of the scaling formalism [2,4,5]. This catalog presents a large sky coverage and a lower average density than the optical catalogs, and it undersamples the cores of rich galaxy clusters. Details about the

scaling formalism can be found in [2,4,5,6,7,8] and in Domínguez-Tenreiro *et al.*, these proccedings.

2. Results and Conclusions

We have considered five volume-limited reference samples defined by the condition $|b| > 10^o$ and with a limiting depth of $V_{max} = 40, 50, 60, 70$ and 80 h^{-1} Mpc, respectively. To analyze different effects, they have been split into different subsamples. Their scaling analysis have produce the following results: a) In contrast with what has been found in optical catalogs [7,9], it has been found out that the effect of peculiar velocities in IRAS galaxy redshifts is very low even for the closer galaxies. b) An important question is to know whether optically selected and IRAS galaxies trace the same density field of not: our results suggest that this is not the case, optically selected galaxies are more clustered than IRAS ones at scales up to $r \simeq 10 - 15$ h^{-1} Mpc both in areas of moderate and low density, so that this difference is not dominated by the rich cluster galaxies, undersampled by the IRAS catalog. c) Northern IRAS galaxies are more clustered and more contamined by peculiar velocities than southern IRAS galaxies, except for the referenced sample at limiting depth 80 h^{-1} Mpc. Moreover, when the reference samples are divided into close and distant subvolumes, the statistics differ without any systematics. In consequence, it is not possible to extract an universal behaviour from the 1.936 Jy IRAS subsamples at the scales they sample. d) No depth effect has been found. Subsamples with different limiting depth but with galaxies belonging to the same absolute flux interval present only very small differences in their clustering properties, and, moreover, they are in the opposite sense to what would be expected for the volume effects. e) Infrared luminosity segregation has been detected, but only in the denser areas of the volumes at limiting depth $40, 50$ and 70 h^{-1} Mpc, and at small scales. This suggests that this segregation merely expresses a correlation between infrared luminosity and average local density in galaxy groups or clusters.

3. References

1.- Peebles, P.J.E. 1980, "The Large Scale Structure of the Universe" (Princeton: Princeton University Press).
2.- Martínez, V.J., Jones, B.J.T., Domínguez-Tenreiro, R. and van de Weygaert, R. 1990, ApJ, 357, 50.
3.- Strauss, M.A. et al., 1992, ApJS,83, 29.
4.- Jones, B.J.T., Martínez, V.J., Saar, E., and Einasto, J., 1988, ApJ Letters, 332, L1.
5.- Borgani, S. 1995, Phys. Rep. in press.
6.- Yepes, G., Domínguez-Tenreiro, R., and Couchman, H.M.P. 1992, ApJ, 401.40.
7.- Domínguez-Tenreiro, R., Gómez-Flechoso, M.A. and Martínez, V.J. 1994, ApJ, 424, 42.
8.- Grassberger, P., Badii, R., and Politi, A. 1988, J. Stat. Phys. 51, 135.
9.- Campos, A., Domínguez-Tenreiro, R., and Yepes, G. 1994, ApJ, 436, 565.

TIDAL EVOLUTION OF DISC GALAXIES IN RICH CLUSTERS

M. Ángeles Gómez-Flechoso. Dpto. Física Teórica, C-XI, UAM, 28049 Madrid, Spain
Rosa Domínguez-Tenreiro. Dpto. Física Teórica, C-XI, UAM, 28049 Madrid, Spain
Julio F. Navarro. Steward Observatory, Univ. of Arizona, Tucson, AZ 85721, USA

Abstract

We study the evolution of disc galaxies as they orbit within the potential of a rich cluster. We use N-body halo-disc models in equilibrium to simulate the galaxy. The cluster is simulated as a rigid spherical potential similar to that inferred from X-ray observations. We focus on the fate of these galaxy models as they pass near the centre of the cluster, with emphasis on the disruption of the disc by tidal shocks and the rearrangement of the halo mass. Implications for the shape of the rotation curves of disc galaxies in clusters and for the absence of disc galaxies in the inner regions of a rich cluster are also discussed.

1. Introduction

It is a well established observational fact that galaxy morphologies depend on the local density of galaxies[2),7),8)]. In clusters, there is also a pronounced trend for the local spiral fraction to increase as a function of the clustercentric distance. Within the inner $\simeq 250\ h^{-1}$ kpc, the spiral fraction typically plummets to almost zero[10),12)]. The rotation curve of cluster spirals seem show signs of decline within the luminous radius of the galaxy[9),11)], in contrast with the typically flat rotation curves of field spirals. The existence of this effect, however, has been challenged in a recent paper[1)].

In this contribution we analyse the possibility that the paucity of spirals near the centre of rich clusters as well as their peculiar rotation curves are a consequence of the mean tidal field of the cluster. We present here the results of N-body simulations intended to estimate quantitatively the effect of tides induced by the cluster potential on a typical disc galaxy orbiting through the cluster. We focus on the possible disruption of the galaxy's disc, and on the modifications to the shape of its rotation curve.

2. Results

We have run a number of simulations, varying systematically the parameters describing the galaxy and cluster models as well as the galaxy's orbital parameters. We assume that discs have an exponential structure and that haloes are well represented by King model[5]. The cluster potential was chosen to match that inferred from X-ray observations [3] or that found in simulations of hierarchical clustering [6]. We find that only in extreme situations (*i.e.* nearly radial orbits, and steep cluster density profiles) the tidal field of a typical cluster has a noticeable effect on the internal dynamics of a spiral galaxy. These effects are seen as: a) halo expansion or truncation, b) a decline in the disc rotation curve, especially manifest for $r \geq 8$ kpc, and c) vertical heating of the disc. The projected density profile of the disc and the V_{rot}/σ ratio are less sensitive to cluster tides.

3. Summary and conclusions

Although the appearance of discs can be substantially modified under some circumstances, cluster tides are unlikely to modify significantly the projected density profile or the V_{rot}/σ ratio of a galaxy. Thus tidally perturbed discs are unlikely to be the progenitors of normal bright ellipticals. The cumulative effect of several pericentric passages is also important; for nearly radial orbits it can lead to the complete destruction of a galaxy's disc. Almost radial orbits are also found to be the only capable of influencing the shape of the rotation curve of the disc. It may therefore be possible to gauge the distribution of orbits of spirals in clusters by observations of the shape of their rotation curves. Our results suggest that, unless the orbits of galaxies in clusters are predominantly radial, the expected change in the shape of disc rotation curves is relatively minor. Large observational samples are therefore required to test this effect observationally.

4. References

1. Amram, P., Balkowski, C., Marcelin, M. & Cayatte, V., 1993. *Ap. J. Lett.* , **403,** L59
2. Dressler, A., 1980. *Ap. J.* , **236,** 351
3. Durret, F., Gerbal, D., Lachièze-Rey, M. & Sadat, R., 1995. *A.& A.* , submitted
4. Hernquist, L., 1987. *Ap. J. Suppl.* , **64,** 715
5. King, I., 1966. *Ap. J.* , **71,** 64
6. Navarro, J.F., Frenk, C.S. & White, S.D.M., 1994. *MNRAS* , submitted
7. Oemler, A., 1974. *Ap. J.* , **194,** 1
8. Postman, M. & Geller, M.J., 1984. *Ap. J.* , **281,** 95
9. Rubin, V.C., Whitmore, B.C. & Ford, W.K., 1988. *Ap. J.* , **333,** 522
10. Sanromá, M. & Salvador-Solé, E., 1990. *Ap. J.* , **360,** 16
11. Whitmore, B.C., Forbes, D.A. & Rubin, V.C., 1988. *Ap. J.* , **333,** 542
12. Whitmore, B.C., Gilmore, D.M. & Jones, C., 1993. *Ap. J.* , **407,** 489

THE STRUCTURE OF COMPACT GROUPS OF GALAXIES

María-Luisa Montoya, Dpto. Física Teórica, Universidad Autónoma de Madrid, Madrid, Spain
Rosa Domínguez-Tenreiro, Dpto. Física Teórica, Universidad Autónoma de Madrid, Madrid, Spain
Guillermo González-Casado, Departament de Matemàtica Aplicada II, Universitat Politècnica de Catalunya, Barcelona, Spain
Gary A. Mamon, Institut d'Astrophysique de Paris, Paris, France; Département d'Astrophysique Extragalactique et Cosmologie, Observatoire de Paris-Meudon, Meudon, France
Eduard Salvador-Solé, Departament d'Astronomia i Meteorologia, Universitat de Barcelona, Barcelona, Spain

Abstract

We present a method to determine the density profiles of galaxy groups based on the study of the galaxy autocorrelation function. By means of Monte-Carlo simulations, we show that this method is capable of recovering the mean profile of such systems, even in the case of poor statistics (low number of galaxies per group). We present first results arising from its application to Hickson's catalog of compact groups.

1. Introduction

The mean projected density profile of a catalog of groups is related to the galaxy two-point correlation function, $\xi(s)$, by[1]:

$$\xi(s) = \frac{\langle N_i^2 (\sigma_i * \sigma_i)(s) \rangle n_G}{n^2}, \tag{1}$$

where $\sigma_i(s)$ is the normalized projected density profile of the $i^{\underline{th}}$ group, N_i is the number of galaxies in the $i^{\underline{th}}$ group, n_G and n are the mean number density of groups and galaxies respectively, $\langle\ \rangle$ is the average taken over the N_G groups of the catalog and $(\sigma_i * \sigma_i)(s)$ is the convolution of the projected density profile of the $i^{\underline{th}}$ group, which can be calculated by[2,3]:

$$(\sigma * \sigma)(s) = \mathcal{F}_1 \circ \mathcal{A} \left\{ \mathcal{A} \circ \mathcal{F}_1^{-1} \left[2 \int_s^\infty P(r) dr \right] \right\}. \tag{2}$$

where $\mathcal{F}_1$ and $\mathcal{A}$ are the one-dimensional Fourier and Abel transforms, respectively, and $P(r)$ is the distribution of intergalactic separations.

2. Statistical method to determine $\sigma(r)$

We create N_{sim} Monte-Carlo realizations of an artificial catalog of N_G groups, each with N_P galaxies, which are all realizations of a certain analytical profile $\sigma_i(r)$ with a given set of parameters. In practice, $N_{sim} = 1000$, N_G and N_P take the typical values in real group catalogs and $\sigma(r)$ is an *analytical King profile*[4] ($\sigma(r) = \sigma_o/(1 + (r/r_c)^2)$ with $\log(r_c/r_c^0) \in N(0, \sigma_{\log})$ with $r_c^0 = 0.16$ and $\sigma_{\log}$ variable. We calculate the following

statistic:

$$X^2(j, r_c^j) = \frac{1}{N_b} \sum_{k=1}^{N_b} \frac{(\xi_k(r_c^j) - \xi_k^T(r_c))^2}{\sigma_k^2}, \quad j = 1, ..., N_{sim}. \tag{3}$$

r_c^j is the value of r_c which minimizes X^2 for the $j^{\underline{th}}$ realization of the artificial catalog, $\xi_k(r_c^j)$ and $\xi_k^T(r_c)$ are the two-point correlation function of the $j^{\underline{th}}$ realization (calculated by means of (2)) and theoretical (calculated analytically as a function of r_c), respectively, N_b is the number of points in which ξ is tabulated and $\sigma_k^2 = \langle(\xi_k - \langle\xi_k\rangle)^2\rangle$. In this way we obtain the distribution of the optimum values of $\log(r_c^j/r_c^0)$ as well as that of the minimum X^2, which show the capability of the method to recover the input value of r_c^0. We also show that the method is capable of distinguishing between different density profiles by creating the artificial catalogs with projected density profiles different from the analytical King profile (in practice a uniform density profile and a modified Hubble profile with $\alpha = 2$). In the first case we were not able to reach the minimum value of X^2 (r_c would be equal to ∞). In the second case the distribution of minimum values of X^2 was found to be much higher than in the previous case, with no intersection between them even in the case of poor statistics.

3. Application to Hickson's catalog of compact groups

We have applied the method explained above to a sample of 42 groups from Hickson's catalog of compact groups[5] selected by choosing groups with 4 galaxies with *accordant* velocities ($\Delta v < 1000$). Simulations of groups of galaxies all of the same size suggest that a rescaling of the groups of the sample is not necessary. We have tested the null hypothesis H_0 that the groups of the sample are realizations of a modified Hubble profile with $1 \leq \alpha \leq 2$ and a certain value of r_c by using the χ^2 test. By means of Monte-Carlo simulations we have obtained the regions of the (α, r_c) plane where we are not forced to reject H_0 at different confidence levels. An optimum fit has been obtained for $\alpha = 1.6$ and $r_c = 18h^{-1}$kpc.

4. Conclusions

The method is able to distinguish between different density profiles and to recover the values of their parameters, even in the case of poor statistics. Its application to a sample of compact groups from Hickson's catalog suggests that the sample is a realization of a modified Hubble profile with an optimum fit when $\alpha = 1.6$ and $r_c \simeq 18h^{-1}$ kpc. Unlike other methods[6], ours uses only information on the intergalactic separations. This circumvents the delicate problem of determining the centre of the group. Moreover, we show that it is not necessary to rescale the sizes of the groups, which would also be a source of uncertainty.

5. References

[1] Peebles, P.J.E., in *The Large Scale Structure of the Universe*, Princeton University Press.

[2] Salvador-Solé, E., González-Casado, G., & Solanes, J.M., 1993, Ap. J., 410, 1.

[3] González-Casado, G., Salvador-Solé, E., & Solanes, J.M., 1993, Ap. J., 410, 15.

[4] King, I.R., 1962, Astr. Astrophys., 67, 471.

[5] Hickson, P., Mendes de Oliveira, C., Huchra, J.P., & Palumbo, G.G.C. 1992, Ap. J., 199, 353.

[6] Hickson, Mendes de Oliveira, C., & Giraud, E. 1994, Ap. J., 437, L103.

DARK MATTER IN CLUSTERS OF GALAXIES AND THE NEUTRINO REST MASS

A. Kull[1], R. A. Treumann[1,2], H. Böhringer[1]
[1] *Max-Planck-Institut für Extraterrestrische Physik, Garching b. München, Germany.*
[2] *Department of Physics and Astronomy, Dartmouth College, Hanover, New Hampshire, USA.*



Abstract

We consider a neutrino sphere in local thermodynamic Fermi equilibrium as a model for dark matter in clusters of galaxies. Integrated neutrino mass profiles are determined and fitted to ROSAT X-ray observations of the Coma cluster with the neutrino-mass as free parameter. The best fit is obtained for a neutrino-mass of $m_\nu = 8$ eV.

The idea that massive neutrinos may form dark matter within clusters of galaxies has been suggested by Cowsik and McClelland [1]. Their work is based on selfgravitating cluster-scale neutrino spheres in global thermal equilibrium of temperature 0 K. It is estimated that the neutrino mass should be of order of ~10 eV. However, observational results and theoretical considerations show that the requirement of global thermal equilibrium as well as that of a fully degenerated neutrino gas may be too strong. We therefore propose to treat the neutrino sphere as a gas in *local thermal equilibrium* which is in *global hydrostatic equilibrium* with its gravitational potential.

The neutrino sphere is described by the hydrostatic equation $\frac{1}{r^2}\frac{d}{dr}\left(\frac{r^2}{\rho}\frac{dP}{dr}\right) = -4\pi G\rho$ and an equation of state. Under the simplifying assumption of only one relevant neutrino family (e.g. electron neutrino ν_e), the equation of state which determines the properties of the neutrino gas is given according to Fermi statistics by

$$\rho_\nu(T_\nu,\mu) = \frac{g_\nu m_\nu^{\frac{5}{2}} k_B T_\nu^{\frac{3}{2}}}{\sqrt{2}\pi^2\hbar^3}\int_0^\infty \frac{\sqrt{z}dz}{e^{z-\frac{\mu}{k_B T_\nu}}+1}, \quad P_\nu(T_\nu,\mu) = \frac{g_\nu\sqrt{2}m_\nu^{\frac{3}{2}}k_B T_\nu^{\frac{5}{2}}}{3\pi^2\hbar^3}\int_0^\infty \frac{z^{\frac{3}{2}}dz}{e^{z-\frac{\mu}{k_B T_\nu}}+1} \qquad (1)$$

(neutrino density and pressure). m_ν denotes the neutrino mass, μ the chemical potential, T_ν the neutrino temperature, k_B the Boltzmann constant and z equals $\frac{\epsilon}{k_B T_\nu}$, where $\epsilon = \frac{p^2}{2m_\nu}$ stands for the neutrino energy and p for the neutrino momentum. The value of the helicity g_ν is

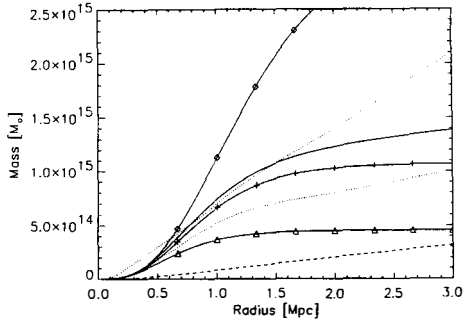


Figure 1: Neutrino-mass profiles for the Coma cluster for neutrino rest masses of 6 eV, 8 eV, and 10 eV. The dotted lines indicate the upper and lower limits for the cluster binding mass derived from ROSAT X-ray observations. The dashed line represents a typical intracluster gas-mass profile and the solid line the total mass of the intracluster gas and the neutrino-mass for a 8 eV neutrino.

chosen to be 2, corresponding to two allowed helicity states. Since we assume that there are no neutrino-neutrino interactions besides the gravitational interaction, the only source of the chemical potential μ is due to the gravitational potential ϕ and thus is given by $\mu = m_\nu \phi$ and the condition $\phi(\infty) = 0$. For a given central density and a given neutrino mass, the solution of this system of equations yields the density and temperature profiles of the neutrino gas.

A cut-off radius of 3 Mpc has been used. Since the neutrino spheres under consideration are well localized within 3 Mpc, the choice of the value of the cut-off radius does not pose a problem and has little effect on the results. In Fig.1 we present neutrino mass profiles adopted to the COMA cluster. They are compared to the limits of the binding mass derived from ROSAT X-ray observations [2]. The calculations have been performed for a central density $\rho_\nu(0) = 3.5 \times 10^{-26}$ g cm^{-3} and for neutrino masses m_ν of 6.0 eV, 8.0 eV, and 10.0 eV. For m_ν =8.0 eV we obtain a total mass profile tight within the binding mass limits. Roughly speaking, the neutrino spheres become too narrow for neutrino masses larger than ~9 eV and too extended for neutrino masses smaller than ~7 eV. More definite limits will be provided by an extended model which takes into account the contribution of the intracluster gas to the total density trough the relation $\rho = \rho_{gas} + \rho_\nu$.

However, at this stage it is already clear that the neutrino mass required by the described model lies close to the upper end of the experimentally obtained limits for the electron neutrino mass which is inferred to be between 5 eV and 7 eV [3].

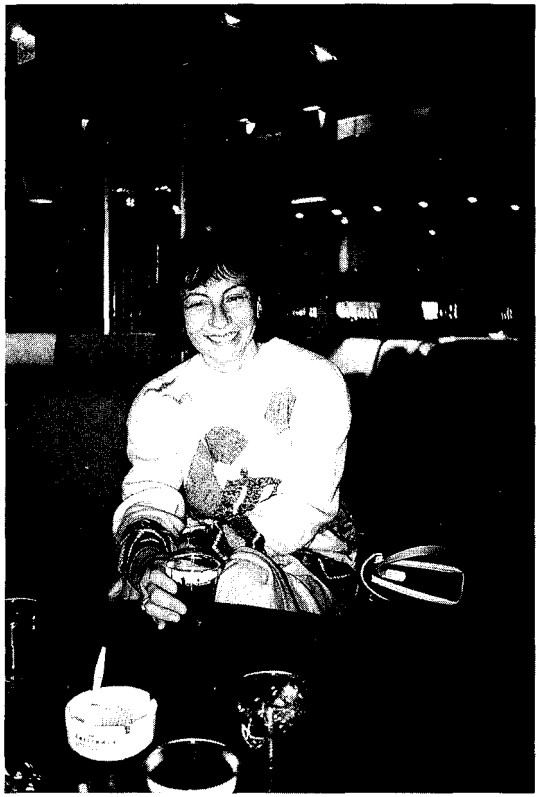
References

[1] R. Cowsik and J. McClelland, 1973, *Astrophys. J.* **180**, 7

[2] U. G. Briel, J. P. Henry, and H. Böhringer, 1992, *Astr. Astrophys.* **259**, L31

[3] The Particle Group, Phys. Rev. D., 1994, **50**, 1

RÉSUMÉS EN FRANCAIS



TRADUCTION DES EXPOSES EN FRANCAIS

De l'étude de la formation des galaxies et des structures grâce aux relevés complets de décalages vers le rouge
L. Nicolaci da Costa

Nous passons brièvement en revue l'histoire des relevés "complets", à grand-angle, de décalages vers le rouge de galaxies, mettant en vedette la contribution apportée par chaque relevé à notre compréhension actuelle de la nature de la distribution des galaxies. Nous passons également en revue et discutons les contraintes imposées aux théories de formation des galaxies et des structures par les résultats des analyses réalisées sur les relevés du CfA2 et SSRS2, qui sont actuellement les plus grands échantillons disponibles pour ce type d'étude.

Le spectre de puissance des fluctuations de densité des galaxies: résultats actuels et techniques d'optimisation.
M. Vogeley

Le spectre de puissance des fluctuations de densité mesuré à partir de catalogues de décalages vers le rouge de galaxies procure des contraintes importantes sur les modèles de formation des structures à grande échelle. Je passe en revue les résultats actuels concernant le spectre de puissance 3D et j'examine les limites des mesures actuelles et des techniques d'estimation. Pour couvrir le facteur dix en longueur d'onde entre les échelles testées par les catalogues de galaxies et par COBE, mesurer la forme détaillée du spectre de puissance, et examiner avec précision la dépendance de la structuration en fonction du type des galaxies, nous avons besoin d' échantillons plus profonds sélectionnés par des critères soigneusement contrôlés et de techniques améliorées pour l'estimation du spectre de puissance. Je décris une nouvelle méthode pour estimer le spectre de puissance qui traite de manière optimale les données provenant de catalogues de géométrie et d'échantillonage arbitraires.

Le biais dans le Relevé SSRS2.
C. Benoist et al.

Nous étudions les propriétés de la distribution des galaxies dans le SSRS2 et mettons en évidence l'existence d'une ségrégation en luminosité, particulièrement forte pour les galaxies plus brillantes que L^*. Puis, nous calculons le biais relatif en fonction de la magnitude.

Contraindre Ω et le biais à partir du catalogue Stromlo-APM

J. Loveday

Les catalogues de décalages vers le rouge de galaxies délivrent une image déformée de l'univers , à cause de la composante non-Hubble du mouvement des galaxies. En mesurant de telles distorsions dans le régime linéaire, on peut contraindre la quantité $\beta = \Omega^{0.6}/b$, où Ω est le paramètre de densité cosmologique et b est le facteur de biais (linéaire) pour les galaxies sélectionnées en optique. Dans ce papier, nous estimons β à partir du catalogue de décalages vers le rouge Stromlo-APM en comparant l'amplitude de la fonction de corrélation moyennée en direction dans l'espace des décalages vers le rouge à la fonction de corrélation dans l'espace réel. Nous trouvons une limite supérieure $\beta = 0.75$, correspondant à un niveau de confiance de 95% avec une meilleure estimation de β à ≈ 0.48. Un paramètre de biais $b \sim 2$ est alors requis si $\Omega \equiv 1$. Cependant, les corrélations d'ordre supérieur mesurées sur le catalogue de galaxies de l'APM indiquent une valeur basse pour le paramètre de biais $b \approx 1$, nécessitant $\Omega \leq 0.6$.

Le spectre de puissance de la distribution des galaxies dans le relevé de décalages vers le rouge de Las Campanas

H. Lin et al.

Nous présentons le spectre de puissance $P(k)$, calculé sur le domaine d'échelles $\lambda = 2\pi/k = 5 - 400h^{-1}$ Mpc, pour un échantillon limité en magnitude du Relevé de décalages vers le rouges de Las Campanas (LCRS) comprenant 19276 galaxies, présentant un décalage vers le rouge moyen $z \approx 0.1$. On peut modéliser le $P(k)$ du LCRS par $\propto k^{-1.8}$ aux petites échelles $\lambda = 5 - 30h^{-1}$ Mpc, se changeant en $\propto k^{1\pm1}$ aux grandes échelles $\lambda \approx 200 - 400h^{-1}$ Mpc. L'amplitude totale correspond à $\sigma_8 = 1$ dans l'espace des décalages vers le rouge. Nous comparons aussi nos résultats à ceux de plusieurs autres relevés en décalages vers le rouge. Pour $\lambda \preceq 100h^{-1}$ Mpc, le $P(k)$ du LCRS est grossièrement similaire en forme au $P(k)$ estimé à partir des autres relevés, mais présente une amplitude différente de celle des autres relevés, peut-être bien à cause des différences de structuration inhérentes entre les différents types de galaxies. Pour $\lambda \succeq 100h^{-1}$ Mpc, les résultats du LCRS sont compatibles avec ceux des autres relevés, étant données les grandes erreurs entre tous les relevés à ces échelles.

Ségrégation en couleur à grande échelle dans le relevé de décalages vers le rouge de Las Campanas
D. Tucker et al.

Le relevé de décalages spectraux vers le rouge de Las Campanas (LCRS) est un relevé de galaxies jusqu'à un décalage spectral de 0.2 composé de 6 tranches de 1.5° x 80° alternées dans les pôles galactiques Sud et Nord. A ce jour environ 26400 décalages spectraux de galaxies ont été recueillis. La combinaison de la photométrie en bande b_J obtenue à la machine automatique à mesurer les plaques (APM) avec la photométrie en bande R du LCRS a permis la détermination des couleurs $(b_J - R)$ dans le référentiel au repos des galaxies de la tranche $\delta = -39^o$ du LCRS. On observe que les galaxies rouges $[(b_J - R)_0 \geq 1.25]$ sont plus regroupées que les galaxies bleues $[(b_J - R)_0 \leq 1.05]$ aux petites échelles ($\preceq 10h^{-1}Mpc$) tandis qu'aux plus grandes échelles, il n'y a aucun signe de ségrégation en couleur.

Premiers résultats du programme ESO ESP
E. Zucca et al.

Le projet de la tranche ESO (ESP) est un relevé de décalages spectraux de galaxies réalisé dans le cadre d'un programme clé ESO, dans une région proche du pôle Sud galactique. La magnitude limite est $b_J = 19.4$. Les observations ont été terminées en octobre 1994 et toutes les données viennent juste d'être réduites, produisant 3348 décalages spectraux de galaxies. Nous présentons quelques résultats préliminaires concernant la distribution des galaxies à grande échelle et la fonction de luminosité.

Estimer le spectre de puissance à partir des catalogues 3D de galaxies.
M. Tegmark

Le spectre de puissance estimé à partir d'un catalogue de décalages vers le rouge de galaxies est le spectre de puissance réel convolué par une fonction fenêtre, donc lorsque l'on estime la puissance aux très grandes échelles (aux faibles k), il est important que cette fonction fenêtre soit aussi étroite que possible. Une méthode réalisant cela est présentée. Il est montré que l'estimation optimale de $P(k)$ est la transformée de Fourier des fluctuations de densité $n/\bar{n} - 1$ pondérée par une fonction ψ_0, et que la ψ_0 optimale est la solution du niveau fondamental de l'équation de Schrödinger, avec la fonction de sélection inverse comme potentiel. Cette analogie à la mécanique quantique apparaît simplement parce que nous voulons que la fonction de pondération soit étroite à la fois dans l'espace de Fourier (pour donner une fenêtre étroite) et dans l'espace réel (pour minimiser la variance due au bruit blanc)

La topologie de la distribution des galaxies.
S. Shandarin

L'historique et les résultats majeurs de l'étude de la topologie de la structure à grande échelle sont brièvement passés en revue. Deux techniques basées sur la théorie de percolation et sur la courbe de genus sont discutées. Les résultats préliminaires de l'analyse en percolation de la reconstruction de Wiener du catalogue de décalages vers le rouge découlant du catalogue IRAS à 1.2 Jy sont présentés.

Les radio-sources et la structure à grande échelle.
J. Wall et C. R. Benn

Les radio-sources extragalactiques ont le potentiel de suivre la structure à grande échelle au travers de l'univers observable: les effets de sélection sérieux qui sont présents aux autres longueurs d'onde sont maitrisés grâce à la luminosité des objets, la linéarité des détecteurs, l'uniformité à grande échelle des relevés, et l'obscurcissement minimal. Deux approches visant à extraire une information sur la structure à partir des relevés radios sont ici décrites, (i) en recouvrant directement la structure à partir des décalages vers le rouge dans les relevés radios, et (ii) en examinant la structure grâce à des analyses statistiques des relevés. Les deux approches confirment qu'une information substantielle sur la structure est présente dans les relevés radios modernes, et que la nouvelle génération de relevés doit receler l'empreinte du squelette de l'univers.

Grandes structures à trois dimensions.
A.P. Fairall et W.R. Paverd

Des vues à trois dimensions sont utilisées afin d'explorer le caractère de la distribution à grande échelle des galaxies de l'hémisphère Sud. Elles montrent qu'à l'intérieur des grands murs de galaxies, tels que celui du Sculpteur, il existe une texture cellulaire avec des vides de taille inférieure à $1000 kms^{-1}$ (tandis que les vides séparant les grands murs sont de l'ordre de $5000 kms^{-1}$ dans l'espace des vitesses). La vue à partir de la position de notre propre galaxie révèle que la concentration de galaxies formant l'équateur supergalactique s'étend en profondeur des galaxies les plus proches jusqu'à approximativement $cz = 1000 kms^{-1}$, avec beaucoup de petits vides emboîtés. Il est ainsi suggéré que notre galaxie est elle même à l'intérieur d'une structure de type "Grande Muraille".

Grandes Structures dévoilées dans la voie lactée Sud.
R.C. Kraan-Korteweg et al.

Au cours de notre recherche de galaxies derrière la voie lactée Sud par inspection de plaques IIIaJ ESO/SRC jusqu'à un diamètre limite de $D \geq 0.2'$, nous avons trouvé plus de 1000 nouvelles galaxies dans une région telle que $265^o \preceq l \preceq 340^o$, $|b| < 10^o$. Notre extension la plus récente couvre une région substantielle autour de la position prédite du Grand Attracteur $(l, b, v) = (320^o, 0^o, 4500km/s)$. Dans cette présentation, nous nous concentrons sur la détection d'une sur-densité extrême centrée sur l'amas A 3627. Cette sur-densité se révèle être un amas riche avec de nombreuses galaxies de type précoce. Les décalages spectraux sont proches du Grand Attracteur dans l'espace des vitesses $(l, b, vobs) = (325^o, -7^o, 4887km/s)$. De plus, les premières estimations de masse montrent que A3627 est un amas très massif, $M \simeq 7.10^{15} M_\odot$. La masse de l'amas lui même ne peut pas totalement expliquer les mouvements de chute vers le GA ($5.10^{16} M_\odot$[11]), mais A3627 semble être le pic central d'une plus grande structure de type super-amas, qui correspond aux prédictions générales de cet excès de matière.

Recherche de galaxies à raies d'émission dans les vides proches.
C. Popescu et al.

Nous présentons les résultats de notre recherche de galaxies à raies d'émission (ELG) dans les vides proches, les premières conclusions concernent leur distribution spatiale à grande échelle. Afin de trouver des galaxies à raies d'émission nous avons utilisé des plaques de prisme objectif du relevé de QSO de Hambourg. Ensuite nous avons obtenu des spectres longue fente pour déterminer le décalage spectral précis des candidats sélectionnés. Un échantillon de 205 objets a été finalement obtenu, dont à peu près la moitié sont de nouveaux objets. Les premiers résultats indiquent qu'il y a très peu d'ELG isolés. La plupart d'entre eux sont distribués en bordure des vides.

Les Galaxies naines et LSB tracent-elles le même champ de densité que les galaxies brillantes?
R. Dominguez-Tenreiro et al.

Un échantillon de galaxies naines et de faible brillance de surface (LSB) de l' hémisphère Nord, sélectionné à partir du catalogue UGC, avec des informations complètes en décalage vers le rouge , ont été analysées au travers du formalisme d'invariance d'échelle. Nous avons construit des sous-ensembles à volume limité que nous avons comparés aux galaxies brillantes du relevé du Centre d'Astrophysique (CfA) dans les mêmes ensembles à volume limité. Le formalisme d'invariance d'échelle permet une analyse séparée des régions appartenant à des zones de densités différentes. L' hypothèse zéro que les galaxies naines et LSB, d'une part, et les galaxies CfA, d'autre part, tracent le même champ de densité, peut être exclue à 95% de niveau de confiance pour des régions de forte à faible densité, les galaxies CfA étant plus regroupées

que les naines et les LSB. Les différences ne sont pas statistiquement significatives pour les régions très denses des galaxies les plus proches, probablement à cause d'un plus fort degré de contamination des vitesses particulières aux décalages vers le rouges des galaxies CfA proches. Ces résultats sont stables par rapport à des modifications d'intervalles de magnitude absolue ou de type morphologique des sous-ensembles CfA considérés.

Mesure de Ω indépendamment du biais des galaxies.
A. Dekel

Je décris des méthodes visant à mesurer le paramètre cosmologique de densité Ω à partir du champ de vitesses particulières à grande échelle indépendamment du biais des galaxies et de Λ. Plusieurs méthodes de ce type reposent sur l'hypothèse que les fluctuations initiales sont Gaussiennes; elles utilisent soit le champ de vitesses près d'un vide, soit l'écart à une distribution Gaussienne de la distribution de probabilité de $\nabla.v$, soit les fluctuations de densité initiales. Toutes conduisent à $\Omega > 0.3$ à un niveau de confiance de 95%. Une nouvelle détermination est basée sur la comparaison du spectre de puissance des fluctuations de densité de *masse* provenant des vitesses observées et des fluctuations à grand-angle du rayonnement de fond cosmologique observées par COBE. Dans le cas d'une cosmologie à univers plat motivée par l'inflation avec $\Omega + \Lambda = 1$ et à base de matière sombre froide, on trouve que si le spectre des fluctuations primordiales a une pente $n = 1$, le maximum de vraisemblance est à $\Omega \sim (0.7 \pm 0.2)h_{50}^{-1.2}$. Si $\Omega = 1$, alors $n \sim (0.8 \pm 0.1)h_{50}^{-0.8}$ sans tenseur des fluctuations, et $n \sim (0.9 \pm 0.1)h_{50}^{-0.8}$ avec tenseur des fluctuations.

Ω et le biais à partir des galaxies sélectionnées en optique versus la masse obtenue par POTENT.
M. Hudson et al.

Le champ de densité de masse dans l'Univers local, reconstruit par la méthode POTENT à partir des vitesses particulières de $\sim$ 3000 galaxies, est comparé au champ de densité des galaxies sélectionnées en optique. Les deux champs de densité sont lissés avec un filtre Gaussien de rayon $12h^{-1}Mpc$. Sous l'hypothèse de l'instabilité gravitationnelle et d'un biais linéaire entre les galaxies optiques et la distribution de masse, nous obtenons $\beta_O \equiv \Omega^{0.6}/b_O = 0.74 \pm 0.13$. Ce résultat est obtenu à partir d'une régression de la densité de masse de POTENT sur la densité optique après avoir corrigé le champ de densité de masse des biais systématiques présentés par les données sur les vitesses et par la méthode POTENT. L'erreur ici citée est juste l'erreur formelle à 1σ estimée à partir de la dispersion observée dans le diagramme de dispersion densité-densité; elle n'inclut pas l'incertitude due à la dispersion cosmique dans la densité moyenne ou dans la relation de biais. Nous ne tenterons pas d'analyse formelle de la qualité de l'ajustement, mais la dispersion de l'ajustement est compatible avec

nos estimations des incertitudes.

Cartographier le champ de vitesses propres des galaxies.
L. Nicolaci da Costa et al.

Nous avons récemment terminé un sondage sur tout le ciel comportant le décalage vers le rouge et la distance de galaxies spirales. L'échantillon est composé d'environ 1600 galaxies Sbc-Sc sélectionnées en fonction d'un diamètre limite dépendant du décalage vers le rouge. De nouvelles données ont été également obtenues pour des galaxies appartenant à plusieurs amas, qui sont utilisées pour déduire une relation de Tully-Fisher indépendante dans la bande I pour estimer les distances. Ces distances sont corrigées du biais en utilisant une approche Monte-Carlo qui tient en compte simultanément des biais de Malmquist homogène et inhomogène, des effets de sélection et de l'incomplétude de l'échantillon. Nous utilisons ce nouvel échantillon pour reconstruire de manière indépendante les fluctuations dans le champ de densité de matière et le champ de vitesse tridimensionnel. Nous présentons ici une brève description de l'échantillon et de la méthode d'analyse. Nous discutons aussi quelques résultats préliminaires.

Le contenu en information des relevés de décalages spectraux et de vitesses.
A. Yahil

La reconstruction d'image basée sur le pixon de Puetter et Pina permet des améliorations notables par rapport aux autres méthodes, résolution spatiale plus grande, plus grande sensibilité aux sources faibles, et immunité dans la production d'artefacts et de résiduels corrélés au signal. La même technique peut être utilisée pour les problèmes de structure à grande échelle qui permettent un lissage variable. La comparaison entre différents ensembles de données n'est pas pénalisée par le lissage variable, parce qu' un champ de densité/potentiel commun sous-jacent peut être appliqué à tous les ensembles de données quelque soit le lissage. En utilisant au mieux les différents ensembles de données, la méthode des pixons peut ainsi apporter la détermination la plus sensible du paramètre de densité cosmologique, Ω, à partir de relevés de décalages spectraux et de vitesses.

Champs dynamiques et Ω simultanément à partir des relevés de décalages vers le rouges et des relevés de vitesses propres.

A. Nusser et A. Dekel

Nous présentons une méthode (dénommée SIMPOT) visant à reconstruire simultanément les champs de densité à grande échelle, de vitesse et de potentiel et le paramètre β (où Ω est le paramètre de densité cosmologique et b est le paramètre de biais linéaire) à partir des vitesses propres radiales mesurées et de la distribution des galaxies dans l'espace des décalages vers le rouge .SIMPOT modélise le champ de potentiel des vitesses par l'intermédiaire d'un développement en harmoniques sphériques et en fonctions radiales de Bessel, et, supposant une valeur pour β , le relie à la distribution des galaxies dans l'espace des décalages vers le rouge en utilisant la théorie linéaire de l'instabilité gravitationelle. La méthode est testée en utilisant des catalogues d'imitation réalistes du catalogue de vitesses propres Mark III et du catalogue de décalages vers le rouge d'IRAS à 1.2Jy. Les données d'imitation sont extraites d'une simulation a N-corps avec $\Omega = 1$ qui reproduit bien l'Univers proche. Si le biais linéaire prévaut dans l'Univers, SIMPOT fournit une estimation non biaisée de β avec une erreur de ± 0.06. On peut appliquer SIMPOT avec des pondérations différentes des données sur les vitesses et les décalages vers le rouge. Lorsqu'un poids important est donné aux vitesses, les champs déduits sont principalement déterminés par les vitesses, mais bel et bien contrôlés par la distribution des galaxies dans les régions où les données sur les vitesses sont pauvres. SIMPOT peut être vu comme une méthode générale permettant de déduire les champs dynamiques à grande échelle à partir d'une multitude de données hétérogènes.

Reconstruction de Wiener et estimation des paramètres des catalogues.

S. Zaroubi

Le formalisme du filtrage du Wiener est utilisé pour reconstruire en terme d' harmoniques sphériques la distribution en galaxies projetée sur 4π d'un catalogue imitation du catalogue IRAS à 1.2 Jy avec une zone vide en $|b| = 15^\circ$. L'algorithme de décomposition en valeur singulière a été utilisé comme un régulateur de plus, afin de stabiliser l'inversion. Ce cas montre la quantité d'informations contenue dans les données, et suggère aussi une méthode pour obtenir une base fonctionnelle "optimale", basée sur notre connaissance première, pour l'utilisation de l'analyse de vraisemblance et la reconstruction de Wiener pour des échantillons de données cosmologiques. L'application d'une telle base fonctionnelle pour des catalogues de décalages spectraux de galaxies est aussi discutée.

Distorsions des décalages vers le rouge et Ω dans les catalogues IRAS.
A. Hamilton

Les distorsions dans l'espace des décalages vers le rouge aux grandes échelles peuvent être utilisées pour mesurer le paramètre de taux de croissance linéaire $f \sim \Omega^{0.6}/b$. Je rapporte ici les mesures de telles distorsions dans les catalogues de décalages vers le rouge issus des catalogues IRAS à 2 Jy, 1.2 Jy, et de de QDOT, trouvant $f = 0.69^{+.21}_{-.19}$ à partir d'un catalogue résultant de la fusion de QDOT et du catalogue IRAS à 1.2 Jy. Malheureusement, le niveau de confiance en ce résultat est indéterminé à cause d'un changement prononcé (4σ) de la structuration dans QDOT au delà d'environ $80h^{-1}Mpc$. Un effet similaire pourrait être présent à un certain point dans le catalogue à 1.2 Jy. L'effet pourrait être causé par une variation systématique dans la limite effective en flux du catalogue IRAS PSC sur le ciel, avec une dispersion de ~ 0.1 Jy aux échelles de $\sim 7°$. Si cela était le cas, alors la valeur de f déduite des distorsions en décalage vers le rouge dans les catalogues IRAS pourrait être systématiquement sous-estimée.

Que prouve la vitesse des paires de galaxies?
A. Blanchard et J. Bartlett

La vitesse de paires des galaxies, c'est à dire la vitesse relative de deux galaxies séparées d'une certaine distance peut être estimée grâce aux catalogues de vitesses radiales. Peebles a souligné qu'il est ainsi possible d'estimer la densité moyenne de l'univers sans avoir recours à un objet individuel. Si la distribution des galaxies reflète fidèlement celle de la masse (scénario non-biaisé), cette méthode est généralement considérée comme permettant une bonne estimation de la densité moyenne de l'univers. Cependant cette vision doit être corrigée pour tenir compte du fait que les galaxies possèdent un halo étendu: de fait, nous montrons, que dans ce cas la vitesse de paires aux petites échelles est indépendante de la densité moyenne de l'univers. Nous concluons que la vitesse de paires reflète le caractère étenclu des halos de galaxies. Les observations actuelles indiquent que les halos des galaxies s'étendent au moins jusqu'à 300kpc.

Statistiques et Dynamiques de la Structuration.
R. Juskiewicz et F. R. Bouchet

Depuis le papier classique de Lifshitz il y a pratiquement un siècle, l'analyse en stabilité linéaire des modèles cosmologiques est bien connue. Cependant, jusqu'à une époque très récente, peu de choses était connu sur le comportement des termes d'ordres supérieurs au cas linéaire dans le développement perturbatif. Ces termes deviennent très importants dans le régime non-linéaire de l'agrégation gravitationnelle, lorsque le contraste de densité de masse r.m.s est seulement légèrement inférieur à l'unité. Dans

le passé, les théoriciens ont montré peu d'intêret à étudier ce régime, avec d'ailleurs une bonne raison: il y a seulement dix ans, cela aurait été un exercice académique;à des échelles suffisamment grandes pour prouver le régime faiblement non linéaire, toutes les mesures de la force de regroupement étaient dominées par le bruit. Ce n'est désormais plus le cas avec les données actuelles; les possibilités d'appliquer l'approche faiblement non linéaire à l'analyse des observations seront encore plus grandes, lorsque les nouveaux relevés, comme le SDSS ou 2DF seront disponibles. Le but de cet exposé est de pourvoir à un bref résumé des avancées récentes dans la théorie de perturbation dans le domaine faiblement non linéaire. Nous présentons des résultats perturbatifs analytiques conjointement aux résultats de simulations à N-corps, effectuées pour tester leur précision. Nous comparons les prédictions perturbatives aux mesures des relevés de galaxies. De telles comparaisons peuvent être utilisées pour tester la théorie de l'instabilité gravitationelle et pour contraindre des déviations possible aux statistiques Gaussiennes dans la distribution de masse initiale; elles peuvent aussi être utilisées pour étudier la nature des processus physiques qui gouvernent la formation des galaxies ("biais"). Nous terminons avec une discussion des prospectives futures pour l'approche perturbative de l'instabilité gravitationnelle. Nous montrons comment les propriétés statistiques du champ de vitesses particulière peuvent être utilisées pour construire une nouvelle méthode visant à mesurer le paramètre de densité cosmologique, Ω, et comment l'ancienne méthode peut être améliorée.

Aspects de l'invariance d'échelle en agrégation gravitationelle.
B. Jain

Les hypothèses sous-jacentes à une description semi-empirique de l'agrégation gravitationelle non-linéaire sont discutées. Le postulat d'invariance d'échelle de Hamilton et al. étend effectivement le concept d'invariance d'échelle auto-similaire à un spectre initial de toute forme générique. Cette contribution examine les deux ingrédients théoriques intervenant dans l'invariance d'échelle: l'évolution auto-similaire et l'hypothèse de l'agrégation stable. La vitesse moyenne des paires de particules peut être calculée précisément partir des simulations à N-corps via l'équation de conservation des paires en utilisant l'évolution de la fonction d'auto-corrélation. Les résultats ainsi obtenus pour des spectres invariants d'échelle d'indice n =0,1,-2 et pour le spectre CDM sont compatibles avec l'hypothèse d' agrégation stable: la vitesse moyenne des paires en coordonnées physiques tend vers zéro aux petites échelles.

Propriétés des fonctions de distribution de densité dans le régime quasi-linéaire.
F. Bernardeau

La théorie perturbative appliquée aux champs cosmologiques à grande échelle, pour des conditions initiales Gaussiennes, prédit une grande variété de propriétés statistiques

pour les champs de densité cosmologiques, tels que les comportements des moments d'ordre élevé des probabilités de comptage dans des cellules. Dans cet article je présente le cadre général de ces calculs et leur domaine de validité. En particulier j'applique ces indicateurs statistiques aux catalogues angulaires de galaxies et souligne que les observations dans le catalogue angulaire APM suggèrent une distribution de galaxies légèrement biaisée.

Méthodes améliorées pour comparer les simulations aux données.
J.R. Primack

Les modèles théoriques de formation des structures avec fluctuations initiales Gaussiennes ont été travaillés en détail et comparés avec les observations à différentes échelles. C'est sur les échelles non-linéaires $\leq 10h^{-1}Mpc$ que les plus grandes différences existent entre les modèles avec $\Omega = 1$ qui ont été normalisés pour être en bon accord aux plus grandes échelles avec les données de COBE; ici en particulier il existe une nécessité de meilleurs tests statistiques qui soient simultanément robustes, discriminatoires et que l'on puisse interpréter. L'ère à laquelle la formation des galaxies et des amas a lieu est aussi un test critique de certains modèles. Parmi les besoins pour le futur, il faut inclure des codes plus rapides et plus intelligents, un meilleur contrôle de la variance cosmique dans les simulations, une meilleure compréhension des processus conduisant à la formation des galaxies, de meilleures méthodes pour comparer les données observationnelles aux modèles, et un meilleur accès aux données observationnelles et résultant des simulations.

A propos des coeurs des amas et des spectres de puissance.
B. C. Bromley et al.

Nous discutons les simulations numériques à haute résolution de formation des structures avec 1) la distribution de la matière sombre dans le coeur des amas d'Abell 2) les effets de la dynamique non linéaire des galaxies sur la mesure du spectre de puissance. Les arguments d'invariance d'échelle suggèrent que les amas massifs ont un coeur mou étendu; cependant, des observations récentes d'optique gravitationnelle impliquent que les coeurs sont bornés à quelques dizaines de kiloparsecs. En travaillant avec une simulation d'un amas isolé à partir de matière sombre froide (CDM) comprenant 1.1 million de particules , nous n'avons pas trouvé de coeur mou étendu, en accord avec les observations. Nous examinons la structuration non linéaire des galaxies dans l'Univers à grande échelle en utilisant une simulation CDM avec 17 millions de particules dans un cube périodique de 250 Mpc. Nous nous concentrerons sur l'effet des vitesses des paires sur le spectre de puissance mesuré dans l'espace des décalages vers le rouge, $P_S(k)$. Les données issues des simulations montrent que les vitesses particulières et la structuration spatiale conspirent pour rendre la détermination de $P_S(k)$ très peu sensible à la normalisation du spectre de puissance primordial, sur des échelles aussi

grandes que $50Mpc$; cet effet est modélisé a l'aide d'un filtre F(k), valable des échelles linéaires aux échelles fortement non linéaires, qui relie le spectre de puissance dans l'espace des décalages vers le rouge à sa contrepartie dans l'espace réel par la relation: $P_R(k) = F(k)P_S(k)$. Nous trouvons que la puissance dans l'espace des décalages vers le rouge est en excellent accord avec les observations, néanmoins nous concluons que cette statistique ne contraint pas fortement les modèles cosmologiques sur le domaine d' échelles étendu qui peut être affecté par le mouvement propre non linéaire.

La structure à grande échelle dans les simulations à N-corps.
A. Doroskhevich

La théorie approximativement quantitative de la formation et de l'évolution de la structure à grande échelle de l'Univers (LSS) est comparée à six simulations à N-corps de spectre de puissance CDM standard et à invariance d' échelle brisée (BSI). La dépendance propre des paramètres de structure et l'histoire de leur évolution sur l'amplitude et la forme des spectres et sur la taille de la boite de calcul sont établis.

Simulations numériques de formation des galaxies: Effets de rétroaction de Supernova.
G. Yepes et al.

Nous présentons les résultats de simulations cosmologiques de formation des galaxies dans lesquelles les effets du refroidissement radiatif et Compton ainsi que les effets de rétroaction des explosions de supernovae ont été pris en compte. Dans nos simulations numériques Hydro+N-corps, la matière est traitée comme un milieu multi-phase à quatre composantes: matière sombre, gaz chaud baryonique, nuages de gaz froid, et étoiles produites par les nuages de gaz froid. Les étoiles de masse $> 10M_{\odot}$ explosent en supernova, provoquant l' évaporation alentour de nuages froids et un réchauffement du gaz chaud. La combinaison de ces effets va contrôler la formation d'étoiles dans les halos de matière sombre. Les modèles de Synthèse de Population Stellaire ont été utilisés pour calculer les luminosités et les couleurs des "galaxies numériques". Les effets de rétroaction des supernova jouent un rôle important sur l'évolution des galaxies naines. La plupart des petits objets présentent des luminosités extrêmement faibles et une couleur très rouge. Cependant, les galaxies naines situées à proximité de galaxies brillantes semblent être significativement plus brillantes que celles qui se trouvent dans des zones de basse densité. La quantité de matière lumineuse qui est formée dans les halos sombres dépend fortement de la modélisation des effets de rétroaction des supernova. La formation stellaire est inhibée lorsqu'une partie importante de l'énergie libérée par la supernova va réchauffer le gaz plutôt que provoquer l'évaporation de nuages froids. La fraction totale de gaz converti en étoiles dans la simulation totale varie de 50%, lorsque la moitié de l'énergie de la supernova est cinétique, à 8% lorsque la majeure partie de l'énergie de la supernova est thermique. La distribution du gaz suit

en grande ligne la distribution de la matière sombre, sauf pour les condensations qui sont beaucoup moins diffuses que la matière sombre locale. Dans le cas de petites et de grandes " galaxies" , la distribution de la matière lumineuse est fortement biaisée par rapport à celle des halos sombres. Cependant, le biais n'est pas une fonction simple de la densité locale, mais dépend fortement de l'environnement.

Simulation de la formation de grandes structures pour le spectre de puissance BSI.
V. Müller

Un modèle double inflationnaire produit des spectres de perturbations avec un pouvoir accru aux grandes échelles (perturbations brisées à invariance d'échelle: BSI), et conduit à un scénario prometteur pour la formation des structures cosmiques. Nous décrivons un série de simulations PM à haute résolution avec un modèle pour l'évolution thermodynamique des baryons dans lesquelles nous sommes capables d'identifier des halos de "galaxies" avec un spectre de puissance raisonnable en suivant la genèse des structures grandes et super-grandes. Le spectre de puissance et les fonctions de corrélation des "galaxies" sont comparées au spectre de puissance reconstruit du catalogue CfA et aux fonctions de corrélation du relevé profond de décalages spectraux de Las Campanas.

Test des modèles de matière sombre par la distribution des amas.
S. Borgani et al.

Nous étudions les propriétés de structuration de simulations numériques de la distribution des amas, qui sont basées sur l'approximation de Zeldovich, et les comparons à celles d'un catalogue étendu comprenant les décalages vers le rouge d'amas Abell/ACO. Une comparaison détaillée de telles simulations aux simulations à N-corps exactes est aussi discutée. Parmi la liste des modèles de matière sombre (DM) simulés, nous trouvons que seuls ceux basés sur un mélange de matière sombre Froide+Chaude (avec $\Omega_{chaud} = 0.3$) et un modèle CDM de faible densité ($\Omega_0 = 0.2$) avec un terme de constante cosmologique ($\Omega_\Lambda = 0.8$) permettent un bon ajustement aux données. Le modèle CDM standard, le modèle CDM tilté (n=0.7) et les modèles CDM avec une faible valeur de la constante de Hubble sont écartés.

Contraintes observationnelles sur les spectres primordiaux dans le bleu.
L. Moscardini et al.

Récemment, un intérêt croissant pour les spectres primordiaux de perturbation "bleus" ($n > 1$) se développe, motivé d'une part par un ensemble varié de données observationnelles à grande échelle (anisotropies du fond cosmologique diffus, les flux

de groupe, etc...), et d'autre part, par la construction de modèles théoriques (c.a.d. inflation hybride). Pour imposer des contraintes observationnelles sur ce type de spectres, à la fois dans le cadre des scenarii de Matière Sombre Froide(CDM) et de Matière Sombre Mélangée(MDM), nous avons fait tourner des simulations à N corps et nous avons fait des analyses statistiques de la distribution de matière, des champs de vitesse et des distributions d'amas. Les résultats principaux montrent qu'un modèle purement CDM avec spectre primordial bleu produit trop de puissance à petite échelle; au contraire, un modèle bleu MDM peut reproduire la variance APM-Stromlo des comptages en cellules, et le résultat d'autres tests, mais il tend à produire trop d'amas massifs.

Structure et formation des trous noirs primordiaux dans les modèles inflationnaires avec la particularité d'un potentiel inflaton.
P. Ivanov

Nous discutons les propriétés inhabituelles du spectre des perturbations adiabatiques primordiales produites dans les modèles cosmologiques inflationnaires avec des coupures (les changements de pentes) dans le potentiel inflaton. Nous montrons qu'un tel spectre devrait être non plat de façon très importante contrairement au cas standard de Harrison-Zeldovich. N coupures dans le potentiel entraînent N traits particuliers dans la forme des bosses ou des dépressions dans la fonction de corrélation à deux points de la distribution de matière. Le potentiel avec deux coupures et une région pratiquement plate entre (un plateau), donne une augmentation dans le spectre de puissance à l'échelle adéquate. Cette bosse dans le spectre peut produire les trous noirs primordiaux en une quantité suffisante pour clore l'Univers ($\Omega = 1$).

Relevés en Optique/Proche-InfraRouge d'amas de galaxies distants
M. Postman

Les résultats d'une analyse d'un catalogue sélectionné en optique/proche IR de 79 amas distribués sur une zone de 5.1 degrés carrés sont présentés. Le catalogue a été construit à partir d'images obtenues avec la caméra à mosaïque de détecteurs à transfert de charge à quatre canaux installée sur le télescope de 5m de Hale fonctionnant en mode balayage. Le relevé, connu jusqu'à présent sous le nom de Relevé d'Amas Distants du Palomar (PDCS), a été entrepris en deux filtres à bande large qui ressemblent de près aux filtres V et I. Les magnitudes limites à 4σ correspondant à nos poses de 300s sont $\sim$ 23.8 (V) et 22.5 (I). Un algorithme d'optimisation du filtre a été développé et utilisé pour identifier les candidats amas en utilisant simultanément les données de position et photométriques. Les amas couvrent le domaine $0.2 \preceq z \preceq 1.2$, à partir des estimations de décalages vers le rouge provenant de la procédure de détection des amas. Une fonction de sélection précise est générée à partir de simulations étendues. Nous trouvons que la densité de surface intégrée des amas de classe de richesse $R \succeq 1$ est environ 5 fois plus grande que la densité extrapolée à partir des amas d'Abell de $R \succeq 1$.

Les résultats du PDCS sont compatibles avec une densité comobile constante d'amas jusqu'à $z \preceq 0.6$, malgré la valeur élevée du niveau de densité précédemment citée. Il sera possible de contraindre l'abondance des amas à $z > 0.6$ lors de l'acquisition de décalages vers le rouge par spectroscopie pour un grand échantillon de ces candidats amas. Nous avons analysé les amas les plus riches de cet échantillon et nous avons trouvé que l'amas typique du Palomar a un profil de densité de surface en $r^{-1.4}$ ($r \succeq 0.15h^{-1}Mpc$) a un rayon de coeur de $0.1h^{-1}Mpc$. Nous avons quelques indications que la pente du profil de densité de surface devient plus raide lorsque le décalage vers le rouge augmente. Notre population d'amas est incompatible à un niveau de confiance de 99.2% avec une population d'amas symétrique en azimuts.

La distribution en densité des amas est-elle gaussienne?
T. Kolatt

La fonction de distribution de probabilité à un point (PDF) est calculée pour le champ de densité des amas riches de galaxies des catalogues Abell/ ACO lissé sur 25 $h^{-1}Mpc$. La PDF observée est comparée aux PDF tirées de manière similaire des catalogues d'imitation de catalogues d'amas extraits de simulations cosmologiques de conditions initiales Gaussiennes et non Gaussiennes. Plusieurs statistiques permettent une exclusion significative des modèles non-Gaussiens testés ici, et ne parviennent pas à écarter le modèle Gaussien. Une comparaison avec les prédictions de la théorie perturbative du second ordre et le modèle log-normal pour des conditions initiales Gaussiennes CDM donnent un facteur de biais linéaire $b_c/b_o \sim 4$ et $b_c/b_o \sim 3.7$ pour les amas de richesse $R \geq 0$.

Le catalogue d'amas de l'APM : Détection des Amas et Structure à Grande Echelle.
G. Dalton

Le catalogue d'amas de l'APM est basé sur une modification de la méthode de classification originelle des amas de galaxies établie par Abell. Nous discutons ici les résultats d'une investigation de la stabilité des propriétés statistiques du catalogue d'amas face au changement des paramètres de sélection. Lorsque les critères de sélection sont mal définis, nous trouvons des indications claires qu'il s'agit d'amas sur la ligne de visée, mais il existe un vaste domaine de paramètres d'entrée pour lesquels les propriétés statistiques du catalogue sont stables. Nous concluons que les amas sélectionnés de cette manière sont bien sûr utiles en tant que traceurs de la structure à grande échelle.

Le spectre de puissance des amas de l'APM.
H. Tadros

Nous présentons l'analyse du spectre de puissance du sondage (en décalages vers le rouge) d'amas de l'APM et le comparons avec les prédictions de plusieurs modèles à base de matière sombre froide (CDM). Nous trouvons que le modèle CDM standard (SCDM) ne parvient pas à expliquer les observations. Les modèles à base de matière sombre mélangée (MDM) et ceux à base de matière sombre froide avec une constante cosmologique (ΛCDM) donnent un meilleur ajustement aux données. Nous examinons aussi la question du biais de la distribution des amas par rapport à celle des galaxies, et nous tentons d'estimer le paramètre de biais entre les galaxies et la masse dans le contexte de modèles cosmologiques spécifiques.

Vitesses propres à grande échelle: effets des superamas.
R. Scaramella

Nous étudions l'influence gravitationnelle des structures à très grande échelle tracées par les amas de galaxies sur le mouvement du groupe local (LG) et les mouvements à grandes échelle. A partir de la distribution des amas d'Abell à l'intérieur de $300Mpc/h$, nous avons dérivé le champ de sur-densité sur une grille 3D avec une maille de $5Mpc/h$, nous avons ensuite résolu l'équation de Poisson pour le potentiel particulier et finalement obtenu le champ de vitesse. A partir de cette solution globale nous trouvons les résultats suivants:

i) nous retrouvons à 10^o près la direction du mouvement du LG dans le repère du fond cosmique (CMB)

ii) nous trouvons que le Grand Attracteur lui même se déplace par rapport au repère du CMB

iii) nous dérivons $\beta_c^{-1} = b_c\Omega^{-0.6} = 5.3\pm0.20$ à partir d'une comparaison préliminaire avec le catalogue de vitesses particulières Mark II

iv) nous dérivons une estimation du mouvement d'ensemble dans des sphères en bon accord avec le niveau estimé à partir de POTENT et des échantillons de spirales

v) nous trouvons que le mouvement d'ensemble de Lauer et Postman (LP) a une amplitude trop grande pour être en accord avec nos résultats.

Relevé de décalages spectraux dans un candidat superamas de l'hémisphère Sud.
K. Singlend et al.

L'analyse récente des amas du catalogue d'Abell et du catalogue d'Abell, Corwin et Olowin (ACO, 1989) des amas riches du Sud révèle l'existence de superamas sur des échelles de 50 à $100Mpc$ et au-delà (Batuski et Burns, 1985 et Huchra et al. 1990). Toutefois les décalages spectraux n'ont été mesurés que pour 35% des amas d'Abell et

d'ACO (et la plupart d'entre eux n'ont qu'une ou deux galaxies mesurées, voir Struble et Rood, 1991). Nous poursuivons un programme utilisant MEFOS au 3.60 m de l'ESO afin d'observer des amas dans une tranche de 10^ox 70^o incluant deux candidats superamas particulièrement intéressants afin de déterminer l'existence réelle de ces superamas. Notre échantillon est limité à des amas de richesse $R \geq 1$, possédant un ou plusieurs décalages spectraux mesurés, à haute latitude galactique (limites de l'échantillon statistique d'Abell, 1958, et $|b| > 30^o$ par les amas ACO), avec $m_{10} \leq 19.0$ (décalage spectral estimé $z < 0.18$). La première mission sur ce programme a eu lieu en août 1994. Nous avons observé 22 amas dans la tranche (10 décalages spectraux ou plus par amas) , concentrés sur les 2 candidats superamas. Nous présentons ici les premiers résultats. Nous avons trouvé une sur-densité d'un facteur 10 d'amas d'Abell et ACO dans cette région. Ce superamas s'ajoute aux 3 autres, de sur-densité similaire, que la théorie devra expliquer.

Oscillation à $140 Mpc$ de la fonction de corrélation des amas.

V. Saar

Nous avons développé une méthode indépendante de tout paramètre afin de détecter les maxima locaux de la fonction de corrélation à deux points. Son application à deux échantillons d'amas d'Abell riches en galaxies avec des limites en décalages spectraux $z < 0.08$ et $z < 0.1$ montre l'existence de 3 maxima centrés à $150 h^{-1} Mpc$, $300 h^{-1} Mpc$ et $430 h^{-1} Mpc$ avec des niveaux de confiance de 80% et plus. Cette séquence de fluctuations est espacée de $140 h^{-1} Mpc$, ce qui peut être expliqué par un spectre de puissance avec un pic à $k = 0.048 \pm 0.005 h Mpc^{-1}$.

Comparaison des corrélations des galaxies brillantes et des amas riches.

A. Cappi et al.

Nous avons utilisé le deuxième Grand Relevé des Décalages vers le rouge des galaxies dans le Ciel Austral (SSRS; voir da Costa et al. 1995), dont la limite est fixée à la magnitude apparente 15,5, pour étudier la distribution spatiale des galaxies intrinsèquement très lumineuses, en la comparant aussi à la distribution des amas de galaxies. Force est de constater que la distribution des ces galaxies ressemble plutôt à celle des amas, bien qu'elles ne se trouvent pas de préférence dans ces derniers, avec une fonction de corrélation qui est amplifiée par rapport à celle des galaxies de plus faible luminosité et qui semble s'adapter assez bien à la fonction de corrélation universelle apparemment suivie par les amas.

Estimer β à partir des vitesses particulières du Groupe Local et des amas.
M. Plionis

En comparant les vitesses particulières observées du Groupe Local et des amas de galaxies d'Abell proches à celles prédites en utilisant la théorie de perturbation linéaire et l'algorithme de reconstruction 3D de Branchini et Plionis (ce volume) la valeur de β peut être estimée. Je montre que l'anisotropie qui cause le mouvement du Groupe Local ne s'étend pas très loin en profondeur ($\sim 160h^{-1}Mpc$) mais est aussi très cohérente, ce qui suggère que la valeur de $\beta \sim 0.21 \pm 0.015$, obtenue à partir de la vitesse du GL, ne devrait pas être affectée de manière significative par la variance cosmique. En comparant les dipôles des amas d'Abell et des galaxies de QDOT dans l'espace réel, leur facteur de biais relatifs sont estimés à: $b_{cI} \sim 3.5 \pm 0.5$. Enfin, en utilisant un échantillon adapté de vitesses particulières d'amas disponibles, j'obtiens une valeur quelque peu plus basse pour $\beta \sim 0.15 - 0.17$ mais avec une grande incertitude (≥ 0.1) lorsque pondérée par les grandes erreurs observationnelles. Des données plus nombreuses et de meilleure qualité sur les vitesses particulières d'amas sont nécessaire pour pouvoir réduire cette incertitude.

Reconstruction des vitesses particulières des amas en deçà de $20000km/s$
E. Branchini et M. Plionis

A partir de la distribution dans l'espace des décalages vers le rouge d'un échantillon limité en volume d'amas Abell et ACO, nous utilisons une procédure de reconstruction pour déduire leurs distances et leurs vitesses propres. Le dipôle 3-D résultant, ainsi que celui dans l'espace des z, convergent à $\sim 170h^{-1}Mpc$ et pointent à environ 10^o de l'apex du CMB. Cependant, à cause des distorsions dans l'espace des décalages vers le rouge le dipôle asymptotique de la distribution des amas dans l'espace des z est surestimé par rapport au dipôle dans l'espace 3D d'environ $\sim 23\%$ conduisant à une valeur de $\beta \sim 0.21$, où b_c est le facteur de biais de la population d'amas par rapport à la distribution sous-jacente de matière. Le champ de vitesses d'amas résultant est dominé par un courant à grande échelle le long de la ligne Perseus-Pisces/Grand Attracteur dirigé vers la concentration de Persée, en accord qualitatif avec le champ de vitesses des galaxies aux plus petites échelles. La vitesse d'ensemble des amas est en bon accord avec celle déduite de l'analyse par POTENT des mouvements des galaxies à $\sim 60h^{-1}Mpc$; celui-ci décroit lorsque l'on pointe dans la direction habituelle du dipôle du Fond diffus cosmologique (CMB), en profond désaccord avec [3].

Le Relevé ESO d'Amas d'Abell Proches (ENACS): distribution en dispersion des vitesses.

A. Mazure et al.

Les données obtenues pour 91 amas de galaxies dans le cadre d'un programme clé de l'ESO (ENACS) auxquelles s'ajoutent celles issues de la littérature pour 37 amas, permettent la construction d'un échantillon d'amas d'Abell proches (z <0.08) avec lequel on étudie la distribution des dispersions de vitesse en rapport avec les prédictions théoriques.

Sondages d'amas de galaxies détectés par ROSAT.

H. Böhringer

Les amas de galaxies, les plus grands objets bien définis de l'univers, sont idéaux pour tracer la structure à grande échelle. L'échantillon d'amas de galaxies à utiliser pour ces études cosmologiques est mieux sélectionné par leur détection en rayons X. Le sondage de tout le ciel par ROSAT est la meilleure base pour une telle étude. Dans cette contribution, nous passons brièvement en revue les propriétés en rayons X des amas, la détermination de la masse des amas avec les données de ROSAT et le statut des projets de catalogues de décalages vers le rouge d'amas détectés par le sondage de tout le ciel par ROSAT.

Fonctions de corrélation non monotones pour les amas d'Abell très riches: histoire, résultats et projets:

T.S. Fetissova

L'échantillon d'amas de galaxies très riches et très compacts contenant tous les amas d'Abell avec $R \geq 2$, $0.06 < z < 0.24$ et $b > 60^o$ (l'échantillon de "Shvortsman", programme initié par V.F. Shvortsman en 1981, et également dénommé "Le Cône Nord") fut initialement étudié en 1984. La fonction de corrélation de cet échantillon d'amas particulièrement profond, complet et homogène donnait alors un maximum $\xi(R) = 0.5$ à $R = 250 Mpc$ ($H_0 = 50 kms^{-1} Mpc^{-1}$). Nous présentons de nouveaux résultats pour les fonctions de corrélation obtenues pour différents échantillons constitués d'amas de richesse différente. Nous analysons leur comportement dans le domaine $100 < R < 600 Mpc$. La possibilité d'utiliser des décalages spectraux estimés pour une partie des amas est aussi discutée.

Évolution des amas et théories d'instabilité gravitationnelle.
S. Colafrancesco

Nous discutons la capacité des amas de galaxies à tester certains aspects des scénarios de structure à grande échelle et de théories d'instabilité gravitationelle. Nous nous concentrerons sur le rôle dynamique que peut peut-être jouer la sous-structuration dans la modification de l'effondrement de l'amas tout entier.

Une revue des expériences de microlentilles gravitationnelles.
C. Magneville

Trois expériences recherchent actuellement de la Matière Noire sous forme d'objets compacts au moyen de microlentilles gravitationnelles. Toutes ont observé des événements candidats. Nous décrirons ici l'effet de microlentille gravitationnelle, les spécifications de chaque expérience et nous discuterons leurs résultats actuels.

Cosmologie avec matière sombre froide + chaude.
J. Primack et al.

Le modèle cosmologique à base de matière froide + chaude semble requérir une masse pour le neutrino d'environ $5eV$, afin de produire une formation des galaxies suffisamment précoce. Ces neutrinos constitueraient la matière sombre chaude, une fraction $\Omega_\nu = 0.2(0.5/h)^2$ de la densité critique, où $h = H_0/(100kms^{-1}Mpc^{-1})$ est le paramètre de Hubble. Des données expérimentales récentes suggèrent que cette masse de neutrino pourrait être répartie suivant deux ou plusieurs espèces de neutrinos. Nous considérons ici les conséquences de telles masses de neutrinos sur la formation des galaxies et des grandes structures de l'univers dans le cadre de modèles cosmologiques qui sont spatialement plats et dans lesquels la majeure partie de la matière sombre est froide. Les calculs linéaires et les simulations à N-corps que nous reportons ici indiquent qu'un modèle cosmologique CHDM avec $\Omega = 1$ et deux neutrinos chacun de masse $\sim 2.4eV$ (nous appellerons ce modèle Cν^2DM) est en bon accord avec toutes les observations disponibles. Cependant, nous trouvons que ceci est vrai uniquement si le paramètre de Hubble $h \sim 0.5$. Nous considérons aussi les modèles à base de matière sombre froide (CDM) avec une constante cosmologique λ et nous montrons que l'évidence de matière sombre chaude dresse des difficultés sérieuses pour les modèles ΛCDM à faible Ω.

Le Problème des neutrinos solaires, 1995.
V. Berezinsky

L'état du problème des neutrinos solaires (SNP), vu en 1995, est passé en revue. Tout simplement, il existe deux solutions au problème des neutrinos solaires: (i) avec des *neutrinos standard* (neutrinos du modèle standard des interactions électrofaibles) et (ii) avec des *neutrinos non standard* (neutrinos au delà du Modèle Standard). En fait, on peut distinguer trois problèmes de neutrinos solaires: le déficit des neutrinos du Bore, le déficit des neutrinos du ^{7}Be et le conflit Homestake/Kamiokande. Le premier pourrait être résolu probablement par des petits changements corrélés des sections efficaces de neutrinos et le changement de la température centrale du Soleil. Le déficit des neutrinos du ^{7}Be semble être le problème clé. Le conflit Homestake/Kamiokande élimine ou au moins ne favorise pas le neutrino standard (solution nucléaire/astrophysique du SNP). La conversion MSW offre l'explication la plus plausible au SNP.

L'expérience de neutrinos solaires Russo-Américaine au Gallium.
S.R. Elliott et al.

L'expérience de neutrinos solaires Russo-Américaine au Gallium (SAGE) est décrite. Le flux de neutrinos solaires mesuré par les 31 extractions jusqu'en Octobre 1993 est présenté. Le résultat de $69 \pm 10\ ^{+5}_{-7}$ est à comparer à la prédiction du modèle standard du soleil de 132 SNU. L'état de l'irradiation de la source de neutrinos du ^{51}Cr pour tester l'opération globale de l'expérience est aussi présentée.

Résultats récents de l'expérience GALLEX.
C. Tao

La collaboration GALLEX a conduit une expérience avec une source intense de neutrinos. Les points principaux de cette expérience sont rapportés dans cette contribution. Les résultats démontrent que l'expérience GALLEX n'a pas de problème imprévu au niveau de 1.04 ± 0.12 (rapport du nombre d'événements mesurés au nombre attendu) et confirment un déficit de neutrinos solaires dans les expériences au gallium.

Physique découverte au LHC
N. Ellis

Le grand collisionneur d'hadrons (LHC) a été récemment approuvé comme le prochain accélérateur de particules majeur pour le CERN, l'organisation européenne de recherche en physique des particules. Au sein du LHC, deux faisceaux de protons de haute intensité, se rencontreront de sorte que l'énergie disponible au barycentre pourra

produire de nouveaux types de particules à un ordre de magnitude plus élevé que la machine de plus haute énergie existant aujourd'hui, et avec un taux d'interaction supérieur de trois ordres de magnitude. Le LHC sera aussi utilisé pour produire des collisions à ultra-haute énergie entre les paires d'ions de plomb, et ensuite entre électrons et protons. Cet article, présenté en session commune avec les astrophysiciens, décrit brièvement la machine LHC et les détecteurs de particules qui lui seront conjointement utilisés, avant de discuter quelques exemples d'études physiques qui seront réalisées. Nous insistons sur les sujets qui sont reliés à la cosmologie: Recherche de bosons de Higgs, recherche de particules Super-symétriques et violation du CP.

Résultats récents sur le Rayonnement de Fond Cosmologique.

J. Silk

Je passe en revue les détections récentes des anisotropies angulaires dans le rayonnement de fond cosmologique, incluant les résultats aux échelles angulaires intermédiaires et grandes. La reconstruction du spectre de puissance primordial des fluctuations de matière est le but désiré et des progrès ont été réalisés dans ce sens: il y a déjà un recoupement entre les fluctuations du CMB et les sondages profonds de décalages vers le rouge de galaxies, sur des échelles de $\sim 100 - 300 Mpc$. Le modèle générique est le modèle inflationnaire à base de matière sombre froide avec une légère digression (ajout d'un mélange de 20% de matière sombre chaude, introduction d'une constante cosmologique avec $\Omega \approx 0.3$ dans un univers plat, ou même un modèle ouvert inflationnaire), créé pour tenir compte de l'excès de puissance à grande échelle requis par les sondages profonds. Une possibilité plus bizarre est discutée, notamment celle d'un univers ouvert dominé par de la matière sombre baryonique. Un tel modèle conduit à des prédictions uniques et qui seront vérifiables de manière imminente.

Anisotropies du rayonnement de fond cosmologique et Structure à grande échelle de l'Univers.
G. Efstathiou

Je passerai en revue les observations récentes du rayonnement de fond cosmologique et de la structuration à grande échelle des galaxies. Les observations sont compatibles avec les modèles à base de matière sombre froide (CDM) invariants d'échelle, mais ne peuvent pas encore permettre de trancher entre des variantes comme un modèle CDM dominé par le vide ou un univers de densité critique fait d'un mélange de matière sombre chaude et froide. Je discuterai les projets futurs qui pourraient résoudre ces problèmes, en particulier le projet ESA COBRAS/SAMBA visant à cartographier les anisotropies du fond cosmologique, les catalogues de décalages vers le rouge des galaxies qui seront entrepris par l'Observatoire Anglo-Australien ainsi que le sondage digital du ciel SLOAN.

Évolution des galaxies et structuration à partir du Relevé Canada-France de décalages vers le rouge.
O. Le Fèvre et al.

L'échantillon de galaxies du Relevé Canada-France de décalages vers le rouge (CFRS) contient 591 galaxies avec des décalages vers le rouge compris entre $0 \leq z \leq 1.2$. Nous présentons plusieurs résultats: (1) la fonction de luminosité des galaxies bleues évolue avec le temps, avec un accroissement de la luminosité de $\sim$1 mag. à $\mathbf{z}\sim$0.8, ou un changement de la densité de galaxies d'un facteur $\sim$3, alors que pour les galaxies les plus rouges elle est compatible avec aucune évolution; (2) L'imagerie HST d'un échantillon de 32 galaxies du CFRS avec $z > 0.5$ montre que la luminosité des disques est plus élevée que localement, de $\sim$1.2 mag. à $\mathbf{z}\sim$0.7; (3) l'amplitude de la fonction de corrélation à deux points, aux échelles $\sim 1h^{-1}$ Mpc, évolue avec le temps, conduisant à une croissance de l'agrégation des galaxies, $0 \leq \epsilon \leq 2$, plus rapide que pour une évolution des unités liées se faisant avec une taille physique constante.

La fonction de corrélation angulaire des galaxies de champ peu lumineuses.
A. Campos et al.

Afin de tester l'existence de structuration forte à grande échelle dans la distribution des galaxies, nous sommes en train de créer un nouveau catalogue de galaxies à partir d'images CCD. Ce catalogue nous permettra de mesurer la fonction de corrélation angulaire des galaxies sur le même domaine d'échelles que l'APM et environ quatre fois plus en profondeur. Les résultats préliminaires semblent indiquer un aplatissement de la pente de la corrélation aux petites échelles avec la profondeur. Nous détectons aussi un signal à $\sim 1^o$, que nous plaçons comme limite supérieure de la fonction de corrélation à ces échelles jusqu'à ce que de nouvelles données deviennent disponibles.

Comptages morphologiques à partir des images HST ultra-profondes.
S. Driver et R. Windhorst

Nous discutons les observations conduisant au problème des Faibles Galaxies Bleues et les incertitudes auxquelles les modèles de galaxies faibles sont soumis. En utilisant le mode imagerie profonde du Télescope Spatial de Hubble pourvu par la Caméra Planétaire à Grand Champ (WFPC2), nous montrons comment l'information sur la morphologie a été utilisée pour éclairer le problème sous un nouvel angle. Les résultats initiaux indiquent que les galaxies géantes (elliptiques et spirales de type avancé), sont bien approchées par les modèles standards sans évolution jusqu'à des magnitudes $m_I \sim 24.5$ ($z \sim 0.8$). Les données montrent aussi que les faibles galaxies bleues ont une morphologie de type avancé/irrégulière et ne peuvent pas être modélisées de manière satisfaisante tant que de meilleures contraintes n'auront été établies sur la densité spatiale locale de cette catégorie de galaxies.

Évolution du taux de paires de galaxies
L. Infante et al.

Afin d'étudier le taux de fusion avec le décalage spectral, des paires de galaxies faibles (de séparations $\leq 20h^{-1}Mpc$) ont été sélectionnées à partir d'images en bande V obtenues au télescope Canada-France-Hawaii (CFHT) et au télescope de Nouvelle Technologie (NTT) de l'ESO. Nous avons observé des champs près du pôle Nord galactique (NGP) et du pôle Sud galactique (SGP). Dans ce papier nous présentons nos résultats obtenus dans la région NGP. Nous faisons une comparaison statistique entre les paires proches et les galaxies de champ. Les décalages spectraux de 14 galaxies ($V \leq 22.5, < z >= 0.36$) en paires serrées ($0.6sec$) et 38 galaxies de champ ($< z >= 0.42$) ont été utilisées dans l'analyse. Nous trouvons que, (a) la similitude des deux distributions en décalage spectral, $\Delta z \leq 0.1$, limite toute augmentation différentielle de luminosité des paires proches à moins d'une demi magnitude. (b) Les paires sont légèrement plus bleues que les galaxies de champ et ont un taux de détection moyen de [O II] à peu près deux fois supérieur, mais les différences ne sont pas significatives. (c) Les paires physiques comprennent à peu près 7% des galaxies faibles de l'échantillon. La même séparation physique appliquée aux galaxies locales donne seulement 2.6% dans des paires.

Propriétés de regroupement des images Lyα.
S. Cristiani et al.

Les spectres des QSOs PKS2126-158 ($z_{em} = 3.27$) et Q0055-269 ($z_{em} = 3.66$) ont été observés à haute résolution ($2.2 - 2.7 \times 10^4$). Un regroupement significatif, avec $\xi \sim 1$ à $\Delta v = 100 kms^{-1}$, est détecté dans les deux cas pour des raies avec $\log N_{HI} \geq 13.8$.

Un résultat similaire est obtenu à partir de données publiées pour Q0014+81. Un anti-regroupement est aussi détecté sur des échelles $\Delta v \sim 600 kms^{-1}$. Deux vides de taille $\sim 200 kms^{-1}$ sont mis en évidence dans le spectre de Q0055-269 avec une probabilité de 2 x 10^{-4}.

Corrélations de la forêt de Lyman α et comptage par cellules:
F. R. Bouchet et A. Meiksin

Nous présentons une nouvelle technique de calcul des corrélations de la forêt de Lyman fondée sur des comptages par intervalles. Cette technique a été appliquée aux listes de raies de 7 quasars observés à haute résolution ($\Delta v < 25 km/s$). Deux des spectres (ceux de Q0055−259 et Q0014+813) semblent suffisamment exempts de biais pour en tirer des estimations crédibles. Nous avons trouvé dans ces deux cas des corrélation positives, atteignant un maximum de $0.5 - 1$, aux échelles comprises entre 0.5 et $3h^{-1}$ Mpc (comobiles), soit $100 - 600 km/s$. Ces résultats s'accordent bien à ce qu'on peut attendre étant donné le spectre de puissance primordial inféré des catalogues de galaxies sélectionnés en optique. De fortes indications de l'existence d'anti-corrélations aux échelles comprises entre 3 et $6h^{-1}$ Mpc ont aussi été mises en évidence. Si cette première détection d'anti-corrélations est bien physique, d'autres facteurs que la seule gravité pourraient jouer un rôle dans la détermination des propriétés de corrélation de la forêt de Lyman aux échelles comobiles $> 3h^{-1} Mpc$.

Quasars et structures à grande échelle de l'Univers.
V.N. Lukash

La majorité des quasars lointains et brillants ($z \succeq 1$) peut se former dans des fusions massives au sein de groupes compacts et / ou dans des amas jeunes. Les tests attendus sont (i) une corrélation importante pour les QSOs de z intermédiaires ($1 \prec z \prec 2$) et (ii) une recherche directe de groupes de quasars (QGs) indiquant les positions de proto-superamas qui évolueront plus tard en des systèmes tels que le Grand Attracteur ou la concentration de Shapley. Nous discutons les grands QGs avec plus de dix membres à l'intérieur de régions de tailles $\leq l_{LS} \sim 100 - 150 h^{-1} Mpc$, traçant des régions de sur-densités à $z \preceq 2$. Ces grandes structures jeunes (i) donnent une voie nouvelle pour "biaiser" la distribution des amas d'Abell, et (ii) suggèrent que le spectre des perturbations primordiales de densité est presque plat à des échelles englobant à la fois amas et Grands Attracteurs, $l = \pi k^{-1} \in (10, 100) h^{-1} Mpc$: $\Delta_k^2 \sim k^3 P(k) \sim k^\gamma, \gamma = 1^{+0.6}_{-0.4}$

La distribution des quasars.
P. Andreani et al.

Nous avons analysé la distribution spatiale des quasars et sa relation au décalage spectral en utilisant la fonction de corrélation à deux points, la variance des comptages de cellules et la densité conditionnelle en fonction du décalage spectral. La comparaison de nos résultats avec ceux d'autres auteurs nous permet de conclure que les quasars ont une fonction de corrélation avec une amplitude similaire ou supérieure à celle des galaxies, mais son évolution doit encore être établie. Nous discutons comment de nouvelles observations comparées à des résultats de simulations peuvent résoudre la question de l'évolution.

Lentille gravitationnelle du quasar 0957 + 561 et détermination de H_0.
G. Rhee et al.

Nous présentons les résultats d'une étude en imagerie profonde de l'amas provoquant l'effet de lentille sur le quasar double 0957 + 561. En utilisant les données obtenues à KPNO et au CFHT nous avons détecté des distorsions dans la population de galaxies bleues de fond soumise aux effets de lentille. A partir des distorsions de ces petits arcs nous avons construit une carte de la densité de masse dans le champ du double QSO. Nous utilisons cette carte pour contraindre les concentrations de masse responsables des effets de lentille. L'utilisation de ces contraintes en conjonction avec des modèles de masse et la connaissance du décalage en temps entre les images A et B nous permettent de placer des contraintes sur la valeur de la constante de Hubble.

L'environnement des quasars à $z < 0.3$.
B.J. Boyle et al.

A partir d'une analyse de corrélation croisée de QSOs sélectionnés en X avec des galaxies faibles ($B_J < 20.5$), nous trouvons un excès de galaxies à 5σ autour de QSOs à faible décalage spectral ($z < 0.3$) avec une amplitude identique à celle de la fonction de corrélation angulaire des galaxies. La similitude entre le regroupement QSO - galaxie et galaxie - galaxie suggère que les QSOs ne sont pas biaisés comparés aux galaxies, ce qui en fait de très bon traceurs des grandes structures de l'Univers.

De grands groupes de quasars.
M.J. Graham et al.

Nous avons développé une méthode générale utilisant un code en arbre (MST) afin de trouver de grands groupes dans des relevés de quasars et d'évaluer leur signification statistique. Nous avons appliqué notre technique à six relevés dont trois d'entre eux avec des grands groupes de quasars. Nous retrouvons les trois groupes communs et

nous mettons de plus en évidence un nouveau groupe de 10 quasars à $z \sim 0.19$ et un regroupement de sept galaxies de Seyfert à $z \sim 0.19$. Le premier groupe a des dimensions de $\sim$ 120 x90x20$h^{-3}Mpc^3$ et le dernier $\sim$ 60 x 30 x 10$h^{-3}Mpc$. Nous présentons aussi une remise à jour du groupe de quasars de Clowes & Campusano découvert en 1991[3].

La nature de la Matière Noire: plaidoyer pour de la Matière Noire non baryonique.

B. Sadoulet

Nous essayons de résumer les indices que la cosmologie obervationnelle nous fournit sur la nature de la Matière Noire de l'Univers: que pouvons-nous apprendre des estimations actuelles sur la densité moyenne, et que pouvons-nous apprendre de nos comparaisons entre les structures à grande échelle et le bruit de fond cosmologique? Les deux ensembles d'observations indiquent l'existence d'une composante non baryonique.

La Matière Noire peut-elle être totalement baryonique?

J-M. Alimi et A. Serna

Les alternatives les plus naturelles à la Relativité Génerale sont les théories scalaires-tenseurs, qui contiennent le tenseur métrique $g_{\mu\nu}$ et un champ scalaire supplémentaire. Cette classe de théories apparaît actuellement en cosmologie primordiale (inflation), et en physique des particules (théories Kaluza- Klein, super-symétriques, limites basses énergies des super-cordes). Nous avons déduit la production des éléments légers et analysé tous les modèles cosmologiques dans les théories scalaires-tenseurs compatibles avec les expériences de systèmes solaires, les dynamiques de pulsars binaires... Nous avons ensuite réussi pour la première fois à construire une classe de modèles tenseurs scalaires qui prédisent les abondances des éléments légers justes pour permettre la fermeture de l'Univers par les baryons. De telles prédictions ont été obtenues parce que le facteur d'accélération (rapport entre le paramètre de Hubble de la théorie et celui obtenu en Relativité Générale) dans ces classes de théories a une évolution en temps non monotone pendant la nucléosynthèse primordiale. Ces théories ont aussi des conséquences importantes sur l'inflation et la formation des grandes structures.

Recherches de Matière Noire non baryonique: plaidoyer pour des WIMPs.

R. Bernabei

Cet article passe en revue les recherches souterraines de Matière Noire sous forme de particules. La plupart des résultats expérimentaux est passée en revue.

Axions: la Matière Noire et le Problème de violation forte de CP.
L. J. Rosenberg

L'axion, une particule élémentaire hypothétique, a été proposée à l'origine pour résoudre le problème de violation forte de CP en QCD. Plus tard, on s'est rendu compte que les axions seraient un bon candidat pour la Matière Noire. Des recherches nouvelles et très sensibles sont en cours qui permettraient de détecter les axions formant notre halo galactique.

La Recherche de WIMPs: l'expérience cryogénique Matière Noire du CfPA.
D.S. Akerib

Notre groupe, la collaboration CDMS, va bientôt commencer la première phase d'une expérience de recherche de WIMPS, ou particules massives interagissant faiblement, dans le halo galactique en utilisant des détecteurs terrestres. Cette classe typique de particules hypothétiques, dont les propriétés sont similaires à celles prédites par des extensions du modèle standard de la physique des particules, pourrait représenter la composante froide de la matière non baryonique. Je décrirai notre expérience, fondée sur des détecteurs au germanium refroidis dans un cryostat blindé de faible radioactivité.

L'expérience Edelweiss: un état des lieux.
D. Yvon

Nous avons fait fonctionné un bolomètre de 24 g avec un seuil de 1,5 keV en tunnel souterrain dans un environnement sélectionné de faible radioactivité. L'installation expérimentale est rapidement décrite. Une analyse préliminaire, basée sur 125 heures de fonctionnement effectif montre une amélioration d'un facteur 10 sur le taux d'évènements entre 10 et 20 keV d'énergie, par rapport aux mesures précédentes de 1991. Cependant le taux est encore 2 ordres de grandeur plus élevé que dans les meilleurs détecteurs dans cette zone. Nous travaillons à identifier l'origine de ces contaminations radioactives et nous développons de nouveaux détecteurs.

Arcs lumineux géants.
F. Hammer et al.

Les amas de galaxies n'étaient pas considérés comme assez massifs et compacts pour atteindre la densité critique nécessaire pour créer des effets de lentille gravitationnelle, et ce, jusqu'aux début des années 1980. En 1981, une structure filamentaire fut observée dans A370, et identifiée en 1985 à un arc géant lumineux. A cette époque, une

structure identique fut aussi découverte dans Cl2244-02. Les arcs furent rapidement modélisés avec succès, dans le cadre de la théorie des lentilles gravitationnelles; cela impliquait que les arcs lumineux étaient les images extrêmement déformées par l'effet gravitationnel des coeurs d'amas situés en avant-plan. La mesure du décalage spectral de l'arc dans A370 (le double de celui de l'amas), prouva définitivement l'origine gravitationnelle des arcs lumineux. Depuis, de nombreux travaux ont été consacrés aux arcs lumineux, généralement dans le but d'estimer la quantité et la distribution de la matière sombre dans les amas, directement responsable des arcs. Plus de 40 arcs lumineux ont été découverts à ce jour. Dans cette courte revue, sont résumés les principaux résultats obtenus à partir des observations des arcs géants lumineux (définis par $R < 22.5$ et un rapport d'axe $l/w > 10$). Les progrès les plus récents concernent le profil de densité dans les coeurs d'amas et la morphologie détaillée des galaxies distantes sources des arcs, au delà de 1 kpc.

Ondes Gravitationnelles et Cosmologie.
T. Damour

Après une brève présentation de la recherche sur les ondes gravitationnelles, on discute l'impact potentiel des observations d'ondes gravitationnelles en cosmologie.

Relativité d'Echelle et Structuration de l'Univers.
L. Nottale

Quelques conséquences du principe de relativité d'échelle en cosmologie sont considérées dans cette contribution. La forme générale des lois d'échelle linéaires qui satisfont à ce principe est celle du groupe de Lorentz. Ceci permet de résoudre le problème de l'horizon sans faire appel à l'inflation, et implique que la dimension fractale des grandes structures doit varier en fonction de l'échelle, d'une manière qui dépend de la valeur de la constante cosmologique. Cette théorie explique la valeur de $\gamma = 1.8$ de la puissance de la fonction d'auto-corrélation, prédit que γ doit décroître quand l'échelle croit et rend compte de la transition à l'uniformité. Elle permet d'obtenir une mesure de la constante cosmologique en accord avec une estimation indépendante à partir de la densité d'énergie du vide.

Programmes clé cosmologique pour le radiotélescope de Nancay.
W. Van Driel

Il existe deux nouveaux projets radio-astronomiques présentant un intérêt certain pour les études des structures à grande échelle dans l'Univers. L'un deux, le projet FORT, a pour but la remise à niveau du radiotélescope décamétrique de Nancay, le troisième plus grand instrument travaillant dans le domaine décamétrique avec une

surface collectrice effective d'une antenne de 94 m diamètre. En 1998, le télescope possédera un nouveau système focal optimisé, incluant un système de miroir Grégorien. Il sera alors disponible par exemple, pour une relevé sensible à long terme dans la raie 21 cm d'un grand échantillon de galaxies. Un programme clé possible, consistera à observer 5000 à 7000 galaxies afin d'améliorer notre connaissance de la relation Tully-Fisher. Une recherche systématique de galaxies cachées derrière la voie lactée est un autre type de relevé possible. L'autre projet est un réseau d'antennes d'un kilomètre carré (SKAI). Il a pour but de préparer la nouvelle génération de radiotélescope métrique et décamétrique avec une surface collective de un kilomètre carré. Ce réseau devrait être une centaine de fois plus sensible que les plus grands radiotélescopes actuels. Il existe en principe plusieurs options quant à sa réalisation technique, mais la technique des réseaux en phase semble être la plus adaptée pour le moment, il en est de même quant à l'aspect budgétaire. Cet instrument géant devrait de toute évidence révolutionner les études cosmologiques et devrait présenter un intérêt pour une large communauté d'astronomes non encore utilisateurs des données radio, dans la mesure où il permettra par exemple la détection du HI dans des galaxies jusqu'à un décalage spectral de 3 et de mégamasers OH jusqu'à $z \sim 8$.

Le projet COBRAS/SAMBA.
F. R. Bouchet et al.

COBRAS/SAMBA est un satellite de deuxième génération qui doit cartographier les anisotropies du Corps Noir Cosmologique, avec une résolution angulaire et une sensibilité permettant d'en extraire toute l'information cosmologique. Cette mission est en phase d'étude de faisabilité (A) à l'ASE. La décision finale est attendue mi-1996, pour un lancement vers 2003.

Spectrographes de Relevés pour la Cosmologie à l'ESO-VLT.
O. Le Fèvre et P. Vettolani

Des spectrographes multi-objets grand champ, dédiés aux grands sondages pour la cosmologie, sont en cours d'étude pour la seconde génération d'instruments du VLT de l'ESO. Ces spectrographes doivent idéalement couvrir une bande passante 5500–1.8μm, pour un champ $\sim$ 16'×16', avec un gain multiplex supérieur à 500. Des concepts de spectro-imageurs avec une transmission élevée sont étudiés, ainsi que des concepts de spectrographes à suppression OH pour le proche IR. Ces instruments sont indispensables pour que le VLT puisse participer, au premier plan, à la cartographie de l'univers lointain et améliorer substantiellement notre connaissance de l'évolution des grandes structures et des galaxies, vers l'époque de formation des structures et des galaxies. La motivation scientifique principale demande d'assembler de très grands échantillons (> plusieurs fois 10^4) de galaxies L_* , jusqu'à des époques très reculées dans le passé, couvrant l'intervalle de décalages vers le rouge $0.3 \leq z \leq\sim 2.5$ (ou plus).

La signification des orientations des amas de galaxies.
F.W. Baier et al.

La structure de 27 amas de galaxies avec des galaxies centrales dominantes est examinée. Les données de balayage automatique de plaques UK Schmidt obtenues au Royal Observatory Edinburgh sont utilisées pour cet examen.

La signification des orientations des amas de galaxies.
F.W. Baier et H. Wipper

Les orientations des galaxies dominantes centrales et les amas les abritant sont considérées pour 201 amas de galaxies de différents types morphologiques. Nous trouvons qu'il existe de grandes incertitudes sur les orientations des amas principalement à cause de l'influence des sous-structures. En dépit de ces incertitudes, il semble exister une tendance à un alignement général des galaxies dominantes centrales et des amas.

Analyse du relevé IRAS à 1.936 Jy à travers le formalisme d'échelle.
R. Dominguez-Tenreiro et al.

Nous présentons les résultats de l'analyse d'échelle du catalogue de décalages spectraux des galaxies IRAS à 1.936 Jy. Des différences de regroupement entre les galaxies IRAS du Nord et du Sud ont été détectées, ainsi qu'entre des galaxies qui occupent des zones différentes dans le volume limité par le relevé. Ceci implique que ce volume ne peut pas être considéré comme un échantillon typique extrait d'une hypothétique distribution universelle des galaxies. Aucun effet de profondeur n'a été trouvé. De plus, les galaxies IRAS ne présentent pas de ségrégation en luminosité, excepté à petite échelle dans les zones les plus denses de quelques sous-volumes. Enfin, la comparaison des priorités de regroupement des galaxies IRAS ou de celles sélectionnées optiquement, a révélé qu'elles sont différentes à la fois dans les régions de densité faible ou modérée. Ceci implique que les différences ne sont pas dominées par les galaxies qui appartiennent aux coeurs des amas riches, sous représentées dans le catalogue IRAS.

Évolution de marée des galaxies à disque dans les amas riches.
M.A. Gomez-Flechoso et al.

Nous étudions l'évolution des galaxies à disque orbitant dans le potentiel d'un amas riche. Nous utilisons des modèles disque-halo à N-corps, en équilibre pour simuler la galaxie. L'amas est simulé comme un potentiel sphérique rigide semblable à celui suggéré par les observations X. Nous nous concertons sur le devenir de ces modèles de galaxies lorsqu'ils passent près du centre de l'amas, en supposant que le disque est détruit par des chocs de marée et que la masse du halo se redistribue. Les implications

sur la forme des courbes de rotation des galaxies à disque dans les amas d'une part et l'absence des galaxies à disque dans les régions internes d'un amas riche d'autre part sont discutées.

La structure des groupes compacts de galaxies.
M.-L. Montoya et al.

Nous présentons une méthode pour déterminer les profils de densités des groupes de galaxies, basée sur l'étude des fonctions d'auto-corrélation des galaxies. Au moyen de simulations Monte-Carlo, nous montrons que cette méthode est capable de retrouver le profil moyen de tels systèmes, même dans le cas de faibles statistiques (nombre faible de galaxies par groupe). Nous présentons des premiers résultats provenant de l'application de cette méthode au catalogue de Hickson des groupes compacts.

Matière Noire dans les amas de galaxies et masse au repos du neutrino.
A. Kull et al.

Nous considérons une sphère de neutrinos en équilibre thermodynamique de Fermi comme modèle de Matière Noire dans les amas de galaxies. Les profils intégrés de masses de neutrino sont déterminés et ajustés aux observations en rayons X de ROSAT de l'amas COMA, en laissant la masse du neutrino comme paramètre libre. Le meilleur ajustement se produit pour une masse de neutrino de 8 eV.

LIST OF PARTICIPANTS

AKERIB D.	University of California, Berkeley, USA
ALIMI J.M.	Observatoire de Meudon, France
ANDREANI P.	Universita' di Padova, Italy
AUDIT E.	Observatoire de Meudon, France
BALKOWSKI C.	Observatoire de Meudon, France
BAIER F.	Postdam University, Germany
BARDELLI S.	Osservatorio Astronomico, Bologne, Italy
BAUER F.	C.E. Saclay, Gif-sur-Yvette, France
BENOIST C.	Observatoire de Meudon, France
BEREZINSKY V.	Laboratori nazionali del Gran Sasso, Assergi, Italy
BERNABEI R.	Universita' "Tor Vergata", Roma, Italy
BERNARDEAU F.	C.E. Saclay, Gif-sur-Yvette, France
BLANCHARD A.	Observatoire de Strasbourg, France
BÖHRINGER H.	Max Planck Institut für Extraterrestriche Physik, Garching, Germany
BORGANI S.	INFN, Sezione di Perugia, Italy
BOUCHET F.	IAP, France
BRANCHINI E.	SISSA/ISAS, Trieste, Italy
BROADHURST T.	Johns Hopkins University, Baltimore Maryland, USA
BOYLE B.	Royal Greenwich Observatory, Cambridge, USA
CAMPOS A.	Instìtuto de Astrofisica de Andalucia, Granada, Spain
CAPPI A.	Osservatorio Astronomico, Bologne, Italy
CHRISTENSEN L.	Copenhagen University Observatory, Denmark
COLAFRANCESCO S.	Osservatorio Astronomico, Roma, Italy
COUTURES C.	C.E. Saclay, Gif-sur-Yvette, France
CRISTIANI S.	Universita' di Padova, Italy
DA COSTA L.	IAP, France
DALTON G.	University of Oxford, UK
DAMOUR T.	I.H.E.S., Bures-sur-Yvette, France
DAW E.	MIT, Cambridge, USA
DEKEL A.	Racah Institute of Physics, Jérusalem, Israël
DE THEIJE P.	Leiden Observatory, The Netherlands
DELABROUILLE N.	C.E. Saclay, Gif-sur-Yvette, France
DELABROUILLE J.	IAS, Orsay, France
DOMINGUEZ-TENREIRO R.	Universidad Autonoma de Madrid, Spain
DOROSHKEVICH A.	Theoretical Astrophysics Center, Copenhagen, Denmark
DRIVER S.	Arizona State University, Tempe, USA
EFSTATHIOU G.	University of Oxford, UK
ELLIS R.	Institute of Astronomy, Cambridge, UK
FAIRALL T.	University of Cape Town, Rondebosch, South Africa
FETISOVA T.	Astro Space Center, Lebedev Institute, Moscow, Russia
GAUCHEREL C.	C.E. Saclay, Gif-sur-Yvette, France
GLICENSTEIN J.F.	C.E. Saclay, Gif-sur-Yvette, France
GOLDMAN B.	C.E. Saclay, Gif-sur-Yvette, France
GRAHAM M.	University of Central Lancashire, Preston,UK
GROS M.	C.E. Saclay, Gif-sur-Yvette, France
HAMILTON A.	University of Oxford, UK
HAMMER F.	Observatoire de Meudon, France
HARDIN D.	C.E. Saclay, Gif-sur-Yvette, France
HUDSON M.	University of Durham, UK
INFANTE L.	Pontificia Universitad Catolica, Santiago, Chili
IVANOV P.	Astro Space Center, P.N. Lebedev Institute, Moscow, Russia
JAIN B.	Max Planck Institut für Astrophysik, Garching, Germany
JUSZKIEWICZ R.	Copernicus Astronomical Center, Warsaw, Poland
KOLATT T.	Centre for Astrophysics, Cambridge, USA
KRAAN-KORTEWEG R.	Observatoire de Meudon, France
KULL A.	Max Planck Institut für Extraterrestriche Physik, Garching, Germany
LE FEVRE O.	Observatoire de Meudon, France
LIANG H.	C.E. Saclay, Gif-sur-Yvette, France

LIN H.	Centre for Astrophysics, Cambridge, USA
LOVEDAY J.	FERMILAB, Batavia, USA
LUKASH V.	Astro Space Center, Moscow, Russia
MAGNEVILLE C.	C.E. Saclay, Gif-sur-Yvette, France
MAOLI R.	Observatoire de Paris, France
MARTIN J.M.	Observatoire de Meudon, France
MASEGOSA P.	Instituto de Astrofisica de Andalucia, Granada, Spain
MAZURE A.	LAS, Marseille, France
MONIEZ M.	LAL, Orsay, France
MAUROGORDATO S.	Observatoire de Meudon, France
MOSCARDINI L.	Universita' di Padova, Italy
MÜLLER V.	Astrophysical Institute Postdam, Germany
NEUMANN D.	Max Planck Institut für extraterrestriche Physik, Garching, Germany
NOTTALE L.	Observatoire de Meudon, France
NUSSER A.	Institute of Astronomy, Cambridge, UK
OUKBIR J.	C.E. Saclay, Gif-sur-Yvette, France
PILKUHN H.	Universität Karlsruhe, Germany
PLIONIS M.	SISSA, Trieste, Italy
PONS-BORDERIA J.	Universitat de Valencia, Spain
POPESCU C.	Max Planck Institut für Astronomie, Heidelberg, Germany
POSTMAN M.	Space Telescope Science Institute, Baltimore Maryland, USA
PRIMACK J.	University of California, Santa Cruz, USA
RHEE G.	Department of Physics, Las Vegas, USA
ROSENBERG L.	MIT, Cambridge, USA
SAAR V.	Toravere Observatory, Tartu, Estonia
SADOULET B.	University of California, Berkeley, USA
SCARAMELLA R.	Osservatorio di Roma, Monteporzio Catone, Italy
SERNA A.	Observatoire de Meudon, France
SHANDARIN S.	University of Kansas, Lawrence, USA
SILK J.	University of California, Berkeley, USA
SLINGLEND K.	University of Maine, Orono, USA
STEINBERGER J.	CERN, Geneva, Switzerland
TADROS H.	University of Oxford, UK
TAO C.	LPC College de France, Paris, France
TEGMARK M.	Max Planck Institut für Physik/Astrophysik, München, Germany
THEUREAU G.	Observatoire de Meudon, France
TEYSSIER R.	CEA, Bruyères-le-Châtel, France
TORMEN G.	IAP, France
TUCKER D.	Astrophysikalisches Institut Potsdam, Germany
VAN DRIEL W.	Observatoire de Meudon, France
VOGELEY M.	Johns Hopkins University, Baltimore Maryland, USA
WALL J.	Royal Greewich Observatory, Cambridge, UK
YAHIL A.	SUNY, Stony Brook, USA
YEPES G.	Universidad Autonoma, Madrid, Spain
ZAROUBI S.	University of California, Berkeley, USA
ZUCCA E.	Istituto di Radioastronomia, Bologna, Italy
ZUREK W.	Theoretical Astrophysics Center, Los Alamos, USA